

# Photophysics and Spin Chemistry of Triptycene Bridge Donor-Acceptor-Triads



Dissertation zur Erlangung des naturwissenschaftlichen Doktorgrades  
an der Fakultät für Chemie und Pharmazie  
der Julius-Maximilians-Universität Würzburg

vorgelegt von  
**Chantal Roger**

aus **Kaufbeuren**

Würzburg, 2024





Eingereicht bei der Fakultät für Chemie und Pharmazie am:

16.04.2024

Gutachter der Dissertation:

1. Gutachter: Prof. Dr. Christoph Lambert

2. Gutachter: Prof. Dr. Frank Würthner

Prüfer des öffentlichen Promotionskolloquiums:

1. Prüfer: Prof. Dr. Christoph Lambert

2. Prüfer: Prof. Dr. Frank Würthner

3. Prüfer: Prof. Dr. Tobias Hertel

Tag des öffentlichen Promotionskolloquiums:

10.06.2024

Doktorurkunde ausgehändigt am:

\_\_\_\_\_



Diese Arbeit wurde in der Zeit von Oktober 2019 bis April 2024 am Institut für Organische Chemie der Universität Würzburg angefertigt.

Mein besonderer Dank gilt

**Prof. Dr. Christoph Lambert**

Für die Vergabe des interessanten und vielseitigen Themas sowie die unzähligen Diskussionen sowie Hilfestellungen.



**Parts of this thesis have previously been published in:**

*The influence of hindered rotation on electron transfer and exchange interaction in triarylamine-triptycene-perylene diimide triads*, C. Roger, A. Schmiedel, M. Holzapfel, N. N. Lukzen, U. E. Steiner and C. Lambert, *Phys. Chem. Chem. Phys.* **2024**.

*Synthese und Charakterisierung einer neuartigen Donor-Akzeptor-Dyade zur Untersuchung von magnetfeldabhängigen Effekten*, C. Roger, Master-Thesis, Julius-Maximilians-Universität (Würzburg), **2019**.

(Bachelor thesis supervised by M. Sc. Chantal Roger and Prof. Dr. Christoph Lambert):

*Synthese und Charakterisierung einer Donor-Akzeptor-Dyade mit chloresubstituierter Triptycenen-Brücke zur Untersuchung photoinduzierter magnetfeldabhängiger Effekte*, F. Fella, Bachelor-Thesis, Julius-Maximilians-Universität (Würzburg), **2021**.



# Contents

<b>1</b>	<b>Introduction</b>	<b>1</b>
<b>1.1</b>	<b>Spin chemistry of radical pairs</b>	<b>2</b>
1.1.1	Radical pair mechanism	2
1.1.2	Coherent and incoherent spin flip mechanisms	4
1.1.2.1	Coherent spin evolution	4
1.1.2.2	Incoherent spin relaxation	7
1.1.3	Classical and semiclassical description of the MFE	9
1.1.4	Level crossing mechanism	13
1.1.5	Molecules with a non-zero exchange interaction determined by magnetic field dependent transient absorption spectroscopy measurements	16
<b>1.2</b>	<b>Triptycene as a bridging unit</b>	<b>21</b>
<b>2</b>	<b>Scope of the work</b>	<b>25</b>
<b>3</b>	<b>Synthesis</b>	<b>29</b>
<b>3.1</b>	<b>Synthesis of the triarylamine donor units</b>	<b>29</b>
<b>3.2</b>	<b>Synthesis of the perylene diimide acceptor units</b>	<b>31</b>
<b>3.3</b>	<b>Synthesis of the bridging units</b>	<b>33</b>
<b>3.4</b>	<b>Synthesis of the triads</b>	<b>37</b>
3.4.1	Rotationally hindered triads	37
3.4.2	Substituted triptycene triads	39
3.4.3	Anthracene bridge triads	41
<b>3.5</b>	<b>Synthesis of the reference compounds</b>	<b>44</b>
<b>4</b>	<b>Steady-state absorption and emission spectroscopy</b>	<b>46</b>
<b>4.1</b>	<b>Steady-state absorption spectroscopy</b>	<b>46</b>
<b>4.2</b>	<b>Steady-state emission spectroscopy</b>	<b>50</b>
<b>5</b>	<b>Cyclic voltammetry</b>	<b>53</b>

<b>6</b>	<b>Rotationally hindered triads.....</b>	<b>57</b>
<b>6.1</b>	<b>Electron transfer processes.....</b>	<b>59</b>
6.1.1	State energies .....	59
6.1.2	Charge separation .....	63
6.1.2.1	fs-Pump probe spectroscopy .....	63
6.1.2.2	Global target analysis .....	73
6.1.3	Charge recombination.....	79
6.1.3.1	Charge recombination at zero external magnetic field .....	79
6.1.3.2	Magnetic field effect.....	86
6.1.4	Quantum mechanical consideration .....	96
6.1.5	Calculation of the electronic couplings $V$ .....	98
<b>6.2</b>	<b>Discussion .....</b>	<b>104</b>
<b>7</b>	<b>Substituted triptycene triads .....</b>	<b>111</b>
<b>7.1</b>	<b>Electron transfer processes.....</b>	<b>112</b>
7.1.1	State energies .....	112
7.1.2	Charge separation .....	114
7.1.2.1	fs-Pump probe spectroscopy .....	114
7.1.2.2	Global target analysis .....	121
7.1.3	Charge recombination.....	125
7.1.3.1	Charge recombination at zero external magnetic field .....	125
7.1.3.2	Magnetic field effect.....	129
7.1.4	Quantum mechanical consideration .....	134
7.1.5	Calculation of the electronic coupling $V$ .....	136
<b>7.2</b>	<b>Discussion .....</b>	<b>141</b>
<b>8</b>	<b>Anthracene bridge triads.....</b>	<b>145</b>
<b>8.1</b>	<b>Electron transfer processes.....</b>	<b>146</b>
8.1.1	State energies .....	146
8.1.2	Charge separation .....	148
8.1.2.1	fs-Pump probe spectroscopy .....	148
8.1.2.2	Global target analysis .....	151
8.1.3	Charge recombination.....	152
8.1.3.1	Charge recombination at zero field .....	152



8.1.3.2	Magnetic field effect.....	155
<b>8.2</b>	<b>Discussion .....</b>	<b>158</b>
<b>9</b>	<b>Summary.....</b>	<b>161</b>
<b>9.1</b>	<b>Summary .....</b>	<b>161</b>
<b>9.2</b>	<b>Zusammenfassung .....</b>	<b>163</b>
<b>10</b>	<b>Experimental section.....</b>	<b>166</b>
<b>10.1</b>	<b>Charge separated state energies.....</b>	<b>166</b>
<b>10.2</b>	<b>Classical simulations .....</b>	<b>168</b>
<b>10.3</b>	<b>Analytical methods.....</b>	<b>173</b>
10.3.1	Steady-state absorption spectroscopy .....	173
10.3.2	Steady-state emission spectroscopy .....	173
10.3.3	Cyclic voltammetry (CV) .....	173
10.3.4	Pump-probe spectroscopy .....	174
10.3.4.1	fs-Pump-probe spectroscopy .....	174
10.3.4.2	ns-Pump-Probe Spectroscopy .....	175
10.3.5	NMR spectroscopy .....	179
10.3.6	Mass spectrometry .....	179
10.3.7	Gel permeation chromatography (GPC).....	179
<b>10.4</b>	<b>Synthesis.....</b>	<b>180</b>
10.4.1	General procedures .....	180
10.4.1.1	General procedure for the synthesis of the triptycene bridging units (GP I).....	180
10.4.1.2	General procedure for the <i>Suzuki-Miaura</i> borylation (GP II).....	180
10.4.1.3	General procedure for the <i>Suzuki-Coupling</i> reaction (GP III) .....	181
10.4.2	Synthesis of the TAA units.....	181
10.4.3	Synthesis of the PDI units.....	183
10.4.4	Synthesis of the bridging units .....	185
10.4.5	Synthesis of the triads.....	199
10.4.5.1	Rotational hindered triads .....	199
10.4.5.2	Substituted triptycene Triads .....	205
10.4.5.3	Anthracene bridge triads.....	214
10.4.6	Synthesis of the references .....	218

<b>11 Table of formulas .....</b>	<b>226</b>
<b>12 Literature .....</b>	<b>235</b>
<b>13 Appendix.....</b>	<b>242</b>
<b>13.1 Conference distributions and distributions to other publications .....</b>	<b>274</b>
<b>13.2 Danksagung .....</b>	<b>275</b>

## Abbreviations

A	acceptor
ahf	anisotropic hyperfine coupling
Bpin <sub>2</sub>	Bis-(pinacolato)diboron
ATC	anthracene
BHJ	bulk heterojunction
CIDNP	chemically induced dynamic electron polarisation
CR	charge recombination
CR <sub>s</sub>	charge recombination via singlet pathway
CR <sub>T</sub>	charge recombination via triplet pathway
CS	charge separation
<sup>(1,3)</sup> CSS	(singlet, triplet) charge separated state
CT	charge transfer
D	donor
DCM	dichloromethane
esdi	electron spin dipolar interaction
dppf	1,1'-Bis(diphenylphosphino)ferrocen
EA	ethyl acetate
EADS	evolution associated difference spectrum
ESA	excited state absorption
ET	electron transfer
GP	general procedure
GPC	gel permeation chromatography
GSB	ground state bleaching
gta	<i>g</i> -tensor anisotropy
hfc	hyperfine coupling
HOMO	highest occupied molecular orbital
IRF	instrument response function
LFE	low field effect
LUMO	lowest unoccupied molecular orbital
MARY	magnetic field affected reaction yield
MFE	magnetic field effect
MTHF	2-methyltetrahydrofuran
OSC	organic solar cell
PDI	perylene diimide
PE	hexanes

PTCDA	perylene tetracarboxylic dianhydride
RP	radical pair
rt	room temperature
SADS	species associated difference spectra
SCRP	spin correlated radical pair
SE	stimulated emission
SEC	spectro electrochemistry
SOC	spin orbit coupling
sri	spin rotational interaction
TAA	triarylamine
TBAHFP	tetrabutylammonium hexafluorophosphate
TTC	tritycene
QY	quantum yield
ZQT	zero quantum transition





# 1 Introduction

In nature, a variety of phenomena are based on light-driven electron transfer processes (ET), such as the ability of plants to photosynthesise and the ability of migratory birds to orient in the earth magnetic field.<sup>[1-10]</sup> Photosynthesis generates chemical energy from sunlight, with the fundamental step being the electron transfer process within molecular energy converting proteins called reaction centres.<sup>[2, 11-17]</sup> Many animals use the earth's magnetic field to orient themselves, a process that has also been attributed to an ET process.<sup>[3, 18-26]</sup> The influence of an external magnetic field on chemical reactions has been a matter of debate for many decades. Compared to the thermal energy  $k_B T$  at room temperature, which amounts to  $2.5 \text{ kJ mol}^{-1}$  and which exceeds the influence of an external magnetic field on an electron ( $1 \text{ T} \approx 11 \text{ J mol}^{-1}$ ) by several orders of magnitude, the influence of the average earth magnetic field of only  $50 \text{ } \mu\text{T}$  strength seems negligibly small. Thus, how migrating birds orient in the weak magnetic field of the earth seems difficult to explain. The explanation can be found in the so-called radical pair mechanism (RPM). This is a light-driven ET process in which an electron is transferred from an electron donor (D) to an electron acceptor (A) forming a so-called spin correlated radical pair (SCRPs). The spin motions of these SCRPs can in turn be influenced by an external magnetic field.<sup>[1, 27-32]</sup> It has been observed that vertebrates, invertebrates and birds such as the European robin (*Erithacus rubecula*) only sense the influence of the geomagnetic field in the presence of light, suggesting an active RPM. The mechanism is assumed to be connected to cryptochrome flavoproteins in the retinas of these magneto sensitive animals.<sup>[18, 21, 33-41]</sup> In nature, the molecules involved in this light activated RPM are complex, which makes the understanding of the underlying electron motions very difficult. To analyse such processes, it is helpful to reduce the complexity by investigating the involved ET processes in smaller model structures. In this way, *Timmel* et al. proved that magnetic fields of comparable strengths to the magnetic field of the earth indeed influence the photophysical and photochemical properties of radical pairs (RP).<sup>[3, 42-46]</sup> In the past decades a multitude of model systems was synthesised and investigated to deepen the understanding of the charge separation (CS) and charge recombination (CR) dynamics of RPs in an external magnetic field.<sup>[47-49]</sup> A better insight into these SCRPs dynamics can open the door to new technologies, such as quantum computers<sup>[50-52]</sup>, and to the possibility of controlling and optimising the performances of new materials.<sup>[53-66]</sup>

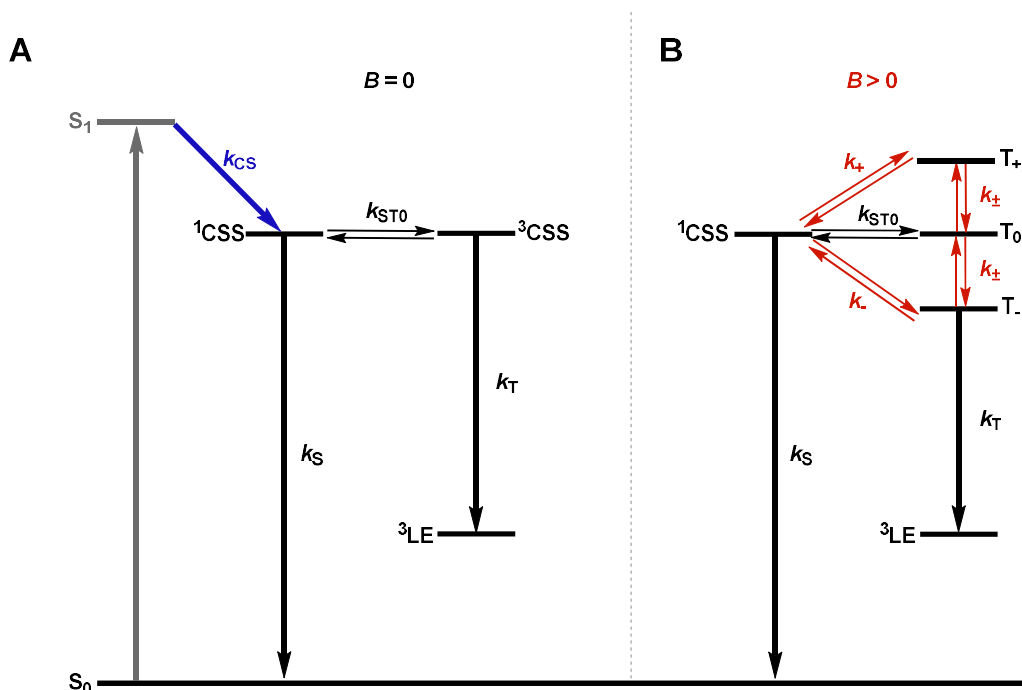
The aim of this work is to investigate small DA model systems to gain further insight into these light-driven ET processes of SCRPs. A short overview of the underlying spin chemistry of radical pairs will be given in this chapter. In **section 2** a short overview of the current state of research will be given and in **sections 6 to 8** the results of this work will be discussed in detail.

## 1.1 Spin chemistry of radical pairs

### 1.1.1 Radical pair mechanism

A radical pair (RP) can occupy four different spin states, the singlet state (S) and one of the three degenerate triplet states ( $T_0$ ,  $T_+$ ,  $T_-$ ). The singlet state exhibits an overall spin of 0 while the three triplet states exhibit a spin of 1. Due to the spin conservation rules, the formed SCRPs always presents the spin multiplicity of its precursor state. Since purely organic molecules generally are excited into their  $S_1$  state, the creation of the RP leads to a singlet charge separated state ( $^1\text{CSS}$ ) in the first place. This  $^1\text{CSS}$  is not a stationary eigenstate but can undergo spin interconversion to form a triplet charge separated state ( $^3\text{CSS}$ ).<sup>[1, 30-31, 67]</sup> Due to spin conservation rules, charge recombination (CR) of  $^1,^3\text{CSS}$  only leads to recombination products of the same spin multiplicity. The  $^1\text{CSS}$  can always recombine in the  $S_0$  state with the rate constant  $k_s$ . CR from the  $^3\text{CSS}$  ( $k_T$ ) can only occur if a triplet state with lower energy ( $^3\text{LE}$ ) is accessible. Thus, the spin evolution directly influences the product ratios and consequently the decay times of the CSS due to the different rate constants.<sup>[1, 31-32, 68-69]</sup> This mechanism was first discussed by *Brocklehurst*, later on extended by *Hayashi* and *Nagakura* and is schematically described in **Figure 1 (A)**.<sup>[67-68]</sup>





**Figure 1:** Schematic description of the radical pair mechanism. **A: ( $B = 0$ ):** after light excitation (grey arrow) an electron is transferred from a donor to an acceptor (CS) and forms a <sup>1</sup>CSS ( $k_{CS}$ , blue arrow). At zero field the radical pair undergoes fast spin interconversion to the <sup>3</sup>CSS ( $k_{ST0}$ ). Due to spin conservation rules the singlet state can only recombine to the S<sub>0</sub> while the triplet state may only recombine to the local excited triplet state (<sup>3</sup>LE). **B: ( $B > 0$ ):** If an external magnetic field is applied the triplet states split up. Since the T<sub>0</sub> state is not affected by an external magnetic field, the conversion rate between <sup>1</sup>CSS and <sup>3</sup>CSS ( $k_{ST0}$ ) stays constant. The outer Zeeman levels otherwise are affected by an external field and therefore the spin evolution is slowed down. The corresponding rate constants are depicted in red.

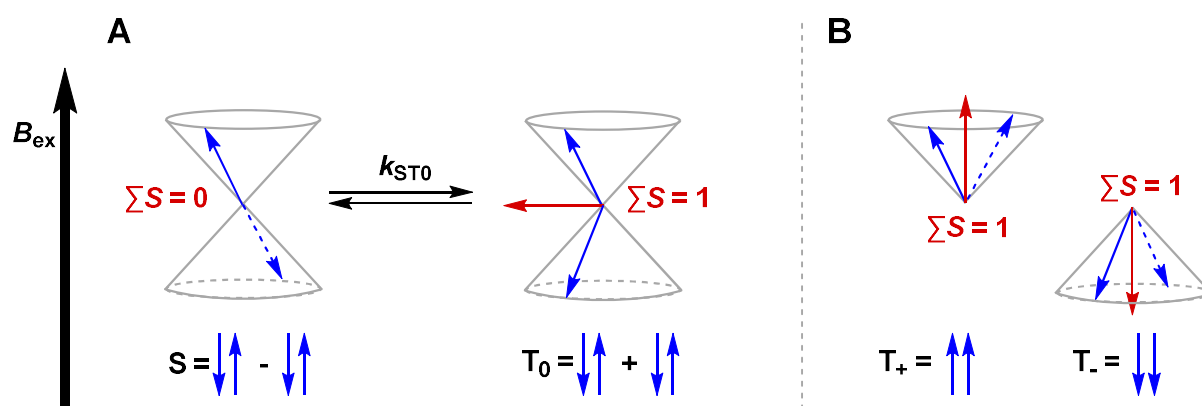
In **Figure 1 (A)** the singlet and triplet levels are degenerate and consequently the spin interconversion is coherent. To distinguish the three triplet substates, an external magnetic field is applied (**Figure 1 B**). The energies of the <sup>1</sup>CSS and the T<sub>0</sub> state are independent of an external magnetic field. Thus, the zero-quantum transition (ZQT) stays coherent. The energies of the triplet levels T<sub>+</sub> and T<sub>-</sub>, however, are split by an external magnetic field (Zeeman splitting), which increasingly inhibits the single quantum transition (SQT) from <sup>1</sup>CSS to T<sub>+</sub> / T<sub>-</sub>. At high external magnetic fields T<sub>+</sub> / T<sub>-</sub> become energetically isolated. Due to the different spin ratios, which change from <sup>1</sup>CSS/<sup>3</sup>CSS 1 : 3 in the zero field case to 1 : 1 in the high field case, a CR product mix is usually produced whose ratios depend on the external magnetic field.<sup>[1, 29, 31, 67, 70-71]</sup> For a better understanding of the spin motions between the <sup>1</sup>CSS and <sup>3</sup>CSS the coherent and incoherent spin flip mechanisms have to be considered.

### 1.1.2 Coherent and incoherent spin flip mechanisms

In the following sections, the physical background of the spin interconversion between the  $^1\text{CSS}$  and the  $^3\text{CSS}$  will be described. First, the case with degenerate singlet and  $T_0$  states will be discussed. The initial spin state of the radical pairs is not stationary and the transitions between the singlet and the triplet state are induced by coherent (elucidated in **section 1.1.2.1**) and incoherent (elucidated in **section 1.1.2.2**) mechanisms, which are influenced by an external magnetic field.

#### 1.1.2.1 Coherent spin evolution

A simple way to describe the spin motion is by using a vector representation of angular momentum, in which electrons and nuclei are decoupled in a strong external magnetic field and precess in cones around the magnetic field direction (**Figure 2**). The spins orientate upwards ( $\alpha$ -spin) and downwards ( $\beta$ -spin) with respect to the external magnetic field direction. The phase relation distinguishing singlet state ( $S$ ) and  $T_0$  does not operate between the spins of single electrons but between the spin function products  $\alpha_1\beta_2$  and  $\alpha_2\beta_1$ . The overall spin of the singlet state is zero whereas it is one for the three triplet states ( $T_0$ ,  $T_+$ ,  $T_-$ ). The  $T$  states can be orientated parallel ( $T_+$ ), antiparallel ( $T_-$ ) or perpendicular ( $T_0$ ) to the axis of quantization. Due to the perpendicular orientation of the overall spin of  $T_0$  relative to the external field, the  $T_0$  state is not influenced by that field in contrast to the  $T_+$  and  $T_-$  states.<sup>[30-31, 67]</sup>



**Figure 2:** **A:** Vector representation in high external magnetic fields wherein spin vectors are depicted in blue and the overall magnetisation in red. Parallel/ antiparallel alignment of the spins ( $S/T_0$ ) with respect to the external magnetic field. **B:** The spins within  $T_+/T_-$  states as well as the overall magnetisation orientate parallel/antiparallel to the external magnetic field direction.

The electronic spin motion is mainly caused by isotropic hyperfine coupling (ihfc) of the radical with the surrounding nuclei. This was described using a semiclassical approximation by *Schulten*<sup>[72]</sup> et al. in which the precession frequencies (*Larmor* frequencies) of the two radicals are given by **equation (1)**.

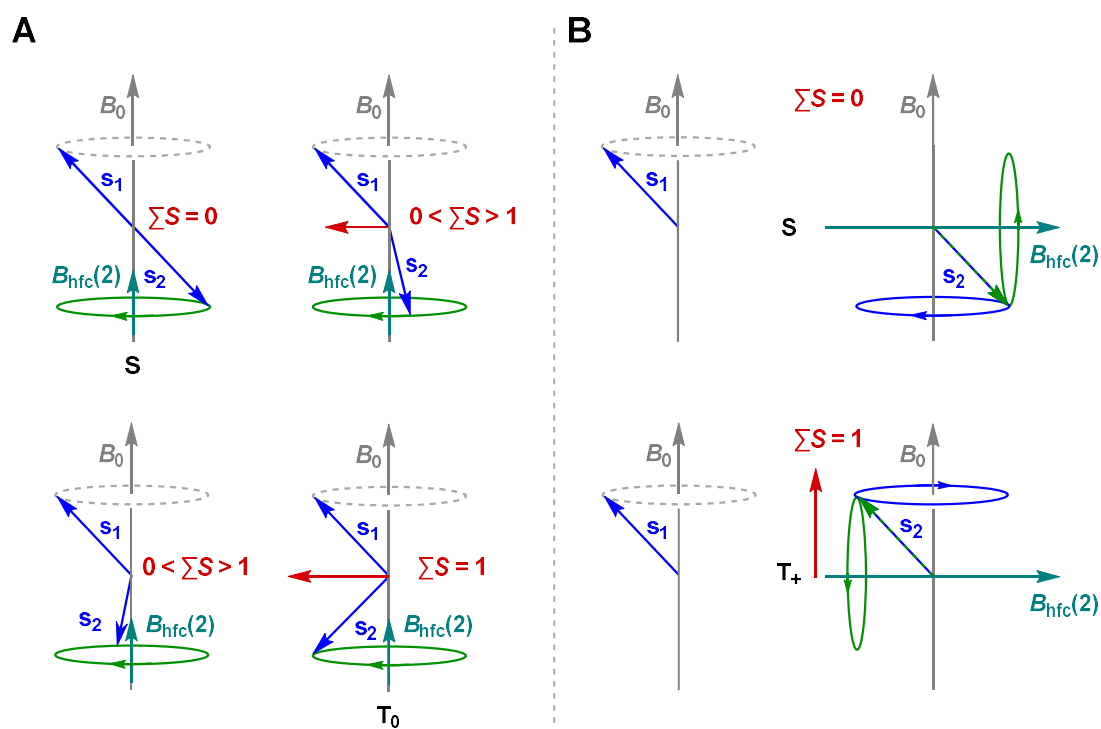
$$\omega_0(i) = \frac{g \mu_B B(i)}{\hbar} \quad (1)$$

Here,  $\mu_B$  is the *Bohr* magneton and  $g$  the isotropic  $g$ -value of the respective radical. In this semiclassical approximation, the active field  $B(i)$  of the respective radical centres is a vector sum of the external magnetic field  $B_0$  and the respective hyperfine field  $B_{\text{hfc}}(i)$  (**equation (2)**).  $B_{\text{hfc}}(i)$  is described by the ihfc constants  $a_k$  and the spin quantum numbers  $I_k$  of the respective involved nuclei  $k$  (**equation (3)**).<sup>[30-31, 73-75]</sup>

$$B(i) = B_0 + B_{\text{hfc}}(i) \quad (2)$$

$$B_{\text{hfc}}(i) = \sqrt{\sum_k a_k^2 I_k(I_k - 1)} \quad (3)$$

This hfc field changes if the two radicals are surrounded by different nuclei. The difference of the hfc fields causes a change of the relative orientation of the two spins over time due to the change in the sum, which causes an ongoing oscillation between S and T<sub>0</sub>. The alignment of the overall spin changes between parallel and antiparallel causing mixed spin states during the transition. The transition takes place even at zero field and is depicted in **Figure 3 (A)** regarding its corresponding spins ( $s_1, s_2$ ).<sup>[30-31, 72-73, 75-76]</sup>



**Figure 3:** **A:** Transition between S and  $T_0$  state through mixed states over time (rotating clockwise beginning with  $S = 0$ ). **B:** Transition between S and  $T_+$  in a weak external field due to rotation around different fields ( $B_0$  and  $B_{hfc}(2)$ ).  $s_1$  appears stationary because the figures are drawn in a reference frame rotating in phase with the precessions of  $s_1$  around  $B_0$ , thus only  $s_2$  experiences a nuclear precession caused by the magnetic field  $B_{hfc}(2)$ .

By increasing the external magnetic field, the precession frequencies of the radical electron spins are still different due to the  $B_{hfc}(i)$  component, though the  $B_0$  component increasingly determines the overall field  $B(i)$ , which retains the transition  $S \leftrightarrow T_0$  at very high fields. When the field  $B(i)$  is determined by  $B_0$ , the spin-flip transitions between S or  $T_0$  and  $T_+$  or  $T_-$  are suppressed because the directions of the precession axes of the two spins coincide. The transition between S/ $T_0$  and  $T_{\pm}$  as well as the corresponding spins ( $s_1$ ,  $s_2$ ) are depicted in **Figure 3 (B)**. It should be noted that the description using only two vectors is not an adequate representation of the spin motion between S and  $T_0$  because their spin functions correspond to a superposition of S and  $T_0$ . Thus, these pure spin states would require an extended model using four vectors<sup>[77-78]</sup> to give a more consistent representation. Nevertheless, two instead of four vectors simplifies the mechanism to give a comprehensible picture. This spin interconversion mechanism is called the hfc-mechanism due to its dependency on the hyperfine field  $B_{hfc}$ . In molecules with negligible or very small spin-orbit coupling (SOC), the hfc-mechanism dominates the spin evolution at zero or very small magnetic fields because the triplet states are degenerate and spin interconversion between S and all T states is possible.<sup>[30-31, 67, 71, 75]</sup>

In RPs with long decay times a so-called low field effect (LFE) can be observed, which is due to splitting of the triplet levels in a non-zero but very low external magnetic field, such that the

*Zeeman* splitting is smaller than the effective hyperfine coupling. The degeneracy at zero magnetic field is repealed, such that the outer T levels are accessible for spin evolution. Thus, the LFE causes an increase of the spin interconversion rate.<sup>[30, 46, 67, 71, 75, 79-81]</sup>

In organic molecules with heavy atoms attached, the SOC increases and if the difference of the respective *g*-values of the two radicals reaches a value of about 0.001 another spin interconversion mechanism is enabled. This coherent spin evolution mechanism is called the  $\Delta g$ -mechanism (see **equation (1)**).<sup>[31, 75]</sup> This  $\Delta g$ -mechanism is unlikely to play a significant role in the triads investigated in this thesis because in similar triads with the same donor and acceptor a  $\Delta g$  value of 0.0002 was found.<sup>[48]</sup>

The increase of the external field leads to an increase of the *Zeeman* splitting. At very high external magnetic fields the outer *Zeeman* levels are no longer accessible via the hfc-mechanism. However, at high fields the outer *Zeeman* levels are still accessible via incoherent spin relaxation.<sup>[71, 75, 82]</sup>

### 1.1.2.2 Incoherent spin relaxation

In the high field case in which the outer *Zeeman* levels are split, the incoherent path of spin evolution is open. The incoherent spin relaxation is primarily caused by spin-lattice (relaxation time  $T_1$ ) and spin-spin relaxations (relaxation time  $T_2$ ). The spin-spin relaxation changes the phase relations between the spins of the electron and therefore interconverts S and  $T_0$ . The spin-lattice relaxation changes the orientation of the spins causing an interconversion between the outer and inner *Zeeman* levels. At zero field  $T_1$  and  $T_2$  are indistinguishable, but in an external field they differ causing a MFE. The spin-lattice relaxation can further be divided in four relaxation mechanisms. Those are the spin rotational interaction (sri), the electron spin dipolar interaction (esdi), the anisotropic hyperfine coupling (ahfc) and the *g*-tensor anisotropy (gta). Those relaxation mechanisms can contribute significantly to the overall spin evolution at higher fields and all four mechanisms are caused by the stochastic modulation of the electron spin *Hamiltonian* due to translational and rotational *Brownian* motions of the radicals.<sup>[1, 30-31, 71, 75, 82-85]</sup>

For a better understanding of the individual relaxation processes, these are presented in detail. All four incoherent mechanisms depend on the rotational correlation time  $\tau_c$ , which describes the mean rotational time of a molecule in solution.  $\tau_c$  is given by the *Debye*-equation (**equation (4)**) and is on the order of nanoseconds.

$$\tau_c = \frac{4\pi R^3}{3k_B T} \eta \quad (4)$$

Here,  $k_B$  is the *Boltzmann* constant,  $R$  is the hydrodynamic radius and  $\eta$  the solvent viscosity.<sup>[31, 75, 82-85]</sup>

The first mechanism is the sri mechanism, which is related to the longitudinal and transversal relaxation times  $T_1$  and  $T_2$  of a radical.<sup>[86-87]</sup> The relaxation of one radical of the radical pair can be described by

$$k_{r,sri} \sim \frac{1}{T_{1,sri}} \sim \frac{1}{T_{2,sri}} \sim \overline{\delta g^2} \frac{1}{\tau_C} \quad (5)$$

in which  $\delta g$  is given as

$$\overline{\delta g^2} = \sum_{i=x,y,z} (g_{ii} - g_e)^2 \quad (6)$$

Thus, the sri mechanism depends on the deviation  $\delta g$  of the  $g$ -value of the free electron  $g_e$ .<sup>[84]</sup> This mechanism depends on the anisotropy of the  $g$ -tensors, which can be modulated through heavy atoms but is not influenced by an external magnetic field.<sup>[50, 75, 83-85]</sup>

The other three mechanisms (gta, esdi, ahf) are all dependent on the *Larmor* frequency (**equation (1)**) which is changed by an external field.

Another incoherent field dependent mechanism is the esdi mechanism, which is strongly dependent on the distance between the two radicals and describes the spin relaxation due to the interaction of two separate electron spins. Thus, the stochastic modulation of translational diffusion of two radicals is the basis for the modulation of the electron spin dipolar interaction of flexible bound radicals, which have translational freedom, such as free radicals in a micelle. An estimation of  $k_{r,esdi}$  can be made if two radical centers are rigidly linked and exhibit a large D-A-distance, thus it only couples  $T_0$  and  $T_{\pm}$  but does not cause a change of the overall spin. In this case the dipole-dipole relaxation of the molecules can be described by

$$k_{r,esdi} = 0.3 \frac{g^4 \mu_B^4}{\hbar^2 r^6} \frac{\tau_C}{1 + \omega_0^2 \tau_C^2} \quad (7)$$

where  $g$  is the mean value of the  $g$ -values,  $\mu_B$  the *Bohr* magneton,  $r$  the mean distance of the two radical centres,  $\tau_C$  the rotation correlation time and  $\omega_0$  the *Larmor* frequency.<sup>[82, 84-85, 88]</sup>

Furthermore, the mechanisms of ahf and gta can be described individually or combined. By taking the anisotropic hyperfine coupling of one nitrogen nucleus into account, the combined representation of the gta and ahf mechanism is given by

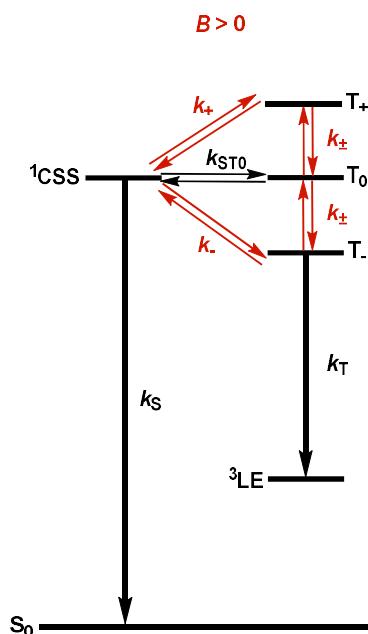
$$k_{r,ahf+gta} = \frac{4}{27} (\Delta A)^2 \frac{\tau_C}{1+\omega_0^2\tau_C^2} - \frac{1}{90} (\Delta g' \Delta A) \frac{\omega_0\tau_C}{1+\omega_0^2\tau_C^2} + \frac{1}{60} (\Delta g')^2 \frac{\omega_0^2\tau_C}{1+\omega_0^2\tau_C^2} \quad (8)$$

Here,  $\Delta A$  is the anisotropy of the hyperfine tensor of the nitrogen nucleus and  $\Delta g'$  is the variance from the anisotropic hyperfine  $g$ -tensor. The effects of the ahf and gta are not simply additive but show an interference term.<sup>[48, 84, 88]</sup> The variance of the anisotropic  $g$ -tensor depends on the SOC and therefore increases for heavy atoms. In purely organic molecules, without heavy atoms attached, the gta relaxation plays a minor role so the ahf-mechanism can be given individually (**equation (9)**).<sup>[75, 83-85]</sup> It describes the effect of the anisotropic component of the hyperfine coupling interaction between the radical electron spin and the nuclear spins and is modulated through molecular rotations and vibrations.<sup>[67, 75, 83-85, 88]</sup>

$$k_{r,ahf} \sim (\Delta A)^2 \frac{\tau_C}{1 + \omega_0^2\tau_C^2} \quad (9)$$

### 1.1.3 Classical and semiclassical description of the MFE

In the previous sections (**section 1.1.2.1** and **1.1.2.2**) the coherent and incoherent spin interconversion mechanisms were discussed. These mechanisms can cause a MFE due to different *Larmor* frequencies of the radical electron spins. If the spin interconversion between the central ( $S$ ,  $T_0$ ) and the outer *Zeeman* levels ( $T_+$ ,  $T_-$ ) is due to relaxation (incoherent processes) and the  $S/T_0$  equilibration is fast, the RP reaction dynamics can be described by a *Hayashi* and *Nagakura* scheme (**Figure 4**).



**Figure 4:** Spin interconversion processes of a RP in an external magnetic field. The rate constants depicted in red are magnetic field dependent and the ones in black are magnetic field independent.

According to *Schulten* and *Wolynes* the spin evolution can be described by a semiclassical approach.<sup>[73-74]</sup> In this semiclassical approach the magnetic field  $B(i)$  is the vector sum of an effective magnetic field resulting from the various nuclear spins in the corresponding radical and the external magnetic field  $B_0$  (see **equation (2)** in **section 1.1.2.1**). This effective nuclear hyperfine field is treated as a constant vector, which is justified in the case of systems with many nuclear spins.<sup>[31, 73]</sup> Using classical rate equations (**equation (10)**) the semiclassical approach from *Schulten* can be approximated. Thus, the kinetics of the RPs can be described by a system of classical linear differential equations, which have to be solved simultaneously because the overall measurable population of CSS comprises to the sum of all four spin substates ( $[CSS] = [S] + [T_0] + [T_+] + [T_-]$ ) (**equation (10)**).<sup>[47, 83]</sup>

$$\begin{aligned}
 \frac{d[S]}{dt} &= -(k_S + 2k_{\pm} + k_{ST_0})[S] + k_{ST_0}[T_0] + k_{\pm}([T_+] + [T_-]) \\
 \frac{d[T_0]}{dt} &= k_{ST_0}[S] - (k_T + 2k_{\pm} + k_{ST_0})[T_0] + k_{\pm}([T_+] + [T_-]) \\
 \frac{d[T_+]}{dt} &= k_{\pm}[S] + k_{\pm}[T_0] - (k_T + 2k_{\pm})[T_+] \\
 \frac{d[T_-]}{dt} &= k_{\pm}[S] + k_{\pm}[T_0] - (k_T + 2k_{\pm})[T_-]
 \end{aligned}
 \tag{10}$$

With this set of rate equations, the incoherent spin motion can be described correctly, however, the coherent parts cannot be described fully in an accurate way. For example, the oscillations of spin substate populations or the LFE are not included.<sup>[47, 79, 82-83, 89-90]</sup> To get a better insight



into coherent spin evolution mechanisms, the spin evolution must be treated with a quantum mechanical approach.<sup>[47-48, 83, 91]</sup> An approximation of the spin evolution of the *Schulten* and *Wolynes* model by classical kinetic equations is needed to apply the classical rate equations (**equation (10)**).<sup>[83]</sup> To describe this evolution of the singlet probability  $p_S$  in the limit of zero field, it can be assumed that  $k_{\pm} \approx k_{ST0}$  yielding

$$p_{S,zf}(t) = \frac{1}{4}(1 - e^{-4k_{ST0}t}) \quad (11)$$

and in the high-field case  $k_{\pm} \rightarrow 0$ , yielding

$$p_{S,hf}(t) = \frac{1}{6}(1 - e^{-2k_{ST0}t}) \quad (12)$$

For a full understanding of the spin evolution a quantum mechanical approach is needed, but to get a rough impression about the spin evolution and to obtain suitable starting values for the quantum mechanical approach, a fit using the classic differential equations (**equation (10)**) can be useful. The rate constants needed for the classical fit are  $k_S$  and  $k_T$  for the singlet and triplet recombination of the CSS,  $k_{ST0}$  for the magnetic field independent ZQT,  $k_+$  for the  $S \leftrightarrow T_+$  transition,  $k_-$  for the  $S \leftrightarrow T_-$  transition, and  $k_{\pm}$  for the identical  $T_{0 \leftrightarrow T_+}$  and  $T_{0 \leftrightarrow T_-}$  interconversions (**Figure 4**).<sup>[68, 79, 82-83, 89]</sup>

The individual rate constants ( $k_{spin}$ ) can be described using a double *Lorentzian* equation (**equation (13)**).<sup>[47, 83]</sup>

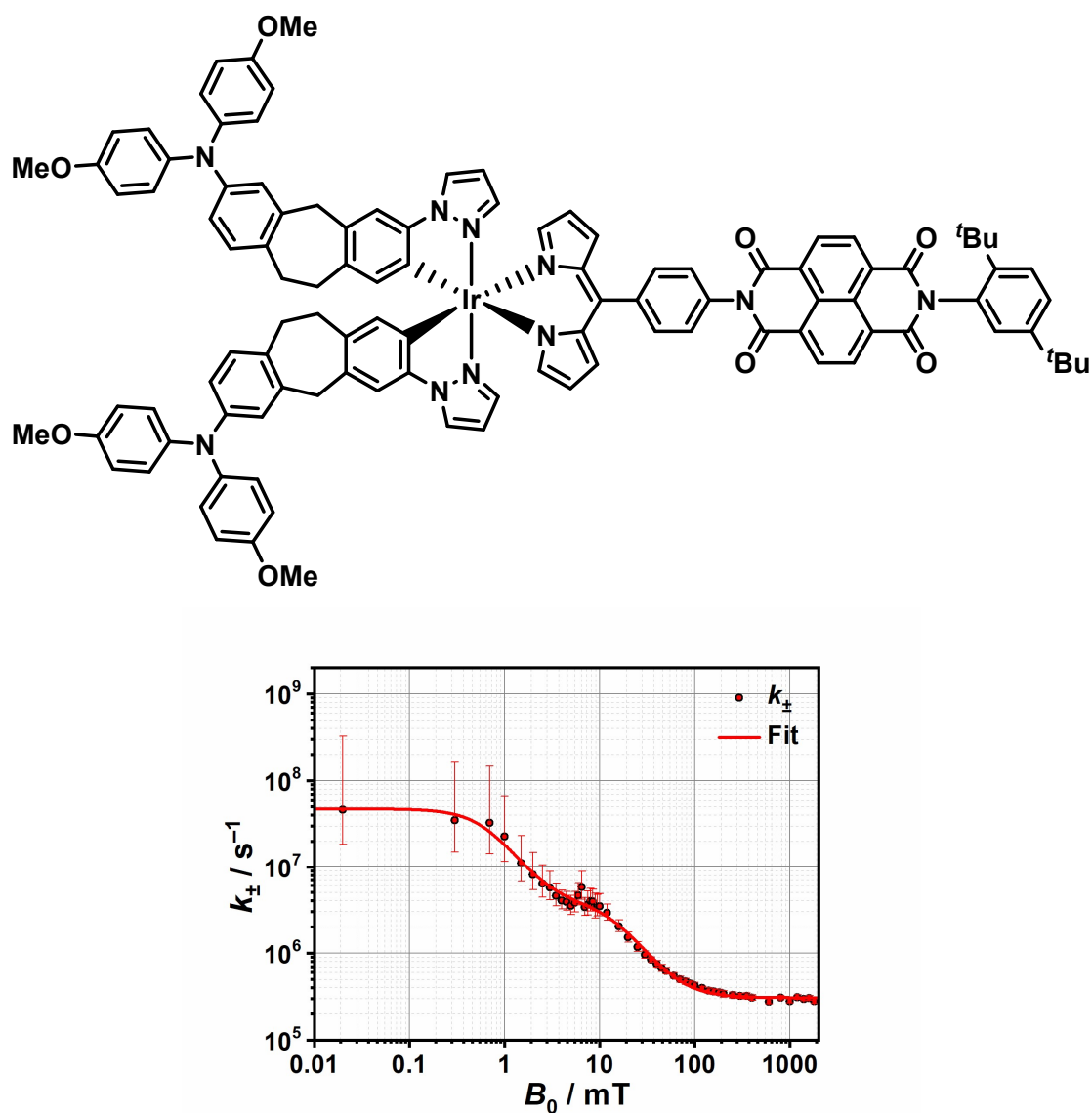
$$k_{spin}[B_{eff}] = \frac{k_1}{1 + (B_{eff}/B_1)^2} + \frac{k_2}{1 + (B_{eff}/B_2)^2} + k_0 \quad (13)$$

$B_{eff}$  describes the field and  $k_1/k_2$  represent the rate constants for the coherent/incoherent parts of the spin evolution. The half-field  $B_1$  ( $B_2$ ) describes the field where the coherent (incoherent) spin interconversion rate constant decreases to half of its zero-field value (**Figure 5**). The first term of the equation accounts for the coherent spin motion ( $B < 10$  mT), the second term describes the incoherent spin flips ( $10$  mT  $< B < 1$  T) and the last term stands for the saturation of the MFE at high fields due to the incoherent spin flips ( $B > 1$  T).

Inserting the double *Lorentzian* equation (**equation (13)**) in the classical differential equations (**equation (10)**) results in a system of coupled differential rate equations including seven global unknown variables ( $k_S$ ,  $k_T$ ,  $k_1$ ,  $k_2$ ,  $B_1$ ,  $B_2$  and  $k_0$ ), none of which are magnetic field dependent.<sup>[83,</sup>

<sup>88]</sup> This allows the experimental data to be fitted numerically.

*Klein et al.*<sup>[83]</sup> showed, for a triad consisting of two TAA donors, a cyclometalated iridium complex sensitiser and a naphthalene diimide acceptor, that by plotting the  $k_{\pm}$  values vs. the magnetic field  $B$ , a clear double *Lorentzian* behaviour (**Figure 5**) can be observed. The coherent and incoherent domains are herein described by the two half-fields  $B_1$  and  $B_2$ .<sup>[83]</sup> This approach can be applied to similar triads as well.<sup>[47-48, 82, 92]</sup>



**Figure 5:** Magnetic field dependence of  $k_{\pm}$  with error bars. The solid line represents the fit of the double *Lorentzian* function to the data.  $k_1 = (4.3 \pm 0.4) \cdot 10^7 \text{ s}^{-1}$ ,  $B_1 = (0.69 \pm 0.07) \cdot \text{mT}$ ,  $k_2 = (3.6 \pm 0.25) \cdot 10^6 \text{ s}^{-1}$ ,  $B_2 = (15 \pm 1) \text{ mT}$ ,  $k_0 = (3.1 \pm 0.1) \cdot 10^5 \text{ s}^{-1}$ . Adapted with permission.<sup>[83]</sup>

### 1.1.4 Level crossing mechanism

In the following section, the energy difference between the S and  $T_0$  CSS (exchange interaction  $2J$ ) will be discussed. Three possible scenarios, how large the energy difference between the S and the  $T_0$  level can be, will be discussed (see **Figure 6 B**).

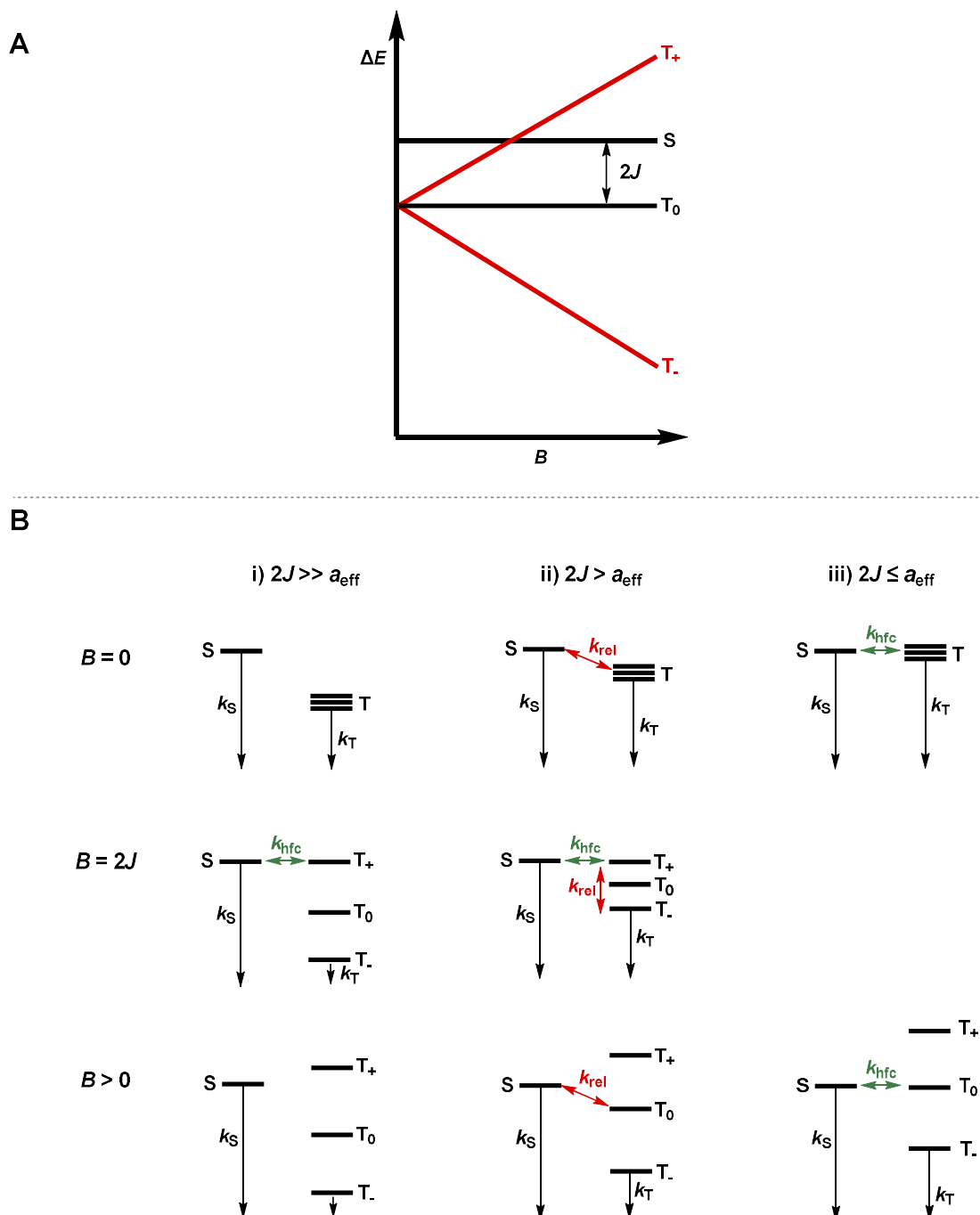
i) The exchange interaction can be much larger than the effective hyperfine interaction ( $2J \gg a_{\text{eff}}$ ). In this case only in the range of  $B \approx 2J$  a coherent spin interconversion between S and  $T_+$ <sup>1</sup> is possible. [28, 31, 67, 93-94]

ii) The exchange interaction can be larger than the effective hyperfine interaction ( $2J > a_{\text{eff}}$ ), but a spin interconversion is possible through the ahf-mechanism at zero field. In this case the singlet triplet gap is too large for the coherent spin flip mechanism (**Figure 6, B:  $B = 0$** ). Increasing the external magnetic field, the outer *Zeeman* levels split until the  $T_+$  level becomes degenerate with S and the spin interconversion is coherent through the hfc-mechanism (**Figure 6, B:  $B = 2J$**  green arrow).<sup>2</sup> The spin interconversion  $S \leftrightarrow T_-$  becomes more ineffective but the coherent effect exceeds the incoherent processes, leading to an overall increase of the spin interconversion rate constant. As the external field further increases, the degeneracy of S and  $T_+$  is lifted, which slows down the spin interconversion (**Figure 6, B:  $B > 2J$** ). The MFE therefore shows a clear resonance peak around the external field  $B = 2J$ , which can be attributed to the level crossing of  $T_+$  and S and is thus called the level crossing mechanism (LCM). [27, 31, 67, 75, 93-94]

iii) The singlet and triplet level can be almost degenerate ( $2J \ll a_{\text{eff}}$ ), consequently, the spin interconversion  $S \leftrightarrow T_0$  is coherent. With increasing external magnetic field, the outer *Zeeman* levels split and the spin flip rate becomes slower until  $T_+$  and  $T_-$  are no longer available and only the coherent spin interconversion between  $S \leftrightarrow T_0$  is taking place. [94]

<sup>1</sup> For the positive  $J$  case.

<sup>2</sup> Example for a positive  $J$  value ( $E_S > E_T$ ).



**Figure 6:** **A:** Energy diagram of electronic spin states of a RP in an external magnetic field for  $2J > 0$ . **B:** Schematic diagram of spin dynamics and spin selective charge recombination pathways in the case of i)  $2J \gg a_{\text{eff}}$  (left column), ii)  $2J > a_{\text{eff}}$  (middle column), iii)  $2J \leq a_{\text{eff}}$  (right column) at zero magnetic field (top row), at  $B = 2J$  (resonance, middle row) and very high fields (bottom row).  $k_{\text{hfc}}$  (green arrows) represent the coherent spin interconversion processes and  $k_{\text{rel}}$  (red arrows) the incoherent spin interconversion processes.

CIDNP or EPR measurements are required to determine the sign of  $J$ , but the absolute value can, in most cases, be obtained directly from the position of the resonance peak in the MARY plots (magnetic field affected reaction yield<sup>3</sup>). Very small exchange interactions cannot be directly read out of the MARY plots because the LFE influences the resonance peak as well.

<sup>3</sup> More detailed description in **section 6.1.3.2**.

Furthermore, in rigidly bound compounds C-C rotation can cause a modulation of the  $2J$  coupling due to S-T-dephasing.<sup>[31, 50, 79-80, 94-95]</sup>

The exchange interaction depends on several factors, where the distance dependence of two radicals can be estimated with **equation (14)**.  $J_0$  describes the dependency of the exchange interaction on the geometry of the RP and can show positive or negative sign. The exponent  $a$  describes how fast the exchange interaction decreases with the radical-radical distance.  $J$  is dependent on the square of the electronic couplings  $V_{\text{CSS}-n}$  and the energetically nearby lying states  $n$  (**equation (15)**).<sup>[75, 96-97]</sup>

$$J(r) = J_0 e^{-ar} \quad (14)$$

$$2J = \Delta E_S - \Delta E_T = \left[ \sum_n \frac{V_{1\text{CSS}-n}^2}{E_{1\text{CSS}} - E_n - \lambda} \right]_S - \left[ \sum_n \frac{V_{3\text{CSS}-n}^2}{E_{3\text{CSS}} - E_n - \lambda} \right]_T \quad (15)$$

This relation between the exchange interaction and the electronic couplings was derived by *Anderson et al.*<sup>[96]</sup> Here,  $V$  represents the singlet ( $^1\text{CSS}$ ) and triplet ( $^3\text{CSS}$ ) couplings of a CSS with its precursor- or successor state of the regarded ET process.  $E_{1,3\text{CSS}}$  are the energy levels of the CSSs and  $E_n$  the energy levels of the precursor- or successor states. The exchange interaction can be obtained by summing over all singlet and triplet permutations divided by the energy difference. A detailed description of the dependence of the electronic coupling from the CS and CR rate constants was given by *Bixon-Jortner* theory, which is not further discussed here.<sup>[47, 71, 80, 93-94, 96-102]</sup> The exchange interaction therefore has a strong influence on the spin evolution but is not only dependent on the radical-radical distance.  $2J$  is also dependent on the coupling between donor and acceptor states. This coupling can be influenced by the modulation of the rotation around C-C bonds, and therefore minimising the  $\pi$ -overlap of the connected parts as well as the variation of the electron density in the bridging unit linking donor and acceptor.<sup>[47, 93, 99, 103-105]</sup>

The  $2J$  coupling can be influenced by several different factors and therefore be tuned. The spin evolution in molecules exhibiting such an exchange interaction can also be approximated by using classical linear differential equations (**equation (10)** in **section 1.1.3**). The  $2J$  coupling can directly be taken from the MARY plots of the experimental data and inserted **equation (13)**. This is possible because the spin interconversion rate constant  $k_+$  ( $k_+$ ,  $k_{\pm}$  and  $k_{\text{ST}0}$ ) can be expressed by **equation (16)** when for  $B_{\text{eff}}$  the effective field taking  $J$  into account is inserted.<sup>[79]</sup> For example, to calculate the rate constant  $k_+$  the energy gap between S and  $T_0$  can be expressed as  $B_{\text{eff}} = 2J - B$  and therefore replace  $B_{\text{eff}}$  in **equation (13)** resulting in **equation (16)**.

$$k_+ = \frac{k_1}{1 + (B_{\text{eff}}/B_1)^2} + \frac{k_2}{1 + (B_{\text{eff}}/B_2)^2} + k_0 \quad (16)$$

The other rate constants can be expressed as:  $k_-: B_{\text{eff}} = 2J + B$ ,  $k_{\pm}: B_{\text{eff}} = B$ ,  $k_{\text{ST}0}: B_{\text{eff}} = 2J$ .<sup>[79]</sup> Using this approach all magnetic field dependent spin flip rate constants are described by the field independent parameters  $k_S$ ,  $k_T$ ,  $k_1$ ,  $k_2$ ,  $B_1$ ,  $B_2$  and  $k_0$ , which are identical for all rate constants at all fields. By inserting the appropriate double *Lorentzian* functions in **equation (13)** (**section 1.1.3**) a system of coupled differential rate equations is obtained. In this equation all parameters ( $k_S$ ,  $k_T$ ,  $k_1$ ,  $k_2$ ,  $B_1$ ,  $B_2$ ,  $k_0$ ) are independent on the magnetic field and the experimental results can be fitted numerically using MATLAB.<sup>[48, 79]</sup><sup>4</sup>

### 1.1.5 Molecules with a non-zero exchange interaction determined by magnetic field dependent transient absorption spectroscopy measurements

As already mentioned, the exchange interaction  $2J$  between the <sup>1</sup>CSS and the <sup>3</sup>CSS ( $S \leftrightarrow T_0$ ) depends on several factors. Changes in the spin distribution can primarily change the overall effective radical ion pair distance ( $r_{\text{DA}}$ ), which changes the interaction of the radical ions. This may create a significant dispersion of  $2J$ , even within a series of molecules that are structurally related.<sup>[99]</sup>

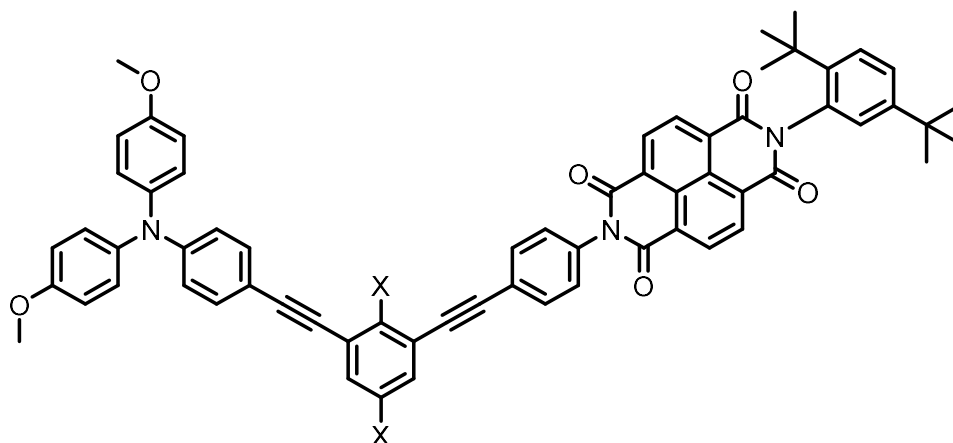
The influence of the radical ion pair distance on the exchange interaction has extensively been studied in the past years.<sup>[94, 106-107]</sup> Those studies showed that  $J$  depends exponentially on the SCR distance (compare **equation (14)**). *Scott et al.*<sup>[106]</sup> analysed a series of molecules with 3,5-dimethyl-4-(9-anthracenyl)julolidine (DMJ-An) as an electron donor and a naphthalene-1,8:4,5-bis(dicarboximide) (NDI) acceptor. Here, donor and acceptor were separated by a *p*-oligophenylene bridge ( $\text{Ph}_n$ ,  $n = 1-4$ ) to create a long-living RP. They analysed how the electronic coupling  $V_{\text{DA}}$  between donor and acceptor depends on the molecular structure by analysing the exchange interaction  $2J$ , since the exchange interaction is proportional to the electronic coupling ( $2J \sim V_{\text{DA}}^2$ ). The  $2J$  coupling of DMJ-An- $\text{Ph}_n$ -NI in toluene shifts from 170 mT ( $\text{Ph}_1$ ) to 0.3 mT ( $\text{Ph}_4$ ) and is therefore a good example for the strong distance dependency. The variation of the donor acceptor distance also leads to the crossover from a *superexchange* ( $n = 1-3$ ) to a *charge hopping* mechanism ( $n = 4$ ). In the *superexchange* mechanism charge transport occurs in a single step with a rate that decays exponentially with distance. In contrast to that, in the *hopping* mechanism the charge is transported sequentially between the donor and the acceptor via bridge sites.<sup>[107-108]</sup> *Goldsmith et al.* found the same

<sup>4</sup> All the experimental CR decays were fitted by this approach, which was developed by *D. Mims* as part of his doctoral thesis. The data implementation in MATLAB is described in **section 10.2**.

behaviour in another series of molecules containing phenothiazine (PTZ) donors, 2,7-oligofluorene (FL<sub>n</sub>, n = 1-4) bridges and perylene-3,4:9,10-bis(dicarboximide) (PDI) acceptors. CR occurs only in the FL<sub>1</sub> bridged molecule by the *superexchange* mechanism, whereas CR within FL<sub>2</sub>-FL<sub>4</sub> occurs by *hopping*. The exchange interaction in these molecules decrease from 30 mT (FL<sub>2</sub>) to about 1 mT (FL<sub>4</sub>) as the radical-radical distance increases.<sup>[108]</sup> The CR dynamics were further investigated by *Miura* et al., who showed that  $2J$  is also modulated by the torsional motions of the single bonds connecting the bridge segments. This results in fluctuations that can induce a S-T dephasing process of the exchange interaction.<sup>[94]</sup>

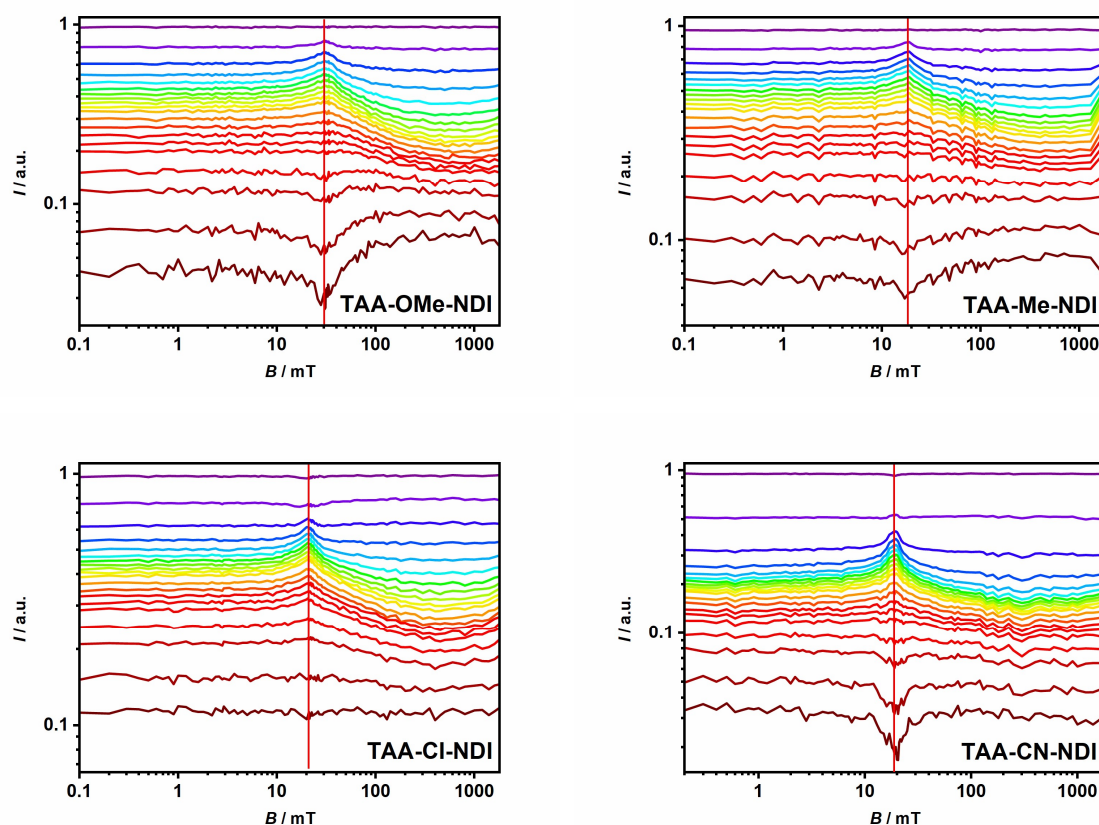
Not only can the distance of the radical centres influence the exchange interaction but a temperature variation can also cause a significant change. *Scott* et al. presented donor acceptor systems with 3,5-dimethyl-4-(9-anthracenyl) julolidine (DMJ-An) electron donors and naphthalene-1,8:4,5-bis(dicarboximide) (NDI) acceptors bridged by either 2,7-fluorenone (FN1-2) or *p*-phenylethynylene (PE1-2P). Hereby, the CR rate constants ( $k_{CR}$ ) were measured over a temperature range of 270 K to 350 K in toluene and  $k_S$  and  $k_T$  were extracted by kinetic analysis. This attempt showed a distinct crossover from a temperature-independent singlet CR pathway to a triplet CR pathway at 300 K, which can be explained by the temperature dependence of the bridge structural dynamics. In the molecules with the longer bridges, the triplet recombination pathway is dominant for CR. Consequently, the CR is gated by the torsional barriers around the single bonds linking the 2,7-fluorenone and *p*-phenylethynylene bridges to D and A. Those data showed that the combination of varying bridge structures along with application of magnetic fields at different temperatures can be used to control the CR dynamics that arise due to the differences in the S-T energy gap between the singlet and triplet RPs.<sup>[109]</sup> The same observation was made by *Weiss* et al, who also showed a change in CR dynamics for different bridge lengths at varying temperatures in donor acceptor systems.<sup>[110]</sup>

Another way to tune the exchange interaction is to vary the electron density in the bridging unit between D and A. This was investigated by *Schäfer* et al.<sup>[47]</sup>, regarding a series of molecules with different electron withdrawing and donating (OMe, Me, Cl, CN) groups at a *meta*-conjugated diethynylbenzene bridge to modify the electronic nature of the bridge. In these molecules the electron donor is a triarylamine (TAA) and the acceptor a naphthalene diimide (NDI) (**Figure 7**).



X = OMe, Me, Cl, CN

TAA-X-NDI



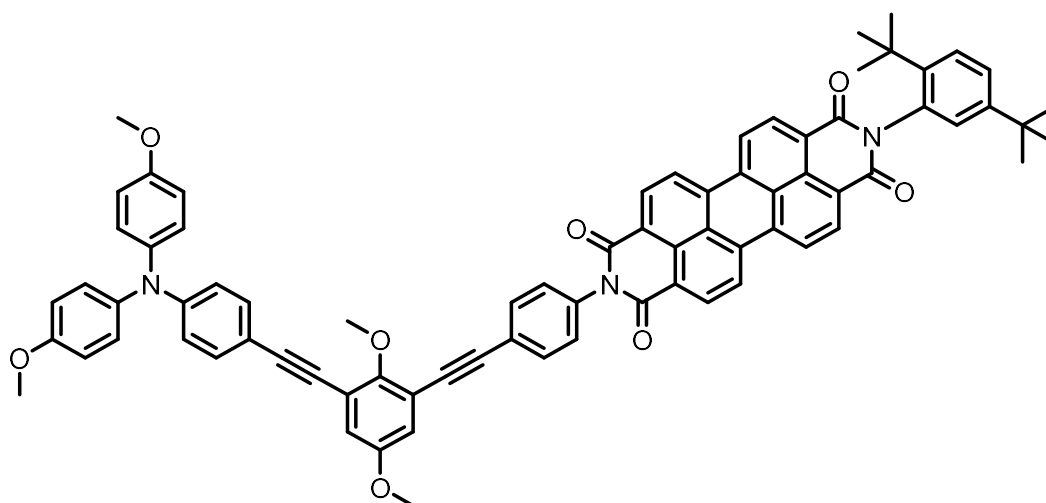
**Figure 7:** Structure of the triad investigated by Schäfer et al. (top). MARY plots of amplitudes vs. magnetic field at different times (from purple to dark red: 0, 0.18, 0.38, 0.58, 0.78, 0.98, 1.18, 1.58, 1.78, 1.98, 2.38, 2.78, 3.18, 3.58, 3.98, 4.98, 5.98, 7.98, 9.98  $\mu$ s) for all four possible bridge substitutions (bottom). The red line highlights the  $2J$  resonance peak.<sup>[47, 111]</sup>

The charge separation in these TAA-X-NDI triads (see **Figure 7**) takes place over a CT state between the donor and the bridge, followed by a charge transfer from this CT state to the CSS. The rise time of the CSS is decreasing from X = Me over OMe and Cl to CN. However, OMe

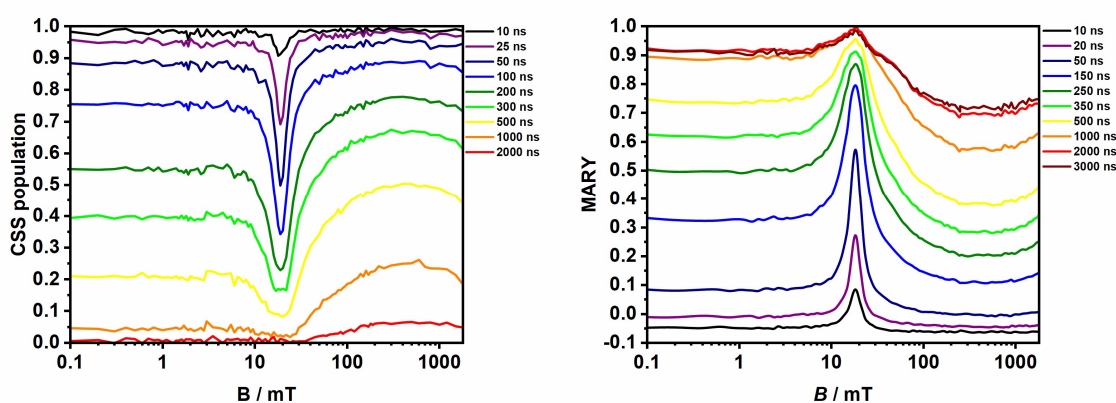


is expected to be a better donor than Me, which was not observed. The OMe group at the 2-position of the *meta*-phenylene group between the two alkyl groups is rotated out of the  $\pi$ -plane for steric reasons, thus the oxygen p-type lone pair orbital cannot overlap with the benzene  $\pi$ -orbitals. This was confirmed by DFT optimisations. Consequently, this OMe group no longer acts as an electron donor via the lone-pair orbital, but as an electron acceptor due to the electronegativity of the oxygen. The electronic couplings  $V^2$  for CS are only slightly changing along the series and these small changes are therefore overcompensated by the influence of the *Marcus* (inverted) barrier. CR in all investigated triads is only possible through the singlet pathway because the NDI triplet is higher in energy than the CSS, and thus not accessible. All triads showed a distinct MFE for the CR with a curve crossing of the CSS decay curves at about 6  $\mu$ s, resulting in a positive resonance peak in the MARY plots at early times and a negative peak at later times (**Figure 7**). The resonance peak at  $B = 2J$  is at 30 mT for X = OMe group and between 19 – 21 mT for X = Me, Cl and CN but does not follow a distinct trend along the series. The sign of  $J$  was evaluated to be positive by CIDNP measurements<sup>[112]</sup>, implying that the <sup>3</sup>CSS is lower in energy than the <sup>1</sup>CSS. The calculated electronic couplings for CR are much smaller than those for CS because for CS the primary state is the CT state, in which the bridge is involved and therefore shares some negative charge, resulting in an enhanced coupling to the NDI. The underlying spin processes have been studied in detail by *Steiner* et al using a classical as well as a quantum mechanical approach.<sup>[79]</sup> However, the bridge substituents appeared to have a minor influence on the exchange interaction in this series of molecules. Thus, the influence of the substituents needs further investigation, which was part of this work in **section 7**.<sup>[47, 79, 113]</sup>

*Mims* et al.<sup>[48]</sup> studied the advantages of a PDI acceptor in a structural similar triad as the ones studied by *Schäfer* et al.<sup>[47]</sup> *Mims* et al. investigated the MFE of a triad using a triarylamine (TAA) donor, a 1,3-diethynyl-2,5-dimethoxy benzene bridge (OMe) and a PDI acceptor (**Figure 8**).<sup>[48]</sup> The NDI was replaced by a PDI acceptor due to its absorption maximum in the visible range at 18900  $\text{cm}^{-1}$  (528 nm) and its good stability in solution after light-excitation. Another advantage of PDI is that the excited state absorption of the PDI radical anion is also in the visible region (14100  $\text{cm}^{-1}$ , 710 nm).



TAA-OMe-PDI



**Figure 8:** Structure of TAA-OMe-PDI triad investigated by *Mims et al* (top). MARY plot of CSS decay with pronounced negative resonance peak at  $B = 2J$  (bottom left). MARY plot of triplet rise with pronounced positive resonance peak at  $B = 2J$  (bottom right). Measured in toluene at 298 K.<sup>[48, 88]</sup>

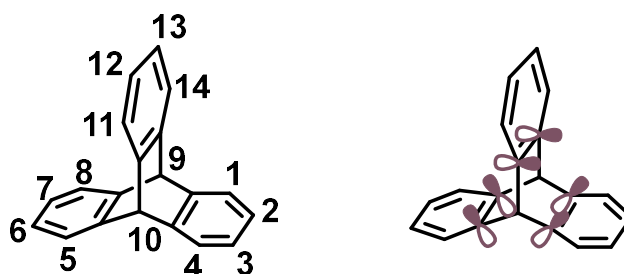
In this triad, the rigidly linked radical ion pair is formed with singlet multiplicity and recombines almost exclusively to the excited local triplet PDI state ( $^3\text{PDI}$ ). It belongs to the  $2J > a_{\text{eff}}$  (compare **section 1.1.4**) case (classification by *Miura et al.*<sup>[94]</sup>) and exhibits a level crossing resonance peak at  $B = 2J = 19.8$  mT. The MARY plots, both from the CSS decay and the formation of the  $^3\text{PDI}$  show a sharp resonance peak at  $B = 2J$  (**Figure 8**). The CSS decay of TAA-OMe-PDI is monoexponential outside the resonance range and can be simulated by a classical model, assuming a single field dependent double *Lorentzian* function for the energy gap dependence of all spin conversion processes (compare **section 1.1.4**). In the resonance region the decay is biexponential, which was proved by quantum simulations to be caused by so called “orphan states<sup>[114]5</sup>”. A subpopulation of singlet hyperfine states coupling strongly with the  $T_+$  level on the one hand, and on the other hand a complementary subpopulation of singlet

<sup>5</sup> Orphan states in EPR mentioned by *Forbes* seem to be closely related.

states that does not couple strongly with  $T_+$ , was the explanation for this phenomenon. The kinetics in this triad are controlled by S-T transitions, where the rates of the coherent and incoherent S- $T_+$  transitions are on a different order of magnitude. This strong difference of the rates causes the strong biexponential behaviour. This observation of kinetic partitioning of nuclear sublevels was pointed out to be rather unique in spin chemistry so far.<sup>[48, 88]</sup>

## 1.2 Triptycene as a bridging unit

9,10-*o*-Benzenoanthracene was first synthesised and reported by *Cohen* et al. in 1942 and was named “triptycene”.<sup>[115]</sup> The paddlewheel-like structure of triptycene consists of three benzene rings (“fins”) bound via two shared bridgehead carbon atoms with  $sp^3$  hybridisation.<sup>[116]</sup> By definition, homoconjugation refers to the orbital overlap between two separated conjugated systems linked by a saturated group.<sup>[117]</sup> The shape of triptycene leads to an electronic communication between the aryl fins through homoconjugation, which is to a large extent mediated by the transannular, through-space overlap of the  $\pi$ -electron clouds over the aryl fins. The structure, numbering and the assembly of the relevant  $\pi$ -electron orbitals mediating homoconjugation in triptycene are depicted in **Figure 9**.<sup>[115-116]</sup>



**Figure 9:** Triptycene with numbering (left) and the array of  $\pi$ -electron orbitals responsible for homoconjugation (right).

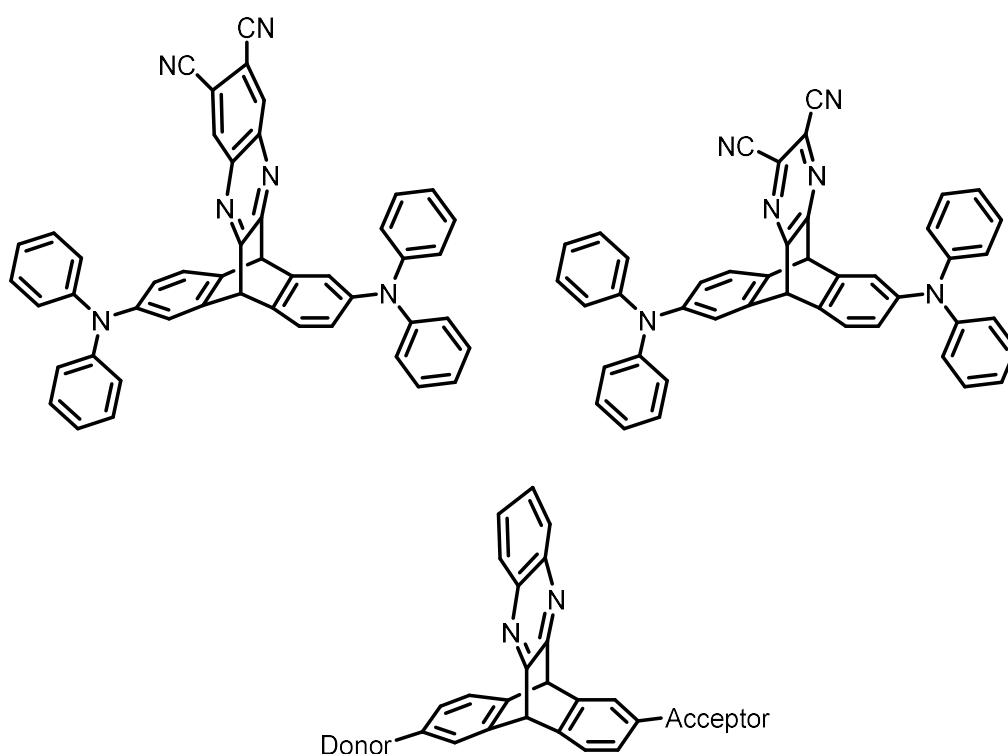
The usefulness of triptycene in various applications, such as molecular gears<sup>[118-119]</sup>, sensors<sup>[120-121]</sup>, photocatalysis<sup>[122-124]</sup> and as a key structural compound of both metal<sup>[125-127]</sup> and covalent organic frameworks<sup>[128]</sup> as well as polymer networks<sup>[129]</sup> has been investigated by many different groups. One reason for the widespread use of triptycene is the ability to tune the properties of the molecules and impart desirable optoelectronic functionality by functionalising the fins.<sup>[116, 130-132]</sup>

In donor acceptor substituted triptycenes, with donor and acceptor on different fins, the electronic communication between the separated parts is not caused by regular conjugation but by homoconjugation, which amounts to 20-30 % of the regular conjugation.<sup>[116-117]</sup>

One example of using homoconjugation of triptycene derivatives is the substitution of all three fins with the same A to create a three-dimensional structure that can be used as a bulk heterojunction (BHJ) in organic solar cells (OSCs).<sup>[133-134]</sup> This three-dimensional acceptor structure interpenetrates charge transport networks, enhancing electron mobility and thus improving the efficiency of OSCs.<sup>[133]</sup> *Menke* et al. synthesised triptycene derivatives substituted by three arylenimidazole units on the triptycene core.<sup>[135]</sup> They reported that these molecules can act as a non-fullerene acceptor material in BHJ OSCs. PDI dyes fused at the bay position to the triptycene core can also act as a BHJ device in OSCs.<sup>[133, 136]</sup>

Other examples of substituted triptycenes were given by *Kawasumi* et al. and *Lei* et al., who synthesised a new kind of thermally activated delayed fluorescence (TADF) materials with a triptycene core for OLEDs (organic light emitting diodes) using donor acceptor substituted triptycenes.<sup>[137-138]</sup> Materials showing TADF have segregated HOMO and LUMO states with a sufficiently small overlap to reduce the exchange energies, which is often achieved by a direct connection with a twisted geometry.<sup>[139-140]</sup>

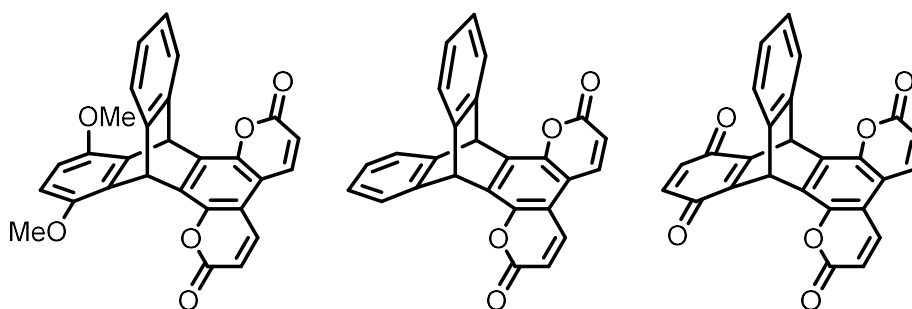
The physical separation of donor and acceptor on different fins of the triptycene scaffold (**Figure 10**) using through-space interaction through homoconjugation can create small singlet-triplet gaps  $\Delta E_{ST}$  and consequently sufficient singlet emission.<sup>[137]</sup>



**Figure 10:** Triptycene based donor acceptor substituted TADF emitters synthesised by *Kawasumi* et al. (top).<sup>[137]</sup> Donor-acceptor substituted triptycenes from *Lei* et al. in which donors carbazole, phenothiazine and acceptors naphthalimide, bromonaphthalimide and BMes (bottom) are used.<sup>[138]</sup>

*Kawasumi et al.* reported structures that provide small  $\Delta E_{ST}$  and exhibit TADF characteristics, achieved by placing two triphenylamine donors on two fins of the triptycene core and a dicyanoquinoxaline or dicyanopyrazine acceptor on the third (**Figure 10**, top).<sup>[137]</sup> Using such triptycene emitters in multilayer OLED devices proved to show yellow emission with an efficiency up to 9.4 %. The molecular design of *Lei et al.* was similar, using a simple non-functionalised quinoxaline unit as acceptor. Those highly emissive molecules cover an emission range from 390 nm to 625 nm, by fine tuning the electron-accepting strength, and therefore could be the basis for future studies of high-performance luminescent materials with applications in sensing and electronic devices.<sup>[138]</sup>

A donor acceptor substituted fluorophore separated by a triptycene core was studied by *Quian et al.*<sup>[117]</sup> They designed a triptycene-coumarin hybrid molecule using a 1,4-dimethoxybenzene donor and a coumarin fluorophore as an acceptor, placed on different fins of a triptycene backbone to investigate the interactions facilitated by homoconjugation and its effect on the photophysical properties of the coumarin fluorophore (**Figure 11**).



**Figure 11:** Chemical structures of the donor acceptor substituted fluorophores by *Quian et al.*<sup>[117]</sup>

The fluorophore attached to a triptycene core by *Quian et al.* exhibits different absorption spectra compared to the fluorophore itself. This could be caused by homoconjugation through the triptycene core. It was shown that the attachment of an electron donor<sup>[141]</sup> to the triptycene leads to a charge separated excited state in solution with emissions sensitive to solvent polarity.<sup>[117, 142]</sup>

*Baumgärtner et al.* reported a number of molecules with 1,2-dimethoxybenzene as donor and furazan-quinoxaline/phenazine as acceptor attached to the triptycene core.<sup>[143]</sup> Those molecules feature one/two electron donors combined with one/two (**Figure 12**, left) phenazine/furazan-quinoxaline acceptors. Furthermore, they investigated molecules with three phenazine/furazan-quinoxaline acceptors attached to the triptycene core (**Figure 12**, right).

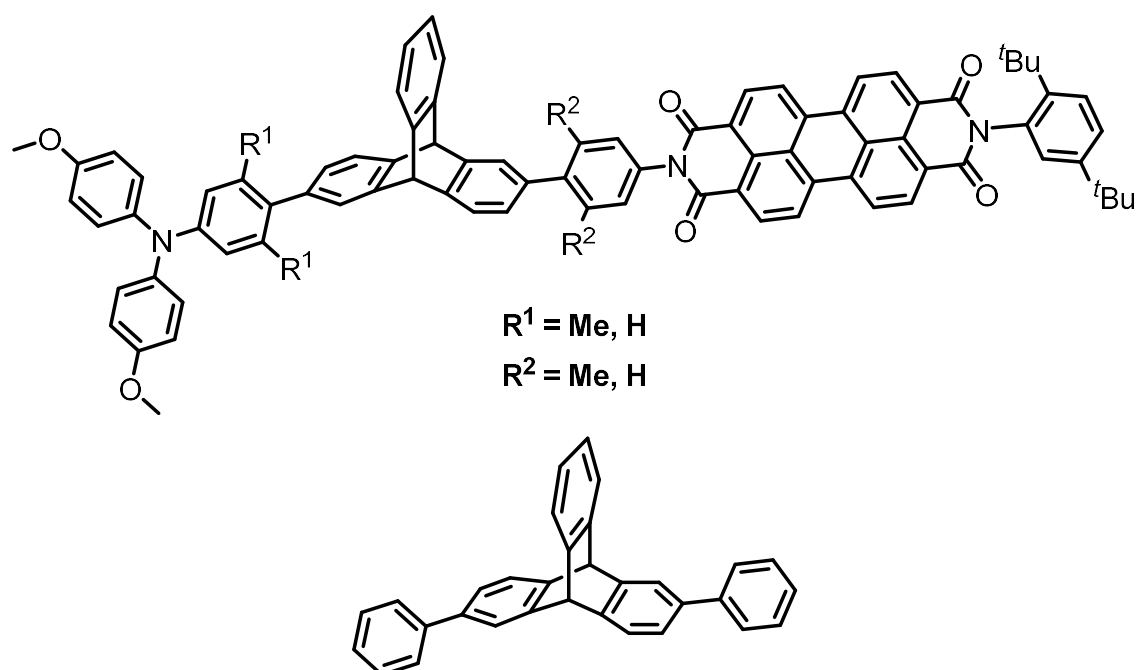


## 2 Scope of the work

This work investigates the influence of rotational hindrance and varying electron density in a connecting bridge moiety on the ET processes and electronic couplings of purely organic rigidly bound donor acceptor systems. All the molecules in this work consist of a triarylamine electron donor (**TAA**) and a perylene diimide electron acceptor (**PDI**). The bridging unit between donor and acceptor is either a triptycene (**TTC**) or an anthracene (**ATC**) moiety. The molecules under consideration are referred to as triads due to their three-part structure, consisting of a donor, bridge (B), and acceptor.

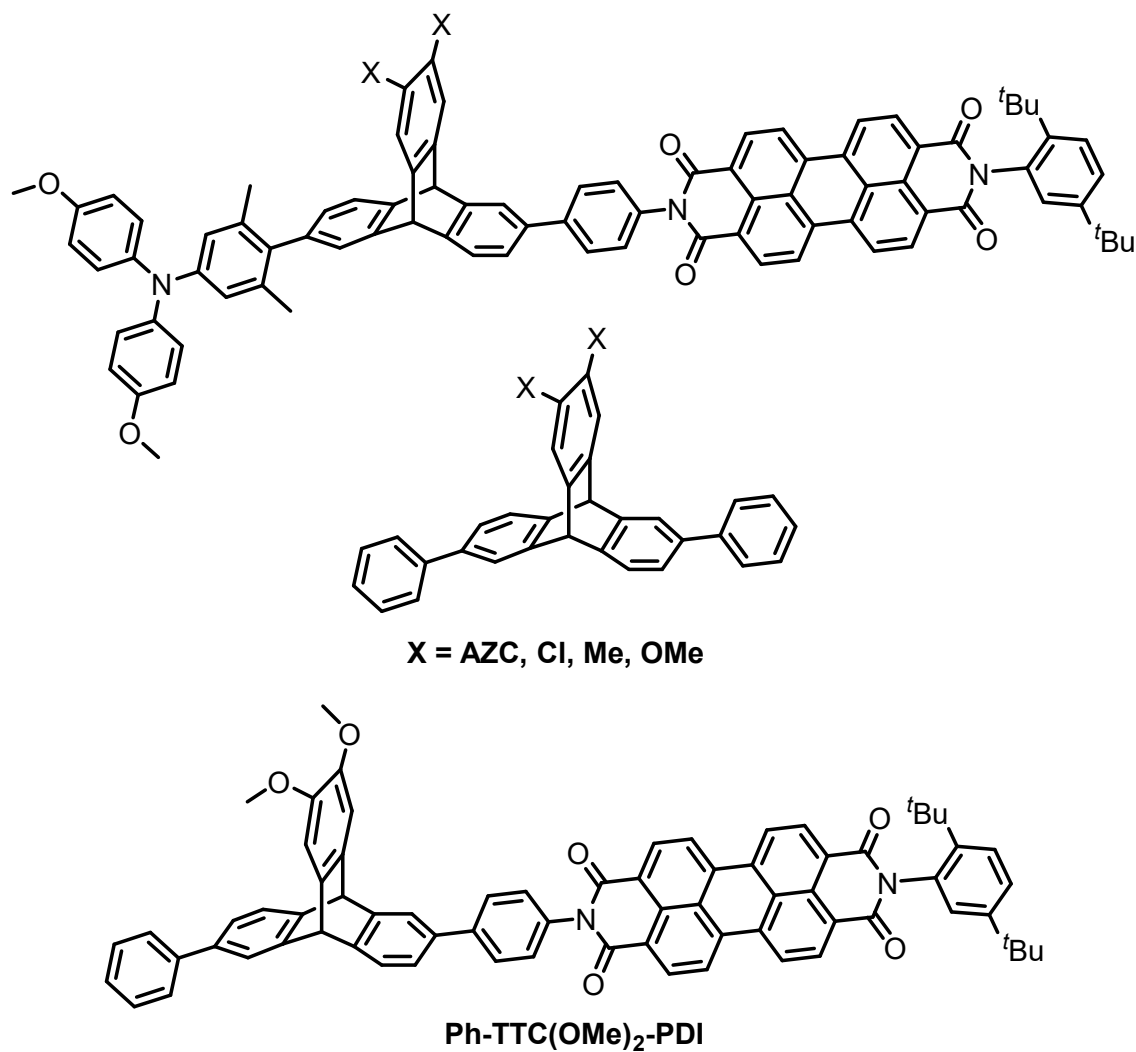
Three series of molecules and the respective bridge reference compounds were synthesised to investigate the influence of rotational hindrance and varying electron density.

The influence of rotational restriction (**chapter 6**) is investigated by tuning the dihedral angle between the **TAA** and the **TTC** as well as between the **TTC** and the **PDI** by attaching *ortho*-methyl groups at the phenylene linkers at the connecting ends to the **TTC** bridge, producing a twist around the linking single bond and therefore minimising the  $\pi$ -overlap (**Figure 13**). Thus, the triads exhibit different degrees of rotational restriction.



**Figure 13:** Series of rotationally hindered triads and reference compound to investigate the influence of rotational restriction.

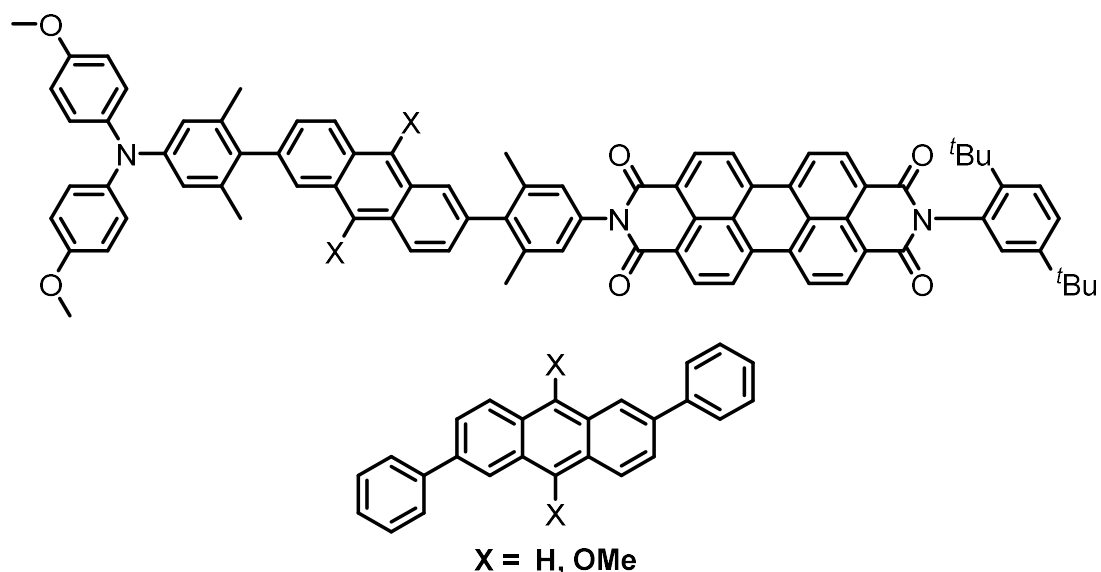
In the series of substituted triptycene triads (**chapter 7**) the impact of different electron densities in the connecting bridge between donor and acceptor is investigated. This is achieved by adjusting the electron density in the **TTC** bridging unit by adding electron donating groups (OMe, Me) and electron withdrawing groups (Cl, AZC) to the 12,13-positions of the triptycene (**Figure 14**). Thus, the **TTC** bridges exhibit different HOMO/LUMO levels.



**Figure 14:** Series of substituted triptycene triads and reference compounds to investigate the influence of varying HOMO/LUMO levels.

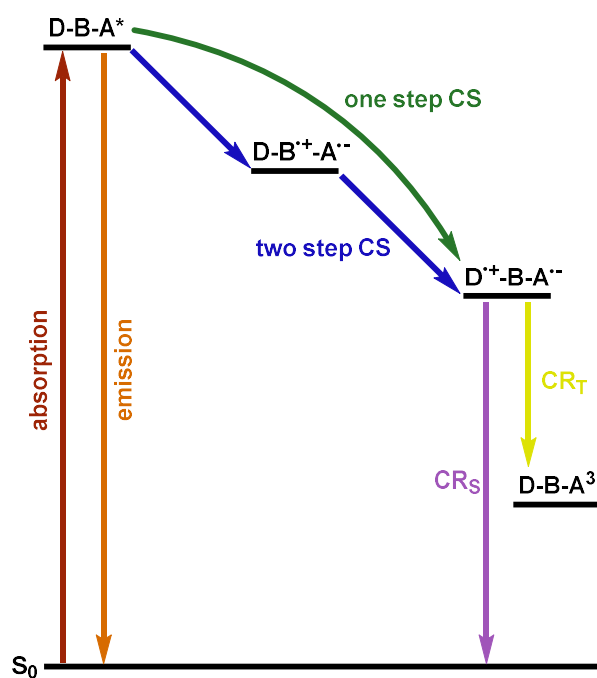
In the anthracene bridge triads (**chapter 8**), the influence of full rotational hindrance combined with varying electron density is investigated. The rotation of the donor and acceptor is prevented by methyl groups, while the electron density is increased by the addition of methoxy groups. (**Figure 15**).





**Figure 15:** Series of the anthracene bridge triads to investigate varying electron density combined with full rotational hindrance.

All investigated triads are structurally very similar. Therefore, the synthesis (**chapter 3**), absorption and emission properties (**chapter 4**) (red and orange arrows in **Figure 16**) as well as the redox properties (**chapter 5**) of all triads will be discussed together. Thereafter, the aforementioned three series of molecules, namely the rotationally hindered triads (**chapter 6**), the substituted triptycene triads (**chapter 7**) and the anthracene bridge triads (**chapter 8**), will be discussed in separate chapters. Those chapters are all structured in the same way. To get a clear overview of all ET processes in the triads, the CSS energies are calculated and the CR dynamics are assigned to the *Marcus* regions. The CS dynamics are investigated using fs-transient absorption (TA) spectroscopy (green and blue arrows in **Figure 16**) and the rate constants for CS are calculated using a global target analysis. The following CR dynamics upon depopulation of the CSS are investigated using magnetic field dependent ns-TA spectroscopy (purple and yellow arrows in **Figure 16**). The CR dynamics of the ns-TA data are further examined by a quantum mechanical simulation to extract the rate constants for CR. Finally, the electronic couplings between the involved states are calculated for the CS and CR processes.



**Figure 16:** Possible photophysical processes in the investigated D-B-A triads.

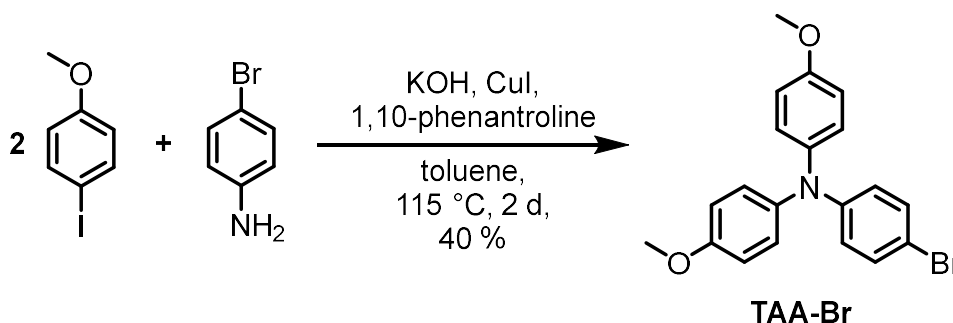
### 3 Synthesis

Due to the structural similarity of all investigated triads, the synthesis is very similar and therefore will be discussed together.

Since the synthesis of the separate building blocks, namely the triaryl amine donor (**TAA**)<sup>[47, 83, 144-148]</sup>, the perylene diimide acceptor (**PDI**)<sup>[149-153]</sup> and the triptycene bridging unit (**TTC**)<sup>[115, 129, 154-156]</sup>, are well known in literature, the building blocks were synthesised following the literature, and subsequently coupled via *Suzuki Miyaura* coupling, according to general procedure **GP III** (section 10.4.1).

#### 3.1 Synthesis of the triarylamine donor units

The one-step synthesis of the non-methylated donor moiety **TAA-Br** was done by an *Ullmann*-condensation reaction using 4-bromoaniline with two equivalents of 4-iodoanisole as educts. Copper (I) catalysis was used with KOH as the base and 1,10-phenanthroline as the ligand (**Figure 17**). The product was isolated with a yield of 40 %.<sup>[157]</sup>



**Figure 17:** *Ullmann*-condensation reaction for **TAA-Br**.

The methylated donor building block **TAAMe<sub>2</sub>-Br** was synthesised in two steps (**Figure 18**). The reaction conditions of the first step are the same as for the **TAA-Br** synthesis but 3,5-dimethylaniline was used instead of 4-bromoaniline.<sup>[157]</sup> This *Ullmann*-condensation yielded only 12 % of **TAA-Me<sub>2</sub>**. The second step was a bromination reaction with NBS<sup>[158]</sup>, from which the product **TAAMe<sub>2</sub>-Br** was isolated with a yield of 70 %.

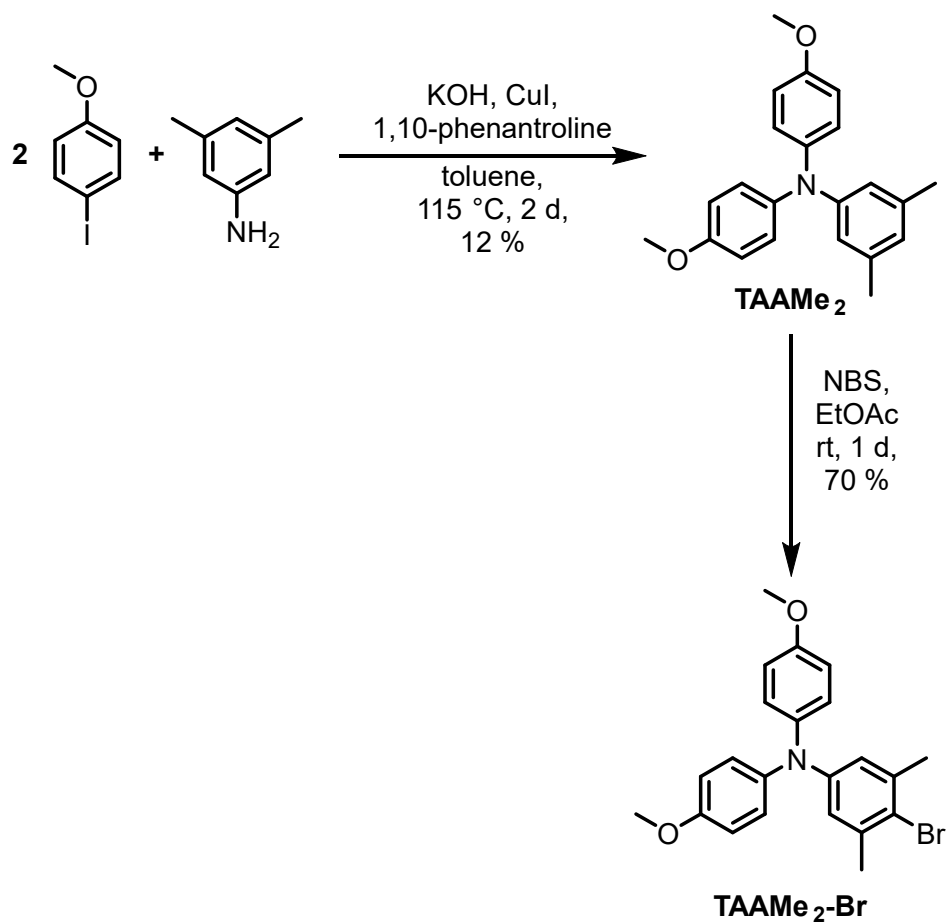


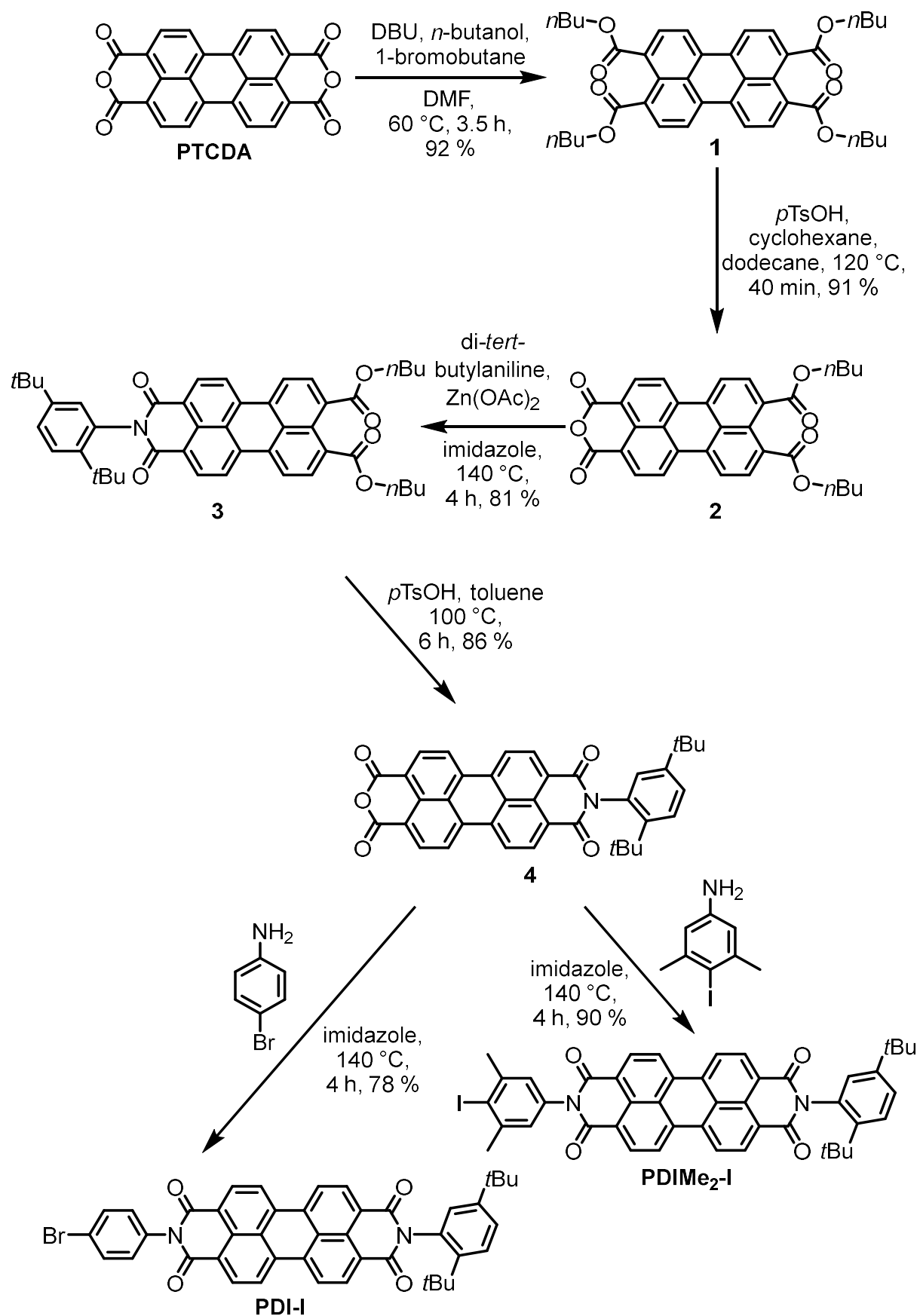
Figure 18: Synthesis of the **TAAMe<sub>2</sub>-Br** moiety.

### 3.2 Synthesis of the perylene diimide acceptor units

To synthesise the **PDI** moieties, **PDIME<sub>2</sub>-I** and **PDI-I** (**Figure 19**), a five-step synthesis was used, starting with the perylene tetracarboxylic dianhydride (PTCDA) (**Figure 19**). PTCDA was converted into its tetra-ester **1** (yield 92 %) using DBU as a non-nucleophilic base in a mixture of *n*-butanol and 1-bromobutane in DMF.<sup>[159]</sup> The saponification to the mono-anhydride diester derivative was carried out in a highly concentrated solution of the tetra-ester in a mixture of cyclohexane and dodecane (10:1) as reported by *Webb* et al.<sup>[152]</sup> The principle of this reaction is based on the different solubilities of product and reactant. Here, the product precipitates by adding one equivalent of *p*-toluene sulfonic acid monohydrate, resulting in 9,10-di(carboxylic acid butyl ester) perylene-3,4-anhydride **2** (91 %). The third step was the imidisation reaction of **2** with 2,5-di-*tert*-butyl aniline in imidazole at 130 °C, using zinc acetate as a catalyst to enhance the reactivity. This step yielded 81 % of 9,10-di(carboxylic acid butyl ester)-*N'*-(2,5-di-*tert*-butyl phenyl) perylene imide **3**. The following saponification with an excess of *p*-toluene sulfonic acid monohydrate in toluene yielded 86 % of *N*-(2,5-di-*tert*-butyl phenyl)-3,4-peryleneimide-anhydride **4**. The last step was a second imidisation reaction of **4** with either *p*-iodoaniline or 4-iodo-3,5-dimethyl aniline in imidazole at 140 °C to give the desired **PDI** building blocks. This step yielded 78 % **PDI-I** and 90 % **PDIME<sub>2</sub>-I**.<sup>6[48, 88, 160]</sup>

---

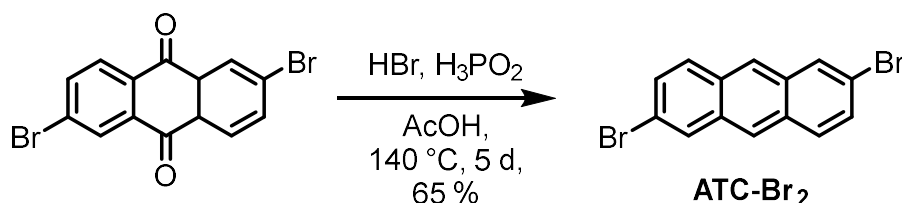
<sup>6</sup> This synthetic route was improved by *D. Mims*, who described the difficulties of other synthetic approaches and highlighted the advantage of the herein described route in his doctoral thesis.



**Figure 19:** Synthetic route of the PDI building blocks.

### 3.3 Synthesis of the bridging units

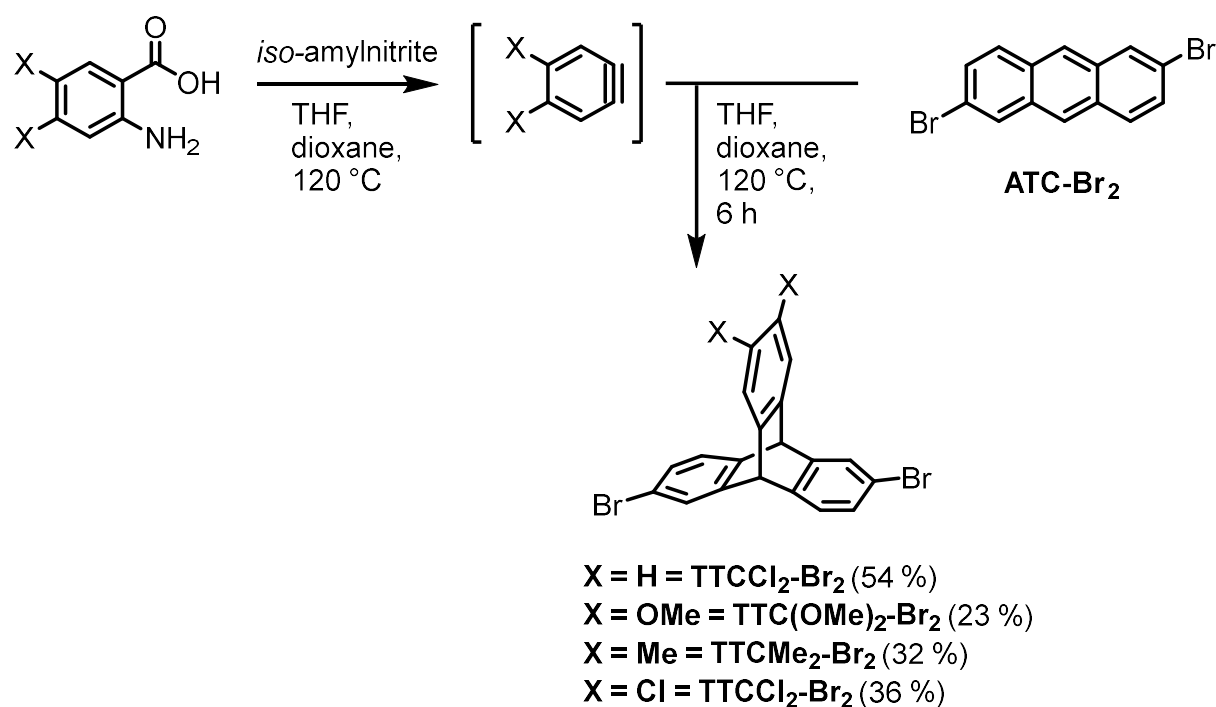
To synthesise the bridging unit, 2,6-dibromoanthraquinone was dissolved in acidic acid, hydrobromic acid and phosphinic acid and then heated to 140 °C for 5 days to yield 2,6-dibromoanthracene (**ATC-Br<sub>2</sub>**) with 65 % (**Figure 20**).<sup>[161]</sup>



**Figure 20:** Reduction of 2,6-dibromoanthraquinone to 2,6-dibromoanthracene under acidic conditions.

The second step of the bridge syntheses was the *Diels-Alder* reaction of the previously synthesised **ATC-Br<sub>2</sub>** with the anthranilic acid derivatives (**Figure 21**). The non-commercially available acid (4,5-dimethyl-anthranilic acid) was synthesised as described by *Shionoya et al.*<sup>[162]</sup> The literature known synthesis was optimized.<sup>[154-155]</sup> A concentrated solution of **ATC-Br<sub>2</sub>** in dioxane was heated to 120 °C and the anthranilic acid derivatives as well as *iso*-amyl nitrite were added simultaneously. The former was added via syringe pump and the latter via a syringe in portions every 10 minutes over a period of 6 hours, which is described in **GP I**. *iso*-amyl nitrite was used in a large excess because decomposition started at about 60 °C, which was indicated by the formation of nitrogen oxides in the reaction flask. A decrease of the temperature was, however, not possible because below 100 °C no product formation was observed. This approach yielded **TTC-Br<sub>2</sub>** with 54 %. The bridging unit **TTC(OMe)<sub>2</sub>-Br<sub>2</sub>** with strong electron donating groups, **TTCMe<sub>2</sub>-Br<sub>2</sub>** with weak electron donating groups and **TTCCl<sub>2</sub>-Br<sub>2</sub>** with weak electron withdrawing groups were obtained with 23 %, 32 % and 36 % yield, respectively. The temperature increase was necessary because of the reduced electron density of dibromo anthracene compared to unsubstituted anthracene used in literature.<sup>[155]</sup> Pure anthracene only requires a temperature of about 40 °C for the [4+2]-cycloaddition with benzyne, generated in situ from anthranilic acid and *iso*-amyl nitrite.<sup>[155]</sup> The reaction time was limited due to the necessity of the continuous addition of the nitrite. Due to the limited reaction time and therefore incomplete conversion, **ATC-Br<sub>2</sub>** always remained in the reaction mixture and had to be separated from the product before column chromatography. This was done by washing the product out of the reaction mixture using a solvent mixture of DCM/PE (v:v 1:20). In this mixture the brominated triptycene derivatives are moderately soluble, but **ATC-Br<sub>2</sub>** is poorly soluble. Consequently, only a small amount of **ATC** remained in the crude product, which made the column chromatography possible. Without the washing step **ATC-Br<sub>2</sub>**

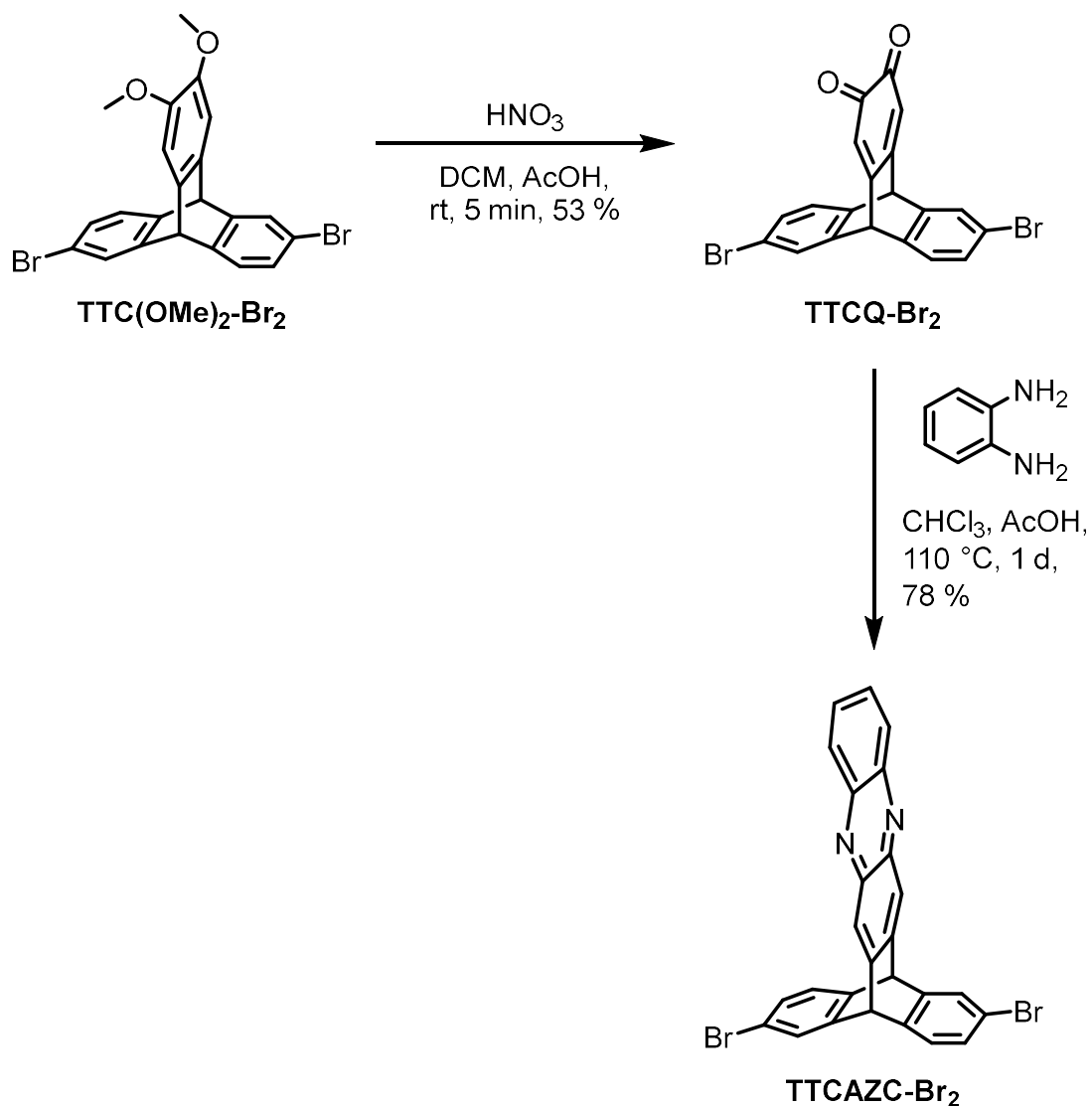
precipitates out of the used solvent mixture at the top of the column and then dissolves in small amounts during column chromatography, consequently the purification would not be possible.



**Figure 21:** Schematic representation of the *Diels-Alder* reaction of the anthranilic acid derivatives with 2,6-dibromoanthracene to the substituted bridging units.

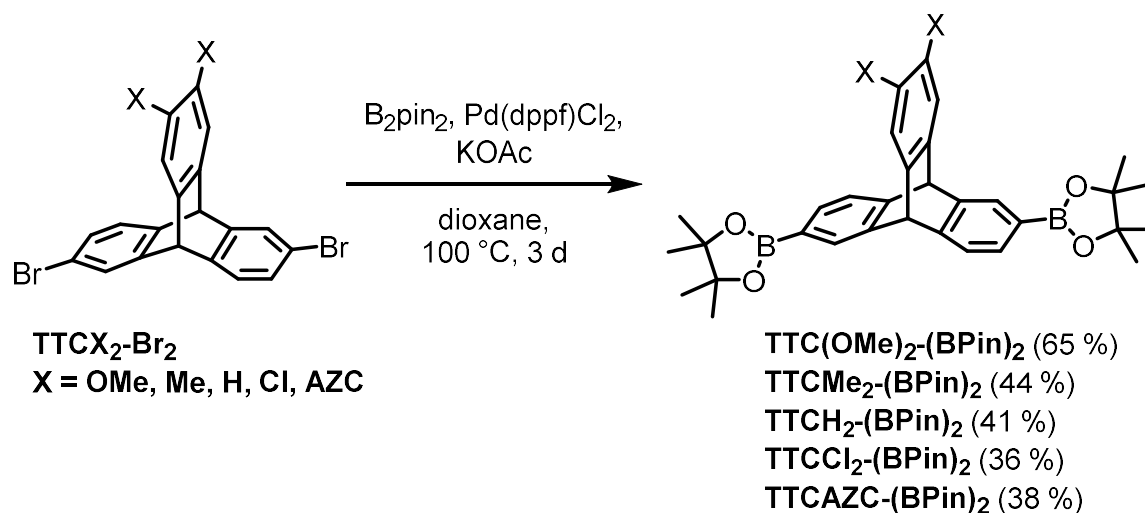
As a strong electron acceptor, a triptycene-azaacene derivative (AZC) **TTCAZC-Br<sub>2</sub>** was synthesised (**Figure 22**). To gain the azaacene moiety attached to the triptycene core, the first step was the oxidation of **TTC(OMe)<sub>2</sub>-Br<sub>2</sub>** with concentrated nitric acid in acidic acid resulting in the *ortho*-quinone derivative **TTCQ-Br<sub>2</sub>** with 53 % yield. The phenazine was subsequently synthesised by the condensation reaction of **TTCQ-Br<sub>2</sub>** with *ortho*-phenylenediamine under acidic conditions to yield 78 % of **TTCAZC-Br<sub>2</sub>**.<sup>[143]</sup>





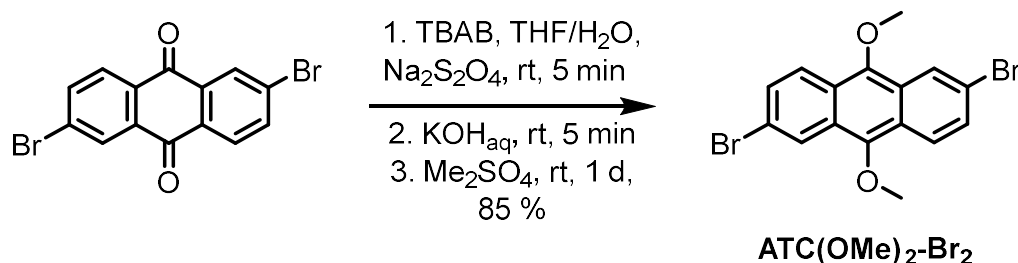
**Figure 22:** Synthetic route to obtain the triptycene-azaacene derivative bridging unit.

The last step of the bridge synthesis was the palladium catalysed borylation reaction of the brominated triptycene derivatives with bis(pinacolato)diboron to **TTC-(Bpin)<sub>2</sub>** (41%), **TTC(OMe)<sub>2</sub>-(Bpin)<sub>2</sub>** (65%), **TTCMe<sub>2</sub>-(Bpin)<sub>2</sub>** (44%), **TTCCl<sub>2</sub>-(Bpin)<sub>2</sub>** (36%) and **TTCAZC-(Bpin)<sub>2</sub>** (38%) (**Figure 23**).<sup>[163]</sup> This reaction is given in **GP II (section 10.4.1.2)**.



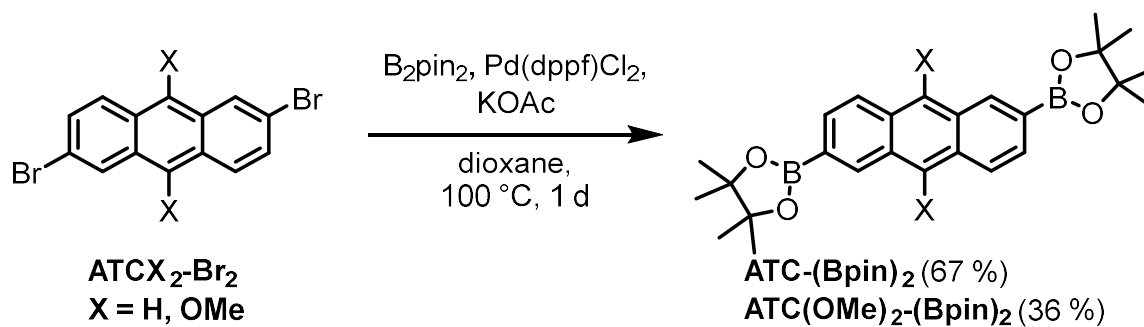
**Figure 23:** Borylation reaction of the substituted **TTC** bridging units.

Two approaches were tested to synthesise the 9,10-methoxy substituted anthracene bridge. First, the reaction conditions reported by *Anthony* et al. were tested, using dimethyl sulphate as a methylating reagent and lithium diisopropyl amide, which only resulted in yields of about 4 %.<sup>[164]</sup> The reductive methylation technique reported by *Kraus* and *Man*, on the other hand, yielded **ATC(OMe)<sub>2</sub>-Br<sub>2</sub>** in 85 % (**Figure 24**).<sup>[165]</sup> Here, dimethyl sulphate was used as a methylation reagent. The phase transfer catalyst tetrabutylammonium bromide was used to improve the solubility of the anion of the reduced quinone.



**Figure 24:** Methylation reaction of 2,6-dibromoanthraquinone.

The borylation reaction of both anthracene derivatives was performed using **GP II** and yielded 67 % **ATC-(BPin)<sub>2</sub>** and 36 % **ATC(OMe)<sub>2</sub>-(BPin)<sub>2</sub>** (**Figure 25**).

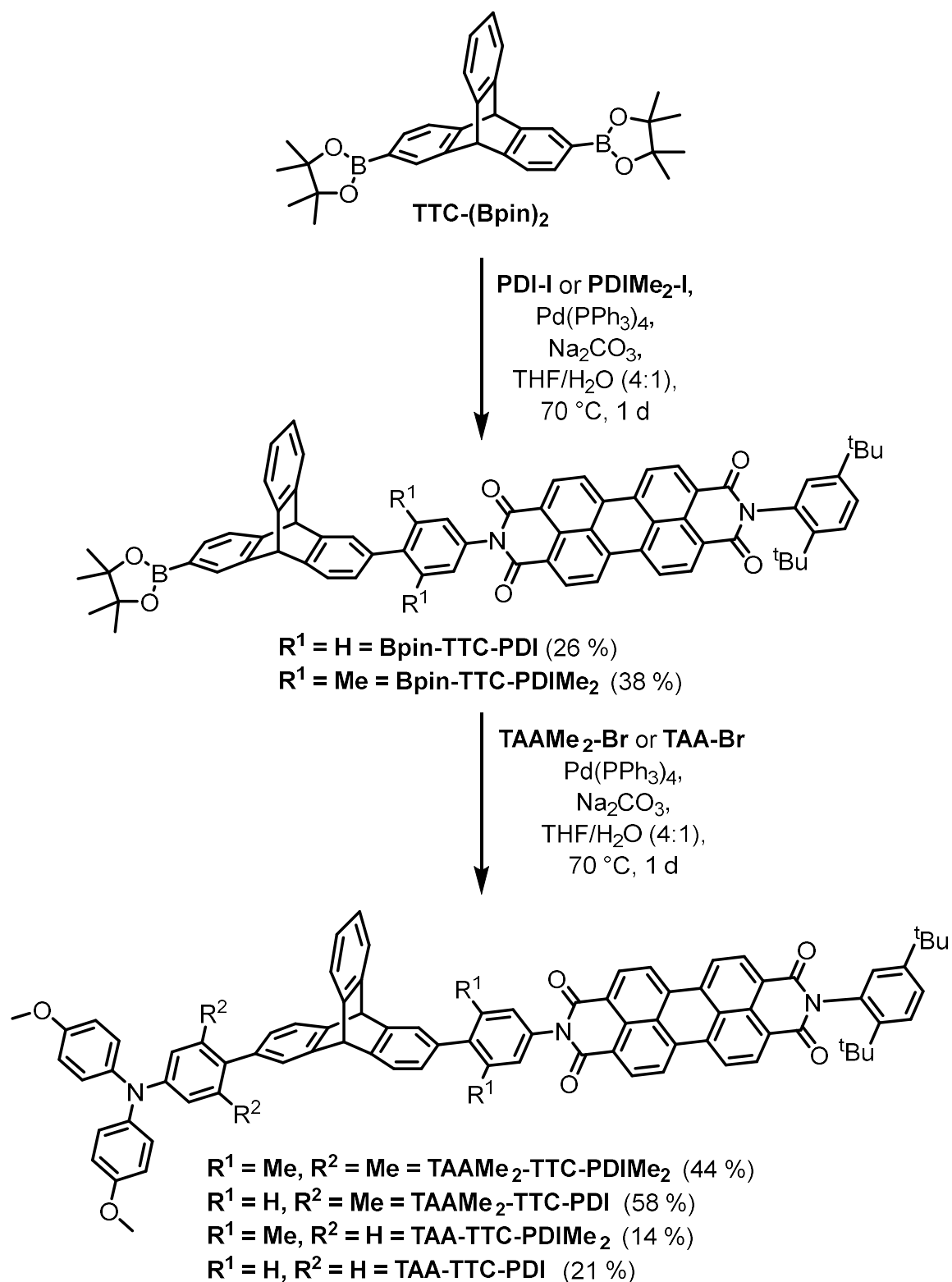


**Figure 25:** Borylation reaction of the anthracene derivatives.

### 3.4 Synthesis of the triads

#### 3.4.1 Rotationally hindered triads

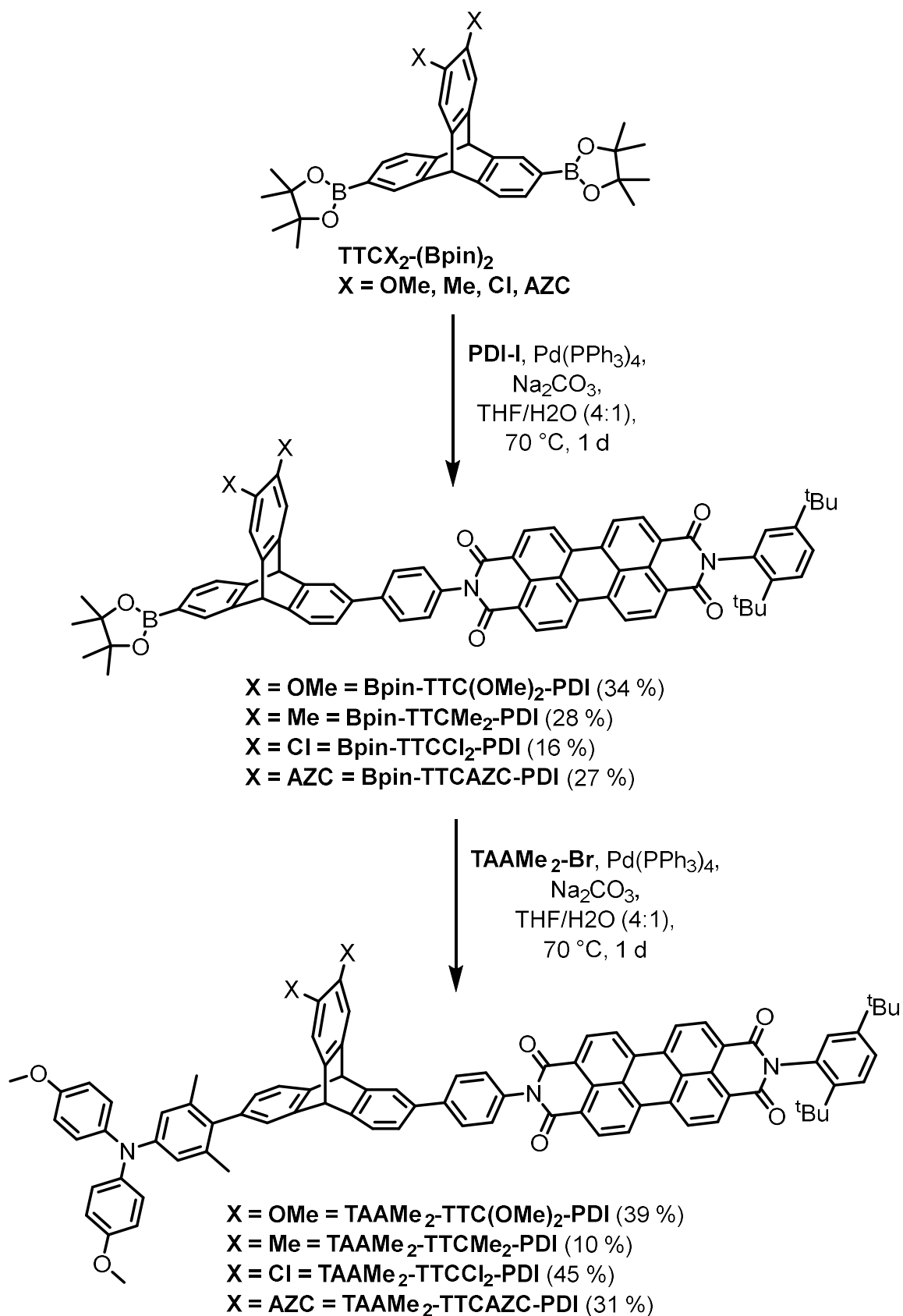
The triads were synthesised by first linking the respective **PDI** building block to the borylated bridging unit via *Suzuki Miyaura* coupling, followed by the coupling of the respective **TAA** moiety (**Figure 26**). The conditions for the *Suzuki Miyaura* coupling reaction is given in **GP III**.<sup>[163]</sup> The bridge was used in an excess to avoid coupling of the **PDI** at both sides of the bridging unit. However, in none of the cases the formation of this side products could completely be avoided, which reduced the yields for this step. The *Suzuki* coupling reaction of the **TTC** bridging unit with the respective **PDI** moieties gave **Bpin-TTC-PDI** with 26 % and **Bpin-TTC-PDIME<sub>2</sub>** with 38 % yield. The attempt of first coupling the **TAA** moiety to the bridge resulted in worse yields for the first coupling step. In the second coupling reaction, on one hand, **Bpin-TTC-PDI** was coupled with **TAAME<sub>2</sub>-Br** and **TAA-Br**, resulting in the respective triads **TAAME<sub>2</sub>-TTC-PDI** (58 %) and **TAA-TTC-PDI** (21 %). On the other hand, **Bpin-TTC-PDIME<sub>2</sub>** was coupled with both **TAA** building blocks to yield **TAAME<sub>2</sub>-TTC-PDIME<sub>2</sub>** (44 %) and **TAA-TTC-PDIME<sub>2</sub>** (14 %). Comparing those four coupling reactions, the yields were better using the methylated **TAA** species, which could be explained by the more effective oxidative addition to the catalytic system due to the higher electron density of the coupling reactant. Longer reaction times did not result in higher yields, but in decomposition of the precursor.



**Figure 26:** Synthetic route of the rotationally hindered triads.

### 3.4.2 Substituted triptycene triads

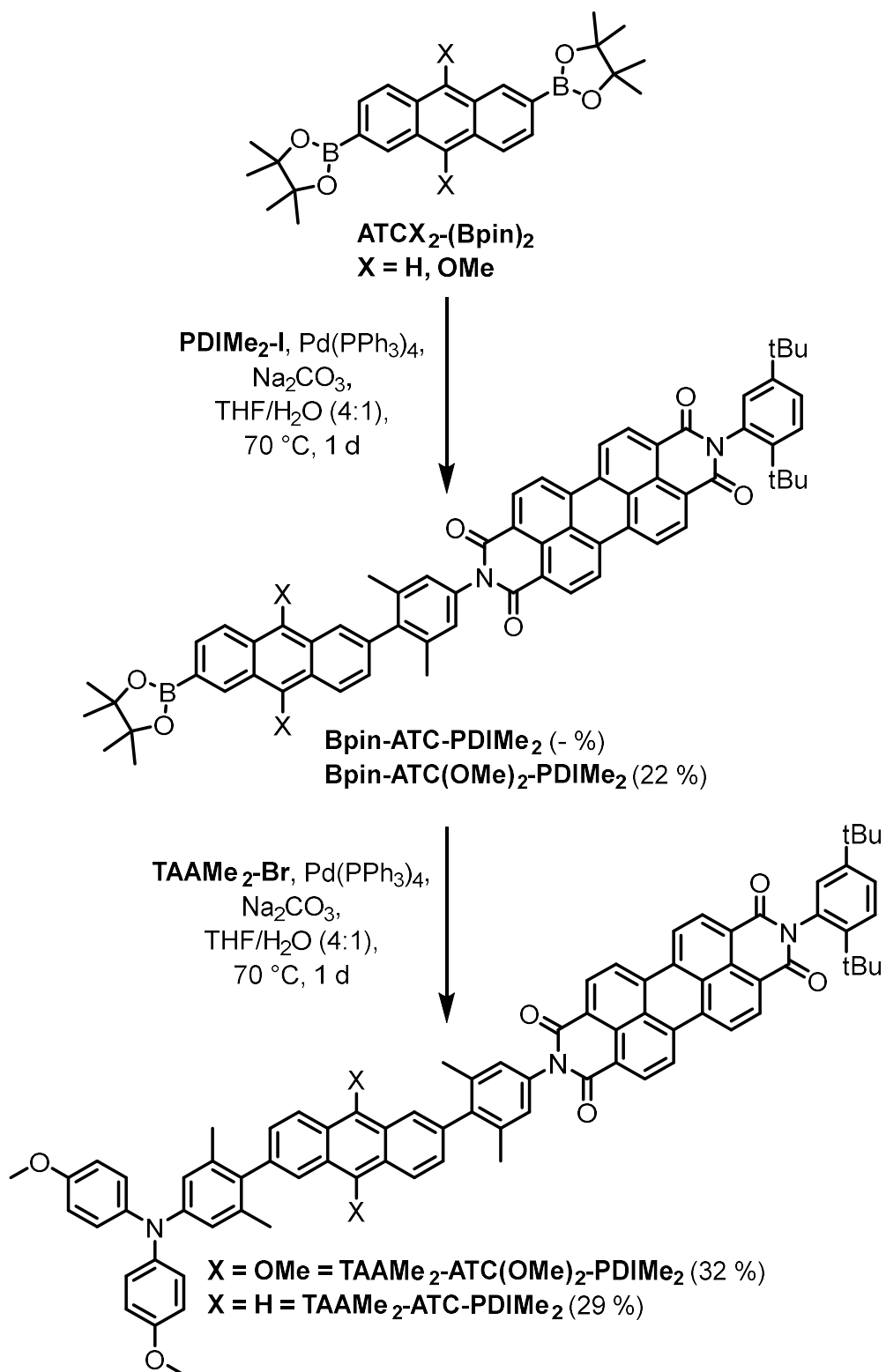
The synthesis of the substituted triptycene triads was done analogous to the synthesis described for the rotationally hindered triads. All borylated bridging units (**TTC(OMe)<sub>2</sub>(Bpin)<sub>2</sub>**, **TTCMe<sub>2</sub>(Bpin)<sub>2</sub>**, **TTCCl<sub>2</sub>(Bpin)<sub>2</sub>** and **TTCAZC-(Bpin)<sub>2</sub>**) were first coupled with **PDI-I** and afterwards with **TAAMe<sub>2</sub>-Br** (**Figure 27**). The first coupling reaction with die **PDI-I** moiety yielded **(Bpin)-TTC(OMe)<sub>2</sub>-PDI** (34 %), **(Bpin)-TTCMe<sub>2</sub>-PDI** (28 %), **(Bpin)-TTCCl<sub>2</sub>-PDI** (16 %) and **(Bpin)-TTCAZC-PDI** (27 %). As described before the bridging unit was used in excess but two times coupling of the **PDI** moiety to the different bridges could never completely be avoided, which decreased the yields. The second coupling reaction of the respective precursors with **TAAMe<sub>2</sub>-Br** gave **TTAMe<sub>2</sub>-TTC(OMe)<sub>2</sub>-PDI** (39 %), **TTAMe<sub>2</sub>-TTCMe<sub>2</sub>-PDI** (10 %), **TTAMe<sub>2</sub>-TTCCl<sub>2</sub>-PDI** (45 %) and **TTAMe<sub>2</sub>-TTCAZC-PDI** (31 %).



**Figure 27:** Synthetic route to prepare the substituted TTC triads.

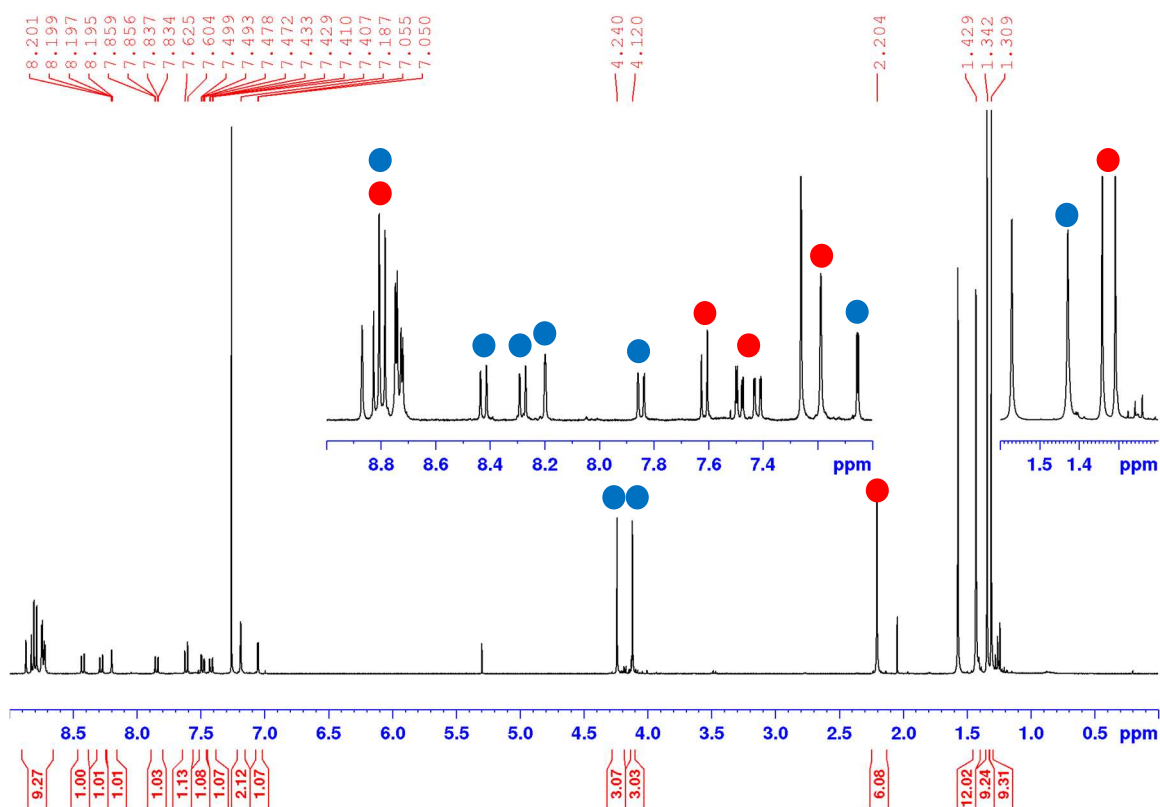
### 3.4.3 Anthracene bridge triads

The anthracene bridge triads were synthesised using **GP III** by two consecutive *Suzuki* coupling reactions similar as previously discussed (**Figure 28**).<sup>[163]</sup> For the synthesis of **(Bpin)-ATC-PDIME<sub>2</sub>** the reaction mixture needed to be highly concentrated (124 mM) to make the *Suzuki* coupling reaction work. Furthermore, the purification of this precursor was not possible due to a side product that could not be separated from the product neither by column chromatography, or recrystallisation, nor by GPC using diverse solvents. Thus, no <sup>13</sup>C NMR of **(Bpin)-ATC-PDIME<sub>2</sub>** was measured and the next coupling reaction with **TAAME<sub>2</sub>-Br** was performed with the remaining impurities. The second coupling reaction, however, yielded 32 % of **TAAME<sub>2</sub>-ATC-PDIME<sub>2</sub>** and the impurities of the precursor step could be removed. **(Bpin)-ATC(OMe)<sub>2</sub>-PDIME<sub>2</sub>** was synthesised with higher dilution (19.4 mM) and a reaction time was reduced to 2 hours, which resulted in 22 % yield. Longer reaction times only led to complete decomposition. The second coupling reaction with **TAAME<sub>2</sub>-Br** yielded 29 % of **TAAME<sub>2</sub>-ATC(OMe)<sub>2</sub>-PDIME<sub>2</sub>**. The methoxy substituted precursor and the triad were very unstable in solution, therefore, no <sup>13</sup>C NMR was measured of either of the two intermediates but <sup>1</sup>H NMR (**Figure 29**) and mass confirmed the formation of the precursor. The successful coupling of the **TAAME<sub>2</sub>** moiety forming the triad could be proved by <sup>1</sup>H NMR (**Figure 30**), by clear **TAAME<sub>2</sub>** signals. In **Figure 29** the red dots refer to the proton signals of the **PDI** moiety and the blue dots to the methoxy substituted bridge. All six aromatic proton signals can be found in the region between 7.00 and 9.00 ppm. The two signals for the methoxy groups in 9,10-position of the anthracene can be found at 4.12 ppm and 4.24 ppm as well as the signal for the Bpin group at 1.43 ppm. The integral of 12 for the Bpin group indicates the successful one time coupling of **PDI** to the bridge. The attachment of the **TAAME<sub>2</sub>** building block to the precursor was shown by <sup>1</sup>H NMR (**Figure 30**) by the distinctive AA'/BB' signals of the triaryl amine at 6.84 ppm and 7.10 ppm as well as the signal at 3.81 ppm, referring to the **TAA** methoxy groups.

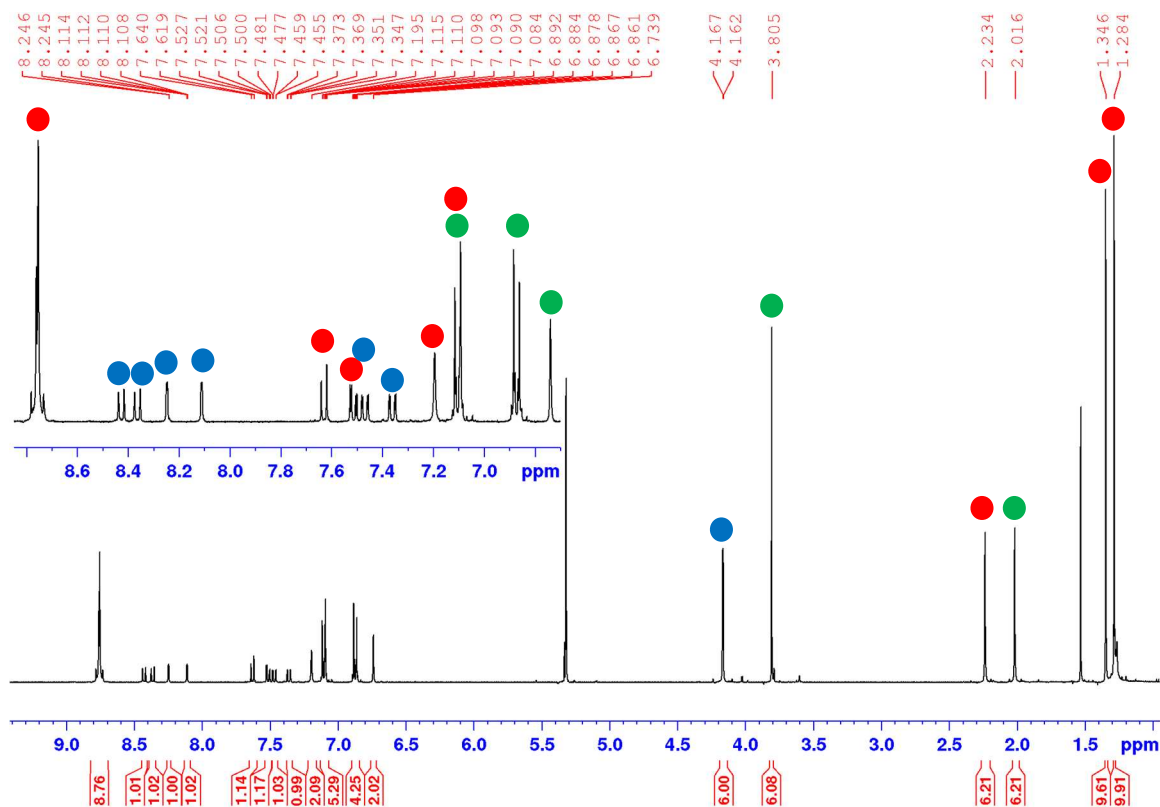


**Figure 28:** Synthetic route for the anthracene bridge triads.





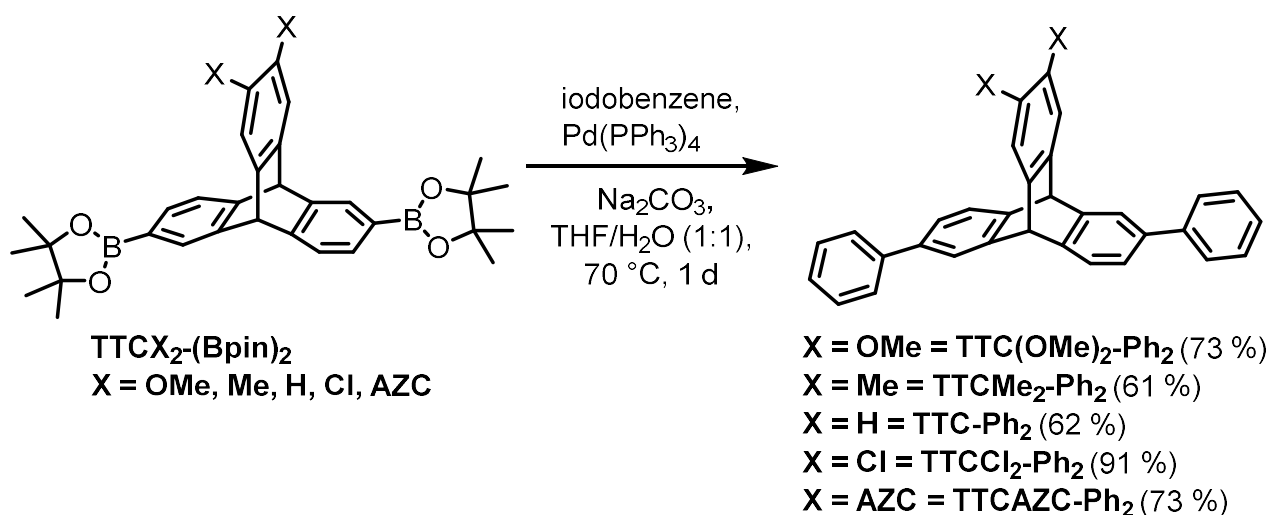
**Figure 29:**  $^1\text{H}$  NMR spectrum of **(Bpin)-ATC(OMe) $_2$ -PDIME $_2$** . The red dots refer to the **PDI** protons and the blue ones to the bridge protons.



**Figure 30:**  $^1\text{H}$  NMR spectrum of **TAAME $_2$ -ATC(OMe) $_2$ -PDIME $_2$** . The red dots refer to the **PDIME $_2$**  protons, the blue ones to the bridge protons and the green ones to the **TAAME $_2$** .

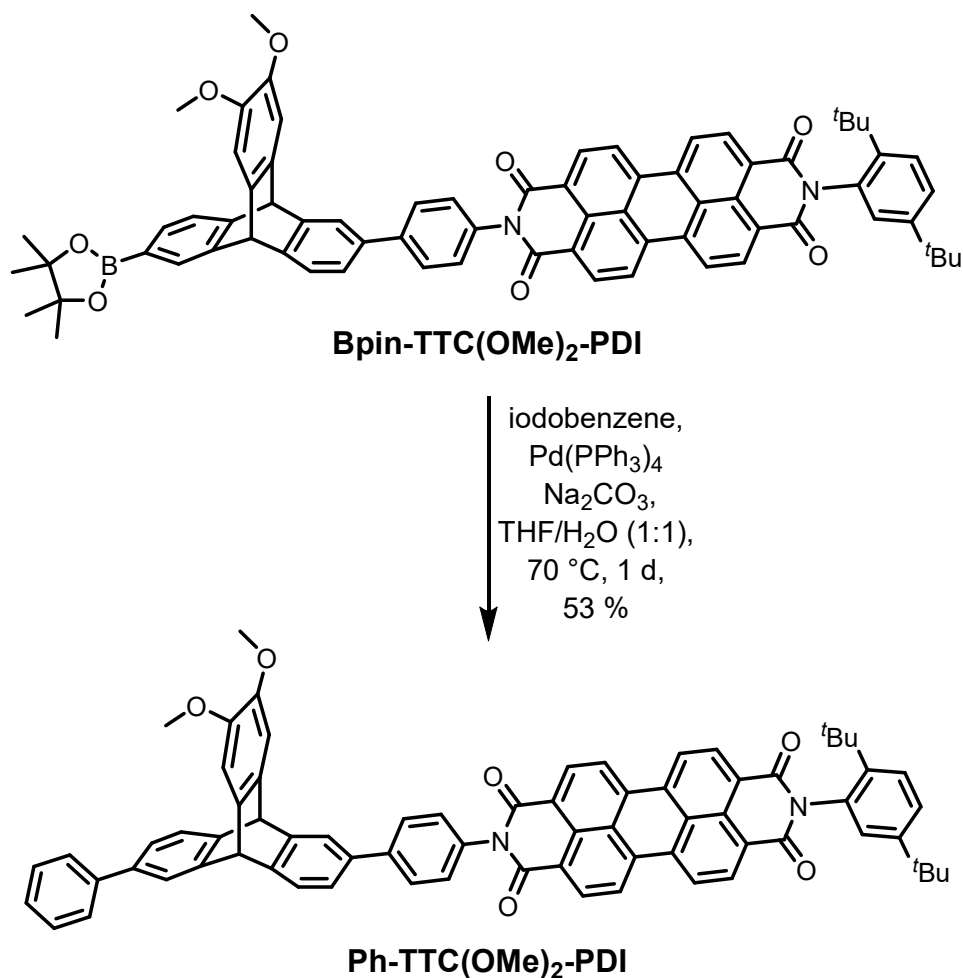
### 3.5 Synthesis of the reference compounds

To synthesise the reference compounds the borylated triptycene derivatives were coupled using a *Suzuki* coupling reaction with iodobenzene (according to **GP III**)<sup>[163]</sup> and yielded **TTC(OMe)<sub>2</sub>-Ph<sub>2</sub>** (73 %), **TTCMe<sub>2</sub>-Ph<sub>2</sub>** (61 %), **TTC-Ph<sub>2</sub>** (62 %), **TTCCl<sub>2</sub>-Ph<sub>2</sub>** (91 %), **TTCAZC-Ph<sub>2</sub>** (73 %).



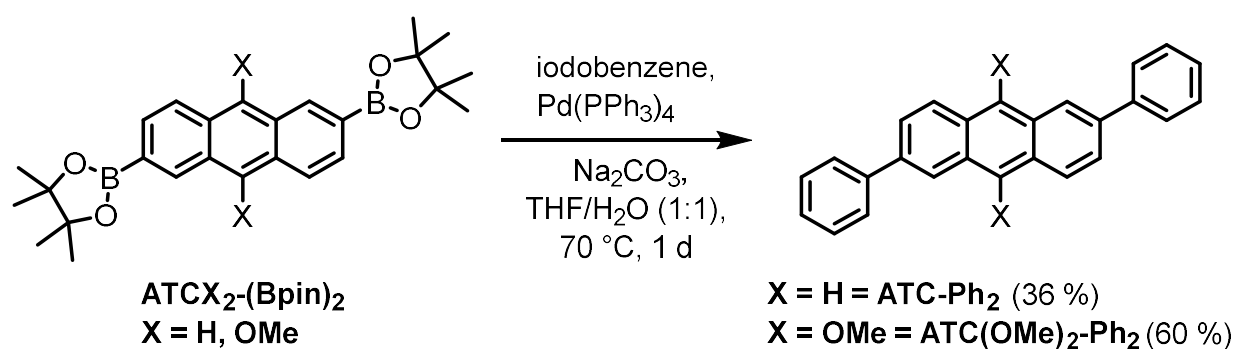
**Figure 31:** Synthesis of the **TTC** reference compounds.

The reference compound consisting of the methoxy substituted bridging unit and the **PDI** acceptor was synthesised by coupling **(Bpin)-TTC(OMe)<sub>2</sub>-PDI** to iodobenzene by a *Suzuki* coupling reaction (according to **GP III**)<sup>[163]</sup> This reaction yielded **Ph-TTC(OMe)<sub>2</sub>-PDI** with 53 %.



**Figure 32:** Synthesis of the **Ph-TTC(OMe)<sub>2</sub>-PDI** reference compound.

The anthracene reference compounds were synthesised via *Suzuki* coupling reaction with iodobenzene (**Figure 33**) as described in **GP III**.<sup>[163]</sup> Both reference compounds **ATC-Ph<sub>2</sub>** and **ATC(OMe)<sub>2</sub>-Ph<sub>2</sub>** were isolated providing 36 % and 60 % yield, respectively.



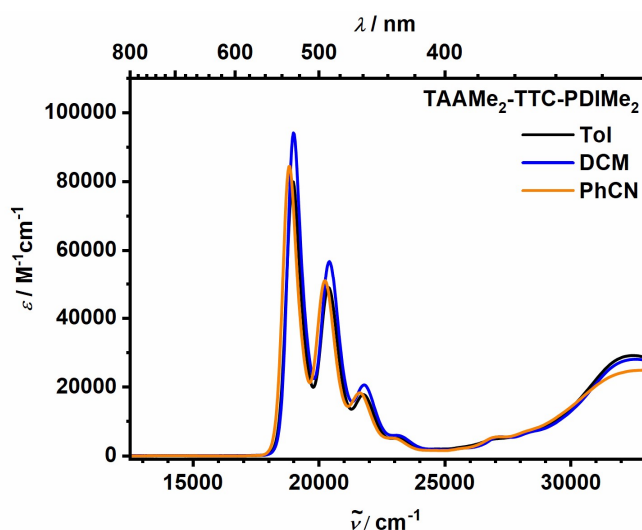
**Figure 33:** Synthesis of the ATC reference compounds.

## 4 Steady-state absorption and emission spectroscopy

Due to the structural similarity of all investigated triads, the steady-state absorption and emission data are very similar and therefore will be discussed together.

### 4.1 Steady-state absorption spectroscopy

In order to investigate the absorption properties steady-state absorption spectra were measured of all triads (**Table 1**). To account for polarity effects, the spectra were measured in three different solvents with increasing polarities, namely toluene, DCM and PhCN. In all solvents a series of concentrations between  $10^{-7}$  –  $10^{-5}$  M was measured to check for aggregation effects, which are known for PDI systems.<sup>[166-170]</sup> However, the investigated triads showed no aggregation effects in the investigated concentration range (example see **Appendix**). Since the absorption spectra of all investigated triads are very similar, only **TAAMe<sub>2</sub>-TTC-PDIME<sub>2</sub>** is shown exemplarily and the absorption spectra of the other triads can be found in the **Appendix (Figure A2, Figure A3 and Figure A4)**.



**Figure 34:** Steady-state absorption spectra of **TAAMe<sub>2</sub>-TTC-PDIME<sub>2</sub>** in toluene (black), DCM (blue) and PhCN (orange) at 298 K.

The **PDI** absorption is located in the lower energetic region between 18000 and 24000  $\text{cm}^{-1}$  (556-417 nm) with the maximum absorption band (0-0-transition) at 18900  $\text{cm}^{-1}$  (528 nm) for all triads. The  $S_1 \leftarrow S_0$  transition of the **PDI** shows the typical vibronic progression with the respective higher transitions with gaps of 1400  $\text{cm}^{-1}$  (0-1: 20400  $\text{cm}^{-1}$  (490 nm), 0-2: 21800  $\text{cm}^{-1}$  (459 nm), 0-3: 23200  $\text{cm}^{-1}$  (431 nm)). The extinction coefficient is approximately 100000  $\text{M}^{-1}\text{cm}^{-1}$  for all triads.<sup>[48, 88, 160, 166]</sup> The **PDI** absorption does neither change due to steric effects caused by the attachment of methyl groups nor due to electronic changes in the bridging unit. This can be explained by the nodal planes of the HOMO and LUMO of the **PDI** acceptor, which cause a strong decoupling from the rest of the triad.<sup>[167, 171]</sup>

In all triads the higher energetic absorption band ( $> 30000 \text{ cm}^{-1}$ , 333 nm) is caused by the **TAA** moiety. Here, the absorption of the **TTC** bridging unit, which is located in the same area, is superimposed by the **TAA** absorption because of its much higher absorption coefficient (approx.  $30000 \text{ M}^{-1}\text{cm}^{-1}$  between  $32000 - 28000 \text{ cm}^{-1}$ , 313-357 nm) compared to the bridging units absorption coefficients (compare to reference compounds in **Table 2**, spectra in the **Appendix** in **Figure A5** and **Figure A6**). Due to the  $C_2$ -symmetry of the **TAA** building block there are two possible transitions. First, the HOMO-LUMO transition ( $S_1 \leftarrow S_0$ ), which is polarised in the direction of the bridging unit and possesses CT character. The possible CT character of the **TAA** absorption is indicated by a bathochromic shift of the absorption maximum. The spectral position of this absorption band is strongly dependent on the electronic coupling between the donor and the bridge.<sup>[47]</sup> Second, the HOMO-LUMO+1 transition ( $S_2 \leftarrow S_0$ ), which is located in the  $\pi$ - $\pi^*$ -system of the dianisyl part of the **TAA**.<sup>[111, 146]</sup> The **TAA** absorption bands in the triads with methyl groups attached to the **TAA** moiety (rotationally hindered triads **TAAMe<sub>2</sub>-TTC-PDIME<sub>2</sub>** and **TAAMe<sub>2</sub>-TTC-PDI** in **Figure A2 A/B** and all substituted triptycene and anthracene bridge triads in **Figure A3** and **Figure A4**) do not show CT-character, which is caused by the almost orthogonal structure of **TAA** and **TTC/ATC**, which destabilises a possible CT-state. The triads without *ortho*-methyl groups attached to the **TAA** moiety (**TAA-TTC-PDIME<sub>2</sub>** and **TAA-TTC-PDI** in **Figure A2 C/D**), on the other hand, show a bathochromic shift of the **TAA** absorption band probably caused by a CT-state. The CT-band indicates an enhanced electronic coupling between the **TAA** and the bridge in those triads.<sup>[88, 158, 172]</sup>

The absorption spectra of most of the triads consist of two separate parts, which can be assigned to the **PDI** and the **TAA** moiety. The triad **TAAMe<sub>2</sub>-TTCAZC-PDI** (**Figure A3 D**), however, shows three distinct absorption maxima, in which the **PDI** and **TAA** absorption are found in the same regions as in the other triads. The absorption between  $24000$  and  $31000 \text{ cm}^{-1}$  (416-323 nm) is caused by the  $\pi$ - $\pi^*$ -transition of the phenazine-like structure attached to the triptycene core of the bridge,<sup>[173-174]</sup> which is confirmed by the absorption spectrum of the reference compound **TTCAZC-Ph<sub>2</sub>** (**Table 2**, **Figure A5 E**).

The anthracene bridge triads show three absorption maxima as well. Here, the absorption between  $24000$  and  $30000 \text{ cm}^{-1}$  (417 nm-333 nm) is assigned to the anthracene bridge with its typical vibronic progression, which was also determined by the absorption spectra of the respective reference compounds (**Table 2**, **Figure A6**). The absorption spectrum of the methoxy substituted anthracene bridge is bathochromically shifted compared to the unsubstituted anthracene, which causes the better resolution of the vibronic fine structure of the bridging unit. Furthermore, because of this bathochromic shift the overlap with the **TAA** absorption is reduced.<sup>[175-177]</sup>

**Table 1:** Data of the steady-state absorption spectra of all triads with the corresponding absorption maxima  $\tilde{\nu}_{\max}$  of the **TAA** and the **PDI** moiety as well as the associated molar extinction coefficients  $\epsilon_{\max}$ .

	solvent	$\tilde{\nu}_{\max\text{PDI}}^a /$ $\text{cm}^{-1}$ ( $\lambda_{\max\text{PDI}} / \text{nm}$ )	$\epsilon_{\max\text{PDI}} /$ $\text{M}^{-1}\text{cm}^{-1}$	$\tilde{\nu}_{\max\text{TAA}} / \text{cm}^{-1}$ ( $\lambda_{\max\text{TAA}} / \text{nm}$ )	$\epsilon_{\max\text{TAA}} /$ $\text{M}^{-1}\text{cm}^{-1}$
<b>TAAMe<sub>2</sub>-TTC-PDIME<sub>2</sub></b>	toluene	18900 (528)	79900	32300 (309)	29200
	DCM	18900 (528)	94200	32300 (309)	28000
	PhCN	18800 (531)	84400	32300 (309)	24700
<b>TAAMe<sub>2</sub>-TTC-PDI</b>	toluene	18900 (528)	84400	-	-
	DCM	18900 (528)	98800	-	-
	PhCN	18800 (531)	87100	-	-
<b>TAA-TTC-PDIME<sub>2</sub></b>	toluene	18900 (528)	83000	29700 (336)	30600
	DCM	18900 (528)	96900	29800 (335)	30900
	PhCN	18800 (531)	84600	29400 (340)	26000
<b>TAA-TTC-PDI</b>	toluene	18900 (528)	84500	29600 (337)	30500
	DCM	18900 (528)	98400	29800 (335)	31400
	PhCN	18700 (534)	87900	29500 (338)	27400
<b>TAAMe<sub>2</sub>-TTC(OMe)<sub>2</sub>-PDI</b>	toluene	18900 (528)	82300	-	-
	DCM	18900 (528)	97200	-	-
	PhCN	18800 (531)	85600	-	-
<b>TAAMe<sub>2</sub>-TTCMe<sub>2</sub>-PDI</b>	toluene	18900 (528)	81000	-	-
	DCM	18900 (528)	93000	-	-
	PhCN	18800 (531)	82000	-	-
<b>TAAMe<sub>2</sub>-TTCCl<sub>2</sub>-PDI</b>	toluene	18900 (528)	85000	-	-
	DCM	19000 (527)	103100	-	-
	PhCN	18800 (531)	88600	-	-
<b>TAAMe<sub>2</sub>-TTCAZC-PDI<sup>b</sup></b>	toluene	18900 (528)	83800	-	-
	DCM	19000 (527)	95300	-	-
	PhCN	18800 (531)	85700	-	-
<b>TAAMe<sub>2</sub>-ATC-PDIME<sub>2</sub></b>	toluene	19000 (526)	84400	32800 (305)	34000
	DCM	19000 (526)	89600	32900 (304)	29500
	PhCN	18800 (532)	78400	-	-
<b>TAAMe<sub>2</sub>-ATC(OMe)<sub>2</sub>- PDIME<sub>2</sub></b>	toluene	19000 (526)	72600	-	-
	DCM	19000 (526)	77800	-	-
	PhCN	18800 (532)	73900	-	-

<sup>a</sup> Vibronic progression of the **PDI**. Only the transition with the lowest energy is given (0-0 transition). The higher energetic transitions ( $\nu = 1-3$ ) are 1400  $\text{cm}^{-1}$  apart from each other.

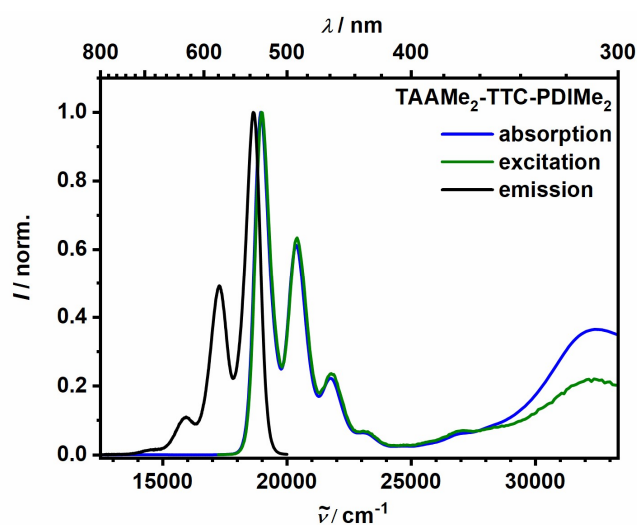
**Table 2:** Data of the steady-state absorption spectra of all reference compounds with the corresponding absorption maxima  $\tilde{\nu}_{\max}$  and the associated molar extinction coefficients  $\epsilon_{\max}$ .

	solvent	$\tilde{\nu}_{\max} / \text{cm}^{-1}$ ( $\lambda_{\max} / \text{nm}$ )	$\epsilon_{\max} /$ $\text{M}^{-1}\text{cm}^{-1}$	$\tilde{\nu}_{\max} / \text{cm}^{-1}$ ( $\lambda_{\max} / \text{nm}$ )	$\epsilon_{\max} /$ $\text{M}^{-1}\text{cm}^{-1}$
<b>TTC(OMe)<sub>2</sub>-Ph<sub>2</sub></b>	toluene	-	-	-	-
	DCM	33800 (296)	9300	39900 (251)	20100
<b>TTCMe<sub>2</sub>-Ph<sub>2</sub></b>	toluene	-	-	-	-
	DCM	34700 <sup>a</sup> (288)	17200	37500 (267)	25400
<b>TTC-Ph<sub>2</sub></b>	toluene	-	-	-	-
	DCM	-	-	38000 (263)	27700
<b>TTCCl<sub>2</sub>-Ph<sub>2</sub></b>	toluene	-	-	-	-
	DCM	34000 <sup>a</sup> (294) 35100 <sup>a</sup> (285)	10800 15200	37400 (267)	21300
<b>TTCAZC-Ph<sub>2</sub></b>	toluene	26000 <sup>b</sup> (385)	16300	-	-
	DCM	26000 <sup>b</sup> (385)	13700	38700 (258)	75000
<b>ATC(OMe)<sub>2</sub>-Ph<sub>2</sub></b>	toluene	25000 <sup>c</sup> (400)	5200	-	-
	DCM	25000 <sup>c</sup> (400)	4800	34000 (294)	77700
<b>ATC-Ph<sub>2</sub></b>	toluene	23500 <sup>c</sup> (426)	7400	33000 (303)	136000
	DCM	23500 <sup>c</sup> (426)	6100	33200 (301)	133600

<sup>a</sup> shoulder. <sup>b</sup> absorption from the phenazine moiety where only the max. absorption peak is given, the vibronic progression is not. <sup>c</sup> only the transition with the lowest energy is given. The higher transitions of the anthracene are 1400  $\text{cm}^{-1}$  apart from each other.<sup>[177]</sup>

## 4.2 Steady-state emission spectroscopy

The emission and excitation spectra of all triads were measured in highly diluted solutions ( $OD \leq 0.03$ ) in PhCN (**Figure A8**) or toluene (**Figure A7**, **Figure A9** and **Figure A10**). The quantum yields (QYs,  $\phi$ ) were determined using an integration sphere<sup>[178]</sup> in oxygen free solutions<sup>7</sup> in a range of  $OD = 0.25 - 1.00$  (**Table 3**). PDI dyes are known to have small Stokes shifts of about  $300 - 400 \text{ cm}^{-1}$ ,<sup>[149]</sup> therefore the emission spectra were measured after exciting the second absorption maximum of the **PDI** unit (0-1-transition,  $20400 \text{ cm}^{-1}$ ,  $490 \text{ nm}$ ). The emission spectra of all triads only show emission from the **PDI** moiety but no emission of the **TAA** or the bridge moiety. The **PDI** emission is the mirror image of its absorption.<sup>[48, 88, 149, 166-167, 179]</sup> The excitation spectra were recorded by probing in the second emission maximum (1-0-transition,  $16900 \text{ cm}^{-1}$ ,  $591 \text{ nm}$ ) of the **PDI**. The emission and excitation spectra of the investigated triads are very similar, therefore, the spectrum of **TAAMe<sub>2</sub>-TTC-PDIME<sub>2</sub>** in toluene is shown exemplarily and the emission/excitation spectra of the other triads can be found in the **Appendix (Figure A7, Figure A8, Figure A9 and Figure A10)**.



**Figure 35:** Normalised steady-state absorption (blue), excitation (green) and emission spectra (black) of **TAAMe<sub>2</sub>-TTC-PDIME<sub>2</sub>** in toluene at 298 K. Emission spectra were recorded after excitation at  $20400 \text{ cm}^{-1}$  ( $490 \text{ nm}$ , 0-1 absorption band of the **PDI**) and excitation spectra were recorded by probing at  $16900 \text{ cm}^{-1}$  ( $590 \text{ nm}$ , 1-0 emission band of the **PDI**).

The fluorescence QYs of all triads (**Table 3**) are significantly smaller compared to the QY of 0.97 of the pure PDI<sup>[48, 88, 166, 180]</sup>, which is a first indication for the existence of an alternative non-radiative quenching mechanism. The QYs of the triads are decreasing with increasing

<sup>7</sup> Oxygen was removed for all emission, QY, and excitation measurements to assure that no fluorescence or phosphorescence was quenched.



rotational freedom (rotationally hindered triads) or increasing electron density in the bridging unit (substituted triptycene triads).

The fluorescence QYs of the rotationally hindered triads in toluene are 0.26 for **TAAMe<sub>2</sub>-TTC-PDIME<sub>2</sub>**, which decreases along the series to 0.05 for **TAA-TTC-PDI**. The QYs in PhCN are on the same order of magnitude as the ones in toluene. The decrease of the fluorescence quantum yields is a first indication for an increase of the electronic coupling between the donor and acceptor state due to decreasing rotational hindrance.

In the series of substituted triptycene triads the methoxy substituted triad (**TAAMe<sub>2</sub>-TTC(OMe)<sub>2</sub>-PDI**) features a QY of about 0.01, increasing over the methylated (**TAAMe<sub>2</sub>-TTCMe<sub>2</sub>-PDI**, 0.03), the unsubstituted (**TAAMe<sub>2</sub>-TTC-PDI**, 0.04), the chlorinated (**TAAMe<sub>2</sub>-TTCCl<sub>2</sub>-PDI**, 0.08) to the azaacene substituted triad (**TAAMe<sub>2</sub>-TTCAZC-PDI**, 0.09). The increase of the fluorescence quantum yield is a first indication for a decreasing electronic coupling due to diminished electron density in the bridging unit.

In the anthracene substituted triads the QY is 0.07 for **TAAMe<sub>2</sub>-ATC-PDIME<sub>2</sub>** and 0.23 for **TAAMe<sub>2</sub>-ATC(OMe)<sub>2</sub>-PDIME<sub>2</sub>**.

The excitation spectra of the triads indicate that the energy transfer from the **TAA** to the **PDI** moiety in toluene is good (**Figure A7**, **Figure A9** and **Figure A10**) but ineffective in PhCN (**Figure A8**). No clear trend along any of the series of triads in the different solvents is observed.

**Table 3:** Data of the steady-state emission spectra of all investigated triads. Fluorescence maximum  $\tilde{\nu}_{\max\text{PDI}}$  of the **PDI** moiety and emission quantum yields of the triads.

	solvent	$\tilde{\nu}_{\max\text{PDI}}^a / \text{cm}^{-1}$ ( $\lambda_{\max\text{PDI}} / \text{nm}$ )	$\phi_f$
<b>TAAMe<sub>2</sub>-TTC-PDIME<sub>2</sub></b>	toluene	18600 (537)	0.26
	PhCN	18500 (540)	0.39
<b>TAAMe<sub>2</sub>-TTC-PDI</b>	toluene	18600 (537)	0.04
	PhCN	18500 (540)	0.06
<b>TAA-TTC-PDIME<sub>2</sub></b>	toluene	18600 (537)	0.11
	PhCN	18500 (540)	0.18
<b>TAA-TTC-PDI</b>	toluene	18600 (537)	0.05
	PhCN	18500 (540)	0.04
<b>TAAMe<sub>2</sub>-TTC(OMe)<sub>2</sub>-PDI</b>	toluene	18600 (537)	0.01
<b>TAAMe<sub>2</sub>-TTCMe<sub>2</sub>-PDI</b>	toluene	18600 (537)	0.03
<b>TAAMe<sub>2</sub>-TTCCl<sub>2</sub>-PDI</b>	toluene	18600 (537)	0.08
<b>TAAMe<sub>2</sub>-TTCAZC-PDI</b>	toluene	18600 (537)	0.09
<b>TAAMe<sub>2</sub>-ATC-PDIME<sub>2</sub></b>	toluene	18600 (537)	0.07
<b>TAAMe<sub>2</sub>-ATC(OMe)<sub>2</sub>-PDIME<sub>2</sub></b>	toluene	18600 (537)	0.23

<sup>a</sup> Vibronic progression of the **PDI**. Only the transition with the highest energy is given (0-0 transition). The lower energetic transitions ( $\nu = 1-3$ ) are 1400  $\text{cm}^{-1}$  apart from each other.

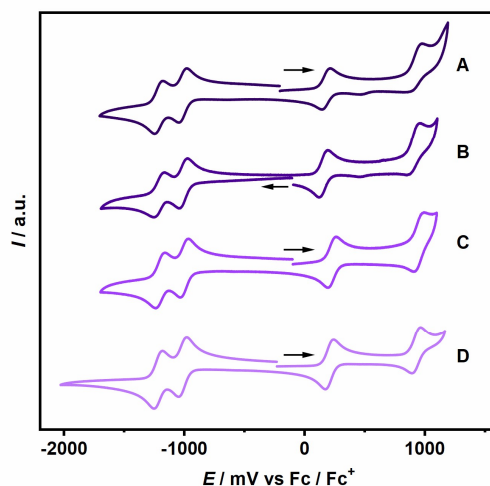
## 5 Cyclic voltammetry

The data of the cyclic voltammetry measurements are very similar due to the structural similarity of the triads and therefore will be discussed together as well.

The strongly decreased fluorescence QYs of all triads are indicative for the existence of an alternative non-radiative quenching mechanism, which could be the formation of a CSS. In order to determine the energetic position of a possible CSS with the *Weller* approach (**equation (24)** in **section 10.1**) the redox potentials of each triad are needed. Therefore, the electrochemical properties of the triads and the reference compounds were investigated using cyclic voltammetry (**Figure 36**, **Figure 37**, **Figure 38** and **Table 4**). All cyclic voltammograms were measured in DCM with 0.2 M TBAHFP (tetrabutylammonium hexafluorophosphate) as a supporting electrolyte under argon atmosphere at 298 K. All measurements were referenced to the ferrocene/ferrocenium (Fc/Fc<sup>+</sup>) redox couple and measured with a scan rate of 100 mV s<sup>-1</sup>. The chemical reversibility of each redox process was tested using multicycle thin layer experiments (minimum 10 cycles).

The two reduction potentials at about -1000 and -1200 mV are identical of all triads within the measurement error. This observation indicates that those potentials are associated to a building block that is identical in all triads. By comparison with the literature, these reduction potentials can be assigned to the **PDI** moiety.<sup>[48, 88, 160, 167, 179, 181]</sup> Those two reductions are fully reversible. The two oxidation potentials at approximately 200 and 900 mV refer to the **TAA** building blocks, whereby the first oxidation is reversible and the second is irreversible.<sup>[48, 144, 148, 160]</sup>

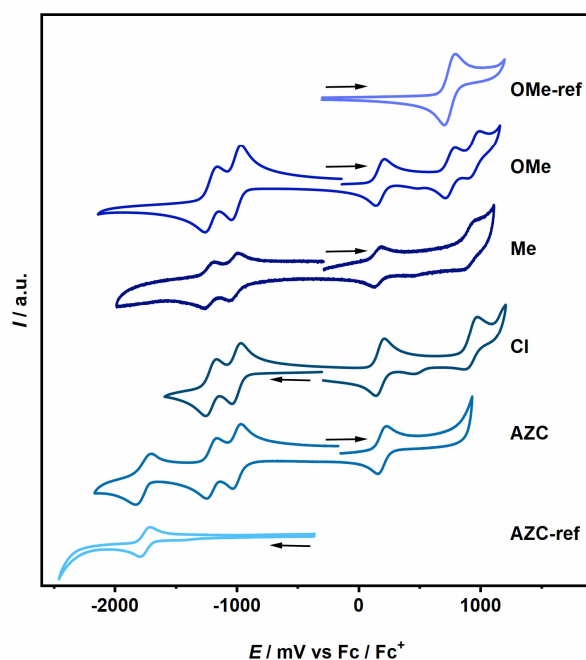
The oxidation potentials of the methylated **TAA**s in the rotationally hindered triads (**Figure 36**) are slightly negatively shifted due to the electron donating character of the attached methyl groups.<sup>[182]</sup> The **TTC** bridge does not exhibit reduction or oxidation potentials in the accessible potential range.



**Figure 36:** Cyclic Voltammetry of **A: TAAMe<sub>2</sub>-TTC-PDIME<sub>2</sub>**, **B: TAAMe<sub>2</sub>-TTC-PDI**, **C: TAA-TTC-PDIME<sub>2</sub>** and **D: TAA-TTC-PDI** in a solution of 0.2 M TBAHFP in DCM at 298 K referenced to Fc/Fc<sup>+</sup>. Black arrows indicate the start of the measurement. The reference compound **TTC-Ph<sub>2</sub>** does not exhibit redox potentials in the measured range.

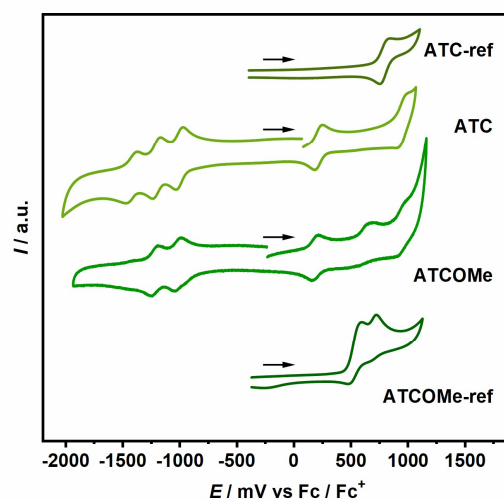
In the series of substituted triptycene triads **TAAMe<sub>2</sub>-TTC(OMe)<sub>2</sub>-PDI** (OMe in **Figure 37**) shows an additional oxidation potential at 749 mV, which is caused by the oxidation of the methoxy substituted bridging unit.<sup>[183-184]</sup> This was confirmed by the measurement of the reference compound **TTC(OMe)<sub>2</sub>-Ph<sub>2</sub>** (OMe-ref in **Figure 37**) showing the same oxidation potential. The third reduction potential that is visible in **TAAMe<sub>2</sub>-TTC-AZC-PDI** (AZC in **Figure 37**) at -1768 mV can be assigned to the reduction of the azaacene-like structure attached to the triptycene core, which was confirmed by the measurement of the reference compound **TTC-AZC-Ph<sub>2</sub>** (OMe-ref).<sup>[143]</sup> The other three bridge reference compounds do not show any redox potentials in the accessible potential range.

These results show that the investigated bridge substitutions cover the whole range of possible electron withdrawing and donating groups that can be attached to the bridging unit. The attachment of a better electron donor like a 5,10-dihydro-5,10-dimethylphenazine unit ( $E_{\text{ox}1} = -0.2$  V) would make the bridge a better donor than the **TAA** moiety.<sup>[185]</sup> Furthermore, replacing the phenazine-like structure with a furazan-quinoxaline unit ( $E_{\text{red}1} = -0.82$  V) would make it a better electron acceptor than the **PDI** unit.<sup>[143]</sup>



**Figure 37:** Cyclic Voltammetry of **TAAMe<sub>2</sub>-TTCX-PDI** (X = OMe, Me, Cl, AZC) in a solution of 0.2 M TBAHFP in DCM at 298 K and referenced against Fc/Fc<sup>+</sup>. Black arrows indicate the start of the measurement. AZC-ref and OMe-ref represent the reference compounds **TTCAZC-Ph<sub>2</sub>** and **TTC(OMe)<sub>2</sub>-Ph<sub>2</sub>** to check the potential of the pure bridging unit.

In the anthracene bridge triads the second oxidation at 621 mV of **TAAMe<sub>2</sub>-ATC(OMe)<sub>2</sub>-PDIME<sub>2</sub>** (ATCOMe in **Figure 38**) can be assigned to the irreversible oxidation of the methoxy substituted anthracene bridge, which is consistent with the oxidation of the reference compound (**Figure 38**, ATCOMe-ref). The second oxidation of this bridge is overlaid by the second oxidation of the **TAA** moiety, which are both irreversible. The reduction of the unsubstituted anthracene bridge is less obvious because the reference compound only shows oxidation at about 800 mV but the triad **TAAMe<sub>2</sub>-ATC-PDIME<sub>2</sub>** shows a reduction at -1417 mV caused by the anthracene. Thus, the redox potentials of the anthracene bridging unit are strongly dependent on the attached substituents.



**Figure 38:** Cyclic voltammetry of **TAAMe<sub>2</sub>-ATC-PDIME<sub>2</sub> (ATC)**, and **TAAMe<sub>2</sub>-ATC(OMe)<sub>2</sub>-PDIME<sub>2</sub> (ATCOMe)** in a solution of 0.2 M TBAHFP in DCM at 298 K and referenced against Fc/Fc<sup>+</sup>. Black arrows indicate the start of the measurement. The reference compounds are **ATC-Ph<sub>2</sub> (ATC-ref)** and **ATC(OMe)<sub>2</sub>-Ph<sub>2</sub> (ATCOMe-ref)**.

**Table 4:** Redox potentials of all triads measured with 0.2 M TBAHFP in DCM at 298 K. All voltammograms are measured with a scan rate of 100 mV s<sup>-1</sup> and referenced against Fc/Fc<sup>+</sup>.

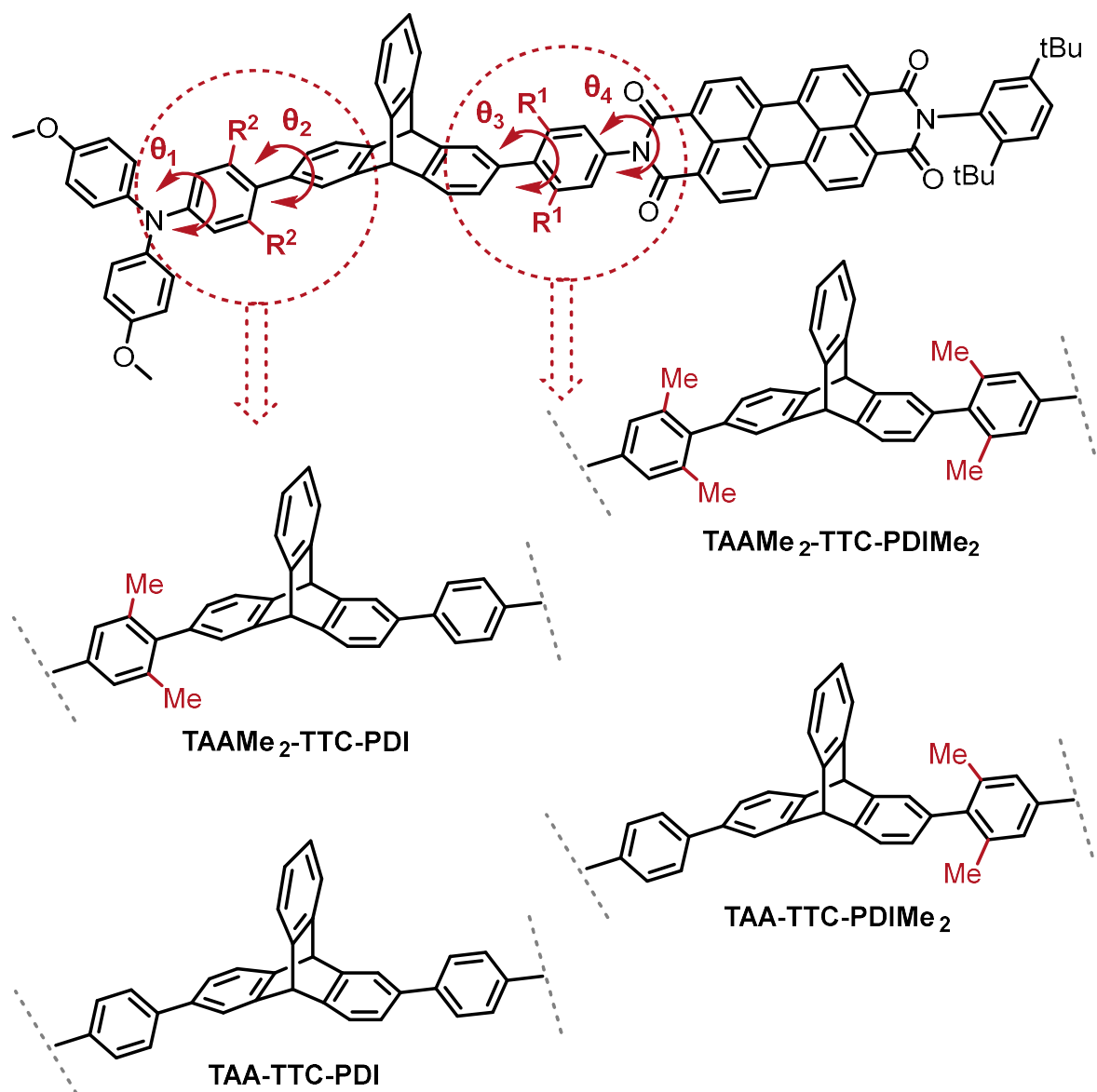
	$E_{1/2}$ / mV					
	ox <sub>1</sub>	ox <sub>2</sub>	ox <sub>3</sub>	red <sub>1</sub>	red <sub>2</sub>	red <sub>3</sub>
<b>TAAMe<sub>2</sub>-TTC-PDIME<sub>2</sub></b>	180 <sup>b</sup>	929 <sup>a,b</sup>		-1011 <sup>d</sup>	-1212 <sup>d</sup>	
<b>TAAMe<sub>2</sub>-TTC-PDI</b>	164 <sup>b</sup>	909 <sup>a,b</sup>		-1015 <sup>d</sup>	-1224 <sup>d</sup>	
<b>TAA-TTC-PDIME<sub>2</sub></b>	230 <sup>b</sup>	951 <sup>a,b</sup>		-997 <sup>d</sup>	-1200 <sup>d</sup>	
<b>TAA-TTC-PDI</b>	210 <sup>b</sup>	932 <sup>a,b</sup>		-1012 <sup>d</sup>	-1216 <sup>d</sup>	
<b>TAAMe<sub>2</sub>-TTC(OMe)<sub>2</sub>-PDI</b>	178 <sup>b</sup>	749 <sup>c</sup>	955 <sup>a,b</sup>	-1001 <sup>d</sup>	-1218 <sup>d</sup>	
<b>TAAMe<sub>2</sub>-TTCMe<sub>2</sub>-PDI</b>	156 <sup>b</sup>	909 <sup>a,b</sup>	-	-1020 <sup>d</sup>	-1222 <sup>d</sup>	-
<b>TAAMe<sub>2</sub>-TTCCl<sub>2</sub>-PDI</b>	179 <sup>b</sup>	924 <sup>a,b</sup>	-	-999 <sup>d</sup>	-1207	-
<b>TAAMe<sub>2</sub>-TTCAZC-PDI</b>	160 <sup>b</sup>	-	-	-1004 <sup>d</sup>	-1214 <sup>d</sup>	-1768 <sup>c</sup>
<b>TAAMe<sub>2</sub>-ATC-PDIME<sub>2</sub></b>	218 <sup>b</sup>	951 <sup>a,b</sup>	-	-1000 <sup>d</sup>	-1204 <sup>d</sup>	-1417 <sup>a,c</sup>
<b>TAAMe<sub>2</sub>-ATC(OMe)<sub>2</sub>-PDIME<sub>2</sub></b>	205 <sup>b</sup>	621 <sup>a,c</sup>	953 <sup>a,b</sup>	-1012 <sup>d</sup>	-1222 <sup>d</sup>	-

<sup>a</sup> irreversible. <sup>b</sup> TAA. <sup>c</sup> bridge. <sup>d</sup> PDI.

## 6 Rotationally hindered triads

Up to now the data of all triads were discussed together because of their strong similarity. From here each series will be discussed separately in order to highlight the influence of the different modifications within each series of molecules, starting with the rotationally hindered triads.

The introduction of methyl groups between two phenylene rings can be used to fine tune the electronic interaction between donor and acceptor units by adapting the dihedral angle between them.<sup>[91, 186]</sup> In the following section, the influence of intramolecular twisting of linked phenylene rings on electron transfer processes in a donor (**TAA**) - acceptor (**PDI**) system, using a triptycene (**TTC**) bridging unit was investigated. The **TTC** bridge was chosen because it keeps the donor and acceptor at a fixed distance but is electronically partially non-conjugating, which becomes important in regard of the electron transfer processes. In order to control the steric hindrance of the intramolecular twisting around the biaryl axes connecting the donor and acceptor to the **TTC**, methyl groups were introduced. A series of four molecules was synthesised, starting from the non-methylated triad **TAA-TTC-PDI**. In **TAAMe<sub>2</sub>-TTC-PDI** and **TAA-TTC-PDIME<sub>2</sub>** one of the two phenyl linkers attached to the **TTC** was *ortho*-substituted by two methyl groups and in **TAAMe<sub>2</sub>-TTC-PDIME<sub>2</sub>** both phenyl linkers were methyl substituted (**Figure 39**). This section was published in reference.<sup>[91]</sup>



**Figure 39:** Series of investigated rotationally hindered triads with the angles ( $\theta$ ) between the donor and acceptor, tuned by *ortho*-methyl groups. Average cosine-square products over the four angles ( $\Pi/\text{Cos}^2\theta_i$ ) are: **TAAMe<sub>2</sub>-TTC-PDIME<sub>2</sub>** (0.0017), **TAAMe<sub>2</sub>-TTC-PDI** (0.012), **TAA-TTC-PDIME<sub>2</sub>** (0.010), **TAA-TTC-PDI** (0.070). See supporting information of reference.<sup>[91]</sup>



## 6.1 Electron transfer processes

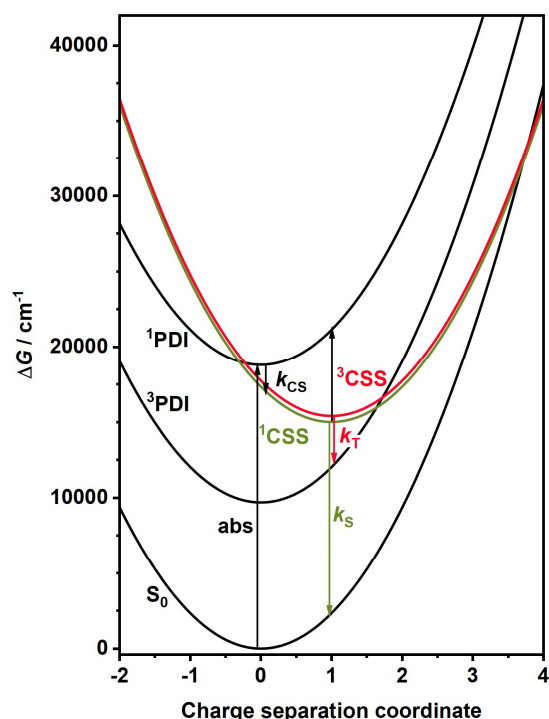
The steady-state emission spectroscopy data (**section 4.2**) already indicate the existence of an alternative non-radiative quenching mechanism in the series of rotationally hindered triads, which could be an electron transfer process. Thus, in order to investigate if electron transfer processes take place the energies of the states involved in the ET processes were considered and possible charge recombination pathways were assigned to the different *Marcus* regions. The formation of a possible CSS can be predicted based on the electrochemical data (**section 5**) and structure related parameters. The charge separation and the possible formation of a CSS were investigated using transient absorption (TA) spectroscopy in the femtosecond time range, showing that CSS formation is observed in all rotationally hindered triads. Thereafter, charge recombination (CR) from the CSS was investigated using ns-TA spectroscopy. The decay kinetics were furthermore investigated by the application of an external magnetic field, resulting in decay curves that exhibit a pronounced magnetic field dependence, giving information on the exchange interaction  $2J$  between  $^1\text{CSS}$  and  $^3\text{CSS}$ . These magnetic field dependent decay kinetics were simulated using quantum dynamical calculations. The quantum dynamic calculations as well as the global target analysis performed on the fs-TA measurements provide rate constants for the CS and CR processes, which were used to calculate the electronic couplings between the CSS and either its precursor or successor states. The calculations give insight into the influence of intramolecular twisting on the electronic couplings.

### 6.1.1 State energies

By calculating the CSS energies in toluene and PhCN, a first impression of whether the formation of a CSS is possible in the regarded solvents can be given. The energies of the CSSs (**Table 36** in **section 10.1**) can be determined from the oxidation and reduction potentials (**Table 4** in **section 5**) using the *Weller*-approximation<sup>8</sup> (**equation (24)** in **section 10.1**) and structure related parameters (state diagram with all regarded energies see **Figure 40**). The  $^1\text{PDI}$  state energy is at  $18800\text{ cm}^{-1}$  (2.33 eV) determined from the intersection of the normalised absorption and emission bands.<sup>[88, 187]</sup> Comparing the CSS energies (approximately  $15000\text{ cm}^{-1}$  (1.86 eV) in toluene and approximately  $8000\text{ cm}^{-1}$  (0.99 eV) in PhCN, see **Table 36** in **section 10.1**) to the  $^1\text{PDI}$  state energy ( $18800\text{ cm}^{-1}$ , 2.33 eV) shows that all CSS energies are located below the  $^1\text{PDI}$  energy, indicating that CS into the CSS is

<sup>8</sup> Calculated by Dr. M. Holzapfel.

possible for all rotationally hindered triads in both solvents. The CR to the  $S_0$  ground state from the CSS is always possible via the singlet pathway ( $CR_S$ ). Since spin interconversion from the singlet to the triplet CSS takes place (**section 1.1**), a possible local triplet state must be considered as possible CR pathway. The  ${}^3TAA$  state is too high in energy to play a role,<sup>[91]</sup> but CR into the lowest  ${}^3PDI$  state ( $9690\text{ cm}^{-1} \pm 810\text{ cm}^{-1}$ ,  $(1.2\text{ eV} \pm 0.1\text{ eV})$ )<sup>[188]</sup> could be possible. The determination of the  ${}^3PDI$  state energy is not possible using simple methods and therefore was taken from the literature.<sup>[188]</sup> Since the lowest energy level of the PDI triplet state is strongly located on the perylene core, the assumption can be made that this energy is not strongly dependent on the imide substituent or the used solvent, which makes it possible to take this energy level from literature.<sup>[189]</sup> Regarding the CSS energies in PhCN (approximately  $8000\text{ cm}^{-1}$ ,  $0.99\text{ eV}$ , **Table 36** in **section 10.1**) shows that the recombination into the lowest  ${}^3PDI$  state ( $9690\text{ cm}^{-1}$ ,  $1.2\text{ eV}$ ) is not possible because the latter is higher in energy. Therefore, CR in PhCN occurs only via the singlet pathway. In comparison to that, the CSS energies in toluene (approximately  $15000\text{ cm}^{-1}$ ,  $1.86\text{ eV}$ , **Table 36** in **section 10.1**) are higher in energy than the  ${}^3PDI$  state making CR via triplet pathway ( $CR_T$ ) possible.



**Figure 40:** Energy level diagram of the states involved in CS and CR with their respective reorganisation energy parabolas. The vertical arrows starting from the equilibrium position of the pertinent initial states depict the ET process.

In order to determine the efficiency of the CR pathways, the CR ET processes were assigned to the *Marcus* regions (**Table 5**). The *Marcus* theory relates electron transfer kinetics to their

compound- and solvent specific energy parameters. Here, the overall reorganization energy  $\lambda_{\text{tot}}$  is compared to the *Gibbs* energy  $\Delta G^{00}$  of the respective ET process. The reorganization energy is composed of the inner reorganization energy  $\lambda_{\text{v}}$ , (determined by quantum chemical optimisations using Gaussian09<sup>[190]</sup>)<sup>9</sup> and the outer reorganization energy  $\lambda_{\text{o}}$  (determined using the *Born*-approach **equation (25)** in **section 10.1**). The inner reorganization energy is 1855 cm<sup>-1</sup> (0.23 eV) and represents the changes of bond length and bond angles of the redox centres while changing their oxidation states. The outer reorganization energy in toluene is 484 cm<sup>-1</sup> (0.06 eV) and 7501 cm<sup>-1</sup> (0.93 eV) in PhCN and describes the reorientation of the solvent molecules induced by the charge redistribution due to the ET.<sup>[48, 88, 191-192]</sup> If  $\lambda_{\text{tot}} > -(\Delta G^{00})$  the ET takes place in the *Marcus* normal (norm.) region, if  $\lambda_{\text{tot}} < -(\Delta G^{00})$  the ET is in the *Marcus* inverted (inv.) region and if  $\lambda_{\text{tot}} \approx -(\Delta G^{00})$  the ET is in the optimal region meaning that the ET process is barrierless.

**Table 5:** *Gibbs* energies of the rotationally hindered triads of CS from <sup>1</sup>PDI to <sup>1</sup>CSS ( $\Delta G_{1\text{PDI-1CSS}}$ ) and of CR from <sup>1</sup>CSS to S<sub>0</sub> ( $\Delta G_{1\text{CSS-S}_0}$ ) or from <sup>3</sup>CSS to <sup>3</sup>PDI ( $\Delta G_{3\text{CSS-3PDI}}$ ) as well as the corresponding assignment of the respective transition in the *Marcus* region.

		$\Delta G_{1\text{PDI-1CSS}}$	$\Delta G_{1\text{CSS-S}_0}$	$\Delta G_{3\text{CSS-3PDI}}$	<i>Marcus</i> region		
		/ cm <sup>-1</sup>	/ cm <sup>-1</sup>	/ cm <sup>-1</sup>	CS	CR <sub>S</sub>	CR <sub>T</sub>
		(eV)	(eV)	(eV)			
<b>TAAMe<sub>2</sub>-TTC- PDIMe<sub>2</sub></b>	toluene	-3798 (-0.47)	-15002 (-1.86)	-5323 (-0.66)	inv.	inv.	inv.
	PhCN	-11138 (-1.38)	-7662 (-0.95)	-	inv.	norm.	-
<b>TAAMe<sub>2</sub>-TTC- PDI</b>	toluene	-3879 (-0.48)	-14921 (-1.85)	-5242 (-0.65)	inv.	inv.	inv.
	PhCN	-11218 (-1.39)	-7582 (-0.94)	-	inv.	norm.	-
<b>TAA-TTC- PDIMe<sub>2</sub></b>	toluene	-3476 (-0.43)	-15324 (-1.90)	-5645 (-0.70)	inv.	inv.	inv.
	PhCN	-10896 (-1.35)	-7904 (-0.98)	-	inv.	norm.	-
<b>TAA-TTC-PDI</b>	toluene	-3556 (-0.44)	-15244 (-1.89)	-5565 (-0.69)	inv.	inv.	inv.
	PhCN	-10898 (-1.35)	-7904 (-0.98)	-	inv.	norm.	-

$\lambda_{\text{v}} = 1855 \text{ cm}^{-1}$  (0.23 eV),  $\lambda_{\text{otol}} = 484 \text{ cm}^{-1}$  (0.06 eV),  $\lambda_{\text{oPhCN}} = 7501 \text{ cm}^{-1}$  (0.93 eV),  $\lambda_{\text{tottol}} = 2340 \text{ cm}^{-1}$  (0.29 eV),  $\lambda_{\text{totPhCN}} = 9356 \text{ cm}^{-1}$  (1.16 eV)

<sup>9</sup> Calculated by Dr. M. Holzapfel.

The CS process takes place in the *Marcus* inverted region in all triads in both solvents because  $\lambda_{\text{tot}} < -(\Delta G^{00})$ . As shown above, in PhCN the CSSs are lower in energy than the local  $^3\text{PDI}$  state and therefore CR is only possible via the singlet pathway. Comparing the overall reorganisation energy in PhCN ( $\lambda_{\text{totPhCN}}$ ,  $9356 \text{ cm}^{-1}$ ,  $1.16 \text{ eV}$ ) to the *Gibbs* energy for the transition from  $^1\text{CSS}$  to  $\text{S}_0$  ( $\Delta G_{1\text{CSS-S}_0}$ , **Table 5**), places  $\text{CR}_\text{S}$  for all rotationally hindered triads in the *Marcus* normal region ( $\lambda_{\text{tot}} > -(\Delta G^{00})$ ). Since the local  $^3\text{PDI}$  state is lower in energy than the CSS, triplet recombination becomes possible in toluene. Comparing the overall reorganisation energy in toluene ( $\lambda_{\text{tottol}}$ ,  $2340 \text{ cm}^{-1}$ ,  $0.29 \text{ eV}$ ) to the *Gibbs* energy for the transition from  $^3\text{CSS}$  to  $^3\text{PDI}$  ( $\Delta G_{3\text{CSS-}^3\text{PDI}}$ , **Table 5**) and from  $^1\text{CSS}$  to  $\text{S}_0$  ( $\Delta G_{1\text{CSS-S}_0}$ ), places  $\text{CR}_\text{T}$  as well as  $\text{CR}_\text{S}$  for all rotationally hindered triads in the *Marcus* inverted region ( $\lambda_{\text{tot}} > -(\Delta G^{00})$ ).  $\text{CR}_\text{T}$  shows a much smaller *Gibbs* energy (approximately  $-5500 \text{ cm}^{-1}$ ,  $-0.68 \text{ eV}$ , **Table 5**) than  $\text{CR}_\text{S}$  (approximately  $-15000 \text{ cm}^{-1}$ ,  $-1.86 \text{ eV}$ , **Table 5**), indicating that the favoured CR pathway in toluene is the triplet pathway for all triads. Comparing the two different solvents, the *Marcus* region is changed due to solvent polarity, as already reported in literature for similar triads.<sup>[88]</sup>

## 6.1.2 Charge separation

In the previous section, the CSS energies were estimated and compared to the  $^1\text{PDI}$  energy. All rotationally hindered triads should be able to undergo CS and form CSSs. fs-TA spectroscopy was used to characterise the CS kinetics. Therefore, fs-TA maps were recorded in PhCN and toluene. A detailed description of the measurement setup and conditions is given in **Section 10.3.4.1**.

### 6.1.2.1 fs-Pump probe spectroscopy

The fs-transient absorption measurements<sup>10</sup> of the triads **TAAMe<sub>2</sub>-TTC-PDIME<sub>2</sub>**, **TAAMe<sub>2</sub>-TTC-PDI**, **TAA-TTC-PDIME<sub>2</sub>** and **TAA-TTC-PDI** yielded transient maps (see **Figure 44** to **Figure 48 (B)**). By applying a sequential model, the TA maps were analysed by a global exponential fit and the resulting EADS (evolution associated difference spectra) (figures **(A)**) were further interpreted.<sup>11</sup>

Excitation of the PDI moiety leads to a ground state bleaching (GSB) at around  $18900\text{ cm}^{-1}$  (528 nm) in the TA-spectra. The excitation causes the formation of an initial (hot) PDI  $S_1$  state observed by excited state absorption (ESA) bands around  $13500\text{ cm}^{-1}$  (740 nm). Subsequently, the hot state relaxes to the final (cold) PDI  $S_1$  state from which fluorescence is emitted. This fluorescence is observed as a stimulated emission (SE) at around  $17200\text{ cm}^{-1}$  (581 nm) in the TA-spectra.<sup>[166, 180, 193-195]</sup> The difference of the hot and cold states can be attributed to different conformations of the solvent shell.<sup>[196]</sup> These processes are well-known in literature and therefore were not investigated in detail.<sup>[88, 194-195]</sup>

### fs-Transient absorption spectroscopy in toluene

All EADS of **TAAMe<sub>2</sub>-TTC-PDI** (**Figure 41**), **TAA-TTC-PDIME<sub>2</sub>** (**Figure 42**) and **TAA-TTC-PDI** (**Figure 43**) consist of five independent spectral components that can be assigned to different processes within the triads. The two EADS associated with  $\tau_1$  and  $\tau_2$  ( $\tau_1$ - $\tau_3$  for **TAAMe<sub>2</sub>-TTC-PDI**, **Figure 41** to **Figure 43**) are spectrally very similar for the three triads and exhibit ESA signals at  $15000\text{ cm}^{-1}$  (667 nm) and  $12000\text{ cm}^{-1}$  (833 nm) as well as a prominent GSB above  $18900\text{ cm}^{-1}$  (528 nm) and SE below  $18900\text{ cm}^{-1}$  (528 nm).<sup>[91]</sup> The time constant  $\tau_1$  ( $\tau_1$  and  $\tau_2$  for **TAAMe<sub>2</sub>-TTC-PDI**, **Table 6**) reflects the vibrational relaxation of the **PDI**  $S_1$  state

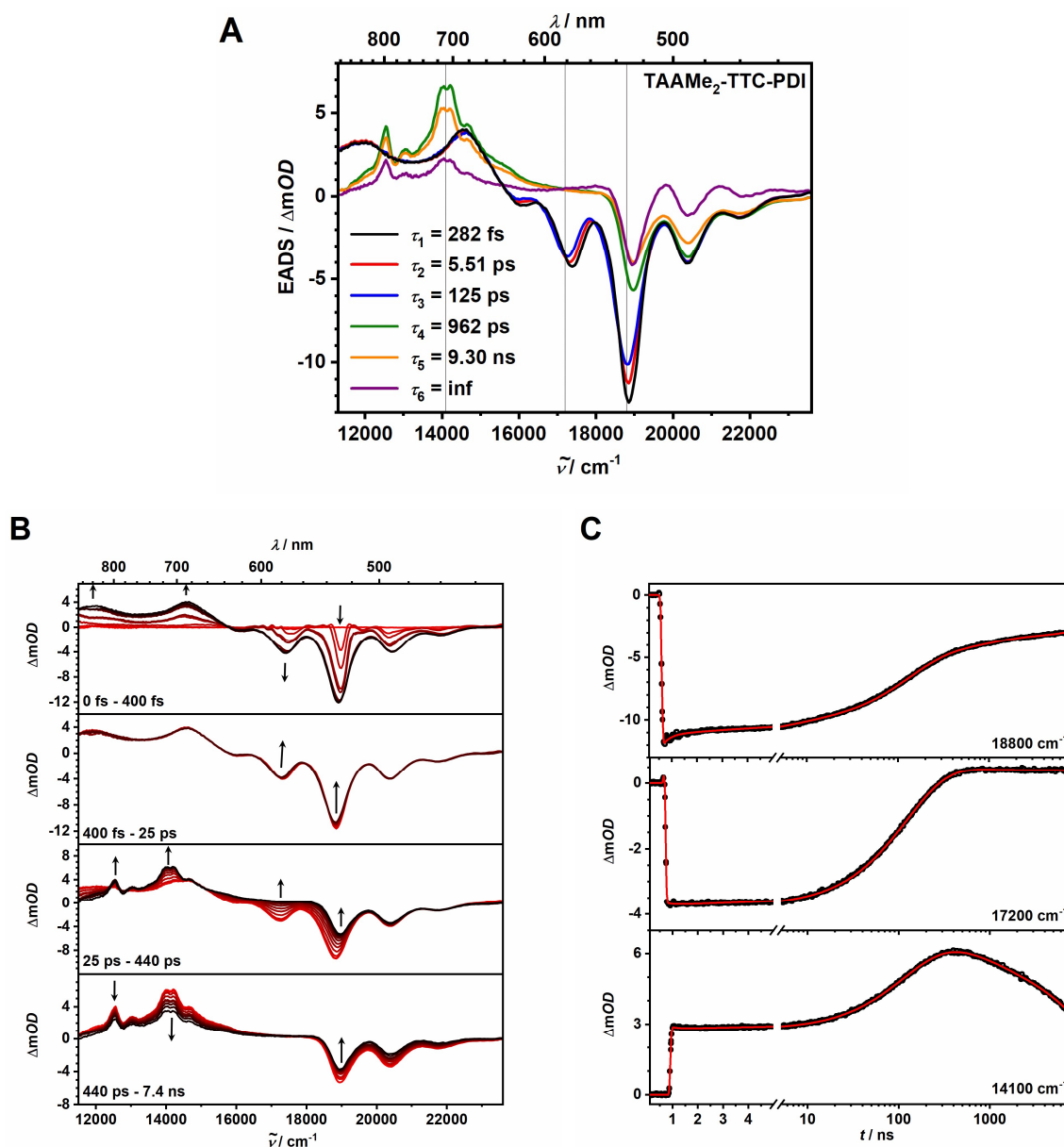
<sup>10</sup> Measurements done by A. Schmiedel.

<sup>11</sup> Global exponential fit was done by Dr. M. Holzappel.

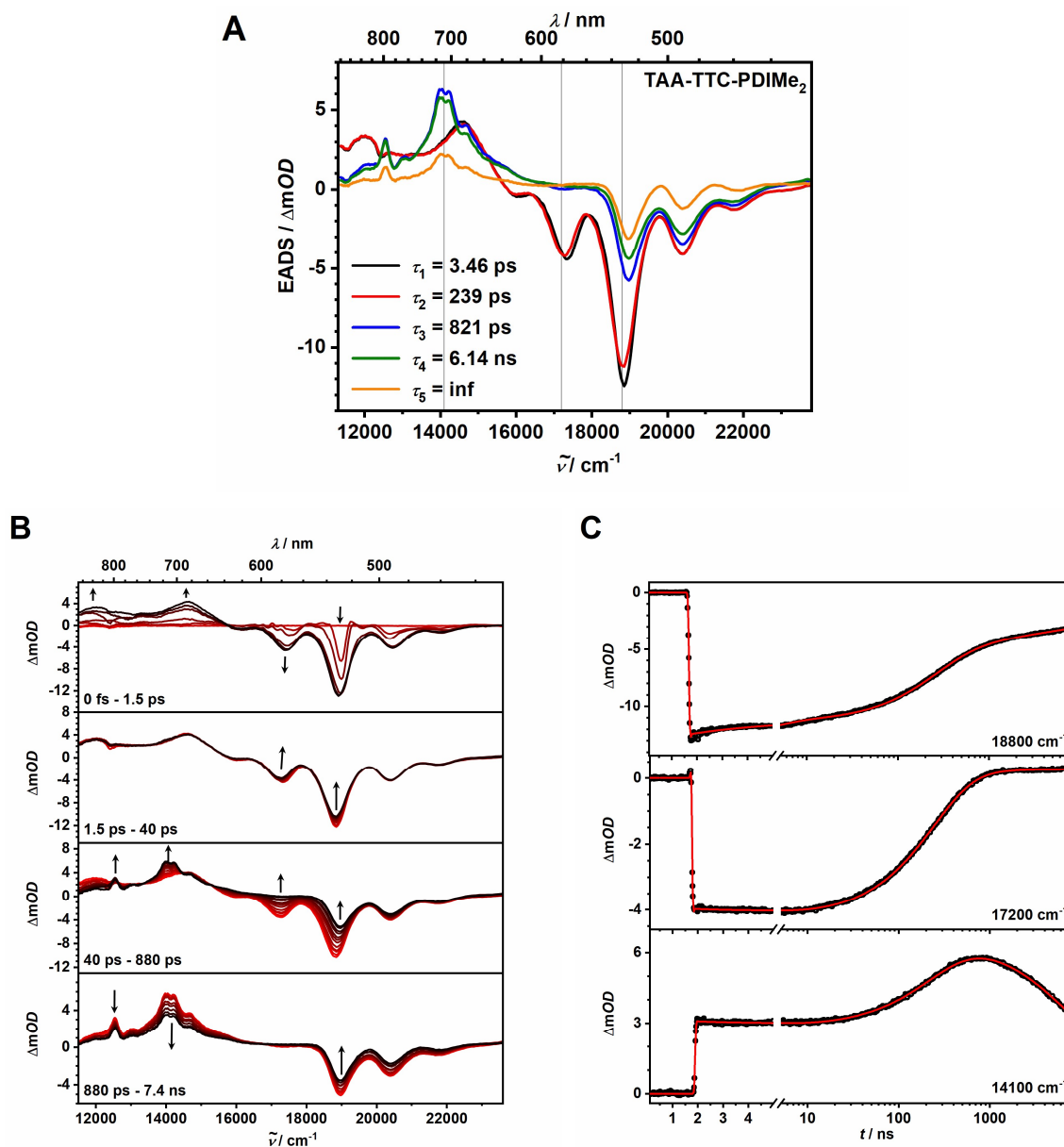
and is within the same order of magnitude for the three triads. The electron transfer process is characterised by the disappearance of the SE band at  $17300\text{ cm}^{-1}$  (578 nm) as well as the rise of new ESA bands at  $12600\text{ cm}^{-1}$  (794 nm),  $13000\text{ cm}^{-1}$  (769 nm) and a double peak at  $14100\text{ cm}^{-1}$  (710 nm). The rise of those signals between  $12500\text{ cm}^{-1}$  (800 nm) and  $15300\text{ cm}^{-1}$  (654 nm) proves the formation of a charge separated state because they are typical for the superposition of absorption signals of a **TAA** radical cation and a **PDI** radical anion.<sup>[48, 88]</sup> Thus, the lifetimes  $\tau_2$  ( $\tau_3$  for **TAAMe<sub>2</sub>-TTC-PDI**, **Table 6**) are associated with the photoinduced electron transfer process in which the **PDI** unit is reduced by an electron of the **TAA** donor.  $\tau_3$  and  $\tau_4$  of the triads **TAA-TTC-PDIME<sub>2</sub>** and **TAA-TTC-PDI** ( $\tau_4$  and  $\tau_5$  for **TAAMe<sub>2</sub>-TTC-PDI**, **Figure 41** to **Figure 43**) both consist of ESA signals between  $12600\text{ cm}^{-1}$  (794 nm) and  $15300\text{ cm}^{-1}$  (654 nm) and the GSB above  $18900\text{ cm}^{-1}$  (528 nm). The structural similarity of the signals could reflect a spin chemical evolution within the RP caused by the spin evolution between <sup>1</sup>CSS and <sup>3</sup>CSS (**section 1.1.1**). The CSSs are structurally indistinguishable but differ in their lifetimes due to the different CR pathways ( $k_T \gg k_S$ ) and, therefore, the shorter lifetime component  $\tau_3$  ( $\tau_4$  for **TAAMe<sub>2</sub>-TTC-PDI**) could be assigned to the <sup>3</sup>CSS.  $\tau_5$  ( $\tau_6$  for **TAAMe<sub>2</sub>-TTC-PDI**, **Table 6**) shows a clear decrease of the ESA between  $12500\text{ cm}^{-1}$  (800 nm) and  $15300\text{ cm}^{-1}$  (654 nm), which indicates that part of the CSS decays within the measured time range. The formation of the <sup>3</sup>PDI can be identified by the rise of another ESA between  $18300\text{ cm}^{-1}$  (546 nm) and  $22500\text{ cm}^{-1}$  (444 nm) overlaid by the GSB of the **PDI**.<sup>[48]</sup> This signal indicates that the <sup>1</sup>CSS undergoes spin evolution to the <sup>3</sup>CSS, which in turn decays into the <sup>3</sup>PDI state.

In **TAAMe<sub>2</sub>-TTC-PDIME<sub>2</sub>** (**Figure 44** figure (A)), other than in the previously described triads, the first three signals are spectrally very similar and  $\tau_1$  and  $\tau_2$  can be assigned to the vibrational relaxation of the PDI S<sub>1</sub> state.  $\tau_3$  refers to the CS process and  $\tau_4$  represents the formation of the CSS. In this triad the CS is much slower compared to the other three triads due to the strong rotational hindrance, which precludes the recording of further processes within the measurable time range. None of the four rotationally hindered triads examined shows an intermediate charge transfer state involved in the CS process. This is consistent with an one-step charge transfer from the **TAA** to the **PDI**.

By comparing the four triads in toluene it becomes clear that the CS processes become faster with decreasing rotational hindrance. **TAAMe<sub>2</sub>-TTC-PDIME<sub>2</sub>** (**Figure 44**, **Table 6**) shows the slowest CS with  $\tau_3 = 953\text{ ps}$  caused by the strong rotational hindrance due to the attached *ortho*-methyl groups. The time constants of the CS process ( $\tau_2$  in **Table 6**) of the triads **TAAMe<sub>2</sub>-TTC-PDI** (**Figure 41**), **TAA-TTC-PDIME<sub>2</sub>** (**Figure 42**) and **TAA-TTC-PDI** (**Figure 43**) strongly decrease with increasing rotational freedom along the series. This proves that the attachment of *ortho*-methyl groups and, therefore, restriction of the intramolecular twisting influences the CS dynamics of **TAA** donor **PDI** acceptor triads.

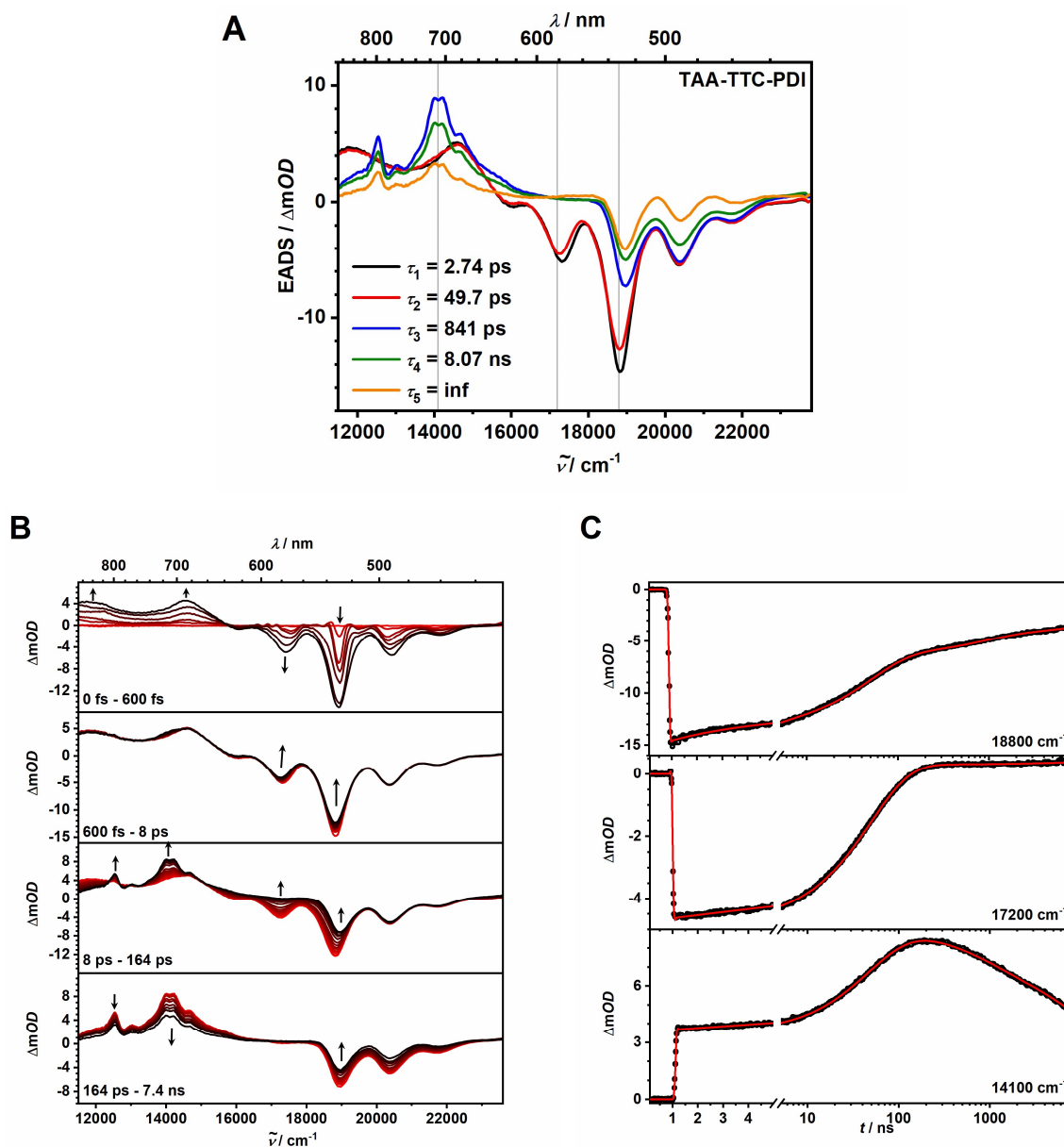


**Figure 41:** Chirp corrected fs-TA spectra of TAAMe<sub>2</sub>-TTC-PDI in toluene after light-excitation at 18900 cm<sup>-1</sup> (528 nm) at 298 K. **A:** EADS **B:** selected TA-spectra from the fs-TA measurements (short times to long times depicted from red to black) **C:** selected time traces at different wavenumbers (grey lines in **A**) with their respective global fits.

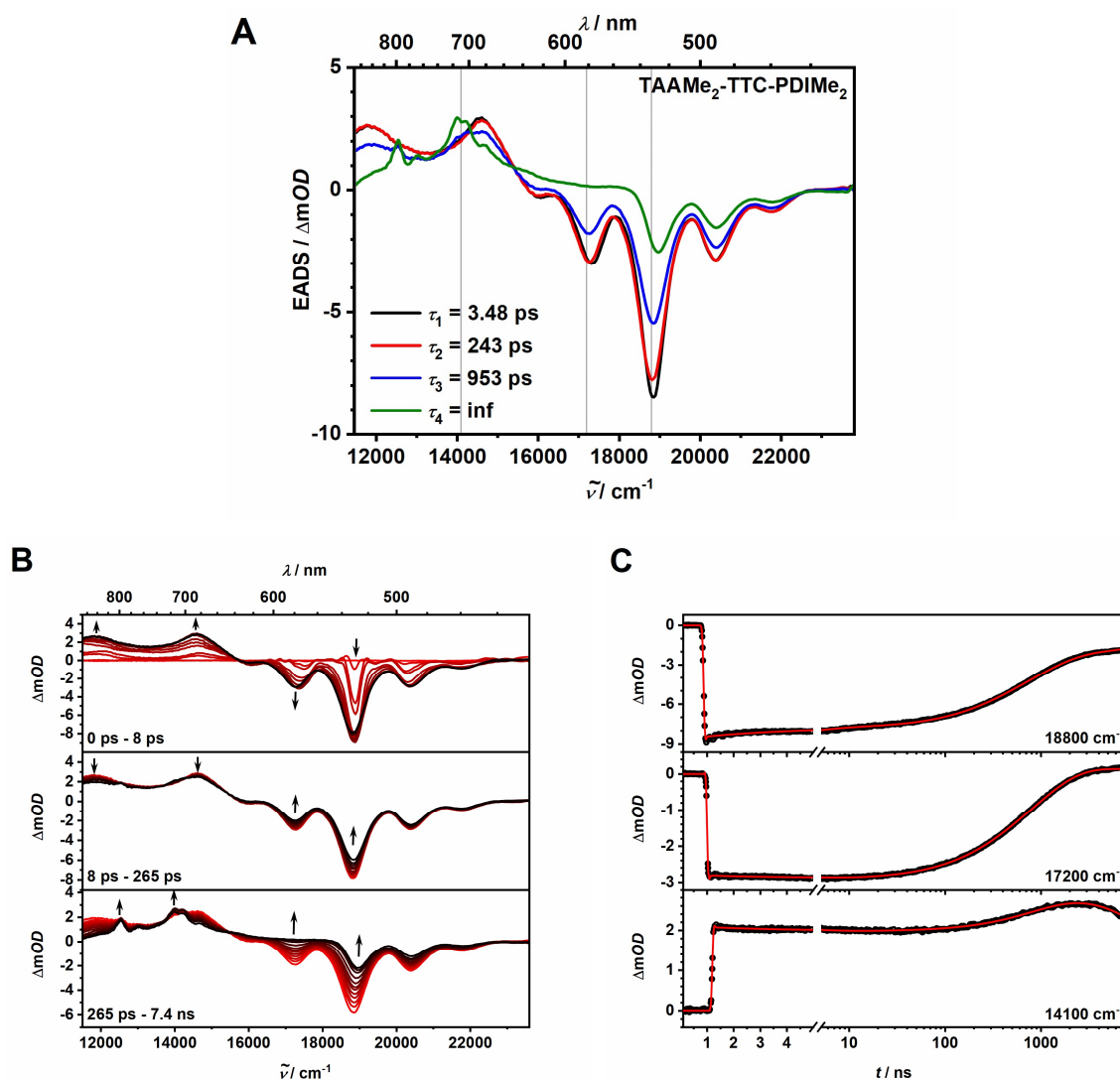


**Figure 42:** Chirp corrected fs-TA spectra of **TAA-TTC-PDIME<sub>2</sub>** in toluene after light-excitation at 18900  $\text{cm}^{-1}$  (528 nm) at 298 K. **A:** EADS **B:** selected TA-spectra from the fs-TA measurements (short times to long times depicted from red to black) **C:** selected time traces at different wavenumbers (grey lines in **A**) with their respective global fits.





**Figure 43:** Chirp corrected fs-TA spectra of **TAA-TTC-PDI** in toluene after light-excitation at  $18900\text{ cm}^{-1}$  ( $528\text{ nm}$ ) at  $298\text{ K}$ . **A:** EADS **B:** selected TA-spectra from the fs-TA measurements (short times to long times depicted from red to black) **C:** selected time traces at different wavenumbers (grey lines in **A**) with their respective global fits.



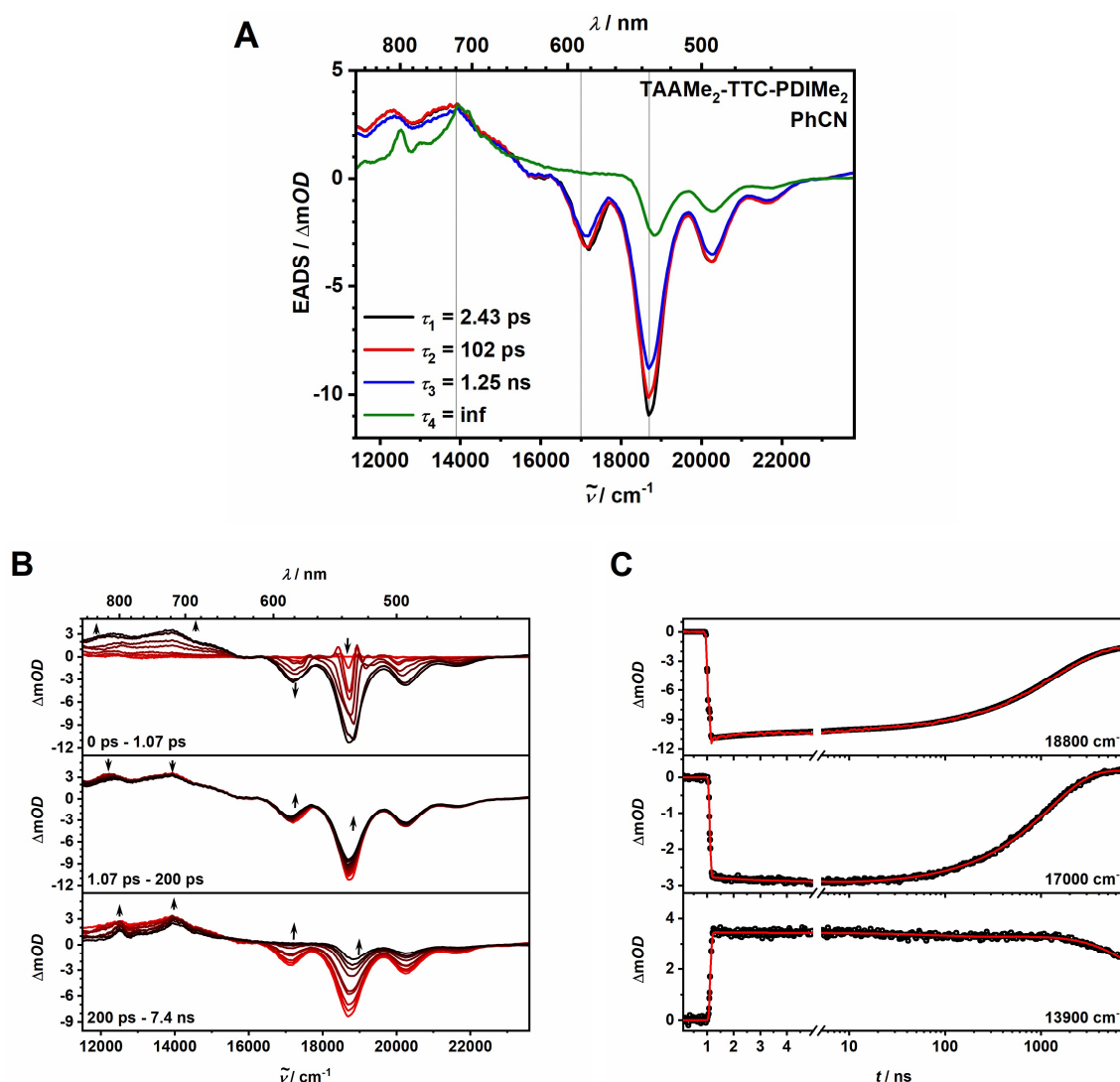
**Figure 44:** Chirp corrected fs-TA spectra of TAAMe<sub>2</sub>-TTC-PDIME<sub>2</sub> in toluene after light-excitation at 18900 cm<sup>-1</sup> (528 nm) at 298 K. **A:** EADS **B:** selected TA-spectra from the fs-TA measurements (short times to long times depicted from red to black) **C:** selected time traces at different wavenumbers (grey lines in **A**) with their respective global fits.

**Table 6:** Time constants of the four rotationally hindered triads obtained by global analysis of the fs-TA measurements in toluene.

	$\tau_1 / \text{ps}$	$\tau_2 / \text{ps}$	$\tau_3 / \text{ps}$	$\tau_4 / \text{ps}$	$\tau_5 / \text{ns}$	$\tau_6 / \text{ns}$
TAAMe <sub>2</sub> -TTC-PDIME <sub>2</sub>	3.48	243	953	inf	-	-
TAAMe <sub>2</sub> -TTC-PDI	0.28	5.51	125	962	9.30	inf
TAA-TTC-PDIME <sub>2</sub>	3.46	239	821	$6.14 \cdot 10^3$	inf	-
TAA-TTC-PDI	2.74	49.7	841	$8.07 \cdot 10^3$	inf	-

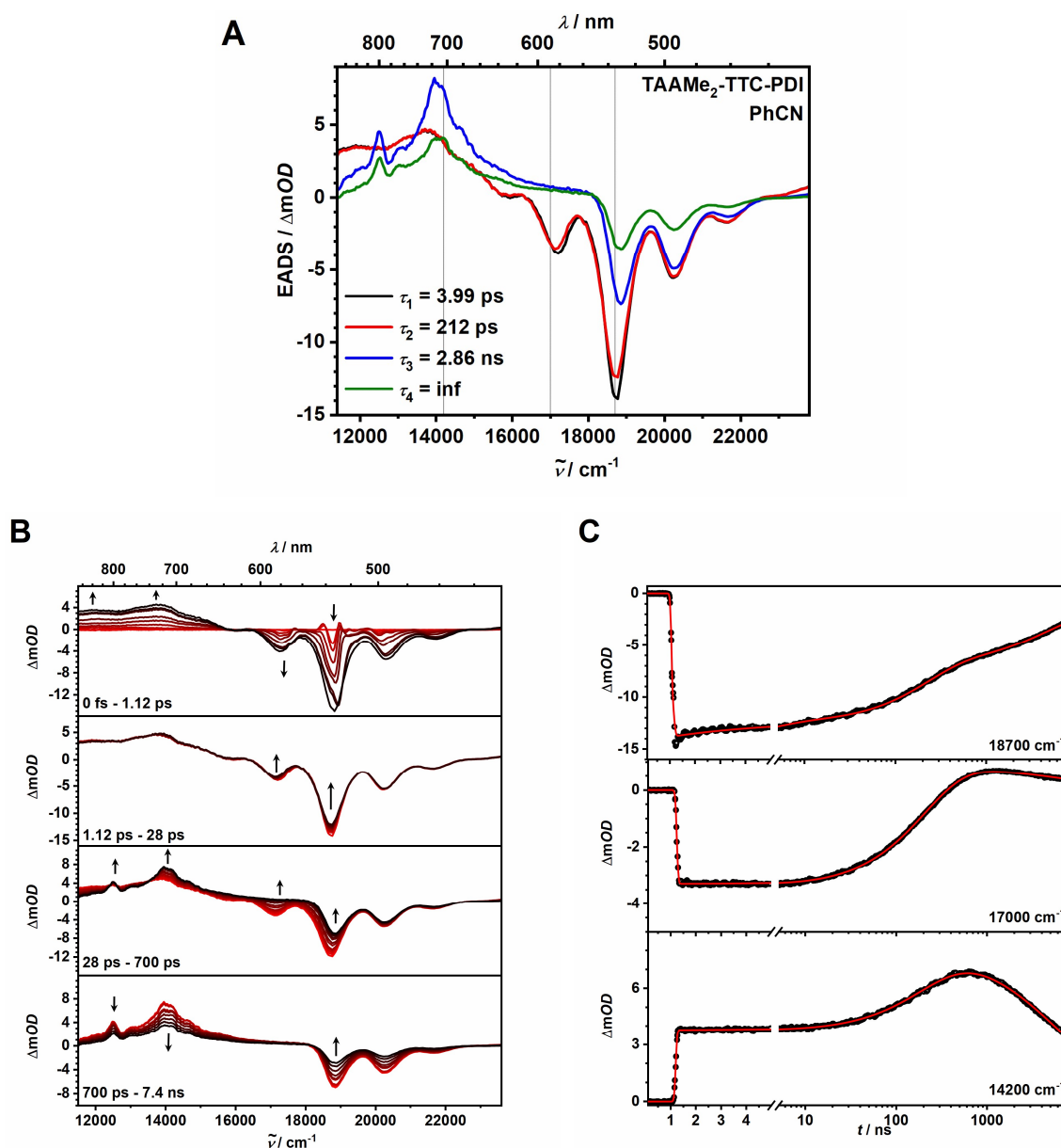
### fs-Transient absorption spectroscopy in PhCN

The CS dynamics of **TAAMe<sub>2</sub>-TTC-PDIME<sub>2</sub>** in PhCN are also slow, like those in toluene, due to the reduced  $\pi$ -overlap caused by the *ortho*-methyl groups.  $\tau_1 = 2.43$  ps and  $\tau_2 = 102$  ps (**Figure 45 (A)**) are assigned to the relaxation within the **PDI** acceptor form the hot to the cold PDI state, which is observed by the ESA signals at 12000 cm<sup>-1</sup> (833 nm) and 15000 cm<sup>-1</sup> (667 nm) as well as a prominent GSB above 18900 cm<sup>-1</sup> (528 nm) overlaid by SE below 18900 cm<sup>-1</sup> (528 nm).  $\tau_3$  refers to the CS process. The formation of the CSS is characterised by the rise of the ESA bands at 12600 cm<sup>-1</sup> (794 nm), 13000 cm<sup>-1</sup> (769 nm) and 14100 cm<sup>-1</sup> (710 nm) as well as the disappearance of the SE at 17300 cm<sup>-1</sup> (578 nm), which is visible in  $\tau_4$ .



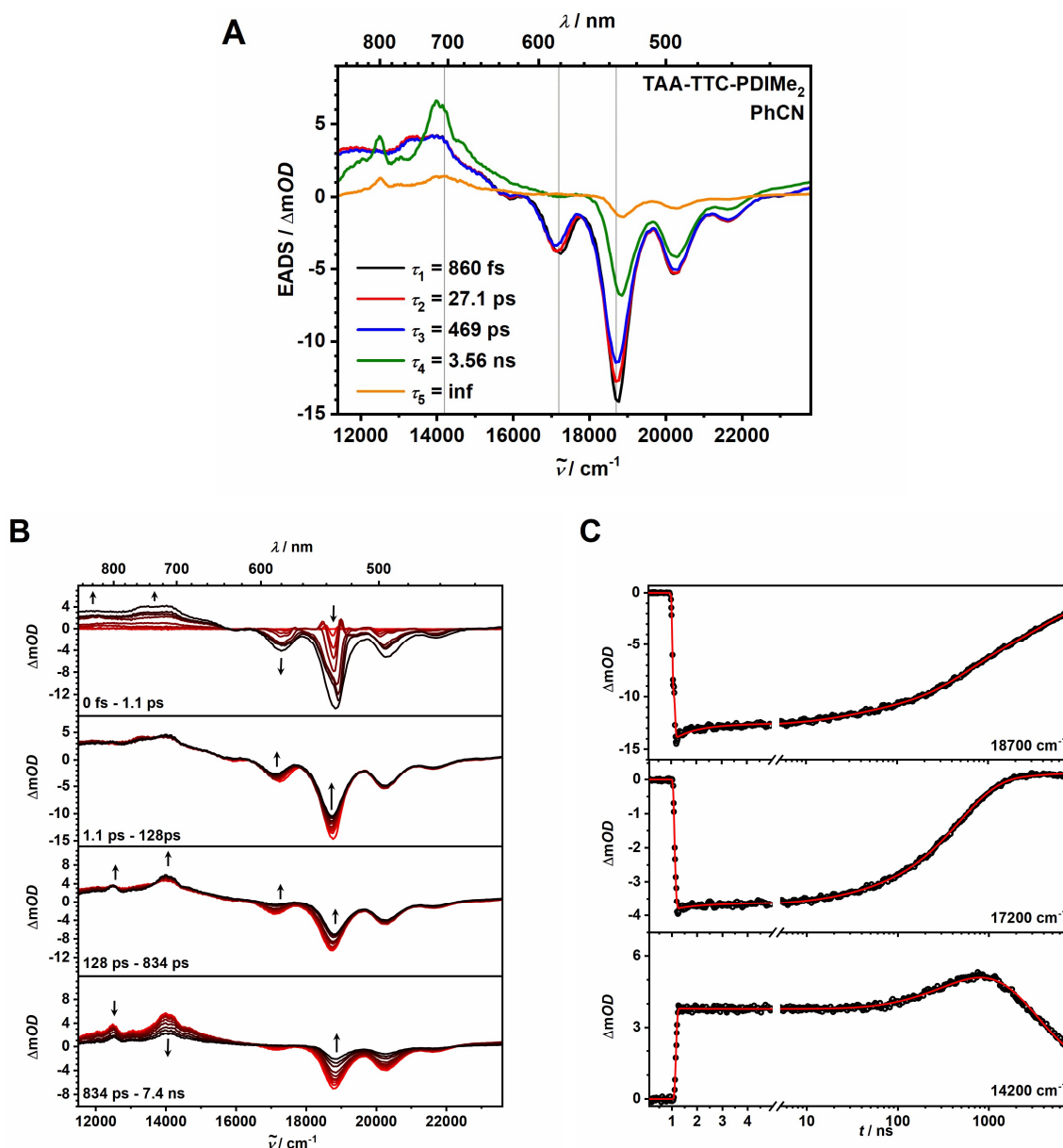
**Figure 45:** Chirp corrected fs-TA spectra of **TAAMe<sub>2</sub>-TTC-PDIME<sub>2</sub>** in PhCN after light-excitation at 18800 cm<sup>-1</sup> (532 nm) at 298 K. **A:** EADS **B:** selected TA-spectra from the fs-TA measurements (short times to long times depicted from red to black) **C:** selected time traces at different wavenumbers (grey lines in **A**) with their respective global fits.

In **TAAMe<sub>2</sub>-TTC-PDI** four time constants are obtained by global analysis, in which the latter two cannot be determined in the measurable time range (**Figure 46 (A)**).  $\tau_1 = 3.99$  ps can be assigned to the relaxation from the hot to the cold <sup>1</sup>PDI state.  $\tau_2 = 212$  ps is associated with the photoinduced CS process. The EADS associated with  $\tau_3$  shows the typical ESA bands at 12600 cm<sup>-1</sup> (794 nm), 13000 cm<sup>-1</sup> (769 nm) and 14100 cm<sup>-1</sup> (710 nm) consistent with the formation of a CSS. The diminished intensity of  $\tau_3$  compared to  $\tau_4$  could indicate a spin chemical process within the triad.



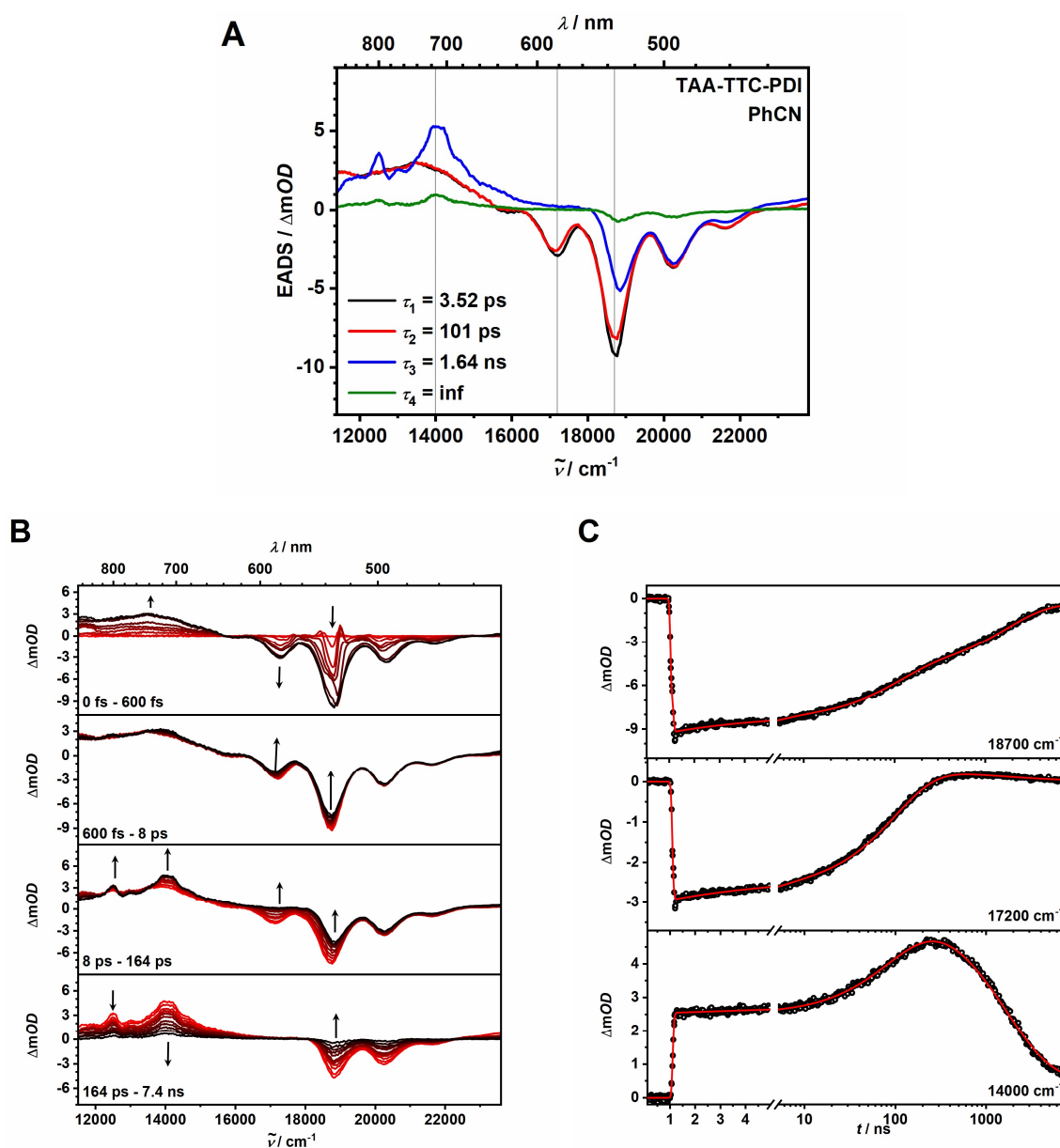
**Figure 46:** Chirp corrected fs-TA spectra of **TAAMe<sub>2</sub>-TTC-PDI** in PhCN after light-excitation at 18800 cm<sup>-1</sup> (532 nm) at 298 K. **A:** EADS **B:** selected TA-spectra from the fs-TA measurements (short times to long times depicted from red to black) **C:** selected time traces at different wavenumbers (grey lines in **A**) with their respective global fits.

In **TAA-TTC-PDIME<sub>2</sub>** five EADS are obtained by global analysis (**Figure 47 (A)**). The EADS with the lifetimes of  $\tau_1 = 860$  fs,  $\tau_2 = 27.1$  ps can be assigned to the relaxation process from the hot to the cold <sup>1</sup>PDI state.  $\tau_3 = 469$  ps is associated with the CS process. The EADS of  $\tau_4$  shows the typical ESA bands at 12600 cm<sup>-1</sup> (794 nm), 13000 cm<sup>-1</sup> (769 nm) and 14100 cm<sup>-1</sup> (710 nm) typically observed during the formation of the CSS. The diminished intensity of  $\tau_5$  between 12600 cm<sup>-1</sup> (794 nm) and 15000 cm<sup>-1</sup> (667 nm) as well as in the region of the GSB indicate the decay of the CSS.



**Figure 47:** Chirp corrected fs-TA spectra of **TAA-TTC-PDIME<sub>2</sub>** in PhCN after light-excitation at 18800 cm<sup>-1</sup> (532 nm) at 298 K. **A:** EADS **B:** selected TA-spectra from the fs-TA measurements (short times to long times depicted from red to black) **C:** selected time traces at different wavenumbers (grey lines in **A**) with their respective global fits.

In **TAA-TTC-PDI** four EADS are obtained by global analysis (**Figure 48 (A)**). The EADS with the lifetime of  $\tau_1 = 3.52$  ps can be assigned to the relaxation process from the hot to the cold  $^1$ PDI state.  $\tau_2 = 101$  ps represents the CS process. The EADS of  $\tau_3$  shows the typical ESA bands at  $12600\text{ cm}^{-1}$  (794 nm),  $13000\text{ cm}^{-1}$  (769 nm) and  $14100\text{ cm}^{-1}$  (710 nm) typically observed during the formation of the CSS. The diminished intensity of  $\tau_4$  between  $12600\text{ cm}^{-1}$  (794 nm) and  $15000\text{ cm}^{-1}$  (667 nm) as well as in the region of the GSB indicate the decay of the CSS.



**Figure 48:** Chirp corrected fs-TA spectra of **TAA-TTC-PDI** in PhCN after light-excitation at  $18800\text{ cm}^{-1}$  (532 nm) at 298 K. **A:** EADS **B:** selected TA-spectra from the fs-TA measurements (short times to long times depicted from red to black) **C:** selected time traces at different wavenumbers (grey lines in **A**) with their respective global fits.

**Table 7:** Time constants of the four rotationally hindered triads obtained by global analysis of the fs-TA measurements in PhCN.

	$\tau_1$ / ps	$\tau_2$ / ps	$\tau_3$ / ps	$\tau_4$ / ns	$\tau_5$ / ns
TAAMe <sub>2</sub> -TTC-PDIME <sub>2</sub>	2.43	102	1.25·10 <sup>3</sup>	inf	-
TAAMe <sub>2</sub> -TTC-PDI	3.99	212	2.86·10 <sup>3</sup>	inf	-
TAA-TTC-PDIME <sub>2</sub>	0.86	27.1	469	3.56	inf
TAA-TTC-PDI	3.52	101	1.64·10 <sup>3</sup>	inf	-

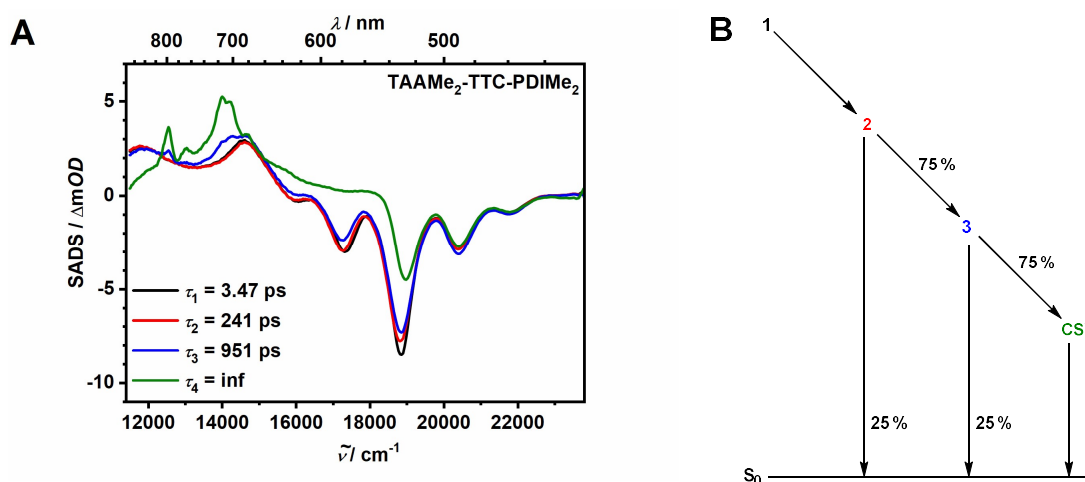
### 6.1.2.2 Global target analysis

The global analysis discussed in the previous section yields EADS with lifetimes, but does not produce rate constants for specific processes when multiple deactivation processes take place. To extract rate constants for the CS, a global target analysis to the transient maps was performed (figure (B) in **Figure 49** to **Figure 56**).<sup>12</sup> The global target analysis allows the inclusion of additionally direct (nonradiative) deactivation processes from all excited states to the ground state. For the procession of the target analysis the assumption was made that the GSB intensity of all excited or reduced PDI species at 20400 cm<sup>-1</sup> (490 nm) is the same, and is not overlaid by ESA or SE. However, this does not hold true for the <sup>3</sup>PDI state, which shows a strong ESA in spectral region between 18300 cm<sup>-1</sup> (546 nm) and 22500 cm<sup>-1</sup> (444 nm). Therefore, the percentages of the triplet formation were estimated. In order to fulfil the afore-mentioned criteria, the efficiencies of the depopulation channels of all pertinent states for all sequential and direct deactivation processes were adjusted during this global target analysis, which then yields species associated difference spectra (SADS). The quotient of the efficiency of the charge separation channel and the lifetime of the excited PDI state then gives the rate constants  $k_{CS}$  for the CS channel (**Table 8**). The QYs of the CS process  $\Phi_{CS}$  resulting from this target analysis (**Table 8**) are in very good agreement with  $(1-\phi)$ , which means that direct nonradiative deactivation of the vibrationally relaxed PDI S<sub>1</sub> state to the ground state is negligible in comparison to fluorescence.<sup>[91]</sup>

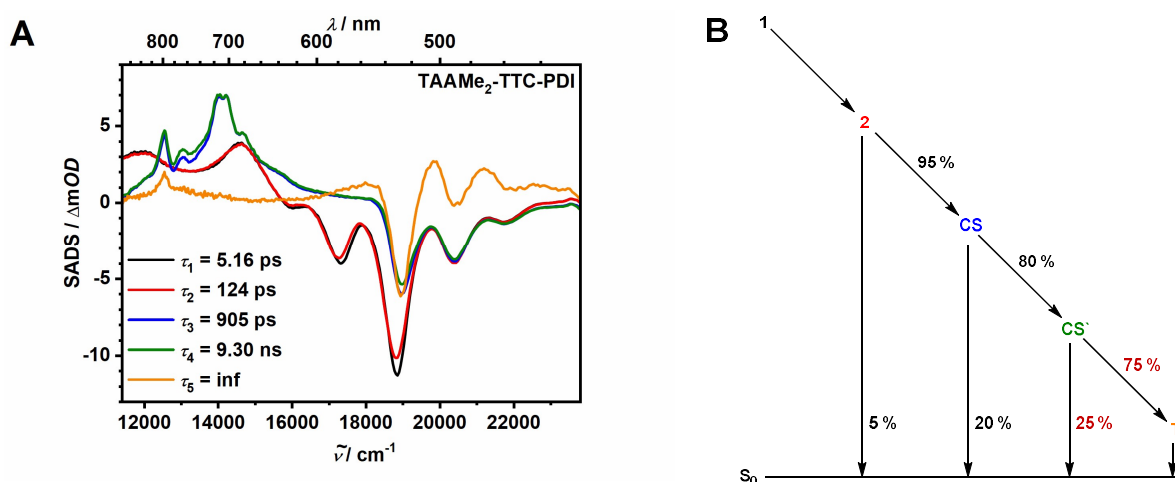
<sup>12</sup> Global target analysis was performed by Dr. M. Holzapfel.

## Global target analysis in toluene

The CS rate constants in toluene increase with increasing rotational freedom from **TAAMe<sub>2</sub>-TTC-PDIME<sub>2</sub>** ( $7.8 \cdot 10^8 \text{ s}^{-1}$ ) to **TAA-TTC-PDI** ( $2.0 \cdot 10^{10} \text{ s}^{-1}$ ) by two orders of magnitude. The efficiencies  $\Phi_{\text{CS}}$  of CS also increase with increasing rotational freedom from **TAAMe<sub>2</sub>-TTC-PDIME<sub>2</sub>** (0.56) to **TAA-TTC-PDI** (1.00). The increasing rate constants along the series indicate that the electronic coupling between the **TAA** donor state and the **PDI** acceptor state rises with increasing rotational freedom for the CS process.

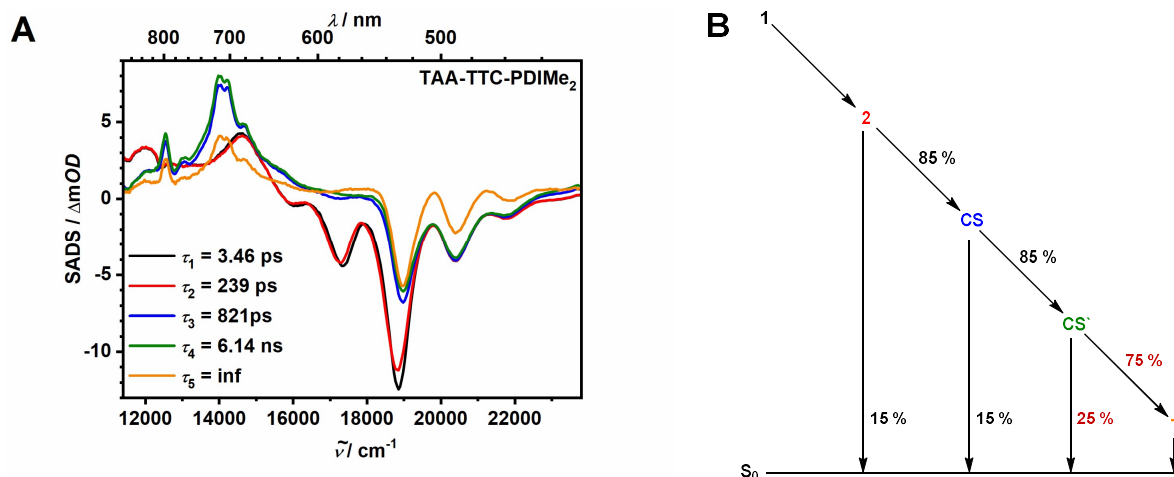


**Figure 49:** **A:** SADS. **B:** Kinetic model used to apply a global target analysis to the transient map of **TAAMe<sub>2</sub>-TTC-PDIME<sub>2</sub>** under the assumption that all SADS spectra with exception of the <sup>3</sup>PDI spectra match at  $20400 \text{ cm}^{-1}$  ( $490 \text{ nm}$ ). The coloured numbers in **B** represent the respective SADS in **A**.

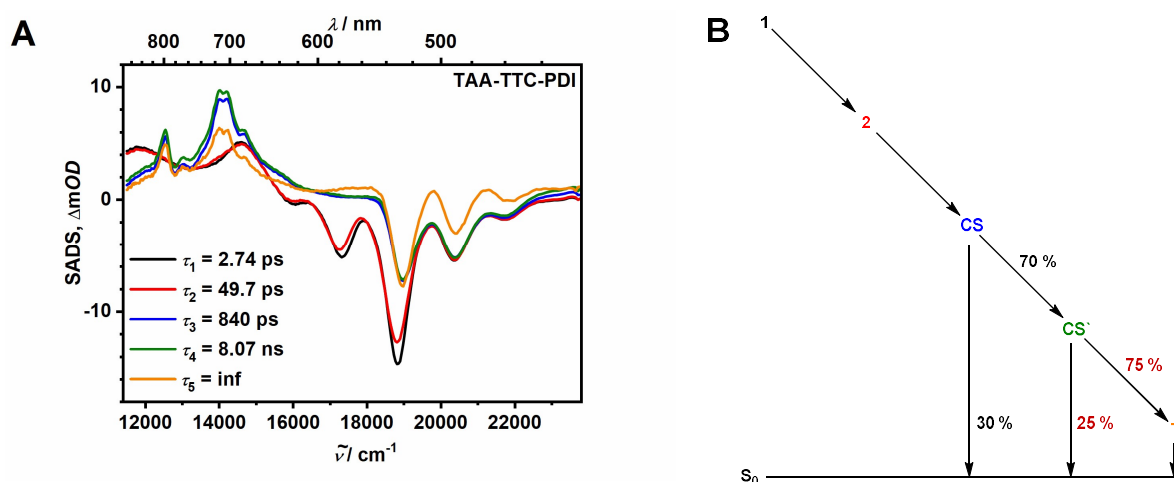


**Figure 50:** **A:** SADS. **B:** Kinetic model used to apply a global target analysis to the transient map of **TAAMe<sub>2</sub>-TTC-PDI** under the assumption that all SADS spectra with exception of the <sup>3</sup>PDI spectra match at  $20400 \text{ cm}^{-1}$  ( $490 \text{ nm}$ ). The red percentages are an estimation for the triplet formation. The coloured numbers in **B** represent the respective SADS in **A**.





**Figure 51: A:** SADS. **B:** Kinetic model used to apply a global target analysis to the transient map of TAA-TTC-PDIME<sub>2</sub> under the assumption that all SADS spectra with exception of the <sup>3</sup>PDI spectra match at 20400 cm<sup>-1</sup> (490 nm). The red percentages are an estimation for the triplet formation. The coloured numbers in **B** represent the respective SADS in **A**.



**Figure 52: A:** SADS. **B:** Kinetic model used to apply a global target analysis to the transient map of TAA-TTC-PDI under the assumption that all SADS spectra with exception of the <sup>3</sup>PDI spectra match at 20400 cm<sup>-1</sup> (490 nm). The red percentages are an estimation for the triplet formation. The coloured numbers in **B** represent the respective SADS in **A**.

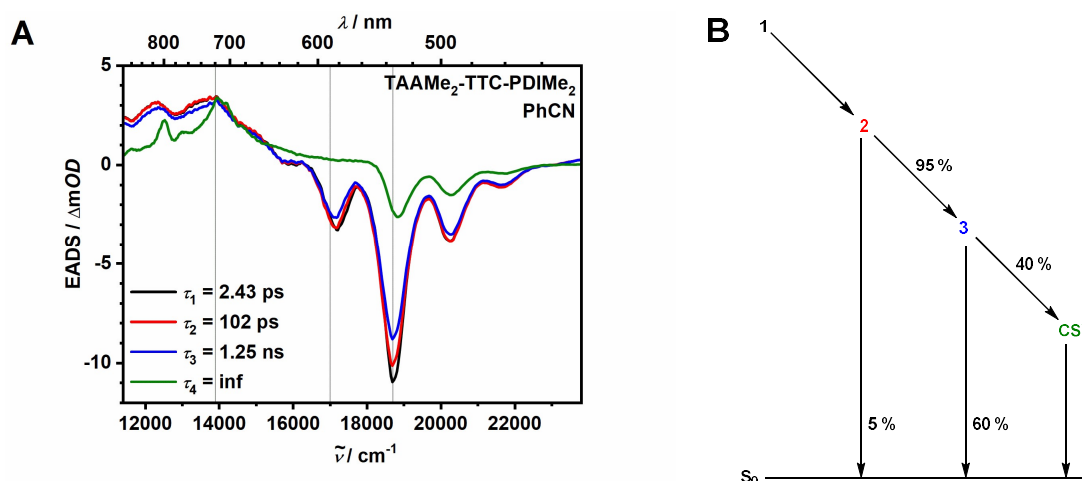
**Table 8:** Lifetimes  $\tau_{S_1}$  of the relaxed  $S_1$  PDI state, quantum yields of the CSS and rate constant of charge separation  $k_{CS}$  in toluene of the triads **TAAMe<sub>2</sub>-TTC-PDIME<sub>2</sub>**, **TAAMe<sub>2</sub>-TTC-PDI**, **TAA-TTC-PDIME<sub>2</sub>** and **TAA-TTC-PDI**.

	$\tau_{S_1} / \text{ps}^a$	$\Phi_{CS}^b$	$k_{CS} / \text{s}^{-1}^c$
<b>TAAMe<sub>2</sub>-TTC-PDIME<sub>2</sub></b>	953	0.56	$7.8 \cdot 10^8$
<b>TAAMe<sub>2</sub>-TTC-PDI</b>	125	0.95	$7.6 \cdot 10^9$
<b>TAA-TTC-PDIME<sub>2</sub></b>	239	0.85	$3.6 \cdot 10^9$
<b>TAA-TTC-PDI</b>	49.7	1.00	$2.0 \cdot 10^{10}$

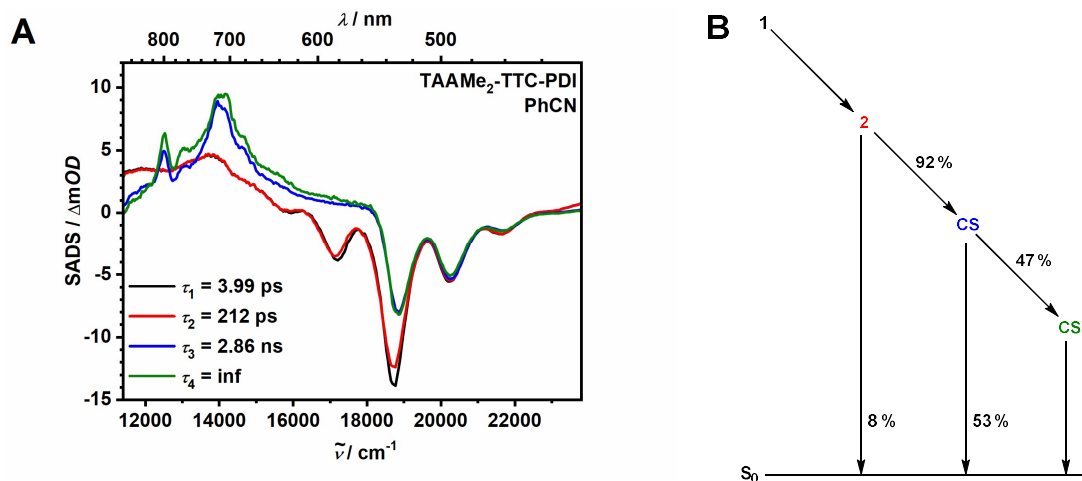
<sup>a</sup> from the fs-TA measurements. <sup>b</sup> quantum yield of CS determined by global target analysis. <sup>c</sup> rate constant for CS from the global target analysis of the fs-TA maps.

### Global target analysis in PhCN

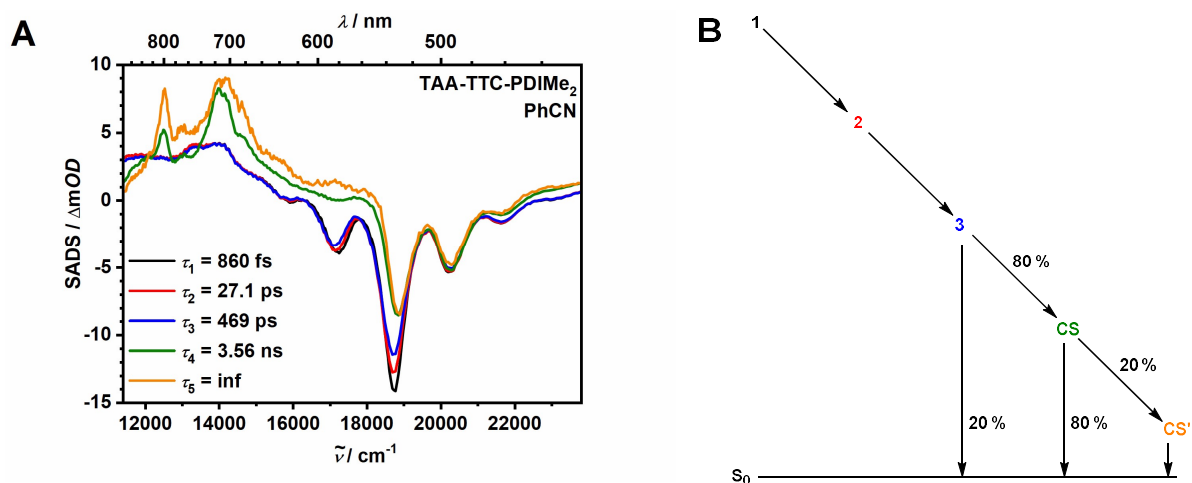
The rate constants  $k_{CS}$  as well as the efficiencies for the CS processes (**Figure 53** to **Figure 56** and **Table 9**) were determined as described above, because the triads show the same processes in PhCN as in toluene. Therefore, the same kinetic model was applied. The CS rate constants of the rotationally hindered triads in PhCN increase with increasing rotational freedom from **TAAMe<sub>2</sub>-TTC-PDIME<sub>2</sub>** ( $3.2 \cdot 10^8 \text{ s}^{-1}$ ) to **TAA-TTC-PDI** ( $9.4 \cdot 10^9 \text{ s}^{-1}$ ) by one order of magnitude. The  $k_{CS}$  values in toluene (**Table 8**) and in PhCN (**Table 9**) show the same trend along the series of rotationally hindered triads. The  $k_{CS}$  rate constants in PhCN are about half as fast compared to those in toluene.  $\Phi_{CS}$  more than doubles with increasing rotational freedom from **TAAMe<sub>2</sub>-TTC-PDIME<sub>2</sub>** (0.38) to **TAA-TTC-PDI** (0.95) but are in all cases smaller than the efficiencies in toluene.



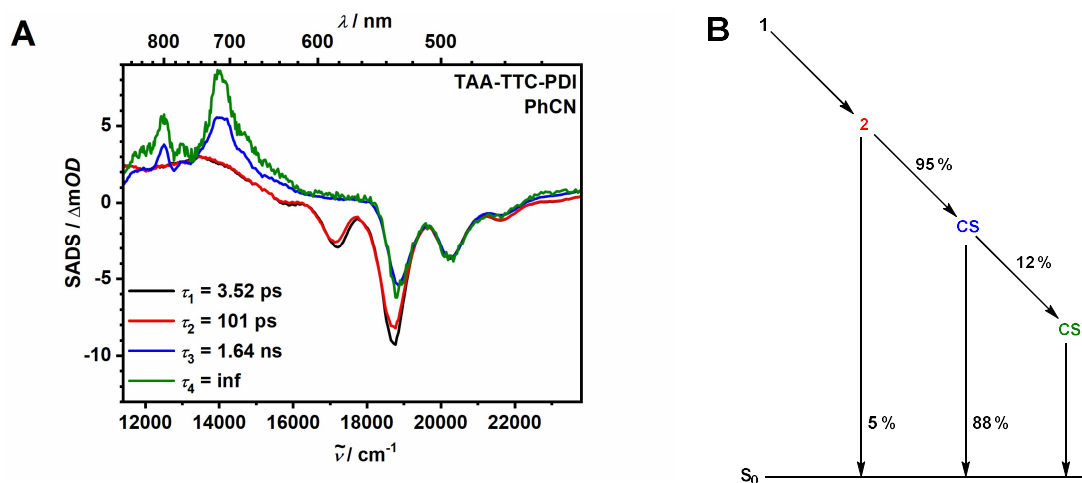
**Figure 53:** **A:** SADS. **B:** Kinetic model used to apply a global target analysis to the transient map of **TAAMe<sub>2</sub>-TTC-PDIME<sub>2</sub>** in PhCN under the assumption that all SADS spectra match at 20400  $\text{cm}^{-1}$  (490 nm). The coloured numbers in **B** represent the respective SADS in **A**.



**Figure 54: A:** SADS. **B:** Kinetic model used to apply a global target analysis to the transient map of TAAMe<sub>2</sub>-TTC-PDI in PhCN under the assumption that all SADS spectra match at 20400 cm<sup>-1</sup> (490 nm). The coloured numbers in **B** represent the respective SADS in **A**.



**Figure 55: A:** SADS. **B:** Kinetic model used to apply a global target analysis to the transient map of TAA-TTC-PDIME<sub>2</sub> in PhCN under the assumption that all SADS spectra match at 20400 cm<sup>-1</sup> (490 nm). The coloured numbers in **B** represent the respective SADS in **A**.



**Figure 56:** **A:** SADS. **B:** Kinetic model used to apply a global target analysis to the transient map of **TAA-TTC-PDI** in PhCN under the assumption that all SADS spectra match at  $20400\text{ cm}^{-1}$  ( $490\text{ nm}$ ). The coloured numbers in **B** represent the respective SADS in **A**.

**Table 9:** Lifetimes  $\tau_{S_1}$  of the relaxed  $S_1$  PDI state, quantum yields of the CSS and rate constant of charge separation  $k_{CS}$  in PhCN of the triads **TAAMe<sub>2</sub>-TTC-PDIME<sub>2</sub>**, **TAAMe<sub>2</sub>-TTC-PDI**, **TAA-TTC-PDIME<sub>2</sub>** and **TAA-TTC-PDI**.

	$\tau_{S_1} / \text{ps}^a$	$\Phi_{CS}^b$	$k_{CS} / \text{s}^{-1}^c$
<b>TAAMe<sub>2</sub>-TTC-PDIME<sub>2</sub></b>	$1.25 \cdot 10^3$	0.38	$3.2 \cdot 10^8$
<b>TAAMe<sub>2</sub>-TTC-PDI</b>	212	0.92	$4.4 \cdot 10^9$
<b>TAA-TTC-PDIME<sub>2</sub></b>	469	0.80	$1.7 \cdot 10^9$
<b>TAA-TTC-PDI</b>	101	0.95	$9.4 \cdot 10^9$

<sup>a</sup> from the fs-TA measurements. <sup>b</sup> quantum yield of CS determined by global target analysis. <sup>c</sup> rate constant for CS from the global target analysis of the fs-TA maps.

### 6.1.3 Charge recombination

In the previous sections it was shown that in all rotationally hindered triads CSSs are formed upon excitation of the **PDI** moiety. The CS dynamics were investigated using fs-TA and the resulting rate constants  $k_{CS}$  as well as the efficiencies of the CS processes were determined using a global target analysis. In this section the kinetics of the CR processes were investigated using magnetic field dependent ns-TA spectroscopy. A detailed description of the used laser setup and the measurement conditions is given in **section 10.3.4.2**. First, the ns-TA experiments at zero field (**section 6.1.3.1**) and thereafter the ns-TA experiments with the application of an external magnetic field (**section 6.1.3.2**) are discussed.

#### 6.1.3.1 Charge recombination at zero external magnetic field

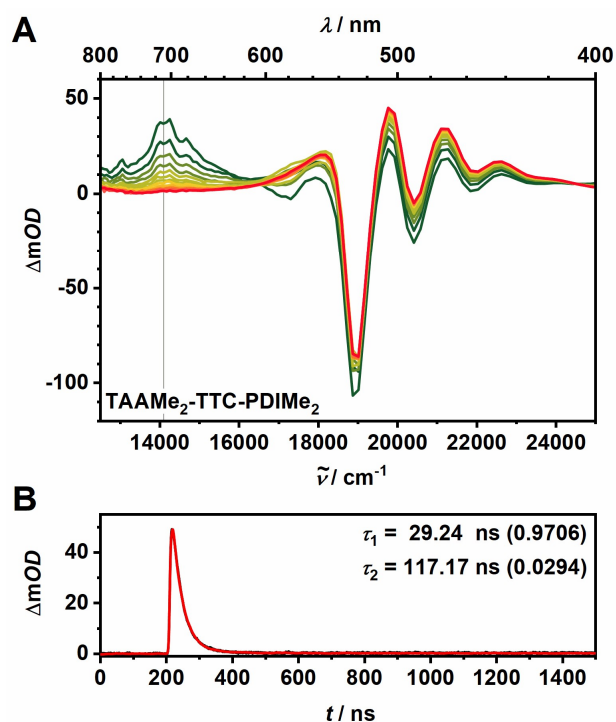
The CR was first investigated at zero external magnetic field. To analyse polarity effects of the solvent on the CR processes the measurements were done in non-polar toluene and polar PhCN.

#### Charge recombination at zero external magnetic field in toluene

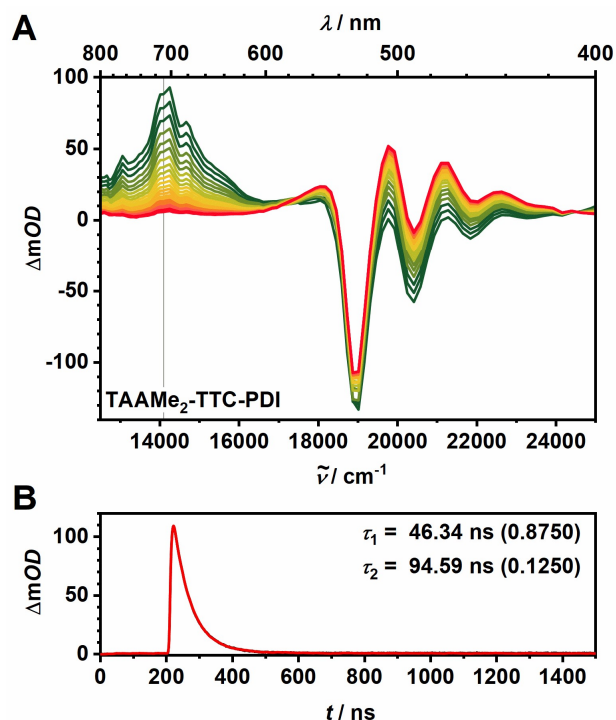
To observe the kinetics of CR ns-TA maps (figure (A)) for the triads **TAAMe<sub>2</sub>-TTC-PDIME<sub>2</sub>** (**Figure 57**), **TAAMe<sub>2</sub>-TTC-PDIME<sub>2</sub>** (**Figure 58**), **TAAMe<sub>2</sub>-TTC-PDIME<sub>2</sub>** (**Figure 59**) and **TAA-TTC-PDI** (**Figure 60**) were measured after light-excitation of the **PDI** moiety in toluene. The ns-TA maps all show the same spectral behaviour. At early times all maps show the GSB of the **PDI** above 18900 cm<sup>-1</sup> (528 nm) as well as an ESA at 14100 cm<sup>-1</sup> (710 nm). The latter is related to the formation of the charge separated state, which is in very good agreement with the fs-TA data (**section 6.1.2.1**). The charge separation process observed in the fs-TA data is, however, not visible in the ns-TA measurements because it is much faster than the shortest time step of the ns-TA measurements. The fs-TA measurements show that after light-excitation the <sup>1</sup>PDI state is formed and thereafter is reduced by an electron from the **TAA** leading to the formation of the <sup>1</sup>CSS (**Figure 44** to **Figure 43** in **section 6.1.2.1**), which may undergo spin interconversion to the <sup>3</sup>CSS. Charge recombination of the <sup>1</sup>CSS directly leads to the singlet ground state, which is forbidden for the <sup>3</sup>CSS. In contrast, the <sup>3</sup>CSS recombines to the local <sup>3</sup>PDI state ( $\Delta G_{3CSS-1PDI}$  approx. -5500 cm<sup>-1</sup>, see **Table 5** in **section 6.1.1**), which is clearly observable in the ns-TA data because at later times the broad, structured ESA between 18300 cm<sup>-1</sup> (546 nm) and 22500 cm<sup>-1</sup> (444 nm) overlaid with the GSB of the **PDI** develops. This ESA band is consistent with the formation of the <sup>3</sup>PDI state, as already described above

(section 6.1.2.1). Furthermore, this is in good agreement with similar triads in literature.<sup>[48, 94, 160]</sup>

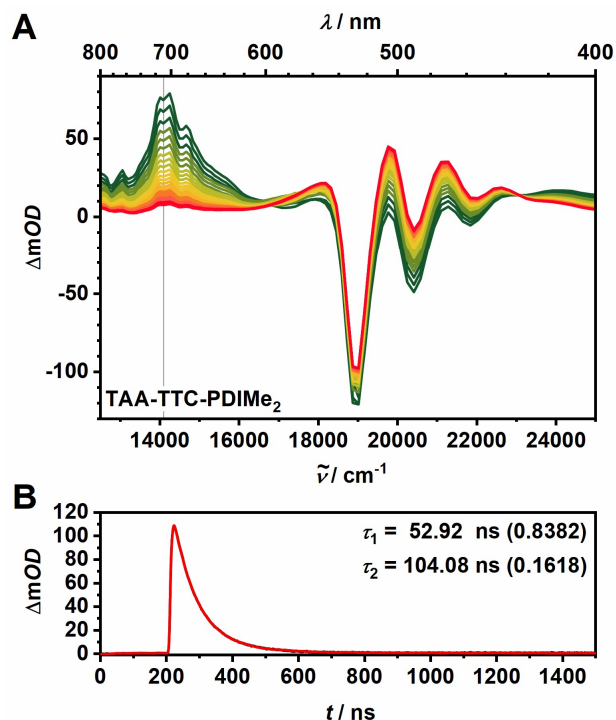
To determine the lifetime of the charge separated state, decay curves were measured in the absence of an external magnetic field and the decay times were extracted using a deconvolution fit (figures (B) in Figure 57 to Figure 60) (description in section 10.3.4.2). The CSS decay times increase in the series from TAAMe<sub>2</sub>-TTC-PDIME<sub>2</sub> over TAAMe<sub>2</sub>-TTC-PDI and TAA-TTC-PDIME<sub>2</sub> to TAA-TTC-PDI (Table 10). As the rotational freedom of the triad increases, the lifetime of the CSS increases. The values for the <sup>3</sup>PDI QYs (Table 39 in section 10.3.4.2) are only approximate because uncertainties in the determination of the <sup>3</sup>PDI extinction coefficients lead to systematic errors in the actinometry measurements (description in section 10.3.4.2). Nevertheless, the QYs of the formation of the CSS and for the <sup>3</sup>PDI are on the same order of magnitude, which indicates that the CSS recombines almost exclusively via the triplet pathway. The distinctly smaller reaction enthalpy of the CR<sub>T</sub> calculated using Marcus theory (section 6.1.1) concurs with this observation.



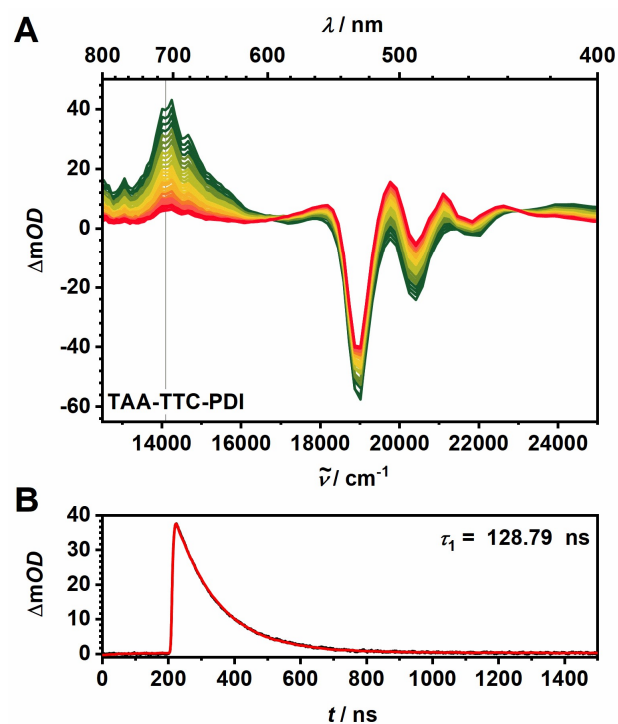
**Figure 57:** **A:** ns-TA spectra of TAAMe<sub>2</sub>-TTC-PDIME<sub>2</sub> in toluene at 293 K after light-excitation at 18900 cm<sup>-1</sup> (528 nm). Early spectra are given in dark green, late spectra in red and the time steps between the spectra are 7 ns. **B:** CSS decay curve (black) with the corresponding deconvolution fit (red) at 14100 cm<sup>-1</sup> (710 nm) (grey line in A).



**Figure 58:** **A:** ns-TA spectra of TAAMe<sub>2</sub>-TTC-PDI in toluene at 293 K after light-excitation at 18900 cm<sup>-1</sup> (528 nm). Early spectra are given in dark green, late spectra in red and the time steps between the spectra are 7 ns. **B:** CSS decay curve (black) with the corresponding deconvolution fit (red) at 14100 cm<sup>-1</sup> (710 nm) (grey line in A).



**Figure 59:** **A:** ns-TA spectra of TAA-TTC-PDIME<sub>2</sub> in toluene at 293 K after light-excitation at 18900 cm<sup>-1</sup> (528 nm). Early spectra are given in dark green, late spectra in red and the time steps between the spectra are 7 ns. **B:** CSS decay curve (black) with the corresponding deconvolution fit (red) at 14100 cm<sup>-1</sup> (710 nm) (grey line in A).



**Figure 60:** **A:** ns-TA spectra of **TAA-TTC-PDI** in toluene at 293 K after light-excitation at 18900  $\text{cm}^{-1}$  (528 nm). Early spectra are given in dark green, late spectra in red and the time steps between the spectra are 7 ns. **B:** CSS decay curve (black) with the corresponding deconvolution fit (red) at 14100  $\text{cm}^{-1}$  (710 nm) (grey line in **A**).

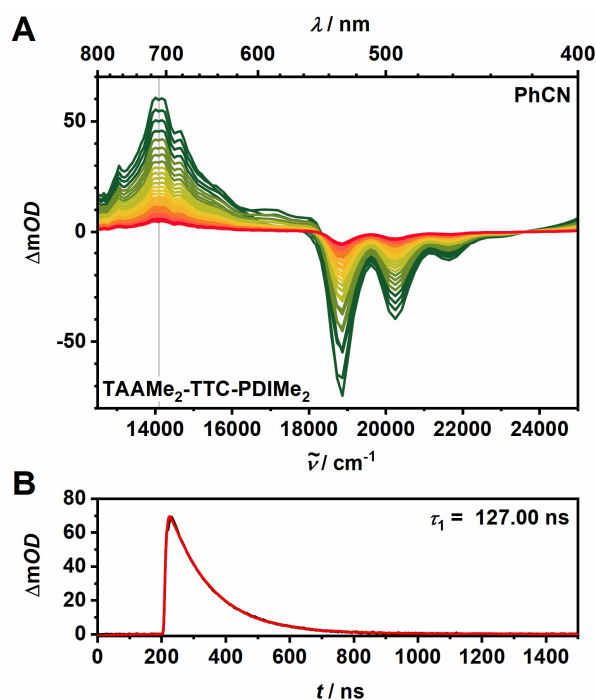
**Table 10:** CSS decay times  $\tau$  and the corresponding amplitudes  $a$  of the four rotationally hindered triads in toluene obtained by a deconvolution fit of the ns-TA decay.

	$\tau_1 / \text{ns}$	$a_1$	$\tau_2 / \text{ns}$	$a_2$
<b>TAAMe<sub>2</sub>-TTC-PDIME<sub>2</sub></b>	29.24	0.9706	117.17	0.0294
<b>TAAMe<sub>2</sub>-TTC-PDI</b>	46.34	0.8750	94.59	0.1250
<b>TAA-TTC-PDIME<sub>2</sub></b>	52.92	0.8382	104.08	0.1618
<b>TAA-TTC-PDI</b>	128.79	-	-	-

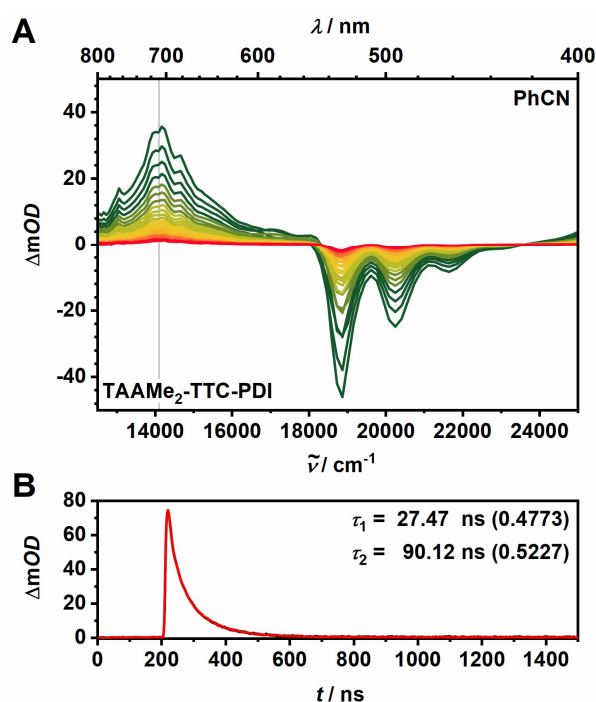


### Charge recombination at zero external magnetic field in PhCN

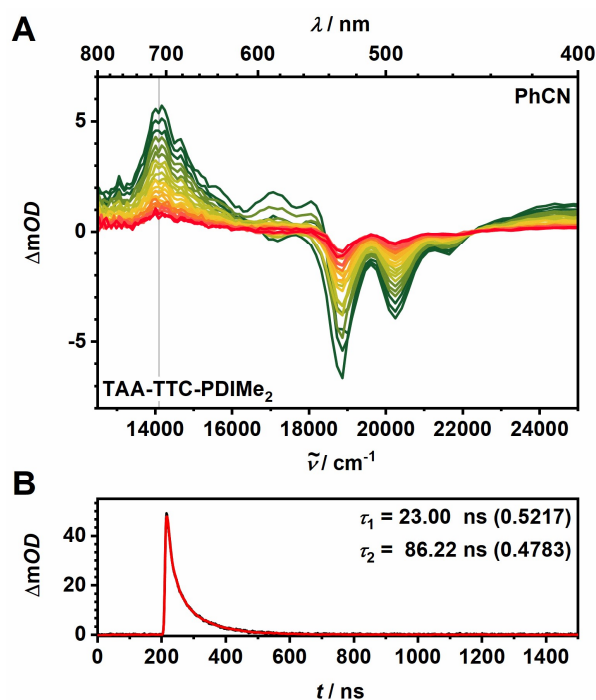
To check whether the solvent polarity influences the CR dynamics, the CR kinetics of **TAAMe<sub>2</sub>-TTC-PDIME<sub>2</sub>** (Figure 61), **TAAMe<sub>2</sub>-TTC-PDI** (Figure 62), **TAA-TTC-PDIME<sub>2</sub>** (Figure 63) and **TAA-TTC-PDI** (Figure 64) were measured using ns-TA spectroscopy after light-exciting of the **PDI** moiety. The ns-TA maps all show the same features. At early times all maps show the GSB of the **PDI** as well as an ESA at 14100 cm<sup>-1</sup> (710 nm). The latter is related to the formation of the charge separated state, which is in very good agreement with the fs-TA data (section 6.1.2.1). The charge separation process observed in the fs-TA data is, however, not visible in the ns-TA measurements because it is much faster than the shortest time step of the ns-TA measurements. The fs-TA measurements show that upon light-excitation the <sup>1</sup>PDI state is formed and is subsequently reduced by an electron from the **TAA**, leading to the formation of the <sup>1</sup>CSS (Figure 44 to Figure 43 in section 6.1.2.1), which may undergo spin interconversion to the <sup>3</sup>CSS. Charge recombination of the <sup>1</sup>CSS directly leads to the singlet ground state, which is forbidden for the <sup>3</sup>CSS. In PhCN the calculated energy level of <sup>1,3</sup>CSS is lower than the energy level of the <sup>3</sup>PDI (compare section 6.1.1), which excludes the CR<sub>T</sub> pathway and therefore the formation of a <sup>3</sup>PDI state. Consequently, in PhCN CR only occurs via singlet pathway. To determine the lifetime of the charge separated state, decay curves without an external magnetic field were measured and the decay times were extracted using a deconvolution fit (figures (B) in Figure 61 to Figure 64) (description in section 10.3.4.2). The CSS decay times decrease from **TAAMe<sub>2</sub>-TTC-PDIME<sub>2</sub>** over **TAAMe<sub>2</sub>-TTC-PDI** and **TAA-TTC-PDIME<sub>2</sub>** to **TAA-TTC-PDI** (Table 11). Thus, with increasing rotational freedom the lifetime of the CSS decrease, which is opposite to the trend observed in toluene. The change of the solvent from non-polar toluene to polar PhCN causes a modification of the *Marcus* region from the *Marcus* inverted region to the *Marcus* normal region for the CR processes (section 6.1.1). This effect was as well observed for other triads.<sup>[197]</sup>



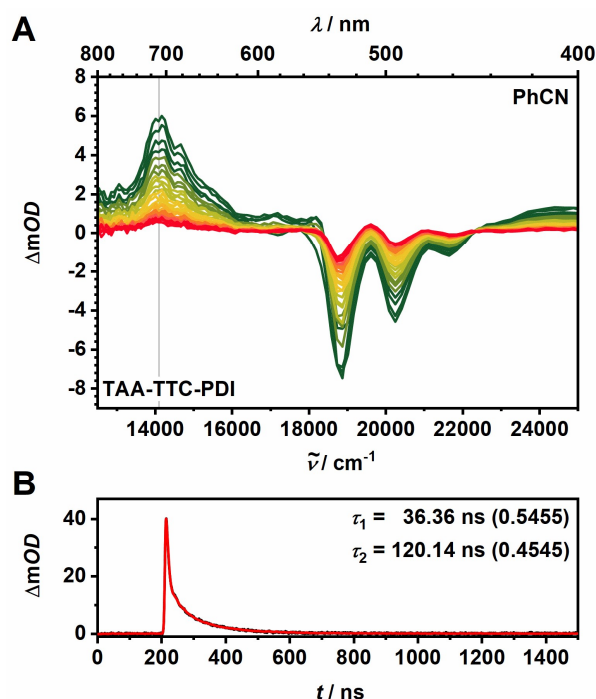
**Figure 61:** **A:** ns-TA spectra of TAAMe<sub>2</sub>-TTC-PDIME<sub>2</sub> in PhCN at 293 K after light-excitation at 18800 cm<sup>-1</sup> (532 nm). Early spectra are given in dark green, late spectra in red and the time steps between the spectra are 7 ns. **B:** CSS decay curve (black) with the corresponding deconvolution fit (red) at 14100 cm<sup>-1</sup> (710 nm) (grey line in A).



**Figure 62 A:** ns-TA spectra of TAAMe<sub>2</sub>-TTC-PDI in PhCN at 293 K after light-excitation at 18800 cm<sup>-1</sup> (532 nm). Early spectra are given in dark green, late spectra in red and the time steps between the spectra are 7 ns. **B:** CSS decay curve (black) with the corresponding deconvolution fit (red) at 14100 cm<sup>-1</sup> (710 nm) (grey line in A).



**Figure 63:** **A:** ns-TA spectra of **TAA-TTC-PDIME<sub>2</sub>** in PhCN at 293 K after light-excitation at 18800 cm<sup>-1</sup> (532 nm). Early spectra are given in dark green, late spectra in red and the time steps between the spectra are 7 ns. **B:** CSS decay curve (black) with the corresponding deconvolution fit (red) at 14100 cm<sup>-1</sup> (710 nm) (grey line in **A**).



**Figure 64:** **A:** ns-TA spectra of **TAA-TTC-PDI** in PhCN at 293 K after light-excitation at 18800 cm<sup>-1</sup> (532 nm). Early spectra are given in dark green, late spectra in red and the time steps between the spectra are 7 ns. **B:** CSS decay curve (black) with the corresponding deconvolution fit (red) at 14100 cm<sup>-1</sup> (710 nm) (grey line in **A**).

**Table 11:** CSS decay times  $\tau$  and the corresponding amplitudes  $a$  of the four rotationally hindered triads in PhCN obtained by a deconvolution fit of the ns-TA decay.

	$\tau_1 / \text{ns}$	$a_1$	$\tau_2 / \text{ns}$	$a_2$
<b>TAAMe<sub>2</sub>-TTC-PDIME<sub>2</sub></b>	127.00		-	-
<b>TAAMe<sub>2</sub>-TTC-PDI</b>	27.47	0.4773	90.12	0.5227
<b>TAA-TTC-PDIME<sub>2</sub></b>	23.00	0.5217	86.22	0.4783
<b>TAA-TTC-PDI</b>	36.36	0.5455	120.14	0.4545

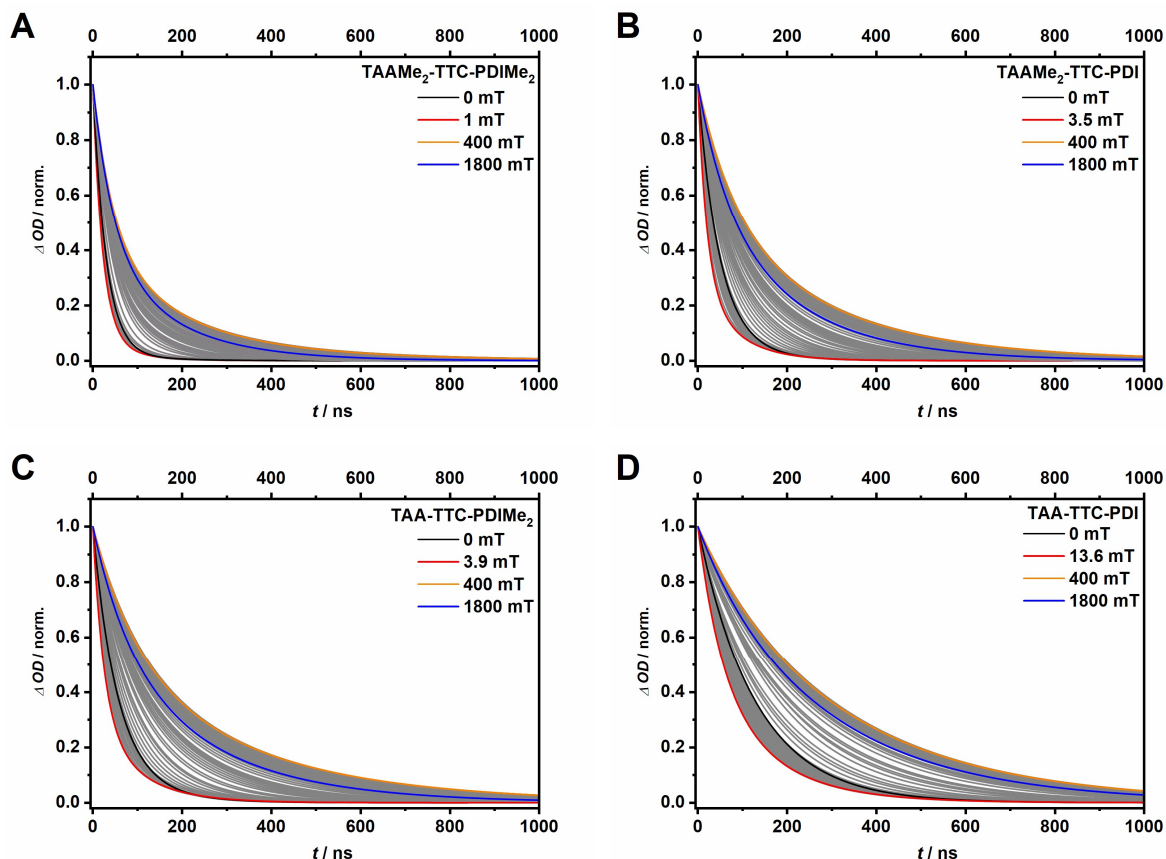
### 6.1.3.2 Magnetic field effect

The formation of CSS was proved in the previous sections for all rotationally hindered triads, using fs- and ns-TA spectroscopy (**section 6.1.2.1** and **6.1.3.1**). The fs-TA measurements show that after light-excitation of the **PDI** moiety the <sup>1</sup>PDI state is populated from which the <sup>1</sup>CSS is populated. The formation of a local <sup>3</sup>PDI state is observed in the ns-TA maps (**section 6.1.3.1**) in toluene, which indicates a spin evolution between the <sup>1</sup>CSS and the <sup>3</sup>CSS, because spin conservation rules restrict that the <sup>1</sup>CSS only recombines to the ground state and the <sup>3</sup>CSS to the local <sup>3</sup>PDI state. This spin evolution as well as the exchange interaction  $2J$  can be investigated in detail using varying external magnetic fields during the ns-TA measurements (**section 1.1**). The CR kinetics of the triads **TAAMe<sub>2</sub>-TTC-PDIME<sub>2</sub>**, **TAAMe<sub>2</sub>-TTC-PDI**, **TAA-TTC-PDIME<sub>2</sub>** and **TAA-TTC-PDI** were therefore investigated by measuring ns-TA at 14100 cm<sup>-1</sup> (710 nm) (setup and analysis details in **section 10.3.4.2**) with applying magnetic fields between 0 and 1800 mT in about 90 steps (exact values and lifetimes in **Appendix**). The decay curves were corrected by deconvolution with the instrumental response function (IRF).

#### Magnetic field effect in toluene

For all the CSS decay curves of **TAAMe<sub>2</sub>-TTC-PDIME<sub>2</sub>**, **TAAMe<sub>2</sub>-TTC-PDI**, **TAA-TTC-PDIME<sub>2</sub>** and **TAA-TTC-PDI** (**Figure 65**) a pronounced magnetic field effect is observed. The decay times decrease at low fields until a minimum is reached (from black to red, **Table 12**), then subsequently increase significantly until a magnetic field of about 400 mT (orange) is reached. Thereafter, a weak decrease of the decay times  $\tau$  upon increasing external magnetic field from 400 mT to 1800 mT (blue) is visible (**Table 12**). The lifetimes at zero magnetic field increase with decreasing rotational hindrance from **TAAMe<sub>2</sub>-TTC-PDIME<sub>2</sub>** to **TAA-TTC-PDI** (black in

**Figure 65** and **Table 12**). The lifetimes of the red curves, which represents the external magnetic field of each triad corresponding to the exchange interaction  $2J$ , are decreasing with decreasing rotational hindrance from **TAAMe<sub>2</sub>-TTC-PDIME<sub>2</sub>** over **TAAMe<sub>2</sub>-TTC-PDI** and **TAA-TTC-PDIME<sub>2</sub>** to **TAA-TTC-PDI** (**Figure 65** and **Table 12**). The lifetimes at higher fields significantly exceed the lifetimes at zero magnetic field.



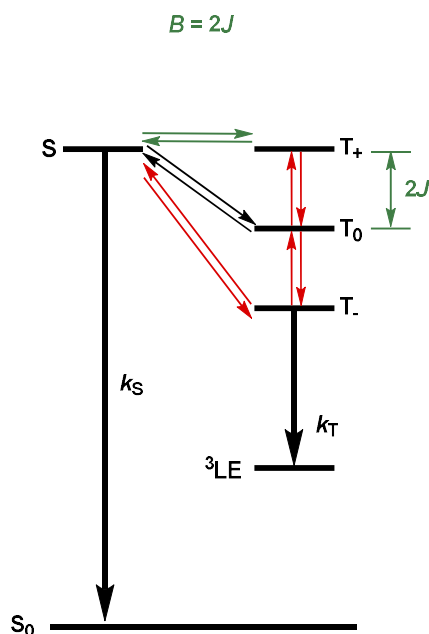
**Figure 65:** Deconvolution fit of the experimental transient decay curves of **A: TAAMe<sub>2</sub>-TTC-PDIME<sub>2</sub>** **B: TAAMe<sub>2</sub>-TTC-PDI** **C: TAA-TTC-PDIME<sub>2</sub>** and **D: TAA-TTC-PDI** at  $14100\text{ cm}^{-1}$  ( $710\text{ nm}$ ) after light-excitation at  $18900\text{ cm}^{-1}$  ( $528\text{ nm}$ ) in toluene at  $298\text{ K}$ . The magnetic field was varied from  $0$  to  $1800\text{ mT}$  in about  $90$  steps. All curves are depicted in grey and only the significant turning points of the MFE are highlighted. The highlighted curves describe the external magnetic fields: black =  $0\text{ mT}$ , red =  $2J$ , hereby the curves not always represent the exact calculated  $2J$  values but correspond to the curves closest to the exact value. Orange =  $400\text{ mT}$ , blue =  $1800\text{ mT}$ .

**Table 12:** Selected CSS lifetimes  $\tau$  and the corresponding amplitudes  $a$  of the four rotationally hindered triads in toluene obtained by using a deconvolution fit to the ns-TA decay curves. The magnetic fields correspond to the highlighted curves in **Figure 65**.

	external magnetic field	$\tau_1$ / ns	$a_1$	$\tau_2$ / ns	$a_2$	$\tau_3$ / ns	$a_3$
<b>TAAMe<sub>2</sub>-TTC-PDIME<sub>2</sub></b>	0 mT	29.24	0.9706	117.17	0.0294	-	-
	1.0 mT	22.16	0.9167	77.91	0.0833	-	-
	400 mT	43.13	0.5366	157.88	0.3415	337.96	0.1220
	1800 mT	45.67	0.5750	162.86	0.4250	-	-
<b>TAAMe<sub>2</sub>-TTC-PDI</b>	0 mT	46.34	0.8750	94.59	0.1250	-	-
	3.5 mT	20.09	0.7105	79.53	0.2895	-	-
	400 mT	84.64	0.4737	284.49	0.5263	-	-
	1800 mT	65.72	0.3919	198.63	0.6081	-	-
<b>TAA-TTC-PDIME<sub>2</sub></b>	0 mT	52.92	0.8382	104.08	0.1618	-	-
	3.9 mT	24.83	0.6944	96.75	0.3056	-	-
	400 mT	100.36	0.4571	332.82	0.5429	-	-
	1800 mT	79.59	0.3944	238.22	0.6056	-	-
<b>TAA-TTC-PDI</b>	0 mT	128.79	-	-	-	-	-
	13.6 mT	54.03	0.5263	144.99	0.4737	-	-
	400 mT	132.33	0.1304	330.58	0.8696	-	-
	1800 mT	99.01	0.1250	290.45	0.8750	-	-

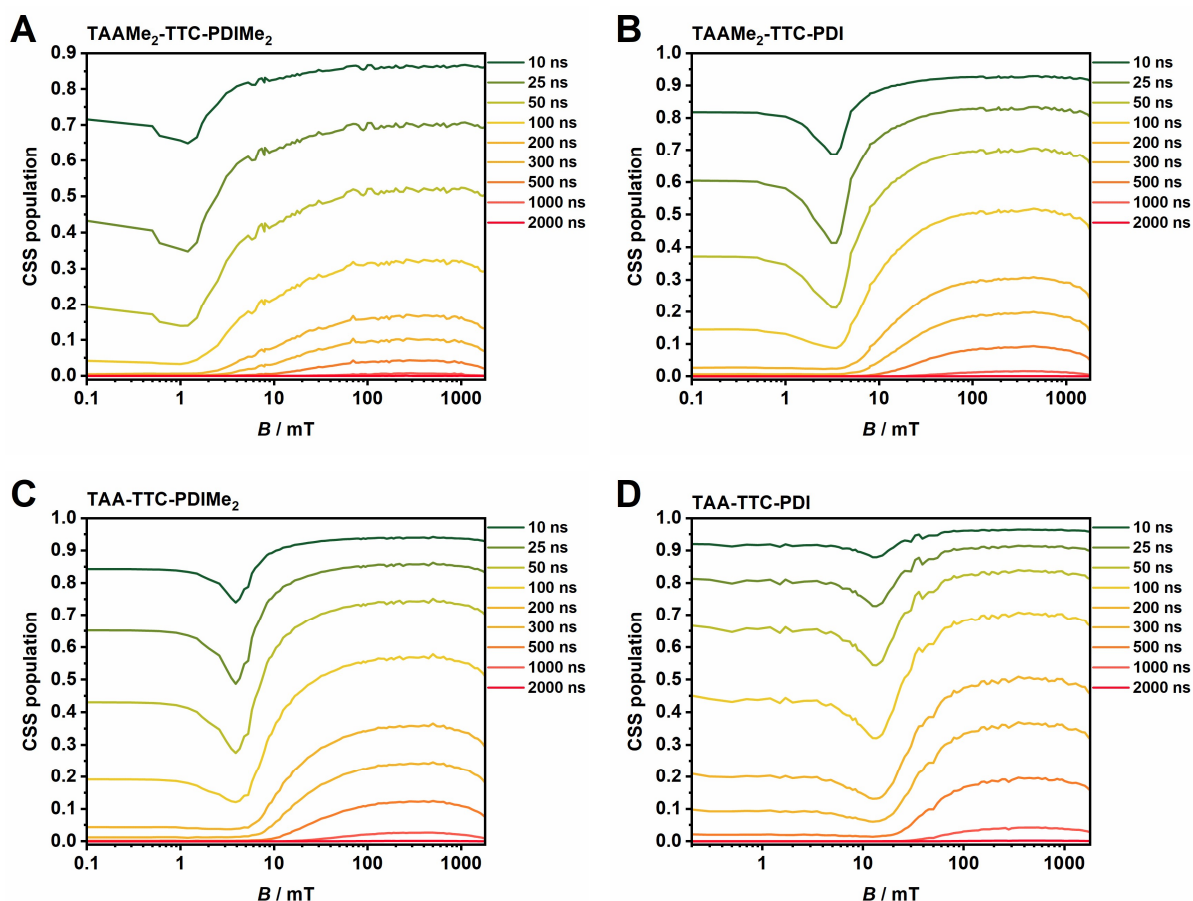
The observation of the decay curves and the corresponding decay times and amplitudes already gives a rough overview of the underlying spin dynamics. In order to get a better understanding of the magnetic field effect on the decay kinetics, the signal amplitudes at different delay times, namely 10 ns, 25 ns, 50 ns, 100 ns, 200 ns, 300 ns, 500 ns, 1000 ns and 2000 ns, can be plotted against the magnetic field. These diagrams are denoted as MARY (magnetic field affected reaction yields) plots because the amplitudes can be conceived as measures of reaction yields.<sup>[91]</sup> Those MARY plots open the possibility of extracting the magnetic field strength associated with the exchange interaction  $2J$  directly from the graph. As already described earlier (**Figure 6** in **section 1.1.4**), this is possible if the exchange interaction is in a range where it is larger than the effective hyperfine interaction ( $2J > a_{\text{eff}}$ ) and a spin interconversion at zero magnetic field is possible through the ahf-mechanism but not through the coherent hfc-mechanism. Structurally similar triads investigated in literature reveal positive exchange interactions.<sup>[112, 160]</sup> Thus, we also assume a positive value for  $J$  of the herein investigated triads, and the application of an external magnetic field results in the rise of the  $T_+$

*Zeeman* level until it becomes degenerate with the  $^1\text{CSS}$  and therefore a coherent spin interconversion between them occurs (**Figure 66**). This coherent process causes an increase of the spin interconversion rate constant  $k_+$ , leading to a more effective transition between the  $^1\text{CSS}$  and the  $^3\text{CSS}$ . This enhanced transition leads to an increased population of the  $T_+$  state, which in turn recombines to the  $^3\text{PDI}$  state. Therefore, the region in which the external field reaches  $B = 2J$  presents as a pronounced negative resonance peak in the MARY plots.



**Figure 66:** Reaction dynamics between the  $^1\text{CSS}$  and the  $^3\text{CSS}$  with a positive exchange interaction  $2J$  ( $\Delta E_{\text{ST}}$ ) in a range where the external magnetic field reaches the value of  $2J$  ( $B = 2J$ ).

The MARY plots of the triads **TAAMe<sub>2</sub>-TTC-PDIME<sub>2</sub>**, **TAAMe<sub>2</sub>-TTC-PDI**, **TAA-TTC-PDIME<sub>2</sub>** and **TAA-TTC-PDI** (**Figure 67**) all show the aforementioned resonance peak and therefore the exchange interaction  $2J$  can directly be determined from this representation. In order to get a precise value, the region around the resonance peak at a delay time of 50 ns of each triad was fitted yielding the value for  $2J$  (**Table 13**, graphs see **Appendix**). This approach ensures comparability of the values, as the differences between the  $2J$  couplings are often small. The calculated values increase from **TAAMe<sub>2</sub>-TTC-PDIME<sub>2</sub>** (1.0 mT) over **TAAMe<sub>2</sub>-TTC-PDI** (3.2 mT) and **TAA-TTC-PDIME<sub>2</sub>** (3.9 mT) to **TAA-TTC-PDI** (13.5 mT).



**Figure 67:** MARY plots of the rotationally hindered triads **A:**  $\text{TAAMe}_2\text{-TTC-PDIME}_2$  **B:**  $\text{TAAMe}_2\text{-TTC-PDI}$  **C:**  $\text{TAA-TTC-PDIME}_2$  and **D:**  $\text{TAA-TTC-PDI}$  in toluene at 298 K.

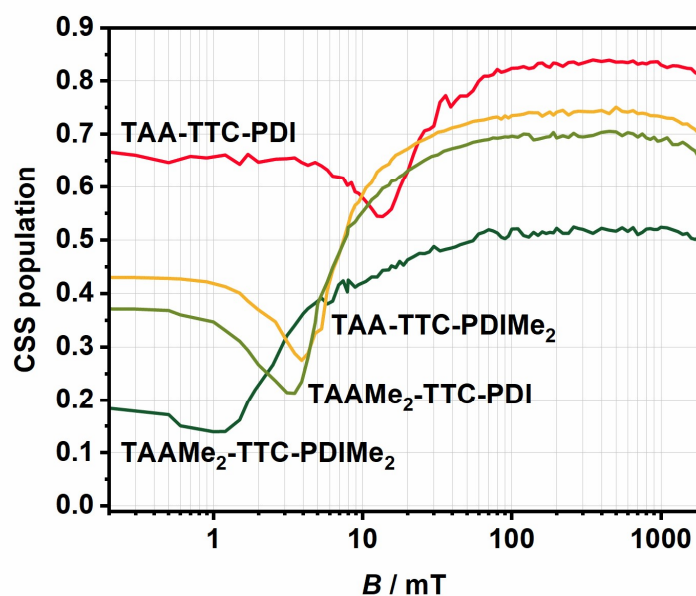
**Table 13:**  $2J$  values of the four rotationally hindered triads in toluene at 298 K determined by fitting the  $2J$  region at a delay time of 50 ns of each rotationally hindered triad using a parabolic fit function.

	$2J / \text{mT}$
$\text{TAAMe}_2\text{-TTC-PDIME}_2$	1.0
$\text{TAAMe}_2\text{-TTC-PDI}$	3.2
$\text{TAA-TTC-PDIME}_2$	3.9
$\text{TAA-TTC-PDI}$	13.5

For better comparability, the CSS populations of all four triads are plotted against the external magnetic field at a delay time of 50 ns, showing the differences between the triads (**Figure 68**). The CSS population of  $\text{TAAMe}_2\text{-TTC-PDIME}_2$  at a delay time of 50 ns is strongly diminished compared to the one of  $\text{TAA-TTC-PDI}$ , which is due to the much shorter decay times of  $\text{TAAMe}_2\text{-TTC-PDIME}_2$  (**Table 12**). The increase of the  $2J$  couplings with decreasing rotational hindrance becomes more obvious in this presentation. The magnetic field dependent



ns-TA measurements show a strong increase in the  $2J$  coupling with decreasing rotational hindrance along the series from **TAAMe<sub>2</sub>-TTC-PDIME<sub>2</sub>** over **TAAMe<sub>2</sub>-TTC-PDI** and **TAA-TTC-PDIME<sub>2</sub>** to **TAA-TTC-PDI**, which indicates that the electronic coupling between the **TAA** donor state and the **PDI** acceptor state is strongly influenced by restricting the rotation.



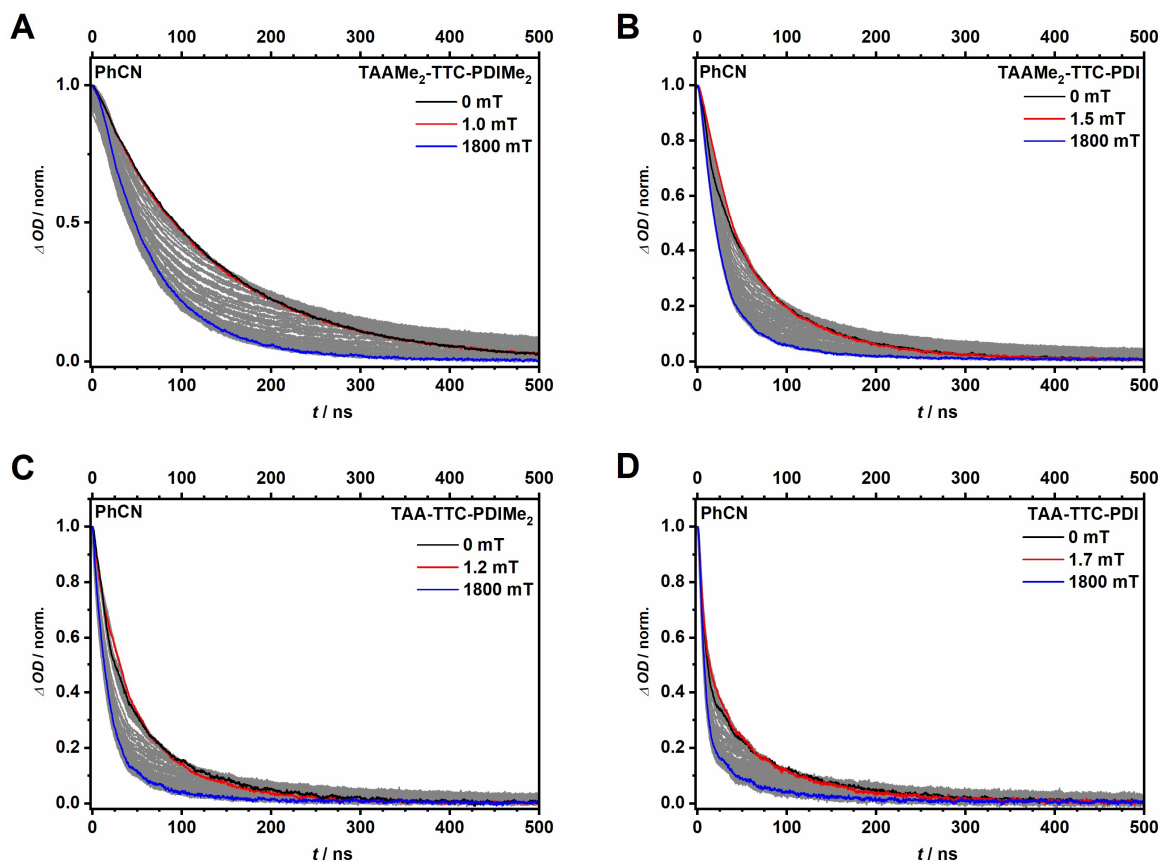
**Figure 68:** Comparison of the MARY plots of the triads **TAAMe<sub>2</sub>-TTC-PDIME<sub>2</sub>**, **TAAMe<sub>2</sub>-TTC-PDI**, **TAA-TTC-PDIME<sub>2</sub>** and **TAA-TTC-PDI** at a delay time of 50 ns.

### Magnetic field effect in PhCN

As described before, in toluene **TAAMe<sub>2</sub>-TTC-PDIME<sub>2</sub>**, **TAAMe<sub>2</sub>-TTC-PDI**, **TAA-TTC-PDIME<sub>2</sub>** and **TAA-TTC-PDI** show a pronounced magnetic field effect as well as  $2J$  couplings that strongly increase with increasing rotational freedom. Changing the solvent from non-polar toluene to polar PhCN causes a strong change in the spin dynamics. It must be noted that the shown decay curves in PhCN as well as the resulting MARY plots depict the original measured data which were not deconvoluted with the IRF. This representation is adequate for a qualitative analysis of the MFE, but a detailed analysis would require the deconvolution with the IRF. Thus, the measured data in PhCN are only briefly described but no deeper analysis is given.

Changing the solvent polarity from non-polar toluene to polar PhCN stabilises the CSS energies and causes a change in the reorganisation energies, which was already found in other triads.<sup>[197]</sup> Regarding the triads in PhCN, the energies of the <sup>1,3</sup>CSSs (approx. 7260 cm<sup>-1</sup>, 0.90 eV) are lower than the <sup>3</sup>PDI state energy<sup>[188]</sup> (9680 cm<sup>-1</sup>, 1.2 eV) (see **section 6.1.1**), which excludes the triplet pathway for the CR process. Therefore, the CR<sub>T</sub> pathway which was favoured in toluene now changes to the CR<sub>S</sub> pathway in PhCN, causing a change in the recombination dynamics. The enhanced spin evolution in the  $2J$  region slows down the CR processes because the coherent spin interconversion between <sup>1</sup>CSS and <sup>3</sup>CSS causes a higher triplet concentration, causing a positive resonance peak in the  $2J$  region.

The CSS decay curves of **TAAMe<sub>2</sub>-TTC-PDIME<sub>2</sub>**, **TAAMe<sub>2</sub>-TTC-PDI**, **TAA-TTC-PDIME<sub>2</sub>** and **TAA-TTC-PDI** (**Figure 69**) all show a magnetic field effect in PhCN. The decay times increase at low fields until they reach a maximum (from black to red, **Table 14**), then they subsequently decrease significantly until a magnetic field of 1800 mT (blue, **Table 14**) is reached. The lifetimes at zero magnetic field decrease with decreasing rotational hindrance from **TAAMe<sub>2</sub>-TTC-PDIME<sub>2</sub>** to **TAA-TTC-PDI** (blue in **Figure 69** and **Table 14**). The lifetimes of the red curves, which represents the external magnetic field of each triad corresponding to the exchange interaction  $2J$ , are decreasing with decreasing rotational hindrance from **TAAMe<sub>2</sub>-TTC-PDIME<sub>2</sub>** over **TAAMe<sub>2</sub>-TTC-PDI** and **TAA-TTC-PDIME<sub>2</sub>** to **TAA-TTC-PDI**. The lifetimes at higher fields significantly exceed the lifetimes at zero magnetic field. The change in the recombination pathway reverses the trend observed in toluene. Thus, in PhCN the decay times decrease from **TAAMe<sub>2</sub>-TTC-PDIME<sub>2</sub>** over **TAAMe<sub>2</sub>-TTC-PDI** and **TAA-TTC-PDIME<sub>2</sub>** to **TAA-TTC-PDI** with increasing rotational freedom.

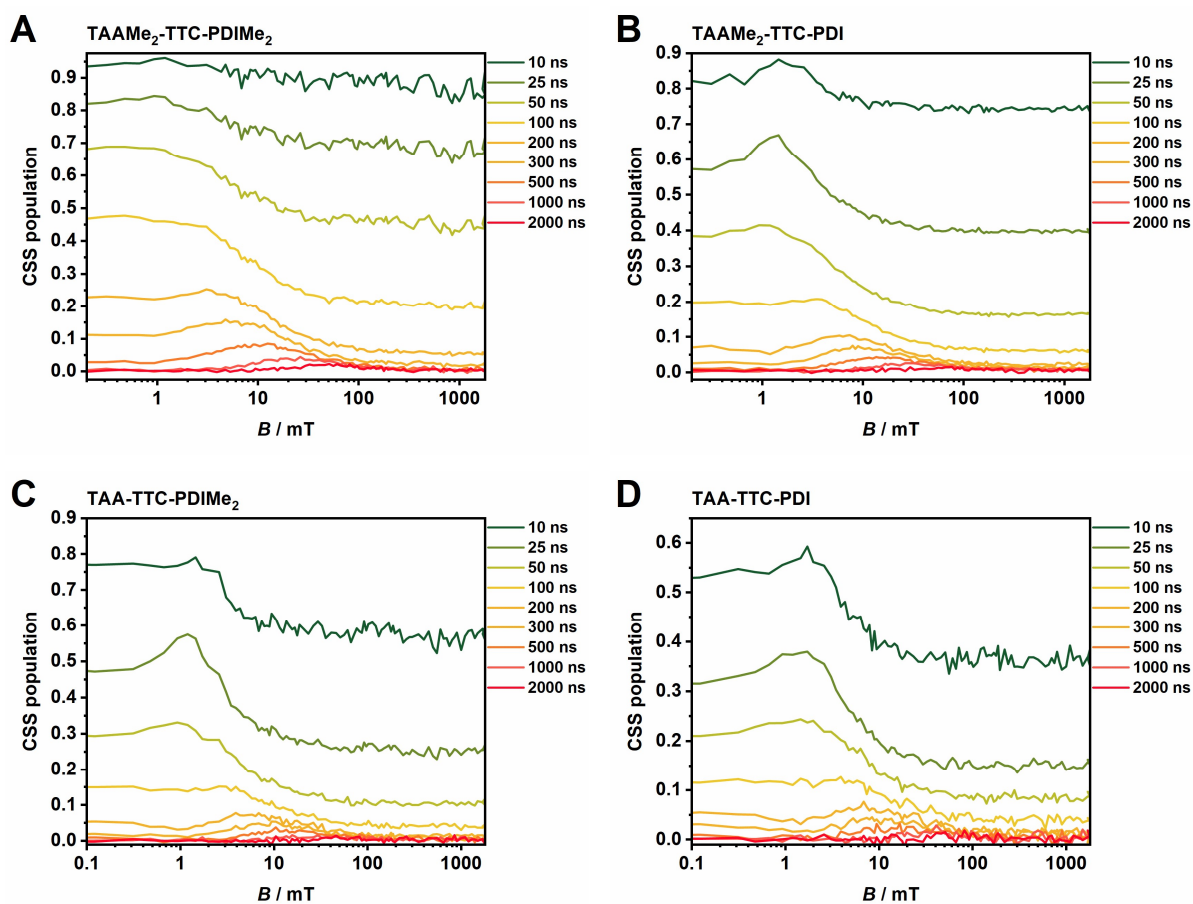


**Figure 69:** Transient decay curves of **A: TAAMe<sub>2</sub>-TTC-PDIME<sub>2</sub>** **B: TAAMe<sub>2</sub>-TTC-PDI** **C: TAA-TTC-PDIME<sub>2</sub>** and **D: TAA-TTC-PDI** at 14100 cm<sup>-1</sup> (710 nm) after light-excitation at 18800 cm<sup>-1</sup> (532 nm) in PhCN at 298 K. The magnetic field was varied from 0 to 1800 mT in about 90 steps. Most curves are depicted in grey and only the significant turning points of the MFE are highlighted. The highlighted curves describe specific magnetic fields: black = 0 mT, red = 2J, blue = 1800 mT.

**Table 14:** Selected CSS lifetimes  $\tau$  and the corresponding amplitudes  $a$  of the four rotationally hindered triads in PhCN obtained using a deconvolution fit on the ns-TA measurements. The lifetimes given correspond to the highlighted curves in **Figure 69**.

	external magnetic field	$\tau_1$ / ns	$a_1$	$\tau_2$ / ns	$a_2$
<b>TAAMe<sub>2</sub>-TTC-PDIME<sub>2</sub></b>	0 mT	127.00		-	-
	1.0 mT	132.45		-	-
	1800 mT	64.03		-	-
<b>TAAMe<sub>2</sub>-TTC-PDI</b>	0 mT	27.47	0.4773	90.12	0.5227
	1.5 mT	32.01	0.6458	99.10	0.3542
	1800 mT	19.65	0.9130	100.00	0.0870
<b>TAA-TTC-PDIME<sub>2</sub></b>	0 mT	23.00	0.5217	86.22	0.4783
	1.2 mT	36.16	0.7308	96.13	0.2692
	1800 mT	17.46	0.9130	102.81	0.0870
<b>TAA-TTC-PDI</b>	0 mT	36.36	0.5455	120.14	0.4545
	1.7 mT	65.60		-	-
	1800 mT	55.08		-	-

On the one hand, for **TAAMe<sub>2</sub>-TTC-PDIME<sub>2</sub>** the value of the  $2J$  coupling is not changed by the solvent polarity, showing a value of 1.0 mT in PhCN compared to 1.0 mT in toluene (**Figure 70** and **Table 15**, toluene values in **Table 13**). On the other hand, the triads **TAAMe<sub>2</sub>-TTC-PDI** and **TAA-TTC-PDIME<sub>2</sub>** show diminished exchange interactions of 1.5 mT and 1.2 mT in PhCN compared to 3.2 mT and 3.9 mT in toluene, respectively. The reduction of the  $2J$  value of the triad **TAA-TTC-PDI** due to solvent polarity from 13.5 mT in toluene to 1.7 mT in PhCN is even more pronounced. The trend of increasing  $2J$  values with increasing rotational freedom, which was observed in toluene still holds true for PhCN but is significantly less pronounced. In changing the energetic levels of the CSSs the energy differences between the possible product and reactant levels for ET processes are influenced as well. Thus, those energetic changes not only influence the rate constants for CR but also the couplings between all accessible energetic states. Due to the proportionality of the electronic couplings involved in the ET processes and the exchange interaction  $2J$  the position of the resonance peak in the MARY plots strongly depends on solvent polarity (**equation (18)** in **section 6.1.5**).<sup>[96, 197]</sup>



**Figure 70:** MARY plots of **A:** TAAMe<sub>2</sub>-TTC-PDIME<sub>2</sub> **B:** TAAMe<sub>2</sub>-TTC-PDI **C:** TAA-TTC-PDIME<sub>2</sub> and **D:** TAA-TTC-PDI in PhCN at 298 K. Hereby, the depicted MARY plots represent the measured data without deconvolution of the raw data with the IRF.

**Table 15:** Experimental  $2J$  values of the four rotationally hindered triads in PhCN at 298 K.

	$2J$ / mT
TAAMe <sub>2</sub> -TTC-PDIME <sub>2</sub>	1.0
TAAMe <sub>2</sub> -TTC-PDI	1.5
TAA-TTC-PDIME <sub>2</sub>	1.2
TAA-TTC-PDI	1.7

#### 6.1.4 Quantum mechanical consideration

In the previous sections, the ET processes of **TAAMe<sub>2</sub>-TTC-PDIME<sub>2</sub>**, **TAAMe<sub>2</sub>-TTC-PDI**, **TAA-TTC-PDIME<sub>2</sub>** and **TAA-TTC-PDI** after light-excitation of the **PDI** moiety were investigated, using fs-TA and magnetic field dependent ns-TA spectroscopy. These measurements showed a strong dependency of the CS rate constant  $k_{CS}$  and the exchange interaction  $2J$  on the degree of rotational restriction. To examine the spin dynamic behaviour, simulations were applied to the experimental data using the classical kinetic approach, as described before (**section 1.1.3**). However, an accurate fit of the data was not obtained (see **section 10.2**). This is due to the strong multi-exponential behaviour of the obtained decay curves over the entire magnetic field range.

In order to access a field dependent representation of the experimental data, a parameter  $k(B)$  was determined and plotted against the magnetic field  $B$ , which produces a kind of magnetic field spectrum of the kinetics (solid lines in **Figure 71**) for each triad. This magnetic field dependent parameter  $k(B)$  was obtained by fitting the first 100 ns of the ns-TA decays using a mono-exponential fit. This function compares well to the first 100 ns of the experimental kinetics but does not fully describe the ns-TA data, particularly towards longer times.

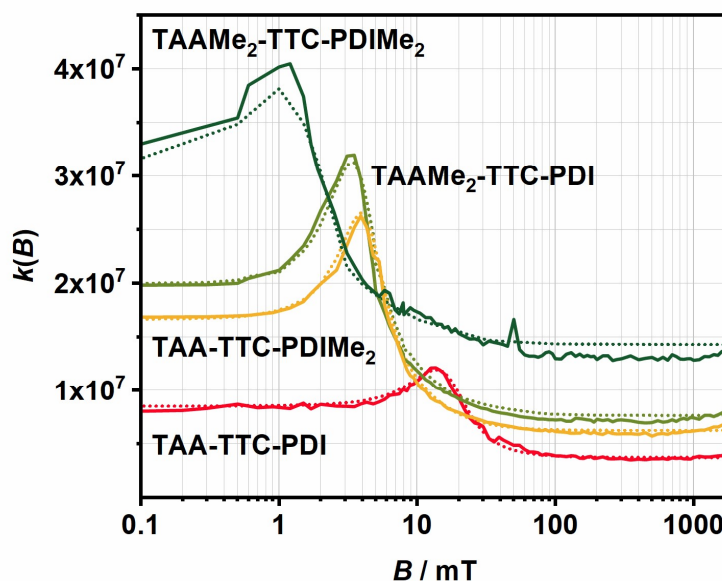
To obtain a complete picture of the spin dynamics, quantum dynamical simulations based on the Stochastic Liouville Equation were provided by *Prof. Dr. U. E. Steiner* (University of Konstanz). The methodology as well as the theoretical background<sup>[79, 89]</sup> are not discussed further in this thesis but can be found in the literature.<sup>[91]</sup>

The set of best fit parameters for the rate constants of CR<sub>S</sub> ( $k_S$ ), of CR<sub>T</sub> ( $k_T$ ), singlet-triplet dephasing ( $k_{STD}$ ) as well as the exchange interaction  $J$  and the observed values for  $B_{max} \approx 2J$  (**Figure 67** and **Figure 68** in **section 6.1.3.2**) are given in **Table 16**.<sup>[91]</sup> Singlet-triplet dephasing is caused by fluctuations of  $2J$  resulting from bridge torsional dynamics.<sup>[94, 198]</sup> For the quantum dynamic simulations only the five strongest hyperfine couplings were taken into account, namely  $a_N = 0.926$  mT<sup>[199-200]</sup> for the **TAA** nitrogen of the donor and  $a_H = 0.18$  mT<sup>[201]</sup> for the four hydrogens of the **PDI** acceptor.

**Table 16:** Best fit parameters that were used for the quantum simulations of the CSS decay curves, whereby  $k_S$  and  $k_T$  are the values of the rate constants for  $CR_S$  and  $CR_T$ , respectively. Hereby, the values for the rotational correlation time  $\tau_r = 0.6$  ns and for the hfc anisotropy of the **TAA** nitrogen  $\Delta a_N = 1.51$  mT were identical for all rotationally hindered triads.  $k_{STD}$  represents the rate for singlet/triplet dephasing and  $J$  the exchange interaction.

	$k_S / s^{-1}$	$k_T / s^{-1}$	$k_{STD} / s^{-1}$	$J / mT$	$B_{max}/2 / mT$
<b>TAAMe<sub>2</sub>-TTC-PDIME<sub>2</sub></b>	0-1.1·10 <sup>5</sup>	0.7-0.9·10 <sup>8</sup>	0-9·10 <sup>6</sup>	0.23-0.27	0.6
<b>TAAMe<sub>2</sub>-TTC-PDI</b>	0-2.0·10 <sup>5</sup>	1.3-1.7·10 <sup>8</sup>	1.3-1.7·10 <sup>8</sup>	1.5-1.6	1.75
<b>TAA-TTC-PDIME<sub>2</sub></b>	0-2.0·10 <sup>5</sup>	0.9-1.1·10 <sup>8</sup>	1.8-2.4·10 <sup>8</sup>	1.8-2.0	1.95
<b>TAA-TTC-PDI</b>	0-1.1·10 <sup>6</sup>	0.8-1.1·10 <sup>8</sup>	1.1-1.6·10 <sup>9</sup>	6.3-6.7	6.8

The  $k(B)$  spectra obtained from the quantum simulations match the experimental data closely and the maxima reflect the increasing rate at the S/T<sub>+</sub> crossing (dashed lines in **Figure 71**). Therefore, quantum dynamics calculated with the parameters obtained by fitting  $k(B)$  is expected to correctly represent the kinetics both for decay times below and above 100 ns.



**Figure 71:**  $k(B)$  versus  $B$  spectra of the CSS decay of the four rotationally hindered triads assuming mono-exponential decay kinetics within the first 100 ns. The solid curves represent the experimental data and the dashed curves the data obtained from the quantum simulations. Adjusted with permission.<sup>[91]</sup>

The quantum dynamical simulations give valuable insight into the spin dynamics of the four rotationally hindered triads. The multi-exponential kinetics of the ns-TA data were attributed to the hyperfine heterogeneity of the kinetics. The heterogeneity is due to hyperfine states with vanishing S/T<sub>0</sub> coupling (so called “orphan-states”) that decay significantly slower and

therefore occupy increasingly larger fractions of the total CSS population.<sup>[91]</sup> Comparing the results found here with similar literature known triads<sup>[48]</sup>, the herein investigated rotationally hindered triads show less pronounced “orphan-states”.<sup>[91]</sup>

The quantum dynamic simulations show a strong influence of the rotational freedom of the triads on the position of the  $2J$ -resonance peak and on the magnitude of the CR rate constants.

### 6.1.5 Calculation of the electronic couplings $V$

In the previous sections the rate constants for CS and CR as well as the exchange interaction  $2J$  were determined using a global target analysis on the fs-TA spectroscopy data and quantum dynamic simulations on the magnetic field dependent ns-TA spectroscopy data. In this part, the electronic couplings<sup>13</sup> between the donor states and the acceptor states for CS, CR<sub>T</sub> and CR<sub>S</sub> were calculated to check whether intramolecular twisting affects the electronic couplings, and if so, how strong the influence is.

In general, by controlling the dihedral angle between aromatic  $\pi$ -systems of bridging units connecting the donor and the acceptor moiety, their electronic coupling is adjusted.<sup>[109, 202-204]</sup>

The literature focus is mainly on the rates of electron or hole transfer. However, the exchange interaction  $2J$  is mostly neglected<sup>[106]</sup> but both the rate constants of electron transfer as well as the exchange interaction depend on the magnitude of the electronic couplings.

For a quantitative analysis, the relation between the rate constant and the electronic couplings  $V$ <sup>[205]</sup> for a specific ET reaction is given by

$$k_{ET,mn} = \frac{2\pi}{\hbar} V_{mn}^2 (\text{FCWDS}_{mn})$$

$$= \frac{2\pi}{\hbar} V_{mn}^2 \sum_{j=0}^{\infty} \frac{e^{-S} S^j}{j!} \sqrt{\frac{1}{4\pi\lambda_0 kT}} \exp\left[-\frac{j\tilde{\nu}_V + \lambda_0 + \Delta G_{mn}}{4\lambda_0 kT}\right] \quad (17)$$

and the relation between the exchange interaction  $2J$  and the electronic couplings<sup>[96]</sup> given by

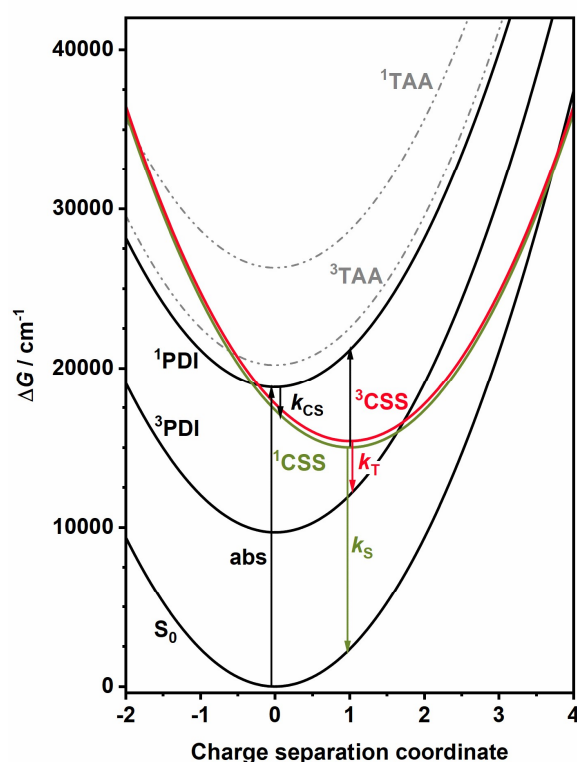
$$2J = \Delta E_S - \Delta E_T = \left[ \sum_n \frac{V_{1CSS-n}^2}{E_{1CSS} - E_n - \lambda} \right]_S - \left[ \sum_n \frac{V_{3CSS-n}^2}{E_{3CSS} - E_n - \lambda} \right]_T \quad (18)$$

<sup>13</sup> Calculated by Dr. M. Holzapfel.



were used. Here, the electronic couplings  $V_{1\text{CSS}-n}$  and  $V_{3\text{CSS}-n}$  represent the coupling of the  $^{1,3}\text{CSS}$  with its precursor- or recombination state of the regarded ET process.

In order to quantify the electronic couplings, the electronic states  $n$  involved in the ET processes are necessary. The states under consideration for the ET processes are the lowest excited singlet state of the **PDI** ( $^1\text{PDI}$  18800  $\text{cm}^{-1}$ , 2.33 eV) determined from the absorption and emission measurements (**section 4**) as well as the lowest excited triplet state of the **PDI** ( $^3\text{PDI}$  9690  $\text{cm}^{-1}$ , 1.20 eV) taken from literature.<sup>[188]</sup> The  $^{1,3}\text{CSS}$  energies of the triads **TAAMe<sub>2</sub>-TTC-PDIME<sub>2</sub>** (15000  $\text{cm}^{-1}$ , 1.86 eV), **TAAMe<sub>2</sub>-TTC-PDI** (15000  $\text{cm}^{-1}$ , 1.86 eV), **TAA-TTC-PDIME<sub>2</sub>** (15300  $\text{cm}^{-1}$ , 1.90 eV) and **TAA-TTC-PDI** (15200  $\text{cm}^{-1}$ , 1.90 eV) (**Table 36** in **section 10.1**) were calculated using the *Weller*-approximation<sup>14</sup> (**equation (24)** in **section 10.1**). The energies of the  $^1\text{TAA}$  and  $^3\text{TAA}$  states are too far off in energy and therefore are not considered to affect the ET processes.<sup>[91]</sup> Based on those results, an energy diagram is formulated with the energetic levels given relative to the ground state  $S_0$  (**Figure 72**).



**Figure 72:** Energy level diagram of the states involved in CS and CR with their respective free energy parabolas. The vertical arrows starting from the equilibrium position of the pertinent initial states depict the ET process.

<sup>14</sup> Calculated by Dr. M. Holzapfel.

The coupling matrix element  $V_{mn}$  between two states  $m$  and  $n$  for CS and CR<sub>S</sub> (**Table 17**) were calculated using the values for  $k_{CS}$  obtained from the global target analysis (**Table 8** in **section 6.1.2.2**) or  $k_T$  obtained from the quantum dynamic simulations (**Table 16** in **section 6.1.4**). This gave the electronic couplings  $V_{1CSS-1PDI}$  and  $V_{3CSS-3PDI}$ , respectively. This was done using the aforementioned relation for diabatic ET given by *Closs and Miller*<sup>[205]</sup> (**equation (17)**) since the electronic couplings are expected to be in the diabatic rate regime ( $V \ll RT$ ), which was also found for similar triads.<sup>[47]</sup>

DFT calculations were used to determine the values for the inner and outer reorganisation energies in toluene, which are  $\lambda_v = 1855 \text{ cm}^{-1}$  (0.23 eV) and  $\lambda_o = 484 \text{ cm}^{-1}$  (0.06 eV), respectively (see **section 10.1**). The reorganisation energies together with an estimated molecular vibrational frequency of  $\tilde{\nu}_v = 1500 \text{ cm}^{-1}$  (0.19 eV) leads to a Huang-Rhys factor  $S = \lambda_v/\tilde{\nu}_v$  of 1.24.

**Table 17:** Rate constants  $k_{CS}$  and  $k_T$  with the resulting electronic couplings  $V_{1PDI-1CSS}$  of CS and  $V_{3CS-3PDI}$  for CR<sub>T</sub> in toluene by applying **equation (17)**.

	$k_{CS} / \text{s}^{-1}$	$V_{1CSS-1PDI}^a / \text{cm}^{-1}$	$k_T / \text{s}^{-1}$	$V_{3CSS-3PDI}^b / \text{cm}^{-1}$
<b>TAAMe<sub>2</sub>-TTC-PDIME<sub>2</sub></b>	$7.8 \cdot 10^8$	2.03	$8.0 \cdot 10^7$	1.03
<b>TAAMe<sub>2</sub>-TTC-PDI</b>	$7.6 \cdot 10^9$	6.77	$1.5 \cdot 10^8$	1.34
<b>TAA-TTC-PDIME<sub>2</sub></b>	$3.6 \cdot 10^9$	3.91	$1.0 \cdot 10^8$	1.61
<b>TAA-TTC-PDI</b>	$2.0 \cdot 10^{10}$	9.26	$9.5 \cdot 10^7$	1.43

<sup>a</sup> from  $k_{CS}$  using **equation (17)**, <sup>b</sup> from  $k_T$  using **equation (17)**

The estimation of the electronic coupling  $V_{1CSS-S_0}$  for CR<sub>S</sub> using  $k_S$  from the quantum dynamical simulations was not possible because the error margins for  $k_S$  are rather wide (**Table 16** in **section 6.1.4**). Therefore, to determine the coupling  $V_{1CSS-S_0}$  for CR<sub>S</sub> *Andersons*<sup>[96]</sup> equation (**equation (18)**) and the exchange interactions resulting from the ns-TA experiments were used.

$E_{1,3CSS}$  represents the energetic level of the respective CSS and  $E_n$  the energetic level from which, or in which the ET process takes place. In the case of the rotationally hindered triads, there are three possible ET processes, namely the transition from  $^1CSS \leftrightarrow ^1PDI$ ,  $^1CSS \leftrightarrow S_0$ , and  $^3CSS \leftrightarrow ^3PDI$ . Those three transitions result in three terms contributing to  $2J$  (**equation (18)**) in which all interactions are lifted in energy by the reorganisation energy  $\lambda$ .

$$2J = \Delta E_S - \Delta E_T = \left[ \sum_n \frac{V_{1CSS-n}^2}{E_{1CSS} - E_n - \lambda} \right]_S - \left[ \sum_n \frac{V_{3CSS-n}^2}{E_{3CSS} - E_n - \lambda} \right]_T = \quad (18)$$

$$\frac{V_{1CSS-1PDI}^2}{E_{1CSS} - E_{1PDI} - \lambda} + \frac{V_{1CSS-1S_0}^2}{E_{1CSS} - E_{1S_0} - \lambda} - \frac{V_{3CSS-3PDI}^2}{E_{3CSS} - E_{3PDI} - \lambda}$$

term1                      term2                      term3

Accordingly, the interaction between  $^1\text{CSS}$  and  $^1\text{PDI}$  is described by term 1, which lowers the energy of the  $^1\text{CSS}$  level.

The interaction between  $^1\text{CSS}$  and  $^1\text{S}_0$  is described by term 2, which rises the energy of the  $^1\text{CSS}$  level.

And the third interaction is between  $^3\text{CSS}$  and  $^3\text{PDI}$ , which is described by term 3 and rises the energy of the  $^3\text{CSS}$  level.

The effects of term 1 and 3 must be overcompensated by term 2 in order to obtain a positive  $J$  value. The required value of term 2 can be obtained using the experimental values of  $J$  together with terms 1 and 3. Thereafter, using the value of term 2 the matrix element  $V_{1CSS-1S_0}^2$  is calculated and by inserting it in **equation (17)** the rate constant  $k_S$  is obtained. The calculated values for  $k_S$  agree well with the theoretical values obtained to the quantum simulations (**Table 18**).<sup>[91]</sup>

**Table 18:** Electronic couplings  $V_{1CSS-1S_0}$  calculated from the experimental  $J$  value and rate constant  $k_S$  calculated from  $V_{1CSS-1S_0}$  using **equation (17)** of the rotationally hindered triads.

	$J / \text{mT}$	$V_{1CSS-1S_0}^a / \text{cm}^{-1}$	$k_S / \text{s}^{-1b}$	$k_{S,\text{qfit}} / \text{s}^{-1c}$
<b>TAAMe<sub>2</sub>-TTC-PDIME<sub>2</sub></b>	0.25	4.36	$1.60 \cdot 10^4$	$0-1.1 \cdot 10^5$
<b>TAAMe<sub>2</sub>-TTC-PDI</b>	1.55	11.7	$1.63 \cdot 10^5$	$0-2.0 \cdot 10^5$
<b>TAA-TTC-PDIME<sub>2</sub></b>	1.85	9.44	$8.20 \cdot 10^4$	$0-2.0 \cdot 10^5$
<b>TAA-TTC-PDI</b>	6.5	18.8	$3.20 \cdot 10^5$	$0-1.1 \cdot 10^6$

<sup>a</sup> calculated from  $J$  using **equation (18)** <sup>b</sup> calculated from  $V_{1CSS-1S_0}$  using **equation (17)** <sup>c</sup> from quantum simulations of the magnetic field dependent CSS decays.

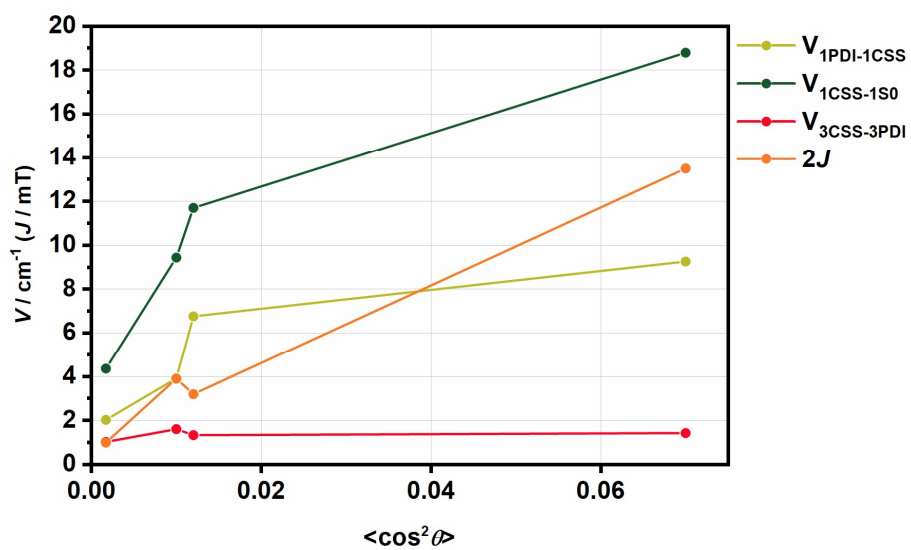
The calculated electronic couplings  $V_{3CSS-3PDI}$  (**Table 17**) are on the order of approximately  $1 \text{ cm}^{-1}$  but  $V_{1CSS-1S_0}$  (**Table 18**) as well as  $V_{1CSS-1PDI}$  (**Table 17**) are significantly higher. The electronic couplings  $V_{1CSS-1S_0}$  and  $V_{1CSS-1PDI}$  as well as the exchange interaction  $2J$  all are increasing with decreasing rotational hindrance (**Figure 73**) but  $V_{3CSS-3PDI}$  is almost the same for all triads. This proves that the restriction of the rotational freedom strongly influences the CS and  $\text{CR}_S$  dynamics in those triads, but the  $\text{CR}_T$  is only slightly influenced. The latter indicates that CR in the local  $^3\text{PDI}$  state is caused by a different electron transfer mechanism than the CR to the ground state and the CS.<sup>[91]</sup>

In order to determine the rotational potentials around the defined angles (see beginning of **section 6** in **Figure 39**), DFT calculations on model fragments were performed. To determine the rotational potential around the angles  $\theta_1$  and  $\theta_2$  a **TAA-TTC** radical cation with or without methyl groups attached to the **TAA** was used. Using uB3LYP/6-31G\* level of theory, this moiety was optimised and thereafter the appropriate molecular fragment was turned around either  $\theta_1$  or  $\theta_2$  in  $10^\circ$  steps while optimising all other geometry parameters. The potentials of the torsion of the **TTC-PDI** radical anion were performed in the same way by turning around the angles  $\theta_3$  and  $\theta_4$ . Analytical functions were then used to fit the potentials. A more detailed description is given in reference.<sup>[91]</sup> Plotting the electronic couplings and the exchange interaction against the average of the four-angle-product of the cosine squares  $\Pi$  (**equation (19)**) of all significant angles in the triads, the correlation between the rotational hindrance and the electronic couplings becomes more obvious (**Figure 73**). The electronic couplings for the singlet pathways are increasing with increasing rotational freedom, however, not in the same progression as the exchange interactions. This shows that rotational restriction can be used to tune electronic couplings in DA systems.

$$\Pi = \prod_{i=1}^4 \cos[\theta_i]^2 \quad (19)$$

**Table 19:** Average of the four-angle-product of the cosine squares using **equation (19)** of the rotationally hindered triads.

	$\Pi$
<b>TAAMe<sub>2</sub>-TTC-PDIME<sub>2</sub></b>	0.0017
<b>TAAMe<sub>2</sub>-TTC-PDI</b>	0.012
<b>TAA-TTC-PDIME<sub>2</sub></b>	0.01
<b>TAA-TTC-PDI</b>	0.07



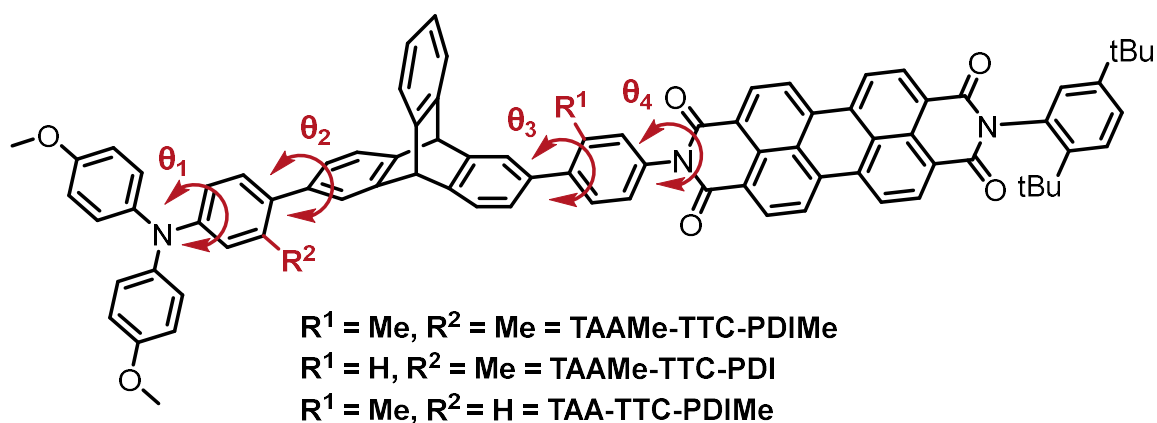
**Figure 73:** Correlation of the electronic couplings and the exchange interaction plotted against the average of the four-angle product.

## 6.2 Discussion

The goal of this chapter was to investigate the influence of rotational restriction on the exchange interaction  $2J$  and the electronic coupling between a donor state and an acceptor state. Therefore, a series of molecules consisting of a **TAA** electron donor, a **TTC** bridging unit and a **PDI** electron acceptor was synthesised (**section 3**). The dihedral angle between the **TAA** and the **TTC** as well as between the **TTC** and the **PDI** were restricted by *ortho*-methyl groups at the phenylene linkers at the connecting ends to the **TTC** bridge, resulting in a fixed geometry with a twist around the linking single bond that minimises the  $\pi$ -overlap. Thus, the rotationally hindered triads **TAAMe<sub>2</sub>-TTC-PDIME<sub>2</sub>**, **TAAMe<sub>2</sub>-TTC-PDI**, **TAA-TTC-PDIME<sub>2</sub>** and **TAA-TTC-PDI** exhibit decreasing numbers of *ortho*-methyl groups and therefore different degrees of rotational restriction. In order to evaluate the electronic properties, steady-state absorption spectra of the triads were measured. All spectra show spectral features associated with the separate absorption bands of **TAA** and the **PDI** moiety (**section 4.1**). Furthermore, all triads show distinctly diminished fluorescence QYs compared to the pure PDI<sup>[166]</sup> in both non-polar toluene and polar PhCN. Here, no emission of the TAA moiety was observed (**section 4.2**). These diminished QYs already give the first indication of a non-radiative quenching mechanism in the triads. The subsequently measured CV data (**section 5**) were used to calculate the energies of possible CSSs using the *Weller* approach, indicating that all triads can undergo CS and form a CSS. Using those results, the CR dynamics were assigned to the different *Marcus* regions placing CR in the *Marcus* normal region in PhCN and in the *Marcus* inverted region in toluene (**section 6.1.1**). CR<sub>T</sub> shows a much smaller *Gibbs* energy than CR<sub>S</sub> in toluene indicating that the favoured CR pathway in toluene is the triplet pathway. In PhCN only the CR<sub>S</sub> pathway is possible. In order to investigate whether the triads actually form CSSs, fs-TA measurements were carried out (**section 6.1.2**). Those measurements show that after light-excitation of the PDI moiety, first a hot (i) PDI S<sub>1</sub> state is populated, which vibrationally relaxes to a cold (f) PDI S<sub>1</sub> state. All triads form a <sup>1</sup>CSS upon depopulation of the <sup>1</sup>PDI state. The respective lifetimes, quantum yields and rate constants  $k_{CS}$  were determined via global exponential fit and global target analysis. Notably, by comparing the QYs of fluorescence and CS, all triads show basically no non-radiative decay besides ET. The CR dynamics upon depopulation of the CSSs were investigated using external magnetic field dependent ns-TA spectroscopy (**section 6.1.3**). The ns-TA maps show that all triads recombine via CR<sub>T</sub> pathway populating the local <sup>3</sup>PDI state in toluene and via CR<sub>S</sub> pathway to the ground state in PhCN, respectively, and provide the respective lifetimes. The QYs of triplet formation were determined using actinometry (**section 10.3.4.2**). The rate determining process upon CR is the spin interconversion from the initially formed <sup>1</sup>CSS to the <sup>3</sup>CSS, which in turn depends on the exchange splitting  $2J$  that, in turn, depends on the electronic coupling

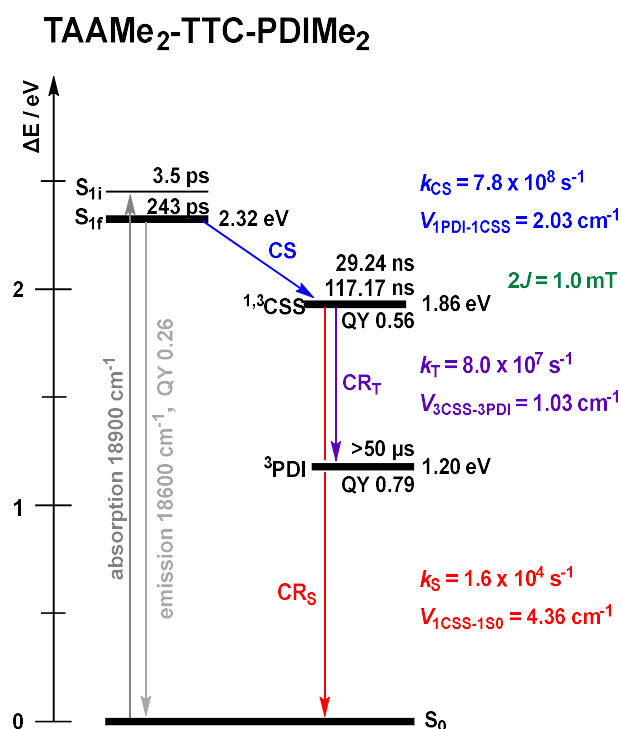
between the donor state and the acceptor state. To investigate the exchange interaction  $2J$  and the associated electronic couplings, CSS decay profiles were recorded and the  $2J$  couplings were obtained from the resulting MARY plots. The magnetic field dependent ns-TA data in toluene were further evaluated using quantum mechanical simulations (done by *U.E. Steiner*<sup>[91]</sup>) to extract the rate constants  $k_T$  and  $k_S$  for  $CR_T$  and  $CR_S$  (**section 6.1.4**). Only the ns-TA data in toluene were used due to the dominant triplet recombination pathway and the thus resulting CR dynamics. This approach was successful for  $k_T$  but the error margins of  $k_S$  were rather wide. Additionally, the electronic couplings were determined using the theoretical relations between the rate constants and the electronic couplings (**section 6.1.5**). In order to do so, the experimentally determined values of  $2J$  and the calculated values of  $k_{CS}$  and  $k_T$  were used. Subsequently, the rate constant  $k_S$  was calculated based on  $V_{1CSS-1S0}$  with good accuracy. The results show that singlet couplings and exchange interaction  $2J$  are sensitive to the effects of rotational restriction. Triplet couplings, on the other hand, seem to be rather independent of the rotational hindrance, indicating a different electron transfer mechanism. Thus, it was proved that the exchange interaction  $2J$  and the singlet couplings between a donor state and an acceptor state are strongly influenced by the restriction of rotational freedom.

As the gap between the cosine square product  $\Pi$  of **TAAMe<sub>2</sub>-TTC-PDI / TAA-TTC-PDIME<sub>2</sub>** and **TAA-TTC-PDI** is large, and the correlation between the exchange interaction and the electronic couplings not linear, the topic of the rotational hindrance needs further investigations. To further investigate the influence of the rotational hindrance the single *ortho*-methylation at the phenylene linkers at the connecting ends to the **TTC** bridge, and therefore a larger cosine square product than **TAAMe<sub>2</sub>-TTC-PDI / TAA-TTC-PDIME<sub>2</sub>**, could give more insight into the correlations (**Figure 74**).



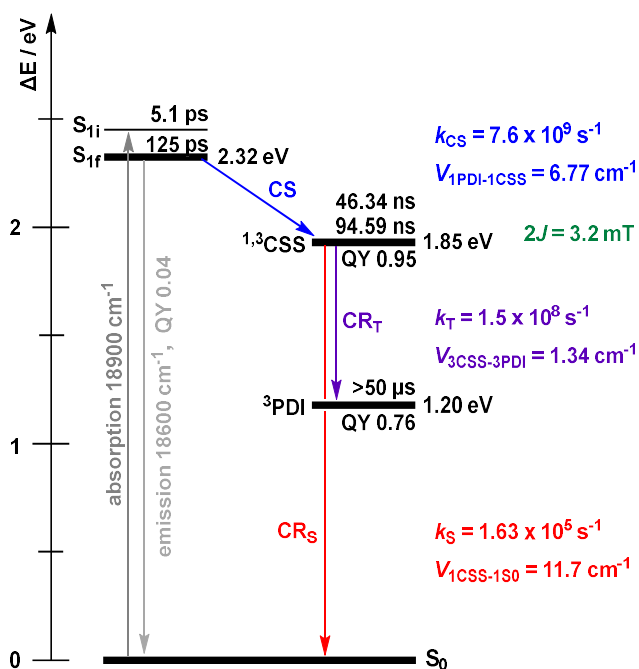
**Figure 74:** Possible series of molecules with one -time *ortho* methylation to further investigate the influence of rotational hindrance.

All investigated processes and the associated values are summarised in energy level diagrams for each triad in both solvents (toluene in **Figure 75** to **Figure 78** and PhCN in **Figure 79** to **Figure 82**).

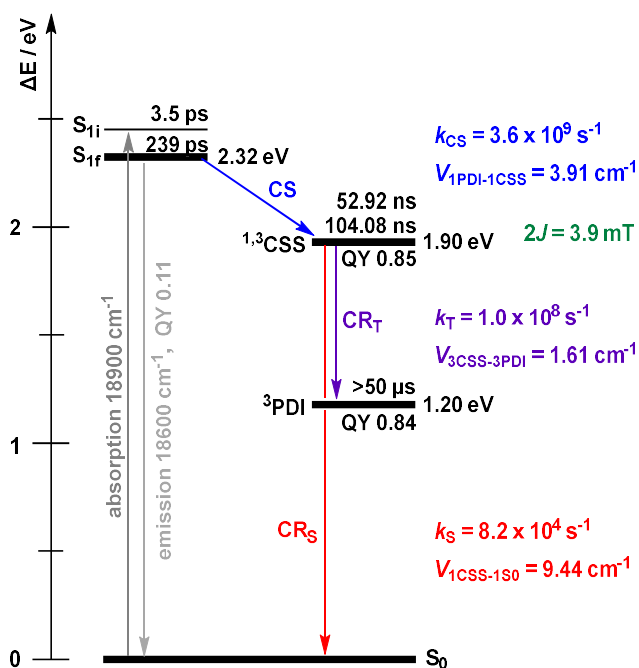


**Figure 75:** Energy level diagram of **TAAMe<sub>2</sub>-TTC-PDIME<sub>2</sub>** in toluene with all herein investigated states including their lifetimes and rate constants as well as the QYs for the formation of the CSS and the local <sup>3</sup>PDI state. The exchange interaction and electronic couplings are given as well. The energy level of the <sup>3</sup>PDI level is taken from literature.<sup>[188]</sup>



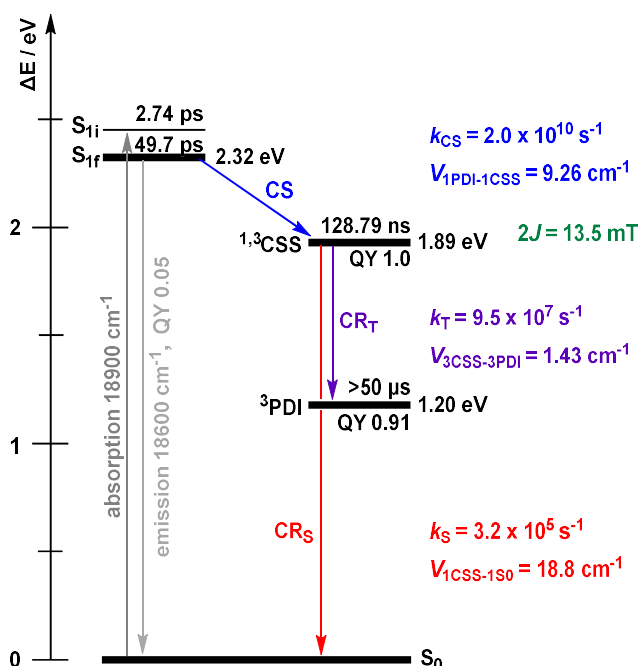
TAAMe<sub>2</sub>-TTC-PDI

**Figure 76:** Energy level diagram of TAAMe<sub>2</sub>-TTC-PDI in toluene with all herein investigated states including their lifetimes and rate constants as well as the QYs for the formation of the CSS and the local  $^3PDI$  state. The exchange interaction and electronic couplings are given as well. The energy level of the  $^3PDI$  level is taken from literature.<sup>[188]</sup>

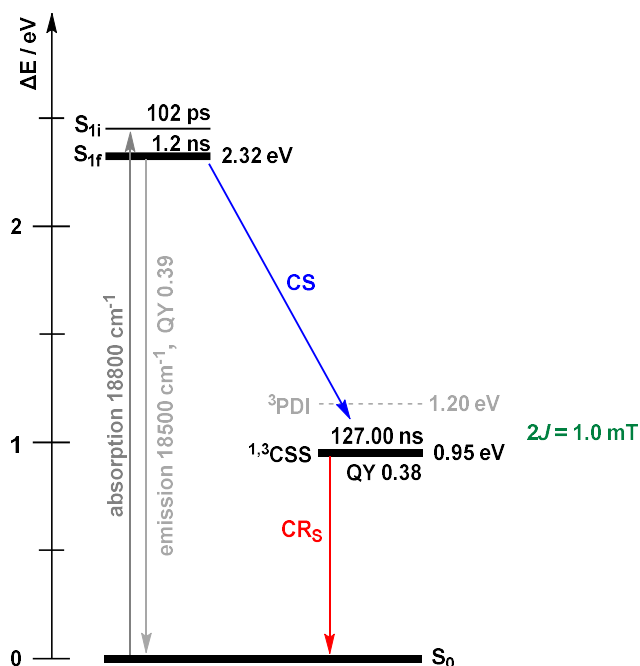
TAA-TTC-PDIME<sub>2</sub>

**Figure 77:** Energy level diagram of TAA-TTC-PDIME<sub>2</sub> in toluene with all herein investigated states including their lifetimes and rate constants as well as the QYs for the formation of the CSS and the local  $^3PDI$  state. The exchange interaction and electronic couplings are given as well. The energy level of the  $^3PDI$  level is taken from literature.<sup>[188]</sup>

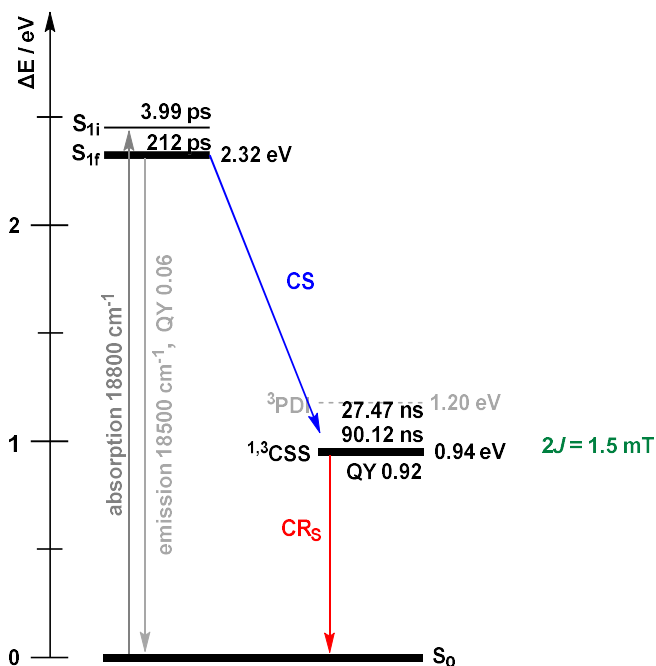
## TAA-TTC-PDI



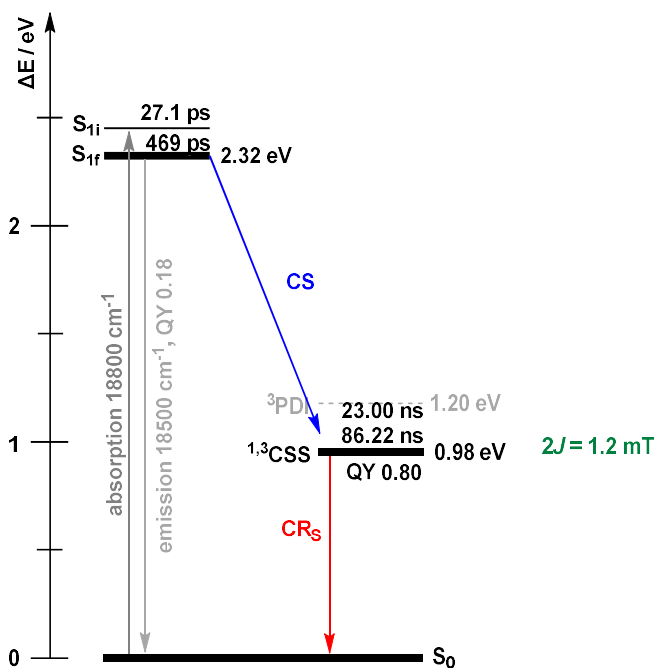
**Figure 78:** Energy level diagram of **TAA-TTC-PDI** in toluene with all herein investigated states including their lifetimes and rate constants. The QYs for the formation of the CSS and the local  $^3\text{PDI}$  as well as the exchange interaction and electronic couplings. The energy level of the  $^3\text{PDI}$  level is taken from literature.<sup>[188]</sup>

 TAAMe<sub>2</sub>-TTC-PDIME<sub>2</sub>


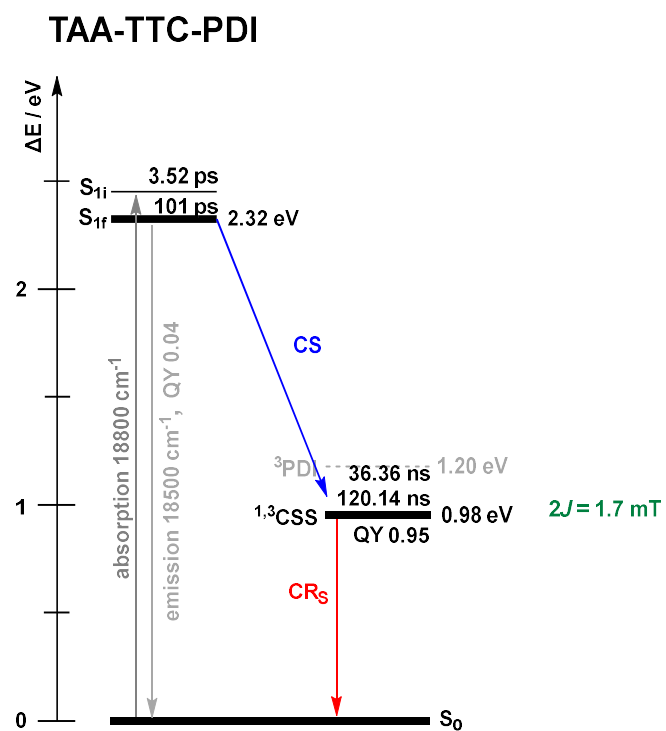
**Figure 79:** Energy level diagram of **TAAMe<sub>2</sub>-TTC-PDIME<sub>2</sub>** in PhCN with all herein investigated states including their lifetimes as well as the QY for the formation of the CSS. The exchange interaction is given as well. The energy level of the  $^3\text{PDI}$  level is taken from literature.<sup>[188]</sup>

TAAMe<sub>2</sub>-TTC-PDI

**Figure 80:** Energy level diagram of TAAMe<sub>2</sub>-TTC-PDI in PhCN with all herein investigated states including their lifetimes as well as the QY for the formation of the CSS. The exchange interaction is given as well. The energy level of the  $^3PDI$  level is taken from literature.<sup>[188]</sup>

TAA-TTC-PDIME<sub>2</sub>

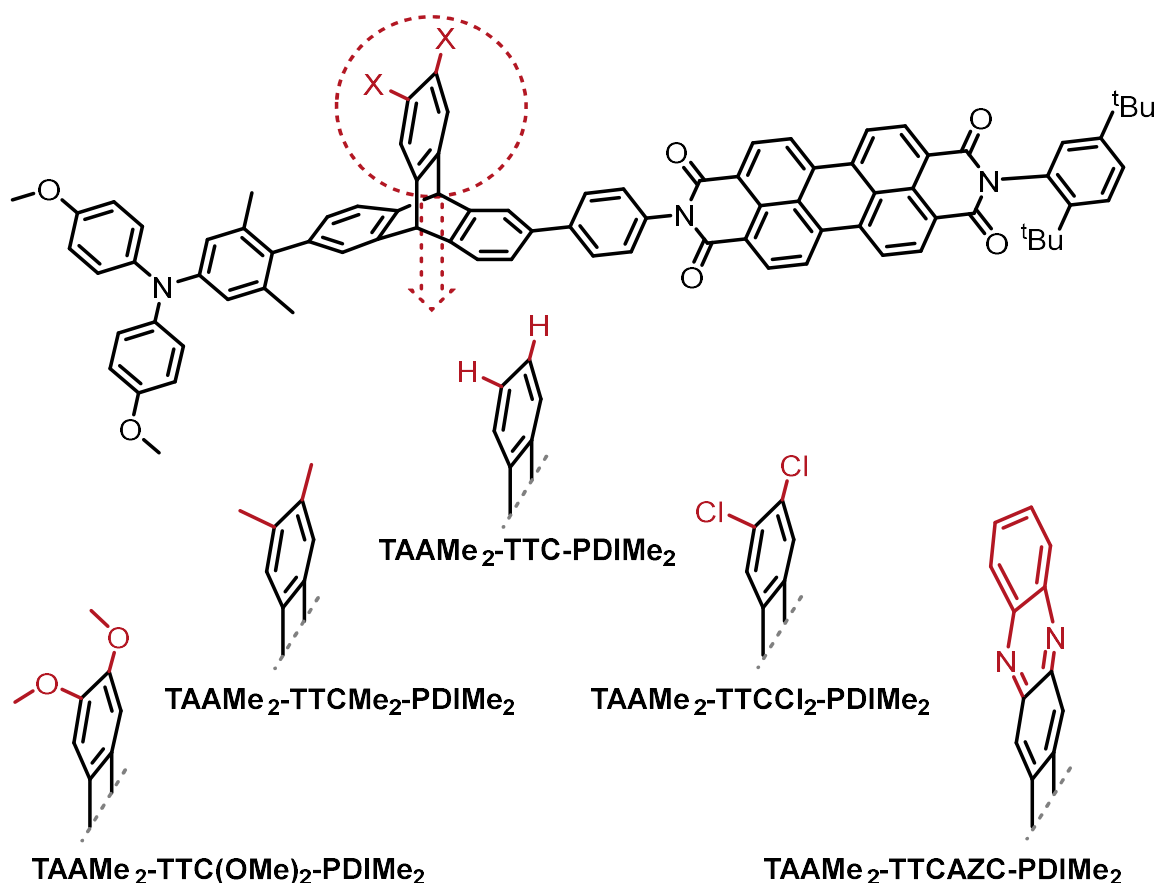
**Figure 81:** Energy level diagram of TAA-TTC-PDIME<sub>2</sub> in PhCN with all herein investigated states including their lifetimes as well as the QY for the formation of the CSS. The exchange interaction is given as well. The energy level of the  $^3PDI$  level is taken from literature.<sup>[188]</sup>



**Figure 82:** Energy level diagram of **TAA-TTC-PDI** in PhCN with all herein investigated states including their lifetimes as well as the QY for the formation of the CSS. The exchange interaction is given as well. The energy level of the <sup>3</sup>PDI level is taken from literature.<sup>[188]</sup>

## 7 Substituted triptycene triads

In the previous chapter, the coupling between donor and acceptor states was influenced by changing the rotational freedom between the D/A and the **TTC** bridging unit. In the present chapter, the electronic coupling between the donor state and the acceptor states was influenced by changing the electron density in the **TTC** bridging unit. In order to do so, the triptycene bridge was substituted with electron donating and withdrawing groups (OMe, Me, Cl, AZC) in the triptycenes 12,13-position (**Figure 83**). The triptycenes were substituted that way in order to utilise the enhanced influence of the 12,13- positioned substituents on the triptycenes homoconjugation compared to 11,14-positioned substitution. The influence of 12,13- positioned substituents on the homoconjugation in triptycene was investigated by the Rathore group and confirmed by DFT calculations.<sup>[206-207]</sup>



**Figure 83:** Series of substituted triptycene triads with the respective electron withdrawing (Cl, AZC) and donating (Me, OMe) groups attached to the **TTC** core.<sup>15</sup>

<sup>15</sup> The triad **TAAMe<sub>2</sub>-TTCCl<sub>2</sub>-PDI** was synthesised and all measurements were done by F. Fella as part of the bachelor thesis *Synthese und Charakterisierung einer Donor-Akzeptor-Dyade mit chloresubstituierter Triptycenen-Brücke zur Untersuchung photoinduzierter magnetfeldabhängiger Effekte*, 2021.

## 7.1 Electron transfer processes

The steady-state emission spectroscopy data (**section 4.2**) already indicate the existence of an alternative non-radiative quenching mechanism in the series of substituted triptycene triads, which similar to the rotationally hindered triads, could be an electron transfer process. Thus, in order to investigate if electron transfer processes take place the energies of the states involved in the ET processes were considered and possible charge recombination pathways assigned to the different *Marcus* regions. The formation of a possible CSS can be predicted based on the electrochemical data (**section 5**) and structure related parameters. The charge separation and the possible formation of a CSS were investigated using transient absorption (TA) spectroscopy in the femtosecond time range, showing that CSS formation is observed in all substituted triptycene triads. Thereafter, charge recombination (CR) from the CSS was investigated using ns-TA spectroscopy. The decay kinetics were furthermore investigated by the application of an external magnetic field, resulting in decay curves that exhibit a pronounced magnetic field dependence, giving information on the exchange interaction  $2J$  between  $^1\text{CSS}$  and  $^3\text{CSS}$ . These magnetic field dependent decay kinetics were simulated using quantum dynamical calculations. The quantum dynamic calculations as well as the global target analysis performed on the fs-TA measurements provide rate constants for the CS and CR processes, which were used to calculate the electronic couplings between the CSS and either its precursor or successor state. The calculations give insight into the influence of electronic changes in the bridging unit on the electronic coupling between the donor state and the acceptor state.

### 7.1.1 State energies

As described before (**section 6.1.1**), the calculation of the CSS energies gives a first impression whether the formation of a CSS is possible. Therefore, the CSS energies (**Table 36** in **section 10.1**) were calculated using the *Weller*-approximation<sup>16</sup> (**equation (24)** in **section 10.1**) and the measured redox potentials (**Table 4** in **section 5**) as well as structure related parameters. Comparing the CSS energies (all approximately  $14900\text{ cm}^{-1}$ , 1.85 eV) see **Table 36** in **section 10.1**) to the  $^1\text{PDI}$  state energy ( $18800\text{ cm}^{-1}$ , 2.33 eV) shows that all CSS energies are located below the  $^1\text{PDI}$  energy and therefore CS into CSSs is possible in all substituted triptycene triads. The CSS energies in toluene (approximately  $14900\text{ cm}^{-1}$ , 1.85 eV, **Table 36** in **section 10.1**) are higher in energy than the  $^3\text{PDI}$  state ( $9680\text{ cm}^{-1}$ , 1.20 eV) and

---

<sup>16</sup> Calculated by Dr. M. Holzapfel.

therefore CR via triplet pathway ( $CR_T$ ) is possible. In order to determine the efficiency of the possible CR pathways the CR ET processes were sorted into the *Marcus* regions (**Table 20**) as described above (**section 6.1.1**).

**Table 20:** *Gibbs* energies of the substituted triptycene triads for the CS process from  $^1PDI$  to  $^1CSS$  ( $\Delta G_{1PDI-1CSS}$ ) and the CR processes from  $^1CSS$  to  $S_0$  ( $\Delta G_{1CSS-S_0}$ ) or from  $^3CSS$  to  $^3PDI$  ( $\Delta G_{3CSS-3PDI}$ ) as well as the corresponding assignment of the respective transition in the *Marcus* region in toluene.

	$\Delta G_{1PDI-1CSS}$	$\Delta G_{1CSS-S_0}$	$\Delta G_{3CSS-3PDI}$	<i>Marcus</i> region		
	/ $cm^{-1}$ (eV)	/ $cm^{-1}$ (eV)	/ $cm^{-1}$ (eV)	CS	$CR_S$	$CR_T$
<b>TAAMe<sub>2</sub>-TTC(OMe)<sub>2</sub>-PDI</b>	-3879 (-0.48)	-14921 (-1.85)	-5242 (-0.65)	inv.	inv.	inv.
<b>TAAMe<sub>2</sub>-TTCMe<sub>2</sub>-PDI</b>	-3879 (-0.48)	-14921 (-1.85)	-5242 (-0.65)	inv.	inv.	inv.
<b>TAAMe<sub>2</sub>-TTCCl<sub>2</sub>-PDI</b>	-3879 (-0.48)	-14921 (-1.85)	-5242 (-0.65)	inv.	inv.	inv.
<b>TAAMe<sub>2</sub>-TTCAZC-PDI</b>	-3999 (-0.50)	-14841 (-1.84)	-5162 (-0.64)	inv.	inv.	inv.

$\lambda_i = 1855 \text{ cm}^{-1}$  (0.23 eV),  $\lambda_{\text{tol}} = 484 \text{ cm}^{-1}$  (0.06 eV),  $\lambda_{\text{tot}} = 2340 \text{ cm}^{-1}$  (0.29 eV). The data for **TAAMe<sub>2</sub>-TTC-PDI** are given in **Table 5** in **section 6.1.1**.

The CS process takes place in the *Marcus* inverted region in all triads because  $\lambda_{\text{tot}} < -(\Delta G^{00})$ . Comparing the overall reorganisation energy in toluene ( $\lambda_{\text{tot}}$ ,  $2340 \text{ cm}^{-1}$ , 0.29 eV) to the *Gibbs* energy of the transition from  $^3CSS$  to  $^3PDI$  ( $\Delta G_{3CSS-3PDI}$ , **Table 20**) and from  $^1CSS$  to  $S_0$  ( $\Delta G_{1CSS-S_0}$ ) places  $CR_T$  as well as  $CR_S$  in the *Marcus* inverted region ( $\lambda_{\text{tot}} < -(\Delta G^{00})$ ) for all substituted triptycene triads.  $CR_T$  (all approximately  $-5200 \text{ cm}^{-1}$ ,  $-0.64 \text{ eV}$ , **Table 20**) shows a much smaller *Gibbs* energy than  $CR_S$  (all approximately  $-14900 \text{ cm}^{-1}$ ,  $-1.85 \text{ eV}$ , **Table 20**), indicating that the favoured CR pathway in toluene is the triplet pathway for all triads.

## 7.1.2 Charge separation

In the previous section the CSS energies were calculated and the assumption was made that all substituted triptycene triads should be able to undergo CS and form CSSs. fs-TA spectroscopy was used to investigate whether this assumption can be proved. Therefore, fs-TA maps were recorded in toluene. A detailed description of the measurement setup and conditions is given in **Section 10.3.4.1**.

### 7.1.2.1 fs-Pump probe spectroscopy

The fs-transient absorption measurements<sup>17</sup> of the triads **TAAMe<sub>2</sub>-TTC(OMe)<sub>2</sub>-PDI**, **TAAMe<sub>2</sub>-TTCMe<sub>2</sub>-PDI**, **TAAMe<sub>2</sub>-TTCCl<sub>2</sub>-PDI** and **TAAMe<sub>2</sub>-TTCAZC-PDI** yielded transient maps (see **Figure 84** to **Figure 88 (B)**). By applying a sequential model, the TA maps were analysed by a global exponential fit and the resulting EADS (figures **(A)**) were further interpreted.<sup>18</sup>

In **TAAMe<sub>2</sub>-TTC(OMe)<sub>2</sub>-PDI** (**Figure 84**), **TAAMe<sub>2</sub>-TTCMe<sub>2</sub>-PDI** (**Figure 86**) **TAAMe<sub>2</sub>-TTCCl<sub>2</sub>-PDI** (**Figure 87**) and **TAAMe<sub>2</sub>-TTCAZC-PDI** (**Figure 88**) five time components are obtained by global analysis (**Table 21**). In the triads with electron donating groups attached to the **TTC** bridge (**TAAMe<sub>2</sub>-TTC(OMe)<sub>2</sub>-PDI** and **TAAMe<sub>2</sub>-TTCMe<sub>2</sub>-PDI**), and therefore enhanced electron density in the bridging unit, the charge separation process takes place within  $\tau_2 = 38$  ps and  $\tau_2 = 94$  ps (**Table 21**). In these two triads the EADS associated with  $\tau_1$  refers to the relaxation from the hot to the cold PDI S<sub>1</sub> state (compare **section 6.1.2.1**). The EADS associated with  $\tau_3$  show ESA bands at 12600 cm<sup>-1</sup> (794 nm), 13000 cm<sup>-1</sup> (769 nm) and a double peak at 14100 cm<sup>-1</sup> (710 nm) that are typically observed for the formation of the CSS. The rise of those ESA bands and the simultaneous disappearance of the SE band at 17200 cm<sup>-1</sup> (581 nm) proves the formation of the CSS.<sup>[48, 88]</sup> The latter is slowed down in the triads with electron withdrawing substituents attached to the bridging unit (**TAAMe<sub>2</sub>-TTCCl<sub>2</sub>-PDI** and **TAAMe<sub>2</sub>-TTCAZC-PDI**). In those triads  $\tau_1$  and  $\tau_2$  can be assigned to the relaxation process from the hot to the cold PDI S<sub>1</sub> state. The CS process takes  $\tau_3 = 268$  ps in **TAAMe<sub>2</sub>-TTCCl<sub>2</sub>-PDI** and  $\tau_3 = 278$  ps in **TAAMe<sub>2</sub>-TTCAZC-PDI** (**Table 21**).  $\tau_4$  shows the ESA bands associated with the CSS. The EADS associated with  $\tau_4$  in **TAAMe<sub>2</sub>-TTC(OMe)<sub>2</sub>-PDI** (**Figure 84 (A)**), **TAAMe<sub>2</sub>-TTCMe<sub>2</sub>-PDI** (**Figure 86 (A)**) is spectrally similar to  $\tau_3$  showing only a slightly diminished intensity, which could indicate the spin chemical

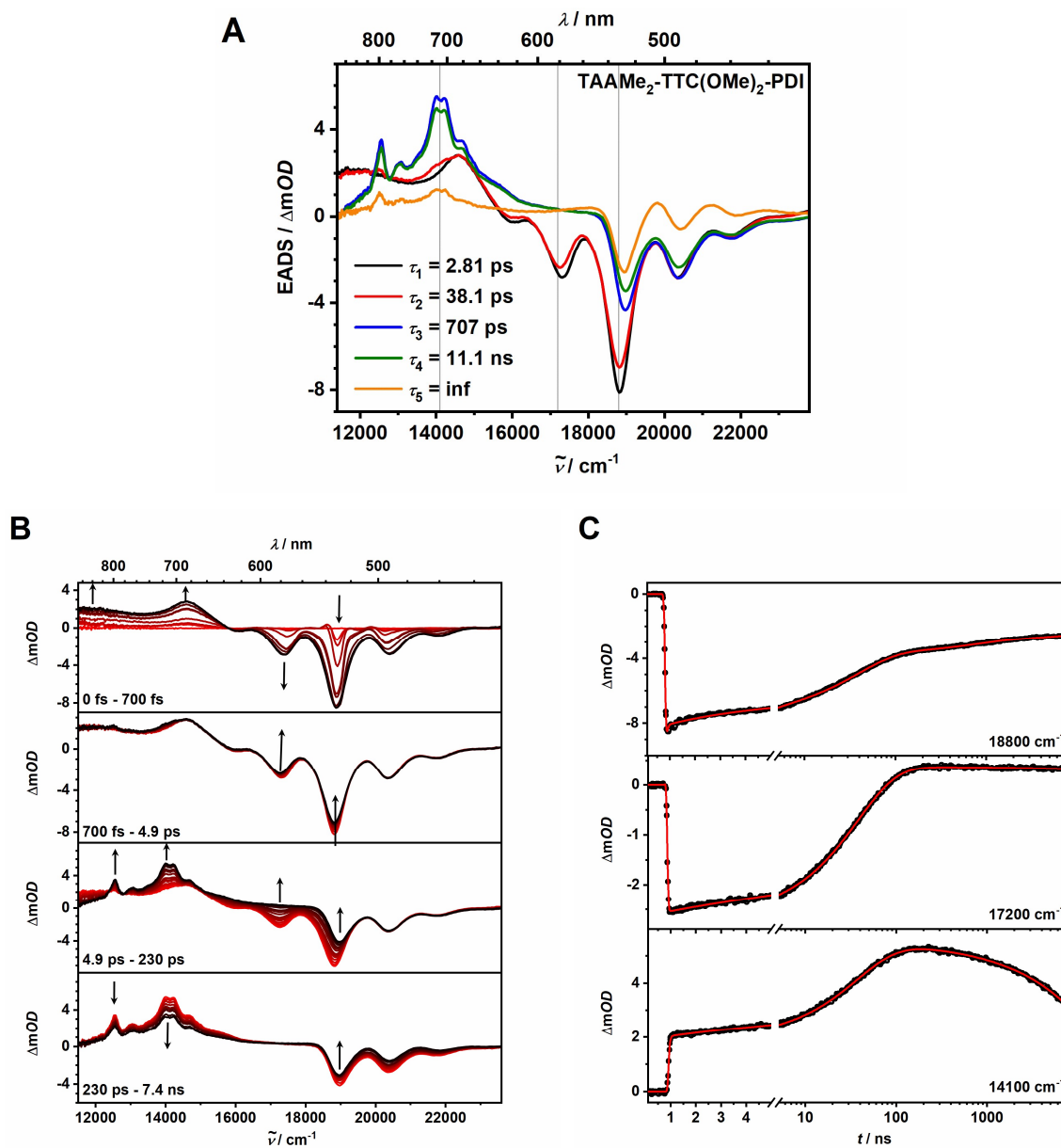
---

<sup>17</sup> Measurements done by A. Schmiedel.

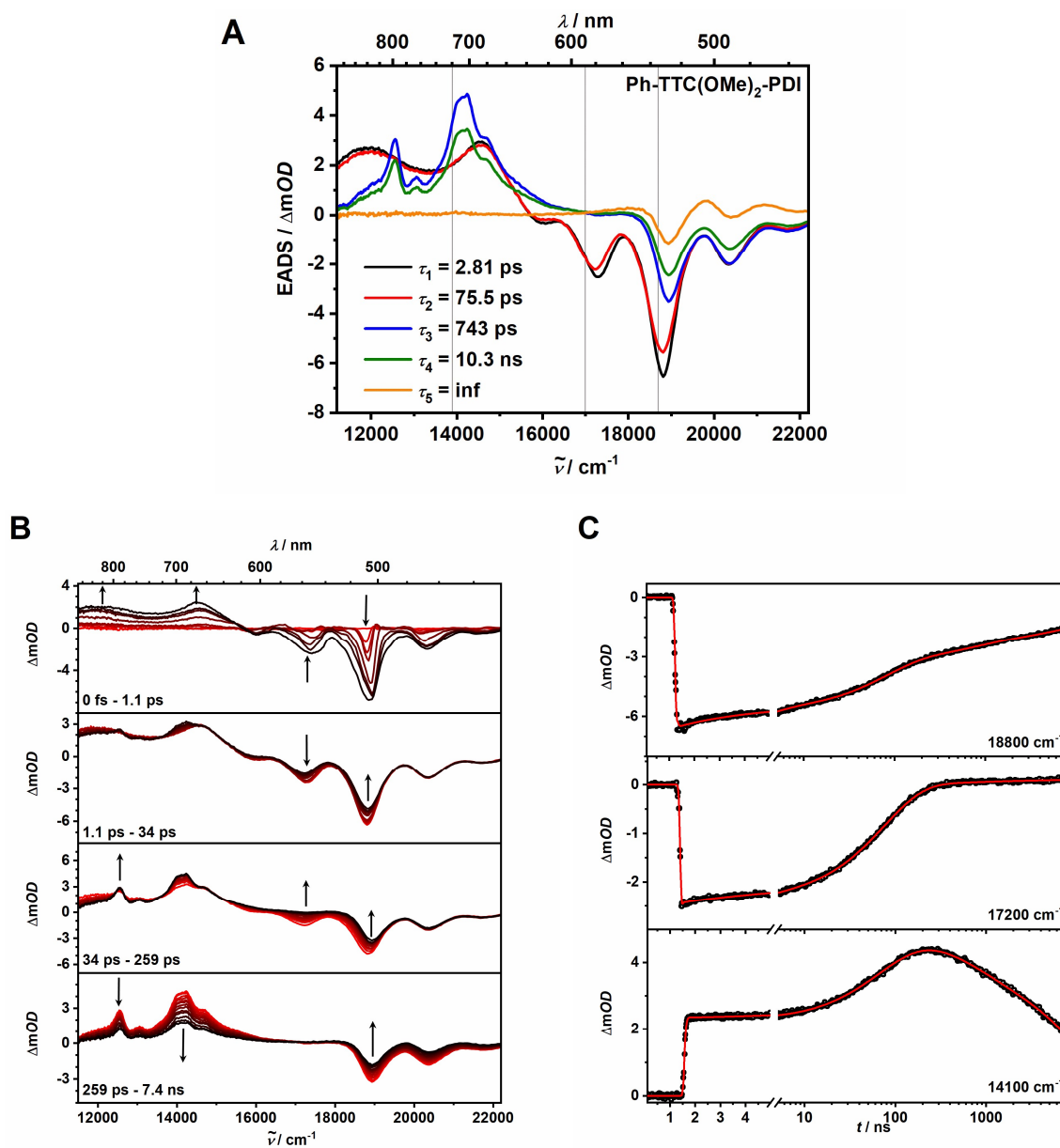
<sup>18</sup> Global exponential fit was performed by Dr. M. Holzapfel.



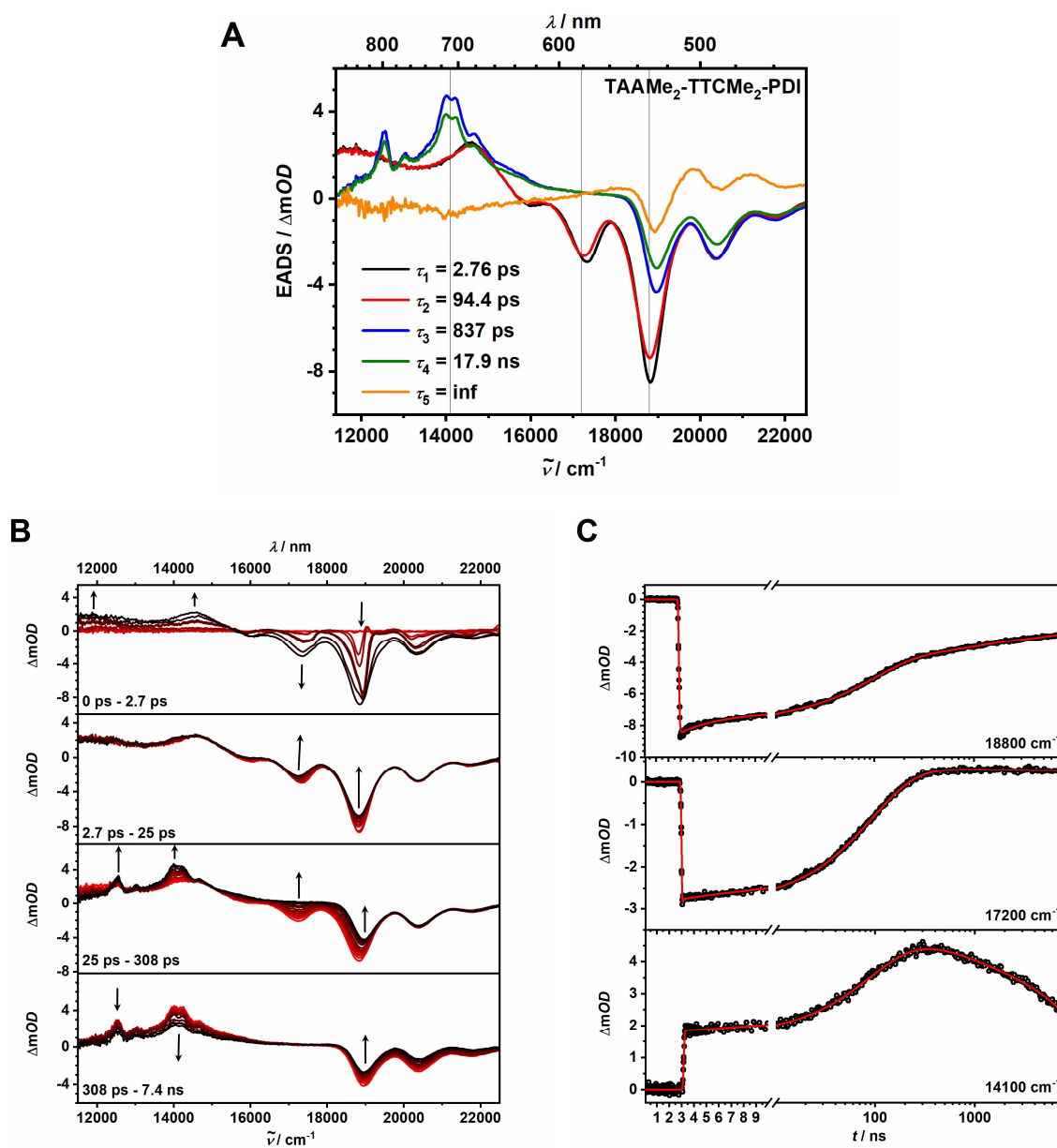
evolution of the RP as described before (section 6.1.2.1). This evolution cannot be seen in **TAAMe<sub>2</sub>-TTCCl<sub>2</sub>-PDI** (Figure 87 (A)) and **TAAMe<sub>2</sub>-TTCAZC-PDI** (Figure 88 (A)) due to the slower CS times. In all four triads the fifth EADS shows an almost complete disappearance of the ESA associated with the CSS (12600 cm<sup>-1</sup> (794 nm), 13000 cm<sup>-1</sup> (769 nm) and 14100 cm<sup>-1</sup> (710 nm)) and the formation of an additional ESA between 18300 cm<sup>-1</sup> (546 nm) and 22500 cm<sup>-1</sup> (444 nm) overlaid by the GSB of the **PDI**. The latter can be assigned to the formation of the <sup>3</sup>PDI state, as described before (section 6.1.2.1).<sup>[48]</sup> None of the triads shows a signal indicative of a charge transfer state, which is consistent with a one-step electron transfer from the **TAA** to the **PDI**. To check whether no CT state is involved in the CS process, a reference compound **Ph-TTC(OMe)<sub>2</sub>-PDI** consisting of a **TTC(OMe)<sub>2</sub>** bridging unit and a **PDI** acceptor (Figure 85) was investigated using fs-TA spectroscopy as well. The methoxy substituted bridge is the one with the highest electron density and therefore the highest HOMO level, which results in a CT state with the lowest energy level. Thus, in the triad **TAAMe<sub>2</sub>-TTC(OMe)<sub>2</sub>-PDI** the involvement of a CT state in the CS process is conceivable. In the reference compound  $\tau_1$  can be assigned to the relaxation of the hot to the cold PDI S<sub>1</sub> state (Table 21).  $\tau_3$  and  $\tau_4$  show (in Table 21) an ESA at 12600 cm<sup>-1</sup> (794 nm) and 14100 cm<sup>-1</sup> (710 nm), which is consistent with the absorption signal of a PDI radical anion.<sup>[48, 88]</sup> The disappearance of the SE at 17200 cm<sup>-1</sup> (581 nm) as well as the ESA at 12600 cm<sup>-1</sup> (794 nm) and 14100 cm<sup>-1</sup> (710 nm) indicate the formation of a CSS, in which the **PDI** is reduced by an electron of the **TTC(OMe)<sub>2</sub>** bridge.  $\tau_5$  shows that the GSB is overlaid by the <sup>3</sup>PDI state.<sup>[48]</sup> Comparing the lifetime components of the formation of the CSS (Table 21), it becomes clear that the formation of the CSS in the triad **TAAMe<sub>2</sub>-TTC(OMe)<sub>2</sub>-PDI** ( $\tau_2 = 38$  ps) is twice as fast as the formation of the CSS in the reference compound **Ph-TTC(OMe)<sub>2</sub>-PDI** ( $\tau_2 = 76$  ps). This indicates that CS in **TAAMe<sub>2</sub>-TTC(OMe)<sub>2</sub>-PDI** does not include a formation of a CT state in which the bridge is oxidised and the **PDI** is reduced. Therefore, CS takes place in one step in **TAAMe<sub>2</sub>-TTC(OMe)<sub>2</sub>-PDI**, proving that the other triads undergo CS in one step as well. Regarding all four substituted triptycene triads, the CS follows a clear trend along the series in which it is slowed down with decreasing electron density in the bridging unit.



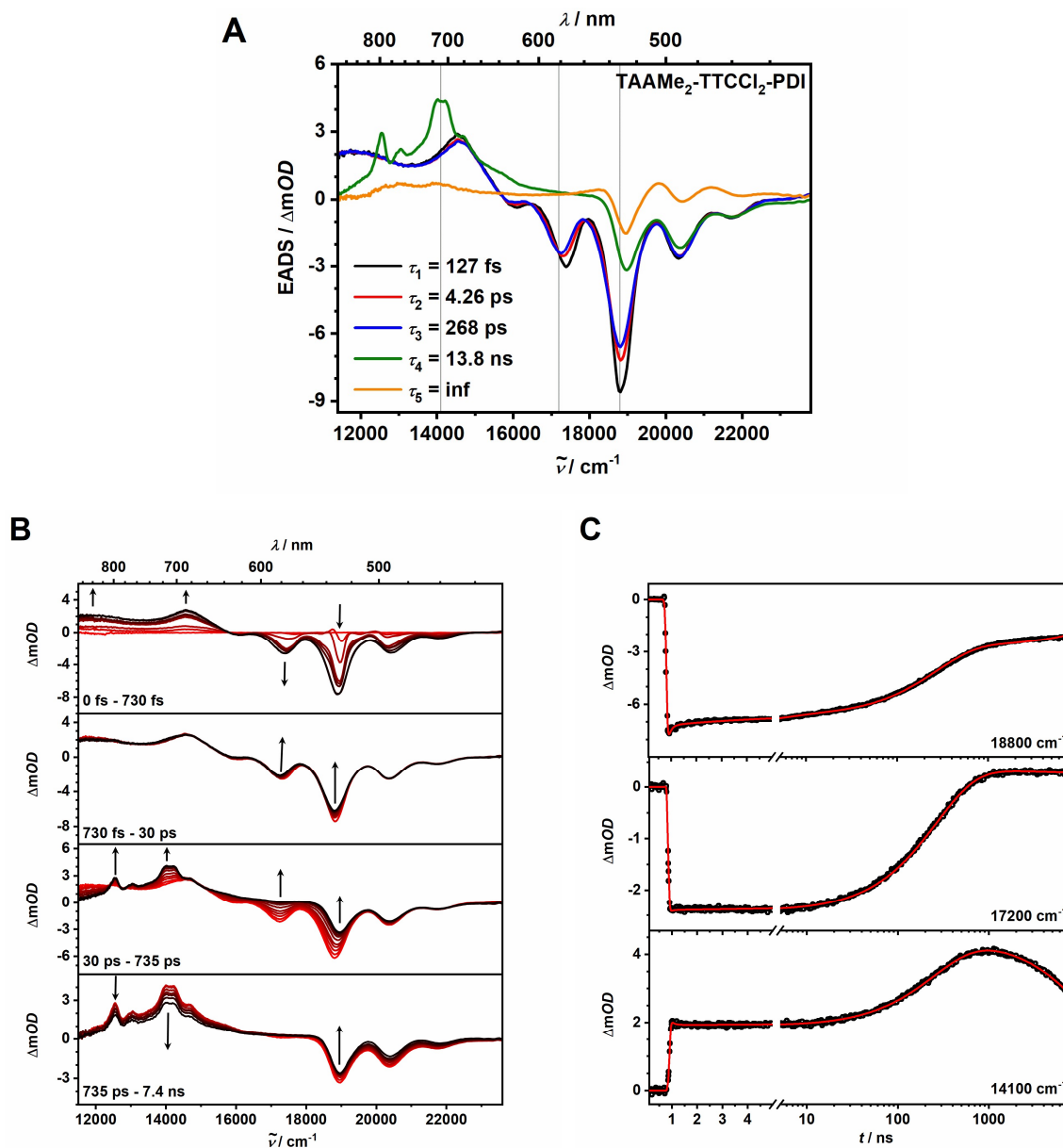
**Figure 84:** Chirp corrected fs-TA spectra of TAAMe<sub>2</sub>-TTC(OMe)<sub>2</sub>-PDI in toluene after light-excitation at 18900 cm<sup>-1</sup> (528 nm) at 298 K. **A:** EADS **B:** selected TA-spectra from the fs-TA measurements (short times to long times depicted from red to black) **C:** selected time traces at different wavenumbers (grey lines in **A**) with their respective global fits.



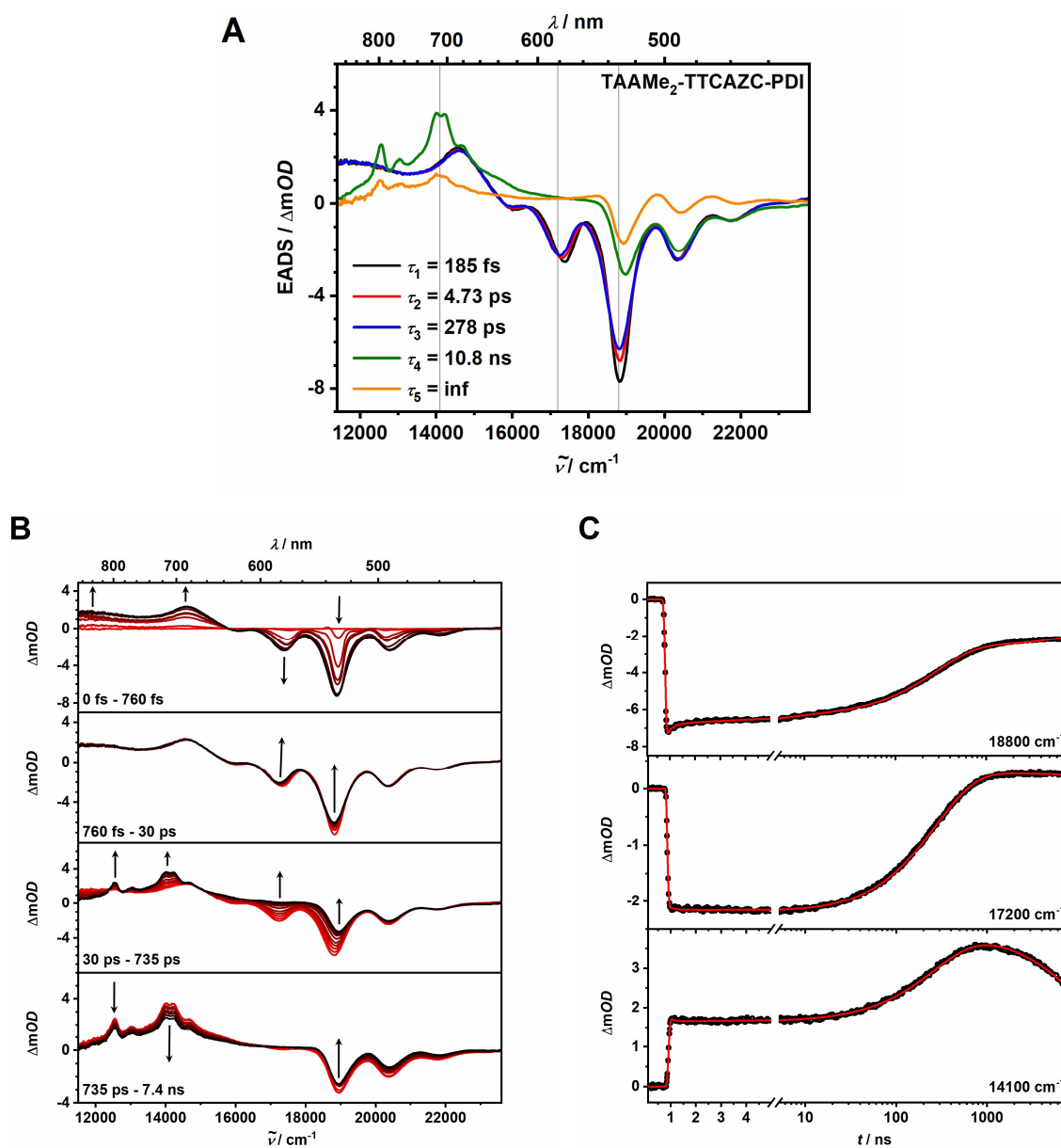
**Figure 85:** Chirp corrected fs-TA spectra of **Ph-TTC(OMe)<sub>2</sub>-PDI** in toluene after light-excitation at 18900 cm<sup>-1</sup> (528 nm) at 298 K. **A:** EADS **B** selected TA-spectra from the fs-TA measurements (short times to long times depicted from red to black) **C:** selected time traces at different wavenumbers (grey lines in **A**) with their respective global fits.



**Figure 86:** Chirp corrected fs-TA spectra of **TAAMe<sub>2</sub>-TTCMe<sub>2</sub>-PDI** in toluene after light-excitation at 18900 cm<sup>-1</sup> (528 nm) at 298 K. **A:** EADS **B:** selected TA-spectra from the fs-TA measurements (short times to long times depicted from red to black) **C:** selected time traces at different wavenumbers (grey lines in **A**) with their respective global fits.



**Figure 87:** Chirp corrected fs-TA spectra of **TAAMe<sub>2</sub>-TTCCl<sub>2</sub>-PDI** in toluene after light-excitation at 18900 cm<sup>-1</sup> (528 nm) at 298 K. **A:** EADS **B:** selected TA-spectra from the fs-TA measurements (short times to long times depicted from red to black) **C:** selected time traces at different wavenumbers (grey lines in **A**) with their respective global fits.



**Figure 88:** Chirp corrected fs-TA spectra of **TAAMe<sub>2</sub>-TTCAZC-PDI** in toluene after light-excitation at 18900 cm<sup>-1</sup> (528 nm) at 298 K. **A:** EADS **B:** selected TA-spectra from the fs-TA measurements (short times to long times depicted from red to black) **C:** selected time traces at different wavenumbers (grey lines in **A**) with their respective global fits.

**Table 21:** EADS lifetime components of the triads **TAAMe<sub>2</sub>-TTC(OMe)<sub>2</sub>-PDI**, **TAAMe<sub>2</sub>-TTCMe<sub>2</sub>-PDI**, **TAAMe<sub>2</sub>-TTCCl<sub>2</sub>-PDI** and **TAAMe<sub>2</sub>-TTCAZC-PDI** as well as the reference compound **Ph-TTC(OMe)<sub>2</sub>-PDI** from the fs-TA measurements.

	$\tau_1$ / ps	$\tau_2$ / ps	$\tau_3$ / ps	$\tau_4$ / ns	$\tau_5$ / ps
<b>Ph<sub>2</sub>-TTC(OMe)<sub>2</sub>-PDI</b>	2.81	75.5	743	10.3	inf
<b>TAAMe<sub>2</sub>-TTC(OMe)<sub>2</sub>-PDI</b>	2.81	38.1	707	11.1	inf
<b>TAAMe<sub>2</sub>-TTCMe<sub>2</sub>-PDI</b>	2.76	94.4	837	17.9	inf
<b>TAAMe<sub>2</sub>-TTC-PDI<sup>a</sup></b>	5.51	125	962	9.30	inf
<b>TAAMe<sub>2</sub>-TTCCl<sub>2</sub>-PDI</b>	0.13	4.26	268	13.8	inf
<b>TAAMe<sub>2</sub>-TTCAZC-PDI</b>	0.19	4.73	278	10.8	inf

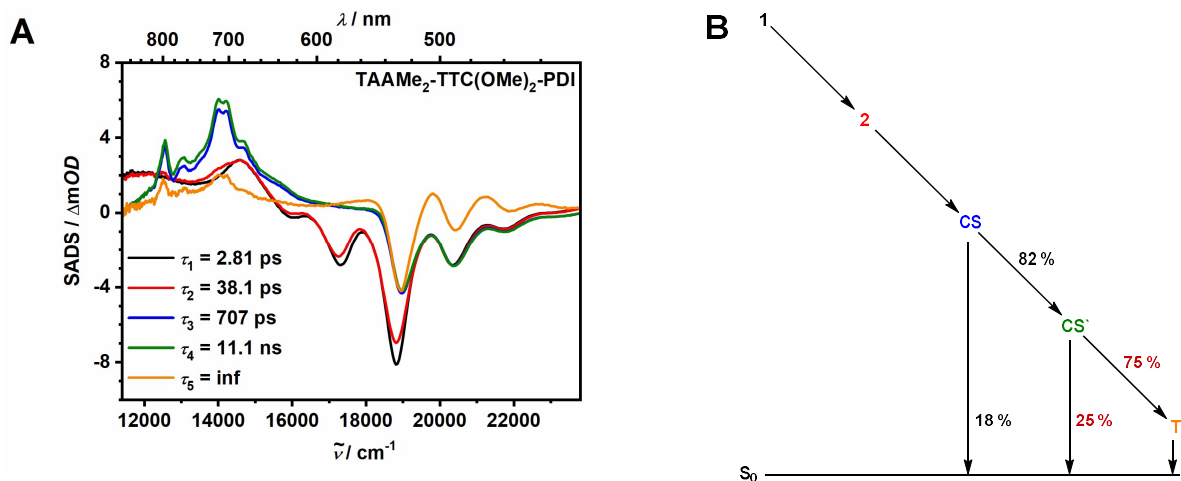
<sup>a</sup> values taken from section 6.1.2.1.

### 7.1.2.2 Global target analysis

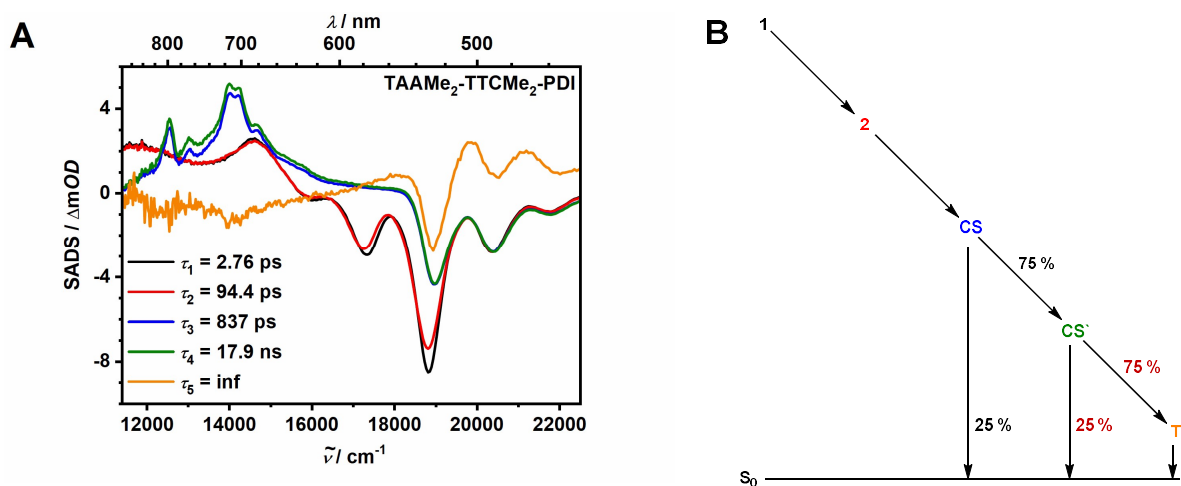
The rate constants  $k_{CS}$  as well as the efficiencies for the CS processes (**Figure 89** to **Figure 92** and **Table 22**) were determined as previously described (**section 6.1.2.2**) because the substituted triptycene triads undergo the same processes as the rotationally hindered triads. Therefore, the same kinetic model was applied.<sup>19</sup>

The analysis of the series of the substituted triptycene triads shows that the attachment of electron donating and withdrawing groups on the **TTC** bridge results in strong changes of the CS dynamics compared to the unsubstituted **TTC**. The triads **TAAMe<sub>2</sub>-TTC(OMe)<sub>2</sub>-PDI** and **TAAMe<sub>2</sub>-TTCMe<sub>2</sub>-PDI**, with electron donating groups exhibit increased values for  $k_{CS}$  of  $2.6 \cdot 10^{10} \text{ s}^{-1}$  and  $1.1 \cdot 10^{10} \text{ s}^{-1}$  compared to  $7.6 \cdot 10^9 \text{ s}^{-1}$  for the unsubstituted triad **TAAMe<sub>2</sub>-TTC-PDI**. Thus, with increasing electron density at the bridging unit the CS process becomes faster by one order of magnitude. In contrast, the triads **TAAMe<sub>2</sub>-TTCCl<sub>2</sub>-PDI** and **TAAMe<sub>2</sub>-TTCAZC-PDI** exhibit decreased values for  $k_{CS}$  of  $3.7 \cdot 10^9 \text{ s}^{-1}$  and  $3.1 \cdot 10^9 \text{ s}^{-1}$ , showing a decrease to half of the value of the unsubstituted triad for the CS rate constants. Thus, varying the electron density in the bridging unit influences the CS kinetics of DA triads, in which electron donating groups increase and electron withdrawing groups decrease the rate of CS.<sup>[47]</sup>

<sup>19</sup> Global target analysis was done by Dr. M. Holzapfel.

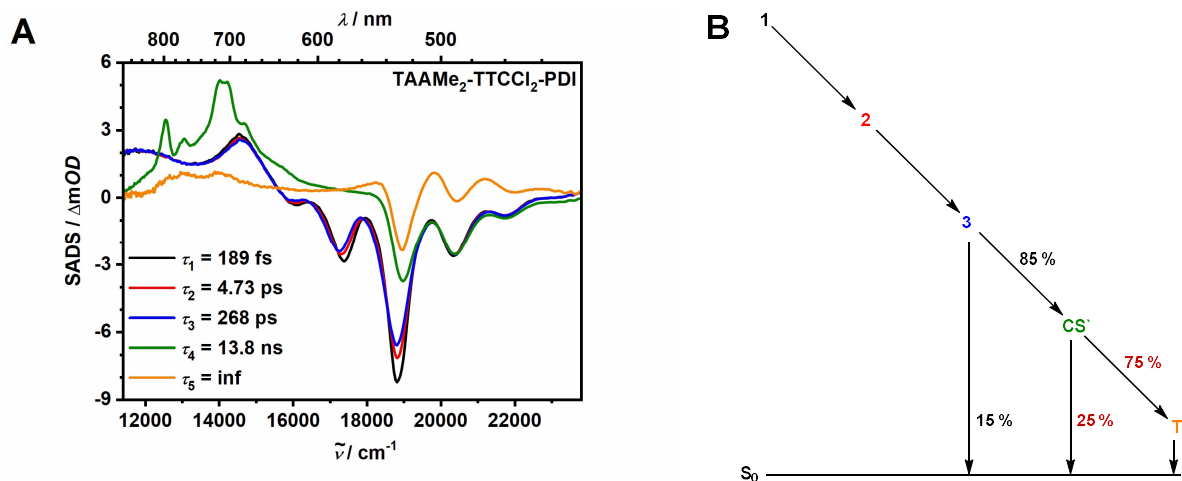


**Figure 89: A:** SADS. **B:** Kinetic model used to apply a global target analysis to the transient map of TAAMe<sub>2</sub>-TTC(OMe)<sub>2</sub>-PDI under the assumption that all SADS spectra with exception of the <sup>3</sup>PDI spectra match at 20400 cm<sup>-1</sup> (490 nm). The dark red percentages are an estimation for the triplet formation. The coloured numbers in **B** represent the respective SADS in **A**.

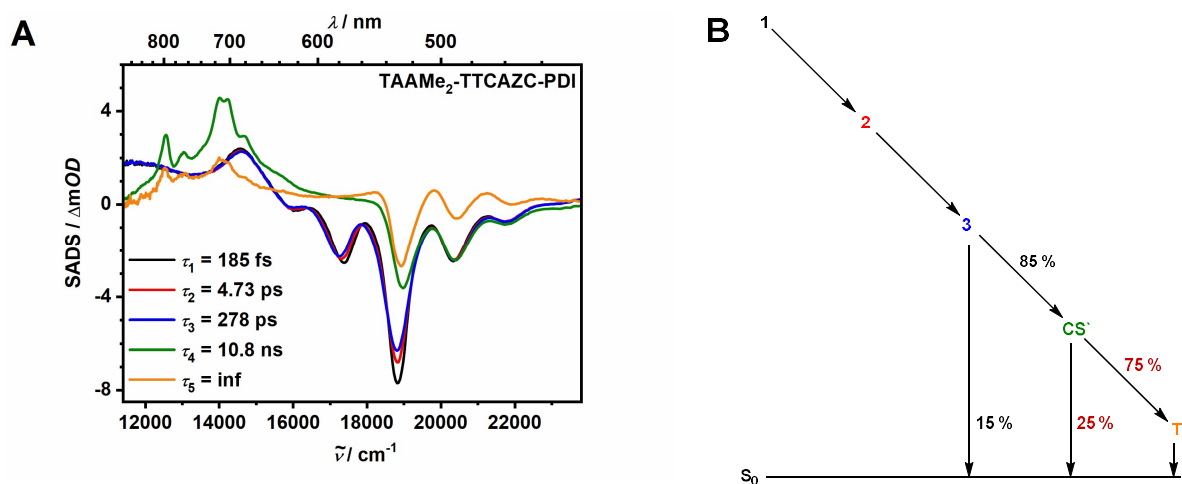


**Figure 90: A:** SADS. **B:** Kinetic model used to apply a global target analysis to the transient map of TAAMe<sub>2</sub>-TTCMe<sub>2</sub>-PDI under the assumption that all SADS spectra with exception of the <sup>3</sup>PDI spectra match at 20400 cm<sup>-1</sup> (490 nm). The dark red percentages are an estimation for the triplet formation. The coloured numbers in **B** represent the respective SADS in **A**.





**Figure 91: A:** SADS. **B:** Kinetic model used to apply a global target analysis to the transient map of TAAMe<sub>2</sub>-TTCCl<sub>2</sub>-PDI under the assumption that all SADS spectra with exception of the <sup>3</sup>PDI spectra match at 20400 cm<sup>-1</sup> (490 nm). The dark red percentages are an estimation for the triplet formation. The coloured numbers in **B** represent the respective SADS in **A**.



**Figure 92: A:** SADS. **B:** Kinetic model used to apply a global target analysis to the transient map of TAAMe<sub>2</sub>-TTCAZC-PDI under the assumption that all SADS spectra with exception of the <sup>3</sup>PDI spectra match at 20400 cm<sup>-1</sup> (490 nm). The dark red percentages are an estimation for the triplet formation. The coloured numbers in **B** represent the respective SADS in **A**.

**Table 22:** Lifetimes  $\tau_{S_1}$  of the relaxed  $S_1$  PDI state, quantum yields of the CSS and rate constant of charge separation  $k_{CS}$  in toluene for the triads **TAAMe<sub>2</sub>-TTC(OMe)<sub>2</sub>-PDI**, **TAAMe<sub>2</sub>-TTCMe<sub>2</sub>-PDI**, **TAAMe<sub>2</sub>-TTCCl<sub>2</sub>-PDI**, and **TAAMe<sub>2</sub>-TTCAZC-PDI**.

	$\tau_{S_1} / \text{ps}^a$	$\Phi_{CS}^b$	$k_{CS} / \text{s}^{-1}{}^c$
<b>TAAMe<sub>2</sub>-TTC(OMe)<sub>2</sub>-PDI</b>	38.1	1.00	$2.6 \cdot 10^{10}$
<b>TAAMe<sub>2</sub>-TTCMe<sub>2</sub>-PDI</b>	94.4	1.00	$1.1 \cdot 10^{10}$
<b>TAAMe<sub>2</sub>-TTC-PDI<sup>d</sup></b>	125	0.95	$7.6 \cdot 10^9$
<b>TAAMe<sub>2</sub>-TTCCl<sub>2</sub>-PDI</b>	268	0.85	$3.7 \cdot 10^9$
<b>TAAMe<sub>2</sub>-TTCAZC-PDI</b>	278	0.85	$3.1 \cdot 10^9$

<sup>a</sup> from the fs-TA measurements. <sup>b</sup> quantum yield of CS determined by global target analysis. <sup>c</sup> rate constant for CS from the global target analysis of the fs-TA maps. <sup>d</sup> values taken from **section 6.1.2.2**.

### 7.1.3 Charge recombination

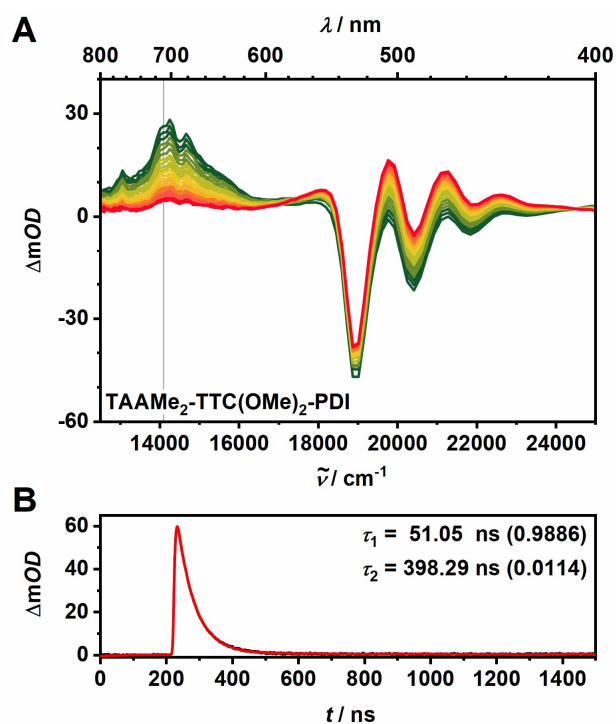
In the previous sections it was shown that all substituted triptycene triads form CSSs upon excitation of the **PDI** moiety. The CS dynamics were investigated using fs-TA spectroscopy and the resulting rate constants  $k_{CS}$  as well as the efficiencies of the CS processes were determined using a global target analysis. In this section, the kinetics of the CR processes will be investigated using magnetic field dependent ns-TA spectroscopy. A detailed description of the used laser setup and the measurement conditions are given in **section 10.3.4.2**. First, the ns-TA experiments at zero field (**section 7.1.3.1**) and thereafter the ns-TA experiments with the application of an external magnetic field (**section 7.1.3.2**) are discussed.

#### 7.1.3.1 Charge recombination at zero external magnetic field

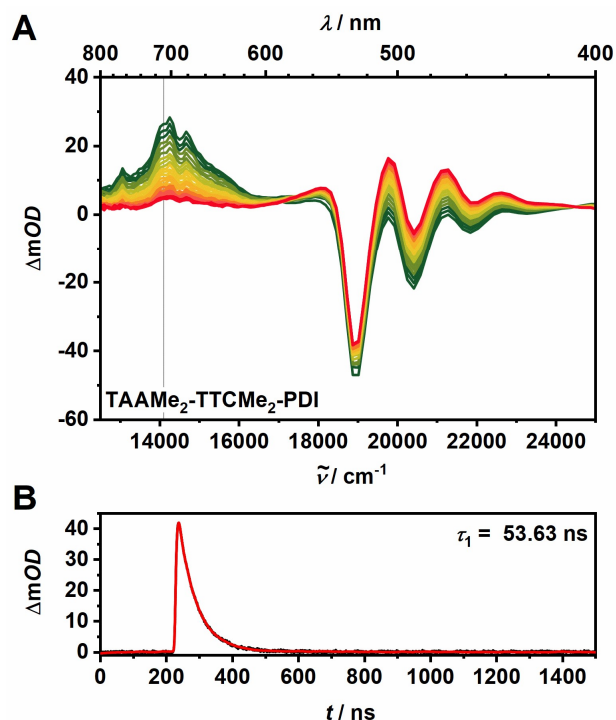
To observe the kinetics of CR, ns-TA maps (figures (A)) for **TAAMe<sub>2</sub>-TTC(OMe)<sub>2</sub>-PDI (Figure 93)**, **TAAMe<sub>2</sub>-TTCMe<sub>2</sub>-PDI (Figure 94)**, **TAAMe<sub>2</sub>-TTCCl<sub>2</sub>-PDI (Figure 95)** and **TAAMe<sub>2</sub>-TTCAZC-PDI (Figure 96)** were measured after light-excitation of the **PDI** moiety in toluene. The resulting ns-TA maps all show the same spectral behaviour. At early times all ns-TA maps exhibit the GSB of the **PDI** above 18900 cm<sup>-1</sup> (528 nm) as well as an ESA at 14100 cm<sup>-1</sup> (710 nm). The latter is related to the formation of the charge separated state, which is in very good agreement with the fs-TA data (**section 7.1.2.1**). The charge separation process observed in the fs-TA data is, however, not visible in the ns-TA measurements because it is much faster than the shortest time step of the ns-TA measurements. The fs-TA measurements show that upon light-excitation the <sup>1</sup>PDI state is formed and subsequently is reduced by an electron from the **TAA**, leading to the formation of the <sup>1</sup>CSS (**Figure 84 to Figure 88 in section 7.1.2.1**), which may undergo spin interconversion to the <sup>3</sup>CSS. Charge recombination of the <sup>1</sup>CSS directly leads to the singlet ground state, which is forbidden for the <sup>3</sup>CSS. In contrast, the <sup>3</sup>CSS recombines to the local <sup>3</sup>PDI state ( $\Delta G_{3CSS-1PDI}$  approx. -5500 cm<sup>-1</sup>, see **Table 20 in section 7.1.1**), which can clearly be observed in the ns-TA data because at later times a broad, structured ESA between 18300 cm<sup>-1</sup> (546 nm) and 22500 cm<sup>-1</sup> (444 nm) overlaid with the GSB of the **PDI** develops. This is in good agreement with similar triads in literature.<sup>[48, 94, 160]</sup>

To determine the lifetime of the CSS, decay curves without an external magnetic field were measured and the decay times were extracted using a deconvolution fit (figures (B) in **Figure 93 to Figure 96**) (description in **section 10.3.4.2**). In comparison to the unsubstituted bridging unit **TAAMe<sub>2</sub>-TTC-PDI (Figure 58 in section 6.1.3.1)**, the CSS decay times increase for the triads **TAAMe<sub>2</sub>-TTC(OMe)<sub>2</sub>-PDI** and **TAAMe<sub>2</sub>-TTCMe<sub>2</sub>-PDI (Table 23)**. Thus, an increasing

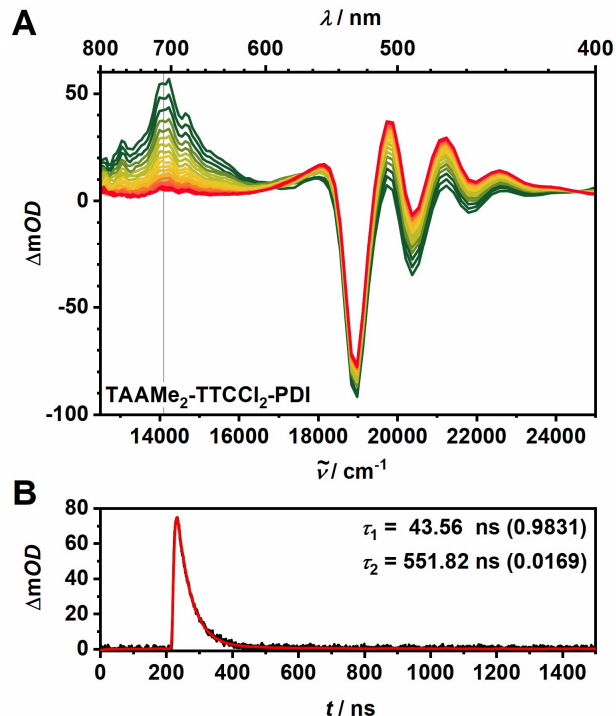
electron density in the bridging unit indicates an increased electronic coupling between the donor state and the acceptor state for CR. In contrast, the CSS decay times decrease in **TAAMe<sub>2</sub>-TTCCl<sub>2</sub>-PDI** and **TAAMe<sub>2</sub>-TTCAZC-PDI** (Table 23) compared to **TAAMe<sub>2</sub>-TTC-PDI**. Thus, decreasing electron density in the bridging unit indicates a decreased electronic coupling between the donor state and the acceptor state for the CR process. The values for the <sup>3</sup>PDI QYs (Table 39 in section 10.3.4.2) are only approximate because uncertainties in the determination of the <sup>3</sup>PDI extinction coefficients lead to systematic errors in the actinometry measurements. Nevertheless, the QYs of the formation of the CSS and for the <sup>3</sup>PDI are on the same order of magnitude, which indicates that the CSS recombines almost exclusively via the triplet pathway. The distinctly smaller *Gibbs* energy of the CR<sub>T</sub> calculated using *Marcus* theory (section 7.1.1) concurs with this observation.



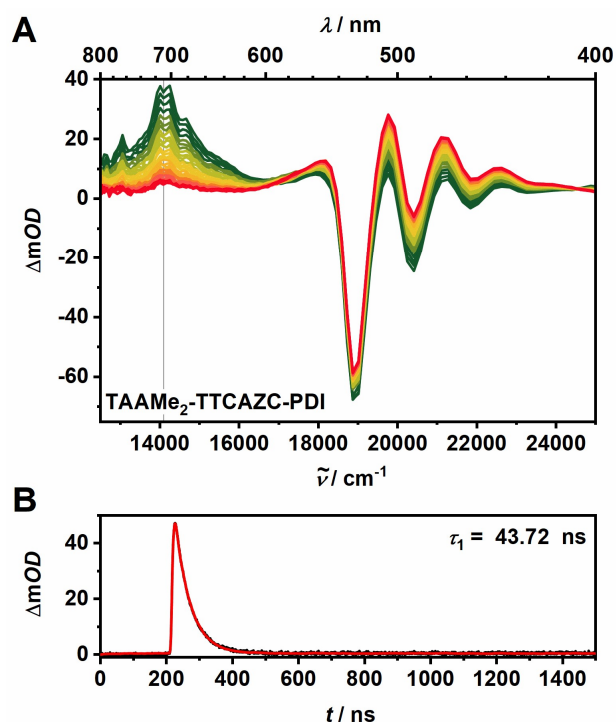
**Figure 93:** **A** ns-TA spectra of **TAAMe<sub>2</sub>-TTC(OMe)<sub>2</sub>-PDI** in toluene at 293 K after light-excitation at  $18900 \text{ cm}^{-1}$  (528 nm). Early spectra are given in dark green, late spectra in red and the time steps between the spectra are 7 ns. **B:** CSS decay curve (black) with the corresponding deconvolution fit (red) at  $14100 \text{ cm}^{-1}$  (grey line in **A**).



**Figure 94:** **A** ns-TA spectra of TAAMe<sub>2</sub>-TTCMe<sub>2</sub>-PDI in toluene at 293 K after light-excitation at 18900 cm<sup>-1</sup> (528 nm). Early spectra are given in dark green, late spectra in red and the time steps between the spectra are 7 ns. **B:** CSS decay curve (black) with the corresponding deconvolution fit (red) at 14100 cm<sup>-1</sup> (grey line in **A**).



**Figure 95:** **A** ns-TA spectra of TAAMe<sub>2</sub>-TTCCl<sub>2</sub>-PDI in toluene at 293 K after light-excitation at 18900 cm<sup>-1</sup> (528 nm). Early spectra are given in dark green, late spectra in red and the time steps between the spectra are 7 ns. **B:** CSS decay curve (black) with the corresponding deconvolution fit (red) at 14100 cm<sup>-1</sup> (grey line in **A**).



**Figure 96:** **A** ns-TA spectra of **TAAMe<sub>2</sub>-TTCAZC-PDI** in toluene at 293 K after light-excitation  $r$  at  $18900\text{ cm}^{-1}$  (528 nm). Early spectra are given in dark green, late spectra in red and the time steps between the spectra are 7 ns. **B:** CSS decay curve (black) with the corresponding deconvolution fit (red) at  $14100\text{ cm}^{-1}$  (grey line in **A**).

**Table 23:** CSS decay times  $\tau$  and the corresponding amplitudes  $a$  of the four substituted triptycene triads in toluene obtained by a deconvolution fit of the ns-TA decay.

	$\tau_1 / \text{ns}$	$a_1$	$\tau_2 / \text{ns}$	$a_2$
<b>TAAMe<sub>2</sub>-TTC(OMe)<sub>2</sub>-PDI</b>	51.05	0.9886	398.29	0.0114
<b>TAAMe<sub>2</sub>-TTCMe<sub>2</sub>-PDI</b>	53.63		-	-
<b>TAAMe<sub>2</sub>-TTC-PDI<sup>a</sup></b>	46.34	0.8750	94.59	0.1250
<b>TAAMe<sub>2</sub>-TTCCl<sub>2</sub>-PDI</b>	43.56	0.9831	551.82	0.0169
<b>TAAMe<sub>2</sub>-TTCAZC-PDI</b>	43.72		-	-

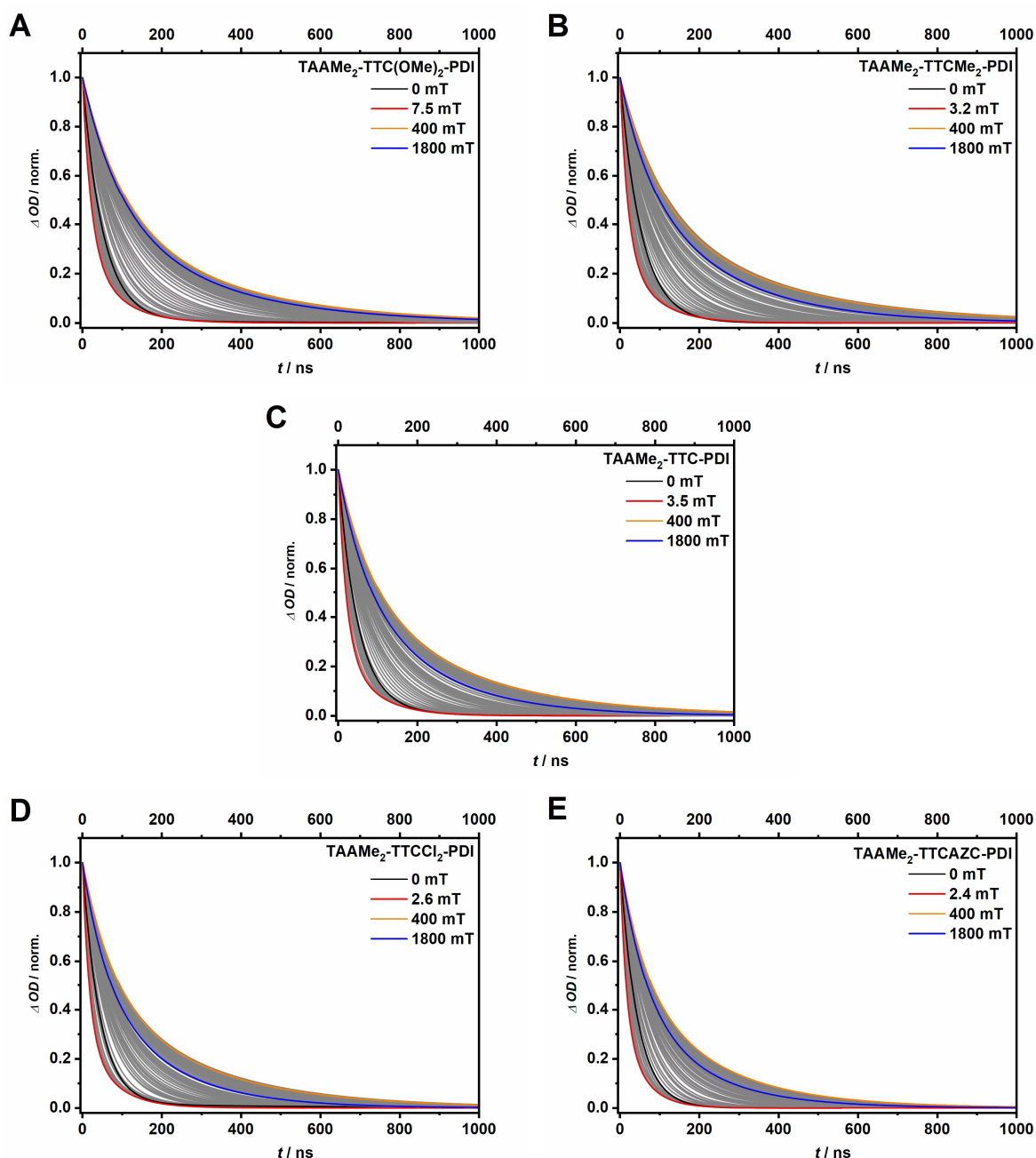
<sup>a</sup> taken from **section 6.1.3.1** for better clarification of the trend of the lifetimes.

### 7.1.3.2 Magnetic field effect

The formation of CSS was proved in the previous sections for all substituted triptycene triads using fs- and ns-TA spectroscopy (**sections 7.1.2.1 and 7.1.3.1**). The fs-TA measurements show that after light-excitation of the **PDI** moiety the  $^1\text{PDI}$  state is formed from which the  $^1\text{CSS}$  is populated. The formation of a local  $^3\text{PDI}$  state is observed in the ns-TA maps (**sections 7.1.3.1 and 6.1.3.1**) in toluene, which indicates a spin evolution between the  $^1\text{CSS}$  and the  $^3\text{CSS}$ . Due to spin conservation rules, the  $^1\text{CSS}$  only recombines to the ground state and the  $^3\text{CSS}$  to the local  $^3\text{PDI}$  state. This spin evolution as well as the exchange interaction  $2J$  can be investigated in detail using varying external magnetic fields (**section 1.1**). The detailed CR kinetics of the triads **TAAMe<sub>2</sub>-TTC(OMe)<sub>2</sub>-PDI**, **TAAMe<sub>2</sub>-TTCMe<sub>2</sub>-PDI**, **TAAMe<sub>2</sub>-TTC-PDI**, **TAAMe<sub>2</sub>-TTCCl<sub>2</sub>-PDI** and **TAAMe<sub>2</sub>-TTCAZC-PDI** were therefore investigated by measuring ns-TA at  $14100\text{ cm}^{-1}$  (710 nm) (setup and analysis details in **section 10.3.4.2**) with applying magnetic fields between 0 and 1800 mT in about 90 steps (exact values and lifetimes in **Appendix**). The initial period of signals was corrected by deconvolution with the IRF.

The CSS decay curves of the triads **TAAMe<sub>2</sub>-TTC(OMe)<sub>2</sub>-PDI**, **TAAMe<sub>2</sub>-TTCMe<sub>2</sub>-PDI**, **TAAMe<sub>2</sub>-TTC-PDI**<sup>20</sup>, **TAAMe<sub>2</sub>-TTCCl<sub>2</sub>-PDI** and **TAAMe<sub>2</sub>-TTCAZC-PDI** (**Figure 97**) all show a pronounced magnetic field effect. The decay times decrease at low fields until they reach a minimum (from black to red, **Table 24**), then subsequently increase significantly until they reach a magnetic field of about 400 mT (orange). Thereafter, a slight decrease of the decay times  $\tau$  upon increasing external magnetic field from 400 mT to 1800 mT (blue) is visible (**Table 24**). The lifetimes of the decay curves at zero magnetic field decrease with decreasing electron density in the bridging unit from **TAAMe<sub>2</sub>-TTC(OMe)<sub>2</sub>-PDI** over **TAAMe<sub>2</sub>-TTCMe<sub>2</sub>-PDI** and **TAAMe<sub>2</sub>-TTC-PDI** and **TAAMe<sub>2</sub>-TTCCl<sub>2</sub>-PDI** to **TAAMe<sub>2</sub>-TTCAZC-PDI** (blue in **Figure 97** and **Table 24**). The lifetimes of the red curves, which represents the external magnetic field of each triad corresponding to the exchange interaction  $2J$ , are decreasing with decreasing electron density in the **TTC** bridging unit from **TAAMe<sub>2</sub>-TTC(OMe)<sub>2</sub>-PDI** over **TAAMe<sub>2</sub>-TTCMe<sub>2</sub>-PDI** and **TAAMe<sub>2</sub>-TTC-PDI** and **TAAMe<sub>2</sub>-TTCCl<sub>2</sub>-PDI** to **TAAMe<sub>2</sub>-TTCAZC-PDI** as well. The lifetimes at higher fields significantly exceed the lifetimes at zero magnetic field.

<sup>20</sup> Data were taken from the rotationally hindered triads in **section 6**.



**Figure 97:** Deconvolution fit of the experimental transient decay curves of **A: TAAMe<sub>2</sub>-TTC(OMe)<sub>2</sub>-PDI** **B: TAAMe<sub>2</sub>-TTCMe<sub>2</sub>-PDI** **C: TAAMe<sub>2</sub>-TTC-PDI** **D: TAAMe<sub>2</sub>-TTCCl<sub>2</sub>-PDI** and **E: TAAMe<sub>2</sub>-TTCAZC-PDI** at 14100 cm<sup>-1</sup> (710 nm) after light-excitation at 18900 cm<sup>-1</sup> (528 nm) in toluene at 298 K. The magnetic field was varied from 0 to 1800 mT in about 90 steps. All curves are depicted in grey and only the significant turning points of the MFE are highlighted. The highlighted curves describe the external magnetic fields: black = 0 mT, red = 2J, hereby the curves not always represent the exact calculated 2J values but correspond to the curves closest to the exact value. Orange = 400 mT, blue = 1800 mT.



**Table 24:** Selected CSS lifetimes  $\tau$  and the corresponding amplitudes  $a$  of the substituted triptycene triads in toluene obtained by using a deconvolution fit on the ns-TA decay curves. The magnetic fields correspond to the highlighted curves in **Figure 97**.

	external magnetic field	$\tau_1$ / ns	$a_1$	$\tau_2$ / ns	$a_2$
<b>TAAMe<sub>2</sub>-TTC(OMe)<sub>2</sub>-PDI</b>	0 mT	51.05	0.9886	398.29	0.0114
	7.5 mT	20.90	0.6771	79.11.	0.3229
	400 mT	98.62	0.5278	313.85	0.4722
	1800 mT	93.20	0.5263	285.65	0.4737
<b>TAAMe<sub>2</sub>-TTCMe<sub>2</sub>-PDI</b>	0 mT	53.63		-	-
	3.2 mT	18.50	0.6765	75.42	0.3235
	400 mT	95.48	0.4923	324.02	0.5077
	1800 mT	70.30	0.3651	227.57	0.6349
<b>TAAMe<sub>2</sub>-TTC-PDI<sup>a</sup></b>	0 mT	46.34	0.8750	94.59	0.1250
	3.5 mT	20.09	0.7105	79.53	0.2895
	400 mT	84.64	0.4737	284.49	0.5263
	1800 mT	65.72	0.3919	198.63	0.6081
<b>TAAMe<sub>2</sub>-TTCCl<sub>2</sub>-PDI</b>	0 mT	43.56	0.9831	551.82	0.0169
	2.6 mT	16.98	0.6887	69.65	0.3113
	400 mT	75.54	0.4941	268.21	0.5059
	1800 mT	58.71	0.4355	180.44	0.5645
<b>TAAMe<sub>2</sub>-TTCAZC-PDI</b>	0 mT	43.72		-	-
	2.4 mT	14.46	0.6129	52.11	0.3871
	400 mT	61.86	0.4426	208.25	0.5574
	1800 mT	64.26	0.5323	176.12	0.4677

<sup>a</sup> taken from **section 6.1.3.2**.

The MARY plots of the triads **TAAMe<sub>2</sub>-TTC(OMe)<sub>2</sub>-PDI**, **TAAMe<sub>2</sub>-TTCMe<sub>2</sub>-PDI**, **TAAMe<sub>2</sub>-TTC-PDI**, **TAAMe<sub>2</sub>-TTCCl<sub>2</sub>-PDI** and **TAAMe<sub>2</sub>-TTCAZC-PDI** (**Figure 98**) all show the aforementioned resonance peak (**section 6.1.3.2**) and therefore the exchange interaction  $2J$  can directly be determined from this representation. In order to obtain a more precise value, the region around the resonance peak at a delay time of 50 ns of each triad was fitted resulting in the value for  $2J$  (**Table 25**, graphs see **Appendix**). This approach ensures comparability of the values, as the differences between the  $2J$  couplings are often small. The thereby calculated values decrease from **TAAMe<sub>2</sub>-TTC(OMe)<sub>2</sub>-PDI** (7.6 mT) over **TAAMe<sub>2</sub>-TTCMe<sub>2</sub>-PDI** (3.2 mT) and **TAAMe<sub>2</sub>-TTC-PDI** (3.2 mT) and **TAAMe<sub>2</sub>-TTCCl<sub>2</sub>-PDI** (2.6 mT) to **TAAMe<sub>2</sub>-TTCAZC-PDI** (2.4 mT).

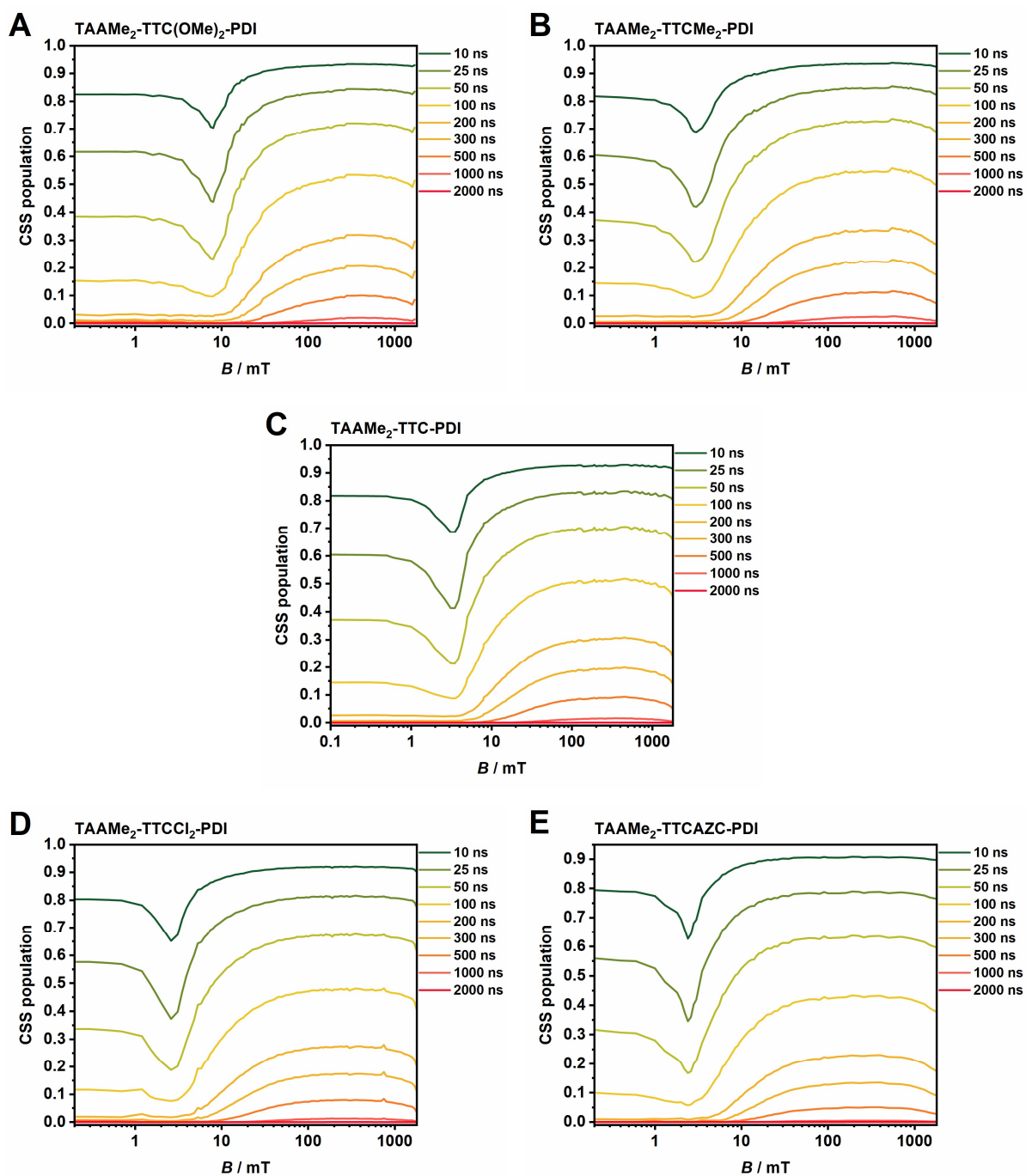
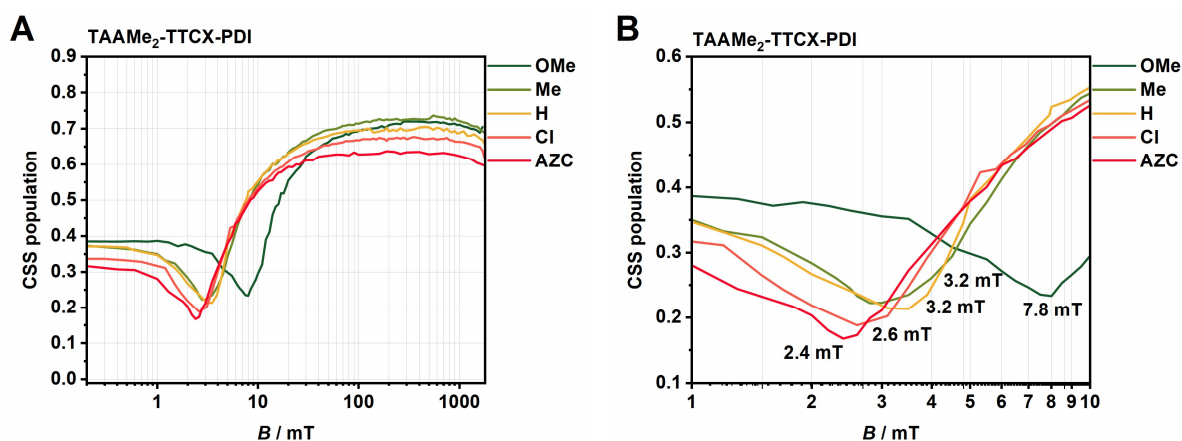


Figure 98: MARY plots of A: TAAMe<sub>2</sub>-TTC(OMe)<sub>2</sub>-PDI B: TAAMe<sub>2</sub>-TTCMe<sub>2</sub>-PDI C: TAAMe<sub>2</sub>-TTC-PDI D: TAAMe<sub>2</sub>-TTCCl<sub>2</sub>-PDI and E: TAAMe<sub>2</sub>-TTCAZC-PDI in toluene at 298 K.

**Table 25:**  $2J$  values of the substituted triptycene triads in toluene at 298 K determined by fitting the  $2J$  region at a delay time of 50 ns of each rotationally hindered triad using a parabolic fit function.

	$2J / \text{mT}$
<b>TAAMe<sub>2</sub>-TTC(OMe)<sub>2</sub>-PDI</b>	7.6
<b>TAAMe<sub>2</sub>-TTCMe<sub>2</sub>-PDI</b>	3.2
<b>TAAMe<sub>2</sub>-TTC-PDI</b>	3.2
<b>TAAMe<sub>2</sub>-TTCCl<sub>2</sub>-PDI</b>	2.6
<b>TAAMe<sub>2</sub>-TTCAZC-PDI</b>	2.4

For better comparability, the CSS populations of all triads at a delay time of 50 ns are plotted against the external magnetic field showing the differences between the triads (**Figure 99**). The magnetic field dependent ns-TA measurements show a strong decrease in the  $2J$  coupling with decreasing electron density in the bridging unit along the series from **TAAMe<sub>2</sub>-TTC(OMe)<sub>2</sub>-PDI** over **TAAMe<sub>2</sub>-TTCMe<sub>2</sub>-PDI** and **TAAMe<sub>2</sub>-TTC-PDI** and **TAAMe<sub>2</sub>-TTCCl<sub>2</sub>-PDI** to **TAAMe<sub>2</sub>-TTCAZC-PDI**, which indicates that the electronic coupling between the **TAA** donor and the **PDI** acceptor can be influenced by modulating the electron density in bridging **TTC** moiety.



**Figure 99:** Comparison of the MARY plots of plots of **TAAMe<sub>2</sub>-TTC(OMe)<sub>2</sub>-PDI**, **TAAMe<sub>2</sub>-TTCMe<sub>2</sub>-PDI**, **TAAMe<sub>2</sub>-TTC-PDI**, **TAAMe<sub>2</sub>-TTCCl<sub>2</sub>-PDI** and **TAAMe<sub>2</sub>-TTCAZC-PDI** in toluene at a delay time of 50 ns. **A:** whole magnetic field range **B:** magnification of the  $2J$  region.

### 7.1.4 Quantum mechanical consideration

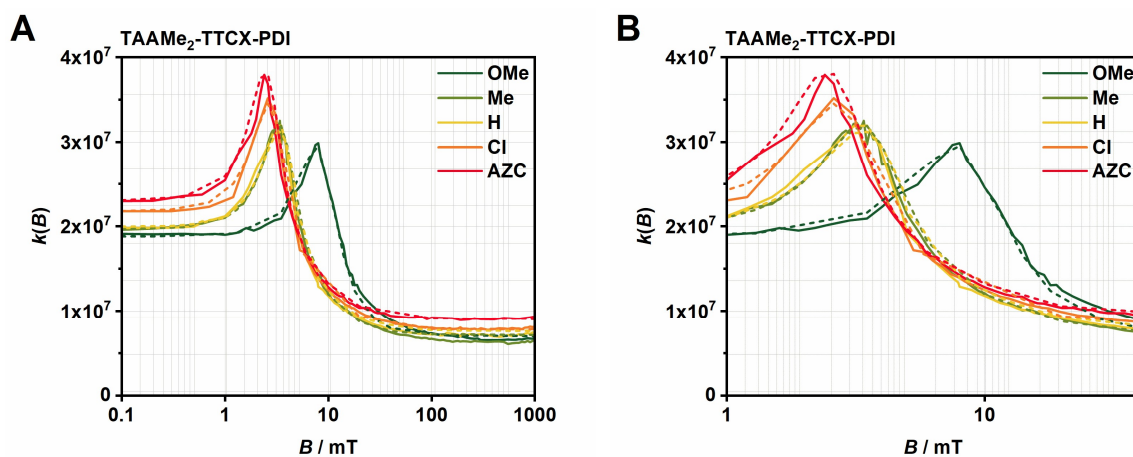
The quantum mechanical simulations were provided by *U. E. Steiner* (University of Konstanz) as described before (section 6.1.4). The rate constant spectra (Figure 100) and the best fit parameters (Table 26 and Table 27) were obtained similar to the rotationally hindered triads. The data shown result from a preliminary fit and require a more careful evaluation. In this context, the isotropic hfc of the TAA nitrogen  $a_N$  had to be modulated individually for a good fit for the  $k(B)$  spectra, while in case of the rotationally hindered triads a good fit with  $a_N = 0.925$  mT for all triads could be obtained. The reason for this difference is still unknown.

**Table 26:** Best fit parameters that were used for the quantum simulations of the CSS decay curves.  $k_S$  and  $k_T$  are the values of the rate constants for CRs and CR<sub>T</sub>, respectively. The values for the rotational correlation time  $\tau_r = 0.6$  ns was identical for all substituted triptycene triads.  $k_{STD}$  represents the rate for singlet/triplet dephasing.

	$k_S / s^{-1}$	$k_T / s^{-1}$	$k_{STD} / s^{-1}$ <sup>a</sup>
TAAMe <sub>2</sub> -TTC(OMe) <sub>2</sub> -PDI	0-2.0·10 <sup>6</sup>	0.84-1.2·10 <sup>9</sup>	7.0-2.4·10 <sup>6</sup>
TAAMe <sub>2</sub> -TTCMe <sub>2</sub> -PDI	0	1.26-1.83·10 <sup>8</sup>	1.20-1.88·10 <sup>7</sup>
TAAMe <sub>2</sub> -TTC-PDI	0-1.7·10 <sup>5</sup>	0.125-1.81·10 <sup>8</sup>	1.21-1.84·10 <sup>8</sup>
TAAMe <sub>2</sub> -TTCCl <sub>2</sub> -PDI	0	2.35-3.30·10 <sup>8</sup>	0.4-1.05·10 <sup>8</sup>
TAAMe <sub>2</sub> -TTCAZC-PDI	0-1.0·10 <sup>6</sup>	3.0-4.1·10 <sup>8</sup>	0.0-3.0·10 <sup>7</sup>

**Table 27:** Best fit parameters that were used for the quantum simulations of the CSS decay curves. The values for the rotational correlation time  $\tau_r = 0.6$  ns was identical for all substituted triptycene triads.  $a_N$  is the hfc isotropy of the TAA nitrogen.  $J$  represents the exchange interaction.

	$B_{max}/2 / mT$	$J / mT$	$a_N / mT$
TAAMe <sub>2</sub> -TTC(OMe) <sub>2</sub> -PDI	3.96	3.63-3.81	1.25
TAAMe <sub>2</sub> -TTCMe <sub>2</sub> -PDI	1.67	1.43-1.64	0.926
TAAMe <sub>2</sub> -TTC-PDI	1.68	1.45-1.65	0.926
TAAMe <sub>2</sub> -TTCCl <sub>2</sub> -PDI	1.34	1.14-1.26	0.800
TAAMe <sub>2</sub> -TTCAZC-PDI	1.22	1.02-1.16	0.820



**Figure 100:**  $k(B)$  spectra of the CSS decay for the substituted triptycene triads assuming mono-exponential decay kinetics within the first 100 ns. The solid curves represent the experimental data and the dashed curves the data obtained from the quantum simulations. **A:** whole magnetic field range **B:** magnification of the  $2J$  region.

### 7.1.5 Calculation of the electronic coupling $V$

The electronic couplings were calculated as described before (**section 6.1.5**) using the same energetic levels involved in the ET processes. The states under consideration for the ET processes (**Figure 72** in **section 6.1.5**) are the lowest excited singlet state ( $^1\text{PDI}$  18800  $\text{cm}^{-1}$ , 2.33 eV) as well as the lowest excited triplet state of the **PDI** ( $^3\text{PDI}$  9690  $\text{cm}^{-1}$ , 1.20 eV). The  $^{1,3}\text{CSS}$  energies (14921  $\text{cm}^{-1}$ , 1.85 eV) were calculated using the *Weller* approximation<sup>21</sup> (**Table 36** and **equation (24)** in **section 10.1**) for all triads.<sup>22</sup> The energies of the  $^1\text{TAA}$  and  $^3\text{TAA}$  states are too far off in energy and therefore are not considered to affect the ET processes.<sup>[91]</sup>

Using DFT calculations, the values for the inner and outer reorganisation energies were determined as  $\lambda_v = 1855 \text{ cm}^{-1}$  (0.23 eV) and  $\lambda_o = 484 \text{ cm}^{-1}$  (0.06 eV), respectively. The reorganisation energies together with an estimated molecular vibration frequency of  $\tilde{\nu}_v = 1500 \text{ cm}^{-1}$  (0.19 eV) leads to a *Huang-Rhys* factor  $S = \lambda_v/\tilde{\nu}_v$  of 1.24. As described before, the relations between the rate constant and the electronic coupling given by *Closs* and *Miller*<sup>[205]</sup> (**equation (17)** in **section 6.1.5**) can be used for a quantitative analysis of  $V_{1\text{CSS-1PDI}}$  and  $V_{3\text{CSS-3PDI}}$  using  $k_{\text{CS}}$  and  $k_{\text{T}}$  (**Table 28**).<sup>23</sup> Since the CS is faster in the substituted triptycene triads with electron donating groups attached to the bridge than in the rotationally hindered triads a modification of **equation (17)** was made. This modification was necessary because the ET processes approach an adiabatic solvent dynamic controlled rate regime. For this regime a simple approach was given by *Jortner* and *Bixon* that considers the solvent dynamics for ET processes using the longitudinal relaxation time  $\tau_L$  of the solvent as the relevant parameter to include the influence of the solvent motion on the ET.<sup>[208-209]</sup> The adiabatic ET rate constant is expressed as

$$k_{\text{ET, mn, solv}} = \frac{k_{\text{ET, mn}}}{1 + H_A} \quad (20)$$

with the adiabatic parameter  $H_A$

$$H_A = \frac{8\pi^2 \cdot c \cdot V^2 \cdot \tau_L}{\lambda_o} \quad (21)$$

<sup>21</sup> Calculated by Dr. M. Holzapfel.

<sup>22</sup>  $^{1,3}\text{CSS}$  energy for **TAAMe<sub>2</sub>-TTC-PDI** was rounded in **section 6.1.5** but the precise value was taken in this section which produces slightly different electronic couplings and rate constants. In the substituted triptycene triads the  $^{1,3}\text{CSS}$  energies are all the same because D and A are identically, which is not the case in the rotationally hindered triads.

<sup>23</sup> Calculated by Prof. C. Lambert.

Inserting these in **equation (17)** in **section 6.1.5** the electron transfer rate constant, that take the solvent dynamics into account is

$$k_{\text{ET},\text{mn},\text{solv}} = \frac{2\pi}{\hbar} V_{\text{mn}}^2 \sum_{j=0}^{\infty} \frac{e^{-S} S^j}{j!} \frac{\sqrt{\frac{1}{4\pi\lambda_0 kT}} \exp\left[-\frac{j\tilde{\nu}_V + \lambda_0 + \Delta G_{\text{mn}}}{4\lambda_0 kT}\right]}{(1 + H_A \cdot \frac{e^{-S} S^j}{j!})} \quad (22)$$

Using the aforementioned data of CS, the electronic couplings  $V_{1\text{CSS-1PDI}}$  were calculated in two different ways. In order to highlight the influence of the longitudinal relaxation time  $\tau_L$ , one time  $\tau_L$  was set zero and in the other time  $\tau_L = 2.7$  ps was taken for toluene (**Table 28**).<sup>[210]</sup> For the electronic coupling  $V_{3\text{CSS-3PDI}}$   $\tau_L$  was not regarded due to its negligible impact.

**Table 28:** Rate constants  $k_{\text{CS}}$  and  $k_{\text{T}}$  with the resulting electronic couplings  $V_{1\text{PDI-1CSS}}$  of CS and  $V_{3\text{CSS-3PDI}}$  for  $\text{CR}_{\text{T}}$  in toluene by applying **equation (22)**.

	$k_{\text{CS}} / \text{s}^{-1}$	$V_{1\text{CSS-1PDI}}^{\text{a}} / \text{cm}^{-1}$ ( $\tau_L = 2.7$ ps)	$V_{1\text{CSS-1PDI}}^{\text{a}} / \text{cm}^{-1}$ ( $\tau_L = 0$ ps)	$k_{\text{T}} / \text{s}^{-1}$	$V_{3\text{CSS-3PDI}}^{\text{b}} / \text{cm}^{-1}$
<b>TAAMe<sub>2</sub>-TTC(OMe)<sub>2</sub>-PDI</b>	$2.6 \cdot 10^{10}$	17.1	12.6	$1.0 \cdot 10^9$	3.5
<b>TAAMe<sub>2</sub>-TTCMe<sub>2</sub>-PDI</b>	$1.1 \cdot 10^{10}$	9.14	8.21	$1.5 \cdot 10^8$	1.3
<b>TAAMe<sub>2</sub>-TTC-PDI</b>	$7.6 \cdot 10^9$	7.33	6.82	$1.5 \cdot 10^8$	1.3
<b>TAAMe<sub>2</sub>-TTCCl<sub>2</sub>-PDI</b>	$3.7 \cdot 10^9$	4.92	4.76	$2.8 \cdot 10^8$	1.8
<b>TAAMe<sub>2</sub>-TTCAZC-PDI</b>	$3.1 \cdot 10^9$	4.85	4.70	$3.5 \cdot 10^8$	2.0

<sup>a</sup> from  $k_{\text{CS}}$  using **equation (22)**, <sup>b</sup> from  $k_{\text{T}}$  using **equation (22)**.

Since  $k_{\text{S}}$  could only be obtained from the quantum simulations with very large error margins, as described before (**section 6.1.5**), this value was calculated by a different approach. Therefore, the electronic couplings  $V_{1\text{CSS-1S0}}$  were calculated from the experimental  $J$  values (**equation (18)** in **section 6.1.5**) combined with the experimental state energies as well as the calculated values for  $V_{1\text{PDI-1CSS}}$  of CS and  $V_{3\text{CSS-3PDI}}$  for  $\text{CR}_{\text{T}}$ . Using these obtained values for  $V_{1\text{CSS-1S0}}$  the rate constants for  $k_{\text{S}}$  were calculated, in which in one case the solvent parameter  $\tau_L$  was taken into account (**Table 30**) and in the other case  $\tau_L$  was set zero (**Table 29**).

**Table 29:** Electronic coupling  $V_{1\text{CSS-1S0}}$  calculated from the experimental  $J$  value and rate constant  $k_S$  calculated from  $V_{1\text{CSS-1S0}}$  using **equation (22)** and  $\tau_L = 0$  ps for the substituted triptycene triads.

	$J / \text{mT}$	$V_{1\text{CSS-1S0}}^a / \text{cm}^{-1}$	$k_S / \text{s}^{-1b}$
<b>TAAMe<sub>2</sub>-TTC(OMe)<sub>2</sub>-PDI</b>	3.80	21.86	$4.58 \cdot 10^5$
<b>TAAMe<sub>2</sub>-TTCMe<sub>2</sub>-PDI</b>	1.55	13.61	$1.77 \cdot 10^5$
<b>TAAMe<sub>2</sub>-TTC-PDI</b>	1.55	11.97	$1.37 \cdot 10^5$
<b>TAAMe<sub>2</sub>-TTCCl<sub>2</sub>-PDI</b>	1.20	9.60	$8.84 \cdot 10^4$
<b>TAAMe<sub>2</sub>-TTCAZC-PDI</b>	1.10	9.58	$8.80 \cdot 10^4$

<sup>a</sup> calculated from  $J$  using **equation (18)** <sup>b</sup> calculated from  $V_{1\text{CSS-1S0}}$  using **equation (22)**.

**Table 30:** Electronic coupling  $V_{1\text{CSS-1S0}}$  calculated from the experimental  $J$  value and rate constant  $k_S$  calculated from  $V_{1\text{CSS-1S0}}$  using **equation (22)** and  $\tau_L = 2.7$  ps for the substituted triptycene triads.

	$J / \text{mT}$	$V_{1\text{CSS-1S0}}^a / \text{cm}^{-1}$	$k_S / \text{s}^{-1b}$
<b>TAAMe<sub>2</sub>-TTC(OMe)<sub>2</sub>-PDI</b>	3.80	27.3	$7.17 \cdot 10^5$
<b>TAAMe<sub>2</sub>-TTCMe<sub>2</sub>-PDI</b>	1.55	14.8	$2.09 \cdot 10^5$
<b>TAAMe<sub>2</sub>-TTC-PDI</b>	1.55	12.6	$1.51 \cdot 10^5$
<b>TAAMe<sub>2</sub>-TTCCl<sub>2</sub>-PDI</b>	1.20	9.77	$9.15 \cdot 10^4$
<b>TAAMe<sub>2</sub>-TTCAZC-PDI</b>	1.10	9.73	$9.08 \cdot 10^4$

<sup>a</sup> calculated from  $J$  using **equation (18)** <sup>b</sup> calculated from  $V_{1\text{CSS-1S0}}$  using **equation (22)**.

Comparing the electronic couplings, the longitudinal relaxation time  $\tau_L$  strongly influences the values of **TAAMe<sub>2</sub>-TTC(OMe)<sub>2</sub>-PDI** and **TAAMe<sub>2</sub>-TTCMe<sub>2</sub>-PDI** with electron donating groups at the bridging unit (compare **Table 29** with **Table 30**). These electronic couplings increase when  $\tau_L$  is taken into account. In contrast, the couplings of the triads **TAAMe<sub>2</sub>-TTCCl<sub>2</sub>-PDI** and **TAAMe<sub>2</sub>-TTCAZC-PDI** are barely influenced by  $\tau_L$ . This illustrates the necessity of considering the influence of the solvent while calculating the electronic couplings in cases of very fast ET processes.

The calculated electronic couplings  $V_{3\text{CSS-3PDI}}$  (**Table 28**) are on the order of approximately  $1 \text{ cm}^{-1}$  but  $V_{1\text{CSS-1S0}}$  (**Table 30**) as well as  $V_{1\text{CSS-1PDI}}$  (**Table 28**) are significantly higher. The electronic couplings  $V_{1\text{CSS-1S0}}$  and  $V_{1\text{CSS-1PDI}}$  as well as the exchange interaction  $2J$  are all decreasing with decreasing electron density in the bridging unit while  $V_{3\text{CSS-3PDI}}$  remains nearly constant. This shows that the variation of the electron density in the connecting bridge strongly influences the CS and CR<sub>S</sub> dynamics in those triads, but the CR<sub>T</sub> is only slightly influenced. The latter indicates that CR in the local <sup>3</sup>PDI state is caused by a different electron transfer mechanism than the CR to the ground state and the CS.<sup>[91]</sup>



In order to get a better understanding of how the varying electron density in the bridging moiety influences the ET processes between donor and acceptor, their influence on the kinetics can be regarded using the *superexchange* model based on perturbation theory.<sup>[211-212]</sup> Here, the orbitals on the bridge moiety are involved in virtual states contributing to the electronic coupling between donor and acceptor subunits. These virtual states can either be included in an ET route, implying the involvement of the lowest-lying unoccupied molecular orbital (LUMO) at the bridge (D<sup>+</sup>-B-A), or in a hole transfer (HT) route, implying the involvement of the highest-lying occupied molecular orbital (HOMO) at the bridge (D-B<sup>+</sup>-A<sup>-</sup>). The bridge-mediated *superexchange* coupling  $V_{DA}$  is given as

$$V_{DA} = \frac{V_{DB} \cdot V_{BA}}{\Delta E} \quad (23)$$

if direct donor acceptor coupling is negligible.<sup>[213-219]</sup> Thus, the coupling between donor state and acceptor state  $V_{DA}$  is given by the product of the couplings between bridge and donor ( $V_{DB}$ ) and between acceptor and bridge ( $V_{BA}$ ) states. The energy difference  $\Delta E$  between the acceptor state and the virtual bridge state may be approximated by the HOMO energy of the bridge. In the herein investigated substituted triptycene triads the **TTC** bridge should formally be oxidised in the virtual two-step ET processes. Thus, in this HT route the energetic level of the bridges HOMO needs to be considered (**Table 31**).

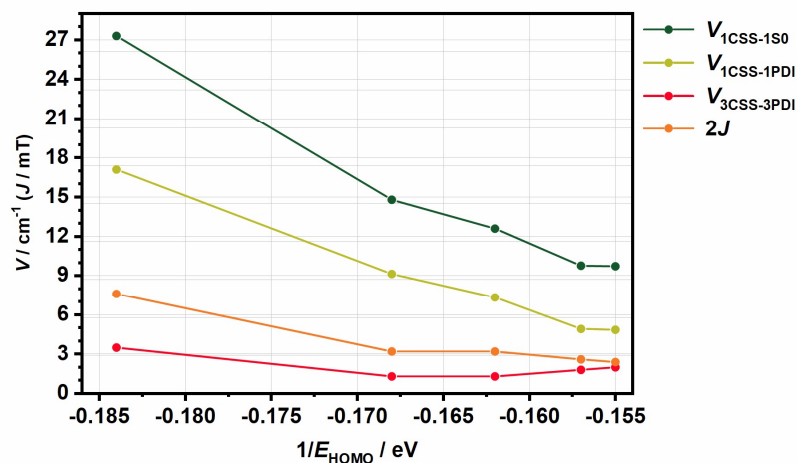
**Table 31:** HOMO levels of the pure bridging units of the substituted triptycene triads were calculated at B3LYP / 6-311+G\*\* level.

	$E_{\text{HOMO}} / \text{cm}^{-1}$	$E_{\text{HOMO}} / \text{eV}$	$1/E_{\text{HOMO}} / \text{eV}$
<b>TTC(OMe)<sub>2</sub></b>	-43900	-5.44	-0.184
<b>TTCMe<sub>2</sub></b>	-47900	-5.94	-0.168
<b>TTC</b>	-47700	-6.16	-0.162
<b>TTCCl<sub>2</sub></b>	-50700	-6.29	-0.157
<b>TTCAZC<sup>a</sup></b>	-51900	-6.44	-0.155

<sup>a</sup> the HOMO-1 level is taken because the HOMO is located only on the phenazine moiety (see **Appendix**) and does not influence the ET processes. **TAA**<sub>HOMO</sub> = -71100 cm<sup>-1</sup> (-8.82 eV), **TAA**<sub>LUMO</sub> = -35400 cm<sup>-1</sup> (-4.39 eV), **PDI**<sub>HOMO</sub> = -14400 cm<sup>-1</sup> (-1.79 eV), **PDI**<sub>LUMO</sub> = 4800 cm<sup>-1</sup> (0.60 eV).

By increasing the electron donating character of the substituents attached to the bridge the energy level of the HOMO is increased, causing a decrease of the  $\Delta E$  value. The decrease of  $\Delta E$  in turn causes an increase of the overall coupling  $V_{DA}$ . Plotting the electronic couplings and the exchange interaction against the HOMO level of the bridging unit, the correlation between the bridge electron density and the electronic couplings becomes clear (**Figure 101**). An almost linear correlation along the series of molecules was observed, in which the electronic couplings

for the singlet pathways are increasing with increasing HOMO level of the bridging unit. This virtual bridge states enter indirectly in **equation (18)** via  $V_{1\text{CSS-1PDI}}$  and  $V_{1\text{CSS-1S0}}$  but are not explicitly included in the *Anderson* approach. Nevertheless, the exchange interaction also displays a linear trend with the bridge HOMO energy. This shows that bridge substitution can be used to tune the electronic properties in donor acceptor systems.



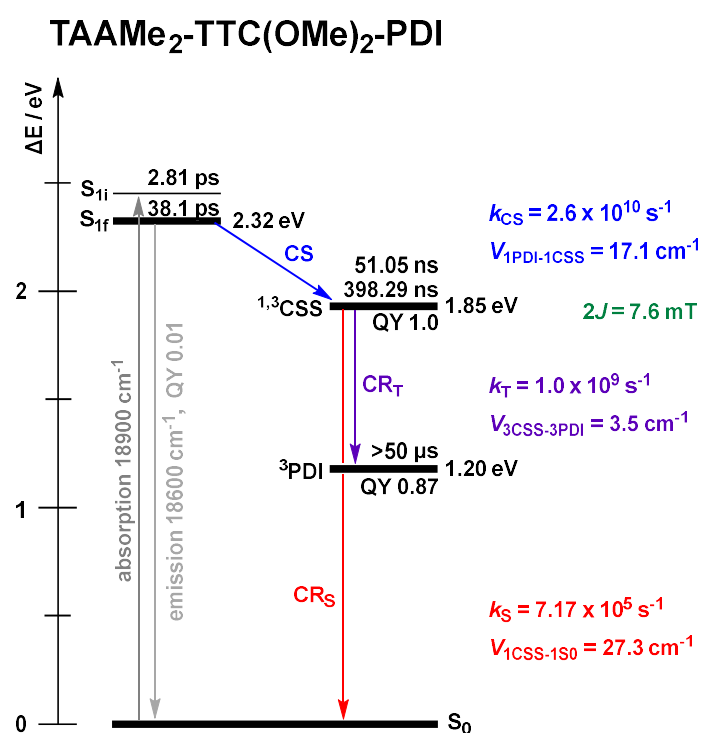
**Figure 101:** Progression of the electronic couplings and exchange interaction plotted against the  $1/E_{\text{HOMO}}$  level of the bridging unit.

## 7.2 Discussion

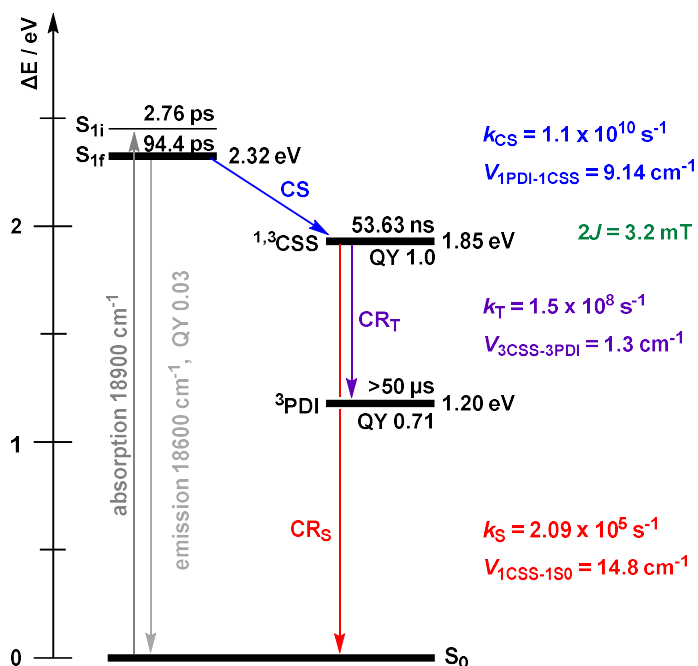
The goal of this chapter was to investigate the influence of varying electron density in the bridging unit on the exchange interaction  $2J$  and thus the electronic coupling between a donor state and an acceptor state. Therefore, a series of molecules consisting of a **TAA** electron donor, a **TTC** bridging unit and a **PDI** electron acceptor was synthesised (**section 3**). The electron density in the **TTC** bridging unit was varied by attaching electron donating groups, such as OMe and Me, and electron withdrawing groups, such as Cl and AZC, in 12,13-position of the triptycene. Thus, the **TTC** bridges of the substituted triptycene triads **TAAMe<sub>2</sub>-TTC(OMe)<sub>2</sub>-PDI**, **TAAMe<sub>2</sub>-TTCMe<sub>2</sub>-PDI**, **TAAMe<sub>2</sub>-TTC-PDI**, **TAAMe<sub>2</sub>-TTCCl<sub>2</sub>-PDI**, and **TAAMe<sub>2</sub>-TTCAZC-PDI** exhibit different HOMO/LUMO energies. In order to evaluate the electronic properties, steady-state absorption spectra of the triads were measured. All triads show spectral features associated with the separate absorption bands of **TAA** and the **PDI** moiety (**section 4.1**). All triads show distinctly diminished fluorescence QYs compared to the pure PDI<sup>[166]</sup> in non-polar toluene. No emission of the **TAA** moiety was observed (**section 4.2**). Those diminished QYs already gave the first indication of a non-radiative quenching mechanism in the triads. The subsequently measured CV data were used to calculate the energies of possible CSSs using the *Weller* approach, which shows that all triads can undergo CS and form a CSS (**section 7.1**). Using those results, the CR dynamics were assigned to the *Marcus* inverted region (**section 7.1.1**).  $CR_T$  shows a much smaller *Gibbs* energy than  $CR_S$  in toluene indicating that the favoured CR pathway in toluene is the triplet pathway. In order to investigate whether the triads actually form the possible CSSs, fs-TA measurements were carried out (**section 7.1.2**). Those measurements show that after light-excitation of the PDI moiety, first a hot (i) PDI  $S_1$  state is populated, which vibrationally relaxes to the cold (f) PDI  $S_1$  state. Afterwards, all triads form a  $^1CSS$  upon depopulation of the  $^1PDI$  state. The respective lifetimes, quantum yields and rate constants  $k_{CS}$  were determined via global exponential fit and global target analysis. Notably, by comparing the QYs of fluorescence and CS, all triads show basically no non-radiative decay besides ET. The CR dynamics upon depopulation of the CSS were investigated using external magnetic field dependent ns-TA spectroscopy (**section 7.1.3**). The ns-TA maps show that all triads recombine via  $CR_T$  pathway populating the local  $^3PDI$  state and provide the respective lifetimes. The QYs of triplet formation were approximately determined using actinometry (**section 10.3.4.2**). The rate determining process upon CR is the spin interconversion from the initially formed  $^1CSS$  to the  $^3CSS$ , which in turn depends on the exchange splitting  $2J$  that, in turn, depends on the electronic coupling between the donor and the acceptor state. To investigate the exchange interaction  $2J$  and the electronic couplings, CSS decays profiles were recorded and the  $2J$  couplings were obtained from the resulting MARY plots. The magnetic field dependent ns-TA data in toluene were furthermore

treated using a quantum mechanical simulation (done by *U. E. Steiner* according to literature<sup>[91]</sup>) to extract the rate constants  $k_T$  and  $k_S$  for  $CR_T$  and  $CR_S$  (**section 7.1.4**). This approach was successful for  $k_T$  but the error margins of  $k_S$  were rather wide. Therefore, the electronic couplings were determined using the theoretical relations between the rate constants and the electronic couplings (**section 7.1.5**). Here, the experimentally determined values of  $2J$  and the calculated values of  $k_{CS}$  and  $k_T$  were used. Subsequently, the rate constant  $k_S$  was calculated based on  $V_{1CSS-1S_0}$  with good accuracy. The results show that singlet couplings and exchange interactions  $2J$  are sensitive to the energy difference  $\Delta E$  between the acceptor state and the virtual bridge state and thus the electron density. Triplet couplings, on the other hand, turned out to be rather independent of the bridge electron density, which indicates a different electron transfer mechanism. Thus, it was proved that the exchange interaction  $2J$  and the singlet couplings between a donor state and an acceptor state are strongly influenced by the variation of the electron density in the bridging unit.

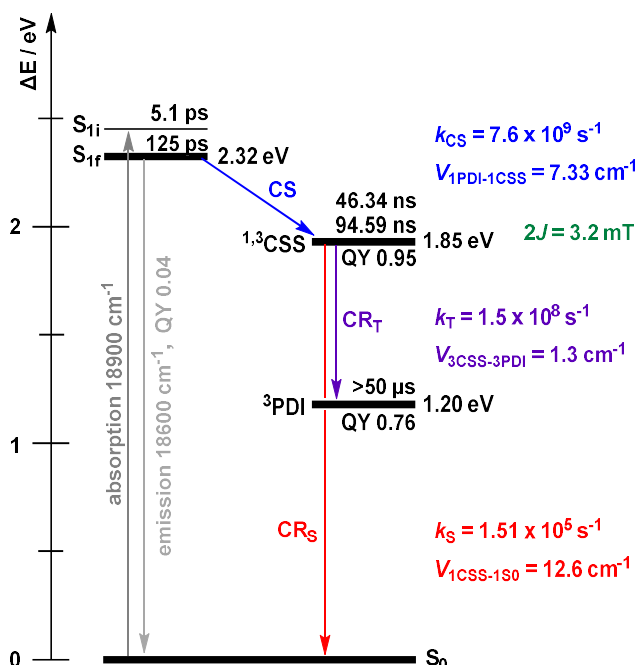
All investigated processes and the associated values are summarised in energy level diagrams for each triad (**Figure 102** to **Figure 106**).



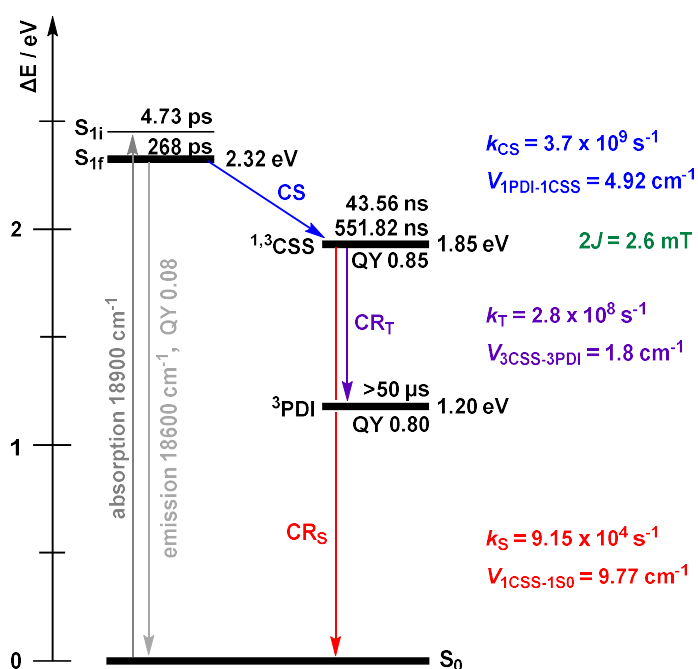
**Figure 102:** Energy level diagram of **TAAMe<sub>2</sub>-TTC(OMe)<sub>2</sub>-PDI** in toluene with all herein investigated states including their lifetimes and rate constants as well as the QYs for the formation of the CSS and the local <sup>3</sup>PDI state. The exchange interaction and electronic couplings are given as well. The energy level of the <sup>3</sup>PDI level is taken from literature.<sup>[188]</sup>

TAAMe<sub>2</sub>-TTCMe<sub>2</sub>-PDI

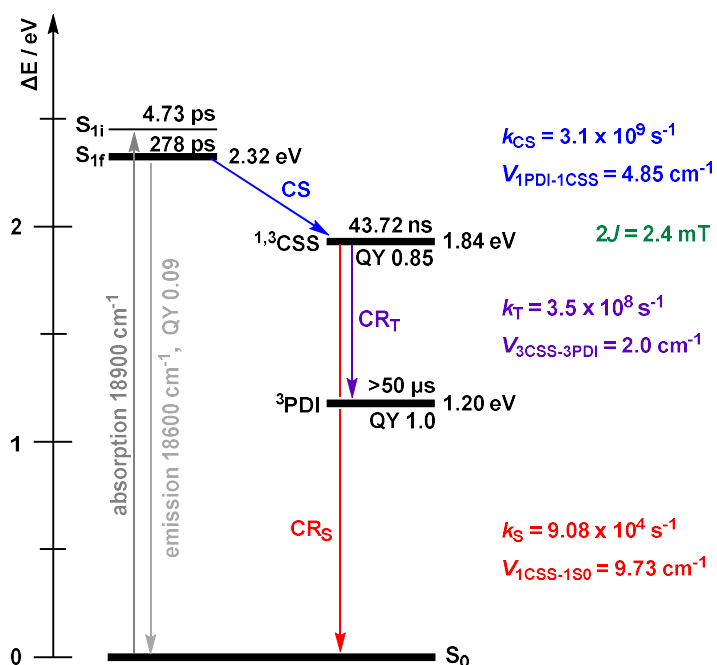
**Figure 103:** Energy level diagram of TAAMe<sub>2</sub>-TTCMe<sub>2</sub>-PDI in toluene with all herein investigated states including its lifetimes and rate constants as well as the QYs for the formation of the CSS and the local  $3\text{PDI}$  state. The exchange interaction and electronic couplings are given as well. The energy level of the  $3\text{PDI}$  level is taken from literature.<sup>[188]</sup>

TAAMe<sub>2</sub>-TTC-PDI

**Figure 104:** Energy level diagram of TAAMe<sub>2</sub>-TTC-PDI in toluene with all herein investigated states including their lifetimes and rate constants as well as the QYs for the formation of the CSS and the local  $3\text{PDI}$  state. The exchange interaction and electronic couplings are given as well. The energy level of the  $3\text{PDI}$  level is taken from literature.<sup>[188]</sup> Adapted from **section 6.2**.

TAAMe<sub>2</sub>-TTCCl<sub>2</sub>-PDI

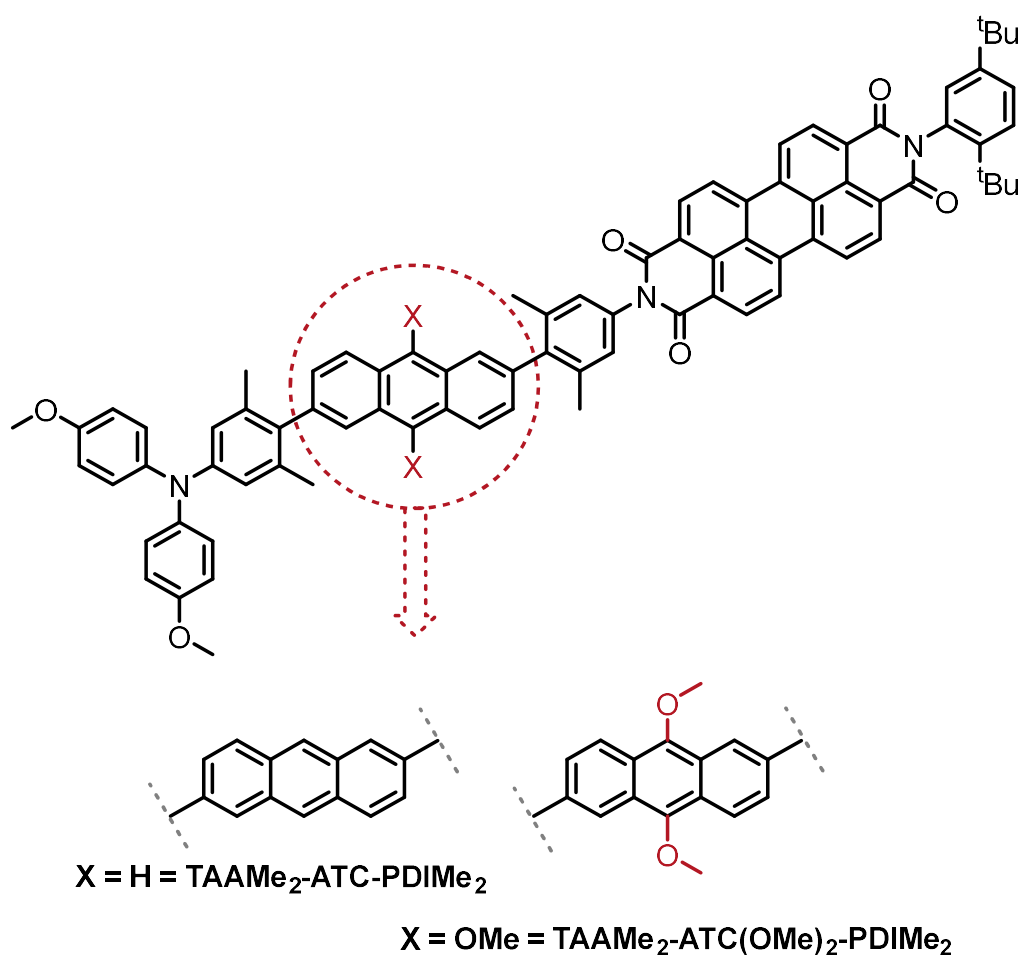
**Figure 105:** Energy level diagram of TAAMe<sub>2</sub>-TTCCl<sub>2</sub>-PDI in toluene with all herein investigated states including their lifetimes and rate constants as well as the QYs for the formation of the CSS and the local <sup>3</sup>PDI state. The exchange interaction and electronic couplings are given as well. The energy level of the <sup>3</sup>PDI level is taken from literature.<sup>[188]</sup>

TAAMe<sub>2</sub>-TTCAZC-PDI

**Figure 106:** Energy level diagram of TAAMe<sub>2</sub>-TTCAZC-PDI in toluene with all herein investigated states including their lifetimes and rate constants as well as the QYs for the formation of the CSS and the local <sup>3</sup>PDI state. The exchange interaction and electronic couplings are given as well. The energy level of the <sup>3</sup>PDI level is taken from literature.<sup>[188]</sup>

## 8 Anthracene bridge triads

In **section 6** the influence of rotational hinderance on the exchange interaction between  $^1\text{CSS}$  and  $^3\text{CSS}$  was shown. In **section 7** the influence of the electron density in the bridging unit, linking donor and acceptor, on the exchange interaction was investigated. Therefore, the rotation in these triads was blocked at the donor moiety, but the acceptor moiety was not hindered in rotation. In both sections a triptycene bridging unit was used. The structure in **section 7** was chosen, because the rotational hindrance of the donor and acceptor leads to a small exchange interaction (as shown in **section 6**), and therefore a reduction of this interaction by electron withdrawing groups would not be observable. Thus, in the following section, the partially non-conjugated triptycene bridge previously investigated was replaced by an anthracene bridge. In order to change the electron density and therefore the exchange interaction this bridging unit was also substituted with an electron donating group (**Figure 107**).



**Figure 107:** Set of investigated anthracene bridge triads.

## 8.1 Electron transfer processes

The steady-state emission spectroscopy data (**section 4.2**) already indicate the existence of an alternative non-radiative quenching mechanism in the two anthracene bridge triads which could be, similar as in the rotationally hindered and in the substituted triptycene triads, an electron transfer process. Thus, in order to investigate if electron transfer processes take place, the energies of the states involved in the ET processes were considered and possible charge recombination pathways assigned to the different *Marcus* regions. The formation of a possible CSS can be predicted on the basis of the electrochemical data (**section 5**) and structure related parameters. The charge separation and the possible formation of a CSS were investigated using TA spectroscopy in the femtosecond time range. CSS formation is observed in both anthracene bridge triads. The CR dynamics out of the CSSs were investigated using ns-TA spectroscopy without an external magnetic field. The decay kinetics were furthermore investigated by the application of an external magnetic field, resulting in decay curves that exhibit a pronounced magnetic field dependence giving information on the exchange interaction  $2J$ .

### 8.1.1 State energies

As described before (**section 6.1.1**), the calculation of the CSS energies gives a first impression whether the formation of a CSS is possible. Therefore, the CSS energies (**Table 36** in **section 10.1**) were calculated using the *Weller* approximation<sup>24</sup> (**equation (24)** in **section 10.1**) and the measured redox potentials (**Table 4** in **section 5**) as well as structure related parameters. Comparing the CSS energies ( $15500\text{ cm}^{-1}$  (1.92 eV), see **Table 36** in **section 10.1**) to the  $^1\text{PDI}$  state energy ( $18800\text{ cm}^{-1}$ , 2.33 eV) shows that all CSS energies are located below the  $^1\text{PDI}$  state energy and therefore a CS into CSSs is possible in both triads. The CSS energies in toluene ( $15500\text{ cm}^{-1}$  (1.92 eV), **Table 36** in **section 10.1**) are higher in energy than the  $^3\text{PDI}$  state and therefore CR via triplet pathway ( $\text{CR}_T$ ) is possible. Furthermore, the anthracene  $^3\text{ATC}/^3\text{ATC}(\text{OMe})_2$  levels ( $14800\text{ cm}^{-1}$  (1.84 eV)<sup>[220-221]</sup> /  $14000\text{ cm}^{-1}$  (1.74 eV)<sup>[222]</sup>) could be accessible for CR as well. In order to determine the efficiency of the possible CR pathways, the CR ET processes were assigned to the *Marcus* regions (**Table 32**) as described above (**section 6.1.1**).

---

<sup>24</sup> Calculated by Dr. M. Holzapfel.



**Table 32:** *Gibbs* energies of the anthracene bridge triads from <sup>1</sup>CSS in S<sub>0</sub> ( $\Delta G_{1\text{CSS-S}_0}$ ) and from <sup>3</sup>CSS in <sup>3</sup>PDI ( $\Delta G_{3\text{CSS-}^3\text{PDI}}$ ) as well as the assignment of the respective transition in the *Marcus* region in toluene.

	$\Delta G_{1\text{PDI-}^1\text{CSS}}$	$\Delta G_{1\text{CSS-S}_0}$	$\Delta G_{1\text{CSS-}^1\text{PDI}}$	<i>Marcus</i> region		
	/ cm <sup>-1</sup> (eV)	/ cm <sup>-1</sup> (eV)	/ cm <sup>-1</sup> (eV)	CS	CR <sub>S</sub>	CR <sub>T</sub>
<b>TAAMe<sub>2</sub>-ATC-PDIME<sub>2</sub></b>	-3314 (-0.41)	-15486 (-1.92)	-5807 (-0.72)	inv.	inv.	inv.
<b>TAAMe<sub>2</sub>-ATC(OMe)<sub>2</sub>- PDIME<sub>2</sub></b>	-3314 (-0.41)	-15486 (-1.92)	-5807 (-0.72)	inv.	inv.	inv.

$\lambda_{\text{v}} = 1855 \text{ cm}^{-1}$  (0.23 eV),  $\lambda_{\text{tot}} = 484 \text{ cm}^{-1}$  (0.06 eV),  $\lambda_{\text{tot}} = 2340 \text{ cm}^{-1}$  (0.29 eV).

The CS process takes place in the *Marcus* inverted region in both triads because  $\lambda_{\text{tot}} < -(\Delta G^{00})$ . Comparing the overall reorganisation energy in toluene ( $\lambda_{\text{tot}}$ , 2340 cm<sup>-1</sup>, 0.29 eV) to the *Gibbs* energy for the transition from <sup>3</sup>CSS in <sup>3</sup>PDI ( $\Delta G_{3\text{CSS-}^3\text{PDI}}$ , **Table 32**) and from <sup>1</sup>CSS in S<sub>0</sub> ( $\Delta G_{1\text{CSS-S}_0}$ ) places CR<sub>T</sub> as well as CR<sub>S</sub> in the *Marcus* inverted region ( $\lambda_{\text{tot}} > -(\Delta G^{00})$ ) for both anthracene bridge triads. Here, CR<sub>T</sub> (-5800 cm<sup>-1</sup>, -0.72 eV, **Table 32**) shows a much smaller reaction enthalpy than CR<sub>S</sub> (-15500 cm<sup>-1</sup>, -1.92 eV, **Table 32**), indicating that the favoured CR pathway in toluene is the triplet pathway.

## 8.1.2 Charge separation

In the previous section the CSS energies were calculated, and the prediction was made that both anthracene bridge triads should be able to undergo CS and form CSSs. fs-TA spectroscopy was used to investigate whether this assumption can be proven. fs-TA maps were recorded in toluene and a detailed description of the measurement setup and conditions is given in **Section 10.3.4.1**.

### 8.1.2.1 fs-Pump probe spectroscopy

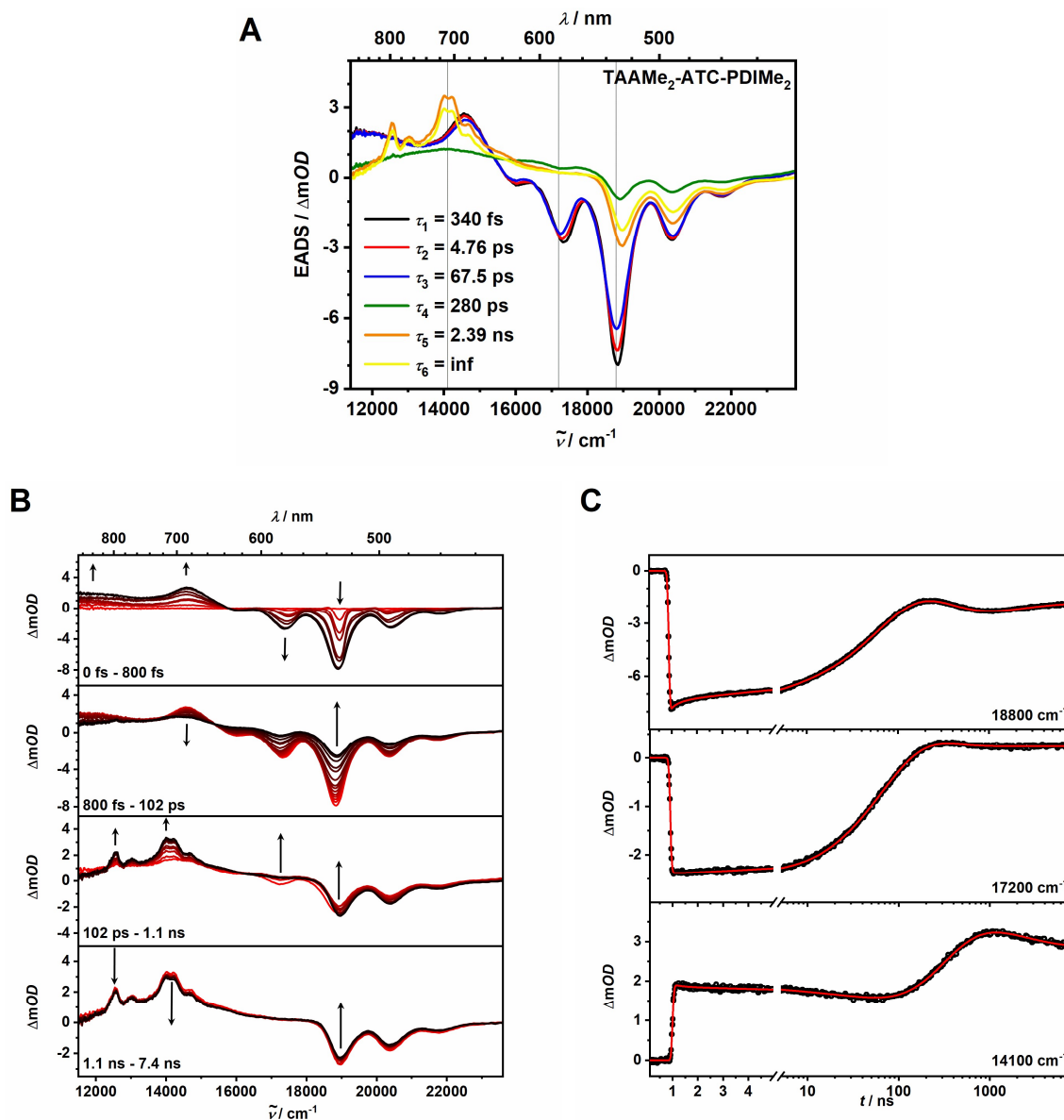
The fs-transient absorption measurements<sup>25</sup> of the triads **TAAMe<sub>2</sub>-ATC-PDIME<sub>2</sub>** and **TAAMe<sub>2</sub>-ATC(OMe)<sub>2</sub>-PDIME<sub>2</sub>** yielded transient maps (see **Figure 108** and **Figure 109 (B)**). By applying a sequential model, the TA maps were analysed by a global exponential fit and the resulting EADS (figures **(A)**) were further interpreted.<sup>26</sup>

The triad **TAAMe<sub>2</sub>-ATC-PDIME<sub>2</sub>** shows six lifetime components, where  $\tau_1 = 340$  fs and  $\tau_2 = 4.76$  ps reflect to the relaxation from the hot to the cold <sup>1</sup>PDI state.  $\tau_3 = 67.5$  ps could reflect a CS process to a CT state, in which the **PDI** is reduced and the anthracene bridge is oxidised. The ESA of ATC<sup>•+</sup> is located around 14100 cm<sup>-1</sup> (710 nm),<sup>[223]</sup> therefore, the EADS associated with  $\tau_4 = 280$  ps could reflect this CT state. The disappearance of the SE band at 17200 cm<sup>-1</sup> (581 nm) as well as the ESA bands at 12600 cm<sup>-1</sup> (794 nm), 13000 cm<sup>-1</sup> (769 nm) and a double peak at 14100 cm<sup>-1</sup> (710 nm) prove the formation of a CSS within  $\tau_4 = 280$  ps. The diminished intensity but structurally similar lifetime components  $\tau_5$  and  $\tau_6$  indicate a spin chemical evolution within the RP.

---

<sup>25</sup> Measurements done by A. Schmiedel.

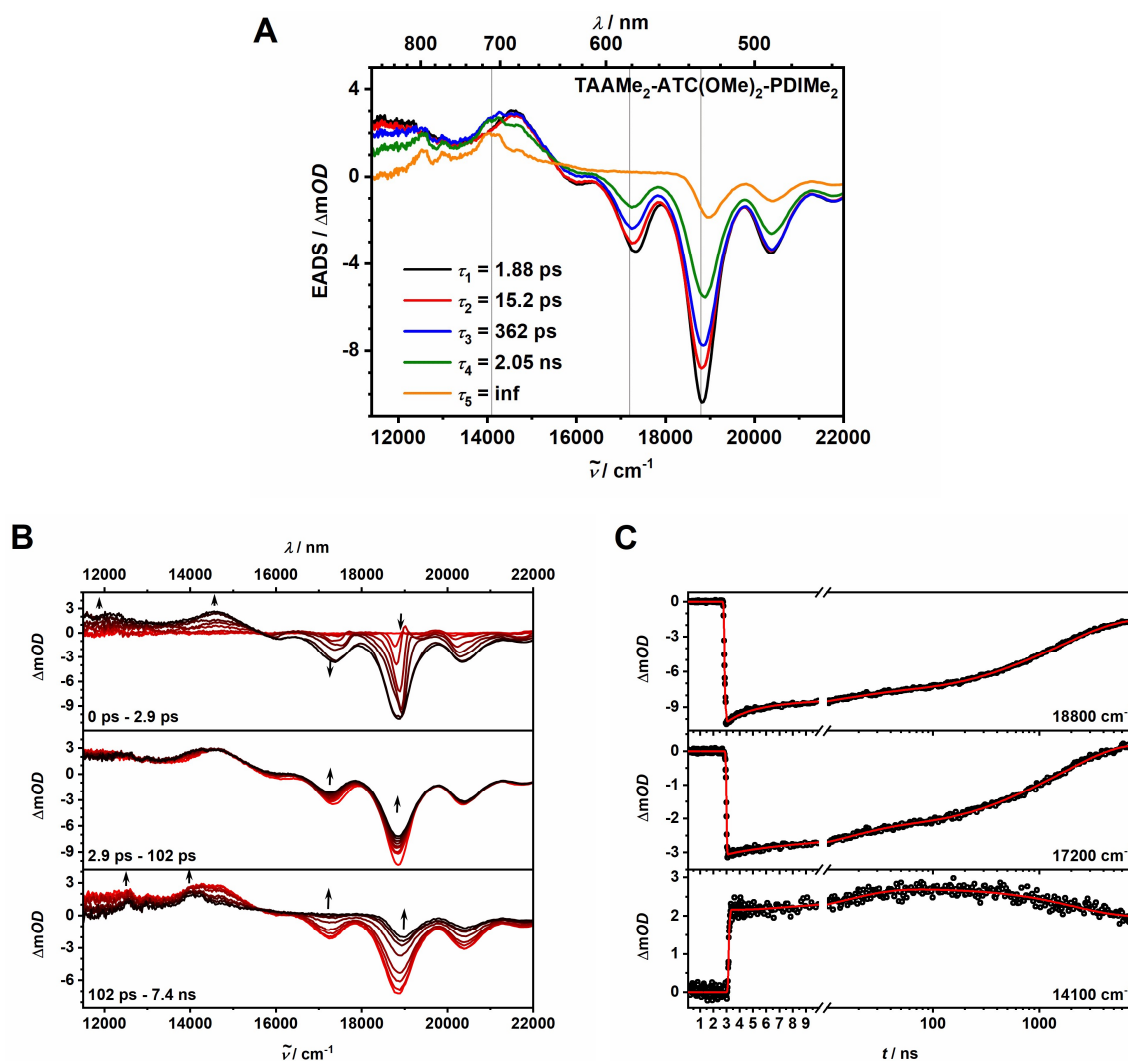
<sup>26</sup> Global exponential fit was performed by Dr. M. Holzapfel.



**Figure 108:** Chirp corrected fs-TA spectra of **TAAMe<sub>2</sub>-ATC-PDI Me<sub>2</sub>** in toluene after light-excitation at 18900 cm<sup>-1</sup> (528 nm) at 298 K. **A:** EADS **B:** selected TA-spectra from the fs-TA measurements (short times to long times depicted from red to black) **C:** selected time traces at different wavenumbers (grey lines in **A**) with their respective global fits.

In **TAAMe<sub>2</sub>-ATC(OMe)<sub>2</sub>-PDIMe<sub>2</sub>** the EADS associated with the lifetime components  $\tau_1 = 1.88$  ps,  $\tau_2 = 15.2$  ps and  $\tau_3 = 362$  ps and  $\tau_4 = 2.05$  ns are spectrally similar and  $\tau_1$ - $\tau_3$  refer to the relaxation process from the hot to the cold <sup>1</sup>PDI state.  $\tau_4$  shows the ESA at 12600 cm<sup>-1</sup> (794 nm), but still exhibits a SE signal at 17200 cm<sup>-1</sup> (581 nm).  $\tau_4 = 2.05$  ns refers to the CS process to the CSS.  $\tau_5$  shows ESA bands at 12600 cm<sup>-1</sup> (794 nm), 13000 cm<sup>-1</sup> (769 nm) and a double peak at 14100 cm<sup>-1</sup> (710 nm) indicating the formation of the CSS. This triad shows no ESA associated with the formation of a CT state, in which the **PDI** is reduced and the **ATC(OMe)<sub>2</sub>** bridging unit is oxidised as in the anthracene triad. The oxidation of the methoxy substituted anthracene is, however, easier than the oxidation of the anthracene due to its low

oxidation potential of 621 mV (see **section 5**). Thus, it is possible that this CT state is too short living to be recorded.

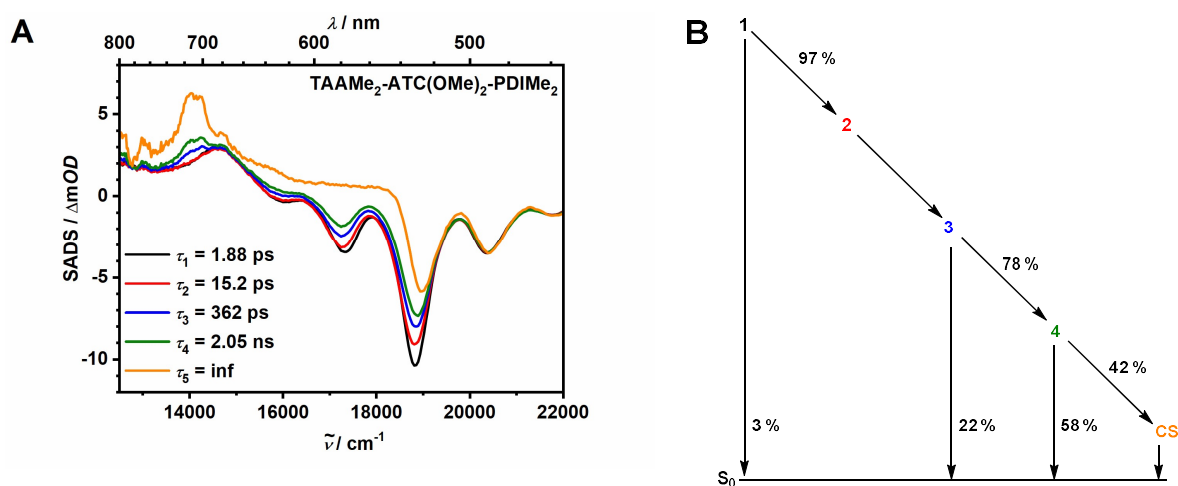


**Figure 109:** Chirp corrected fs-TA spectra of TAAMe<sub>2</sub>-ATC(OMe)<sub>2</sub>-PDIME<sub>2</sub> in toluene after light-excitation at 18900 cm<sup>-1</sup> (528 nm) at 298 K. **A:** EADS **B:** selected TA-spectra from the fs-TA measurements (short times to long times depicted from red to black) **C:** selected time traces at different wavenumbers (grey lines in **A**) with their respective global fits.

### 8.1.2.2 Global target analysis

The rate constants  $k_{CS}$  as well as the efficiencies for the CS processes (**Figure 110** and **Table 33**) were determined as previously described (**section 6.1.2.2**) because the anthracene bridge triads undergo the same processes as the rotationally hindered triads. Therefore, the same kinetic model was applied.<sup>27</sup>

The analysis of the series of the anthracene bridge triads shows that the application the global target analysis was only possible for **TAAMe<sub>2</sub>-ATC(OMe)<sub>2</sub>-PDIMe<sub>2</sub>** but not for **TAAMe<sub>2</sub>-ATC-PDIMe<sub>2</sub>**. This is the case because the assumption that all SADS spectra with exception of the <sup>3</sup>PDI spectra match at 20400 cm<sup>-1</sup> (490 nm) does not hold true for the latter. CS in **TAAMe<sub>2</sub>-ATC(OMe)<sub>2</sub>-PDIMe<sub>2</sub>** occurs with a rate of  $k_{CS} = 2.2 \cdot 10^9 \text{ s}^{-1}$  with an efficiency of 0.76.



**Figure 110:** **A:** SADS. **B:** Kinetic model used to apply a global target analysis to the transient map of **TAAMe<sub>2</sub>-ATC(OMe)<sub>2</sub>-PDIMe<sub>2</sub>** under the assumption that all SADS spectra match at 20400 cm<sup>-1</sup> (490 nm) and no <sup>3</sup>PDI formation is visible in  $\tau_5$ . The coloured numbers in **B** represent the respective SADS in **A**.

**Table 33:** Lifetimes  $\tau_{S1}$  of the relaxed S<sub>1</sub> PDI state, quantum yields of the CSS and rate constant of charge separation  $k_{CS}$  in toluene for the triads **TAAMe<sub>2</sub>-ATC-PDIMe<sub>2</sub>** and **TAAMe<sub>2</sub>-ATC(OMe)<sub>2</sub>-PDIMe<sub>2</sub>**.

	$\tau_{S1} / \text{ns}^a$	$\Phi_{CS}^b$	$k_{CS} / \text{s}^{-1}^c$
<b>TAAMe<sub>2</sub>-ATC-PDIMe<sub>2</sub></b>	-	-	-
<b>TAAMe<sub>2</sub>-ATC(OMe)<sub>2</sub>-PDIMe<sub>2</sub></b>	2.05	0.32	$2.0 \cdot 10^8$

<sup>a</sup> from the fs-TA measurements. <sup>b</sup> quantum yield of CS determined by global target analysis. <sup>c</sup> rate constant for CS from the global target analysis of the fs-TA maps.

<sup>27</sup> Global target analysis was done by Dr. M. Holzapfel.

### 8.1.3 Charge recombination

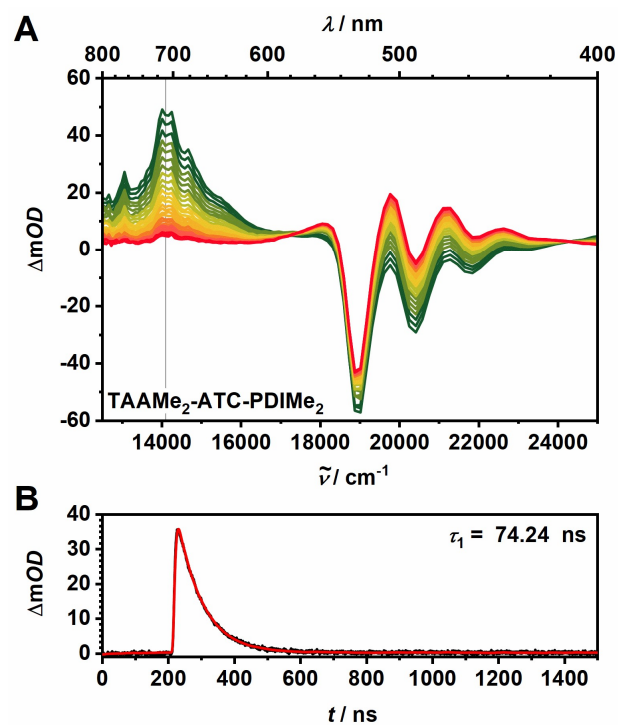
In the previous sections it was shown that both anthracene bridge triads form CSSs upon excitation of the **PDI** moiety. The CS dynamics were investigated using fs-TA. In this section, the kinetics of the CR processes upon depopulation of the CSS were investigated using magnetic field dependent ns-TA spectroscopy. A detailed description of the laser setup and the measurement conditions is given in **section 10.3.4.2**. First, the ns-TA experiments at zero field (**section 8.1.3.1**) and thereafter the ns-TA experiments with the application of an external magnetic field (**section 8.1.3.2**) are discussed.

#### 8.1.3.1 Charge recombination at zero field

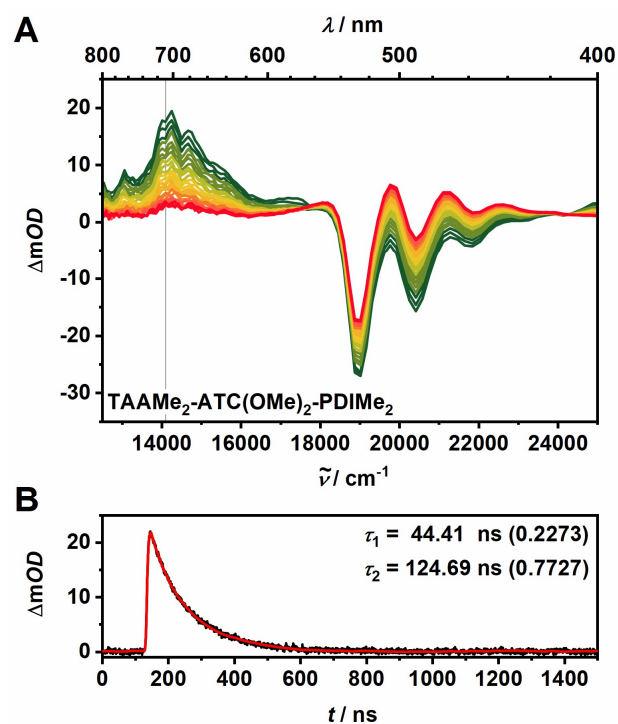
To observe the kinetics of CR, ns-TA maps (figures **(A)**) for the triads **TAAMe<sub>2</sub>-ATC-PDIME<sub>2</sub>** (**Figure 111**) and **TAAMe<sub>2</sub>-ATC(OMe)<sub>2</sub>-PDIME<sub>2</sub>** (**Figure 112**) were measured after light-excitation of the **PDI** moiety in toluene. The resulting ns-TA maps both show the same spectral behaviour. At early times both show the GSB of the **PDI** above 18900 cm<sup>-1</sup> (528 nm) as well as an ESA at 14100 cm<sup>-1</sup> (710 nm). The latter is related to the formation of the charge separated state, which is in very good agreement with the fs-TA data (**section 8.1.2**). The charge separation process observed in the fs-TA data is, however, not visible in the ns-TA measurements because it is faster than the shortest time step of the ns-TA measurements. The fs-TA measurements show that after light-excitation the <sup>1</sup>PDI state is formed, which is subsequently reduced by an electron from the **TAA** leading to the formation of the <sup>1</sup>CSS (**Figure 108** and **Figure 109** in **section 8.1.2**), which may undergo spin interconversion to the <sup>3</sup>CSS. Charge recombination of the <sup>1</sup>CSS directly leads to the singlet ground state, which is forbidden for the <sup>3</sup>CSS. In contrast, the <sup>3</sup>CSS recombines to the local <sup>3</sup>PDI state ( $\Delta G_{3\text{CSS}-1\text{PDI}} = 5807 \text{ cm}^{-1}$ , see **Table 32** in **section 8.1.1**), which is clearly observable in the ns-TA data because at later times a broad, structured ESA between 18300 cm<sup>-1</sup> (546 nm) and 22500 cm<sup>-1</sup> (444 nm) overlaid with the GSB of the **PDI** develops. This is in good agreement with similar triads in literature.<sup>[48, 94, 160]</sup> The recombination to the triplet anthracene states <sup>3</sup>ATC/<sup>3</sup>ATC(OMe)<sub>2</sub> (14800 cm<sup>-1</sup> (1.84 eV)<sup>[220-221]</sup> / 14000 cm<sup>-1</sup> (1.74 eV)<sup>[222]</sup>) would be possible as well, but is not visible in the ns-TA maps.

To determine the lifetime of the charge separated state, decay curves without an external magnetic field were measured and the decay times were extracted using a deconvolution fit (figures **(B)** in **Figure 111** and **Figure 112**) (description in **section 10.3.4.2**). The CSS decay times increase in from **TAAMe<sub>2</sub>-ATC-PDIME<sub>2</sub>** (74.24 ns) to **TAAMe<sub>2</sub>-ATC(OMe)<sub>2</sub>-PDIME<sub>2</sub>**

(44.41 ns (0.2273), 124.69 ns (0.7727)) thus, with increasing electron density in the bridging anthracene unit the lifetime of the CSS increases.



**Figure 111:** **A:** ns-TA spectra of TAAMe<sub>2</sub>-ATC-PDIME<sub>2</sub> in toluene at 293 K after light-excitation at 18900 cm<sup>-1</sup>(528 nm). Early spectra are given in dark green, late spectra in red and the time steps between the spectra are 7 ns. **B:** CSS decay curve (black) with the corresponding deconvolution fit (red) at 14100 cm<sup>-1</sup> (grey line in **A**).



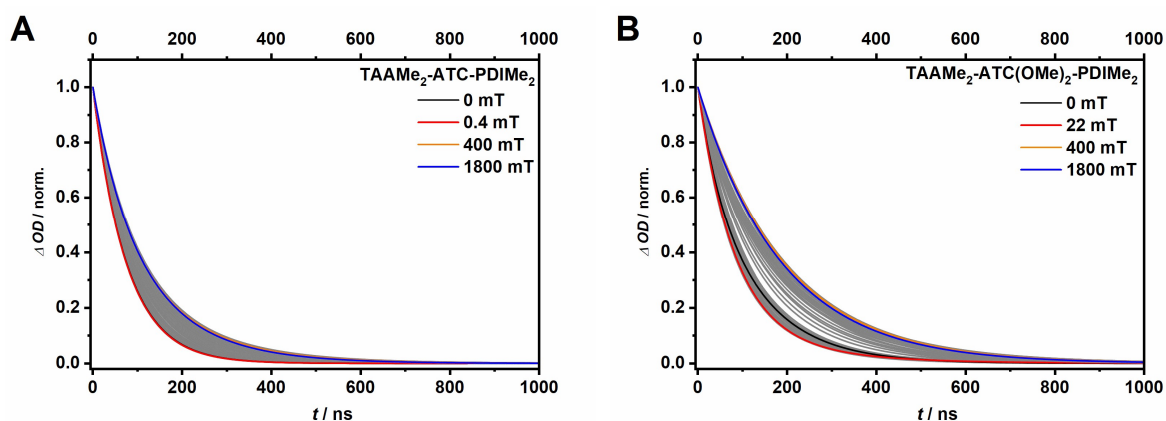
**Figure 112 A:** ns-TA spectra of TAAMe<sub>2</sub>-ATC(OMe)<sub>2</sub>-PDIME<sub>2</sub> in toluene at 293 K after light-excitation at 18900 cm<sup>-1</sup>(528 nm). Early spectra are given in dark green, late spectra in red and the time steps between the spectra are 7 ns. **B:** CSS decay curve (black) with the corresponding deconvolution fit (red) at 14100 cm<sup>-1</sup> (grey line in A).



### 8.1.3.2 Magnetic field effect

The formation of CSS was proved in the previous sections for both anthracene bridge triads using fs- and ns-TA spectroscopy (**section 8.1.1** and **8.1.3.1**). The fs-TA measurements show that after light-excitation of the **PDI** moiety, the  $^1\text{PDI}$  state is populated, from which the  $^1\text{CSS}$  is populated. The formation of a local  $^3\text{PDI}$  state is observed in the ns-TA maps (**section 8.1.3.1**) in toluene, which indicates a spin evolution between the  $^1\text{CSS}$  and the  $^3\text{CSS}$ . This spin evolution as well as the exchange interaction  $2J$ , can be investigated in detail using varying external magnetic fields (**section 1.1**). The detailed CR kinetics of the triads **TAAMe<sub>2</sub>-ATC-PDIME<sub>2</sub>** and **TAAMe<sub>2</sub>-ATC(OMe)<sub>2</sub>-PDIME<sub>2</sub>** were investigated by measuring ns-TA at  $14100\text{ cm}^{-1}$  (710 nm) (setup and analysis details in **section 10.3.4.2**) with applying magnetic fields between 0 and 1800 mT in about 90 steps (exact values and lifetimes in **Appendix**). The initial period of signals was corrected by deconvolution with the IRF.

The CSS decay curves of the triads **TAAMe<sub>2</sub>-ATC-PDIME<sub>2</sub>** and **TAAMe<sub>2</sub>-ATC(OMe)<sub>2</sub>-PDIME<sub>2</sub>** (**Figure 113**) all show a pronounced magnetic field effect. The decay times decrease at low fields until they reach a minimum (from black to red, **Table 34**), then subsequently increase significantly until they reach a magnetic field of about 400 mT (orange). Thereafter, a slight decrease of the decay times  $\tau$  upon increasing external magnetic field from 400 mT to 1800 mT (blue) is visible (**Table 34**). The lifetimes of the decays at zero magnetic field increase with increasing electron density in the bridging unit from **TAAMe<sub>2</sub>-ATC-PDIME<sub>2</sub>** to **TAAMe<sub>2</sub>-ATC(OMe)<sub>2</sub>-PDIME<sub>2</sub>** (black in **Figure 113** and **Table 34**). The lifetimes of the red curves, which represents the external magnetic field of each triad corresponding to the exchange interaction  $2J$  (**Figure 113** and **Table 34**), are increasing with increasing electron density in the bridging unit from **TAAMe<sub>2</sub>-ATC-PDIME<sub>2</sub>** to **TAAMe<sub>2</sub>-ATC(OMe)<sub>2</sub>-PDIME<sub>2</sub>** as well. The lifetimes at higher fields significantly exceed the lifetimes at zero magnetic field.



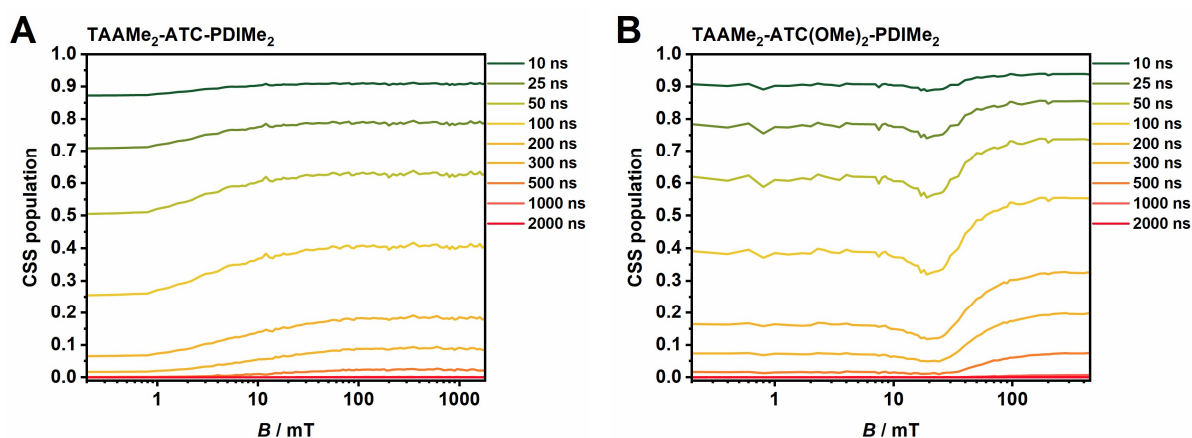
**Figure 113:** Deconvolution fit of the experimental transient decay curves of **A: TAAMe<sub>2</sub>-ATC-PDIME<sub>2</sub>** **B: TAAMe<sub>2</sub>-ATC(OMe)<sub>2</sub>-PDIME<sub>2</sub>** at 14100 cm<sup>-1</sup> (710 nm) after light-excitation at 18900 cm<sup>-1</sup> (528 nm) in toluene at 298 K. The magnetic field was varied from 0 to 1800 mT in about 90 steps. All curves are depicted in grey and only the significant turning points of the MFE are highlighted. The highlighted curves describe the external magnetic fields: black = 0 mT, red = 2J, hereby the curves not always represent the exact calculated 2J values but correspond to the curves closest to the exact value. Orange = 400 mT, blue = 1800 mT.

**Table 34:** Selected CSS lifetimes  $\tau$  and the corresponding amplitudes  $a$  of the two anthracene bridge triads in toluene obtained by using a deconvolution fit on the ns-TA decay curves. The magnetic fields given correspond to the highlighted curves in **Figure 113**.

	external magnetic field	$\tau_1$ / ns	$a_1$	$\tau_2$ / ns	$a_2$
<b>TAAMe<sub>2</sub>-ATC-PDIME<sub>2</sub></b>	0 mT	74.24	-	-	-
	0.4 mT	73.70	-	-	-
	400 mT	72.63	0.4444	156.79	0.5556
	1800 mT	73.38	0.4048	147.16	0.5952
<b>TAAMe<sub>2</sub>-ATC(OMe)<sub>2</sub>-PDIME<sub>2</sub></b>	0 mT	44.41	0.2273	124.69	0.7727
	22 mT	78.78	0.8571	201.70	0.1429
	400 mT	82.02	0.2069	210.00	0.7931
	1800 mT	185.46	-	-	-

The MARY plot of **TAAMe<sub>2</sub>-ATC(OMe)<sub>2</sub>-PDIME<sub>2</sub>** (**Figure 114**) shows the aforementioned resonance peak and therefore the exchange interaction  $2J$  can directly be determined from this representation. In order to get a precise value, the region around the resonance peak at a delay time of 50 ns of **TAAMe<sub>2</sub>-ATC(OMe)<sub>2</sub>-PDIME<sub>2</sub>** was fitted giving the value for  $2J$  (**Table 35**, graph see **Appendix**). Here, the methoxy substituted triad **TAAMe<sub>2</sub>-ATC(OMe)<sub>2</sub>-PDIME<sub>2</sub>** shows a  $2J$  coupling at 20.8 mT. The unsubstituted anthracene triad **TAAMe<sub>2</sub>-ATC-PDIME<sub>2</sub>** shows no  $2J$  coupling. The slight decrease in CSS population between 0 and 1 mT can be

caused by the LFE, where the degeneracy of the triplet *Zeeman* levels is lifted at low magnetic fields, which makes the outer levels accessible and causes a slight increase in the CR rate constants (see section 1.1.2.1).<sup>[224]</sup> The ns-TA measurements show that the influence of the methoxy groups in **TAAMe<sub>2</sub>-ATC-PDIME<sub>2</sub>** is very strong. The impact of changing electron density in the bridging unit is much stronger in the anthracene bridge triads compared to the substituted triptycene triads (section 7.1.3.2). This can be explained by different conjugations in the **TTC** than in the **ATC** bridge. **TTC** is not fully conjugated and thus, the impact of electron withdrawing and donating groups at this unit shows less impact than in the fully conjugated **ATC** moiety.



**Figure 114:** MARY plots of **A: TAAMe<sub>2</sub>-ATC-PDIME<sub>2</sub>** and **B: TAAMe<sub>2</sub>-ATC(OMe)<sub>2</sub>-PDIME<sub>2</sub>** in toluene at 298 K.

**Table 35:**  $2J$  values of the anthracene bridge triads in toluene at 298 K determined by fitting the  $2J$  region at a delay time of 50 ns of each triad using a parabolic fit function.

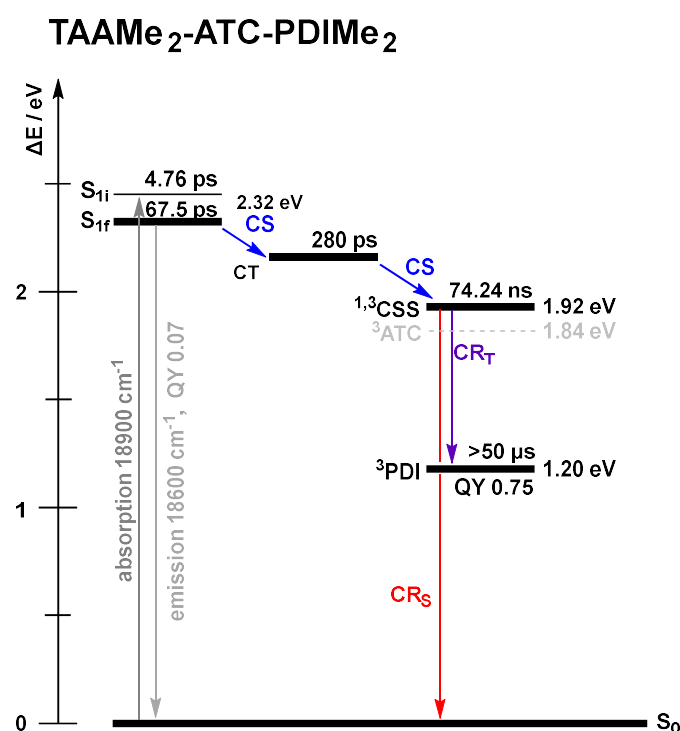
	$2J / \text{mT}$
<b>TAAMe<sub>2</sub>-ATC-PDIME<sub>2</sub></b>	-
<b>TAAMe<sub>2</sub>-ATC(OMe)<sub>2</sub>-PDIME<sub>2</sub></b>	20.8

## 8.2 Discussion

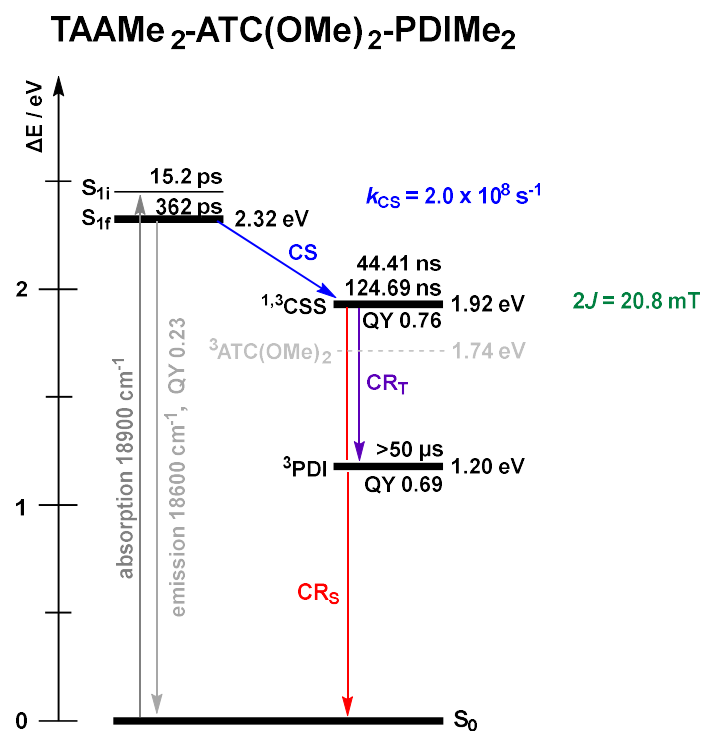
The goal of this chapter was to investigate the influence of varying electron density in the connecting bridge moiety, combined with full rotational hindrance, on the exchange interaction  $2J$  and thus the electronic coupling between an electron donor state and an electron acceptor state. To this end, a set of molecules consisting of a **TAA** electron donor, an **ATC** bridging unit and a **PDI** electron acceptor was synthesised (**section 3**). The electron density in the **ATC** bridging unit was varied by attaching electron donating OMe groups in 9,10-position. The dihedral angle between the **TAA** and the **ATC** as well as between the **ATC** and the **PDI** was restricted by attaching *ortho*-methyl groups at the phenylene linkers at the connecting ends to the **ATC** bridge, which resulted in a twist around the linking single bond, minimising the  $\pi$ -overlap. Thus, the **ATC** bridges of the anthracene bridge triads **TAAMe<sub>2</sub>-ATC-PDIME<sub>2</sub>** and **TAAMe<sub>2</sub>-ATC(OMe)<sub>2</sub>-PDIME<sub>2</sub>** exhibit different HOMO/LUMO energies and the rotation in both triads is fully restricted. In order to evaluate the electronic properties, steady-state absorption spectra of the triads were measured. Both triads show spectral features associated with the separate absorption bands of **TAA**, the bridge and the **PDI** moiety (**section 4.1**). The triads show distinctly diminished fluorescence QYs compared to the pure PDI<sup>[166]</sup> in non-polar toluene. No emission of the **TAA** or the **ATC** moiety was observed (**section 4.2**). Those diminished QYs already give the first indication of a non-radiative quenching mechanism. The subsequently measured CV data (**section 5**) were used to calculate the energies of possible CSSs using the *Weller* approach, which shows that all triads can undergo CS and form a CSS. Using those results, the CR dynamics were assigned to the different *Marcus* regions placing CR in the *Marcus* inverted region in toluene (**section 8.1.1**). CR<sub>T</sub> shows a much smaller *Gibbs* energy than CR<sub>S</sub> in toluene indicating that the favoured CR pathway in toluene is the triplet pathway. In order to investigate whether the triads actually form CSSs, fs-TA measurements were carried out (**section 8.1.2**). Those measurements show that after light-excitation of the **PDI** moiety, first a hot (i) PDI S<sub>1</sub> state is populated, which vibrationally relaxes to the cold (f) PDI S<sub>1</sub> state. Afterwards, all triads form a <sup>1</sup>CSS upon depopulation of the <sup>1</sup>PDI state. The respective lifetimes, quantum yields and rate constants  $k_{CS}$  were determined via global exponential fit and global target analysis for **TAAMe<sub>2</sub>-ATC(OMe)<sub>2</sub>-PDIME<sub>2</sub>**. The quantum yields and rate constants  $k_{CS}$  could not be determined for **TAAMe<sub>2</sub>-ATC-PDIME<sub>2</sub>**. The following CR dynamics upon depopulation of the CSSs were investigated by external magnetic field dependent ns-TA spectroscopy (**section 8.1.3**). The ns-TA maps show that both triads recombine via CR<sub>T</sub> pathway populating the local <sup>3</sup>PDI state and provided the respective lifetimes. The QYs of triplet formation were approximately determined using actinometry (**section 10.3.4.2**). It can therefore be shown that the rate determining process upon CR is the spin interconversion from the initially formed <sup>1</sup>CSS to the <sup>3</sup>CSS, which is dependent on the

exchange splitting  $2J$ , that in turn, depends on the electronic coupling between the donor state and the acceptor state. To investigate the exchange interaction  $2J$ , CSS decay profiles were recorded and the  $2J$  couplings were obtained from the resulting MARY plots. The exchange interaction  $2J$  is strongly influenced by the electron density in the anthracene bridge and increases with increasing electron density. The influence of varying bridge energies in the **ATC** bridged triads is much stronger than in the **TTC** bridged triads.

All investigated processes and the associated values are summarised in energy level diagrams for each triad (**Figure 115** and **Figure 116**).



**Figure 115:** Energy level diagram of **TAAMe<sub>2</sub>-ATC-PDIME<sub>2</sub>** in toluene with all herein investigated states including their lifetimes as well as the QY for the formation the local <sup>3</sup>PDI state. The exchange interaction is given as well. The energy level of the <sup>3</sup>PDI and the <sup>3</sup>ATC level is taken from literature.<sup>[188, 221]</sup>



**Figure 116:** Energy level diagram of TAAMe<sub>2</sub>-ATC(OMe)<sub>2</sub>-PDIMe<sub>2</sub> in toluene with all herein investigated states including their lifetimes as well as the QYs for the formation of the CSS the local <sup>3</sup>PDI state. The exchange interaction is given as well. The energy level of the <sup>3</sup>PDI and <sup>3</sup>ATC(OMe)<sub>2</sub> level is taken from literature.<sup>[188, 222]</sup>

## 9 Summary

### 9.1 Summary

The goal of this thesis was to investigate the influence of rotational restriction between individual parts and of the varying electron density in the bridging unit of D-B-A systems on the exchange interaction  $2J$ , and thus the electronic coupling between a donor state and an acceptor state. A better understanding of how to influence the underlying spin dynamics in such donor acceptor systems can open up the door to new technologies, such as modern molecular electronics or optoelectronic devices.

Therefore, three series of molecules consisting of a **TAA** electron donor, a **TTC** or **ATC** bridging unit and a **PDI** electron acceptor were studied. To investigate the influence of rotational restriction on  $2J$  and the electronic coupling, a series of four rotationally hindered triads (**chapter 6**) was synthesised. The dihedral angle between the **TAA** and the **TTC** as well as between the **TTC** and the **PDI** was restricted by *ortho*-methyl groups at the phenylene linkers of the connecting ends to the **TTC** bridge, producing a twist around the linking single bond which minimises the  $\pi$ -overlap. The triads exhibit varying numbers of *ortho*-methyl groups and therefore different degrees of rotational restriction. In order to shine light on the influence of varying electron density on  $2J$  and the electronic coupling, a series of four substituted triptycene triads (**chapter 7**) was synthesised. The electron density in the **TTC** bridging unit was varied by electron donating and electron withdrawing groups in 12,13-position of the **TTC** bridging unit and thus varying its HOMO/LUMO energy. The last series of two anthracene bridge triads (**chapter 8**) connected both approaches by restricting the rotation with *ortho*-methyl groups and simultaneously by varying the bridge energies.

In order to obtain the electronic properties, steady-state absorption and emission spectra of all triads were investigated (**chapter 4**). Here, all triads show spectral features associated with the separate absorption bands of **TAA** and the **PDI** moiety. The reduced QYs, compared to the unsubstituted **PDI** acceptor, indicate a non-radiative quenching mechanism in all triads. The CV data (**chapter 5**) were used to calculate the energies of possible CSSs and those results were used to assign the CR dynamics into the different *Marcus* regions. fs-TA measurements reveal that all triads form a CSS upon excitation of the **PDI** moiety. The lifetimes of the involved states and the rate constants were determined by global exponential fits and global target analysis. The CR dynamics upon depopulation of the CSSs were investigated using external magnetic field dependent ns-TA spectroscopy. The ns-TA maps show that all triads recombine via CR<sub>T</sub> pathway populating the local <sup>3</sup>PDI state in toluene and provided the respective lifetimes. The approximate QYs of triplet formation were determined using

actinometry. The magnetic field dependent ns-TA data reveal the exchange interaction  $2J$  between singlet and triplet CSS for each triad. Those magnetic field dependent ns-TA data in toluene were furthermore treated using a quantum mechanical simulation (done by *U.E. Steiner*<sup>[91]</sup>) to extract the rate constants  $k_T$  and  $k_S$  for  $CR_T$  and  $CR_S$ , respectively. However, the error margins of  $k_S$  were rather wide. Finally, the electronic couplings between the donor and the acceptor states were obtained by combining the aforementioned experimental results of the rate constants and applying the *Bixon-Jortner* theoretical description of diabatic ET and *Andersons* perturbative theory of the exchange coupling. Therefore, the experimentally determined values of  $2J$  and the calculated values of  $k_{CS}$  and  $k_T$  were used. The rate constant  $k_S$  was calculated based on the electronic coupling  $V_{1CSS-1S0}$ .

The rotationally hindered triads (**chapter 6**) show a strong influence of the degree of rotational restriction on the lifetimes and rate constants of the CS processes. The rate constants of CS are increasing with increasing rotational freedom. The magnetic field dependent decay data show that the exchange interactions increase with increasing rotational freedom. Based on the CR dynamics, the calculated electronic couplings of the ET processes reflect the same trend along the series. Here, only singlet couplings turned out to be strongly influenced while the triplet couplings are not. Therefore, this series shows that the ET dynamics of donor acceptor systems can strongly be influenced by restricting the rotational freedom.

In the substituted triptycene triads (**chapter 7**), decreasing electron density in the bridging unit causes a decrease of the CS rate constants. The magnetic field dependent decay data show that with decreasing electron density in the bridge the exchange interaction decreases. The CR dynamics-based rate constants and the electronic couplings follow the same trend as the exchange interaction. This series shows that varying the HOMO/LUMO levels of the connecting bridge between donor and acceptor strongly influences the ET processes.

In the anthracene bridge triads (**chapter 8**), the CS process is slow in both triads. The CR was fast in the anthracene triad and is slowed down in the methoxy substituted anthracene bridge triad. The increase of the exchange interaction with increasing electron density in the bridge was more pronounced than in the substituted triptycene triads. Thus, the variation of electron density in the bridge strongly influences the ET processes even though the rotation is restricted.

In this thesis, it was shown that the influence of the rotational hindrance as well as the electron density in a connecting bridge have strong influence on all ET processes and the electronic coupling in donor acceptor systems. These approaches can therefore be used to modify magnetic properties of new materials.



## 9.2 Zusammenfassung

Das Ziel dieser Arbeit war es, den Einfluss von Rotationshinderung zwischen einzelnen Bausteinen und Variation der Elektronendichte in der Brückeneinheit eines Donor-Brücke-Akzeptor-Systems auf die Austauschwechselwirkung  $2J$  und somit die elektronische Kopplung zwischen dem Donor- und dem Akzeptor-Zustand zu untersuchen. Ein besseres Verständnis der zugrundeliegenden Spindynamiken in solchen Donor-Akzeptor-Systemen - und wie diese beeinflusst werden können - kann einen Zugang zu neuen Technologien wie molekularer Elektronik oder optoelektronischen Geräten ermöglichen.

Im Zuge dessen wurden drei Molekülreihen, bestehend aus einem **TAA**-Elektronendonator, einer **TTC**- oder **ATC**-Brücke und einem **PDI**-Elektronenakzeptor, untersucht. Der Einfluss von eingeschränkter Rotation zwischen den einzelnen Bausteinen auf die Austauschwechselwirkung und die elektronische Kopplung wurde anhand einer Reihe von rotationsgehinderten Triaden (**Kapitel 6**) untersucht. Der Winkel zwischen der **TAA**- und der **TTC**-Einheit sowie zwischen der **TTC**- und der **PDI**-Einheit wurde durch *ortho*-ständige Methylgruppen eingeschränkt. Dies führt zu einer Verdrillung um die verbrückende Einfachbindung. Um unterschiedliche Grade der Rotationshinderung zu erzielen, wurden die Triaden mit einer unterschiedlichen Anzahl von *ortho*-Methylgruppen substituiert. Des Weiteren wurde eine Reihe, bestehend aus vier Triptycen substituierten Triaden (**Kapitel 7**), synthetisiert, um den Einfluss variierender Elektronendichte auf  $2J$  und die elektronische Kopplung zu untersuchen. Die Elektronendichte in der **TTC**-Brückeneinheit wurde durch elektronenschiebende und elektronenziehende Gruppen in 12,13-Position an der **TTC**-Brückeneinheit variiert, was eine Änderung der HOMO/LUMO-Energien der Brücke zur Folge hat. Die letzte Reihe besteht aus zwei Anthracen-verbrückten Triaden (**Kapitel 8**) und stellt die Kombination beider Ansätze dar. Um dies zu erzielen wurde die Rotation durch *ortho*-Methylgruppen vollständig unterdrückt und gleichzeitig die Brückenenergie verändert.

Um die elektronischen Eigenschaften der Triaden zu untersuchen, wurden zunächst die stationären Absorptions- und Emissionseigenschaften betrachtet (**Kapitel 4**). Die Absorptionsbanden können in allen Triaden der **TAA**- sowie der **PDI**-Einheit zugeordnet werden. Die Fluoreszenz-Quantenausbeuten weisen, verglichen mit dem reinen **PDI**-Akzeptor, deutlich geringere Werte auf. Dies deutet auf einen alternativen, nicht-strahlenden Desaktivierungspfad hin. Mit Hilfe der CV-Daten (**Kapitel 5**) wurde die Energie des ladungstrennten Zustandes für jede Triade berechnet und die Ladungsrekombinationspfade in die jeweiligen *Marcus*-Regionen eingeordnet. fs-transiente Absorptionsmessungen zeigen, dass alle Triaden einen ladungstrennten Zustand ausbilden. Die Lebenszeiten der beteiligten Zustände wurden mit Hilfe eines globalen

exponentiellen Fits und die Ratenkonstanten mit Hilfe einer globalen Targetanalyse bestimmt. Die Ladungsrekombinationsdynamiken wurden mit Hilfe magnetfeldabhängiger ns-transienter Absorptionsmessungen betrachtet. Die ns-transienten Karten zeigen, dass alle Triaden in Toluol über den Triplett-Rekombinationspfad in den lokalen Triplettzustand des **PDI** rekombinieren. Des Weiteren lieferten diese Messungen die Lebenszeiten des ladungsgetrenten Zustandes. Die Quantenausbeuten der Bildung des Triplettzustandes wurden mittels Actinometrie abgeschätzt. Mit Hilfe der magnetfeldabhängigen ns-transienten Messungen konnte die Austauschwechselwirkung zwischen dem singulett und dem triplett ladungsgetrenten Zustand für jede Triade bestimmt werden. Um die Ratenkonstanten  $k_T$  and  $k_S$  der Triplett- und Singulett-Rekombination zu erhalten, wurden die Daten der magnetfeldabhängigen ns-transienten Messungen mittels einer quantendynamischen Simulation untersucht (durchgeführt von *U. E. Steiner*, Universität Konstanz). Hierbei waren die Fehlergrenzen für  $k_S$  jedoch sehr groß. Die elektronischen Kopplungen wurden mit Hilfe der *Bixon-Jortner* Theorie des diabatischen elektronen Transfers und *Andersons* störungstheoretischem Ansatz zur Beschreibung der Austauschwechselwirkung aus den experimentellen Daten sowie den Ratenkonstanten berechnet. Hierfür wurden die die experimentell bestimmten  $2J$ -Werte sowie die berechneten Werte von  $k_{CS}$  und  $k_T$  verwendet. Um ein umfassendes Bild zu erhalten wurden die Ratenkonstanten  $k_S$  aus den elektronischen Kopplungen  $V_{1CSS-1S0}$  berechnet.

Die rotationsgehinderten Triaden (**Kapitel 6**) weisen eine starke Abhängigkeit der Ratenkonstanten des Ladungstrennungsprozesses vom Grad der Rotationseinschränkung auf. Hierbei steigen die Werte der Ratenkonstanten mit zunehmender Rotationsfreiheit. Der selbe Trend kann in der Austauschwechselwirkung bei Betrachtung der magnetfeldabhängigen Abklingkurven beobachtet werden. Des Weiteren zeigen die berechneten elektronischen Kopplungen ebenfalls eine Zunahme bei gesteigerter Rotationsfreiheit. Hierbei war zu beobachten, dass nur die Singulett-Kopplungen von der Rotation beeinflusst wurden, Triplett-Kopplungen jedoch nahezu unverändert blieben. Mit Hilfe dieser Reihe wurde gezeigt, dass Elektrontransferdynamiken durch Rotationseinschränkung beeinflusst werden können.

In der Reihe der substituierten Triptycenen Triaden (**Kapitel 7**) führt eine Abnahme der Elektronendichte in der Brücke zu einer Verringerung der Ratenkonstanten des Ladungstrennungsprozesses. Die Daten der magnetfeldabhängigen Abklingkurven zeigen, dass die Austauschwechselwirkung ebenfalls mit verringerter Elektronendichte in der Brücke abnimmt. Die berechneten elektronischen Kopplungen folgen dem Trend der Austauschwechselwirkung. Anhand dieser Reihe konnte gezeigt werden, dass Elektrontransferprozesse durch Veränderung der Brückenenergien beeinflusst werden können.

In den Anthracen Brücken Triaden (**Kapitel 8**) ist die Ladungstrennung für beide Triaden langsam. Die Ladungsrekombination wird durch den elektronenschiebenden Effekt der Methoxygruppen, verlangsamt. Die Austauschwechselwirkung nimmt mit steigender Elektronendichte in der Brücke zu, wobei dieser Effekt stärker ausgeprägt ist als in den Triptycenen substituierten Triaden. Die Variation der Elektronendichte hat somit, trotz vollständig gehinderter Rotation, einen starken Einfluss auf die Elektronentransferdynamiken.

In dieser Arbeit konnte gezeigt werden, dass gehinderte Rotation und variierende Elektronendichte in einer Brückeneinheit einen starken Einfluss auf die Elektronentransferdynamiken und die elektronischen Kopplungen in Donor-Akzeptor-Systemen haben. Diese Ansätze können somit dazu verwendet werden die magnetischen Eigenschaften von neuen Materialien zu verändern.

## 10 Experimental section

### 10.1 Charge separated state energies

CSS energies ( $\Delta G^0_{(CS \rightarrow S_0)}$ ) were determined using the *Weller*<sup>[225]</sup> approach (**equation (24)**).

$$\Delta G^0_{(CS \rightarrow S_0)} = \frac{N_A z e}{1000} \cdot [E_{\text{ox}}(D/D^+) - (E_{\text{red}}(A/A^-))] - \frac{N_A z e}{1000} \frac{1}{4\pi\epsilon_0} \cdot \left[ \left( \frac{1}{2r_D} + \frac{1}{2r_A} \right) \left( \frac{1}{\epsilon_r} - \frac{1}{\epsilon_s} \right) + \frac{1}{\epsilon_s d_{DA}} \right] \quad (24)$$

The donor ( $E_{\text{ox}}$ ) and acceptor ( $E_{\text{red}}$ ) redox potentials were measured using cyclic voltammetry.  $N_A$  is the Avogadro constant,  $z$  the number of transferred charges,  $e$  is the elementary charge,  $\epsilon_0$  the vacuum permittivity,  $r_D$  and  $r_A$ , are the radii of the D and the A moiety,  $d_{DA}$  the donor acceptor centre to centre distance between the D and A,  $\epsilon_r$  the permittivity of the solvent used for CV and  $\epsilon_s$  is the permittivity of the solvent in which the free energy needs to be calculated. Conolly molecular surface calculations (ChemBio3D Ultra) were used to obtain the radical radii. The donor acceptor distance was calculated via Gaussian09<sup>[190]</sup> using a hybrid density B3LYP functional with a 6-31G\* basis set. Differences in solvation energies between DCM ( $\epsilon_s = 8.93$ , CV), toluene ( $\epsilon_r = 2.38$ ) and PhCN ( $\epsilon_r = 25.2$ ) were accounted for in the Coulomb term. The CSS energies and the data required for the calculation can be found in **Table 36**.

**Table 36:** Energies of the CSS determined by *Weller*-approach with the required radii. The oxidation and reduction potentials are given in **section 5**.

	$r_D$ / Å	$r_A$ / Å	$d_{DA}$ / Å	$\Delta E_{1,3CSS}$ / cm <sup>-1</sup> (eV)
<b>TAAMe<sub>2</sub>-TTC-PDIME<sub>2</sub></b>	4.81	4.64	22.08	15002 <sup>a</sup> (1.86) 7662 <sup>b</sup> (0.95)
<b>TAAMe<sub>2</sub>-TTC-PDI</b>	4.81	4.64	22.09	14921 <sup>a</sup> (1.85) 7582 <sup>b</sup> (0.94)
<b>TAA-TTC-PDIME<sub>2</sub></b>	4.81	4.64	22.11	15324 <sup>a</sup> (1.90) 7904 <sup>b</sup> (0.98)
<b>TAA-TTC-PDI</b>	4.81	4.64	22.10	15244 <sup>a</sup> (1.89) 7904 <sup>b</sup> (0.98)
<b>TAAMe<sub>2</sub>-TTC(OMe)<sub>2</sub>-PDI</b>	4.81	4.64	22.09	14921 <sup>a</sup> (1.85)
<b>TAAMe<sub>2</sub>-TTCMe<sub>2</sub>-PDI</b>	4.81	4.64	22.08	14921 <sup>a</sup> (1.85)
<b>TAAMe<sub>2</sub>-TTCCl<sub>2</sub>-PDI</b>	4.81	4.64	22.09	14921 <sup>a</sup> (1.85)
<b>TAAMe<sub>2</sub>-TTCAZC-PDI</b>	4.81	4.64	22.22	14841 <sup>a</sup> (1.84)
<b>TAAMe<sub>2</sub>-ATC-PDIME<sub>2</sub></b>	4.81	4.64	24.43	15486 <sup>a</sup> (1.92)
<b>TAAMe<sub>2</sub>-ATC(OMe)<sub>2</sub>-PDIME<sub>2</sub></b>	4.81	4.64	24.43	15486 <sup>a</sup> (1.92)

$\Delta E_{1PDI_{tol}} = 18700 \text{ cm}^{-1}$ [48],  $\Delta E_{1PDI_{PhCN}} = 18600 \text{ cm}^{-1}$ [88],  $\Delta E_{3PDI} = 9679 \text{ cm}^{-1}$ [188]. <sup>a</sup> in toluene. <sup>b</sup> in PhCN.

The internal reorganization energies  $\lambda_v$  for CR (CSS $\rightarrow$ S<sub>0</sub>) were estimated from DFT calculations at B3LYP/6-31G\* level with a NICG (neutral in cation geometry) method (or a respective method for anions).<sup>[226-227]</sup> The outer reorganization energies were estimated using the *Born* model (**equation (25)**).

$$\lambda_o = \frac{e^2}{4\pi\epsilon_0} \left( \frac{1}{2r_D} + \frac{1}{2r_A} - \frac{1}{d_{DA}} \right) \left( \frac{1}{n_D^2} - \frac{1}{\epsilon_S} \right) \quad (25)$$

## 10.2 Classical simulations

It was shown for triads similar to the ones investigated in this thesis, that classical first order rate equations (**equation (10)**) can be used to describe the CR processes qualitatively.<sup>[47-48, 82-83, 92]</sup> Thus, the kinetics of the RPs can be presented in a system of classical linear differential equations, that have to be solved simultaneously because the overall population of CSS combines to the sum of all four spin substates ( $[CSS] = [S] + [T_0] + [T_+] + [T_-]$ ) (**equation (10)**).<sup>[47, 83]</sup>

$$\begin{aligned}
 \frac{d[S]}{dt} &= - (k_S + 2k_{\pm} + k_{ST_0})[S] + k_{ST_0}[T_0] + k_{\pm}([T_+] + [T_-]) \\
 \frac{d[T_0]}{dt} &= k_{ST_0}[S] - (k_T + 2k_{\pm} + k_{ST_0})[T_0] + k_{\pm}([T_+] + [T_-]) \\
 \frac{d[T_+]}{dt} &= k_{\pm}[S] + k_{\pm}[T_0] - (k_T + 2k_{\pm})[T_+] \\
 \frac{d[T_-]}{dt} &= k_{\pm}[S] + k_{\pm}[T_0] - (k_T + 2k_{\pm})[T_-]
 \end{aligned}
 \tag{10}$$

Here, the  $CR_S$  and  $CR_T$  are described by the rate constants  $k_S$  and  $k_T$ , the ZQT by  $k_{ST_0}$ , the  $S \leftrightarrow T_+$  transition by  $k_+$ , the  $S \leftrightarrow T_-$  transition by  $k_-$  and the  $T_0 \leftrightarrow T_+ / T_0 \leftrightarrow T_-$  transition by  $k_{\pm}$ .<sup>[68, 79, 83]</sup> The initial spin population of the singlet and triplet state are  $p_S(0)$  and  $p_T(0)$ , where  $p_S(0) = 1 - p_T(0)$  applies. The initial triplet population is evenly distributed over the three substates  $p_{T_-}(0) = p_{T_0}(0) = p_{T_+}(0) = 1/3 p_T(0)$ .<sup>[79, 83, 89]</sup> As described before (**section 1.1.3** and **1.1.4**) a double *Lorentzian* type equation (**equation (13)**) can be used to describe the spin evolution rate constant. The respective spin evolution rate constants can be described by the effective field  $B_{eff}$  resulting in **equation (16)** for the example of  $k_+$ :  $B_{eff} = 2J - B$ .<sup>[83]</sup> Furthermore, the other rate constants can be expressed as:  $k_-$ :  $B_{eff} = 2J + B$ ,  $k_{\pm}$ :  $B_{eff} = B$ ,  $k_{ST_0}$ :  $B_{eff} = 2J$ .<sup>[79]</sup>

$$k_+ = \frac{k_1}{1 + (B_{eff}/B_1)^2} + \frac{k_2}{1 + (B_{eff}/B_2)^2} + k_0
 \tag{16}$$

Applying this approach, all magnetic field dependent spin flip rate constants can be expressed by the magnetic field independent parameters  $k_S$ ,  $k_T$ ,  $k_1$ ,  $k_2$ ,  $B_1$ ,  $B_2$  and  $k_0$ . The value for the exchange interaction in this equation is taken directly from the MARY plots of the respective triad. A more detailed description is given in the literature.<sup>[88]</sup> This numerically fitting approach using the simulated curves (description in **section 10.3.4.2**) of each triad by applying a MATLAB fitting routine<sup>28</sup> resulted in the values given in **Table 37**.

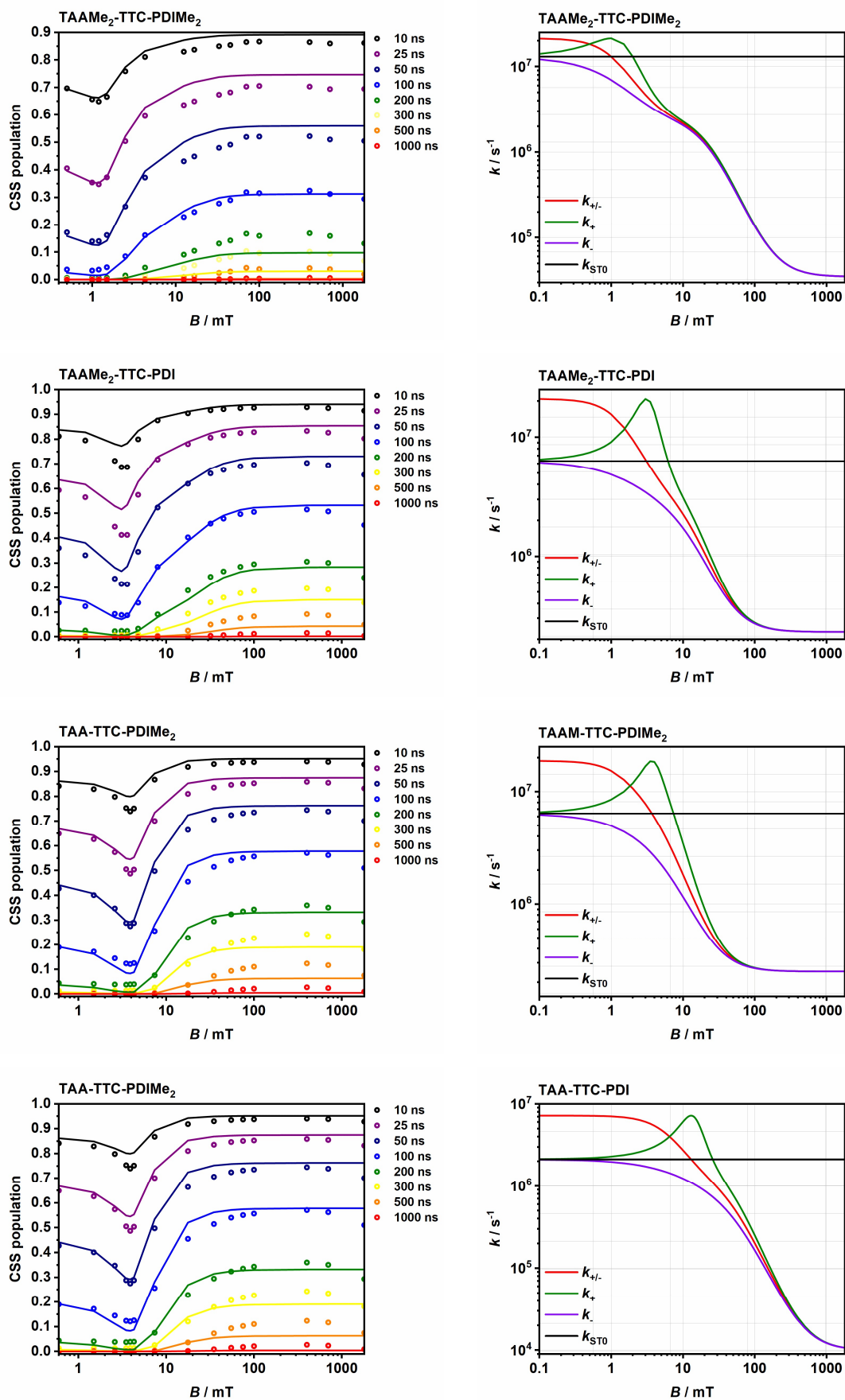
<sup>28</sup> Fitting routine was written by D. Mims.

The obtained values, however, could not describe the CR processes in an accurate way (see **Figure 117**, **Figure 118** and **Figure 119**).

**Table 37:** Magnetic field independent parameters for the CR processes resulting from the classical simulation of all investigated triads using MATLAB.

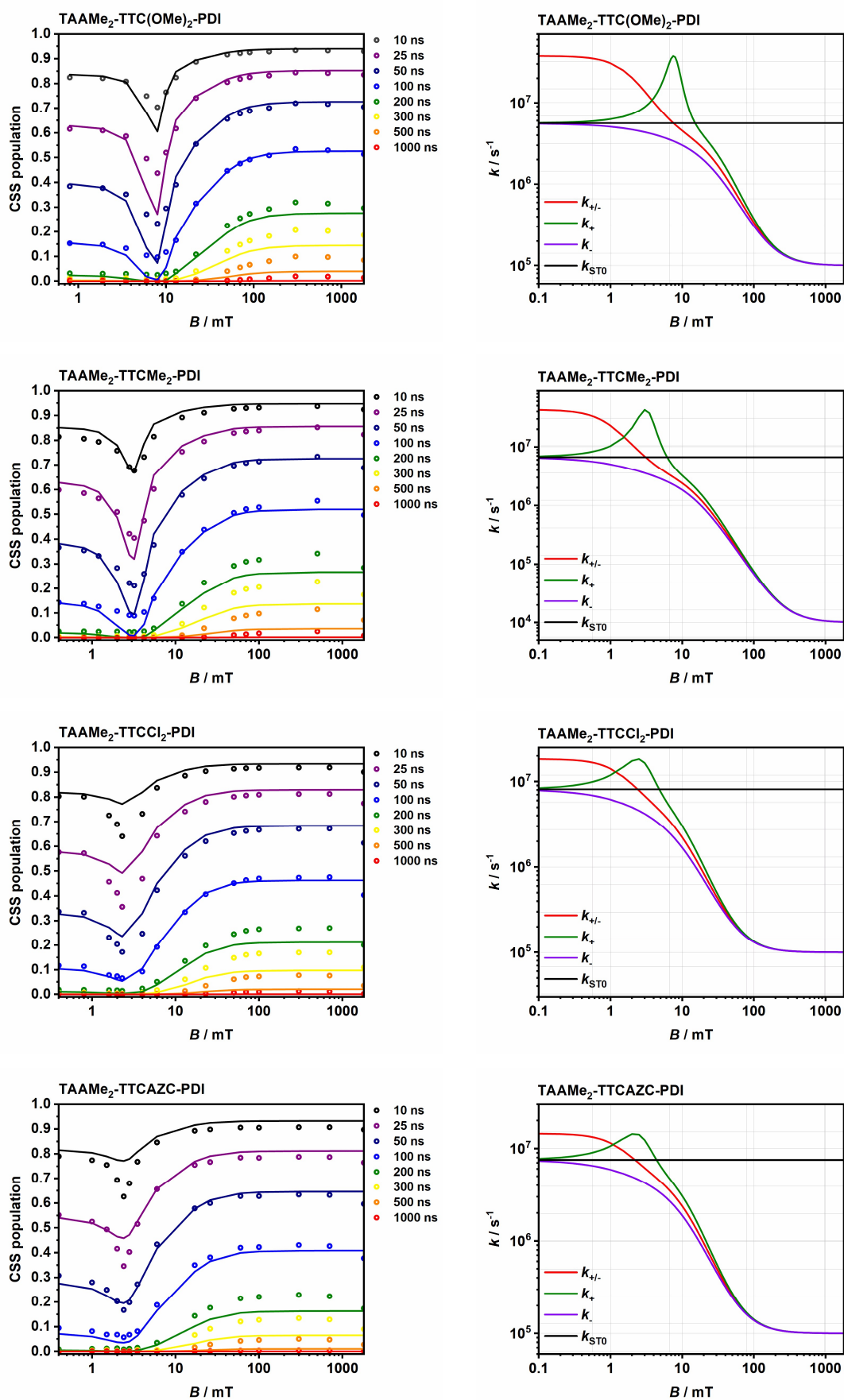
	$k_S$ / s <sup>-1</sup>	$k_T$ / s <sup>-1</sup>	$k_1$ / s <sup>-1</sup>	$k_2$ / s <sup>-1</sup>	$k_{inf}$ / s <sup>-1</sup>	$B_1$ / mT	$B_2$ / mT
<b>TAAMe<sub>2</sub>-TTC-PDIME<sub>2</sub></b> <b>(2J = 1.0 mT)</b>	8.5·10 <sup>5</sup>	8.1·10 <sup>8</sup>	1.9·10 <sup>7</sup>	2.3·10 <sup>6</sup>	3.5·10 <sup>4</sup>	1.14	21.4
<b>TAAMe<sub>2</sub>-TTC-PDI</b> <b>(2J = 3.2 mT)</b>	7.5·10 <sup>5</sup>	4.8·10 <sup>8</sup>	1.8·10 <sup>7</sup>	2.7·10 <sup>6</sup>	2.3·10 <sup>5</sup>	1.53	12.2
<b>TAA-TTC-PDIME<sub>2</sub></b> <b>(2J = 3.9 mT)</b>	9.5·10 <sup>5</sup>	3.3·10 <sup>8</sup>	1.2·10 <sup>7</sup>	6.5·10 <sup>6</sup>	2.5·10 <sup>5</sup>	1.65	4.91
<b>TAA-TTC-PDI</b> <b>(2J = 13.6 mT)</b>	8.0·10 <sup>5</sup>	4.1·10 <sup>8</sup>	6.2·10 <sup>6</sup>	9.9·10 <sup>5</sup>	1.0·10 <sup>4</sup>	6.35	45.0
<b>TAAMe<sub>2</sub>-TTC(OMe)<sub>2</sub>-PDI</b> <b>(2J = 7.6 mT)</b>	5.0·10 <sup>4</sup>	2.0·10 <sup>9</sup>	3.4·10 <sup>7</sup>	3.7·10 <sup>6</sup>	1.0·10 <sup>5</sup>	1.95	25.3
<b>TAAMe<sub>2</sub>-TTCMe<sub>2</sub>-PDI</b> <b>(2J = 3.2 mT)</b>	1.0·10 <sup>5</sup>	5.0·10 <sup>8</sup>	4.0·10 <sup>7</sup>	3.0·10 <sup>6</sup>	1.0·10 <sup>4</sup>	1.00	14.0
<b>TAAMe<sub>2</sub>-TTCCl<sub>2</sub>-PDI</b> <b>(2J = 2.6 mT)</b>	4.0·10 <sup>4</sup>	8.0·10 <sup>8</sup>	1.4·10 <sup>7</sup>	4.3·10 <sup>6</sup>	1.0·10 <sup>5</sup>	1.53	8.50
<b>TAAMe<sub>2</sub>-TTCAZC-PDI</b> <b>(2J = 2.4 mT)</b>	4.0·10 <sup>4</sup>	8.0·10 <sup>8</sup>	1.3·10 <sup>7</sup>	4.4·10 <sup>6</sup>	1.0·10 <sup>5</sup>	1.53	9.35
<b>TAAMe<sub>2</sub>-ATC-PDIME<sub>2</sub><sup>a</sup></b> <b>(2J = 0 mT)</b>	9.0·10 <sup>5</sup>	9.0·10 <sup>8</sup>	4.0·10 <sup>6</sup>	1.5·10 <sup>6</sup>	9.0·10 <sup>5</sup>	0.16	12.9
<b>TAAMe<sub>2</sub>-ATC(OMe)<sub>2</sub>-PDIME<sub>2</sub><sup>a</sup></b> <b>(2J = 20.8 mT)</b>	9.9·10 <sup>5</sup>	1.0·10 <sup>9</sup>	1.6·10 <sup>6</sup>	3.2·10 <sup>6</sup>	8.3·10 <sup>5</sup>	7.47	24.4

<sup>a</sup> due to the strong similarity of the values  $k_1/k_2$  an  $k_{inf}$  there is doubt whether the classical fit is applicable.

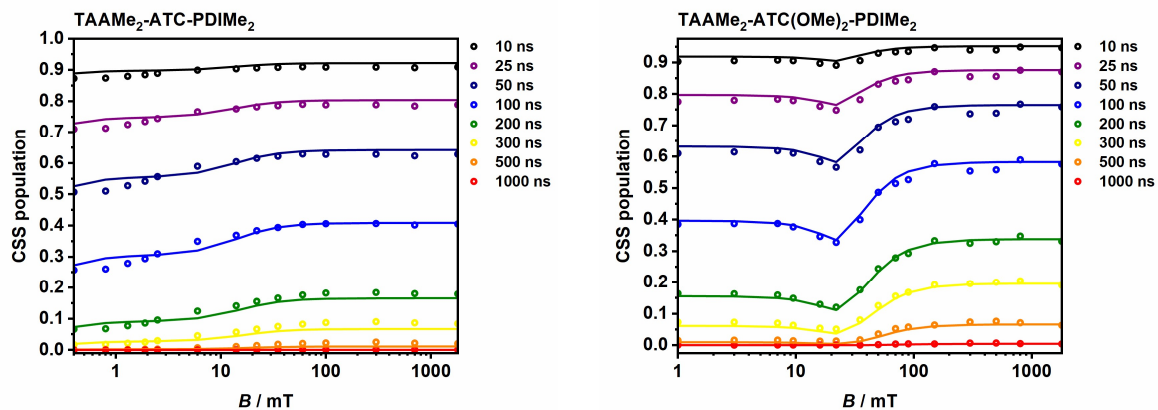


**Figure 117:** Comparison of the experimental data (dots) with the data received from the classical simulation (solid line) for the rotationally hindered triads in toluene. Rate constants obtained by inserting the classical fit parameters in **Table 37** in **equation (16)** and plotted against the magnetic field.





**Figure 118:** Comparison of the experimental data (dots) with the data received from the classical simulation (solid line) for the substituted triptycene triads in toluene. Rate constants obtained by inserting the classical fit parameters in **Table 37** in **equation (16)** and plotted against the magnetic field.



**Figure 119:** Comparison of the experimental data (dots) with the data received from the classical simulation (solid line) for the anthracene bridge triads in toluene. Rate constants are not depicted because the classical fit did not work properly in those triads.

## 10.3 Analytical methods

### 10.3.1 Steady-state absorption spectroscopy

Absorption spectra were recorded on a JASCO V-670 UV/Vis/NIR spectrometer using spectroscopic grade solvents from Sigma Aldrich and Acros Organics in 10 x 10 mm quartz-cuvettes from Starna (Pflugstadt, Germany) at rt. A cuvette with pure solvent was used as reference. In the examined concentration range of  $10^{-7}$  –  $10^{-5}$  M no concentration dependent effects were observed.

### 10.3.2 Steady-state emission spectroscopy

Emission spectroscopy was measured at r.t. in 10 x 10 mm quartz-cuvettes from Starna (Pfungstadt, Germany) using an Edinburgh Instruments FLS980 fluorescence lifetime spectrometer equipped with a 450 W Xenon lamp and a single photon counting photomultiplier R928P (working range 250-850 nm). All solvents were of spectroscopic grade (Sigma Aldrich, Acros Organics) and were used without further purification. The samples used to measure emission and excitation spectra exhibited an OD  $\leq$  0.03 at the maximum absorption of the respective compound. Oxygen was removed by bubbling argon through the sample for at least 30 min before each measurement. All emission spectra were reduced by division by  $\nu^3$  while the absorption spectra were reduced by division by  $\tilde{\nu}$ .

Fluorescence quantum yields were determined using a calibrated integrating sphere and corrected for self-absorption.<sup>[178]</sup>

### 10.3.3 Cyclic voltammetry (CV)

For electrochemical measurements a Gamry Instruments Reference 600 Potentiostat/Galvanostat/ZRA (v. 6.2.2, Warminster, PA, USA) with a conventional three electrode setup (platinum disc working electrode,  $\varnothing = 1$  mm, Ag/AgCl 'LEAK FREE' reference electrode (Warner Instruments, Hamden, CT, USA), platinum wire as counter electrode) was used. The measurements were performed under an argon atmosphere at a concentration of a few mM and referenced against the ferrocene/ferrocenium (Fc/Fc<sup>+</sup>) redox couple. The measurements were performed at a scan rate of 100 mV s<sup>-1</sup> To check chemical and electrochemical reversibility, multiple thin layer experiments were performed.

### 10.3.4 Pump-probe spectroscopy

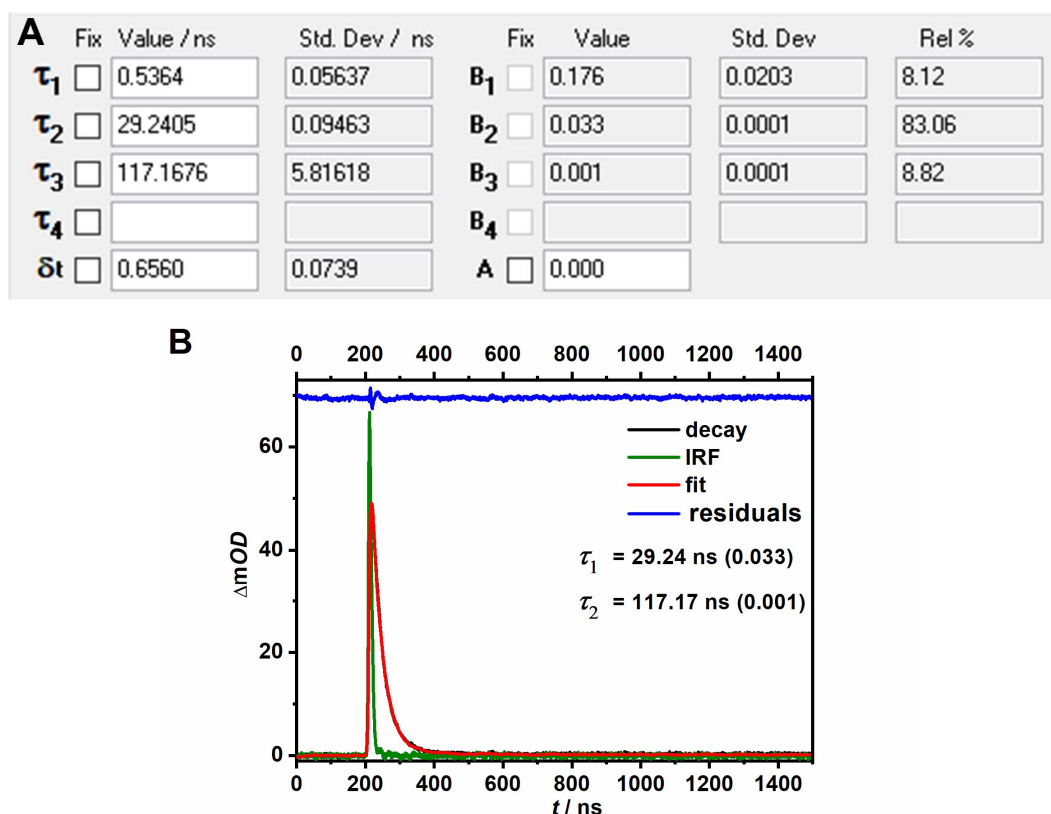
#### 10.3.4.1 fs-Pump-probe spectroscopy

The transient absorption setup (TAS) consists of a one-box femtosecond laser system "Solstice" from Newport Spectra Physics, a "HELIOS" transient absorption spectrometer (TASp) from Ultrafast Systems, a home-built NOPA, and a "TOPAS-C" from LightConversion. The fundamental wavelength from the Solstice is 800 nm with a repetition rate of 1 kHz and a pulse length of 100 fs. The HELIOS spectrometer is equipped with two channels, one for measurement and one for the reference. Furthermore, it has a fibre-coupled linear CMOS sensor with a sensitivity from  $31700\text{ cm}^{-1}$  (315 nm) to  $10800\text{ cm}^{-1}$  (925 nm) and an intrinsic spectral resolution of 1.5 nm. The white light continuum (WLC) is created by an oscillating 3 mm thick  $\text{CaF}_2$  crystal. This crystal was pumped by the TOPAS-C output at  $10000\text{ cm}^{-1}$  (1000 nm) to obtain a gapless WLC from  $29400\text{ cm}^{-1}$  (340 nm) to  $10900\text{ cm}^{-1}$  (915 nm). The probe wavelength range was chopped with a  $25000\text{ cm}^{-1}$  (400 nm) long pass filter and a  $11100\text{ cm}^{-1}$  (900 nm) short pass filter to reach the evaluated region from  $23800\text{ cm}^{-1}$  –  $11500\text{ cm}^{-1}$  (420 nm - 870 nm). A time delay up to 7 ns can be provided by guiding the pump beam from the TOPAS-C for the WLC over a linear stage. The step size for the first 4 ps is 20 fs and afterwards the steps increase exponentially up to 200 fs, whereby the measurements were carried out under magic angle conditions. The angle between the polarization directions between pump and probe was  $54.7^\circ$  and the angle in space between both beams was  $10^\circ$ . The pump beam for the samples was produced from a home-built NOPA at  $18900\text{ cm}^{-1}$  (528 nm) in toluene and  $18800\text{ cm}^{-1}$  (532 nm) in PhCN and the pulse lengths were shorter than 40 fs in a Gaussian fit and the pulse shape was close to the bandwidth limitation. The instrument response function derived from the coherent artefact was ca. 100 fs. All samples were dissolved in toluene from Merck and measured in a cuvette with an optical path length of 0.2 mm, a window thickness of 0.1 mm and pumped with 30 nJ.

GLOTARAN (v. 1.2) was used to analyse the recorded time resolved spectra by a global deconvolution using a sequential model to yield evolution associated difference spectra (EADS).<sup>[228]</sup> By fitting a third order polynomial to the cross-phase modulation signal of the pure solvent the white light dispersion (chirp) was corrected.

#### 10.3.4.2 ns-Pump-Probe Spectroscopy

An Edinburgh LP 920 laser flash spectrometer using an EKSPLA NT340 Nd:YAG laser with integrated optical parametric oscillator was used to perform the ns-transient absorption spectroscopy measurements. The white light was generated by a 450 W Xe arc flash lamp in which the white light and the pump light beams were perpendicular to each other. The solvent was of spectroscopic grade from Sigma Aldrich and degassed by 7 freeze pump thaw cycles. Sample preparation was carried out in a nitrogen filled glovebox in 10 x 10 mm quartz-cuvettes equipped with a *Young's* valve. No bimolecular processes were observed in a concentration range of  $10^{-6}$  to  $10^{-5}$  M. All samples were excited with ca. 5 ns laser pulses (ca. 1.2 mJ pulse energy) with a 10 Hz repetition rate. They were excited at the maximum ground state absorption of the respective PDI moiety at  $18900\text{ cm}^{-1}$  (528 nm) in toluene and at  $18800\text{ cm}^{-1}$  (532 nm) in PhCN. Measuring temporal decay profiles in 4 nm steps between  $25000\text{ cm}^{-1}$  (400 nm) and  $12500\text{ cm}^{-1}$  (800 nm) gave the transient maps. The decay profiles were also corrected for fluorescence. The decay curves of the CSS were measured by light-excitation at  $18900\text{ cm}^{-1}$  (529 nm) in toluene and at  $18800\text{ cm}^{-1}$  (532 nm) in PhCN and probing at  $14100\text{ cm}^{-1}$  (710 nm), consistent with the overlaid signals of the PDI radical anion and the TAA radical cation.<sup>[48, 91]</sup> The decays of all the investigated triads show short lifetimes, which causes a flattening of the CSS decay after the excitation pulse. This is caused because a part of the CSS already decayed in the width of the laser pulse (approximately 5 ns). To eliminate this problem each decay curve (**Figure 120 B**, black) (at all different external magnetic fields) was deconvoluted with the instrumental response function (IRF, **Figure 120 B**, green) using L900 software from Edinburgh Instruments (**Figure 120 A**). The IRF was determined by measuring the scattered light using a LUDOX AS-30 colloidal silica suspension in water. Each curve of all recorded decays was deconvolution fitted and the received mono- /bi- /trixponential decay times  $\tau$  with the respective amplitudes  $a$  (**Figure 120**) are given as determined by the program.



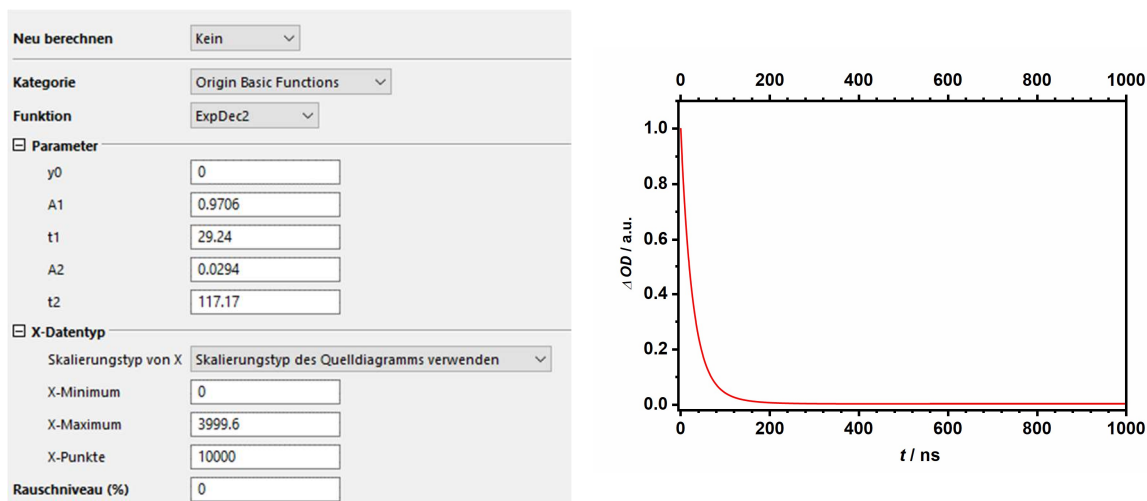
**Figure 120:** **A:** Deconvolution fit with L900 software using the example of **TAAMe<sub>2</sub>-TTC-PDIME<sub>2</sub>** (0 mT) in toluene. **B:** Fit shown with Origin.

After deconvolution the amplitudes were normalised to one (**Table 38**, complete tables in the **Appendix**).

**Table 38:** Normalised amplitudes using the example of **TAAMe<sub>2</sub>-TTC-PDIME<sub>2</sub>** in toluene (0 mT).

$\tau_1 / \text{ns}$	$a_1$	$\tau_2 / \text{ns}$	$a_2$
29.24	0.9706	117.17	0.0294

The decay times and the normalised amplitudes were thereafter used to simulate the actual decay curve by using OriginPro 2019 (**Figure 121**). For the simulation the interception of the y-axis was set to be zero because the small offset made by the measurement is already regarded in the fit results. The curve was simulated from 0 ns to 3999.6 ns in 10000 steps resulting in a step size of 0.4 ns. This corresponds to the exact time range and step size of the original measurement data. Those simulations were used for all further considerations. So, all shown decay curves and MARY plots correspond to the simulated curves. The original data are shown in the **Appendix**.

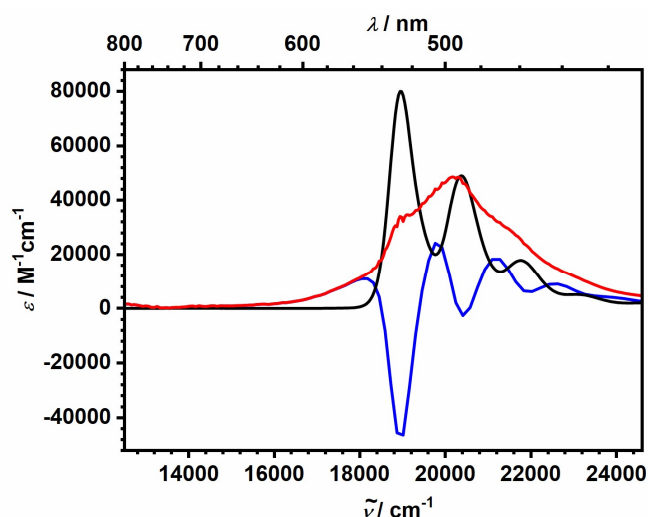


**Figure 121:** Simulated curve of **TAAMe<sub>2</sub>-TTC-PDIME<sub>2</sub>** (0 mT) in toluene using OriginPro2019.

The rise of the <sup>3</sup>PDI was measured by light-excitation with its maximum wavenumber of 18900 cm<sup>-1</sup> (529 nm) in toluene and probing at 21300 cm<sup>-1</sup> (470 nm).<sup>[48, 91]</sup> The quantum yields of the <sup>3</sup>PDI formation were determined by actinometric measurements at 21700 cm<sup>-1</sup> (460 nm) vs. Ru(bpy)<sub>3</sub>Cl<sub>2</sub> and the ε<sub>3PDI</sub> was estimated by using **equation (26)**.

$$\phi_{3\text{PDI}} = \phi_{\text{ref}} \frac{\Delta OD_{3\text{PDI}} \epsilon_{\text{ref}} OD_{\text{ref}}}{\Delta OD_{\text{ref}} \epsilon_{3\text{PDI}} OD_{\text{sam}}} \quad (26)$$

with ε<sub>ref</sub> = 11300 L M<sup>-1</sup> cm<sup>-1</sup> for Ru(bpy)<sub>3</sub>Cl<sub>2</sub> at 22300 cm<sup>-1</sup> (448 nm)<sup>[229]</sup> and ϕ<sub>ref</sub> = 1<sup>[230-231]</sup>. The values for ε<sub>3PDI</sub> were estimated by addition of the <sup>3</sup>PDI's transient spectrum to the absorption spectrum of the neutral compound (example in **Figure 122** for **TAAMe<sub>2</sub>-TTC-PDIME<sub>2</sub>**). The values for ΔOD<sub>3PDI</sub> and ΔOD<sub>ref</sub> were measured at four different laser intensities to ensure a linear dependence of OD with the laser intensity. The estimated values for ε<sub>3PDI</sub> are summarised in **Table 39**.



**Figure 122:** Molar triplet-triplet extinction coefficient (red) for **TAAMe<sub>2</sub>-TTC-PDIME<sub>2</sub>** in toluene obtained by summation of the transient spectrum of the <sup>3</sup>PDI state (blue) and the neutral PDI spectrum (black).

**Table 39:** Extinction coefficients of transient species of all triads in toluene (including GSB). The wavenumber used in actinometric measurements is 21300 cm<sup>-1</sup> (470 nm) for <sup>3</sup>PDI species. Quantum yields  $\Phi_T$  of the triplet formation estimated using actinometric measurements and **equation (26)**.

	$\epsilon_{3\text{PDI}} / \text{M}^{-1}\text{cm}^{-1}$	$\Phi_T$
<b>TAAMe<sub>2</sub>-TTC-PDIME<sub>2</sub></b>	21000	0.79
<b>TAAMe<sub>2</sub>-TTC-PDI</b>	22000	0.76
<b>TAA-TTC-PDIME<sub>2</sub></b>	20000	0.84
<b>TAA-TTC-PDI</b>	21000	0.91
<b>TAAMe<sub>2</sub>-TTC(OMe)<sub>2</sub>-PDIME<sub>2</sub></b>	18000	0.87
<b>TAAMe<sub>2</sub>-TTCMe<sub>2</sub>-PDIME<sub>2</sub></b>	20000	0.71
<b>TAAMe<sub>2</sub>-TTCCl<sub>2</sub>-PDIME<sub>2</sub></b>	21000	0.80
<b>TAAMe<sub>2</sub>-TTCAZC-PDIME<sub>2</sub></b>	19000	1.00
<b>TAAMe<sub>2</sub>-ATC-PDIME<sub>2</sub></b>	19000	0.75
<b>TAAMe<sub>2</sub>-ATC(OMe)<sub>2</sub>-PDIME<sub>2</sub></b>	17000	0.69

The magnetic field dependent measurements were performed using a GMW Associates C-frame electromagnet 5403 (pole diameter = 76 mm, pole face = 38 mm, axial hole in poles 6.35 mm, pole gap = 13 mm) implemented in the aforementioned laser set-up. To control the magnetic field strength a Hall sensor (Projekt Elektronik GmbH Berlin) was used, where the sensor was embedded in a neutral cuvette placed at the side of the pole face. The stability of all samples was checked by repeatedly testing selected magnetic fields as well as comparing steady-state absorption spectra that were recorded at the beginning and the end of all measurements.



### 10.3.5 NMR spectroscopy

All NMR spectra were measured either at a Bruker Avance III HD 400 FT-Spectrometer ( $^1\text{H}$ : 400.13 MHz,  $^{13}\text{C}$ : 100.61 MHz), with a Bruker Ultrashield Magnet, a Bruker Avance III HD 400 FT-Spectrometer ( $^1\text{H}$ : 400.03 MHz,  $^{13}\text{C}$ : 100.59 MHz), with a Bruker Ascend Magnet or a Bruker Avance III HD 600 FT-Spectrometer ( $^1\text{H}$ : 600.13 MHz,  $^{13}\text{C}$ : 150.90 MHz) equipped with a cryoprobe unit.  $^1\text{H}$  and  $^{13}\text{C}$  NMR spectra were measured in deuterated solvents as indicated (e.g. acetone- $d_6$ , chloroform- $d$  ( $\text{CDCl}_3$ ) and dichloromethane- $d_2$  ( $\text{CD}_2\text{Cl}_2$ )). Chemical shifts are given in ppm ( $\delta$ -scale) referenced to the residual proton signal of the respective deuterated solvents ( $^1\text{H}$ ) or to the signal of the present  $^{13}\text{C}$  isotope. The proton signals and their coupling patterns are given as follows: s (singlet), d (doublet), dd (doublet of doublets), m (multiplet), m' (overlapping signals of chemically non-equivalent protons that could not be assigned to first-order couplings). The order of declaration for proton spectra is: chemical shift (spin multiplicity, coupling constant, number of protons). The carbon signals are given as: Cq (quaternary), CH (tertiary),  $\text{CH}_3$  (primary).

### 10.3.6 Mass spectrometry

Mass spectra were recorded on a Bruker Daltonic microTOF focus (ESI, APCI) or a Bruker Daltonics UltrafleXtreme (MALDI). For MALDI spectra DCTB (trans-2-[3-(4-*tert*-butylphenyl)-2-methyl-2-propenylidene]malononitrile) was used as a matrix. Respective theoretical masses were calculated using the software Bruker Daltonics Isotope Pattern. The given measured mass refers to the 100 % peak calculated by the software.

### 10.3.7 Gel permeation chromatography (GPC)

A JASCO gel permeation chromatography system interface box (LC-NetII ADC) with an intelligent HPLC pump (PU-2008 plus), an inline degasser (DG-2080-53), a solvent selection valve unit (LV-2080-03), a multi wavelength UV/Vis detector (UV-2077, range 195-700 nm) and the software Chrompass (v. 6.1) were used. Gel permeation chromatography (GPC) was done using two preparative GPC columns (styrene-divinylbenzene-copolymer, 500 x 500 Å, 600 x 20.8 mm) from PSS (Mainz, Germany) and a four channel UV/Vis-detector (195-700 nm). The flow rate was 4 ml  $\text{min}^{-1}$  and the used solvents were HPLC grade  $\text{CHCl}_3$  or DCM.

## 10.4 Synthesis

Commercially available compounds and standard solvents were purchased from either Acros, Chempur, Fluka, Honeywell, Merck or TCI and used without further purification. DCM, ethyl acetate and hexane were distilled prior to usage. All moisture and oxygen sensitive reactions were performed under a nitrogen atmosphere (dried with Sicapent® from Merck and deoxygenated by a copper oxide catalyst R3-11 from BASF) using dry solvents obtained by a solvent purification system from Inert and degassed in a gentle stream of nitrogen for at least 10 min. Thin layer chromatography (TLC) was performed on pre-coated TLC sheets ALUGRAMR Xtra SIL G/UV254 from Macherey Nagel.

### 10.4.1 General procedures

#### 10.4.1.1 General procedure for the synthesis of the triptycene bridging units (GP I)

2,6-Dibromoanthracene (1 eq.) was dissolved in dioxane and heated to 120 °C. The appropriate anthranilic acid derivative (2-4 eq.) was dissolved in dioxane / THF (v:v; 1:1) and added to the anthracene solution via syringe pump over 6 h. Isoamyl nitrite (20 eq.) was added dropwise simultaneously to the reaction mixture. After complete addition, the mixture was stirred at 120 °C for another 30 min and afterwards cooled to rt. The solvent was removed under reduced pressure and the product was separated from the reactant by washing the solid with hexanes/DCM (v:v 20:1 – 10:1). The crude product was purified by column chromatography on silica gel.<sup>[154-155]</sup>

#### 10.4.1.2 General procedure for the *Suzuki-Miaura* borylation (GP II)

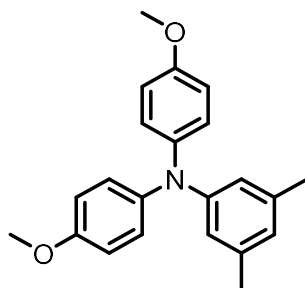
The appropriate triptycene/anthracene derivative (1 eq.), bis(pinacolato)diboron (2.5 eq.), Pd(dppf)Cl<sub>2</sub> (5 mol%) and potassium acetate (4 eq.) were dissolved in dioxane under inert gas atmosphere. After heating the reaction mixture to 100 °C for 3 d the solvent was removed under reduced pressure and the residue was dissolved in DCM. The organic phase was washed with water and dried over Na<sub>2</sub>SO<sub>4</sub>. The solvent was removed under reduced pressure and the crude product was purified by column chromatography on silica gel.<sup>[163]</sup>

### 10.4.1.3 General procedure for the Suzuki-Coupling reaction (GP III)

The appropriate borylated species (1 eq), the halogenated species (varying eq.) and sodium carbonate (4 eq) were dissolved in a mixture of THF and degassed water (v:v 4:1) under an inert gas atmosphere. Afterwards Pd(PPh<sub>3</sub>)<sub>4</sub> (5 mol%) was added and the reaction mixture was heated to 70 °C for 12 h. The solvent was removed under reduced pressure, the residue dissolved in DCM and the organic layer washed with water. The aqueous phases were extracted with DCM and the combined organic phases were dried over Na<sub>2</sub>SO<sub>4</sub>. The solvent was removed under reduced pressure and the crude product was purified by column chromatography on silica gel.

### 10.4.2 Synthesis of the TAA units

#### *N,N*-Bis(4'-methoxyphenyl)-3,5-dimethylaniline (TAAMe<sub>2</sub>)



Synthesis according to literature.<sup>[158]</sup>

CA: [220093-15-4]

3,5-Dimethylaniline (3.00 g, 24.8 mmol) 4-iodoanisole (12.8 g, 54.7 mmol), copper(I)-iodide (377 mg, 1.98 mmol), 1,10-phenanthroline (357 mg, 1.98 mmol) and potassium hydroxide (3.61 g, 64.3 mmol) has been suspended in dry toluene (50 ml) under nitrogen atmosphere. The reaction mixture was heated to 110 °C for 3 d. The solvent was removed under reduced pressure and the residue was dissolved with DCM. The organic phase was washed with water (60 ml) and the solvent was removed under reduced pressure. The crude product was purified by column chromatography on silica gel (eluent: DCM/hexanes 3:2). The crude solid was dissolved in DCM, put in an excess of MeOH and precipitated at -30 °C.

**Yield:** 990 mg (2.97 mmol, 12 %) of a colourless solid.

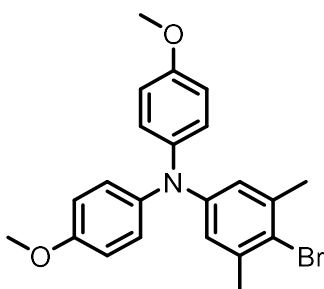
C<sub>22</sub>H<sub>23</sub>NO<sub>2</sub> [333.42 g/mol]

**<sup>1</sup>H-NMR** (400.1 MHz, acetone-d<sub>6</sub>):

δ [ppm] = 6.88 (AA', 4H), 6.86 (BB', 4H), 6.52 (m, 1H), 6.50 (m, 2H), 3.78 (s, 6H), 2.15 (s, 6H).

**Maldi-MS** (pos): m/z calc. [M]<sup>+</sup> 333.17, found [M]<sup>+</sup> 333.17.

#### 4-Bromo-*N,N*-bis(4-methoxyphenyl)3,5-dimethylaniline (TAAMe<sub>2</sub>-Br)



Synthesis according to literature.<sup>[158]</sup>

CA: [220093-24-5]

*N,N*-Bis(4'-methoxyphenyl)-3,5-dimethylaniline (200 mg, 600 μmol) was dissolved in EtOAc (20 ml) and was cooled to 0 °C. *N*-Bromosuccinimide (107 mg, 601 μmol) was added within 1 h, afterwards the reaction mixture was warmed up to rt and stirred for 1 d under light exclusion. The organic layer was washed with brine (50 ml) and dried over MgSO<sub>4</sub>. The crude product was dissolved in DCM, put in an excess of MeOH and precipitated at -30 °C.

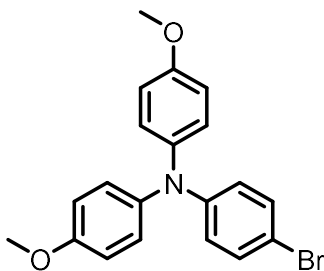
**Yield:** 174 mg (422 μmol, 70 %) of a colourless solid.

C<sub>22</sub>H<sub>22</sub>BrNO<sub>2</sub> [412.32 g/mol]

**<sup>1</sup>H-NMR** (400.1 MHz, acetone-d<sub>6</sub>):

δ [ppm] = 7.02 (AA', 4H), 6.90 (BB', 4H), 6.64 (m, 2H), 3.78 (s, 6H), 2.24 (s, 6H).

**MALDI-MS** (pos): m/z calc. [M]<sup>+</sup> 413.08, found [M]<sup>+</sup> 413.08.

***N,N*-Bis(4'-methoxyphenyl)-4-bromoaniline (TAA-Br)**

Synthesis according to literature.<sup>[158]</sup>

CA: [194416-45-0]

4-Bromoaniline (6.80 g, 39.5 mmol) 4-iodoanisole (19.4 g, 82.9 mmol), copper(I)-iodide (317 mg, 1.67 mmol), 1,10-phenanthroline (300 mg, 1.67 mmol) and potassium hydroxide (6.07 g, 108 mmol) has been suspended in dry toluene (50 ml) under nitrogen atmosphere. The reaction mixture was heated to 110 °C for 5 d. The solvent was removed under reduced pressure and the residue was dissolved with DCM. The organic phase was washed with water (60 ml) and the solvent was removed under reduced pressure. The crude product was purified by column chromatography (silica gel: DCM/hexanes 3:2). The crude solid was dissolved in DCM, put in an excess of MeOH and precipitated at -30 °C.

**Yield:** 6.11 g (15.9 mmol, 40 %) of a colourless solid.

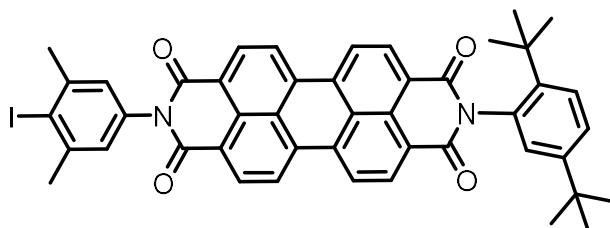
$C_{20}H_{18}BrNO_2$  [384.27 g/mol]

**<sup>1</sup>H-NMR** (400.1 MHz, acetone-*d*<sub>6</sub>):

$\delta$  [ppm] = 6.88 (AA', 4H), 6.86 (BB', 4H), 6.52 (m, 1H), 6.50 (m, 2H), 3.78 (s, 6H), 2.15 (s, 6H).

### 10.4.3 Synthesis of the PDI units

3,4-Anhydride-9,10-di(butylcarboxylate) perylene, *N*-(2,5-di-*tert*-butylphenyl)-9,10-di(butyl carboxylate) perylene monoimide, *N*-(2,5-di-*tert*-butylphenyl)-3,4-anhydride perylene monoimide and *N*-(2,5-di-*tert*-butylphenyl)-*N'*-(4-iodophenyl) perylene diimide were synthesised as *Mims et al.* reported.<sup>[48]</sup>

**N-(2,5-Di-*tert*-butylphenyl)-N'-(4-iodo-3,5-dimethylphenyl) perylene diimide**

Synthesis according to literature.<sup>[48]</sup>

CA: [-]

*N*-(2,5-Di-*tert*-butylphenyl)-3,4-anhydride perylene monoimide (1.00 g, 1.73 mmol) 4-iodo-3,5-dimethylaniline (853 mg, 3.45 mmol) and ZnOAc·2H<sub>2</sub>O (189 mg, 861 μmol) were added to 1*H*-imidazole (15 g) under a nitrogen atmosphere, heated to 140 °C and stirred for 5 h. After cooling aqueous HCl (2 M) was added and stirred until all 1*H*-imidazole was dissolved. The red solid was filtered off, washed with water and dried *in vacuo*. The crude product was purified by column chromatography on silica gel (eluent: CH<sub>2</sub>Cl<sub>2</sub> – CH<sub>2</sub>Cl<sub>2</sub> containing 1% EtOAc).

**Yield:** 1.26 g (1.56 mmol, 90 %) of a red solid.

C<sub>46</sub>H<sub>37</sub>IN<sub>2</sub>O<sub>4</sub> [808.70 g/mol]

**<sup>1</sup>H-NMR** (400.1 MHz, CDCl<sub>3</sub>):

δ [ppm] = 8.75 (m', 8H), 7.61 (d, <sup>3</sup>J<sub>H,H</sub> = 8.6 Hz, 1H), 7.48 (dd, <sup>3</sup>J<sub>H,H</sub> = 8.6 Hz, <sup>4</sup>J<sub>H,H</sub> = 2.3 Hz, 1H), 7.08 (s, 2H), 7.05 (d, <sup>4</sup>J<sub>H,H</sub> = 2.3 Hz, 1H), 2.56 (s, 6H), 1.33 (s, 9H), 1.29 (s, 9H).

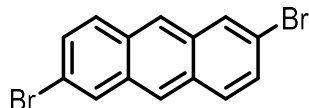
**<sup>13</sup>C-NMR** (100.6 MHz, CDCl<sub>3</sub>):

δ [ppm] = . 164.4 (C<sub>q</sub>), 163.6 (C<sub>q</sub>), 150.4 (C<sub>q</sub>), 143.8 (C<sub>q</sub>), 143.7 (C<sub>q</sub>), 135.2 (C<sub>q</sub>), 134.8 (C<sub>q</sub>), 134.6 (C<sub>q</sub>), 132.6 (C<sub>q</sub>), 131.95 (CH), 131.93 (CH), 129.9 (C<sub>q</sub>), 129.8 (C<sub>q</sub>), 128.9 (CH), 128.0 (CH), 126.9 (CH), 126.8 (C<sub>q</sub>), 126.7 (C<sub>q</sub>), 126.5 (CH), 124.0 (C<sub>q</sub>), 123.5 (CH), 123.4 (CH), 123.3 (C<sub>q</sub>), 109.4 (C<sub>q</sub>), 35.7 (C<sub>q</sub>), 34.4 (C<sub>q</sub>), 31.9 (CH<sub>3</sub>), 31.3 (CH<sub>3</sub>), 29.9 (CH<sub>3</sub>).

**APCI-MS** (pos): *m/z* calc. [M+H]<sup>+</sup> 809.19, found [M+H]<sup>+</sup> 809.18.

#### 10.4.4 Synthesis of the bridging units

##### 2,6-Dibromoanthracene (ATC-Br<sub>2</sub>)



Synthesis according to literature.<sup>[161]</sup>

CAS: [186517-01-1]

2,6-Dibromoanthraquinone (3.00 g, 8.20 mmol) was suspended in acetic acid (170 ml) and stirred with hydrobromic acid (19.3 ml, 355 mmol, 48 % in H<sub>2</sub>O) and phosphinic acid (14.5 ml, 265 mmol, 50 % in H<sub>2</sub>O) for 5 d at 140 °C. The reaction mixture was poured into ice water and stirred for 30 min. The precipitate was filtered and washed with water (2 x 50 ml), methanol (2 x 40 ml), toluene (3 x 20 ml) and was dried under vacuum.

**Yield:** 1.78 g (5.30 mmol, 65 %) of a yellow solid.

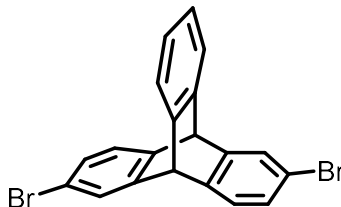
C<sub>14</sub>H<sub>8</sub>Br<sub>2</sub> [336.02 g/mol]

**<sup>1</sup>H-NMR** (400.1 MHz, CDCl<sub>3</sub>):

$\delta$  [ppm] = 8.33 (s, 2H), 8.19 (d, <sup>4</sup>J<sub>H,H</sub> = 2.0 Hz, 2H), 7.90 (d, <sup>3</sup>J<sub>H,H</sub> = 9.0 Hz, 2H), 7.56 (dd, <sup>3</sup>J<sub>H,H</sub> = 9.1 Hz <sup>4</sup>J<sub>H,H</sub> = 2.0 Hz, 2H).

**Maldi-MS** (pos): m/z calc. [M]<sup>+</sup> 335.90, found [M]<sup>+</sup> 335.98.

##### 2,6-Dibromotriptycene (TTC-Br<sub>2</sub>)



CAS: [186517-01-1]

Synthesis according to **GP I**.<sup>[154-155, 232]</sup>

2,6-Dibromoanthracene (1.00 g, 2.98 mmol) in dry dioxane (70 ml). Anthranilic acid (816 mg, 5.95 mmol) in dry THF (20 ml) and dry dioxane (20 ml). Isoamyl nitrite (6.00 ml, 44.6 mmol) column chromatography (silica gel, hexanes/DCM 1:1, hexanes/tol 100:3).

**Yield:** 669 mg (1.62 mmol, 54 %) of a colourless solid.

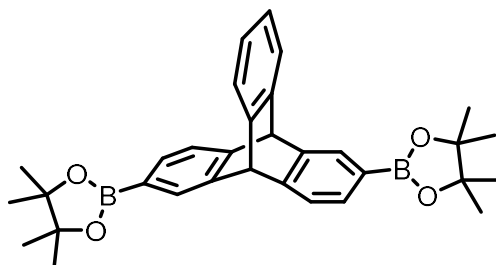
$C_{20}H_{12}Br_2$  [412.12 g/mol]

**$^1H$ -NMR** (400.1 MHz,  $CDCl_3$ ):

$\delta$  [ppm] = 7.52 (d,  $^4J_{H,H} = 1.9$  Hz, 2H), 7.37 (m, 2H), 7.24 (d,  $^3J_{H,H} = 7.8$  Hz, 2H), 7.14 (dd,  $^3J_{H,H} = 7.8$  Hz,  $^4J_{H,H} = 1.9$  Hz, 2H), 7.02 (m, 2H), 5.35 (s, 2H).

**APCI-DIP-MS** (pos): m/z calc.  $[M]^+$  411.93, found  $[M]^+$  411.94.

### 2,6-Di(pinacolboron)tritycene (TTC-(Bpin) $_2$ )



CA: [-]

Synthesis according to **GP II**.<sup>[163]</sup>

2,6-Dibromotriptycene (300 mg, 728  $\mu$ mol), bis(pinacolato)diboron (462 mg, 1.82 mmol), Pd(dppf)Cl $_2$  (29.7 mg, 40.6  $\mu$ mol) und potassium acetate (250 mg, 2.55 mmol) in dry dioxane (25 ml), column chromatography (silica gel, DCM/hexanes 3:2 – DCM).

**Yield:** 152 mg (300  $\mu$ mol, 41 %) of a colourless solid.

$C_{32}H_{36}B_2O_4$  [506.25 g/mol]

**$^1H$ -NMR** (400.1 MHz,  $CDCl_3$ ):

$\delta$  [ppm] = 7.82 (m, 2H), 7.47 (dd,  $^3J_{H,H} = 7.3$  Hz,  $^4J_{H,H} = 1.1$  Hz, 2H), 7.37 (m,  $^3J_{H,H} = 7.3$  Hz, 2H), 7.34 (m, 2H), 6.96 (m, 2H), 5.44 (s, 2H), 1.30 (s, 24H).

**$^{13}C$ -NMR** (100.6 MHz,  $CDCl_3$ ):

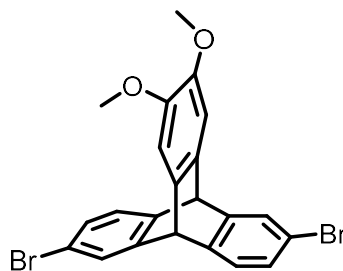
$\delta$  [ppm] = 148.6 ( $C_q$ ), 144.9 ( $C_q$ ), 144.3 ( $C_q$ ), 132.5 (CH), 129.7 (CH), 125.4 (CH), 123.8 (CH), 123.3 (CH), 83.8 ( $C_q$ ), 54.2 (CH), 24.9 (CH $_3$ ).<sup>29</sup>

**Maldi-MS** (pos): m/z calc.  $[M]^+$  506.28, found  $[M]^+$  506.29.

---

<sup>29</sup> C-atom next to Bpin is not visible.



**2,6-Dibromo-14,15-dimethoxytryptycene (TTC(OMe<sub>2</sub>)-Br<sub>2</sub>)**

CA: [-]

Synthesis according to **GP I**. [154-155]

2,6-Dibromoanthracene (1.00 g, 2.98 mmol) in dry dioxane (70 ml). 4,5-Dimethoxyanthranilic acid (2.35 g, 11.9 mmol) in dry THF (20 ml) and dry dioxane (20 ml). Isoamyl nitrite (7.00 ml, 52.0 mmol). Column chromatography (silica gel, eluent: hexanes/DCM 1:1, hexanes/EA 5:1).

**Yield:** 323 mg (684  $\mu$ mol, 23 %) of a colourless solid.

C<sub>22</sub>H<sub>16</sub>Br<sub>2</sub>O<sub>2</sub> [472.17 g/mol]

**<sup>1</sup>H-NMR** (400.1 MHz, CDCl<sub>3</sub>):

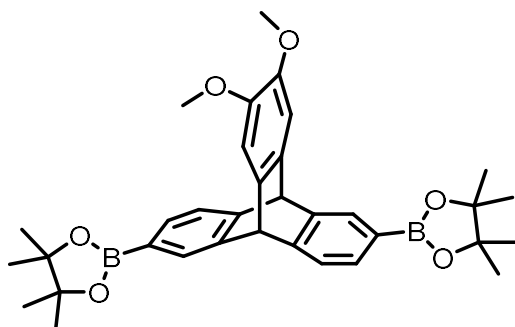
$\delta$  [ppm] = 7.51 (d, <sup>4</sup>J<sub>H,H</sub> = 1.9 Hz, 2H), 7.22 (d, <sup>3</sup>J<sub>H,H</sub> = 7.8 Hz, 2H), 7.12 (dd, <sup>3</sup>J<sub>H,H</sub> = 7.8 Hz, <sup>4</sup>J<sub>H,H</sub> = 1.9 Hz, 2H), 7.00 (s, 2H), 5.27 (s, 2H), 3.84 (s, 6H).

**<sup>13</sup>C-NMR** (100.6 MHz, CDCl<sub>3</sub>):

$\delta$  [ppm] = 147.7 (C<sub>q</sub>); 146.5 (C<sub>q</sub>), 144.3 (C<sub>q</sub>), 136.8 (C<sub>q</sub>), 128.1 (CH), 126.6 (CH), 125.0 (CH), 118.8 (C<sub>q</sub>), 108.7 (CH), 56.3 (CH<sub>3</sub>), 52.9 (CH).

**APCI-MS:** m / z: calc. [M+H]<sup>+</sup> 472.95707; found [M+H]<sup>+</sup> 472.95608,  $\Delta$  = 2.09 ppm.

### TTC(OMe)<sub>2</sub>-(Bpin)<sub>2</sub>



CA: [-]

Synthesis according to **GP II**.<sup>[163]</sup>

**TTC(OMe)<sub>2</sub>-Br<sub>2</sub>** (1.16 g, 2.46 mmol), bis(pinacolato)diboron (1.56 g, 6.14 mmol), Pd(dppf)Cl<sub>2</sub> (100 mg, 137 μmol), potassium acetate (964 mg, 9.83 mmol) in dry dioxane (30 ml) 3 d, 80 °C  
Column chromatography (silica gel, eluent: EA/hexanes 1:4).

**Yield:** 902 mg (1.59 mmol, 65 %) of a colourless solid.

C<sub>34</sub>H<sub>40</sub>B<sub>2</sub>O<sub>6</sub> [566.30 g/mol].

**<sup>1</sup>H-NMR** (400.1 MHz, CDCl<sub>3</sub>):

δ [ppm] = 7.81 (s, 2H), 7.47 (dd, <sup>3</sup>J<sub>H,H</sub> = 7.3 Hz, <sup>4</sup>J<sub>H,H</sub> = 1.1 Hz, 2H), 7.35 (d, <sup>3</sup>J<sub>H,H</sub> = 7.3 Hz, 2H), 6.97 (s, 2H), 5.37 (s, 2H), 3.81 (s, 6H), 1.29 (s, 24H).

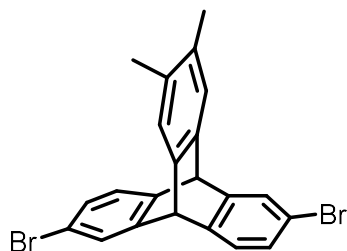
**<sup>13</sup>C-NMR** (100.6 MHz, CDCl<sub>3</sub>):

δ [ppm] = 149.0 (C<sub>q</sub>), 146.1 (C<sub>q</sub>), 144.7 (C<sub>q</sub>), 137.6 (C<sub>q</sub>), 132.4 (CH), 129.3 (CH), 123.0 (CH), 108.6 (CH), 83.8 (C<sub>q</sub>), 56.3 (CH<sub>3</sub>), 53.9 (CH), 24.9 (CH<sub>3</sub>).<sup>30</sup>

**APCI-MS:** m / z: calc. [M+H]<sup>+</sup> 567.3095; found [M+H]<sup>+</sup> 567.3099.

---

<sup>30</sup> The C atom next to the Bpin group is not visible.

**2,6-Dibromo-14,15-dimethyltryptcene (TTCMe<sub>2</sub>-Br<sub>2</sub>)**

CA: [-]

Synthesis according to **GP I**.<sup>[154-155]</sup>

2,6-Dibromoanthracene (1.00 g, 2.98 mmol) in dry dioxane (20 ml). 4,5-Dimethylantranilic acid (1.48 g, 8.96 mmol) in dry THF (20 ml) and dry dioxane (30 ml). Isoamyl nitrite (9.21 ml, 68.4 mmol). Column chromatography (silica gel, eluent: DCM, hexanes/toluene 100:6).

**Yield:** 420 mg (954  $\mu$ mol, 32 %) of a colourless solid.

C<sub>22</sub>H<sub>16</sub>Br<sub>2</sub> [440.17 g/mol]

**<sup>1</sup>H-NMR** (400.1 MHz, CDCl<sub>3</sub>):

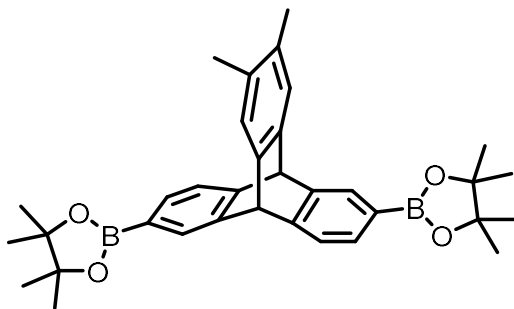
$\delta$  [ppm] = 7.50 (d, <sup>4</sup>J<sub>H,H</sub> = 2.0 Hz, 2H), 7.22 (d, <sup>3</sup>J<sub>H,H</sub> = 7.9 Hz, 2H), 7.18 (s, 2H), 7.12 (dd, <sup>3</sup>J<sub>H,H</sub> = 7.9 Hz, <sup>4</sup>J<sub>H,H</sub> = 2.0 Hz, 2H), 5.28 (s, 2H), 2.17 (s, 6H).

**<sup>13</sup>C-NMR** (100.6 MHz, CDCl<sub>3</sub>):

$\delta$  [ppm] = 147.5 (C<sub>q</sub>), 144.1 (C<sub>q</sub>), 141.8 (C<sub>q</sub>), 133.8 (C<sub>q</sub>), 128.2 (CH), 126.9 (CH), 125.4 (CH), 125.2 (CH), 118.9 (C<sub>q</sub>), 52.8 (CH), 19.7 (CH<sub>3</sub>).

**APCI-HRMS:** m / z: calc. [M+H]<sup>++</sup> 440.96723; found [M+H]<sup>++</sup> 440.96804,  $\Delta$  = 1.84 ppm.

**TTCMe<sub>2</sub>-(Bpin)<sub>2</sub>**



CA: [-]

Synthesis according to **GP II**.<sup>[163]</sup>

**TTCMe<sub>2</sub>-Br<sub>2</sub>** (900 mg, 2.04 mmol), bis(pinacolato)diboron (1.25 g, 4.92 mmol), Pd(dppf)Cl<sub>2</sub> (83.5 mg, 114 μmol), potassium acetate (803 mg, 8.18 mmol) in dry dioxane (50 ml) 3 d, 80 °C  
 Column chromatography (silica gel, eluent: DCM/hexanes 9:1).

**Yield:** 484 mg (906 μmol, 44 %) of a colourless solid.

C<sub>34</sub>H<sub>40</sub>B<sub>2</sub>O<sub>4</sub> [534.30 g/mol].

**<sup>1</sup>H-NMR** (400.1 MHz, CDCl<sub>3</sub>):

δ [ppm] = 7.78 (s, 2H), 7.44 (dd, <sup>3</sup>J<sub>H,H</sub> = 7.2 Hz, <sup>4</sup>J<sub>H,H</sub> = 1.1 Hz, 2H), 7.33 (d, <sup>3</sup>J<sub>H,H</sub> = 7.2 Hz, 2H), 7.12 (s, 2H), 5.36 (s, 2H), 2.12 (s, 6H), 1.28 (s, 24H).

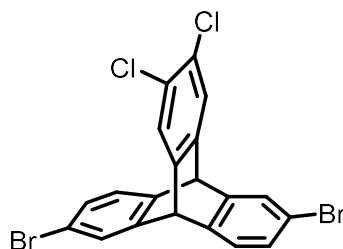
**<sup>13</sup>C-NMR** (100.6 MHz, CDCl<sub>3</sub>):

δ [ppm] = 148.9 (C<sub>q</sub>), 144.6 (C<sub>q</sub>), 142.5 (C<sub>q</sub>), 133.1 (C<sub>q</sub>), 132.4 (CH), 129.5 (CH), 125.3 (CH), 123.1 (CH), 83.7 (C<sub>q</sub>), 53.8 (CH), 24.95 (CH<sub>3</sub>), 24.90 (CH<sub>3</sub>), 19.6 (CH<sub>3</sub>).<sup>31</sup>

**APCI-MS:** m / z: calc. [M+H]<sup>+</sup> 535.3197; found [M+H]<sup>+</sup> 535.3197.

---

<sup>31</sup> The C atom next to the Bpin group is not visible.

**2,6-Dibromo-14,15-dichlorotriptycene (TTCCl<sub>2</sub>-Br<sub>2</sub>)**

CA: [-]

Synthesis according to **GP I**.<sup>[154-155]</sup>

2,6-Dibromoanthracene (1.00 g, 2.98 mmol) in dry dioxane (70 ml). 4,5-Dichloroanthranilic acid (1.23 g, 5.97 mmol) in dry THF (20 ml) and dry dioxane (20 ml), Isoamyl nitrite (6.00 ml, 44.6 mmol). Column chromatography (silica gel, hexanes/DCM 1:1, hexanes/tol 100:3).

**Yield:** 516 mg (1.07 mmol, 36 %) of a colourless solid.

C<sub>20</sub>H<sub>10</sub>Br<sub>2</sub>Cl<sub>2</sub> [481.01 g/mol]

**<sup>1</sup>H-NMR** (400.1 MHz, CDCl<sub>3</sub>):

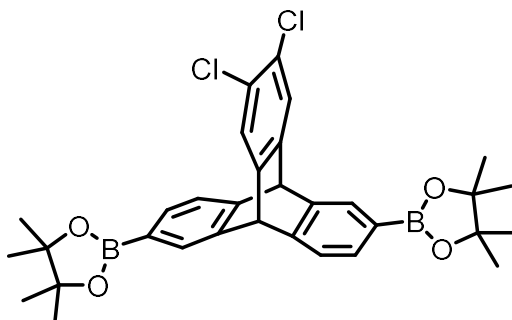
δ [ppm] = 7.51 (d, <sup>4</sup>J<sub>H,H</sub> = 1.9 Hz, 2H), 7.43 (s, 2H), 7.23 (d, <sup>3</sup>J<sub>H,H</sub> = 7.9 Hz, 2H), 7.17 (dd, <sup>3</sup>J<sub>H,H</sub> = 7.8 Hz, <sup>4</sup>J<sub>H,H</sub> = 1.9 Hz, 2H), 5.28 (s, 2H).

**<sup>13</sup>C-NMR** (100.6 MHz, CDCl<sub>3</sub>):

δ [ppm] = 146.6 (C<sub>q</sub>), 144.2 (C<sub>q</sub>), 142.7 (C<sub>q</sub>), 129.2 (C<sub>q</sub>), 128.8 (CH), 127.3 (CH), 125.9 (CH), 125.3 (CH), 119.4 (C<sub>q</sub>), 52.5 (CH).

**APCI-MS:** m / z: calc. [M]<sup>++</sup> 479.8499; found [M]<sup>++</sup> 479.8507.

**TTCCl<sub>2</sub>-(Bpin)<sub>2</sub>**



CA: [-]

Synthesis according to **GP II**.<sup>[163]</sup>

**TTCCl<sub>2</sub>-Br<sub>2</sub>** (300 mg, 624 μmol), bis(pinacolato)diboron (348 mg, 1.37 mmol), Pd(dppf)Cl<sub>2</sub> (22.8 mg, 31.2 μmol), potassium acetate (245 mg, 2.50 mmol) in dry dioxane (15 ml), 1 d, 80 °C. Column chromatography (silica gel, eluent: DCM/hexanes 3:2 – DCM).

**Yield:** 129 mg (224 μmol, 36 %) of a colourless solid.

C<sub>32</sub>H<sub>34</sub>B<sub>2</sub>Cl<sub>2</sub>O<sub>4</sub> [575.14 g/mol].

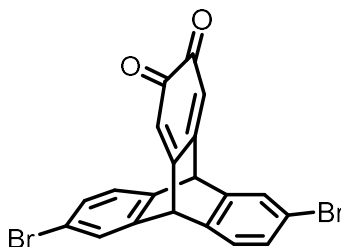
**<sup>1</sup>H-NMR** (400.1 MHz, CDCl<sub>3</sub>):

δ [ppm] = 7.82 (s, 2H), 7.50 (dd, <sup>3</sup>J<sub>H,H</sub> = 7.3 Hz, <sup>4</sup>J<sub>H,H</sub> = 1.1 Hz, 2H) 7.41 (s, 2H), 7.36 (d, <sup>3</sup>J<sub>H,H</sub> = 7.3 Hz, 2H), 5.39 (s, 2H), 1.30 (s, 24H).

**<sup>13</sup>C-NMR** (100.6 MHz, CDCl<sub>3</sub>):

δ [ppm] = 147.4 (C<sub>q</sub>), 145.0 (C<sub>q</sub>), 143.3 (C<sub>q</sub>), 132.9 (CH), 129.9 (CH), 128.7 (C<sub>q</sub>), 125.8 (CH), 123.5 (CH), 83.9 (C<sub>q</sub>), 53.4 (CH), 25.0 (CH<sub>3</sub>), 24.9 (CH<sub>3</sub>).

**APCI-MS:** m / z: calc. [M]<sup>++</sup> 574.2027; found [M]<sup>++</sup> 574.2034.

**TTCO<sub>2</sub>-Br<sub>2</sub>**

Synthesis according to literature.<sup>[143]</sup>

CA: [-]

**TTC(OMe)<sub>2</sub>-Br<sub>2</sub>** (2.07 g, 4.38 mmol) was dissolved in DCM (100 ml) and acetic acid (100 ml) was added. Concentrated nitric acid (21 ml) was added dropwise until a colour change to dark red appeared. The reaction mixture was poured on ice water immediately. The product was extracted with DCM, the organic phases were combined and washed with sodium bicarbonate solution (10 %, 70 ml). The organic phase was dried over Na<sub>2</sub>CO<sub>3</sub> and the solvent removed under reduced pressure. The crude product was purified by column chromatography (silica gel, eluent: DCM).

**Yield:** 1.03 g (2.33 mmol, 53 %) of a red solid.

C<sub>20</sub>H<sub>10</sub>Br<sub>2</sub>O<sub>2</sub> [442.10 g/mol].

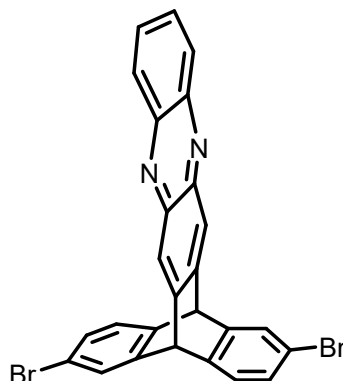
**<sup>1</sup>H-NMR** (400.1 MHz, CDCl<sub>3</sub>):

δ [ppm] = 7.59 (d, <sup>4</sup>J<sub>H,H</sub> = 1.9 Hz, 2H), 7.42 (dd, <sup>3</sup>J<sub>H,H</sub> = 8.0 Hz, <sup>4</sup>J<sub>H,H</sub> = 1.9 Hz, 2H), 7.30 (d, <sup>3</sup>J<sub>H,H</sub> = 8.0 Hz, 2H), 6.36 (s, 2H), 5.08 (s, 2H).

**<sup>13</sup>C-NMR** (100.6 MHz, CDCl<sub>3</sub>):

δ [ppm] = 179.5 (C<sub>q</sub>), 151.7 (C<sub>q</sub>), 140.6 (C<sub>q</sub>), 137.3 (C<sub>q</sub>), 131.3 (CH), 127.9 (CH), 126.2 (CH), 122.3 (CH), 122.2 (C<sub>q</sub>), 51.3 (CH).

**APCI-HRMS:** m / z: calc. [M+H]<sup>+</sup> 442.91010; found [M+H]<sup>+</sup> 442.91084, Δ = 1.67 ppm.

**TTCAZC-Br<sub>2</sub>**

Synthesis according to literature.<sup>[143]</sup>

CA: [-]

**TTCO<sub>2</sub>-Br<sub>2</sub>** (500 mg, 1.13 mmol) and benzene-1,2-diamine (245 mg, 2.27 mmol) were dissolved in chloroform (80 ml) and acetic acid (80 ml) was added. The reaction mixture was stirred for 1 d at 110 °C and then poured on ice water (100 ml). The aqueous phase was neutralised with sodium carbonate solution (10 %) and the product was extracted with DCM (200 ml). The organic phases were combined, washed with sodium carbonate solution (10 %, 100 ml) and dried over Na<sub>2</sub>CO<sub>3</sub>. The solvent was removed under reduced pressure. The crude product was purified by column chromatography (silica gel, eluent: DCM).

**Yield:** 456 mg (887 μmol, 78 %) of a yellow solid.

C<sub>26</sub>H<sub>14</sub>Br<sub>2</sub>N<sub>2</sub> [514.21 g/mol].

**<sup>1</sup>H-NMR** (400.1 MHz, CDCl<sub>3</sub>):

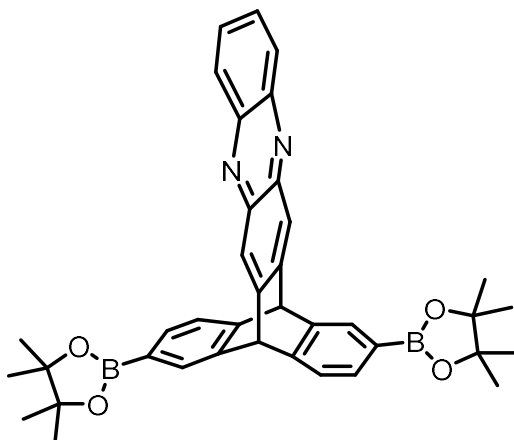
δ [ppm] = 8.18 (m, 2H), 8.08 (s, 2H), 7.77 (m, 2H), 7.64 (d, <sup>4</sup>J<sub>H,H</sub> = 1.8 Hz, 2H), 7.34 (d, <sup>3</sup>J<sub>H,H</sub> = 7.9 Hz, 2H), 7.24 (dd, <sup>3</sup>J<sub>H,H</sub> = 7.9 Hz, <sup>4</sup>J<sub>H,H</sub> = 1.8 Hz, 2H), 5.59 (s, 2H).

**<sup>13</sup>C-NMR** (100.6 MHz, CDCl<sub>3</sub>):

δ [ppm] = 145.1 (C<sub>q</sub>), 145.0 (C<sub>q</sub>), 143.3 (C<sub>q</sub>), 142.8 (C<sub>q</sub>), 141.8 (C<sub>q</sub>), 130.2 (CH), 129.6 (CH), 129.4 (CH), 127.6 (CH), 125.9 (CH), 123.1 (CH), 120.0 (C<sub>q</sub>), 52.6 (CH).

**APCI-HRMS:** m / z: calc. [M+H]<sup>+</sup> 514.95778; found [M+H]<sup>+</sup> 514.95746, Δ = 0.62 ppm.



**TTCAZC-(Bpin)<sub>2</sub>**

CA: [-]

Synthesis according to **GP II**.<sup>[163]</sup>

**TTCAZC-Br<sub>2</sub>** (440 mg, 856  $\mu$ mol), bis(pinacolato)diboron (543 mg, 2.14 mmol), Pd(dppf)Cl<sub>2</sub> (34.9 mg, 47.7  $\mu$ mol), potassium acetate (336 mg, 3.42 mmol) in dry dioxane (10 ml) 3 d, 80 °C. Column chromatography (silica gel, eluent: DCM – DCM/EA 500:25).

**Yield:** 198 mg (325  $\mu$ mol, 38 %) of a yellow solid.

C<sub>38</sub>H<sub>38</sub>B<sub>2</sub>N<sub>2</sub>O<sub>4</sub> [608.34 g/mol].

**<sup>1</sup>H-NMR** (400.1 MHz, CDCl<sub>3</sub>):

$\delta$  [ppm] = 8.17 (m, 2H), 8.05 (s, 2H), 7.94 (s, 2H), 7.76 (m, 2H), 7.57 (dd, <sup>3</sup>J<sub>H,H</sub> = 7.3 Hz, <sup>4</sup>J<sub>H,H</sub> = 1.1 Hz, 2H), 7.49 (d, <sup>3</sup>J<sub>H,H</sub> = 7.3 Hz, 2H), 5.68 (s 2H), 1.30 (s, 24H).

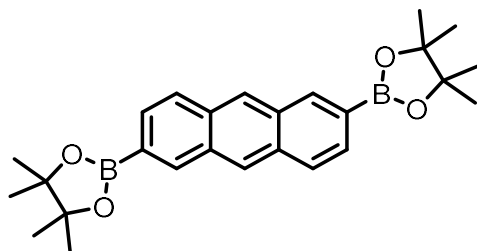
**<sup>13</sup>C-NMR** (100.6 MHz, CDCl<sub>3</sub>):

$\delta$  [ppm] = 146.5 (C<sub>q</sub>), 146.3 (C<sub>q</sub>), 143.2 (C<sub>q</sub>), 143.0 (C<sub>q</sub>), 142.3 (C<sub>q</sub>), 133.4 (CH), 130.3 (CH), 129.9 (CH), 129.6 (CH), 123.8 (CH), 122.7 (CH), 84.0 (C<sub>q</sub>), 53.8 (CH), 25.0 (CH<sub>3</sub>), 24.9 (CH<sub>3</sub>).<sup>32</sup>

**APCI-MS:** m / z: calc. [M+H]<sup>+</sup> 609.3103; found [M+H]<sup>+</sup> 609.3096.

<sup>32</sup> The C<sub>q</sub> next to the Bpin group is not visible.

## ATC-(Bpin)<sub>2</sub>



CA: [849138-20-1]

Synthesis according to **GP II**.<sup>[163, 233]</sup>

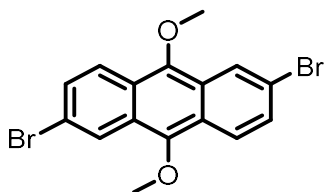
**ATC-Br<sub>2</sub>** (1.00 g, 2.98 mmol), bis(pinacolato)diboron (1.89 g, 7.44 mmol), Pd(dppf)Cl<sub>2</sub> (109 mg, 148 μmol), potassium acetate (1.67 g, 11.9 mmol) in dry dioxane (10 ml) 3 d, 80 °C. Column Filtration (silica gel, eluent: DCM – DCM/EA 500:25). Recrystallisation from toluene (11 ml)

**Yield:** 860 mg (2.00 mmol, 67 %) of a yellow solid.

C<sub>26</sub>H<sub>32</sub>B<sub>2</sub>O<sub>4</sub> [430.15 g/mol].

**<sup>1</sup>H-NMR** (400.1 MHz, CDCl<sub>3</sub>):

δ [ppm] = 8.56 (s, 2H), 8.45 (s, 2H), 7.99 (d, <sup>3</sup>J<sub>H,H</sub> = 8.4 Hz, 2H), 7.79 (dd, <sup>3</sup>J<sub>H,H</sub> = 8.9 Hz, <sup>5</sup>J<sub>H,H</sub> = 0.4 Hz, 2H), 1.41 (s, 24H).

**ATC(OMe)<sub>2</sub>-Br<sub>2</sub>**

Synthesis according to literature.<sup>[165, 234]</sup>

CA: [1424372-34-8]

2,6-Dibromoanthraquinone (1.65 g, 4.51 mmol) and tetrabutylammonium bromide (150 mg, 465  $\mu$ mol) were dissolved in water/THF (4 ml/10 ml). Sodium dithionite (4.18 g, 24.0 mmol) was added and the reaction mixture was stirred at rt for 15 min. conc. potassium hydroxide solution (3.60 ml) and dimethyl sulfate (10.6 g, 84.0 mmol) were added. The reaction mixture was stirred at rt for 1 d. Water (30 ml) was added, the mixture neutralised with hydrochloric acid and then extracted with DCM. The residue was purified by column chromatography (silica gel, eluent: PE - PE/toluene 1:9 - 1:4).

**Yield:** 990 mg (2.50 mmol, 55 %) of a yellow solid.

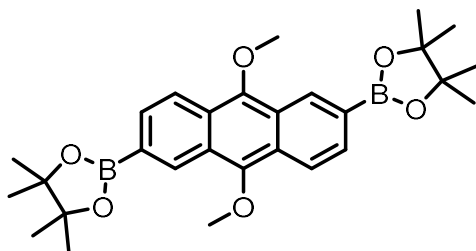
C<sub>16</sub>H<sub>12</sub>Br<sub>2</sub>O<sub>2</sub> [396.07 g/mol].

**<sup>1</sup>H-NMR** (400.1 MHz, CDCl<sub>3</sub>):

$\delta$  [ppm] = 8.43 (dd, <sup>4</sup>J<sub>H,H</sub> = 2.0 Hz, <sup>5</sup>J<sub>H,H</sub> = 0.6 Hz, 2H), 8.15 (dd, <sup>3</sup>J<sub>H,H</sub> = 9.2 Hz, <sup>5</sup>J<sub>H,H</sub> = 0.6 Hz, 2H), 7.55 (dd, <sup>3</sup>J<sub>H,H</sub> = 9.2 Hz, <sup>4</sup>J<sub>H,H</sub> = 2.0 Hz, 2H), 4.09 (s, 6H).

**APCI-HRMS:** m / z: calc. [M+H]<sup>+</sup> 396.92571; found [M+H]<sup>+</sup> 396.92525,  $\Delta$  = 1.16 ppm.

### ATC(OMe)<sub>2</sub>-(Bpin)<sub>2</sub>



CA: [-]

Synthesis according to **GP II**.<sup>[163]</sup>

**ATC(OMe)<sub>2</sub>-Br<sub>2</sub>** (900 mg, 2.27 mmol), bis(pinacolato)diboron (1.44 g, 5.67 mmol), Pd(dppf)Cl<sub>2</sub> (83.1 mg, 114 μmol), potassium acetate (892 mg, 9.09 mmol) in dry toluene (50 ml) 3 d , 120 °C. Filtration (silica gel, eluent: DCM/EA 1:1). Recrystallisation from EtOH/CHCl<sub>3</sub> (v:v / 1:1, 10 ml).

**Yield:** 400 mg (816 μmol, 36 %) of a yellow solid.

C<sub>28</sub>H<sub>36</sub>B<sub>2</sub>O<sub>6</sub> [490.20 g/mol].

**<sup>1</sup>H-NMR** (400.1 MHz, CDCl<sub>3</sub>):

δ [ppm] = 8.84 (s, 2H), 8.28 (dd, <sup>3</sup>J<sub>H,H</sub> = 8.8 Hz, <sup>5</sup>J<sub>H,H</sub> = 0.8 Hz, 2H), 7.82 (dd, <sup>3</sup>J<sub>H,H</sub> = 8.8 Hz, <sup>5</sup>J<sub>H,H</sub> = 0.1 Hz, 2H), 4.15 (s, 6H), 1.41 (s, 24H).

**<sup>13</sup>C-NMR** (100.6 MHz, CDCl<sub>3</sub>):

δ [ppm] = 149.4 (C<sub>q</sub>), 131.6 (CH), 129.4 (CH), 125.8 (C<sub>q</sub>), 125.3 (C<sub>q</sub>), 121.9 (CH), 84.1 (C<sub>q</sub>), 63.8 (CH<sub>3</sub>), 25.1 (CH<sub>3</sub>).<sup>33</sup>

**APCI-MS:** m / z: calc. [M+H]<sup>+</sup> 491.2781; found [M+H]<sup>+</sup> 491.2763.

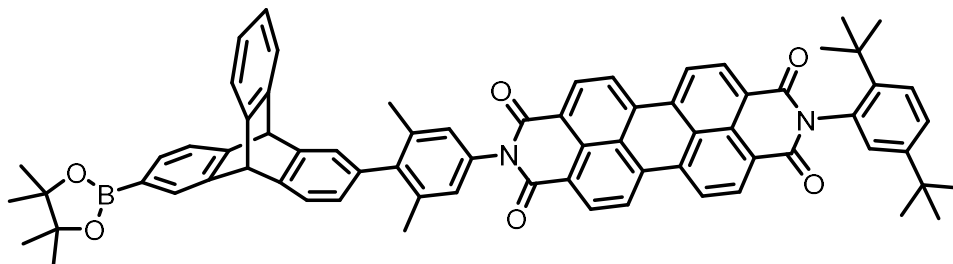
---

<sup>33</sup> The C<sub>q</sub> next to the Bpin group is not visible.

## 10.4.5 Synthesis of the triads

### 10.4.5.1 Rotational hindered triads

#### (Bpin)-TTC-PDIME<sub>2</sub>



CA: [-]

Synthesis according to **GP III**.<sup>[163]</sup>

**TTC-(Bpin)<sub>2</sub>** (100 mg, 198 μmol), **PDI-Me<sub>2</sub>-I** (80.5 mg, 99.5 μmol), sodium carbonate (39.8 mg, 376 μmol) in THF (6 ml) and water (1.5 ml). Pd(PPh<sub>3</sub>)<sub>4</sub> (5.42 mg, 4.69 μmol) Column chromatography on silica gel (eluent: DCM – DCM/tol (5:1) – DCM/toluene/EA (500:100:3)).

**Yield:** 40.0 mg (37.7 μmol, 38 %) of a red solid.

C<sub>72</sub>H<sub>61</sub>BN<sub>2</sub>O<sub>6</sub> [1061.08 g/mol]

**<sup>1</sup>H-NMR** (400.1 MHz, CDCl<sub>3</sub>):

δ [ppm] = 8.75 (m<sup>r</sup>, 8H), 7.88 (s, 2H), 7.61 (d, <sup>3</sup>J<sub>H,H</sub> = 7.3 Hz, 1H), 7.52 (dd, <sup>3</sup>J<sub>H,H</sub> = 7.3 Hz, <sup>4</sup>J<sub>H,H</sub> = 1.1 Hz, 1H), 7.48 (dd, <sup>3</sup>J<sub>H,H</sub> = 8.6 Hz, <sup>4</sup>J<sub>H,H</sub> = 2.3 Hz, 1H), 7.43 (m<sup>r</sup>, 4H), 7.25 (d, <sup>4</sup>J<sub>H,H</sub> = 1.5 Hz, 1H), 7.02 (m<sup>r</sup>, 5H), 6.85 (dd, <sup>3</sup>J<sub>H,H</sub> = 7.5 Hz, <sup>4</sup>J<sub>H,H</sub> = 1.6 Hz, 1H), 5.49 (s, 1H), 5.46 (s, 1H), 2.00 (s, 3H), 1.98 (s, 3H), 1.34 (s, 9H), 1.31 (s, 12H), 1.30 (s, 12H).

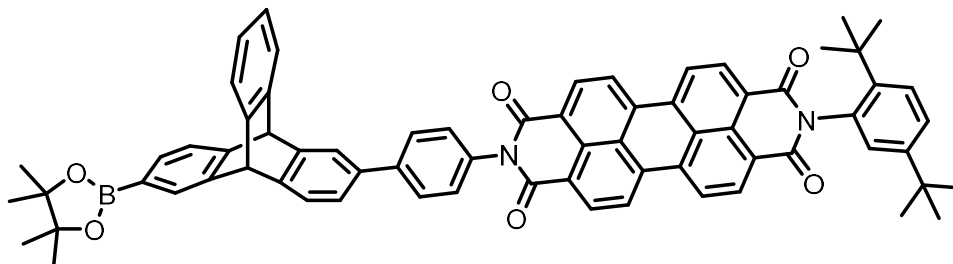
**<sup>13</sup>C-NMR** (100.6 MHz, CDCl<sub>3</sub>):

δ [ppm] = 164.6 (C<sub>q</sub>), 163.9 (C<sub>q</sub>), 150.3 (C<sub>q</sub>), 149.0 (C<sub>q</sub>), 145.5 (C<sub>q</sub>), 145.22 (C<sub>q</sub>), 145.20 (C<sub>q</sub>), 145.0 (C<sub>q</sub>), 143.9 (C<sub>q</sub>), 143.8 (C<sub>q</sub>), 142.5 (C<sub>q</sub>), 138.21 (C<sub>q</sub>), 138.15 (C<sub>q</sub>), 137.4 (C<sub>q</sub>), 135.2 (C<sub>q</sub>), 135.1 (C<sub>q</sub>), 133.5 (C<sub>q</sub>), 132.7 (C<sub>q</sub>), 132.4 (CH), 132.12 (CH), 132.07 (CH), 130.1 (C<sub>q</sub>), 129.3 (C<sub>q</sub>), 129.6 (CH), 129.0 (CH), 127.8 (CH), 127.0 (2 x CH), 126.9 (2 x C<sub>q</sub>), 126.6 (CH), 126.0 (CH), 125.4 (CH), 125.3 (CH), 124.4 (CH), 123.93 (CH), 123.89 (C<sub>q</sub>), 123.8 (2 x CH), 123.7 (C<sub>q</sub>), 123.51 (CH), 123.48 (CH), 123.40 (CH), 83.9 (C<sub>q</sub>), 54.5 (CH), 54.0 (CH), 35.7 (C<sub>q</sub>), 34.5 (C<sub>q</sub>), 31.9 (CH<sub>3</sub>), 31.4 (CH<sub>3</sub>), 25.0 (CH<sub>3</sub>), 21.43 (CH<sub>3</sub>), 21.41 (CH<sub>3</sub>).<sup>34</sup>

**ESI-HRMS** (pos): m/z calc. [M+Na]<sup>+</sup> 1083.45264, found [M+Na]<sup>+</sup> 1083.45149, Δ = 1.06 ppm.

<sup>34</sup> C-atom next to Bpin unit is not visible.

**(Bpin)-TTC-PDI**



CA: [-]

Synthesis according to **GP III**.<sup>[163]</sup>

**TTC-(Bpin)<sub>2</sub>** (463 mg, 915  $\mu$ mol), **PDI-I** (357 mg, 457  $\mu$ mol) sodium carbonate (194 mg, 1.83 mmol) in THF (12 ml) and water (3 ml). Pd(PPh<sub>3</sub>)<sub>4</sub> (26.4 mg, 22.8  $\mu$ mol) Column chromatography on silica gel (eluent: DCM - DCM/toluene (5:1) - DCM/toluene/EA (500:100:3)).

**Yield:** 123 mg (119  $\mu$ mol, 26 %) of a red solid.

C<sub>70</sub>H<sub>57</sub>BN<sub>2</sub>O<sub>6</sub> [1033.03 g/mol]

**<sup>1</sup>H-NMR** (400.1 MHz, CDCl<sub>3</sub>):

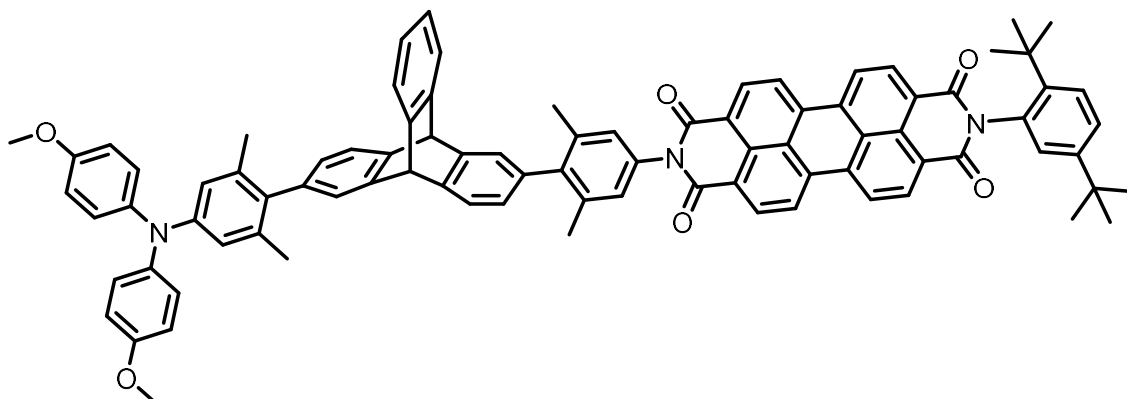
$\delta$  [ppm] = 8.77 (m', 8H), 7.88 (s, 1H), 7.69 (m', 3H), 7.61 (d, <sup>3</sup>J<sub>H,H</sub> = 8.6 Hz, 1H), 7.52 (dd, <sup>3</sup>J<sub>H,H</sub> = 7.3 Hz, <sup>4</sup>J<sub>H,H</sub> = 1.1 Hz, 1H), 7.43 (m', 7H), 7.26 (m', 1H), 7.02 (m', 3H), 5.53 (s, 1H), 5.51 (s, 1H), 1.33 (s, 9H), 1.31 (s, 12H), 1.30 (s, 9H).

**<sup>13</sup>C-NMR** (100.6 MHz, CDCl<sub>3</sub>):

$\delta$  [ppm] = 164.6 (C<sub>q</sub>), 163.8. (C<sub>q</sub>), 150.4. (C<sub>q</sub>), 148.6. (C<sub>q</sub>), 145.7. (C<sub>q</sub>), 145.1. (C<sub>q</sub>), 144.83. (C<sub>q</sub>), 144.81. (C<sub>q</sub>), 144.6. (C<sub>q</sub>), 143.9. (C<sub>q</sub>), 142.3. (C<sub>q</sub>), 137.9. (C<sub>q</sub>), 135.3. (C<sub>q</sub>), 135.1. (C<sub>q</sub>), 134.0. (C<sub>q</sub>), 132.7. (C<sub>q</sub>), 132.6 (CH), 132.1 (CH, 2C), 130.1. (C<sub>q</sub>), 130.0. (C<sub>q</sub>), 129.7 (CH), 129.0 (CH), 128.9 (CH), 128.5 (CH), 127.8 (CH), 127.0. (C<sub>q</sub>), 126.9. (C<sub>q</sub>), 126.6 (CH), 125.6 (CH), 125.4 (CH), 124.6 (CH), 124.1 (CH), 124.0 (CH), 123.9. (C<sub>q</sub>), 123.8 (CH), 123.6. (C<sub>q</sub>), 123.54 (CH), 123.47 (CH), 123.42 (CH), 123.1 (CH), 83.8. (C<sub>q</sub>), 54.6 (CH), 53.8 (CH), 35.7. (C<sub>q</sub>), 34.2. (C<sub>q</sub>), 31.9 (CH<sub>3</sub>), 31.4 (CH<sub>3</sub>), 24.9 (CH<sub>3</sub>).<sup>35</sup>

**ESI-HRMS** (pos): m/z calc. [M+Na]<sup>+</sup> 1055.42131, found [M+Na]<sup>+</sup> 1055.41985;  $\Delta$  = 1.38 ppm.

<sup>35</sup> C-atom next to Bpin unit is not visible.

**TAAMe<sub>2</sub>-TTC-PDIME<sub>2</sub>**

CA: [-]

Synthesis according to **GP III**.<sup>[163]</sup>

**Bpin-TTC-PDIME<sub>2</sub>** (23.0 mg, 21.7  $\mu\text{mol}$ ), **TAAMe<sub>2</sub>-Br** (13.4 mg, 32.5  $\mu\text{mol}$ ), sodium carbonate (9.17 mg, 86.5  $\mu\text{mol}$ ) in THF (12 ml) and water (3 ml). Pd(PPh<sub>3</sub>)<sub>4</sub> (1.25 mg, 10.8  $\mu\text{mol}$ ) Column chromatography on silica gel (eluent: DCM containing 1 % of EA; toluene/EA 7:1). The product was dissolved in DCM and precipitated by addition of hexane.

**Yield:** 12.0 mg (9.47  $\mu\text{mol}$ , 44 %) of a red solid.

C<sub>88</sub>H<sub>71</sub>N<sub>3</sub>O<sub>6</sub> [1266.53 g/mol]

**<sup>1</sup>H-NMR** (600.1 MHz, CD<sub>2</sub>Cl<sub>2</sub>):

$\delta$  [ppm] = 8.76 (m', 8H), 7.63 (d, <sup>3</sup>J<sub>H,H</sub> = 8.7 Hz, 1H), 7.54 (d, <sup>3</sup>J<sub>H,H</sub> = 8.7 Hz, 1H), 7.51 (dd, <sup>3</sup>J<sub>H,H</sub> = 8.7 Hz, <sup>4</sup>J<sub>H,H</sub> = 2.3 Hz, 1H), 7.49 (d, <sup>3</sup>J<sub>H,H</sub> = 7.6 Hz, 1H), 7.47 (m', 2H), 7.37 (d, <sup>4</sup>J<sub>H,H</sub> = 1.5 Hz, 1H), 7.26 (d, <sup>4</sup>J<sub>H,H</sub> = 1.6 Hz, 1H), 7.06 (m', 5H), 7.04 (AA', 4H), 6.96 (dd, <sup>3</sup>J<sub>H,H</sub> = 7.3 Hz, <sup>4</sup>J<sub>H,H</sub> = 1.6 Hz, 1H), 6.83 (m', 5H), 6.63 (m, 2H), 5.55 (s, 1H), 5.53 (s, 1H), 3.78 (s, 6H), 2.09 (s, 3H), 2.04 (s, 3H), 1.88 (s, 3H), 1.82 (s, 3H), 1.34 (s, 9H), 1.28 (s, 9H).

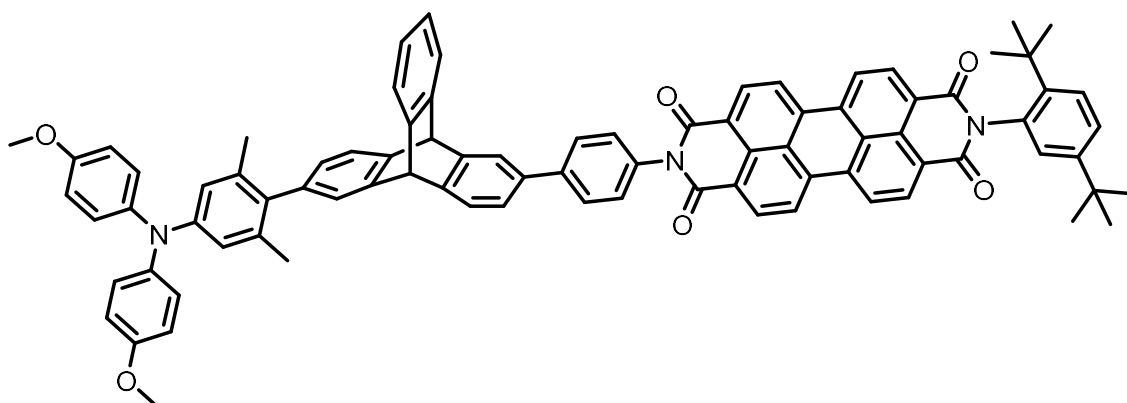
**<sup>13</sup>C-NMR** (150.9 MHz, CD<sub>2</sub>Cl<sub>2</sub>):

$\delta$  [ppm] = 164.9 (C<sub>q</sub>), 164.1 (C<sub>q</sub>), 156.1 (C<sub>q</sub>), 150.8 (C<sub>q</sub>), 147.7 (C<sub>q</sub>), 146.3 (C<sub>q</sub>), 146.2 (C<sub>q</sub>), 145.8 (C<sub>q</sub>), 144.8 (C<sub>q</sub>), 144.5 (C<sub>q</sub>), 143.8 (C<sub>q</sub>), 142.6 (C<sub>q</sub>), 141.6 (C<sub>q</sub>), 139.7 (C<sub>q</sub>), 138.5 (C<sub>q</sub>), 138.24 (C<sub>q</sub>), 138.15 (C<sub>q</sub>), 137.6 (C<sub>q</sub>), 137.2 (C<sub>q</sub>), 137.1 (C<sub>q</sub>), 135.5 (C<sub>q</sub>), 135.4 (C<sub>q</sub>), 134.8 (C<sub>q</sub>), 134.5 (C<sub>q</sub>), 133.6 (C<sub>q</sub>), 132.1 (CH), 132.0 (CH), 130.3 (C<sub>q</sub>), 130.2 (C<sub>q</sub>), 129.3 (CH), 128.3 (CH), 127.6 (CH), 127.23 (C<sub>q</sub>), 127.15 (C<sub>q</sub>), 126.9 (2 x CH), 126.8 (CH), 126.6 (CH), 126.5 (CH), 126.3 (CH), 125.5 (CH), 125.4 (CH), 142.7 (CH), 124.2 (CH), 124.07 (CH), 124.06 (C<sub>q</sub>), 124.02 (CH), 123.97 (CH), 123.89 (CH), 123.88 (C<sub>q</sub>), 123.87 (CH), 120.1 (2 x CH), 114.9 (CH), 55.8

(CH<sub>3</sub>), 54.2 (CH), 54.1 (CH), 35.8 (C<sub>q</sub>), 35.6 (C<sub>q</sub>), 31.8 (CH<sub>3</sub>), 13.3 (CH<sub>3</sub>), 21.29 (CH<sub>3</sub>), 21.27 (CH<sub>3</sub>), 21.25 (CH<sub>3</sub>), 21.23 (CH<sub>3</sub>).

**ESI-HRMS** (pos): m/z calc. [M]<sup>+</sup> 1265.53374, found [M]<sup>+</sup> 1265.53712, Δ = 2.67 ppm.

### TAAMe<sub>2</sub>-TTC-PDI



CA: [-]

Synthesis according to **GP III**.<sup>[163]</sup>

**Bpin-TTC-PDI** (36.0 mg, 34.8 μmol), **TAAMe<sub>2</sub>-Br** (28.7 mg, 69.6 μmol) sodium carbonate (14.7 mg, 139 μmol) in THF (6 ml) and water (1.5 ml). Pd(PPh<sub>3</sub>)<sub>4</sub> (2.01 mg, 1.74 μmol) Column chromatography (eluent: DCM). The product was dissolved in DCM and precipitated by addition of hexane.

**Yield:** 25.0 mg (20.2 μmol, 58 %) of a red solid.

C<sub>86</sub>H<sub>67</sub>N<sub>3</sub>O<sub>6</sub> [1238.47 g/mol]

**<sup>1</sup>H-NMR** (600.1 MHz, CD<sub>2</sub>Cl<sub>2</sub>):

δ [ppm] = 8.75 (m', 8H), 7.77 (d, <sup>4</sup>J<sub>H,H</sub> = 1.8 Hz, 1H), 7.75 (AA', 2H), 7.62 (d, <sup>3</sup>J<sub>H,H</sub> = 8.7 Hz, 1H), 7.54 (d, <sup>3</sup>J<sub>H,H</sub> = 7.7 Hz, 1H), 7.51 (m', 2H), 7.49 (m', 1H), 7.45 (m', 1H), 7.40 (BB', 2H), 7.36 (dd, <sup>3</sup>J<sub>H,H</sub> = 7.7 Hz, <sup>4</sup>J<sub>H,H</sub> = 1.8 Hz, 1H), 7.25 (d, <sup>4</sup>J<sub>H,H</sub> = 1.7 Hz, 1H), 7.07 (m', 3H), 7.04 (AA', 4H), 6.83 (m', 5H), 6.62 (s, 2H), 5.60 (s, 1H), 5.53 (s, 1H), 3.78 (s, 6H), 1.84 (s, 3H), 1.82 (s, 3H), 1.33 (s, 9H), 1.28 (s, 9H).

**<sup>13</sup>C-NMR** (150.9 MHz, CD<sub>2</sub>Cl<sub>2</sub>):

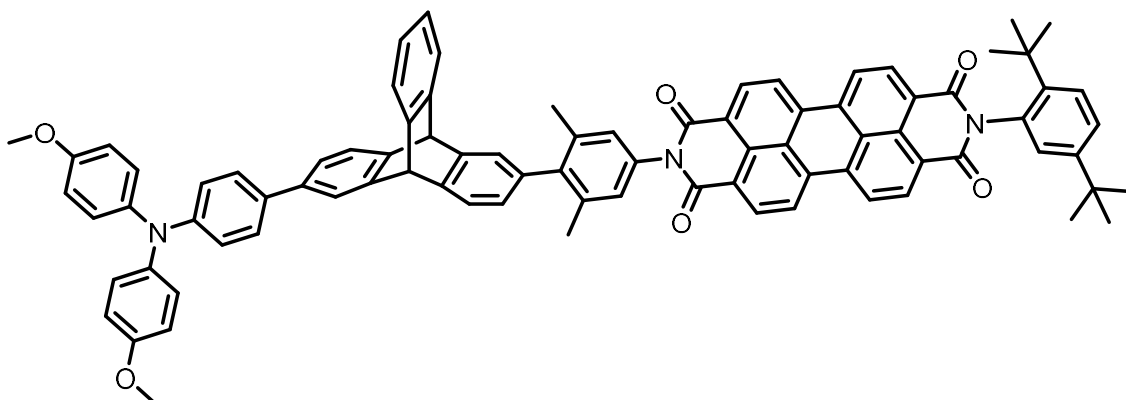
δ [ppm] = 164.9 (C<sub>q</sub>), 164.0 (C<sub>q</sub>), 156.1 (C<sub>q</sub>), 150.8 (C<sub>q</sub>), 147.7 (C<sub>q</sub>), 146.8 (C<sub>q</sub>), 145.84 (C<sub>q</sub>), 145.81 (C<sub>q</sub>), 145.6 (C<sub>q</sub>), 145.5 (C<sub>q</sub>), 144.6 (C<sub>q</sub>), 143.5 (C<sub>q</sub>), 142.1 (C<sub>q</sub>), 141.6 (C<sub>q</sub>), 138.6 (C<sub>q</sub>), 138.0 (C<sub>q</sub>), 137.16 (C<sub>q</sub>), 137.15 (C<sub>q</sub>), 135.5 (C<sub>q</sub>), 135.4 (C<sub>q</sub>), 134.9 (C<sub>q</sub>), 134.8 (C<sub>q</sub>), 133.6 (C<sub>q</sub>), 132.1 (CH), 132.0 (CH), 130.24 (C<sub>q</sub>), 130.16 (C<sub>q</sub>), 129.4 (CH), 129.3 (CH), 128.4 (CH), 128.3



(CH), 127.2 (C<sub>q</sub>), 127.1 (C<sub>q</sub>), 127.0 (CH), 126.8 (CH), 2C), 126.5 (CH), 125.7 (CH), 125.6 (CH), 125.4 (CH), 124.7 (CH), 124.4 (CH), 124.09 (C<sub>q</sub>), 124.08 (CH, 2C), 124.0 (CH), 123.9 (C<sub>q</sub>), 123.89 (CH), 123.88 (CH), 123.2 (CH), 120.1 (CH), 114.9 (CH), 55.8 (CH<sub>3</sub>), 54.22 (CH), 54.18 (CH), 35.8 (C<sub>q</sub>), 35.6 (C<sub>q</sub>), 31.8 (CH<sub>3</sub>), 31.3 (CH<sub>3</sub>), 21.31 (CH<sub>3</sub>), 21.27 (CH<sub>3</sub>).

**ESI-HRMS** (pos): m/z calc. [M]<sup>+</sup> 1237.50244, found [M]<sup>+</sup> 1237.50133,  $\Delta$  = 0.90 ppm.

### TAA-TTC-PDIME<sub>2</sub>



CA: [-]

Synthesis according to **GP III**.<sup>[163]</sup>

**Bpin-TTC-PDIME<sub>2</sub>** (73.0 mg, 68.7  $\mu$ mol), **TAA-Br** (52.8 mg, 137  $\mu$ mol), sodium carbonate (29.1 mg, 275  $\mu$ mol) in THF (12 ml) and water (3 ml). Pd(PPh<sub>3</sub>)<sub>4</sub> (3.97 mg, 3.43  $\mu$ mol). Column chromatography (eluent: DCM). The product was dissolved in DCM and precipitated by addition of hexane.

**Yield:** 12.0 mg (9.69  $\mu$ mol, 14 %) of a red solid.

C<sub>86</sub>H<sub>67</sub>N<sub>3</sub>O<sub>6</sub> [1238.47 g/mol]

**<sup>1</sup>H-NMR** (600.1 MHz, CD<sub>2</sub>Cl<sub>2</sub>):

$\delta$  [ppm] = 8.76 (m', 8H), 7.65 (d, <sup>4</sup>J<sub>H,H</sub> = 1.7 Hz, 1H), 7.63 (d, <sup>3</sup>J<sub>H,H</sub> = 8.7 Hz, 1H), 7.55 (d, <sup>3</sup>J<sub>H,H</sub> = 7.4 Hz, 1H), 7.51 (dd, <sup>3</sup>J<sub>H,H</sub> = 8.7 Hz, <sup>4</sup>J<sub>H,H</sub> = 2.2 Hz, 1H), 7.47 (m', 3H), 7.38 (AA', 2H), 7.35 (d, <sup>4</sup>J<sub>H,H</sub> = 1.5 Hz, 1H), 7.21 (dd, <sup>3</sup>J<sub>H,H</sub> = 7.7 Hz, <sup>4</sup>J<sub>H,H</sub> = 1.7 Hz, 1H), 7.06 (m', 9H), 6.95 (dd, <sup>3</sup>J<sub>H,H</sub> = 7.4 Hz, <sup>4</sup>J<sub>H,H</sub> = 1.6 Hz, 1H), 6.93 (BB', 2H), 6.84 (BB', 4H), 5.57 (s, 1H), 5.53 (s, 1H), 3.78 (s, 6H), 2.05 (s, 3H), 2.04 (s, 3H), 1.34 (s, 9H), 1.27 (s, 9H).

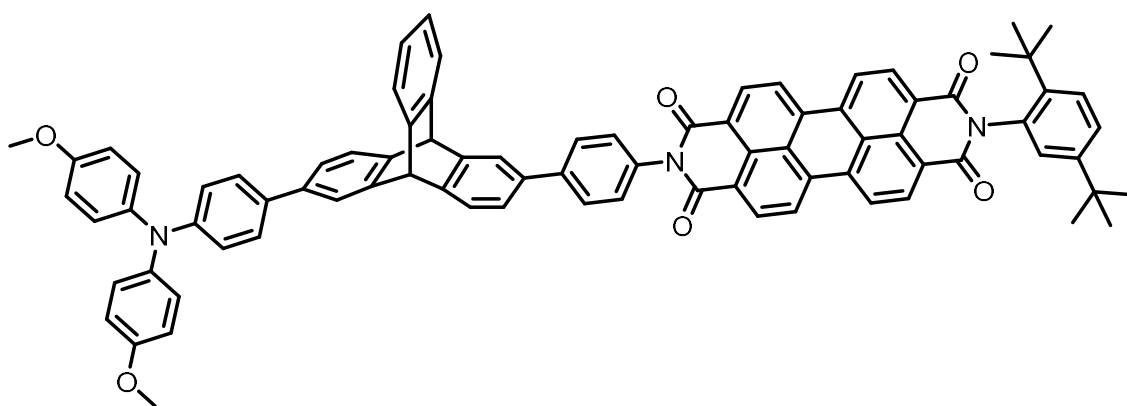
**<sup>13</sup>C-NMR** (150.9 MHz, CD<sub>2</sub>Cl<sub>2</sub>):

$\delta$  [ppm] = 164.9 (C<sub>q</sub>), 164.1 (C<sub>q</sub>), 156.5 (C<sub>q</sub>), 150.8 (C<sub>q</sub>), 148.5 (C<sub>q</sub>), 146.4 (C<sub>q</sub>), 146.0 (C<sub>q</sub>), 145.4 (C<sub>q</sub>), 145.8 (C<sub>q</sub>), 144.6 (C<sub>q</sub>), 144.3 (C<sub>q</sub>), 144.2 (C<sub>q</sub>), 142.6 (C<sub>q</sub>), 141.2 (C<sub>q</sub>), 138.5 (C<sub>q</sub>),

138.19 (C<sub>q</sub>), 138.18 (C<sub>q</sub>), 137.7 (C<sub>q</sub>), 135.5 (C<sub>q</sub>), 135.4 (C<sub>q</sub>), 134.5 (C<sub>q</sub>), 133.6 (C<sub>q</sub>), 133.2 (C<sub>q</sub>), 132.1 (CH), 132.0 (CH), 130.3 (C<sub>q</sub>), 130.2 (C<sub>q</sub>), 129.3 (CH), 128.3 (CH), 127.8 (CH, 2C), 127.6 (CH), 127.24 (C<sub>q</sub>), 127.16 (C<sub>q</sub>), 127.1 (CH), 126.6 (CH), 126.4 (CH), 125.7 (CH), 125.6 (CH), 124.7 (CH), 124.3 (CH), 124.2 (CH) 124.08 (CH), 124.05 (C<sub>q</sub>), 124.04 (CH), 124.02 (C<sub>q</sub>), 123.9 (CH), 123.87 (CH), 123.6 (CH), 122.4 (CH), 120.8 (CH), 115.0 (CH), 55.8 (CH<sub>3</sub>), 54.3 (CH), 54.0 (CH), 35.8 (C<sub>q</sub>), 35.6 (C<sub>q</sub>), 31.8 (CH<sub>3</sub>), 31.4 (CH<sub>3</sub>), 21.3 (CH<sub>3</sub>), 21.2 (CH<sub>3</sub>).

**ESI-HRMS** (pos): m/z calc. [M]<sup>+</sup> 1237.50244, found [M]<sup>+</sup> 1237.49840, Δ = 3.62 ppm.

### TAA-TTC-PDI



CA: [-]

Synthesis according to **GP III**.<sup>[163]</sup>

**Bpin-TTC-PDI** (123 mg, 119 μmol), **TAA-Br** (91.3 mg, 238 μmol), sodium carbonate (50.4 mg, 476 μmol) in THF (12 ml) and water (3 ml). Pd(PPh<sub>3</sub>)<sub>4</sub> (6.87 mg, 5.95 μmol). Column chromatography (eluent: DCM; DCM/tol/EA 400:100:4). The product was dissolved in DCM and precipitated by addition of hexane.

**Yield:** 30.0 mg (24.8 μmol, 21 %) of a red solid.

C<sub>84</sub>H<sub>63</sub>N<sub>3</sub>O<sub>6</sub> [1210.42 g/mol]

**<sup>1</sup>H-NMR** (600.1 MHz, CD<sub>2</sub>Cl<sub>2</sub>):

δ [ppm] = 8.74 (m', 8H), 7.75 (d, <sup>4</sup>J<sub>H,H</sub> = 1.7 Hz, 1H), 7.73 (AA', 2H), 7.64 (d, <sup>4</sup>J<sub>H,H</sub> = 1.8 Hz, 1H), 7.62 (d, <sup>3</sup>J<sub>H,H</sub> = 8.7 Hz, 1H), 7.45 (d, <sup>3</sup>J<sub>H,H</sub> = 7.6 Hz, 1H), 7.51 (dd, <sup>3</sup>J<sub>H,H</sub> = 8.7 Hz, <sup>4</sup>J<sub>H,H</sub> = 2.2 Hz, 1H), 7.48 (m', 3H), 7.40 (BB', 2H) 7.36 (m', 3H), 7.21 (dd, <sup>3</sup>J<sub>H,H</sub> = 7.7 Hz, <sup>4</sup>J<sub>H,H</sub> = 1.8 Hz, 1H), 7.08 (d, <sup>4</sup>J<sub>H,H</sub> = 2.2 Hz, 1H), 7.06 (m', 6H), 6.92 (BB', 2H), 6.84 (BB', 4H), 5.58 (s, 1H), 5.57 (s, 1H), 3.78 (s, 6H), 1.33 (s, 9H), 1.28 (s, 9H).

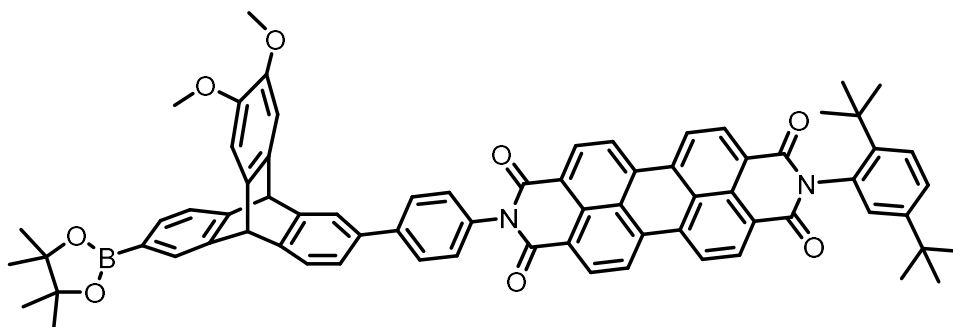
**<sup>13</sup>C-NMR** (150.9 MHz, CD<sub>2</sub>Cl<sub>2</sub>):

$\delta$  [ppm] = .164.8 (C<sub>q</sub>), 164.0 (C<sub>q</sub>), 156.5 (C<sub>q</sub>), 150.8 (C<sub>q</sub>), 148.5 (C<sub>q</sub>), 146.5 (C<sub>q</sub>), 146.1 (C<sub>q</sub>), 145.52 (C<sub>q</sub>), 145.45 (C<sub>q</sub>), 145.3 (C<sub>q</sub>), 144.6 (C<sub>q</sub>), 143.8 (C<sub>q</sub>), 142.1 (C<sub>q</sub>), 141.2 (C<sub>q</sub>), 138.7 (C<sub>q</sub>), 138.1 (C<sub>q</sub>), 135.5 (C<sub>q</sub>), 135.4 (C<sub>q</sub>), 134.9 (C<sub>q</sub>), 133.6 (C<sub>q</sub>), 133.2 (C<sub>q</sub>), 132.1 (CH), 132.0 (CH), 130.23 (C<sub>q</sub>), 130.15 (C<sub>q</sub>), 129.4 (CH), 129.3 (CH), 128.4 (CH), 128.3 (CH), 127.8 (CH), 127.2 (C<sub>q</sub>), 127.12 (C<sub>q</sub>), 127.07 (CH), 126.5 (CH), 125.8 (CH), 125.7 (CH), 124.8 (CH), 124.4 (CH), 124.3 (CH), 124.081 (2 x CH), 124.077 (C<sub>q</sub>), 123.89 (2 x CH), 123.88 (C<sub>q</sub>), 123.7 (CH), 123.1 (CH), 122.4 (CH), 120.8 (CH), 115.0 (CH), 55.8 (CH<sub>3</sub>), 54:1 (CH); 54:0 (CH); 35.8 (C<sub>q</sub>), 34.6 (C<sub>q</sub>), 31.8 (CH<sub>3</sub>), 31.3 (CH<sub>3</sub>).

**ESI-HRMS** (pos): m/z calc. [M]<sup>+</sup> 1209.47114, found [M]<sup>+</sup> 1209.47015,  $\Delta$  = 0.82 ppm.

#### 10.4.5.2 Substituted triptycene Triads

##### (Bpin)-TTC(OMe)<sub>2</sub>-PDI



CA: [-]

Synthesis according to **GP III**.<sup>[163]</sup>

**TTC(OMe)<sub>2</sub>-(Bpin)<sub>2</sub>** (300 mg, 530  $\mu$ mol), **PDI-I** (103 mg, 132  $\mu$ mol), sodium carbonate (225 mg, 2.12 mmol) in THF (6 ml) and water (1.5 ml). Pd(PPh<sub>3</sub>)<sub>4</sub> (30.6 mg, 26.5  $\mu$ mol). Column chromatography on silica gel (eluent: DCM – DCM/toluene (4:1) – DCM/toluene/EA (400:100:1)).

**Yield:** 50.0 mg (45.7  $\mu$ mol, 34 %) of a red solid.

C<sub>72</sub>H<sub>61</sub>BN<sub>2</sub>O<sub>8</sub> [1093.08 g/mol]

**<sup>1</sup>H-NMR** (400.1 MHz, CDCl<sub>3</sub>):

$\delta$  [ppm] = 8.75 (m', 8H), 7.86 (s, 1H), 7.68 (AA', 2H), 7.65 (d, <sup>4</sup>J<sub>H,H</sub> = 1.7 Hz, 1H), 7.61 (d <sup>3</sup>J<sub>H,H</sub> = 8.6 Hz, 1H), 7.51 (dd, <sup>3</sup>J<sub>H,H</sub> = 7.3 Hz, <sup>4</sup>J<sub>H,H</sub> = 1.1 Hz, 1H), 7.48 (dd, <sup>3</sup>J<sub>H,H</sub> = 8.6 Hz,

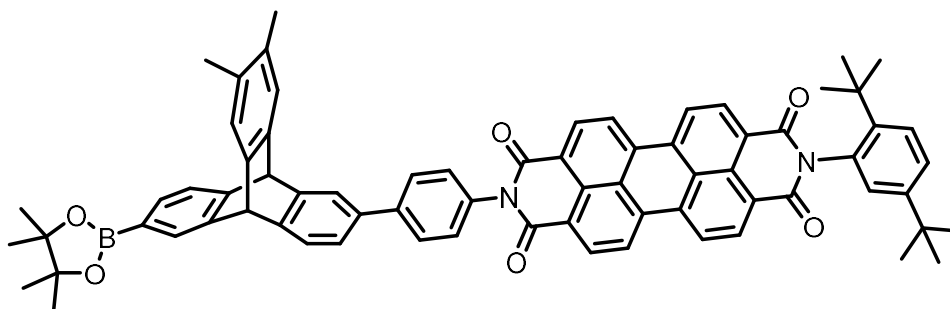
$^4J_{H,H} = 2.3$  Hz, 1H), 7.44 (m', 2H), 7.38 (BB', 2H), 7.25 (m, 1H), 7.05 (m', 3H), 5.44 (s, 1H), 5.43 (s, 1H), 3.85 (s, 3H), 3.84 (s, 3H), 1.33 (s, 9H), 1.31 (s, 12H), 1.30 (s, 9H).

$^{13}\text{C-NMR}$  (100.6 MHz,  $\text{CDCl}_3$ ):

$\delta$  [ppm] = 164.5 ( $\text{C}_q$ ), 163.8 ( $\text{C}_q$ ), 150.3 ( $\text{C}_q$ ), 149.0 ( $\text{C}_q$ ), 146.3 ( $\text{C}_q$ ), 146.2 ( $\text{C}_q$ ), 146.1 ( $\text{C}_q$ ), 145.2 ( $\text{C}_q$ ), 145.1 ( $\text{C}_q$ ), 143.9 ( $\text{C}_q$ ), 142.2 ( $\text{C}_q$ ), 137.9 ( $\text{C}_q$ ), 137.8 ( $\text{C}_q$ ), 137.5 ( $\text{C}_q$ ), 135.3 ( $\text{C}_q$ ), 135.1 ( $\text{C}_q$ ), 134.0 ( $\text{C}_q$ ), 132.7 ( $\text{C}_q$ ), 132.5 (CH), 132.1 (CH), 132.08 (CH), 130.0 ( $\text{C}_q$ ), 129.98 ( $\text{C}_q$ ), 129.3 (CH), 129.0 (CH), 128.9 (CH), 128.5 (CH), 127.8 (CH), 126.94 ( $\text{C}_q$ ), 126.87 ( $\text{C}_q$ ), 126.6 (CH), 124.5 (CH), 123.9 ( $\text{C}_q$ ), 123.8 (CH), 123.6 ( $\text{C}_q$ ), 123.54 (CH), 123.46 (CH), 123.1 (CH), 122.9 (CH), 108.8 (CH), 108.6 (CH), 83.8 ( $\text{C}_q$ ), 56.4 ( $\text{CH}_3$ ), 56.3 ( $\text{CH}_3$ ), 54.2 (CH), 53.5 (CH), 35.7 ( $\text{C}_q$ ), 34.4 ( $\text{C}_q$ ), 31.9 ( $\text{CH}_3$ ), 31.4 ( $\text{CH}_3$ ), 25.0 ( $\text{CH}_3$ ), 24.9 ( $\text{CH}_3$ ).<sup>36</sup>

**MALDI-MS** (pos): m/z calc.  $[\text{M}]^+$  1092.45270, found  $[\text{M}]^+$  1092.44710.

### (Bpin)-TTCMe<sub>2</sub>-PDI



CA: [-]

Synthesis according to **GP III**.<sup>[163]</sup>

**TTCMe<sub>2</sub>-(Bpin)<sub>2</sub>** (100 mg, 187  $\mu\text{mol}$ ), **PDI-I** (73.1 mg, 93.6  $\mu\text{mol}$ ), sodium carbonate (49.6 mg, 468  $\mu\text{mol}$ ) in THF (12 ml) and water (3 ml).  $\text{Pd}(\text{PPh}_3)_4$  (5.41 mg, 4.68  $\mu\text{mol}$ ). Column chromatography on silica gel (eluent: DCM – DCM/toluene/EA (400:100:10)).

**Yield:** 28.0 mg (26.4  $\mu\text{mol}$ , 28 %) of a red solid.

$\text{C}_{72}\text{H}_{61}\text{BN}_2\text{O}_6$  [1061.08 g/mol]

$^1\text{H-NMR}$  (400.1 MHz,  $\text{CDCl}_3$ ):

$\delta$  [ppm] = 8.74 (m', 8H), 7.85 (s, 1H), 7.66 (AA', 2H), 7.63 (d,  $^4J_{H,H} = 1.8$  Hz, 1H), 7.61 (d,  $^3J_{H,H} = 8.6$  Hz, 1H), 7.49 (m', 2H), 7.42 (m' 2H), 7.37 (BB', 2H), 7.22 (m', 3H), 7.04 (d,  $^4J_{H,H} = 2.2$  Hz, 1H), 5.45 (s, 1H), 5.43 (s, 1H), 2.17 (s, 3H), 2.16 (s, 3H), 1.33 (s, 9H), 1.30 (m', 21H).

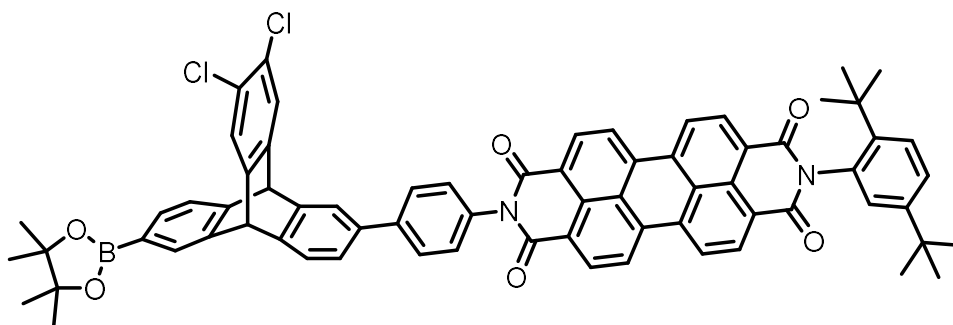
<sup>36</sup>  $\text{C}_q$  next to the Bpin group is not visible.

**<sup>13</sup>C-NMR** (100.6 MHz, CDCl<sub>3</sub>):

$\delta$  [ppm] = 164.6 (C<sub>q</sub>), 163.8 (C<sub>q</sub>), 150.3 (C<sub>q</sub>), 148.9 (C<sub>q</sub>), 146.0 (C<sub>q</sub>), 145.1 (C<sub>q</sub>), 144.9 (C<sub>q</sub>), 143.9 (C<sub>q</sub>), 142.8 (C<sub>q</sub>), 142.5 (C<sub>q</sub>), 142.4 (C<sub>q</sub>), 137.8 (C<sub>q</sub>), 135.3 (C<sub>q</sub>), 135.1 (C<sub>q</sub>), 133.9 (C<sub>q</sub>), 133.4 (C<sub>q</sub>), 133.2 (C<sub>q</sub>), 132.7 (C<sub>q</sub>), 132.5 (CH), 132.10 (CH), 132.09 (CH), 130.00 (C<sub>q</sub>), 129.99 (C<sub>q</sub>), 129.5 (CH), 129.0 (2 x CH), 128.5 (CH), 127.8 (CH), 127.0 (C<sub>q</sub>), 126.9 (C<sub>q</sub>), 126.6 (CH), 125.4 (CH), 125.3 (CH), 124.6 (CH), 123.94 (CH), 123.91 (C<sub>q</sub>), 123.6 (C<sub>q</sub>), 123.5 (CH), 123.47 (CH), 123.3 (CH), 123.0 (CH), 83.8 (C<sub>q</sub>), 54.1 (CH), 53.4 (CH), 35.7 (C<sub>q</sub>), 34.4 (C<sub>q</sub>), 31.9 (CH<sub>3</sub>), 31.4 (CH<sub>3</sub>), 25.0 (CH<sub>3</sub>), 24.9 (CH<sub>3</sub>), 19.68 (CH<sub>3</sub>), 19.67 (CH<sub>3</sub>).<sup>37</sup>

**MALDI-MS** (pos): m/z calc. [M]<sup>+</sup> 1060.46287, found [M]<sup>+</sup> 1060.46272.

**(Bpin)-TTCCl<sub>2</sub>-PDI**



CA: [-]

Synthesis according to **GP III**.<sup>[163]</sup>

**TTCCl<sub>2</sub>-(Bpin)<sub>2</sub>** (320 mg, 556  $\mu$ mol), **PDI-I** (217 mg, 278  $\mu$ mol) sodium carbonate (118 mg, 1.11 mmol) in THF (24 ml) and water (6 ml). Pd(PPh<sub>3</sub>)<sub>4</sub> (16.1 mg, 13.9  $\mu$ mol) Column chromatography on silica gel (eluent: DCM – DCM/toluene (5:1) – DCM/toluene/EA (400:100:20)).

**Yield:** 49.0 mg (44.5  $\mu$ mol, 16 %) of a red solid.

C<sub>70</sub>H<sub>55</sub>BCl<sub>2</sub>N<sub>2</sub>O<sub>6</sub> [1101.91 g/mol]

**<sup>1</sup>H-NMR** (400.1 MHz, CDCl<sub>3</sub>):

$\delta$  [ppm] = 8.74 (m', 8H), 7.88 (s, 1H), 7.67 (m', 3H), 7.61 (d, <sup>3</sup>J<sub>H,H</sub> = 8.7 Hz, 1H), 7.55 (dd, <sup>3</sup>J<sub>H,H</sub> = 7.3 Hz, <sup>4</sup>J<sub>H,H</sub> = 1.1 Hz, 1H), 7.48 (m', 5H), 7.39 (AA', 2H), 7.30 (dd, <sup>3</sup>J<sub>H,H</sub> = 7.6 Hz, <sup>4</sup>J<sub>H,H</sub> = 1.8 Hz, 1H), 7.05 (d, <sup>4</sup>J<sub>H,H</sub> = 2.2 Hz, 1H), 5.48 (s, 1H), 5.45 (s, 1H), 1.33 (s, 9H), 1.32 (s, 12H), 1.30 (s, 9H).

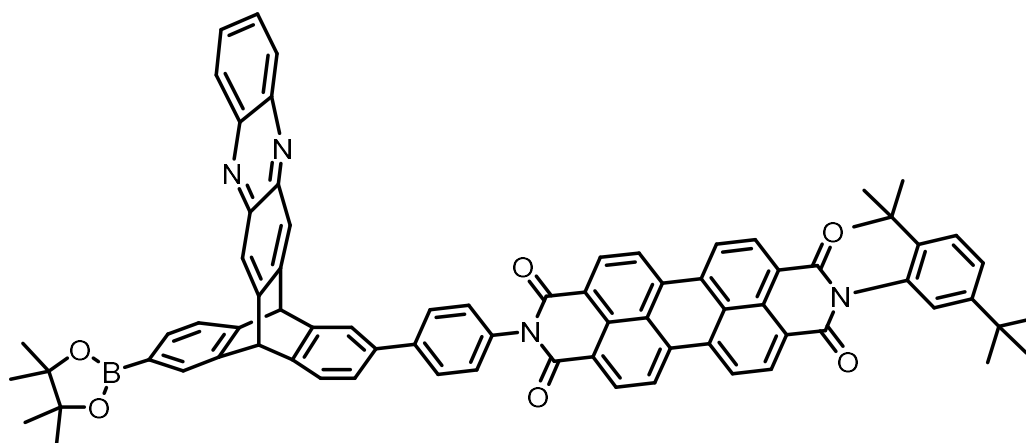
<sup>37</sup> C<sub>q</sub> next to the Bpin group is not visible.

**<sup>13</sup>C-NMR** (100.6 MHz, CDCl<sub>3</sub>):

δ [ppm] = 164.5 (C<sub>q</sub>), 163.8 (C<sub>q</sub>), 150.4 (C<sub>q</sub>), 147.4 (C<sub>q</sub>), 145.3 (C<sub>q</sub>), 145.0 (C<sub>q</sub>), 144.7 (C<sub>q</sub>), 143.9 (C<sub>q</sub>), 143.7 (C<sub>q</sub>), 143.6 (C<sub>q</sub>), 141.9 (C<sub>q</sub>), 138.4 (C<sub>q</sub>), 135.3 (C<sub>q</sub>), 135.0 (C<sub>q</sub>), 134.2 (C<sub>q</sub>), 133.0 (CH), 132.6 (C<sub>q</sub>), 132.1 (CH), 132.1 (CH), 130.0 (C<sub>q</sub>), 130.0 (C<sub>q</sub>), 129.9 (CH), 129.0 (2 x CH), 128.9 (C<sub>q</sub>), 128.8 (C<sub>q</sub>), 128.5 (CH), 127.9 (CH), 126.92 (C<sub>q</sub>), 126.86 (C<sub>q</sub>), 126.6 (CH), 126.0 (CH), 125.8 (CH), 125.0 (CH), 124.3 (CH), 124.0 (C<sub>q</sub>), 123.6 (CH), 123.54 (CH), 123.53 (C<sub>q</sub>), 123.5 (CH), 123.3 (CH), 84.0 (C<sub>q</sub>), 53.6 (CH), 52.9 (CH), 35.7 (C<sub>q</sub>), 34.4 (C<sub>q</sub>), 31.9 (CH<sub>3</sub>), 31.3 (CH<sub>3</sub>), 25.0 (CH<sub>3</sub>), 24.9 (CH<sub>3</sub>).<sup>38</sup>

**APCI-MS:** (pos): m/z calc. [M+H]<sup>+</sup> 1101.3614, found [M+H]<sup>+</sup> 1101.3489.

### (Bpin)-TTCAZC-PDI



Synthesis according to literature.<sup>[163]</sup>

CA: [-]

Synthesis according to **GP III**.

**TTCAZC-(Bpin)<sub>2</sub>** (150 mg, 247 μmol), **PDI-I** (96.2 mg, 123 μmol), sodium carbonate (52.3 mg, 493 μmol) in THF (6 ml) and water (1.5 ml). Pd(PPh<sub>3</sub>)<sub>4</sub> (7.12 mg, 6.16 μmol). Column chromatography on silica gel (eluent: DCM/EA (10:1)).

**Yield:** 38.0 mg (33.5 μmol, 27 %) of a red solid.

C<sub>76</sub>H<sub>59</sub>BN<sub>4</sub>O<sub>6</sub> [1135.12 g/mol]

**<sup>1</sup>H-NMR** (400.1 MHz, CDCl<sub>3</sub>):

---

<sup>38</sup> C<sub>q</sub> next to Bpin-group not visible in NMR.

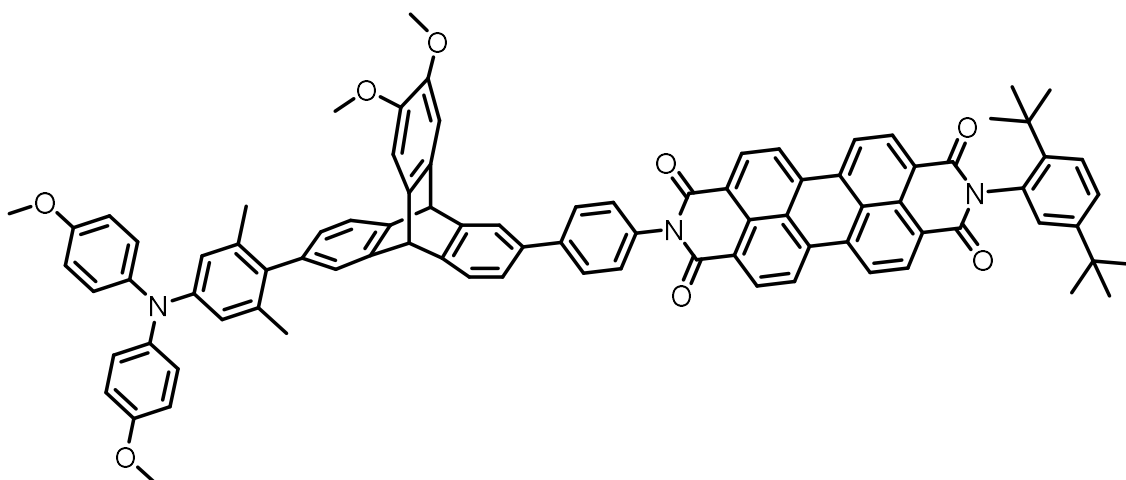
$\delta$  [ppm] = 8.73 (m', 8H), 8.18 (m, 2H), 8.14 (s, 1H), 8.10 (s, 1H), 8.00 (s, 1H), 7.78 (m', 3H), 7.71 (AA', 2H), 7.61 (m', 4H), 7.48 (dd,  $^3J_{H,H} = 8.6$  Hz,  $^4J_{H,H} = 2.3$  Hz, 1H), 7.40 (m', 3H), 7.05 (d,  $^4J_{H,H} = 2.3$  Hz, 1H), 5.78 (s, 1H), 5.75 (s, 1H), 1.33 (s, 9H), 1.32 (s, 12H), 1.30 (s, 9H).

$^{13}\text{C-NMR}$  (100.6 MHz,  $\text{CDCl}_3$ ):

$\delta$  [ppm] = 164.5 ( $\text{C}_q$ ), 163.8 ( $\text{C}_q$ ), 150.3 ( $\text{C}_q$ ), 146.41 ( $\text{C}_q$ ), 146.38 ( $\text{C}_q$ ), 146.2 ( $\text{C}_q$ ), 143.9 ( $\text{C}_q$ ), 143.7 ( $\text{C}_q$ ), 143.20 ( $\text{C}_q$ ), 143.18 ( $\text{C}_q$ ), 143.13 ( $\text{C}_q$ ), 143.06 ( $\text{C}_q$ ), 142.8 ( $\text{C}_q$ ), 142.6 ( $\text{C}_q$ ), 141.8 ( $\text{C}_q$ ), 139.0 ( $\text{C}_q$ ), 135.3 ( $\text{C}_q$ ), 135.0 ( $\text{C}_q$ ), 134.3 ( $\text{C}_q$ ), 133.5 (CH), 132.7 ( $\text{C}_q$ ), 132.09 (CH), 132.07 (CH), 130.3 (CH), 130.00 ( $\text{C}_q$ , CH), 129.98 ( $\text{C}_q$ ), 129.97 (CH), 129.6 (2 x CH), 129.0 (2 x CH), 128.5 (CH), 127.9 (CH), 126.92 ( $\text{C}_q$ ), 126.86 ( $\text{C}_q$ ), 126.6 (CH), 125.7 (CH), 124.7 (CH), 123.9 ( $\text{C}_q$ , CH), 123.6 (CH), 123.5 (CH), 123.45 ( $\text{C}_q$ ), 123.4 (CH), 122.9 (CH), 122.7 (CH), 84.0 ( $\text{C}_q$ ), 54.0 (CH), 54.3 (CH), 35.7 ( $\text{C}_q$ ), 34.4 ( $\text{C}_q$ ), 31.9 ( $\text{CH}_3$ ), 31.4 ( $\text{CH}_3$ ), 25.0 ( $\text{CH}_3$ ), 24.9 ( $\text{CH}_3$ ).

**MALDI-MS** (pos): m/z calc.  $[\text{M}+\text{H}]^+ 1135.46124$ , found  $[\text{M}]^+ 1135.46246$ .

### TAAMe<sub>2</sub>-TTC(OMe)<sub>2</sub>-PDI



CA: [-]

Synthesis according to **GP III**.<sup>[163]</sup>

**Bpin-TTC(OMe)<sub>2</sub>-PDI** (50.0 mg, 45.7  $\mu\text{mol}$ ), **TAAMe<sub>2</sub>-Br** (37.7 mg, 91.4  $\mu\text{mol}$ ), sodium carbonate (19.4 mg, 183  $\mu\text{mol}$ ) in THF (6 ml) and water (1.5 ml).  $\text{Pd}(\text{PPh}_3)_4$  (2.64 mg, 2.28  $\mu\text{mol}$ ). Column chromatography (eluent: DCM – DCM/EA (50:1)). The product was dissolved in DCM and precipitated by addition of hexane.

**Yield:** 23.0 mg (17.7  $\mu\text{mol}$ , 39 %) of a red solid.

$\text{C}_{88}\text{H}_{71}\text{N}_3\text{O}_8$  [1298.52 g/mol]

**<sup>1</sup>H-NMR** (600.1 MHz, CD<sub>2</sub>Cl<sub>2</sub>):

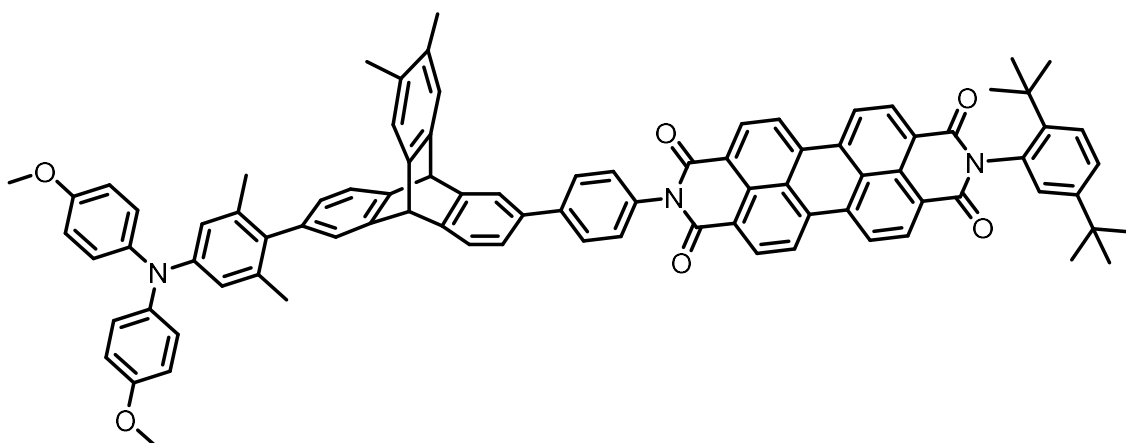
δ [ppm] = 8.74 (m', 8H), 7.75 (m', 3H), 7.62 (d, <sup>3</sup>J<sub>H,H</sub> = 8.6 Hz, 1H), 7.50 (m', 3H), 7.41 (AA', 2H), 7.35 (dd, <sup>3</sup>J<sub>H,H</sub> = 7.6 Hz, <sup>4</sup>J<sub>H,H</sub> = 1.8 Hz, 1H), 7.23 (dd, <sup>4</sup>J<sub>H,H</sub> = 1.5 Hz, 1H), 7.09 (m', 3H), 7.04 (AA', 4H), 6.83 (m', 5H), 6.63 (s, 2H), 5.51 (s, 1H), 5.43 (s, 1H), 3.83 (s, 3H), 3.82 (s, 3H), 3.78 (s, 6H), 1.84 (s, 6H), 1.33 (s, 9H), 1.28 (s, 9H).

**<sup>13</sup>C-NMR** (150.9 MHz, CD<sub>2</sub>Cl<sub>2</sub>):

δ [ppm] = 164.8 (C<sub>q</sub>), 164.0 (C<sub>q</sub>), 156.1 (C<sub>q</sub>), 150.8 (C<sub>q</sub>), 147.7 (C<sub>q</sub>), 147.3 (C<sub>q</sub>), 146.71 (C<sub>q</sub>), 146.70 (C<sub>q</sub>), 146.1 (C<sub>q</sub>), 146.0 (C<sub>q</sub>), 144.6 (C<sub>q</sub>), 144.0 (C<sub>q</sub>), 142.1 (C<sub>q</sub>), 141.6 (C<sub>q</sub>), 138.44 (C<sub>q</sub>), 138.41 (C<sub>q</sub>), 137.7 (C<sub>q</sub>), 137.2 (C<sub>q</sub>), 137.1 (C<sub>q</sub>), 135.5 (C<sub>q</sub>), 135.4 (C<sub>q</sub>), 134.9 (C<sub>q</sub>), 134.8 (C<sub>q</sub>), 133.6 (C<sub>q</sub>), 132.1 (CH), 132.0 (CH), 130.2 (C<sub>q</sub>), 130.1 (C<sub>q</sub>), 129.5 (CH), 129.3 (CH), 128.4 (CH), 128.3 (CH), 127.2 (C<sub>q</sub>), 127.1 (C<sub>q</sub>), 126.6 (CH), 126.5 (C<sub>q</sub>, CH), 125.1 (CH), 124.6 (CH), 124.09 (CH), 124.07 (C<sub>q</sub>), 123.9 (CH), 123.88 (CH), 123.87 (C<sub>q</sub>), 123.7 (CH), 123.4 (CH), 122.9 (CH), 120.1 (2 x CH), 114.9 (CH), 109.5 (CH), 109.4 (CH), 56.6 (2 x CH<sub>3</sub>), 55.8 (CH<sub>3</sub>), 54.2 (2 x CH), 50.8 (C<sub>q</sub>), 35.8 (C<sub>q</sub>), 34.6 (C<sub>q</sub>), 31.8 (CH<sub>3</sub>), 31.3 (CH<sub>3</sub>), 21.31 (CH<sub>3</sub>), 21.29 (CH<sub>3</sub>).

**MALDI-HRMS** (pos): m/z calc. [M]<sup>+</sup> 1297.52357, found [M]<sup>+</sup> 1297.52841, Δ = 3.73 ppm.

#### TAAMe<sub>2</sub>-TTCMe<sub>2</sub>-PDI



CA: [-]

Synthesis according to **GP III**.<sup>[163]</sup>

**(Bpin)-TTCMe<sub>2</sub>-PDI** (35.0 mg, 33.0 μmol), **TAAMe<sub>2</sub>-Br** (27.2 mg, 66.0 μmol), sodium carbonate (14.0 mg, 132 μmol) in THF (6 ml) and water (1.5 ml). Pd(PPh<sub>3</sub>)<sub>4</sub> (1.91 mg, 1.65 μmol). Column chromatography (eluent: DCM – DCM/EA (100:1)). The product was dissolved in DCM and precipitated by addition of hexane.

**Yield:** 4.00 mg (3.16 μmol, 10 %) of a red solid.



$C_{88}H_{71}N_3O_6$  [1266.53 g/mol]

**$^1H$ -NMR** (600.1 MHz,  $CD_2Cl_2$ ):

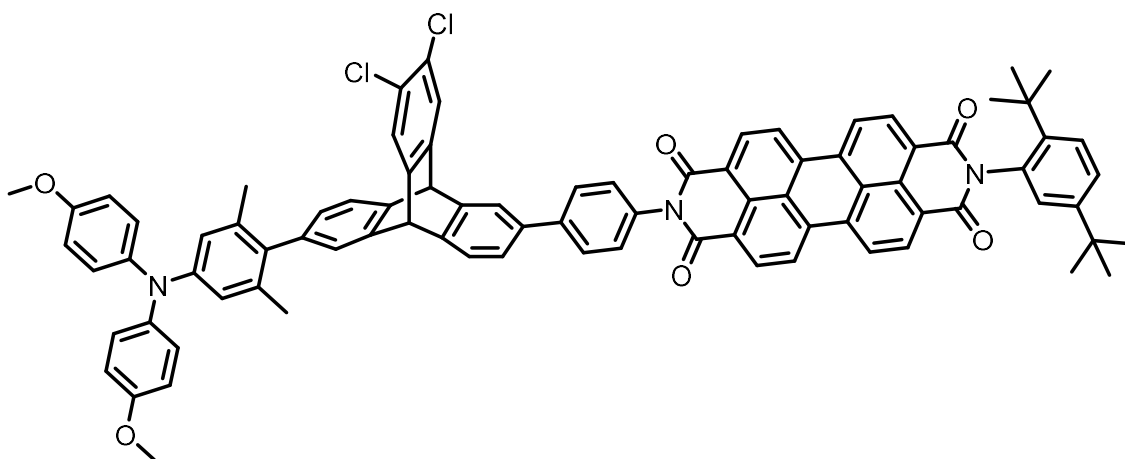
$\delta$  [ppm] = 8.74 (m', 8H), 7.74 (m', 3H), 7.63 (d,  $^3J_{H,H} = 8.7$  Hz, 1H), 7.49 (m', 3H), 7.40 (BB', 2H), 7.34 (dd,  $^3J_{H,H} = 7.6$  Hz,  $^4J_{H,H} = 1.8$  Hz, 1H), 7.24 (m', 3H), 7.07 (d,  $^4J_{H,H} = 2.3$  Hz, 1H), 7.04 (AA', 4H), 6.83 (m', 5H), 6.62 (s, 2H), 5.51 (s, 1H), 5.44 (s, 1H), 3.78 (s, 6H), 2.21 (s, 3H), 2.20 (s, 3H), 1.84 (s, 3H), 1.82 (s, 3H), 1.33 (s, 9H), 1.28 (s, 9H).

**$^{13}C$ -NMR** (150.9 MHz,  $CD_2Cl_2$ ):

$\delta$  [ppm] = 164.9 (C<sub>q</sub>), 164.0 (C<sub>q</sub>), 156.1 (C<sub>q</sub>), 150.8 (C<sub>q</sub>), 147.6 (C<sub>q</sub>), 147.1 (C<sub>q</sub>), 145.9 (C<sub>q</sub>), 145.8 (C<sub>q</sub>), 144.6 (C<sub>q</sub>), 143.8 (C<sub>q</sub>), 143.29 (C<sub>q</sub>), 143.26 (C<sub>q</sub>), 142.2 (C<sub>q</sub>), 141.6 (C<sub>q</sub>), 138.4 (C<sub>q</sub>), 137.8 (C<sub>q</sub>), 137.2 (C<sub>q</sub>), 137.1 (C<sub>q</sub>), 135.5 (C<sub>q</sub>), 135.4 (C<sub>q</sub>), 134.9 (2 x C<sub>q</sub>), 133.60 (C<sub>q</sub>), 133.59 (C<sub>q</sub>), 133.58 (C<sub>q</sub>), 132.1 (CH), 132.0 (CH), 130.23 (C<sub>q</sub>), 130.16 (C<sub>q</sub>), 129.4 (CH), 129.3 (CH), 128.4 (CH), 128.3 (CH), 127.2 (C<sub>q</sub>), 127.1 (C<sub>q</sub>), 126.8 (CH), 126.7 (CH), 126.5 (CH), 125.5 (CH), 125.4 (CH), 125.2 (CH), 124.6 (CH), 124.2 (CH), 124.1 (C<sub>q</sub>), 123.90 (CH), 123.89 (CH), 123.88 (C<sub>q</sub>), 123.81 (CH), 122.9 (CH), 120.11 (CH), 120.09 (CH), 114.9 (CH), 55.8 (CH<sub>3</sub>), 54.2 (CH), 54.0 (CH), 35.8 (C<sub>q</sub>), 34.6 (C<sub>q</sub>), 31.8 (CH<sub>3</sub>), 31.3 (CH<sub>3</sub>), 21.31 (CH<sub>3</sub>), 21.27 (CH<sub>3</sub>), 19.6 (2 x CH<sub>3</sub>).

**MALDI-HRMS** (pos): m/z calc. [M]<sup>+</sup> 1265.53374, found [M]<sup>+</sup> 1265.53127,  $\Delta = 1.95$  ppm.

### TAAMe<sub>2</sub>-TTCCl<sub>2</sub>-PDI



CA: [-]

Synthesis according to **GP III**.<sup>[163]</sup>

**Bpin-TTCCl<sub>2</sub>-PDI** (49.0 mg, 44.5  $\mu$ mol), **TAAMe<sub>2</sub>-Br** (36.7 mg, 89.0  $\mu$ mol), sodium carbonate (18.9 mg, 178  $\mu$ mol) in THF (6 ml) and water (1.5 ml). Pd(PPh<sub>3</sub>)<sub>4</sub> (2.57 mg, 2.22  $\mu$ mol). Column

chromatography (eluent: DCM – DCM/toluene (4:1) – DCM/toluene/EA (400:100:3)). The product was dissolved in DCM and precipitated by addition of hexane.

**Yield:** 26.0 mg (19.9  $\mu$ mol, 45 %) of a red solid.

$C_{86}H_{65}Cl_2N_3O_6$  [1307.36 g/mol]

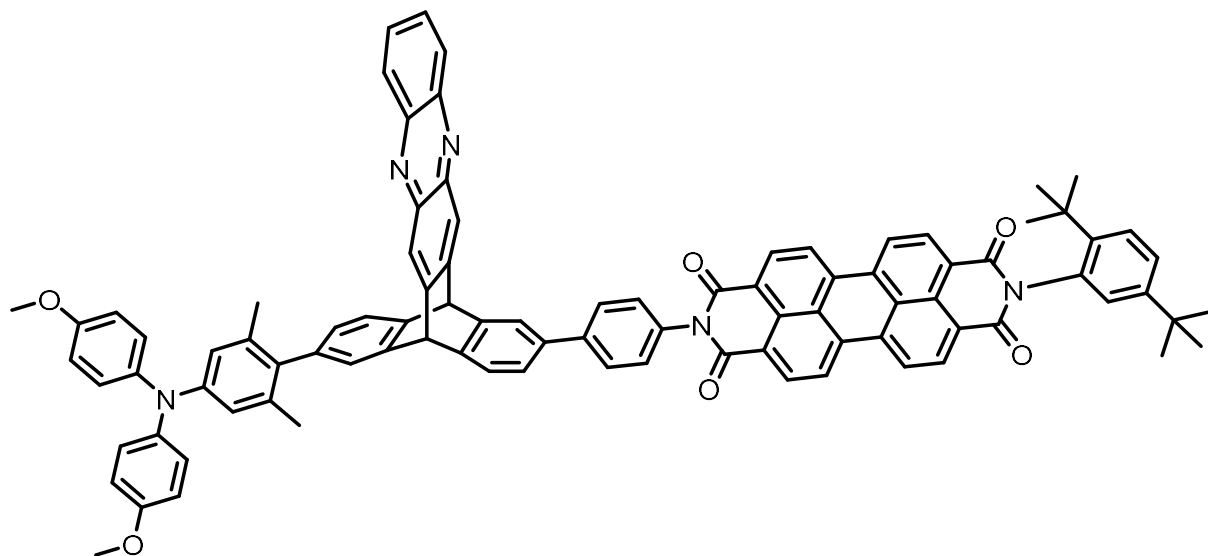
**$^1H$ -NMR** (600.1 MHz,  $CD_2Cl_2$ ):

$\delta$  [ppm] = 8.73 (m', 8H), 7.78 (d,  $^4J_{H,H} = 1.8$  Hz, 1H), 7.75 (AA', 2H), 7.62 (d,  $^3J_{H,H} = 8.7$  Hz, 1H), 7.55 (m', 5H), 7.42 (BB', 2H), 7.39 (dd,  $^3J_{H,H} = 7.5$  Hz,  $^4J_{H,H} = 1.8$  Hz, 1H), 7.25 (d,  $^4J_{H,H} = 1.5$  Hz, 1H), 7.09 (d,  $^3J_{H,H} = 2.2$  Hz, 1H), 7.04 (AA', 4H), 6.86 (dd,  $^3J_{H,H} = 7.5$  Hz,  $^4J_{H,H} = 1.7$  Hz, 1H), 6.83 (BB', 4H), 6.62 (s, 2H), 5.57 (s, 1H), 5.49 (s, 1H), 3.78 (s, 6H), 1.83 (s, 3H), 1.81 (s, 3H), 1.33 (s, 9H), 1.27 (s, 9H).

**$^{13}C$ -NMR** (150.9 MHz,  $CD_2Cl_2$ ):

$\delta$  [ppm] = 164.8 (C<sub>q</sub>), 164.0 (C<sub>q</sub>), 156.1 (C<sub>q</sub>), 150.8 (C<sub>q</sub>), 147.8 (C<sub>q</sub>), 146.2 (C<sub>q</sub>), 146.1 (C<sub>q</sub>), 145.7 (C<sub>q</sub>), 144.6 (2 x C<sub>q</sub>), 144.5 (C<sub>q</sub>), 142.5 (C<sub>q</sub>), 141.8 (2 x C<sub>q</sub>), 141.6 (C<sub>q</sub>), 139.1 (C<sub>q</sub>), 137.14 (C<sub>q</sub>), 137.06 (C<sub>q</sub>), 135.43 (C<sub>q</sub>), 135.36 (C<sub>q</sub>), 135.1 (C<sub>q</sub>), 134.5 (C<sub>q</sub>), 133.6 (C<sub>q</sub>), 132.04 (CH), 131.98 (CH), 130.2 (C<sub>q</sub>), 130.1 (C<sub>q</sub>), 129.5 (CH), 129.2 (CH), 128.79 (C<sub>q</sub>), 128.77 (C<sub>q</sub>), 128.4 (CH), 128.3 (CH), 127.4 (CH), 127.13 (C<sub>q</sub>), 127.07 (C<sub>q</sub>), 126.8 (CH), 126.5 (CH), 126.03 (CH), 126.00 (CH), 125.6 (CH), 125.1 (CH), 124.7 (CH), 124.2 (CH), 124.1 (C<sub>q</sub>), 123.89 (CH), 123.87 (CH), 123.84 (C<sub>q</sub>), 123.4 (CH), 120.01 (CH), 119.99 (CH), 114.9 (CH), 55.8 (CH<sub>3</sub>), 53.4 (CH), 53.2 (CH), 35.8 (C<sub>q</sub>), 34.6 (C<sub>q</sub>), 31.8 (CH<sub>3</sub>), 31.3 (CH<sub>3</sub>), 21.3 (CH<sub>3</sub>), 21.2 (CH<sub>3</sub>).

**MALDI-HRMS** (pos): m/z calc.  $[M]^+$  1307.42552, found  $[M]^+$  1307.42616,  $\Delta = 0.49$  ppm.

TAAMe<sub>2</sub>-TTCAZC-PDI

CA: [-]

Synthesis according to **GP III**.<sup>[163]</sup>

**Bpin-TTCAZC-PDI** (38.0 mg, 33.5  $\mu\text{mol}$ ), **TAAMe<sub>2</sub>-Br** (27.6 mg, 66.9  $\mu\text{mol}$ ) sodium carbonate (14.2 mg, 134  $\mu\text{mol}$ ) in THF (6 ml) and water (1.5 ml). Pd(PPh<sub>3</sub>)<sub>4</sub> (1.94 mg, 1.68  $\mu\text{mol}$ ) Column chromatography (eluent: DCM/EA (10:1)). The product was dissolved in DCM and precipitated by addition of hexane.

**Yield:** 14.0 mg (10.4  $\mu\text{mol}$ , 31 %) of a red solid.

C<sub>92</sub>H<sub>69</sub>N<sub>5</sub>O<sub>6</sub> [1340.57 g/mol]

**<sup>1</sup>H-NMR** (600.1 MHz, CD<sub>2</sub>Cl<sub>2</sub>):

$\delta$  [ppm] = 8.74 (m', 8H), 8.18 (m, 2H), 8.16 (s, 1H), 8.13 (s, 1H), 7.90 (d, <sup>4</sup>J<sub>H,H</sub> = 1.5 Hz, 1H), 7.78 (m', 4H), 7.67 (d, <sup>3</sup>J<sub>H,H</sub> = 7.9 Hz, 1H), 7.63 (m', 2H), 7.51 (dd, <sup>3</sup>J<sub>H,H</sub> = 8.7 Hz, <sup>4</sup>J<sub>H,H</sub> = 2.2 Hz, 1H), 7.48 (dd, <sup>3</sup>J<sub>H,H</sub> = 7.7 Hz, <sup>4</sup>J<sub>H,H</sub> = 1.7 Hz, 1H), 7.42 (AA', 2H), 7.37 (s, 1H), 7.07 (d, <sup>4</sup>J<sub>H,H</sub> = 2.3 Hz, 1H), 7.04 (AA', 4H), 6.95 (dd, <sup>3</sup>J<sub>H,H</sub> = 7.6 Hz, <sup>4</sup>J<sub>H,H</sub> = 1.5 Hz, 1H), 6.83 (BB', 4H), 6.62 (m, 2H), 5.87 (s, 1H), 5.79 (s, 1H), 3.78 (s, 6H), 1.87 (s, 3H), 1.77 (s, 3H), 1.33 (s, 9H), 1.28 (s, 9H).

**<sup>13</sup>C-NMR** (150.9 MHz, CD<sub>2</sub>Cl<sub>2</sub>):

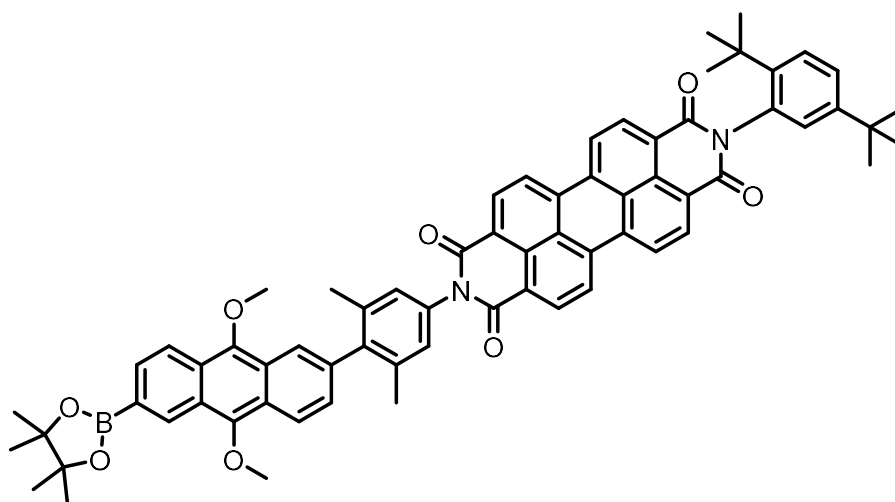
$\delta$  [ppm] = 164.9 (C<sub>q</sub>), 164.0 (C<sub>q</sub>), 156.1 (C<sub>q</sub>), 150.8 (C<sub>q</sub>), 147.8 (C<sub>q</sub>), 147.0 (C<sub>q</sub>), 146.97 (C<sub>q</sub>), 144.8 (C<sub>q</sub>), 144.6 (C<sub>q</sub>), 143.59 (C<sub>q</sub>), 143.58 (C<sub>q</sub>), 143.53 (C<sub>q</sub>), 143.45 (C<sub>q</sub>), 143.44 (C<sub>q</sub>), 141.8 (C<sub>q</sub>), 141.62 (C<sub>q</sub>), 141.57 (C<sub>q</sub>), 139.7 (C<sub>q</sub>), 139.0 (C<sub>q</sub>), 137.13 (C<sub>q</sub>), 137.05 (C<sub>q</sub>), 135.5 (C<sub>q</sub>),



**<sup>1</sup>H-NMR** (400.1 MHz, CDCl<sub>3</sub>):

$\delta$  [ppm] = 8.73 (m, 8H), 8.60 (s, 1H), 8.53 (s, 1H), 8.42 (s, 1H), 8.12 (m, 1H), 8.00 (m, 1H), 7.87 (m, 1H), 7.81 (m, 1H), 7.61 (d, <sup>3</sup>J = 8.7 Hz, 1H), 7.48 (dd, <sup>3</sup>J<sub>H,H</sub> = 8.7 Hz, <sup>4</sup>J<sub>H,H</sub> = 2.2 Hz, 1H), 7.38 (dd, <sup>3</sup>J<sub>H,H</sub> = 8.6 Hz, <sup>4</sup>J<sub>H,H</sub> = 1.6 Hz, 1H), 7.18 (s, 2H), 7.09 (d, <sup>4</sup>J<sub>H,H</sub> = 2.2 Hz, 1H), 2.18 (s, 6H), 1.44 (s, 12H), 1.34 (s, 9H), 1.31 (s, 9H).

**(Bpin)-ATC(OMe)<sub>2</sub>-PDIME<sub>2</sub>**



Synthesis according to literature.<sup>[163]</sup>

CA: [-]

Synthesis according to **GP III**.

**ATC(OMe)<sub>2</sub>-(Bpin)<sub>2</sub>** (100 mg, 204  $\mu$ mol), **PDIME<sub>2</sub>-I** (82.5 mg, 102  $\mu$ mol), sodium carbonate (43.2 mg, 408  $\mu$ mol) in THF (12 ml) and water (3 ml). Pd(PPh<sub>3</sub>)<sub>4</sub> (5.89 mg, 5.10  $\mu$ mol). Column chromatography on silica gel (eluent: DCM/EA (25:1)).

**Yield:** 24.0 mg (23.0  $\mu$ mol, 23 %) of a red solid.

C<sub>68</sub>H<sub>61</sub>BN<sub>2</sub>O<sub>8</sub> [1045.03 g/mol]

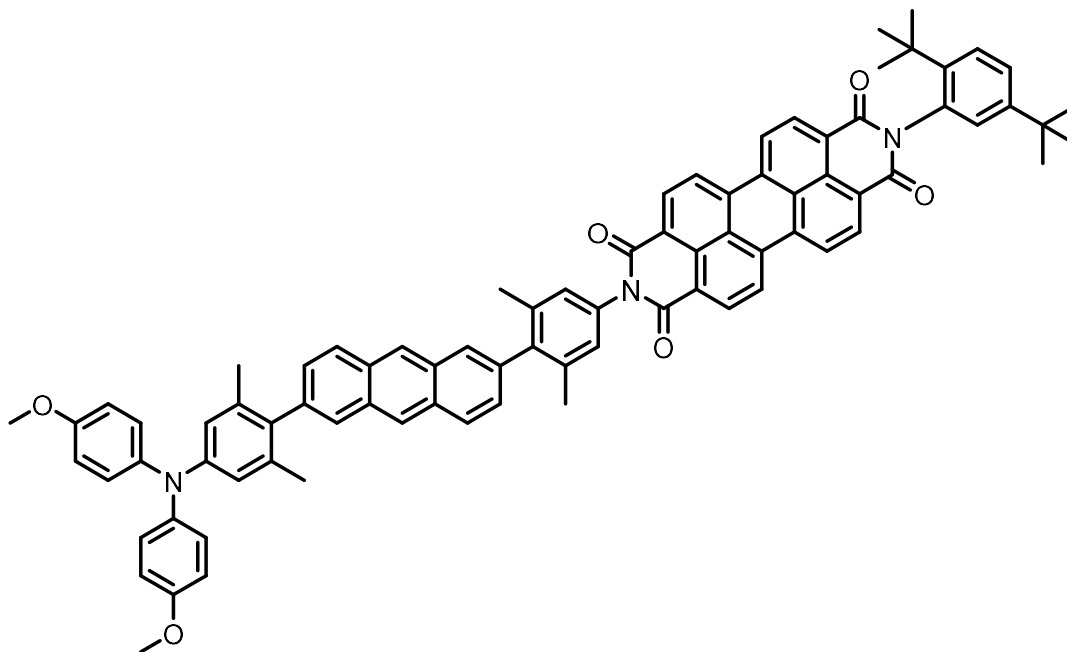
**<sup>1</sup>H-NMR** (400.1 MHz, CDCl<sub>3</sub>):

$\delta$  [ppm] = 8.79 (m', 9H), 8.42 (m, 1H), 8.28 (m, 1H), 8.20 (m, 1H), 7.85 (dd, <sup>3</sup>J<sub>H,H</sub> = 8.7 Hz, <sup>4</sup>J<sub>H,H</sub> = 1.0 Hz, 1H), 7.61 (d, <sup>3</sup>J<sub>H,H</sub> = 8.7 Hz, 1H), 7.48 (dd, <sup>3</sup>J<sub>H,H</sub> = 8.7 Hz, <sup>4</sup>J<sub>H,H</sub> = 2.3 Hz, 1H), 7.42 (dd, <sup>3</sup>J<sub>H,H</sub> = 8.8 Hz, <sup>4</sup>J<sub>H,H</sub> = 1.6 Hz, 1H), 7.19 (s, 2H), 7.05 (d, <sup>4</sup>J<sub>H,H</sub> = 2.2 Hz, 1H), 4.24 (s, 3H), 4.12 (s, 3H), 2.20 (s, 6H), 1.43 (s, 12H), 1.34 (s, 9H), 1.31 (s, 9H).<sup>41</sup>

**MALDI-MS** (pos): m/z calc. [M]<sup>+</sup> 1044.45265, found [M]<sup>+</sup> 1044.45285.

<sup>41</sup> No <sup>13</sup>C NMR and mass could be measured due to strong decomposition.

**TAAMe<sub>2</sub>-ATC-PDIME<sub>2</sub>**



Synthesis according to literature.<sup>[163]</sup>

CA: [-]

Synthesis according to **GP III**.

**(Bpin)<sub>2</sub>-ATC-PDIME<sub>2</sub>** (20.0 mg, 20.3 μmol), **TAAMe<sub>2</sub>-Br** (20.8 mg, 50.4 μmol), sodium carbonate (8.57 mg, 80.9 μmol) in THF (6 ml) and water (1.5 ml). Pd(PPh<sub>3</sub>)<sub>4</sub> (1.17 mg, 1.01 μmol). Column chromatography on silica gel (eluent: DCM – DCM/EA (500:3); toluene/EA (6:1)).

**Yield:** 7.80 mg (6.55 μmol, 32 %) of a red solid.

C<sub>82</sub>H<sub>67</sub>N<sub>3</sub>O<sub>6</sub> [1190.43 g/mol]

**<sup>1</sup>H-NMR** (400.1 MHz, CDCl<sub>3</sub>):

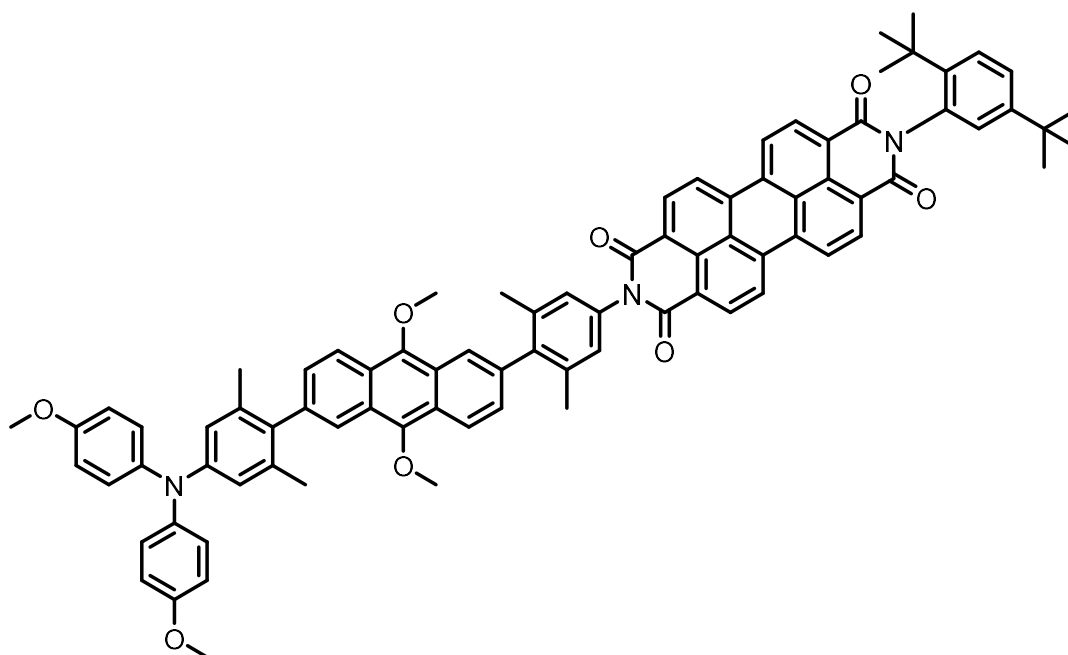
δ [ppm] = 8.78 (m', 10H), 8.44 (m, 1H), 8.38 (m, 1H), 8.28 (m, 1H), 8.16 (m, 1H), 7.78 (dd, <sup>3</sup>J<sub>H,H</sub> = 7.8 Hz, <sup>4</sup>J<sub>H,H</sub> = 1.7 Hz, 1H), 7.66 (dd, <sup>3</sup>J<sub>H,H</sub> = 7.8 Hz, <sup>4</sup>J<sub>H,H</sub> = 1.7 Hz, 1H), 7.63 (d, <sup>3</sup>J<sub>H,H</sub> = 8.7 Hz, 1H), 7.52 (dd, <sup>3</sup>J<sub>H,H</sub> = 8.7 Hz, <sup>4</sup>J<sub>H,H</sub> = 2.3 Hz, 1H), 7.18 (s, 2H), 7.09 (AA', 4H), 7.06 (d, <sup>4</sup>J<sub>H,H</sub> = 2.3 Hz, 1H), 6.87 (BB', 4H), 6.70 (s, 2H), 3.80 (s, 6H), 2.17 (s, 6H), 1.94 (s, 6H), 1.34 (s, 9H), 1.28 (s, 9H).

**<sup>13</sup>C-NMR** (100.6 MHz, CDCl<sub>3</sub>):

δ [ppm] = 183.5 (C<sub>q</sub>), 183.3 (C<sub>q</sub>), 164.9 (C<sub>q</sub>), 164.1 (C<sub>q</sub>), 156.4 (C<sub>q</sub>), 150.8 (C<sub>q</sub>), 148.7 (C<sub>q</sub>), 148.4 (C<sub>q</sub>), 147.2 (C<sub>q</sub>), 144.6 (C<sub>q</sub>), 141.3 (C<sub>q</sub>), 141.0 (C<sub>q</sub>), 137.6 (2 x C<sub>q</sub>), 136.6 (2 x C<sub>q</sub>), 136.3

(CH), 135.53 (C<sub>q</sub>), 135.49 (CH), 135.45 (C<sub>q</sub>), 134.4 (C<sub>q</sub>), 134.0 (C<sub>q</sub>), 133.6 (C<sub>q</sub>), 132.9 (C<sub>q</sub>), 132.4 (C<sub>q</sub>), 132.1 (CH, 2C), 132.0 (2 x CH), 130.3 (C<sub>q</sub>), 130.2 (C<sub>q</sub>), 129.3 (CH), 128.9 (CH), 128.3 (CH), 128.2 (CH), 128.04 (CH), 128.01 (CH, 2C), 127.7 (CH), 127.3 (C<sub>q</sub>), 127.2 (C<sub>q</sub>), 127.1 (CH), 126.6 (CH), 124.1 (C<sub>q</sub>), 124.0 (C<sub>q</sub>), 123.9 (2 x CH), 119.8 (2 x CH), 115.0 (CH), 55.8 (CH<sub>3</sub>), 35.8 (C<sub>q</sub>), 34.6 (C<sub>q</sub>), 31.8 (CH<sub>3</sub>), 31.3 (CH<sub>3</sub>), 21.14 (2 x CH<sub>3</sub>), 21.10 (2 x CH<sub>3</sub>).<sup>42</sup>

### TAAMe<sub>2</sub>-ATC(OMe)<sub>2</sub>-PDIMe<sub>2</sub>



CA: [-]

Synthesis according to **GP III**.<sup>[163]</sup>

**(Bpin)-ATC(OMe)<sub>2</sub>-PDIMe<sub>2</sub>** (20.0 mg, 19.1 μmol), **TAAMe<sub>2</sub>-Br** (15.8 mg, 38.3 μmol), sodium carbonate (8.10 mg, 76.4 mmol) in THF (3 ml) and water (750 μl). Pd(PPh<sub>3</sub>)<sub>4</sub> (1.10 mg, 952 nmol). Column chromatography on silica gel (eluent: DCM/EA (50:1); DCM/EA (50:1); DCM/toluene/EA (400:100:4)).

**Yield:** 7.00 mg (5.55 μmol, 29 %) of a red solid.

C<sub>84</sub>H<sub>71</sub>BN<sub>3</sub>O<sub>8</sub> [1261.29 g/mol]

**<sup>1</sup>H-NMR** (400.1 MHz, CDCl<sub>3</sub>):

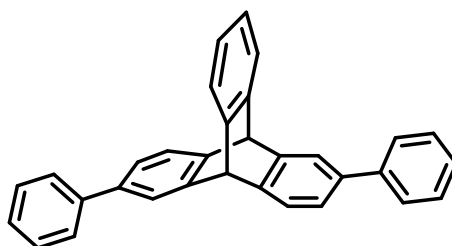
δ [ppm] = 8.76 (m', 8H), 8.43 (dd, <sup>3</sup>J<sub>H,H</sub> = 8.8 Hz, <sup>4</sup>J<sub>H,H</sub> = 0.6 Hz, 1H), 8.36 (dd, <sup>3</sup>J<sub>H,H</sub> = 8.8 Hz, <sup>4</sup>J<sub>H,H</sub> = 0.6 Hz, 1H), 8.23 (m, 1H), 8.11 (m, 1H), 7.63 (d, <sup>3</sup>J<sub>H,H</sub> = 8.6 Hz, 1H), 7.51 (dd,

<sup>42</sup> No mass due to strong decomposition.

$^3J_{H,H} = 8.7$  Hz,  $^4J_{H,H} = 2.3$  Hz, 1H), 7.47 (dd,  $^3J_{H,H} = 8.8$  Hz,  $^4J_{H,H} = 1.6$  Hz, 1H), 7.36 (dd,  $^3J_{H,H} = 8.8$  Hz,  $^4J_{H,H} = 1.6$  Hz, 1H), 7.19 (s, 2H), 7.10 (m', 5H), 6.87 (BB', 4H), 6.74 (s, 2H), 4.17 (s, 3H), 4.16 (s, 3H), 3.81 (s, 6H), 2.23 (s, 6H), 2.02 (s, 6H), 1.35 (s, 9H), 1.28 (s, 9H).<sup>43</sup>

#### 10.4.6 Synthesis of the references

##### TTC-Ph<sub>2</sub>



Synthesis according to literature.<sup>[163]</sup>

CA: [-]

Synthesis according to **GP III**.

**TTC-(Bpin)<sub>2</sub>** (20.0 mg, 39.5  $\mu$ mol), iodobenzene (20.2 mg, 99.0  $\mu$ mol), sodium carbonate (16.8 mg, 159  $\mu$ mol) in THF (6 ml) and water (1.5 ml). Pd(PPh<sub>3</sub>)<sub>4</sub> (2.28 mg, 1.97  $\mu$ mol). Column chromatography on silica gel (eluent: DCM/PE (50:5)).

**Yield:** 10.0 mg (24.6  $\mu$ mol, 62 %) of a colourless solid.

C<sub>32</sub>H<sub>22</sub> [406.52 g/mol]

**<sup>1</sup>H-NMR** (400.1 MHz, CDCl<sub>3</sub>):

$\delta$  [ppm] = 7.64 (d,  $^4J_{H,H} = 1.8$  Hz, 2H), 7.51 (m', 4H), 7.47 (d,  $^3J_{H,H} = 7.6$  Hz, 2H), 7.44 (m, 2H), 7.39 (m, 4H), 7.07 (s, 2H), 7.30 (m', 2H), 7.23 (dd,  $^3J_{H,H} = 7.6$  Hz,  $^4J_{H,H} = 1.8$  Hz, 2H), 5.53 (s, 2H).

**<sup>13</sup>C-NMR** (100.6 MHz, CDCl<sub>3</sub>):

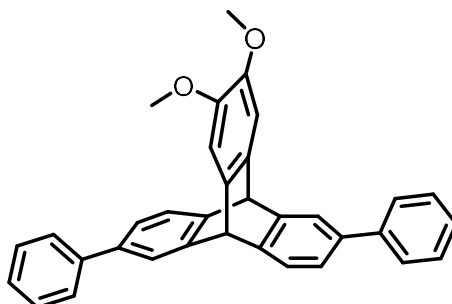
$\delta$  [ppm] = 145.9 (C<sub>q</sub>), 145.2 (C<sub>q</sub>), 144.4 (C<sub>q</sub>), 141.4 (C<sub>q</sub>), 138.8 (C<sub>q</sub>), 128.8 (CH), 127.4 (CH), 127.1 (CH), 125.5 (CH), 124.3 (CH), 124.1 (CH), 123.8 (CH), 122.9 (CH), 55.1 (CH).

**APCI-MS** (pos): m/z calc. [M+H]<sup>+</sup> 407.1794, found [M]<sup>+</sup> 407.1800.

---

<sup>43</sup> No <sup>13</sup>C NMR and mass could be measured because of strong decomposition.



**TTC(OMe)<sub>2</sub>-Ph<sub>2</sub>**

CA: [-]

Synthesis according to **GP III**.<sup>[163]</sup>

**TTC(OMe)<sub>2</sub>-(Bpin)<sub>2</sub>** (20.0 mg, 35.3  $\mu$ mol), iodobenzene (28.8 mg, 141  $\mu$ mol), sodium carbonate (15.0 mg, 142  $\mu$ mol) in THF (6 ml) and water (1.5 ml). Pd(PPh<sub>3</sub>)<sub>4</sub> (2.04 mg, 1.77  $\mu$ mol). Column chromatography on silica gel (eluent: DCM/PE (5:1)).

**Yield:** 12.0 mg (25.7  $\mu$ mol, 73 %) of a colourless solid.

C<sub>34</sub>H<sub>26</sub>O<sub>2</sub> [466.57 g/mol]

**<sup>1</sup>H-NMR** (400.1 MHz, CDCl<sub>3</sub>):

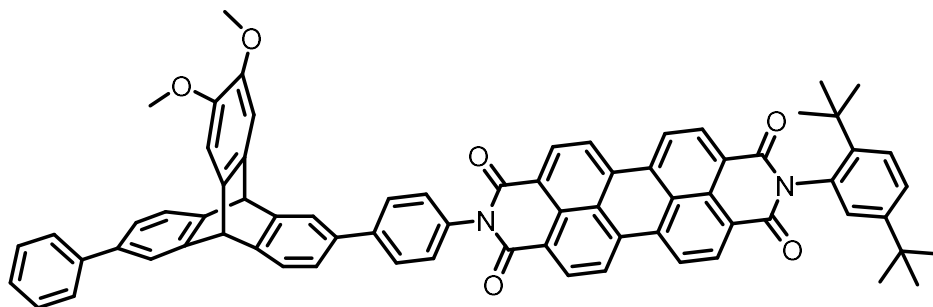
$\delta$  [ppm] = 7.62 (d, <sup>4</sup>J<sub>H,H</sub> = 1.8 Hz, 2H), 7.51 (m', 4H), 7.46 (d, <sup>3</sup>J<sub>H,H</sub> = 7.5 Hz, 2H), 7.39 (m', 4H), 7.30 (m, 2H), 7.22 (dd, <sup>3</sup>J<sub>H,H</sub> = 7.5 Hz, <sup>4</sup>J<sub>H,H</sub> = 1.8 Hz, 2H), 7.07 (s, 2H), 5.45 (s, 2H), 3.85 (s, 6H).

**<sup>13</sup>C-NMR** (100.6 MHz, CDCl<sub>3</sub>):

$\delta$  [ppm] = 146.34 (C<sub>q</sub>), 146.30 (C<sub>q</sub>), 144.8 (C<sub>q</sub>), 141.4 (C<sub>q</sub>), 138.7 (C<sub>q</sub>), 137.9 (C<sub>q</sub>), 128.8 (CH), 127.4 (CH), 127.1 (CH), 124.2 (CH), 123.8 (CH), 122.7 (CH), 108.7 (CH), 56.4 (CH<sub>3</sub>), 53.7 (CH).

**APCI-MS** (pos): m/z calc. [M+H]<sup>+</sup> 467.2006, found [M]<sup>+</sup> 467.2014.

**Ph-TTC(OMe)<sub>2</sub>-PDI**



CA: [-]

Synthesis according to **GP III**.<sup>[163]</sup>

**(Bpin)-TTC(OMe)<sub>2</sub>-PDI** (20.0 mg, 18.3  $\mu$ mol), iodobenzene (7.45 mg, 36.5  $\mu$ mol), sodium carbonate (7.74 mg, 73.0  $\mu$ mol) in THF (6 ml) and water (1.5 ml). Pd(PPh<sub>3</sub>)<sub>4</sub> (1.06 mg, 0.917  $\mu$ mol). Column chromatography on silica gel (eluent: DCM/EA (10:1), Toluene/EA (7:1)).

**Yield:** 10.0 mg (9.59  $\mu$ mol, 52 %) of a red solid.

C<sub>72</sub>H<sub>54</sub>N<sub>2</sub>O<sub>6</sub> [1043.21 g/mol]

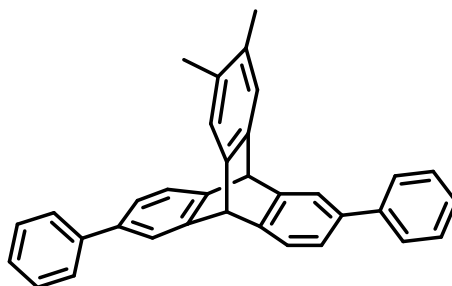
**<sup>1</sup>H-NMR** (400.1 MHz, CDCl<sub>3</sub>):

$\delta$  [ppm] = 8.73 (m', 8H), 7.70 (m', 3H), 7.65 (d, <sup>4</sup>J<sub>H,H</sub> = 1.7 Hz, 1H), 7.61 (d, <sup>3</sup>J<sub>H,H</sub> = 8.6 Hz, 1H), 7.51 (m', 5H), 7.40 (m', 4H), 7.30 (m', 2H), 7.24 (dd, <sup>3</sup>J<sub>H,H</sub> = 7.6 Hz, <sup>4</sup>J<sub>H,H</sub> = 1.7 Hz, 1H), 7.10 (s, 1H), 7.09 (s, 1H), 7.06 (dd, <sup>4</sup>J<sub>H,H</sub> = 2.2 Hz, 1H), 5.49 (s, 1H), 5.48 (s, 1H), 3.88 (s, 3H), 3.87 (s, 3H), 1.33 (s, 9H), 1.30 (s, 9H).

**<sup>13</sup>C-NMR** (100.6 MHz, CDCl<sub>3</sub>):

$\delta$  [ppm] = 164.5 (C<sub>q</sub>), 163.8 (C<sub>q</sub>), 150.3 (C<sub>q</sub>), 146.4 (C<sub>q</sub>), 146.35 (C<sub>q</sub>), 146.33 (C<sub>q</sub>), 146.30 (C<sub>q</sub>), 145.2 (C<sub>q</sub>), 144.8 (C<sub>q</sub>), 143.8 (C<sub>q</sub>), 142.2 (C<sub>q</sub>), 141.4 (C<sub>q</sub>), 138.7 (C<sub>q</sub>), 137.94 (C<sub>q</sub>), 137.87 (C<sub>q</sub>), 137.82 (C<sub>q</sub>), 135.3 (C<sub>q</sub>), 135.0 (C<sub>q</sub>), 134.1 (C<sub>q</sub>), 132.7 (C<sub>q</sub>), 132.07 (CH), 132.04 (CH), 130.00 (C<sub>q</sub>), 129.96 (C<sub>q</sub>), 129.0 (CH), 128.9 (CH), 128.8 (CH), 128.5 (CH), 127.9 (CH), 127.4 (CH), 127.3 (CH), 127.2 (CH), 126.91 (C<sub>q</sub>), 126.85 (C<sub>q</sub>), 126.6 (CH), 124.5 (CH), 124.3 (CH), 123.9 (C<sub>q</sub>), 123.87 (CH), 123.84 (CH), 123.545 (C<sub>q</sub>), 123.53 (CH), 123.45 (CH), 122.8 (CH), 122.7 (CH), 108.7 (CH), 56.4 (2 x CH), 53.8 (CH<sub>3</sub>), 53.7 (CH<sub>3</sub>), 35.7 (C<sub>q</sub>), 34.4 (C<sub>q</sub>), 31.9 (CH<sub>3</sub>), 31.4 (CH<sub>3</sub>).

**MALDI-MS** (pos): m/z calc. [M+H]<sup>+</sup> 1042.397639.

**TTCMe<sub>2</sub>-Ph<sub>2</sub>**

CA: [-]

Synthesis according to **GP III**.<sup>[163]</sup>

**TTCMe<sub>2</sub>-(Bpin)<sub>2</sub>** (20.0 mg, 37.4 μmol), iodobenzene (22.9 mg, 112 μmol), sodium carbonate (15.9 mg, 150 μmol) in THF (6 ml) and water (1.5 ml). Pd(PPh<sub>3</sub>)<sub>4</sub> (2.16 mg, 1.87 μmol). Column chromatography on silica gel (eluent: DCM/PE (1:8)).

**Yield:** 10.0 mg (23.0 μmol, 61 %) of a colourless solid.

C<sub>34</sub>H<sub>26</sub> [434.57 g/mol]

**<sup>1</sup>H-NMR** (400.1 MHz, CDCl<sub>3</sub>):

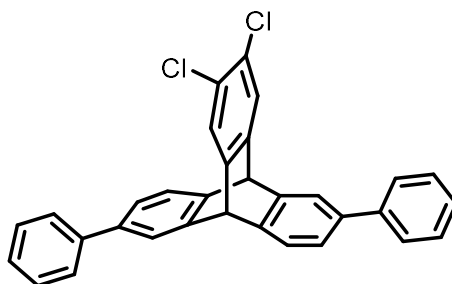
δ [ppm] = 7.61 (d, <sup>4</sup>J<sub>H,H</sub> = 1.8 Hz, 2H), 7.49 (m', 4H), 7.44 (d, <sup>3</sup>J<sub>H,H</sub> = 7.7 Hz, 2H), 7.38 (m', 4H), 7.29 (m, 2H), 7.24 (s, 2H), 7.20 (dd, <sup>3</sup>J<sub>H,H</sub> = 7.7 Hz, <sup>4</sup>J<sub>H,H</sub> = 1.8 Hz, 2H), 5.46 (s, 2H), 2.18 (s, 6H).

**<sup>13</sup>C-NMR** (100.6 MHz, CDCl<sub>3</sub>):

δ [ppm] = 146.2 (C<sub>q</sub>), 144.7 (C<sub>q</sub>), 142.8 (C<sub>q</sub>), 141.6 (C<sub>q</sub>), 138.7 (C<sub>q</sub>), 133.4 (C<sub>q</sub>), 128.8 (CH), 127.4 (CH), 127.1 (CH), 125.3 (CH), 124.2 (CH), 123.9 (CH), 122.8 (CH), 53.6 (CH), 19.7 (CH<sub>3</sub>).

**APCI-MS** (pos): m/z calc. [M+H]<sup>+</sup> 435.2107, found [M+H]<sup>+</sup> 435.2119.

## TTCCl<sub>2</sub>-Ph<sub>2</sub>



CA: [-]

Synthesis according to **GP III**.<sup>[163]</sup>

**TTCCl<sub>2</sub>-(Bpin)<sub>2</sub>** (20.0 mg, 34.8 μmol), iodobenzene (17.7 mg, 86.8 μmol) sodium carbonate (14.7 mg, 139 μmol) in THF (6 ml) and water (1.5 ml). Pd(PPh<sub>3</sub>)<sub>4</sub> (2.01 mg, 1.74 μmol) Column chromatography on silica gel (eluent: DCM/PE (1:5)).

**Yield:** 15.0 mg (31.6 μmol, 91 %) of a colourless solid.

C<sub>32</sub>H<sub>20</sub>Cl<sub>2</sub> [475.41 g/mol]

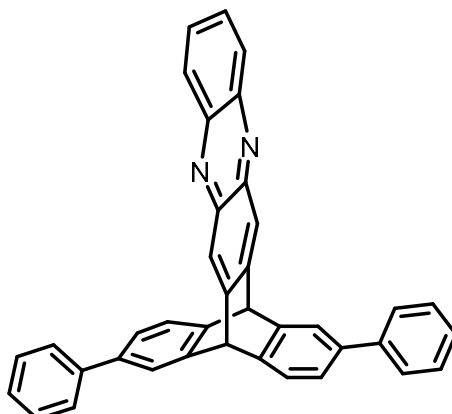
**<sup>1</sup>H-NMR** (400.1 MHz, CDCl<sub>3</sub>):

δ [ppm] = 7.39 (d, <sup>4</sup>J<sub>H,H</sub> = 1.8 Hz, 2H), 7.26 (m', 5H), 7.23 (d, <sup>3</sup>J<sub>H,H</sub> = 7.6 Hz, 2H), 7.16 (m', 4H), 7.07 (m', 2H), 7.02 (m', 3H), 5.23 (s, 2H).

**<sup>13</sup>C-NMR** (100.6 MHz, CDCl<sub>3</sub>):

δ [ppm] = 145.3 (C<sub>q</sub>), 144.9 (C<sub>q</sub>), 143.3 (C<sub>q</sub>), 141.1 (C<sub>q</sub>), 139.3 (C<sub>q</sub>), 128.9 (CH), 128.7 (C<sub>q</sub>), 127.36 (CH), 127.35 (CH), 125.8 (CH), 124.7 (CH), 124.3 (CH), 123.1 (CH), 53.1 (CH).

**APCI-MS** (pos): m/z calc. [M+H]<sup>+</sup> 475.1015, found [M+H]<sup>+</sup> 475.1019.

TTCAZC-Ph<sub>2</sub>

CA: [-]

Synthesis according to **GP III**.<sup>[163]</sup>

**TTCAZC-(Bpin)<sub>2</sub>** (23.0 mg, 37.8  $\mu$ mol), iodobenzene (30.9 mg, 151  $\mu$ mol), sodium carbonate (20.0 mg, 189  $\mu$ mol) in THF (6 ml) and water (1.5 ml). Pd(PPh<sub>3</sub>)<sub>4</sub> (2.18 mg, 1.89  $\mu$ mol). Column chromatography on silica gel (eluent: DCM).

**Yield:** 14.0 mg (27.5  $\mu$ mol, 73 %) of a yellow solid.

C<sub>38</sub>H<sub>24</sub>N<sub>2</sub> [508.61 g/mol]

**<sup>1</sup>H-NMR** (400.1 MHz, CDCl<sub>3</sub>):

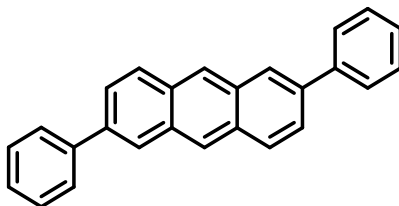
$\delta$  [ppm] = 8.19 (m, 2H), 8.14 (s, 2H), 7.77 (m', 4H), 7.60 (d, <sup>3</sup>J<sub>H,H</sub> = 7.8 Hz, 2H), 7.53 (m', 4H), 7.41 (m', 4H), 7.33 (m', 4H), 5.78 (s, 2H).

**<sup>13</sup>C-NMR** (100.6 MHz, CDCl<sub>3</sub>):

$\delta$  [ppm] = 146.4 (C<sub>q</sub>), 143.9 (C<sub>q</sub>), 143.2 (C<sub>q</sub>), 143.1 (C<sub>q</sub>), 142.3 (C<sub>q</sub>), 141.1 (C<sub>q</sub>), 139.9 (C<sub>q</sub>), 130.0 (CH), 129.6 (CH), 128.9 (CH), 127.42 (CH), 127.38 (CH), 125.4 (CH), 124.7 (CH), 123.4 (CH), 122.7 (CH), 53.5 (CH).

**APCI-MS** (pos): m/z calc. [M+H]<sup>+</sup> 509.2012, found [M+H]<sup>+</sup> 509.2008.

**ATC-Ph<sub>2</sub>**



CA: [95950-70-2]

Synthesis according to **GP III**.<sup>[163, 235]</sup>

**ATC-(Bpin)<sub>2</sub>** (50.0 mg, 116  $\mu\text{mol}$ ), iodobenzene (71.1 mg, 349  $\mu\text{mol}$ ), sodium carbonate (49.3 mg, 465  $\mu\text{mol}$ ) in THF (6 ml) and water (1.5 ml). Pd(PPh<sub>3</sub>)<sub>4</sub> (6.72 mg, 5.82  $\mu\text{mol}$ ). Column chromatography on silica gel (eluent: toluene/PE (1:4)). The product was recrystallized from CHCl<sub>3</sub>/EtOH (1:1).

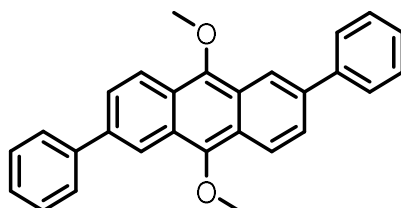
**Yield:** 14.0 mg (42.4  $\mu\text{mol}$ , 37 %) of a yellow solid.

C<sub>26</sub>H<sub>18</sub> [330.42 g/mol]

**<sup>1</sup>H-NMR** (400.1 MHz, CDCl<sub>3</sub>):

$\delta$  [ppm] = 8.50 (s, 2H), 8.22 (d, <sup>4</sup>J<sub>H,H</sub> = 1.8 Hz, 2H), 8.10 (d, <sup>3</sup>J<sub>H,H</sub> = 8.8 Hz, 2H), 7.79 (m', 6H), 7.52 (m', 4H), 7.42 (m, 2H).

**APCI-MS** (pos): m/z calc. [M+H]<sup>+</sup> 331.1481, found [M]<sup>+</sup> 331.1487.

**ATC(OMe)<sub>2</sub>-Ph<sub>2</sub>**

CA: [-]

Synthesis according to **GP III**.<sup>[163]</sup>

**ATC(OMe)<sub>2</sub>-(Bpin)<sub>2</sub>** (50.0 mg, 102  $\mu$ mol), iodobenzene (62.4 mg, 306  $\mu$ mol), sodium carbonate (43.2 mg, 408  $\mu$ mol) in THF (6 ml) and water (1.5 ml). Pd(PPh<sub>3</sub>)<sub>4</sub> (5.89 mg, 5.10  $\mu$ mol). Column chromatography on silica gel (eluent: DCM/PE (1:1)). The product was recrystallized from CHCl<sub>3</sub>/EtOH (v/v 1:1, 2 ml).

**Yield:** 24.0 mg (61.5  $\mu$ mol, 60 %) of a yellow solid.

C<sub>28</sub>H<sub>22</sub>O<sub>2</sub> [390.47 g/mol]

**<sup>1</sup>H-NMR** (400.1 MHz, CDCl<sub>3</sub>):

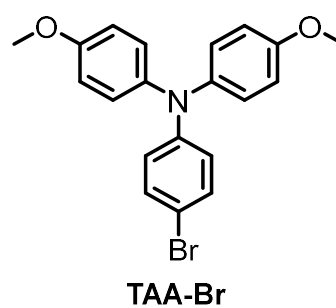
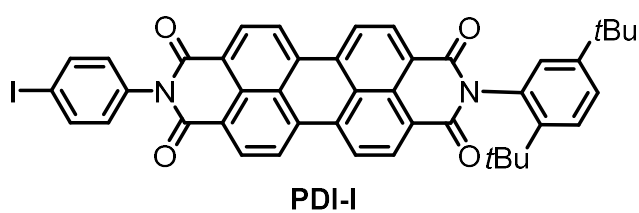
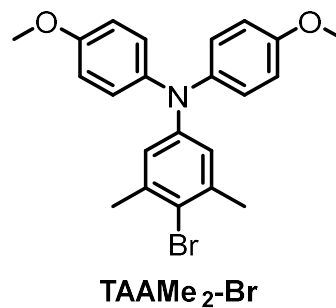
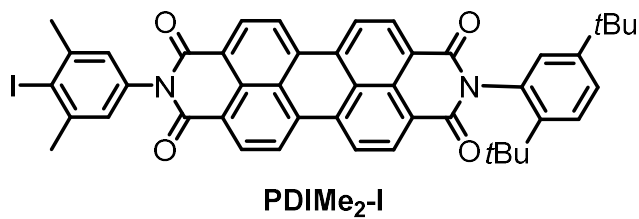
$\delta$  [ppm] = 8.49 (d, <sup>4</sup>J<sub>H,H</sub> = 1.4 Hz, 2H), 8.39 (d, <sup>3</sup>J<sub>H,H</sub> = 9.2 Hz, 2H), 7.81 (m', 6H), 7.54 (m', 4H), 7.42 (m', 2H), 4.19 (s, 6H).

**APCI-MS** (pos): m/z calc. [M+H]<sup>+</sup> 391.1693, found [M+H]<sup>+</sup> 331.1696.<sup>44</sup>

<sup>44</sup> No <sup>13</sup>C NMR could be measured because of strong decomposition during the measurement.

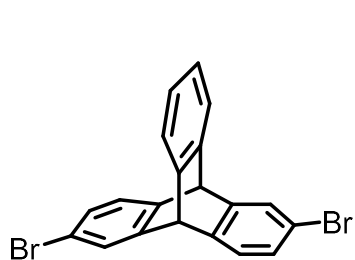
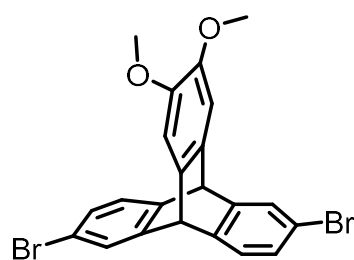
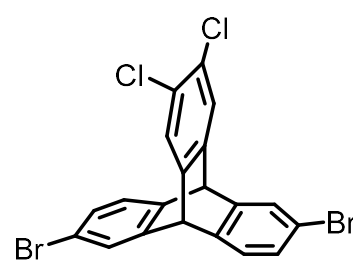
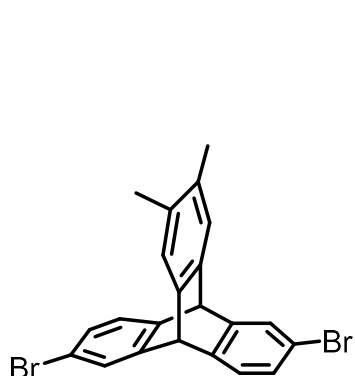
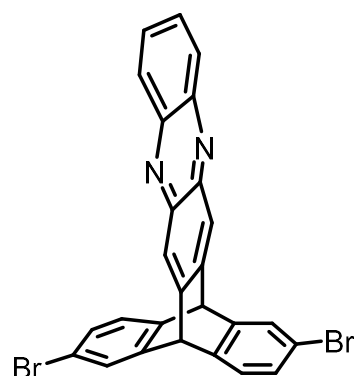
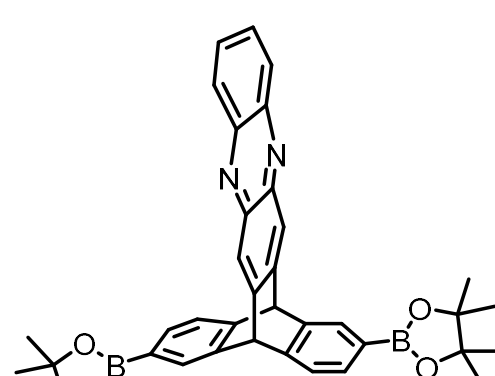
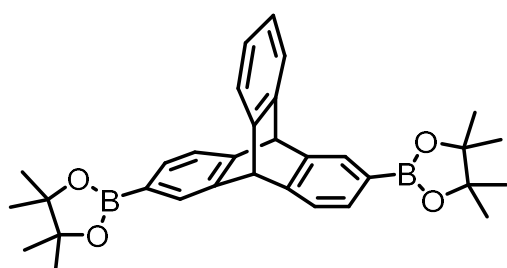
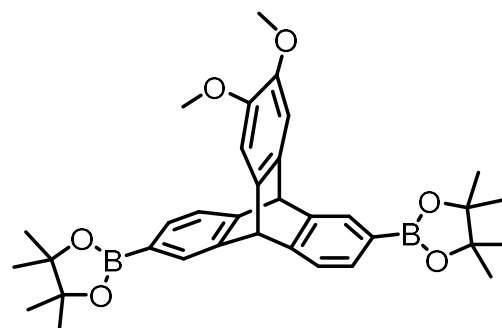
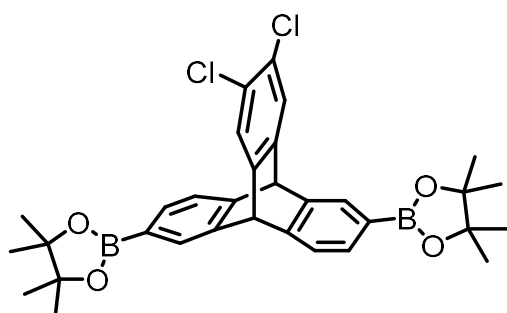
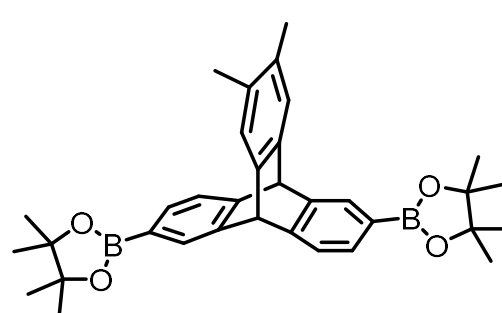
## 11 Table of formulas

### Donors and acceptors

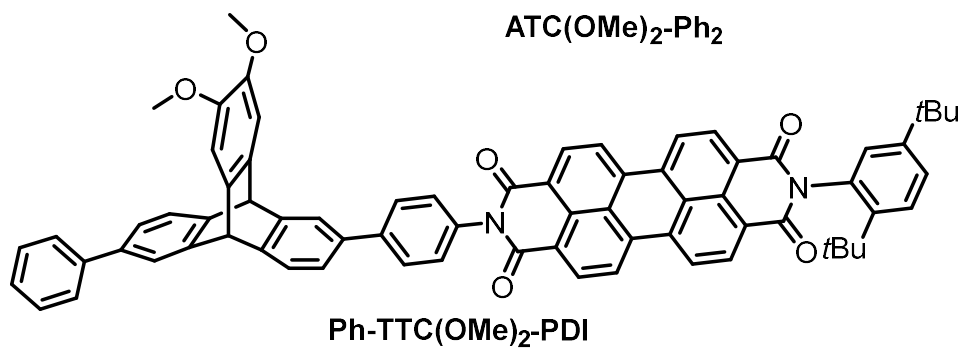
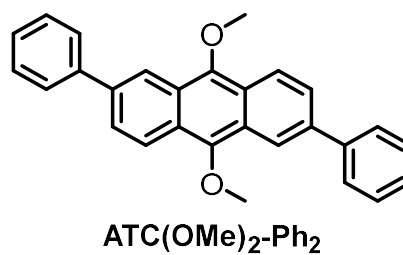
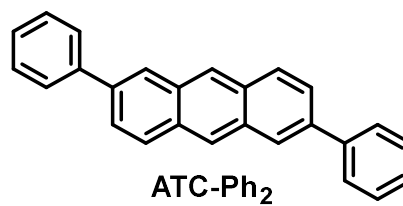
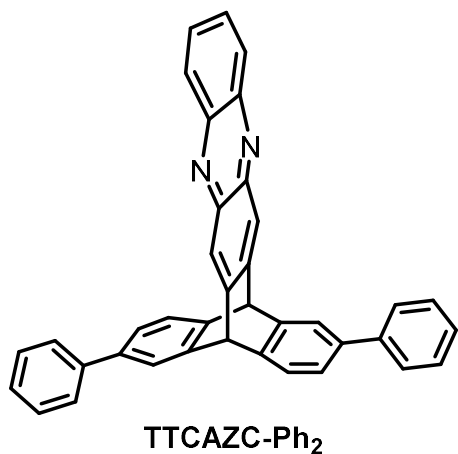
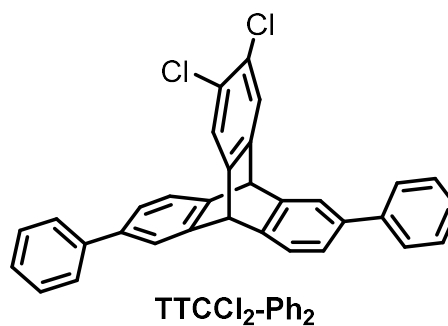
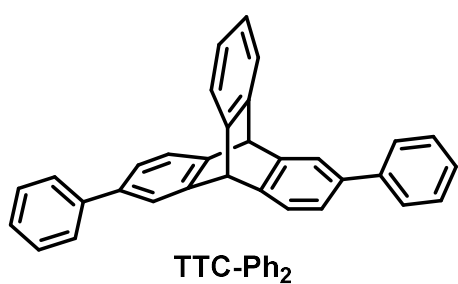
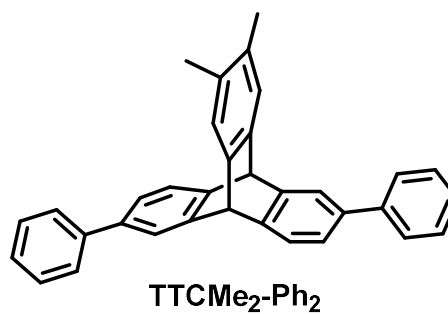
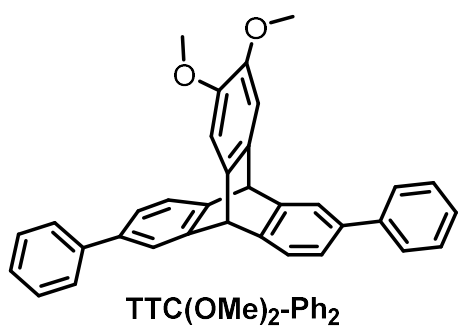




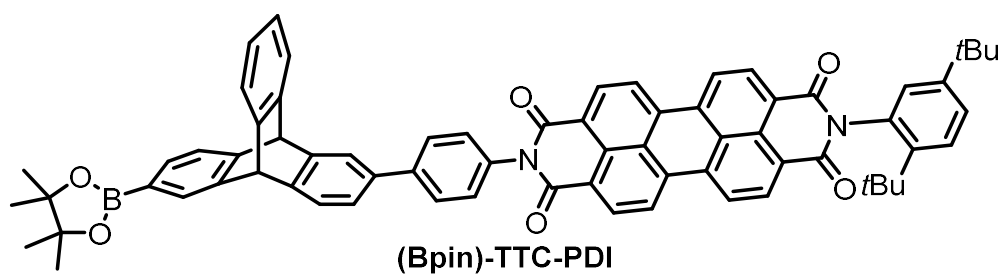
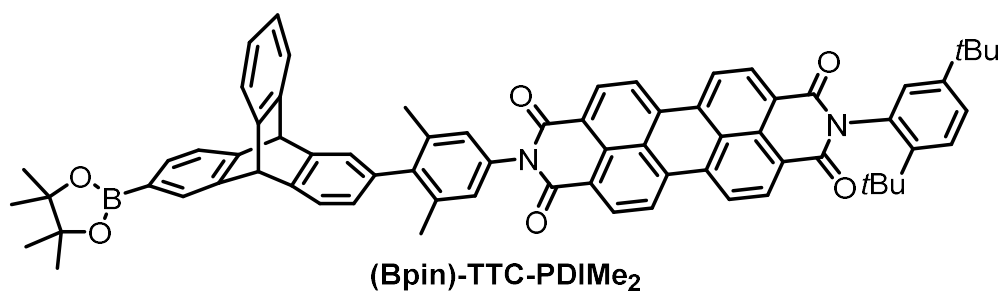
## Triptycene bridges

TTC-Br<sub>2</sub>TTC(OMe)<sub>2</sub>-Br<sub>2</sub>TTCCl<sub>2</sub>-Br<sub>2</sub>TTCMe<sub>2</sub>-Br<sub>2</sub>TTCAZC-Br<sub>2</sub>TTCAZC-(Bpin)<sub>2</sub>TTC-(Bpin)<sub>2</sub>TTC(OMe)<sub>2</sub>-(Bpin)<sub>2</sub>TTCCl<sub>2</sub>-Br<sub>2</sub>TTCMe<sub>2</sub>-Br<sub>2</sub>

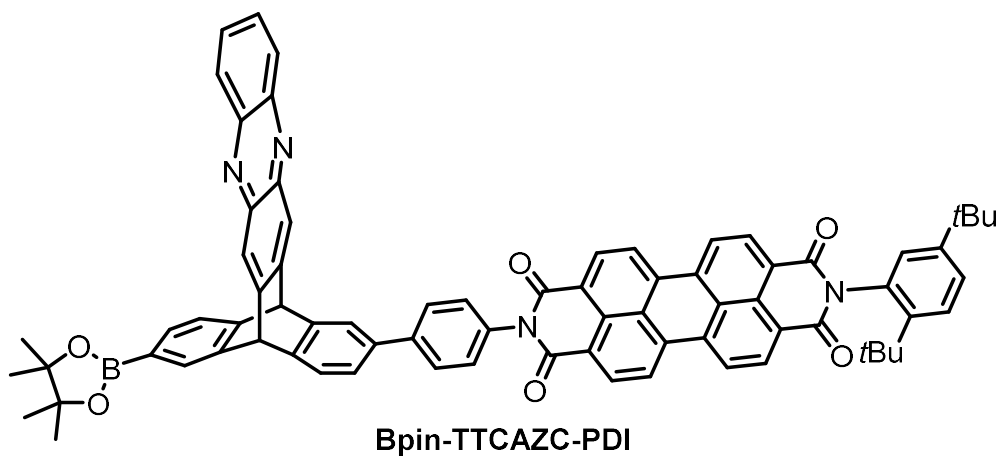
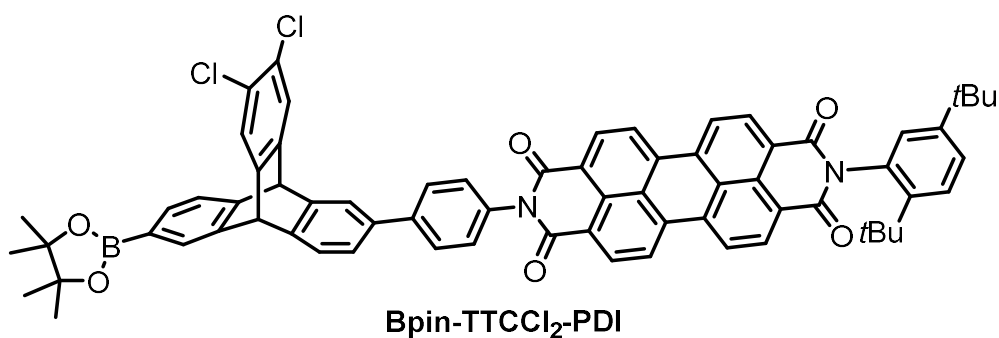
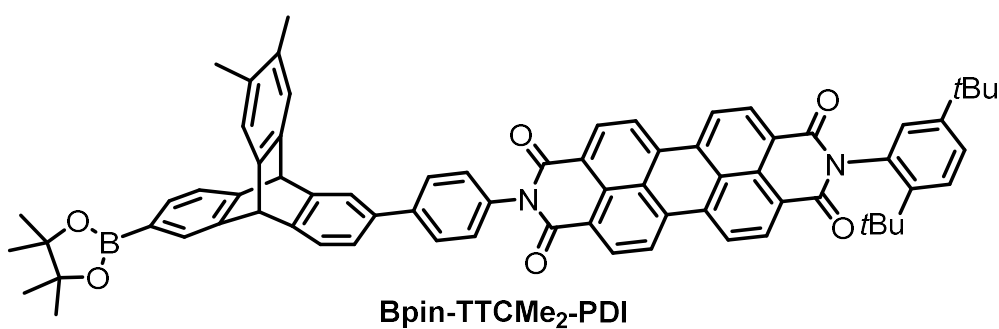
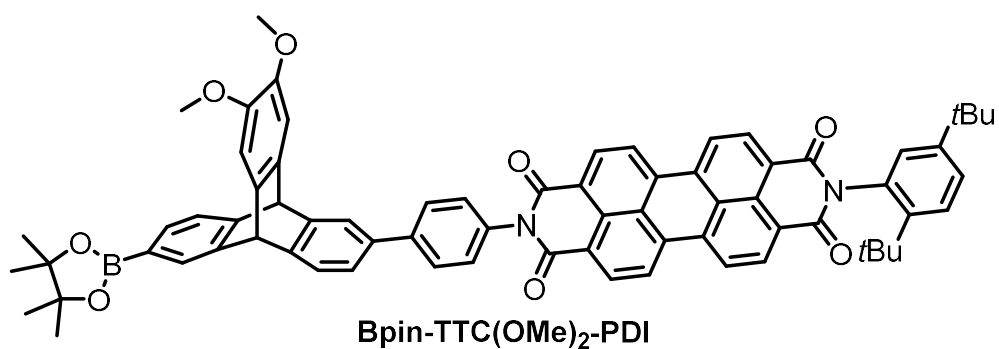
Reference compounds



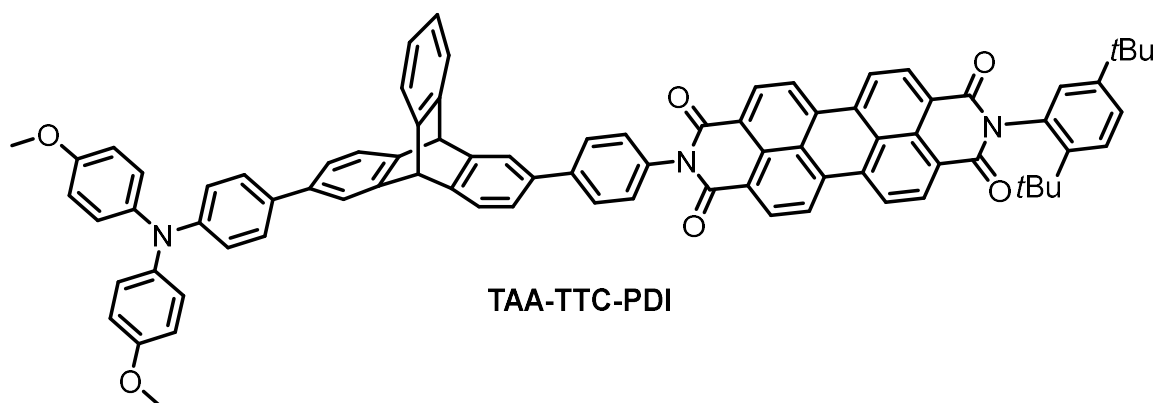
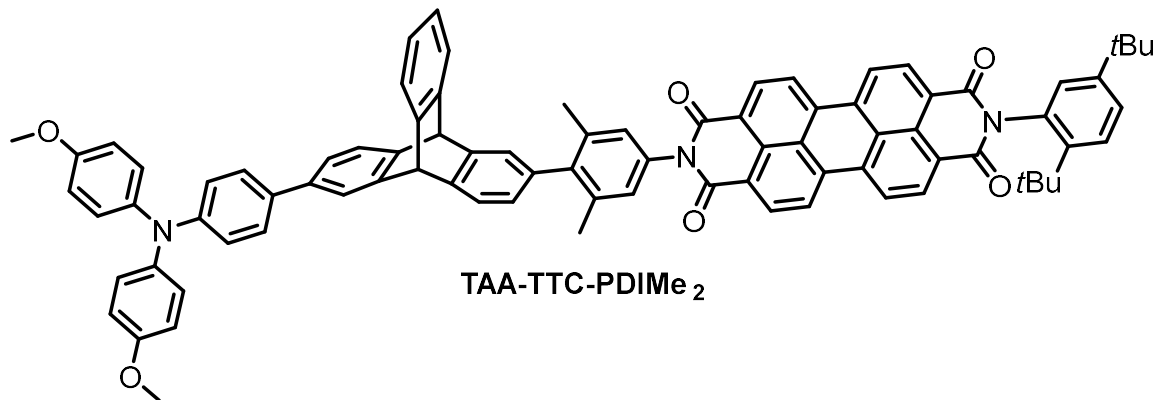
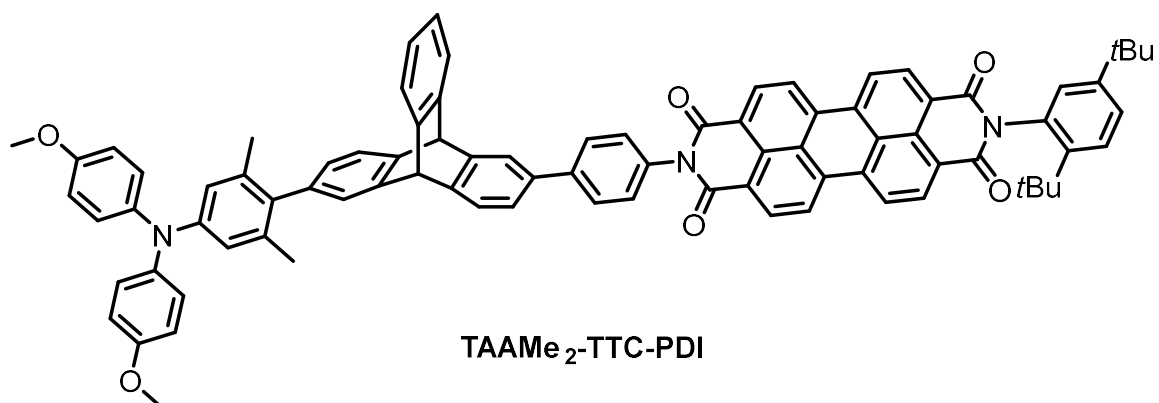
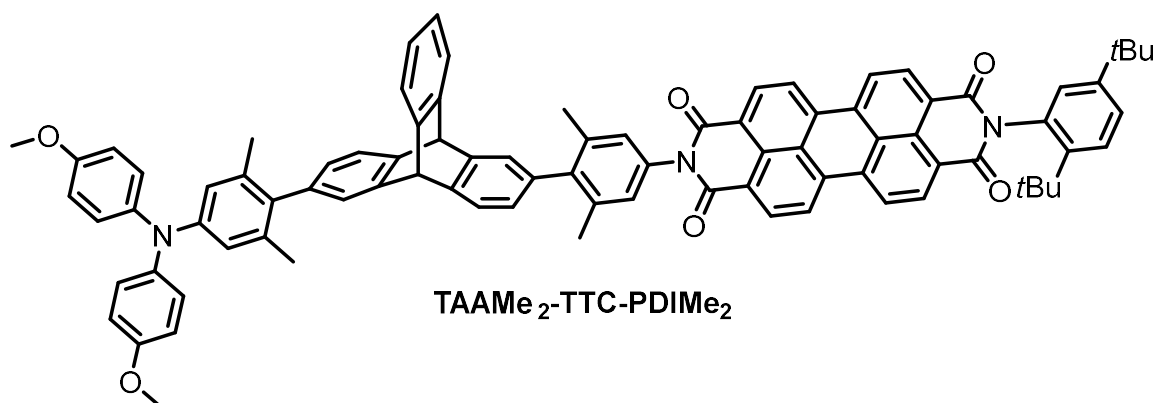
## Bridges coupled to PDI moiety of the rotationally hindered triads



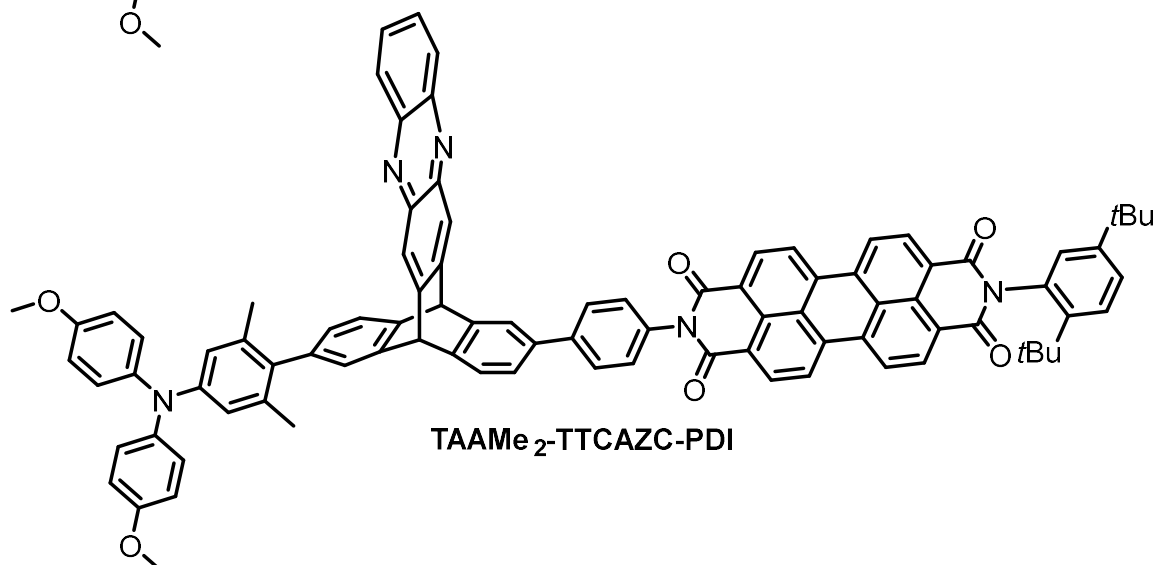
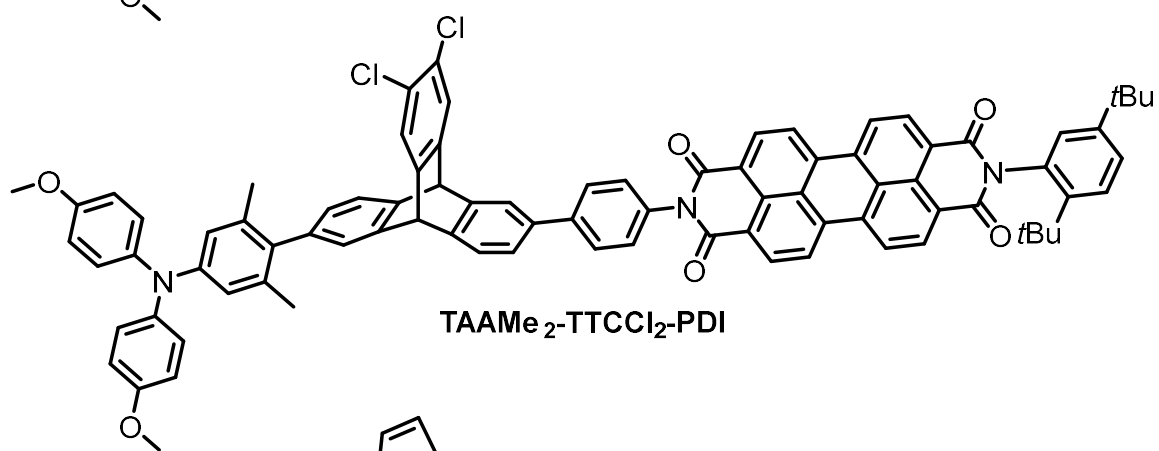
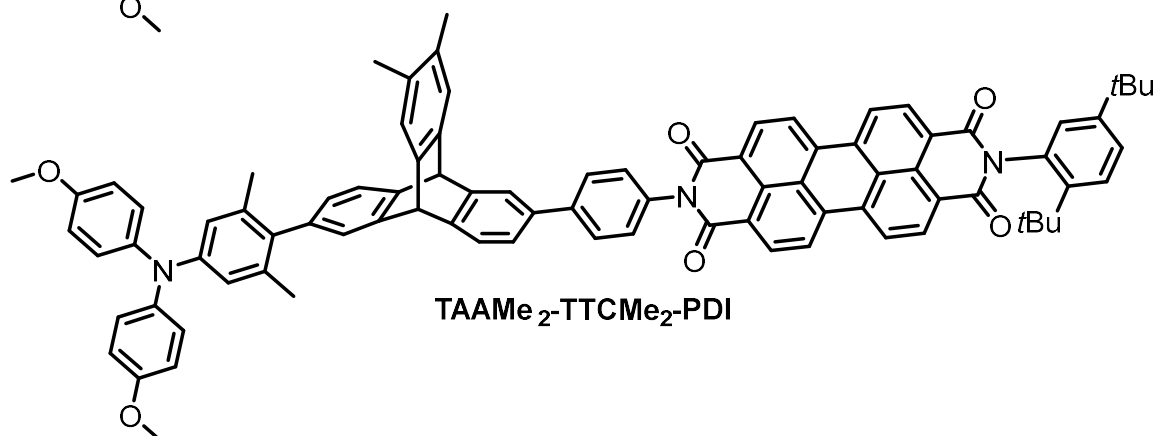
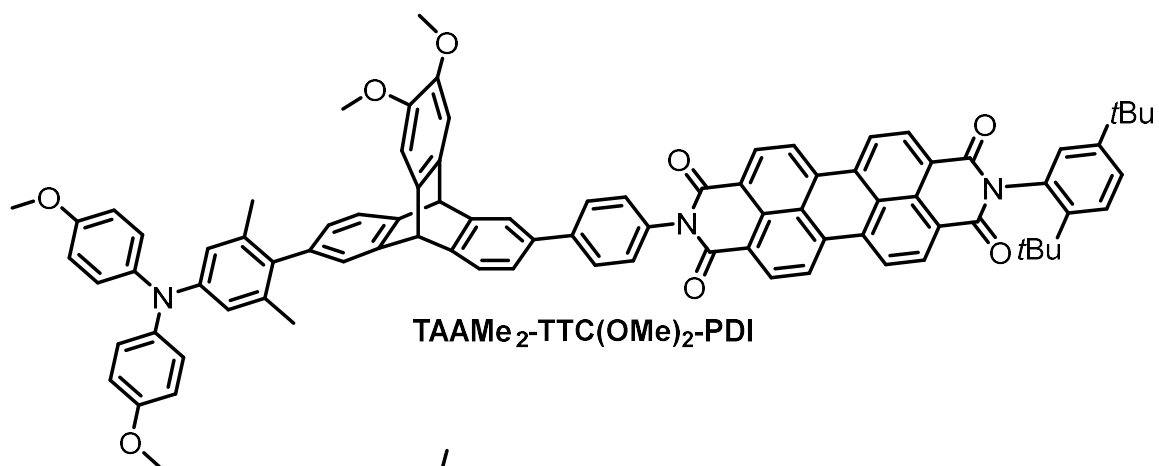
Bridges coupled to PDI moiety of the substituted triptycene triads



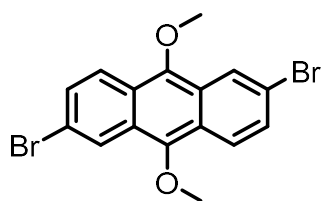
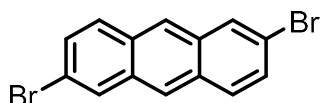
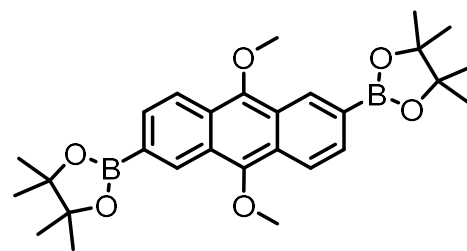
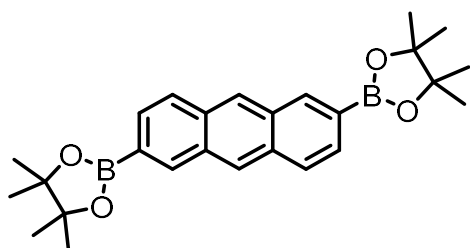
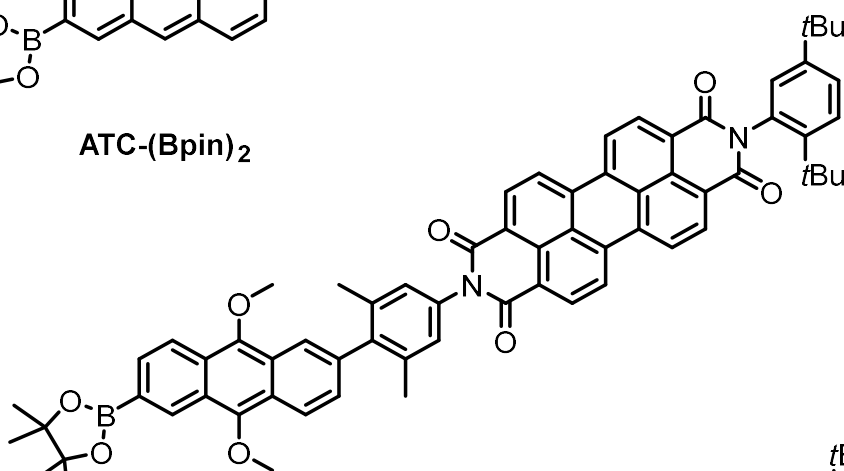
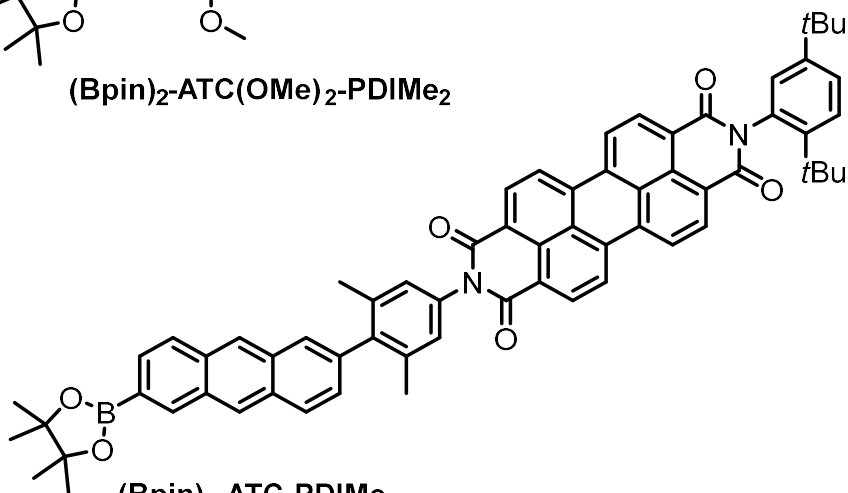
## Rotationally hindered triads



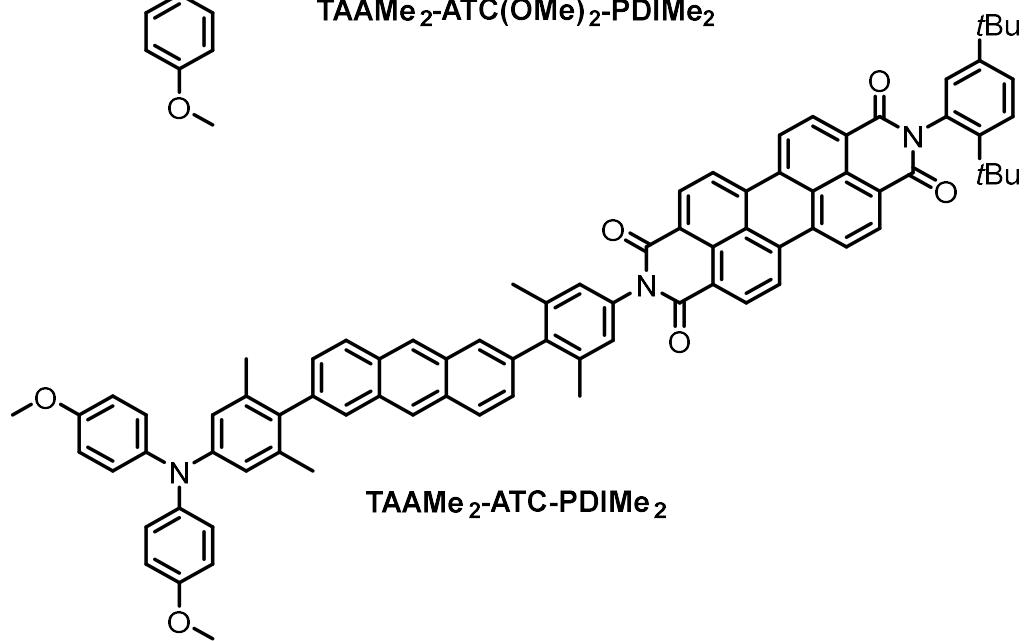
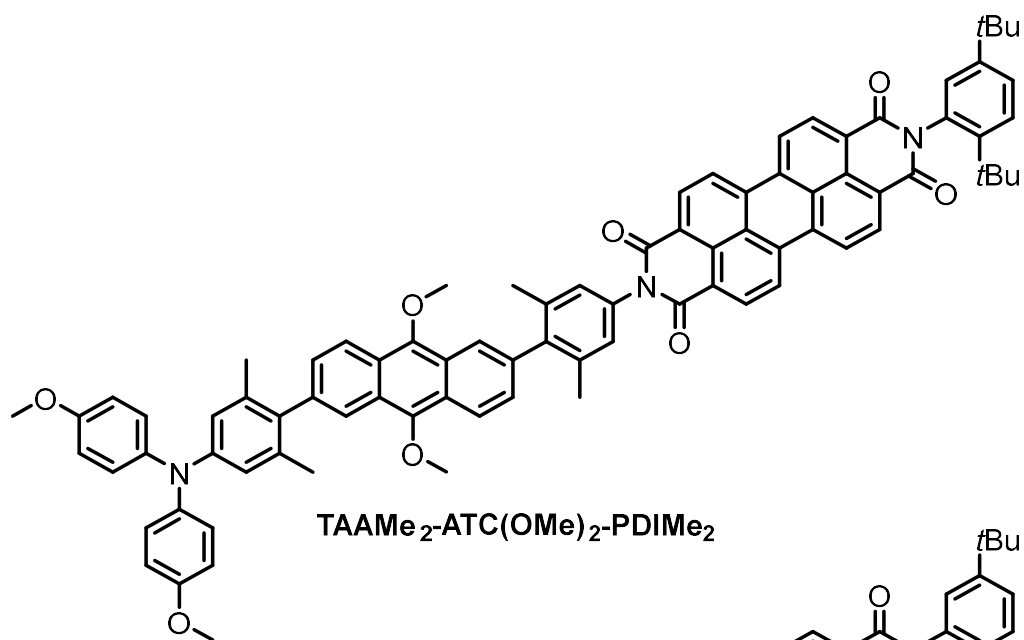
Substituted triptycene triads



## Anthracene bridges and bridges coupled to the PDI moiety

ATC(OMe)<sub>2</sub>-Br<sub>2</sub>ATC-Br<sub>2</sub>ATC(OMe)<sub>2</sub>-(Bpin)<sub>2</sub>ATC-(Bpin)<sub>2</sub>(Bpin)<sub>2</sub>-ATC(OMe)<sub>2</sub>-PDIME<sub>2</sub>(Bpin)<sub>2</sub>-ATC-PDIME<sub>2</sub>

### Anthracene bridge triads





## 12 Literature

- [1] P. J. Hore, H. Mouritsen, *Annu. Rev. Biophys.* **2016**, *45*, 299-344.
- [2] V. Krishnan, *Resonance* **1997**, *2*, 77-86.
- [3] C. T. Rodgers, P. J. Hore, *PNAS* **2009**, *106*, 353-360.
- [4] P. Schertl, H.-P. Braun, *Front. Plant Sci.* **2014**, *5*.
- [5] P. Joliot, A. Joliot, *PNAS* **2002**, *99*, 10209-10214.
- [6] R. E. Blankenship, W. W. Parson, *Annu. Rev. Biochem.* **1978**, *47*, 635-653.
- [7] E. Stevens, M. L. Marco, *FEMS Microbiology Reviews* **2023**, *47*, fuad019.
- [8] K. Krab, M. J. Wagner, A. M. Wagner, I. M. Møller, *Eur. J. Biochem.* **2000**, *267*, 869-876.
- [9] M. Hervás, J. A. Navarro, M. A. De la Rosa, *Acc. Chem. Res.* **2003**, *36*, 798-805.
- [10] W. Leibl, P. Mathis, *Series on photoconversion of solar energy* **2004**, *2*, 117.
- [11] G. McDermott, S. Prince, A. Freer, A. Hawthornthwaite-Lawless, M. Papiz, R. Cogdell, N. Isaacs, *Nature* **1995**, *374*, 517-521.
- [12] M. Medina, *The FEBS journal* **2009**, *276*, 3942-3958.
- [13] J. Deisenhofer, O. Epp, K. Miki, R. Huber, H. Michel, *Nature* **1985**, *318*, 618-624.
- [14] R. Huber, *Angew. Chem.* **1989**, *101*, 849-871.
- [15] J. Deisenhofer, H. Michel, *Angew. Chem.* **1989**, *101*, 872-892.
- [16] L. M. Utschig, D. M. Tiede, O. G. Poluektov, *Biochem.* **2010**, *49*, 9682-9684.
- [17] S. N. Datta, B. Mallik, *Int. J. Quantum Chem* **1997**, *61*, 865-879.
- [18] M. M. Walker, C. E. Diebel, C. V. Haugh, P. M. Pankhurst, J. C. Montgomery, C. R. Green, *Nature* **1997**, *390*, 371-376.
- [19] D. Presti, J. D. Pettigrew, *Nature* **1980**, *285*, 99-101.
- [20] J. L. Kirschvink, J. L. Gould, *Biosyst.* **1981**, *13*, 181-201.
- [21] R. Wiltschko, W. Wiltschko, *Bioessays* **2006**, *28*, 157-168.
- [22] N. F. Putman, *J. Comp. Physiol.* **2022**, *208*, 1-7.
- [23] G. C. Nordmann, T. Hochstoeger, D. A. Keays, *PLoS biology* **2017**, *15*, e2003234.
- [24] S. Krichen, L. Liu, P. Sharma, *Phys. Rev. E* **2017**, *96*, 042404.
- [25] S. Johnsen, K. J. Lohmann, **2008**.
- [26] R. Wiltschko, W. Wiltschko, *J. R. Soc. Interface.* **2019**, *16*, 20190295.
- [27] H. Hayashi, *J. Chin. Chem. Soc.* **2002**, *49*, 137-160.
- [28] J. Woodward, T. Foster, A. Jones, A. Salaoru, N. Scrutton, *Biochem. Soc. Trans.* **2009**, *37*, 358-362.
- [29] K. L. Ivanov, A. Wagenpfahl, C. Deibel, J. Matysik, *Beilstein J. Nanotechnol.* **2017**, *8*, 1427-1445.
- [30] B. Brocklehurst, *Chem. Soc. Rev.* **2002**, *31*, 301-311.
- [31] U. E. Steiner, T. Ulrich, *Chem. Rev.* **1989**, *89*, 51-147.
- [32] I. K. Kominis, *Mod. Phys. Lett. B* **2015**, *29*, 1530013.
- [33] W. Wiltschko, F. W. Merkel, *Verh. Dtsch. Zool. Ges* **1966**, *59*, 362-367.
- [34] W. Wiltschko, *Z. Tierpsychol.* **1968**, *25*, 537-558.
- [35] W. Wiltschko, R. Wiltschko, *Science* **1972**, *176*, 62-64.
- [36] W. Wiltschko, R. Wiltschko, *J. Exp. Biol.* **1996**, *199*, 29-38.
- [37] K. J. Lohmann, C. M. Lohmann, *Nature* **1996**, *380*, 59-61.
- [38] M. Deutschlander, S. Borland, J. Phillips, *Nature* **1999**, *400*, 324-325.
- [39] J. Phillips, O. Sayeed, *J. Comp. Physiol.* **1993**, *172*, 303-308.
- [40] S. D. Cain, L. C. Boles, J. H. Wang, K. J. Lohmann, *Integr. Comp. Biol.* **2005**, *45*, 539-546.
- [41] S. Marhold, W. Wiltschko, H. Burda, *Naturwissenschaften* **1997**, *84*, 421-423.
- [42] T. Ritz, S. Adem, K. Schulten, *Biophys. J.* **2000**, *78*, 707-718.
- [43] K. Maeda, K. B. Henbest, F. Cintolesi, I. Kuprov, C. T. Rodgers, P. A. Liddell, D. Gust, C. R. Timmel, P. J. Hore, *Nature* **2008**, *453*, 387-390.
- [44] K. Maeda, A. J. Robinson, K. B. Henbest, H. J. Hogben, T. Biskup, M. Ahmad, E. Schleicher, S. Weber, C. R. Timmel, P. J. Hore, *PNAS* **2012**, *109*, 4774-4779.

- [45] E. W. Evans, C. A. Dodson, K. Maeda, T. Biskup, C. Wedge, C. R. Timmel, *Interface focus* **2013**, 3, 20130037.
- [46] C. R. Timmel, K. B. Henbest, *Proc. R. Soc. A: Math. Phys. Eng. Sci.* **2004**, 362, 2573-2589.
- [47] J. Schäfer, M. Holzapfel, A. Schmiedel, U. E. Steiner, C. Lambert, *Phys. Chem. Chem. Phys.* **2018**, 20, 27093-27104.
- [48] D. Mims, A. Schmiedel, M. Holzapfel, N. N. Lukzen, C. Lambert, U. E. Steiner, *J. Chem. Phys.* **2019**, 151, 244308.
- [49] M. T. Colvin, A. B. Ricks, A. M. Scott, A. L. Smeigh, R. Carmieli, T. Miura, M. R. Wasielewski, *J. Am. Chem. Soc.* **2011**, 133, 1240-1243.
- [50] J. N. Nelson, J. Zhang, J. Zhou, B. K. Rugg, M. D. Krzyaniak, M. R. Wasielewski, *J. Phys. Chem. A* **2018**, 122, 9392-9402.
- [51] S. von Kugelgen, M. D. Krzyaniak, M. Gu, D. Puggioni, J. M. Rondinelli, M. R. Wasielewski, D. E. Freedman, *J. Am. Chem. Soc.* **2021**, 143, 8069-8077.
- [52] S. M. Harvey, M. R. Wasielewski, *J. Am. Chem. Soc.* **2021**, 143, 15508-15529.
- [53] Z. Shuai, H. Geng, W. Xu, Y. Liao, J.-M. André, *Chem. Soc. Rev.* **2014**, 43, 2662-2679.
- [54] V. Coropceanu, J. Cornil, D. A. da Silva Filho, Y. Olivier, R. Silbey, J.-L. Brédas, *Chem. Rev.* **2007**, 107, 926-952.
- [55] J.-L. Brédas, D. Beljonne, V. Coropceanu, J. Cornil, *Chem. Rev.* **2004**, 104, 4971-5004.
- [56] F. Bella, C. Gerbaldi, C. Barolo, M. Grätzel, *Chem. Soc. Rev.* **2015**, 44, 3431-3473.
- [57] K. Sharma, V. Sharma, S. Sharma, *Nanoscale Res. Lett.* **2018**, 13, 1-46.
- [58] A. Hagfeldt, G. Boschloo, L. Sun, L. Kloo, H. Pettersson, *Chem. Rev.* **2010**, 110, 6595-6663.
- [59] L. Lu, T. Zheng, Q. Wu, A. M. Schneider, D. Zhao, L. Yu, *Chem. Rev.* **2015**, 115, 12666-12731.
- [60] A. Wadsworth, M. Moser, A. Marks, M. S. Little, N. Gasparini, C. J. Brabec, D. Baran, I. McCulloch, *Chem. Soc. Rev.* **2019**, 48, 1596-1625.
- [61] C. Zhao, J. Wang, J. Jiao, L. Huang, J. Tang, *J. Mater. Chem. C* **2020**, 8, 28-43.
- [62] M. N. Paddon-Row, *Aust. J. Chem.* **2003**, 56, 729-748.
- [63] C. Schubert, J. Margraf, T. Clark, D. Guldi, *Chem. Soc. Rev.* **2015**, 44, 988-998.
- [64] J. R. Heath, *Annu. Rev. Mater. Res.* **2009**, 39, 1-23.
- [65] J. Jortner, Washington: American Chemical Society, **1997**.
- [66] X. Wen, A. Nowak-Król, O. Nagler, F. Kraus, N. Zhu, N. Zheng, M. Müller, D. Schmidt, Z. Xie, F. Würthner, *Angew. Chem. Int. Ed.* **2019**, 58, 13051-13055.
- [67] B. Brocklehurst, K. A. McLauchlan, *Int. J. Radiat. Biol.* **1996**, 69, 3-24.
- [68] H. Hisaharu, N. Saburo, *Bull. Chem. Soc. Jpn.* **1984**, 57, 322-328.
- [69] A. M. Lewis, D. E. Manolopoulos, P. Hore, *J. Chem. Phys.* **2014**, 141.
- [70] Y. Wu, J. Zhou, J. N. Nelson, R. M. Young, M. D. Krzyaniak, M. R. Wasielewski, *J. Am. Chem. Soc.* **2018**, 140, 13011-13021.
- [71] J. R. Woodward, *Prog. React. Kinet. Mech.* **2002**, 27, 165-207.
- [72] K. Schulten, C. E. Swenberg, A. Weller, *Z. Phys. Chem.* **1978**, 111, 1-5.
- [73] K. Schulten, P. G. Wolynes, *J. Chem. Phys.* **1978**, 68, 3292-3297.
- [74] E. W. Knapp, K. Schulten, *J. Chem. Phys.* **1979**, 71, 1878-1883.
- [75] K. A. McLauchlan, U. Steiner, *Mol. Phys.* **1991**, 73, 241-263.
- [76] K. Schulten, *J. Chem. Phys.* **1985**, 82, 1312-1316.
- [77] J. A. Syage, *Chem. Phys. Lett.* **1982**, 91, 378-382.
- [78] P. W. Atkins, *Chem. Phys. Lett.* **1966**, 66, 403.
- [79] U. E. Steiner, J. Schäfer, N. N. Lukzen, C. Lambert, *J. Phys. Chem. C* **2018**, 122, 11701-11708.
- [80] O. Efimova, P. Hore, *Biophys. J.* **2008**, 94, 1565-1574.
- [81] A. R. O'Dea, A. F. Curtis, N. J. Green, C. R. Timmel, P. Hore, *J. Phys. Chem. A* **2005**, 109, 869-873.
- [82] S. Riese, L. Mungenast, A. Schmiedel, M. Holzapfel, N. N. Lukzen, U. E. Steiner, C. Lambert, *Mol. Phys.* **2019**, 117, 2632-2644.
- [83] J. H. Klein, D. Schmidt, U. E. Steiner, C. Lambert, *J. Am. Chem. Soc.* **2015**, 137, 11011-11021.

- [84] M. T. Rawls, G. Kollmannsberger, C. M. Elliott, U. E. Steiner, *J. Phys. Chem. A* **2007**, *111*, 3485-3496.
- [85] J. Q. Wu, D. Baumann, U. E. Steiner, *Mol. Phys.* **1995**, *84*, 981-994.
- [86] P. Atkins, D. Kivelson, *J. Chem. Phys.* **1966**, *44*, 169-174.
- [87] U. E. Steiner, Y. A. Serebrennikov, *J. Chem. Phys.* **1994**, *100*, 7503-7507.
- [88] D. Mims, *Dissertation: Einblicke in die Spinchemie durch Untersuchung des Magnetfeldeffektes in rigide gebundenen Radikalpaarionen*, Julius-Maximilians-Universität Würzburg (Würzburg), **2022**.
- [89] N. N. Lukzen, J. H. Klein, C. Lambert, U. E. Steiner, *Z. Phys. Chem.* **2017**, *231*, 197-223.
- [90] T. P. Fay, D. E. Manolopoulos, *J. Chem. Phys.* **2019**, *150*.
- [91] C. Roger, A. Schmiedel, M. Holzapfel, N. N. Lukzen, U. E. Steiner, C. Lambert, *Phys. Chem. Chem. Phys.* **2024**, *26*, 4954-4967.
- [92] S. Riese, J. S. Brand, D. Mims, M. Holzapfel, N. N. Lukzen, U. E. Steiner, C. Lambert, *J. Chem. Phys.* **2020**, *153*, 054306.
- [93] A. S. Lukas, P. J. Bushard, E. A. Weiss, M. R. Wasielewski, *J. Am. Chem. Soc.* **2003**, *125*, 3921-3930.
- [94] T. Miura, A. M. Scott, M. R. Wasielewski, *J. Phys. Chem. C* **2010**, *114*, 20370-20379.
- [95] I. Zhukov, N. Fishman, A. Kiryutin, N. Lukzen, M. Panov, U. Steiner, H.-M. Vieth, J. Schäfer, C. Lambert, A. Yurkovskaya, *J. Chem. Phys.* **2020**, *152*.
- [96] P. W. Anderson, *Phys. Rev.* **1959**, *115*, 2.
- [97] P. W. Anderson, *Phys. Rev.* **1950**, *79*, 350.
- [98] F. J. Adrian, *Rev. Chem. Intermed.* **1979**, *3*, 3-43.
- [99] E. A. Weiss, M. A. Ratner, M. R. Wasielewski, *J. Phys. Chem. A* **2003**, *107*, 3639-3647.
- [100] N. R. Kestner, J. Logan, J. Jortner, *J. Phys. Chem.* **1974**, *78*, 2148-2166.
- [101] M. Bixon, J. Jortner, *J. Chem. Phys.* **1968**, *48*, 715-726.
- [102] M. Bixon, J. Jortner, *Chem. Phys.* **1993**, *176*, 467-481.
- [103] A. M. Scott, A. Butler Ricks, M. T. Colvin, M. R. Wasielewski, *Angew. Chem. Int. Ed.* **2010**, *49*, 2904-2908.
- [104] M. R. Wasielewski, *J. Org. Chem.* **2006**, *71*, 5051-5066.
- [105] T. Miura, D. Fujiwara, K. Akiyama, T. Horikoshi, S. Suzuki, M. Kozaki, K. Okada, T. Ikoma, *J. Phys. Chem. Lett.* **2017**, *8*, 661-665.
- [106] A. M. Scott, T. Miura, A. B. Ricks, Z. E. X. Dance, E. M. Giacobbe, M. T. Colvin, M. R. Wasielewski, *J. Am. Chem. Soc.* **2009**, *131*, 17655-17666.
- [107] Z. E. X. Dance, M. J. Ahrens, A. M. Vega, A. B. Ricks, D. W. McCamant, M. A. Ratner, M. R. Wasielewski, *J. Am. Chem. Soc.* **2008**, *130*, 830-832.
- [108] R. H. Goldsmith, L. E. Sinks, R. F. Kelley, L. J. Betzen, W. Liu, E. A. Weiss, M. A. Ratner, M. R. Wasielewski, *PNAS* **2005**, *102*, 3540-3545.
- [109] A. M. Scott, M. R. Wasielewski, *J. Am. Chem. Soc.* **2011**, *133*, 3005-3013.
- [110] E. A. Weiss, M. J. Tauber, R. F. Kelley, M. J. Ahrens, M. A. Ratner, M. R. Wasielewski, *J. Am. Chem. Soc.* **2005**, *127*, 11842-11850.
- [111] J. Schäfer, *Dissertation: Synthesis and photophysical investigation of donor-acceptor-substituted meta- and para-benzene derivatives*, Julius-Maximilians-Universität Würzburg (Würzburg), **2017**.
- [112] I. Zhukov, N. Fishman, A. Kiryutin, N. Lukzen, M. Panov, U. Steiner, H.-M. Vieth, J. Schäfer, C. Lambert, A. Yurkovskaya, *J. Chem. Phys.* **2020**, *152*, 014203.
- [113] R. Marcus, *J. Phys. Chem.* **1989**, *93*, 3078-3086.
- [114] M. D. Forbes, in *Electron Paramagnetic Resonance*, The Royal Society of Chemistry, **2012**, pp. 58-78.
- [115] P. D. Bartlett, M. J. Ryan, S. G. Cohen, *J. Am. Chem. Soc.* **1942**, *64*, 2649-2653.
- [116] J.-R. Mistry, S. Montanaro, I. A. Wright, *Materials Advances* **2023**, *4*, 787-803.
- [117] R. Qian, H. Tong, C. Huang, J. Li, Y. Tang, R. Wang, K. Lou, W. Wang, *Org. Biomol. Chem.* **2016**, *14*, 5007-5011.
- [118] D. K. Frantz, A. Linden, K. K. Baldrige, J. S. Siegel, *J. Am. Chem. Soc.* **2012**, *134*, 1528-1535.

- [119] S. Toyota, K. Kawahata, K. Sugahara, K. Wakamatsu, T. Iwanaga, *Eur. J. Org. Chem.* **2017**, 2017, 5696-5707.
- [120] F. Bertani, N. Riboni, F. Bianchi, G. Brancatelli, E. S. Sterner, R. Pinalli, S. Geremia, T. M. Swager, E. Dalcanale, *Chem. Eur. J.* **2016**, *22*, 3312-3319.
- [121] S. Barman, J. A. Garg, O. Blacque, K. Venkatesan, H. Berke, *Chem. Commun.* **2012**, *48*, 11127-11129.
- [122] Q. Liang, J. Liu, Y. Wei, Z. Zhao, M. J. MacLachlan, *Chem. Commun.* **2013**, *49*, 8928-8930.
- [123] Q. Liang, G. Jiang, Z. Zhao, Z. Li, M. J. MacLachlan, *Catal. Sci. Technol.* **2015**, *5*, 3368-3374.
- [124] A. M. Elewa, M. H. Elsayed, A. F. El-Mahdy, C.-L. Chang, L.-Y. Ting, W.-C. Lin, C.-Y. Lu, H.-H. Chou, *Appl. Catal., B* **2021**, *285*, 119802.
- [125] Z. Chen, P. Li, R. Anderson, X. Wang, X. Zhang, L. Robison, L. R. Redfern, S. Moribe, T. Islamoglu, D. A. Gómez-Gualdrón, *Science* **2020**, *368*, 297-303.
- [126] Z. Chen, P. Li, X. Zhang, M. R. Mian, X. Wang, P. Li, Z. Liu, M. O'Keeffe, J. F. Stoddart, O. K. Farha, *Nano Res.* **2021**, *14*, 376-380.
- [127] A. Beyeler, P. Belser, *Coord. Chem. Rev.* **2002**, *230*, 29-39.
- [128] Y. Wang, C. Wu, W. Sun, Q. Pan, W. Hao, H. Liu, J. Sun, Z. Li, J. Sun, Y. Zhao, *Mater. Chem. Front.* **2021**, *5*, 944-949.
- [129] N. Baig, S. Shetty, S. Al-Mousawi, F. Al-Sagheer, B. Alameddine, *React. Funct. Polym.* **2019**, *139*, 153-161.
- [130] H. Quast, H. L. Fuchsbauer, *Chem. Ber.* **1986**, *119*, 2414-2429.
- [131] S. Zhang, J.-F. Chen, G. Hu, N. Zhang, N. Wang, X. Yin, P. Chen, *Organometallics* **2021**, *41*, 99-104.
- [132] A. Izuoka, S. Murata, T. Sugawara, H. Iwamura, *J. Am. Chem. Soc.* **1987**, *109*, 2631-2639.
- [133] X. Liu, Y. Cai, X. Huang, R. Zhang, X. Sun, *J. Mater. Chem. C* **2017**, *5*, 3188-3194.
- [134] H. Li, T. Earmme, G. Ren, A. Saeki, S. Yoshikawa, N. M. Murari, S. Subramaniyan, M. J. Crane, S. Seki, S. A. Jenekhe, *J. Am. Chem. Soc.* **2014**, *136*, 14589-14597.
- [135] E. H. Menke, V. Lami, Y. Vaynzof, M. Mastalerz, *Chem. Commun.* **2016**, *52*, 1048-1051.
- [136] H. S. Kang, T. J. Sisto, S. Peurifoy, D. H. Arias, B. Zhang, C. Nuckolls, J. L. Blackburn, *J. Phys. Chem. C* **2018**, *122*, 14150-14161.
- [137] K. Kawasumi, T. Wu, T. Zhu, H. S. Chae, T. Van Voorhis, M. A. Baldo, T. M. Swager, *J. Am. Chem. Soc.* **2015**, *137*, 11908-11911.
- [138] P. Lei, S. Zhang, N. Zhang, X. Yin, N. Wang, P. Chen, *ACS omega* **2020**, *5*, 28606-28614.
- [139] H. Uoyama, K. Goushi, K. Shizu, H. Nomura, C. Adachi, *Nature* **2012**, *492*, 234-238.
- [140] G. Méhes, H. Nomura, Q. Zhang, T. Nakagawa, C. Adachi, *Angew. Chem. Int. Ed.* **2012**, *51*, 11311-11315.
- [141] G. L. Gaines III, M. P. O'Neil, W. A. Svec, M. P. Niemczyk, M. R. Wasielewski, *J. Am. Chem. Soc.* **1991**, *113*, 719-721.
- [142] T. Ikai, Y. Wada, S. Awata, C. Yun, K. Maeda, M. Mizuno, T. M. Swager, *Org. Biomol. Chem.* **2017**, *15*, 8440-8447.
- [143] K. Baumgärtner, M. Hoffmann, F. Rominger, S. M. Elbert, A. Dreuw, M. Mastalerz, *J. Org. Chem.* **2020**, *85*, 15256-15272.
- [144] J. Schäfer, M. Holzappel, B. Mladenova, D. Kattinig, I. Krummenacher, H. Braunschweig, G. n. Grampp, C. Lambert, *J. Am. Chem. Soc.* **2017**, *139*, 6200-6209.
- [145] C. Lambert, G. Nöll, *J. Am. Chem. Soc.* **1999**, *121*, 8434-8442.
- [146] S. Amthor, B. Noller, C. Lambert, *Chem. Phys.* **2005**, *316*, 141-152.
- [147] C. Lambert, J. Schelter, T. Fiebig, D. Mank, A. Trifonov, *J. Am. Chem. Soc.* **2005**, *127*, 10600-10610.
- [148] F. Zieschang, M. H. Schreck, A. Schmiedel, M. Holzappel, J. H. Klein, C. Walter, B. Engels, C. Lambert, *J. Phys. Chem. C* **2014**, *118*, 27698-27714.
- [149] C. Huang, S. Barlow, S. R. Marder, *J. Org. Chem.* **2011**, *76*, 2386-2407.
- [150] J. Kelber, H. Bock, O. Thiebaut, E. Grelet, H. Langhals, Wiley Online Library, **2011**.

- [151] Y. Nagao, *Prog. Org. Coat.* **1997**, *31*, 43-49.
- [152] J. E. Webb, K. Chen, S. K. Prasad, J. P. Wojciechowski, A. Falber, P. Thordarson, J. M. Hodgkiss, *Phys. Chem. Chem. Phys.* **2016**, *18*, 1712-1719.
- [153] C. Xue, R. Sun, R. Annab, D. Abadi, S. Jin, *Tetrahedron Lett.* **2009**, *50*, 853-856.
- [154] J. C. C. Atherton, S. Jones, *Tetrahedron* **2003**, *59*, 9039-9057.
- [155] L. Friedman, F. M. Logullo, *J. Am. Chem. Soc.* **1963**, *85*, 1549-1549.
- [156] A. Streitwieser Jr, G. Ziegler, *J. Am. Chem. Soc.* **1969**, *91*, 5081-5084.
- [157] H. B. Goodbrand, N.-X. Hu, *J. Org. Chem.* **1999**, *64*, 670-674.
- [158] K. Hu, A. D. Blair, E. J. Piechota, P. A. Schauer, R. N. Sampaio, F. G. L. Parlane, G. J. Meyer, C. P. Berlinguette, *Nat. Chem.* **2016**, *8*, 853-859.
- [159] Y. Li, C. Wang, C. Li, S. Di Motta, F. Negri, Z. Wang, *Org. Lett.* **2012**, *14*, 5278-5281.
- [160] D. Mims, J. Herpich, N. N. Lukzen, U. E. Steiner, C. Lambert, *Science* **2021**, *374*, 1470-1474.
- [161] H. Kang, H. Shin, B. Kim, J. Park, *J. Nanosci. Nanotechnol.* **2016**, *16*, 3045-3048.
- [162] K. Sanada, H. Ube, M. Shionoya, *J. Am. Chem. Soc.* **2016**, *138*, 2945-2948.
- [163] N. Miyaura, A. Suzuki, *J. Chem. Soc., Chem. Commun.* **1979**, 866-867.
- [164] K. J. Thorley, Y. Song, S. R. Parkin, J. E. Anthony, *Org. Lett.* **2020**, *22*, 7193-7196.
- [165] G. A. Kraus, T. O. Man, *Synth. Commun.* **1986**, *16*, 1037-1042.
- [166] F. Würthner, *Chem. Commun.* **2004**, 1564-1579.
- [167] F. Würthner, C. R. Saha-Möller, B. Fimmel, S. Ogi, P. Leowanawat, D. Schmidt, *Chem. Rev.* **2016**, *116*, 962-1052.
- [168] M. Lehmann, M. Hecht, S. Herbst, K. Cui, F. Würthner, *Chem. Commun.* **2020**, *56*, 14015-14018.
- [169] M. Hecht, F. Würthner, *Acc. Chem. Res.* **2021**, *54*, 642-653.
- [170] M. Hecht, T. Schlossarek, S. Ghosh, Y. Tsutsui, A. Schmiedel, M. Holzapfel, M. Stolte, C. Lambert, S. Seki, M. Lehmann, F. Würthner, *ACS Appl. Nano Mater.* **2020**, *3*, 10234-10245.
- [171] F. Würthner, V. Stepanenko, Z. Chen, C. R. Saha-Möller, N. Kocher, D. Stalke, *J. Org. Chem.* **2004**, *69*, 7933-7939.
- [172] R. S. Nobuyasu, J. S. Ward, J. Gibson, B. A. Laidlaw, Z. Ren, P. Data, A. S. Batsanov, T. J. Penfold, M. R. Bryce, F. B. Dias, *J. Mater. Chem. C* **2019**, *7*, 6672-6684.
- [173] S. Dutta Choudhury, S. Basu, *J. Phys. Chem. A* **2005**, *109*, 8113-8120.
- [174] G. Wheaton, L. Stoel, N. Stevens, C. Frank, *Appl. Spectrosc.* **1970**, *24*, 339-343.
- [175] J. B. Birks, D. Dyson, *Proc. R. Soc. Lond. Ser. A. Math. Phys. Sci.* **1963**, *275*, 135-148.
- [176] J. Birks, *Proc. Phys. Soc.* **1962**, *79*, 494.
- [177] K. Kobayashi, H. Masu, A. Shuto, K. Yamaguchi, *Chem. Mater.* **2005**, *17*, 6666-6673.
- [178] C. Würth, M. Grabolle, J. Pauli, M. Spieles, U. Resch-Genger, *Nat. Protoc.* **2013**, *8*, 1535-1550.
- [179] X. Zhan, A. Facchetti, S. Barlow, T. J. Marks, M. A. Ratner, M. R. Wasielewski, S. R. Marder, *Adv. Mater.* **2011**, *23*, 268-284.
- [180] A. Rademacher, S. Märkle, H. Langhals, *Chem. Ber* **1982**, *115*, 2927-2934.
- [181] A. Nowak-Król, F. Würthner, *Org. Chem. Front.* **2019**, *6*, 1272-1318.
- [182] C. Nagaraja, T. V. Venkatesha, *Electrochim. Acta* **2018**, *260*, 221-234.
- [183] P. Luo, E. C. Feinberg, G. Guirado, S. Farid, J. P. Dinnocenzo, *J. Org. Chem.* **2014**, *79*, 9297-9304.
- [184] A. Zweig, W. G. Hodgson, W. H. Jura, *J. Am. Chem. Soc.* **1964**, *86*, 4124-4129.
- [185] G. Kwon, S. Lee, J. Hwang, H.-S. Shim, B. Lee, M. H. Lee, Y. Ko, S.-K. Jung, K. Ku, J. Hong, K. Kang, *Joule* **2018**, *2*, 1771-1782.
- [186] L. S. Cui, H. Nomura, Y. Geng, J. U. Kim, H. Nakanotani, C. Adachi, *Angew. Chem. Int. Ed.* **2017**, *56*, 1571-1575.
- [187] M. J. Ahrens, M. J. Fuller, M. R. Wasielewski, *Chem. Mater.* **2003**, *15*, 2684-2686.
- [188] W. E. Ford, P. V. Kamat, *J. Phys. Chem.* **1987**, *91*, 6373-6380.
- [189] D. Veldman, S. M. Chopin, S. C. Meskers, M. M. Groeneveld, R. M. Williams, R. A. Janssen, *J. Phys. Chem. A* **2008**, *112*, 5846-5857.
- [190] R. A. Gaussian09, *Inc., Wallingford CT* **2009**, *121*, 150-166.
- [191] A. Heckmann, C. Lambert, *Angew. Chem. Int. Ed.* **2012**, *51*, 326-392.

- [192] B. Albinsson, J. Mårtensson, *J. Photochem. Photobiol., B: Photochem. Rev.* **2008**, *9*, 138-155.
- [193] M. Sadrai, L. Hadel, R. R. Sauers, S. Husain, K. Krogh-Jespersen, J. D. Westbrook, G. R. Bird, *J. Phys. Chem.* **1992**, *96*, 7988-7996.
- [194] A. Prodi, C. Chiorboli, F. Scandola, E. Iengo, E. Alessio, R. Dobrawa, F. Würthner, *J. Am. Chem. Soc.* **2005**, *127*, 1454-1462.
- [195] M. Ghirotti, C. Chiorboli, C.-C. You, F. Würthner, F. Scandola, *J. Phys. Chem. A* **2008**, *112*, 3376-3385.
- [196] M. Maroncelli, *J. Mol. Liq.* **1993**, *57*, 1-37.
- [197] E. A. Weiss, M. J. Ahrens, L. E. Sinks, M. A. Ratner, M. R. Wasielewski, *J. Am. Chem. Soc.* **2004**, *126*, 9510-9511.
- [198] T. Miura, *Mol. Phys.* **2020**, *118*, e1643510.
- [199] D. R. Kattinig, B. Mladenova, G. n. Grampp, C. Kaiser, A. Heckmann, C. Lambert, *J. Phys. Chem. C* **2009**, *113*, 2983-2995.
- [200] K. Maeda, T. Miura, T. Arai, *Mol. Phys.* **2006**, *104*, 1779-1788.
- [201] S.-G. Chen, H. M. Branz, S. S. Eaton, P. C. Taylor, R. A. Cormier, B. A. Gregg, *J. Phys. Chem. B* **2004**, *108*, 17329-17336.
- [202] A. C. Benniston, A. Harriman, *Chem. Soc. Rev.* **2006**, *35*, 169-179.
- [203] A. Mishchenko, L. A. Zotti, D. Vonlanthen, M. Bürkle, F. Pauly, J. C. Cuevas, M. Mayor, T. Wandlowski, *J. Am. Chem. Soc.* **2011**, *133*, 184-187.
- [204] O. S. Wenger, *Chem. Soc. Rev.* **2011**, *40*, 3538-3550.
- [205] G. L. Closs, J. R. Miller, *Science* **1988**, *240*, 440-447.
- [206] M. V. Ivanov, S. A. Reid, R. Rathore, *J. Phys. Chem. Lett.* **2018**, *9*, 3978-3986.
- [207] M. R. Talipov, T. S. Navale, R. Rathore, *Angew. Chem.* **2015**, *127*, 14676-14680.
- [208] J. Jortner, M. Bixon, *J. Chem. Phys.* **1988**, *88*, 167-170.
- [209] R. Maksimenka, M. Margraf, J. Köhler, A. Heckmann, C. Lambert, I. Fischer, *Chem. Phys.* **2008**, *347*, 436-445.
- [210] L. Reynolds, J. Gardecki, S. Frankland, M. Horng, M. Maroncelli, *J. Phys. Chem.* **1996**, *100*, 10337-10354.
- [211] H. M. McConnell, *J. Chem. Phys.* **1961**, *35*, 508-515.
- [212] M. Natali, S. Campagna, F. Scandola, *Chem. Soc. Rev.* **2014**, *43*, 4005-4018.
- [213] J. N. Onuchic, D. N. Beratan, *J. Am. Chem. Soc.* **1987**, *109*, 6771-6778.
- [214] K. V. Mikkelsen, M. A. Ratner, *J. Phys. Chem.* **1989**, *93*, 1759-1770.
- [215] M. D. Newton, *Chem. Rev.* **1991**, *91*, 767-792.
- [216] K. D. Jordan, M. N. Paddon-Row, *Chem. Rev.* **1992**, *92*, 395-410.
- [217] P. F. Barbara, T. J. Meyer, M. A. Ratner, *J. Phys. Chem.* **1996**, *100*, 13148-13168.
- [218] J. R. Miller, J. V. Beitz, *J. Chem. Phys.* **1981**, *74*, 6746-6756.
- [219] D. E. Richardson, H. Taube, *J. Am. Chem. Soc.* **1983**, *105*, 40-51.
- [220] H. D. Becker, *Chem. Rev.* **1993**, *93*, 145-172.
- [221] Y. Lei, K. Chen, G. Tang, J. Zhao, G. G. Gurzadyan, *Journal of Photochemistry and Photobiology A: Chemistry* **2020**, *398*, 112573.
- [222] F. Tanaka, T. Furuta, M. Okamoto, S. Hirayama, *Phys. Chem. Chem. Phys.* **2004**, *6*, 1219-1226.
- [223] K. Chen, J. Zhao, X. Li, G. G. Gurzadyan, *J. Phys. Chem. A* **2019**, *123*, 2503-2516.
- [224] C. R. Timmel, U. Till, B. Brocklehurst, K. A. Mclauchlan, P. J. Hore, *Mol. Phys.* **1998**, *95*, 71-89.
- [225] A. Weller, *Z. Phys. Chem.* **1982**, *133*, 93-98.
- [226] S. F. Nelsen, S. C. Blackstock, Y. Kim, *J. Am. Chem. Soc.* **1987**, *109*, 677-682.
- [227] S. F. Nelsen, H. Chang, J. J. Wolff, J. Adamus, *J. Am. Chem. Soc.* **1993**, *115*, 12276-12289.
- [228] J. K. Hurley, N. Sinai, H. Linschitz, *Photochem. Photobiol.* **1983**, *38*, 9-14.
- [229] P. Müller, K. Brettel, *Photochem. Photobiol. Sci.* **2012**, *11*, 632-636.
- [230] G. A. Crosby, J. N. Demas, *J. Am. Chem. Soc.* **1970**, *92*, 7262-7270.
- [231] I. Carmichael, G. L. Hug, *J. Phys. Chem. Ref. Data* **1986**, *15*, 1-250.
- [232] Z. Chen, T. M. Swager, *Macromol.* **2008**, *41*, 6880-6885.
- [233] O. Ryota, Y. Kenji, K. Kenji, *Chem. Lett.* **2011**, *40*, 941-943.

- [234] N. Seidel, T. Hahn, S. Liebing, W. Seichter, J. Kortus, E. Weber, *New J. Chem.* **2013**, *37*, 601-610.
- [235] J. Liu, H. Dong, Z. Wang, D. Ji, C. Cheng, H. Geng, H. Zhang, Y. Zhen, L. Jiang, H. Fu, Z. Bo, W. Chen, Z. Shuai, W. Hu, *Chem. Commun.* **2015**, *51*, 11777-11779.

## 13 Appendix

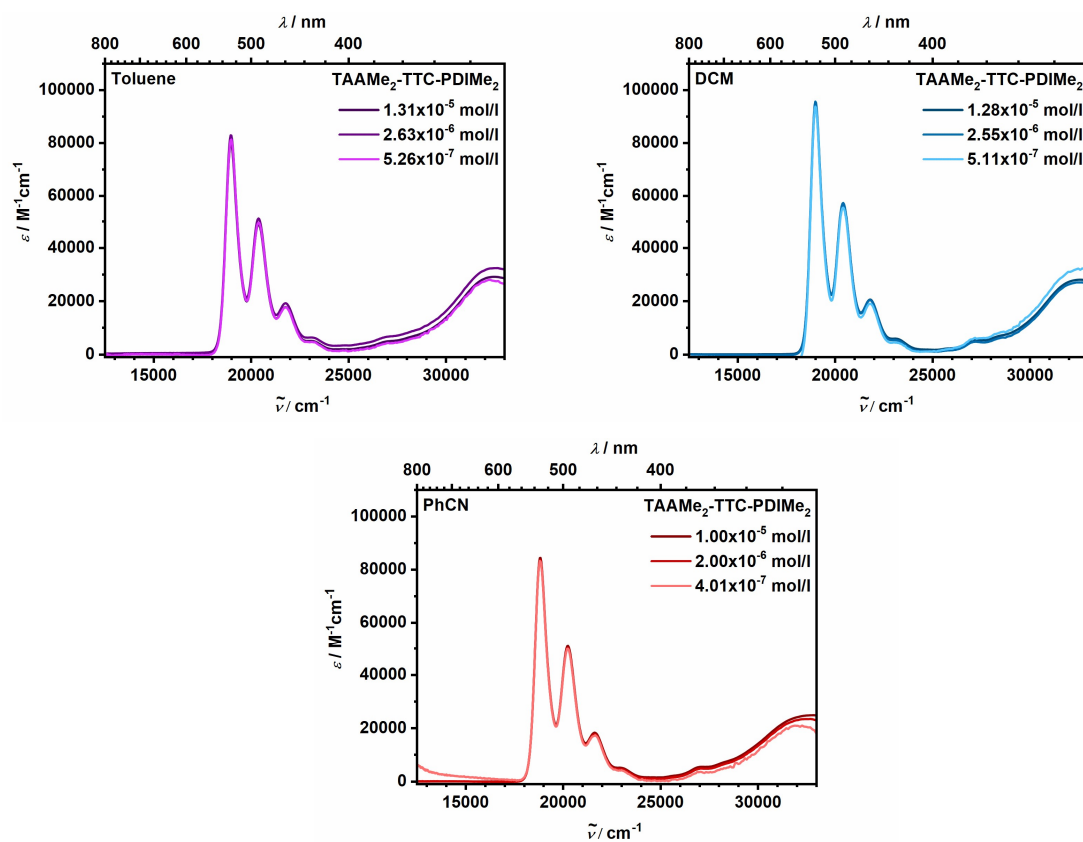
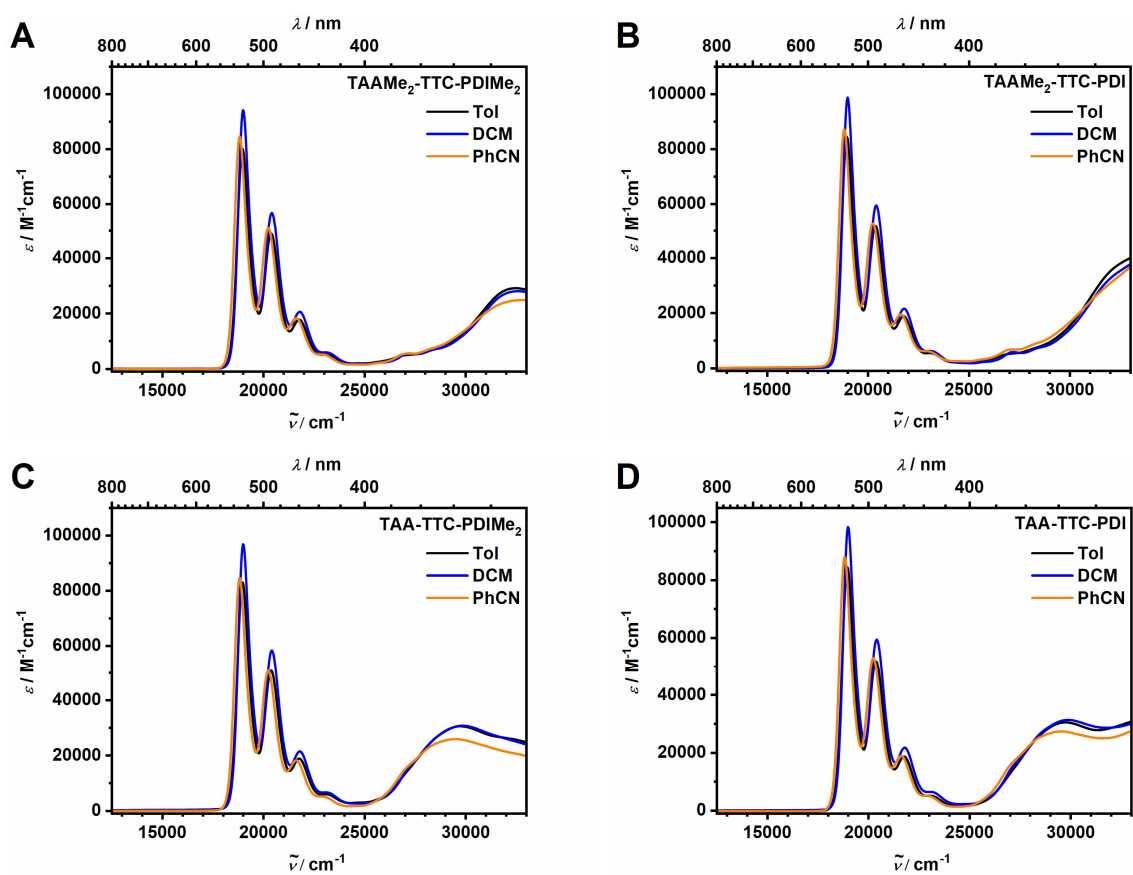
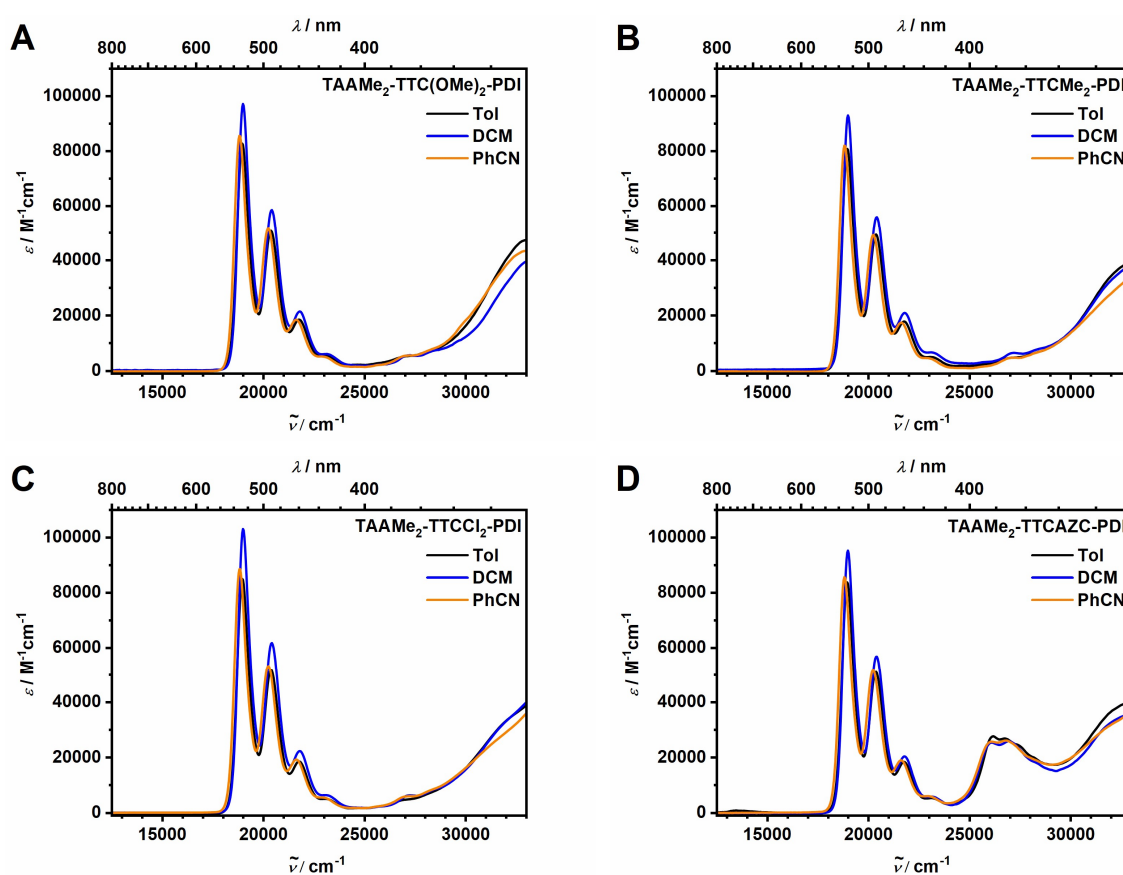


Figure A1: Concentration effects of TAAMe<sub>2</sub>-TTC-PDIME<sub>2</sub> in toluene, DCM and PhCN at 293 K.

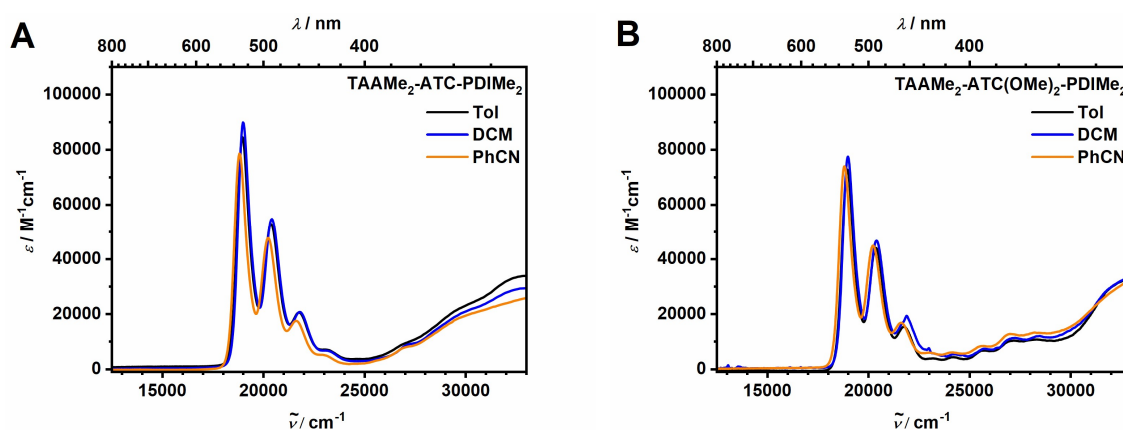




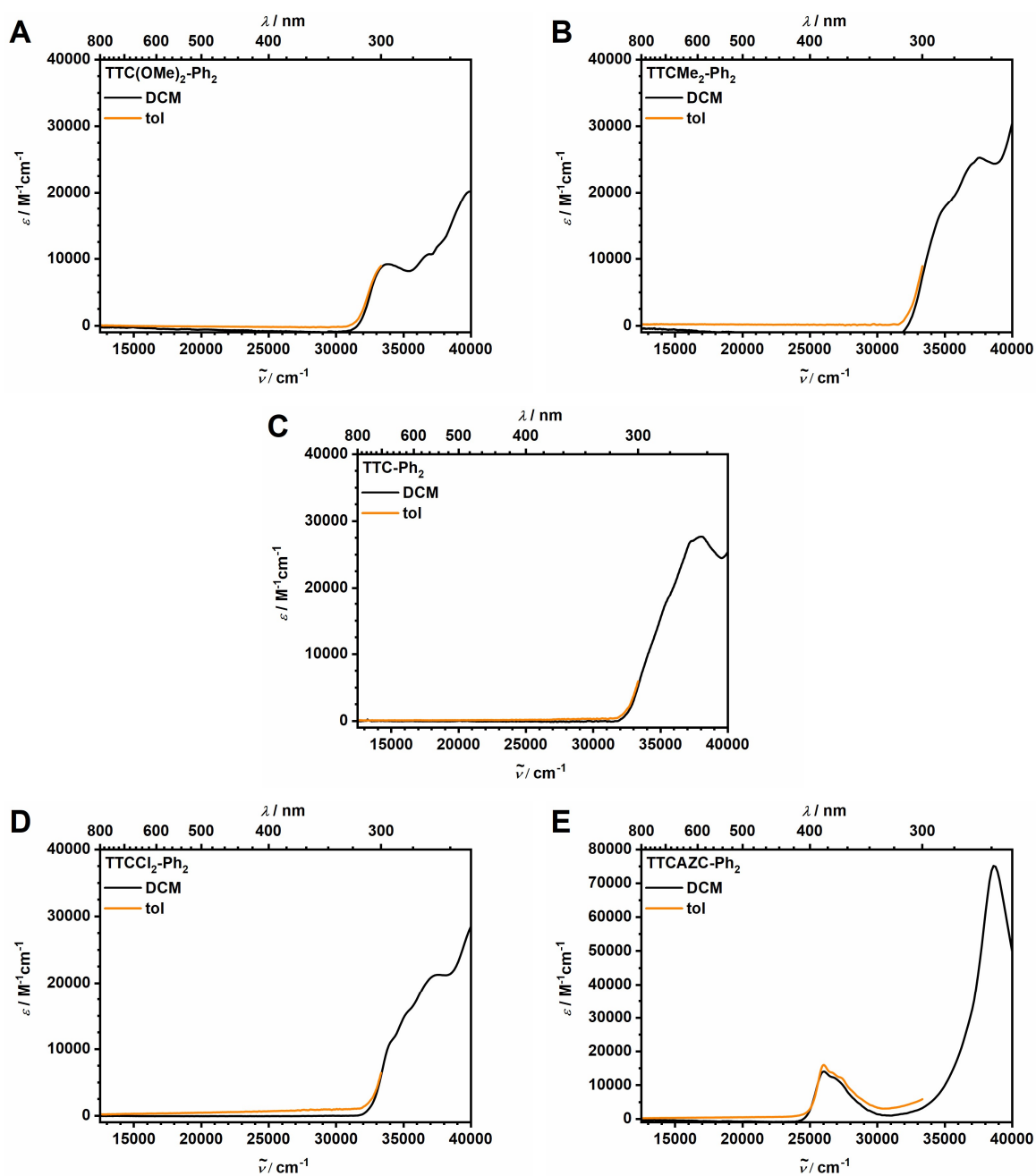
**Figure A2:** Steady-state absorption spectra of **A: TAAMe<sub>2</sub>-TTC-PDIME<sub>2</sub>** **B: TAAMe<sub>2</sub>-TTC-PDI** **C: TAA-TTC-PDIME<sub>2</sub>** and **D: TAA-TTC-PDI** in toluene (black), DCM (blue) and PhCN (orange) at 298 K.



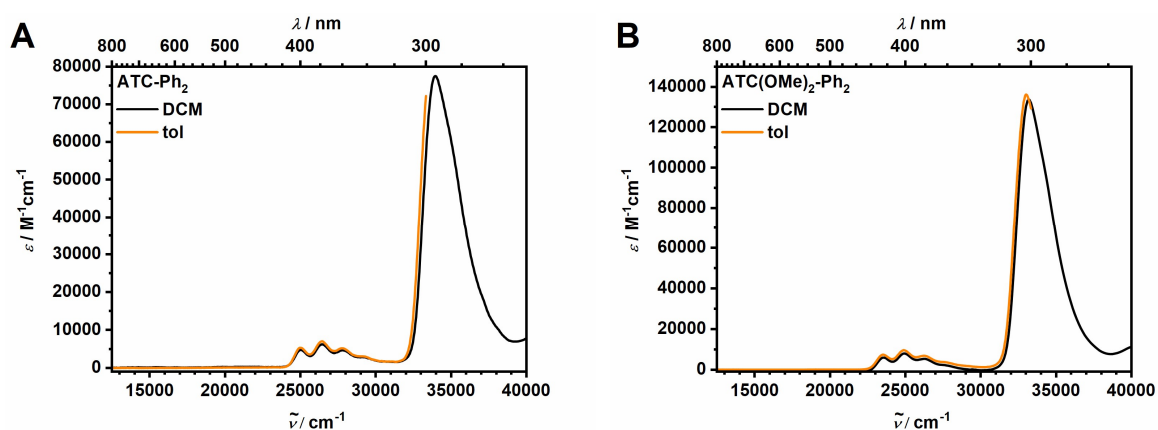
**Figure A3:** Steady-state absorption spectra of the four substituted triptycene triads in toluene (black), DCM (blue) and PhCN (orange) at 298 K. **A:** TAAMe<sub>2</sub>-TTC(OMe)<sub>2</sub>-PDI **B:** TAAMe<sub>2</sub>-TTCMe<sub>2</sub>-PDI **C:** TAAMe<sub>2</sub>-TTCCl<sub>2</sub>-PDI and **D:** TAAMe<sub>2</sub>-TTCACZ-PDI.



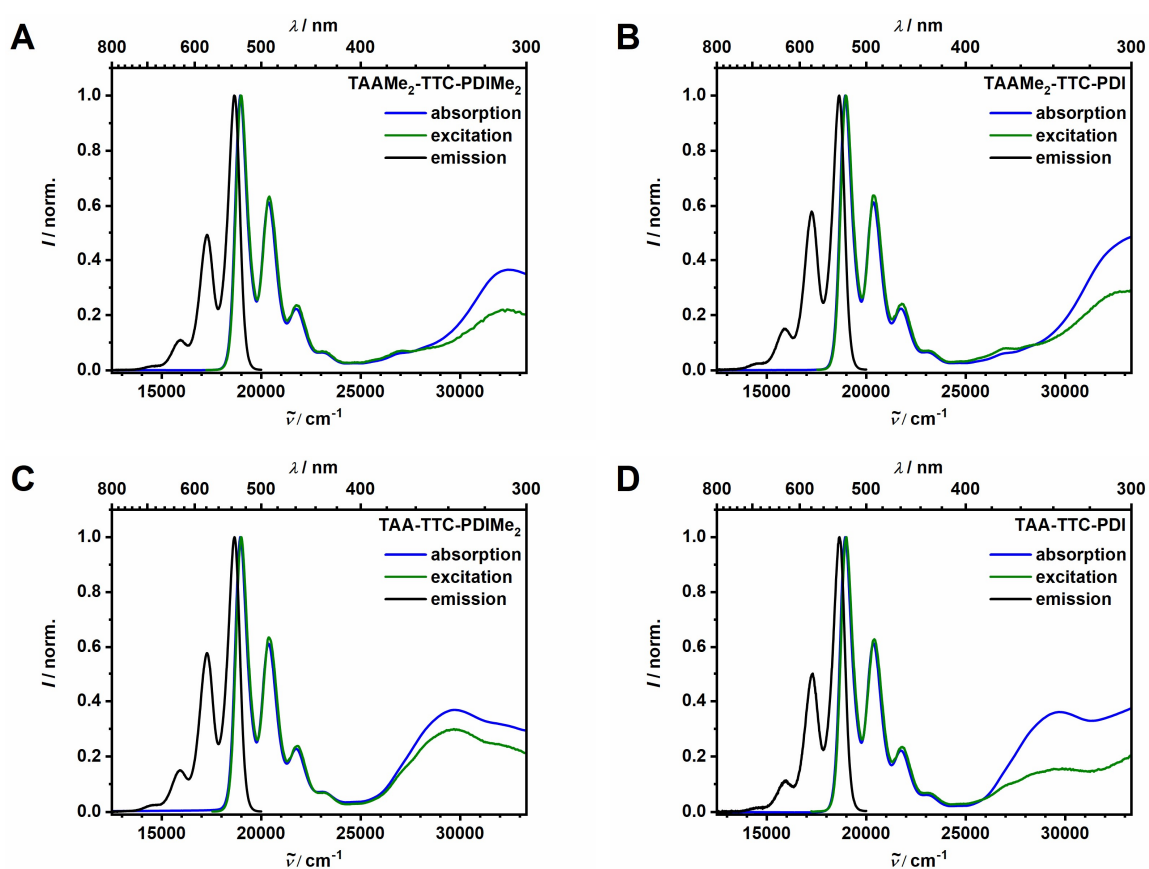
**Figure A4:** Steady-state absorption spectra of the two anthracene bridge triads at rt in toluene (black), DCM (blue) and PhCN (orange).



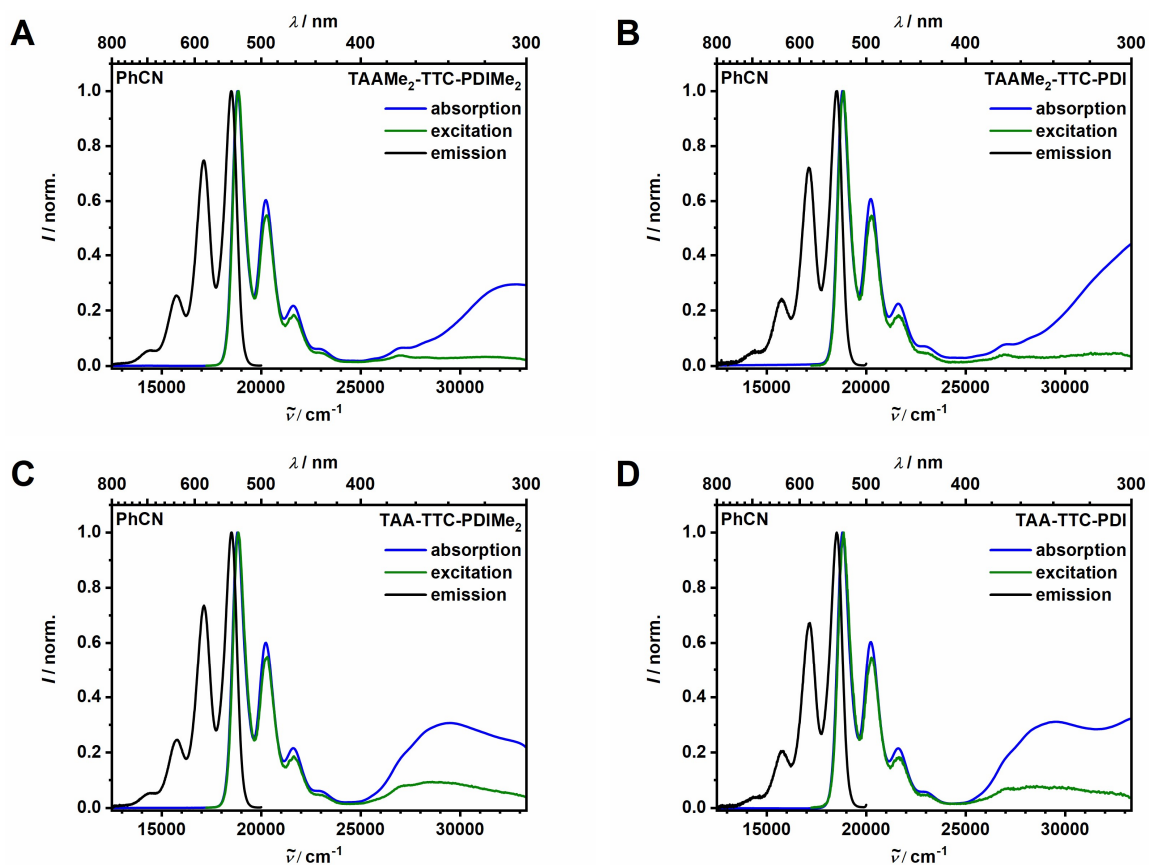
**Figure A5:** Steady-state absorption spectra of the triptycene reference compounds in DCM (black) and toluene (orange) at 298 K. **A:** TTC(OMe)<sub>2</sub>-Ph<sub>2</sub>, **B:** TTCMe<sub>2</sub>-Ph<sub>2</sub>, **C:** TTC-Ph<sub>2</sub>, **D:** TTCCl<sub>2</sub>-Ph<sub>2</sub> and **E:** TTCAZC-Ph<sub>2</sub>.



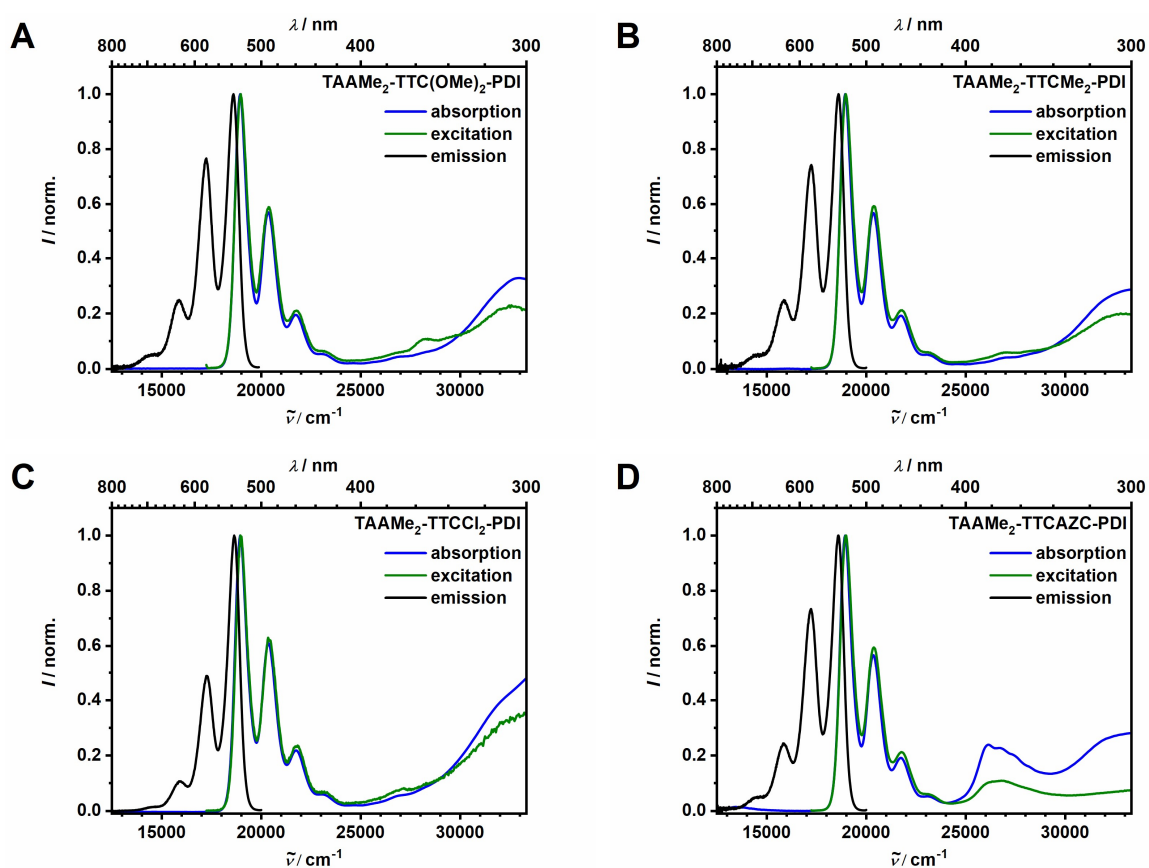
**Figure A6:** Steady-state absorption spectra of the two anthracene reference compounds in DCM (black) and toluene (orange) at 298 K.



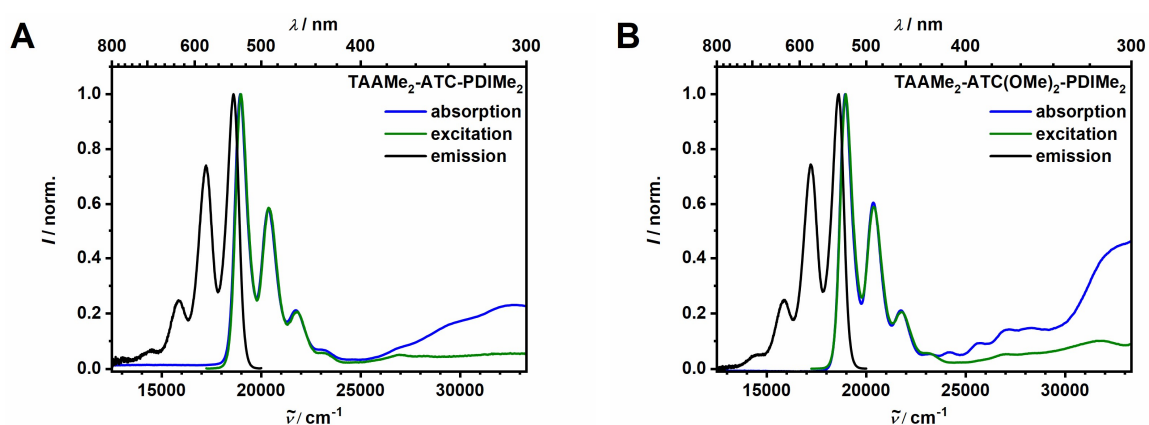
**Figure A7:** Normalised steady-state absorption (blue), excitation (green) and emission spectra (black) of the triads TAAMe<sub>2</sub>-TTC-PDIME<sub>2</sub>, TAAMe<sub>2</sub>-TTC-PDI, TAA-TTC-PDIME<sub>2</sub> and TAA-TTC-PDI in toluene at 298 K. Emission spectra were recorded after excitation at 20400  $\text{cm}^{-1}$  (490 nm, 0-1 absorption band of the PDI) and excitation spectra were recorded by probing at 16900  $\text{cm}^{-1}$  (590 nm, 1-0 emission band of the PDI).



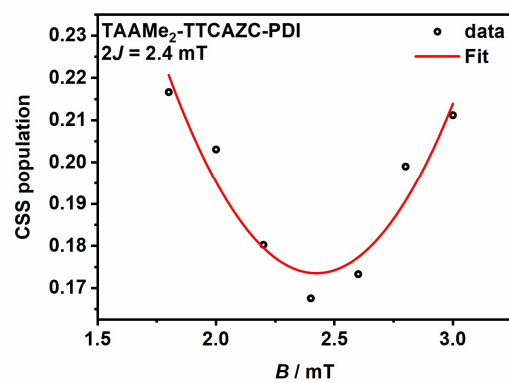
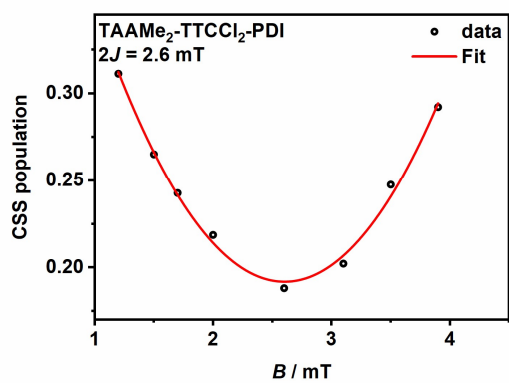
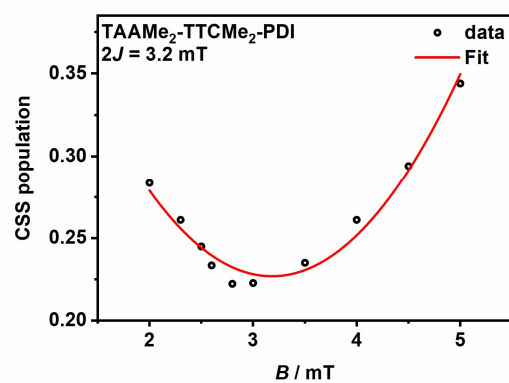
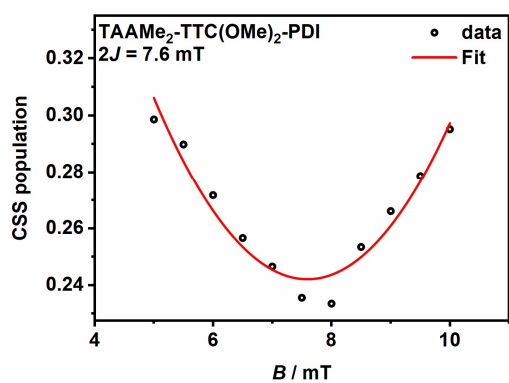
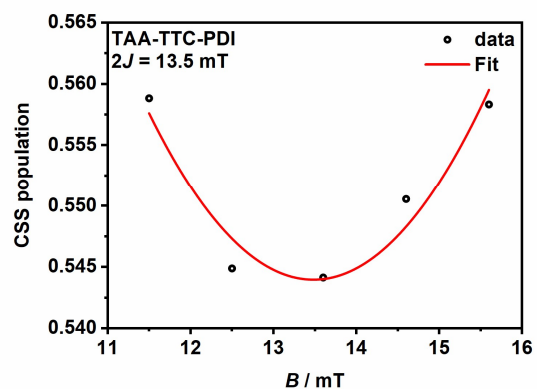
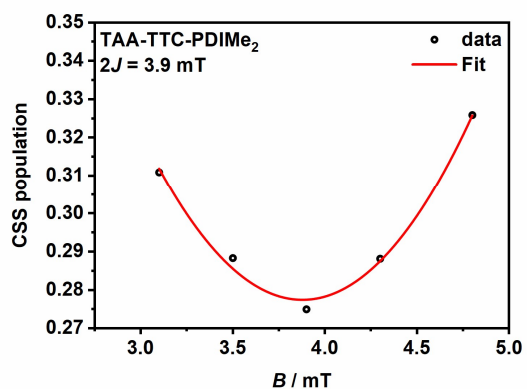
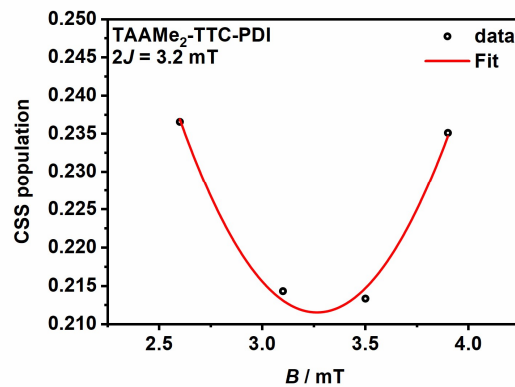
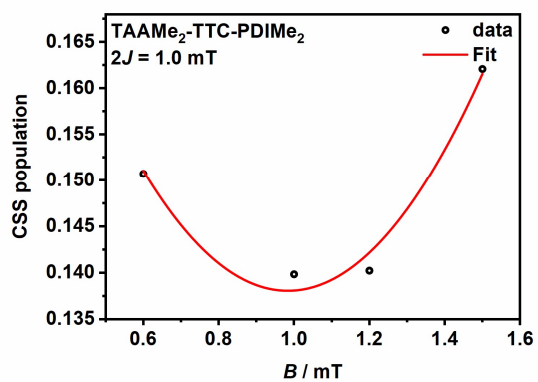
**Figure A8:** Normalised steady-state absorption (blue), excitation (green) and emission spectra (black) of the triads **TAAMe<sub>2</sub>-TTC-PDIME<sub>2</sub>**, **TAAMe<sub>2</sub>-TTC-PDI**, **TAA-TTC-PDIME<sub>2</sub>** and **TAA-TTC-PDI** in PhCN at 298 K. Emission spectra were recorded after excitation at 20400 cm<sup>-1</sup> (490 nm, 0-1 absorption band of the **PDI**) and excitation spectra were recorded by probing at 16900 cm<sup>-1</sup> (590 nm, 1-0 emission band of the **PDI**).

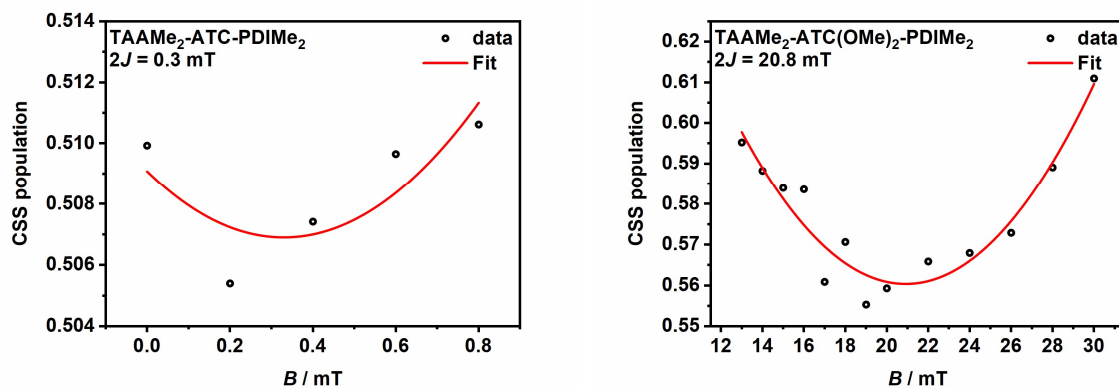


**Figure A9:** Normalised steady-state absorption (blue), excitation (green) and emission spectra (black) of the triads  $\text{TAAMe}_2\text{-TTC(OMe)}_2\text{-PDI}$ ,  $\text{TAAMe}_2\text{-TTCMe}_2\text{-PDI}$ ,  $\text{TAAMe}_2\text{-TTCCl}_2\text{-PDI}$ , and  $\text{TAAMe}_2\text{-TTCAZC-PDI}$  in toluene at 298 K. Emission spectra were recorded after excitation at  $20400\text{ cm}^{-1}$  (490 nm, 0-1 absorption band of the **PDI**) and excitation spectra were recorded by probing at  $16900\text{ cm}^{-1}$  (590 nm, 1-0 emission band of the **PDI**).

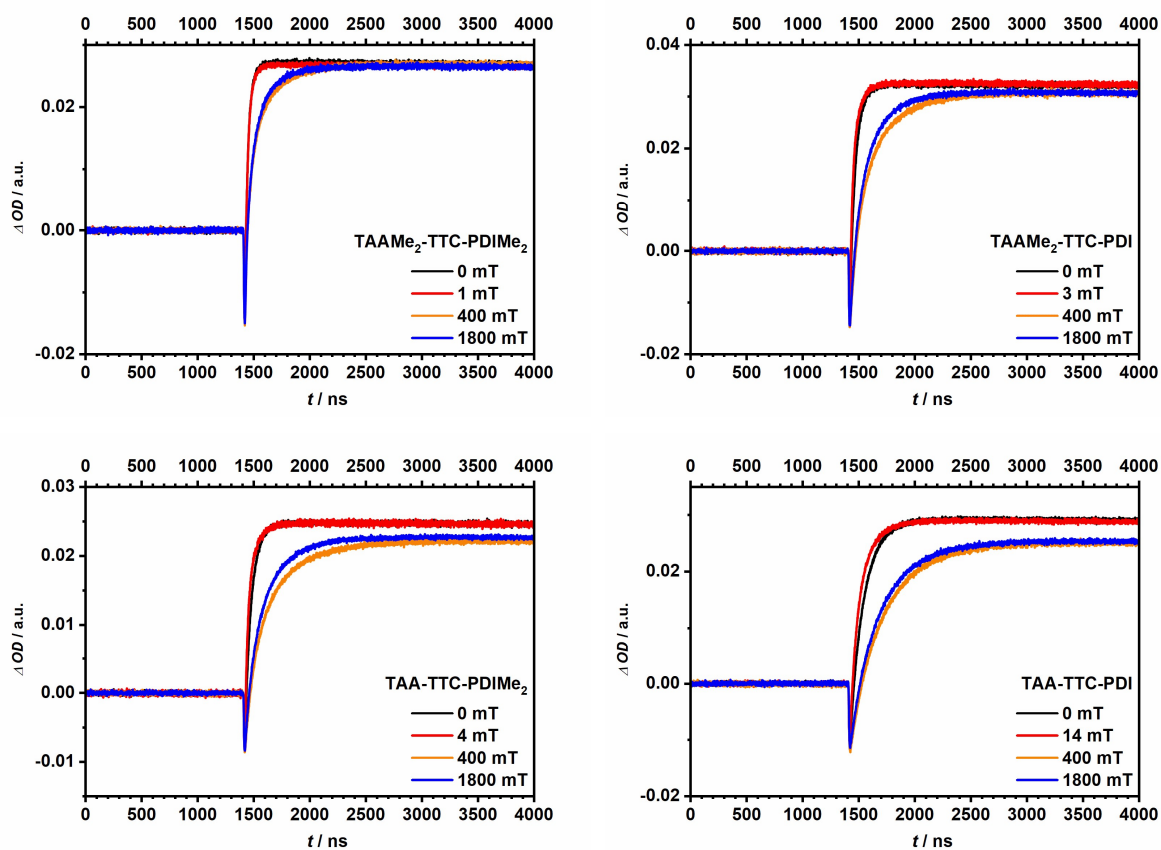


**Figure A10:** Normalised steady-state absorption (blue), excitation (green) and emission spectra (black) of the triads  $\text{TAAMe}_2\text{-ATC-PDIME}_2$  and  $\text{TAAMe}_2\text{-ATC(OMe)}_2\text{-PDIME}_2$  in toluene at 298 K. Emission spectra were recorded after excitation at  $20400\text{ cm}^{-1}$  (490 nm, 0-1 absorption band of the **PDI**) and excitation spectra were recorded by probing at  $16900\text{ cm}^{-1}$  (590 nm, 1-0 emission band of the **PDI**).

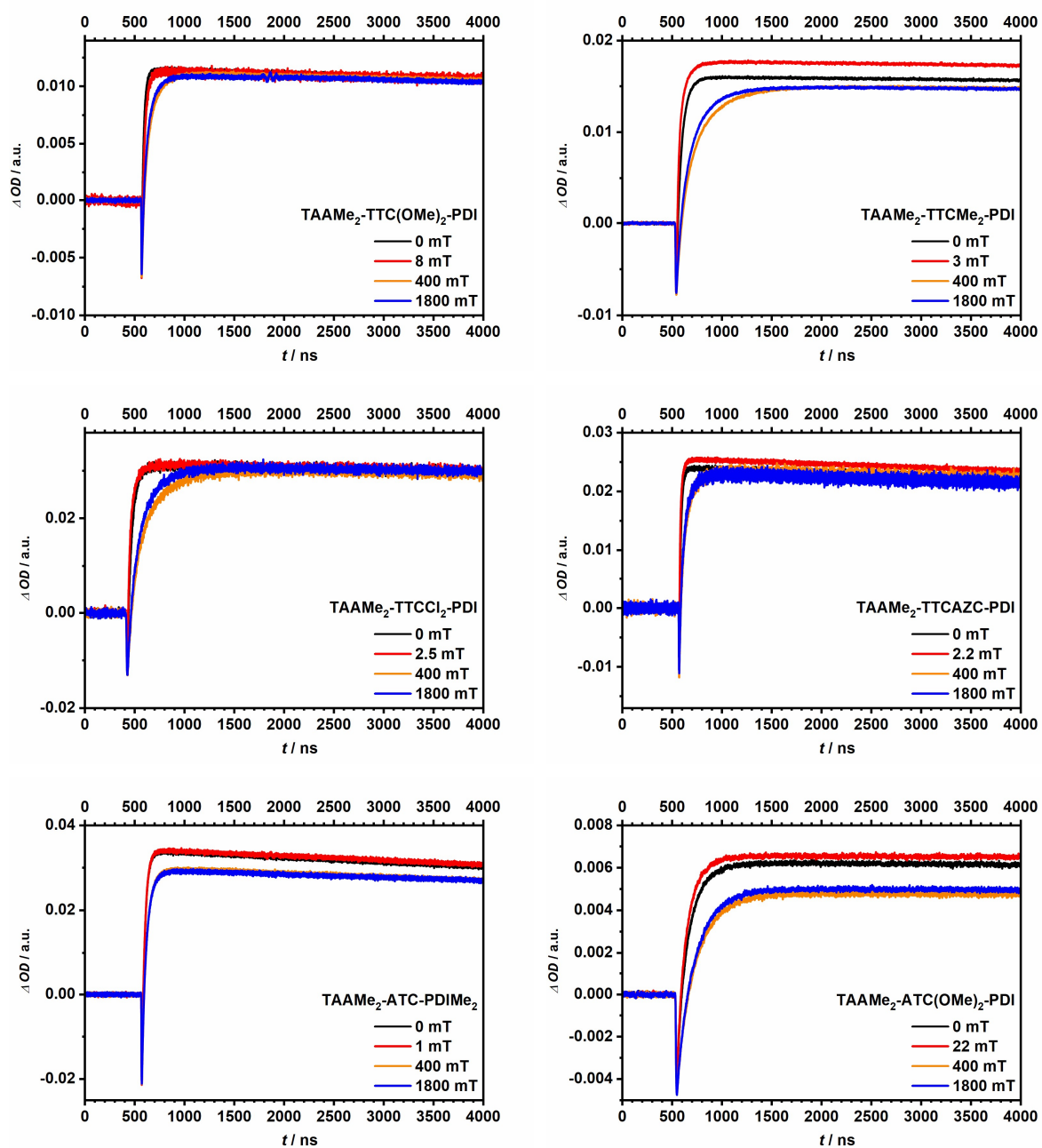




**Figure A11:**  $2J$  region of all investigated triads at a delay time of 50 ns and the corresponding parabolic fit to determine the  $2J$  coupling of each triad. The minimum of the parabolic fit gives the  $2J$  values depicted in the respective sections.

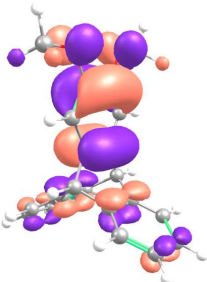
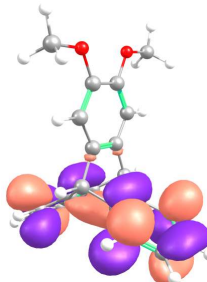
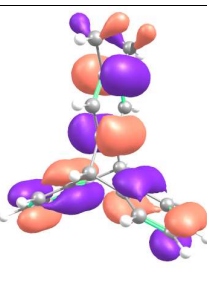
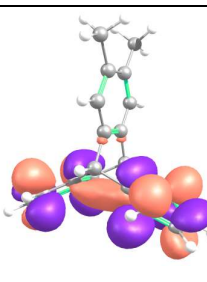
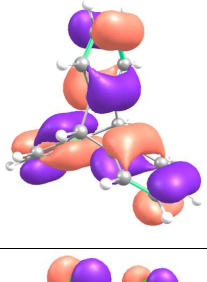
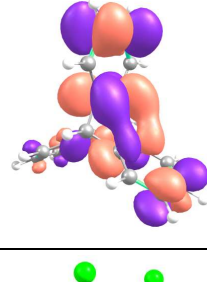
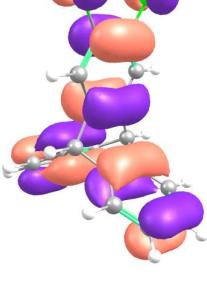
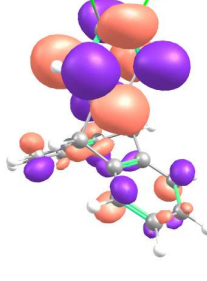
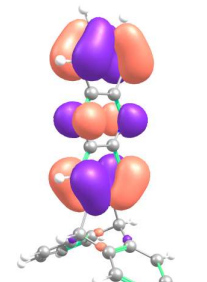
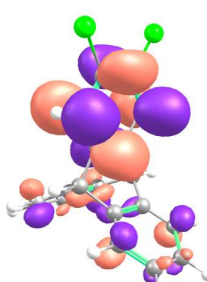






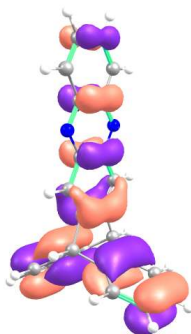
**Figure A12:** Triplet rise of all investigated triads whereby the curve of the 2J coupling corresponds to the measured curve nearest to the calculated value.

**Table A1:** HOMO/LUMO energies of the **TTC** bridges as well as the **TAA** and **PDI** moiety.

B3LYP / 6-311+G**	$E_{\text{HOMO}} / \text{eV}$	HOMO	$E_{\text{LUMO}} / \text{eV}$	LUMO
<b>TTC(OMe)<sub>2</sub></b>	-5.44		-0.58	
<b>TTCMe<sub>2</sub></b>	-5.94		-0.58	
<b>TTC</b>	-6.16		-0.64	
<b>TTCCl<sub>2</sub></b>	-6.37		-1.12	
<b>TTCAZC</b>	-6.29		-2.62	

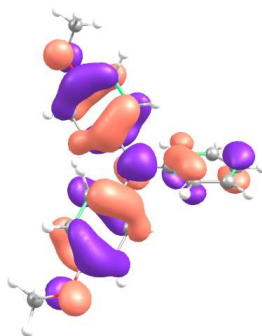
TTCAZC HOMO-1

-6.44

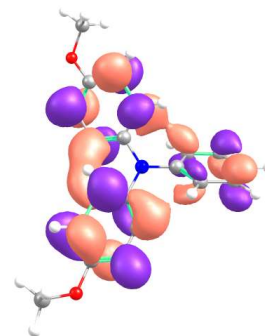


TAA

-8.82

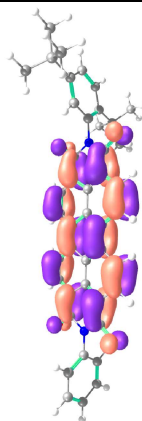


-4.39

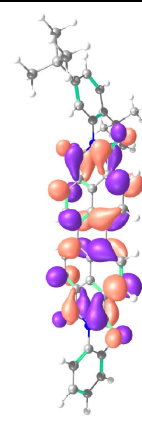


PDI

-1.79



0.60



**Data of all fit results**

All decay times with the corresponding amplitudes after deconvolution fit with the L900 software and after normalisation of the amplitudes to 1.

<b>TAAMe<sub>2</sub>-TTC-PDIME<sub>2</sub></b>	<b>t<sub>1</sub> / ns</b>	<b>a<sub>1</sub></b>	<b>t<sub>2</sub> / ns</b>	<b>a<sub>2</sub></b>	<b>t<sub>3</sub> / ns</b>	<b>a<sub>3</sub></b>
<b>0,0</b>	29,24	0,9706	117,17	0,0294		
<b>0,1</b>	29,24	0,9706	97,48	0,0294		
<b>0,5</b>	27,02	0,9714	127,00	0,0286		
<b>0,6</b>	23,34	0,9167	75,89	0,0833		
<b>1,0</b>	22,16	0,9167	77,91	0,0833		
<b>1,2</b>	20,67	0,8649	65,89	0,1351		
<b>1,5</b>	20,76	0,7838	58,21	0,2162		
<b>1,7</b>	24,34	0,7714	59,20	0,2286		
<b>1,9</b>	28,11	0,8485	72,60	0,1515		
<b>2,5</b>	32,70	0,8485	82,65	0,1515		
<b>3,1</b>	36,47	0,7750	84,49	0,2250		
<b>3,5</b>	35,62	0,6829	82,22	0,3171		
<b>4,0</b>	38,95	0,7317	96,59	0,2683		
<b>4,3</b>	38,42	0,7000	99,50	0,3000		
<b>4,8</b>	39,13	0,6905	102,27	0,3095		
<b>5,3</b>	38,63	0,6585	104,08	0,3415		
<b>5,8</b>	37,06	0,6667	105,65	0,3333		
<b>6,3</b>	34,85	0,6061	102,24	0,3939		
<b>6,9</b>	39,46	0,6341	115,70	0,3659		
<b>7,4</b>	39,16	0,6098	116,46	0,3902		
<b>7,9</b>	35,31	0,5882	109,03	0,4118		
<b>8,0</b>	40,64	0,6429	122,89	0,3571		
<b>8,9</b>	36,62	0,6061	117,42	0,3939		
<b>9,4</b>	36,67	0,5938	117,01	0,4063		
<b>10,5</b>	36,96	0,5938	121,51	0,4063		
<b>11,5</b>	38,25	0,6061	128,80	0,3939		
<b>12,5</b>	37,60	0,6061	133,46	0,3939		
<b>13,6</b>	38,41	0,5938	136,87	0,4063		
<b>15,0</b>	38,07	0,5938	140,73	0,4063		
<b>15,6</b>	39,06	0,5938	143,84	0,4063		
<b>16,7</b>	38,99	0,6061	147,44	0,3939		
<b>17,7</b>	40,49	0,6061	153,16	0,3939		
<b>18,8</b>	39,26	0,6061	152,29	0,3939		
<b>20,0</b>	40,51	0,6061	157,90	0,3939		
<b>22,0</b>	40,13	0,5938	162,24	0,4063		
<b>24,0</b>	40,81	0,5938	166,78	0,4063		
<b>26,0</b>	42,00	0,6176	174,22	0,3824		
<b>28,0</b>	42,28	0,6176	177,72	0,3824		
<b>30,0</b>	44,24	0,6250	185,65	0,3750		
<b>33,0</b>	42,87	0,6250	182,96	0,3750		
<b>36,0</b>	43,80	0,6364	190,05	0,3636		
<b>39,0</b>	43,15	0,6250	191,53	0,3750		

<b>42,0</b>	43,49	0,6250	193,33	0,3750		
<b>45,0</b>	43,95	0,6250	197,20	0,3750		
<b>50,0</b>	17,27	0,2703	60,07	0,4595	219,66	0,2703
<b>55,0</b>	44,73	0,6250	207,03	0,3750		
<b>60,0</b>	47,15	0,6250	209,05	0,3750		
<b>65,0</b>	47,56	0,6250	212,25	0,3750		
<b>70,0</b>	47,36	0,6250	213,55	0,3750		
<b>75,0</b>	48,52	0,6341	218,05	0,3659		
<b>80,0</b>	47,01	0,6250	215,98	0,3750		
<b>85,0</b>	38,02	0,4651	104,82	0,3023	267,09	0,2326
<b>90,0</b>	35,83	0,4286	93,43	0,3095	255,46	0,2619
<b>95,0</b>	38,53	0,1550	113,44	0,7752	272,56	0,0698
<b>100,0</b>	49,02	0,6341	222,28	0,3659		
<b>110,0</b>	48,90	0,6341	225,56	0,3659		
<b>120,0</b>	36,18	0,4286	100,83	0,3333	271,56	0,2381
<b>130,0</b>	40,67	0,5238	126,86	0,2857	284,30	0,1905
<b>140,0</b>	43,51	0,5610	159,59	0,3171	333,30	0,1220
<b>150,0</b>	41,90	0,5500	153,47	0,3250	330,98	0,1250
<b>160,0</b>	41,09	0,5122	125,40	0,2683	280,93	0,2195
<b>170,0</b>	45,51	0,6000	193,68	0,3750	520,10	0,0250
<b>180,0</b>	37,23	0,4048	82,58	0,2857	248,17	0,3095
<b>190,0</b>	41,42	0,5250	131,45	0,2750	294,00	0,2000
<b>200,0</b>	46,20	0,5897	192,29	0,3590	432,21	0,0513
<b>220,0</b>	39,97	0,5122	137,17	0,3171	316,17	0,1707
<b>240,0</b>	41,54	0,5250	134,14	0,3000	304,81	0,1750
<b>260,0</b>	45,37	0,5750	197,71	0,4000	619,64	0,0250
<b>280,0</b>	43,66	0,5500	162,03	0,3250	343,35	0,1250
<b>300,0</b>	44,04	0,5610	170,18	0,3415	371,69	0,0976
<b>350,0</b>	40,08	0,5000	118,60	0,2750	284,35	0,2250
<b>400,0</b>	43,13	0,5366	157,88	0,3415	337,96	0,1220
<b>450,0</b>	41,55	0,5122	126,64	0,2683	285,64	0,2195
<b>500,0</b>	40,71	0,5000	125,39	0,3000	295,90	0,2000
<b>550,0</b>	42,78	0,5122	120,47	0,2439	273,06	0,2439
<b>600,0</b>	40,83	0,5000	120,27	0,2750	277,04	0,2250
<b>650,0</b>	44,23	0,5500	162,81	0,3250	319,58	0,1250
<b>700,0</b>	41,76	0,5366	147,88	0,3415	328,23	0,1220
<b>750,0</b>	42,57	0,5366	145,73	0,3171	299,32	0,1463
<b>800,0</b>	42,17	0,5122	137,19	0,3171	293,83	0,1707
<b>850,0</b>	44,56	0,5610	173,73	0,3659	397,37	0,0732
<b>900,0</b>	42,00	0,5122	129,95	0,2683	263,68	0,2195
<b>950,0</b>	45,59	0,5750	185,21	0,4000	521,05	0,0250
<b>1000,0</b>	46,09	0,5750	188,63	0,4000	573,09	0,0250
<b>1100,0</b>	48,81	0,6154	206,81	0,3846		
<b>1200,0</b>	47,60	0,6154	201,41	0,3846		
<b>1300,0</b>	46,85	0,6000	195,00	0,4000		
<b>1400,0</b>	46,23	0,6000	189,73	0,4000		
<b>1500,0</b>	46,90	0,6000	186,78	0,4000		

<b>1600,0</b>	46,77	0,6154	182,05	0,3846
<b>1700,0</b>	45,90	0,6000	172,63	0,4000
<b>1800,0</b>	45,67	0,5750	162,86	0,4250

<b>TAAMe<sub>2</sub>-TTC-PDI</b>	<b>t<sub>1</sub> / ns</b>	<b>a<sub>1</sub></b>	<b>t<sub>2</sub> / ns</b>	<b>a<sub>2</sub></b>	<b>t<sub>3</sub> / ns</b>	<b>a<sub>3</sub></b>
<b>0,0</b>	46,34	0,8750	94,59	0,1250		
<b>0,1</b>	46,46	0,8714	92,17	0,1286		
<b>0,3</b>	45,79	0,8571	92,82	0,1429		
<b>0,5</b>	46,09	0,8857	99,54	0,1143		
<b>0,6</b>	43,57	0,8219	85,84	0,1781		
<b>1,0</b>	41,00	0,8028	85,61	0,1972		
<b>1,2</b>	38,06	0,7857	86,27	0,2143		
<b>1,5</b>	34,24	0,7465	81,77	0,2535		
<b>1,7</b>	30,84	0,7083	78,05	0,2917		
<b>2,0</b>	25,88	0,6714	75,60	0,3286		
<b>2,6</b>	21,88	0,6712	74,64	0,3288		
<b>3,1</b>	19,94	0,7067	79,81	0,2933		
<b>3,5</b>	20,09	0,7105	79,53	0,2895		
<b>3,9</b>	21,64	0,6849	78,89	0,3151		
<b>4,3</b>	27,54	0,6901	81,89	0,3099		
<b>4,8</b>	37,57	0,7465	92,63	0,2535		
<b>5,0</b>	43,89	0,7778	97,19	0,2222		
<b>5,8</b>	49,88	0,7639	98,08	0,2361		
<b>6,3</b>	51,30	0,6338	89,90	0,3662		
<b>6,9</b>	54,05	0,5915	93,31	0,4085		
<b>7,4</b>	52,40	0,4429	91,74	0,5571		
<b>7,9</b>	54,32	0,4225	95,78	0,5775		
<b>8,0</b>	53,51	0,3750	98,60	0,6250		
<b>8,9</b>	52,91	0,3611	103,32	0,6389		
<b>9,4</b>	51,94	0,3286	105,77	0,6714		
<b>10,5</b>	55,93	0,3699	115,87	0,6301		
<b>11,5</b>	55,88	0,3472	122,56	0,6528		
<b>12,5</b>	55,24	0,3333	126,47	0,6667		
<b>13,6</b>	59,82	0,3662	135,77	0,6338		
<b>15,0</b>	56,21	0,3239	137,63	0,6761		
<b>15,6</b>	58,08	0,3333	143,15	0,6667		
<b>16,7</b>	57,28	0,3380	147,92	0,6620		
<b>17,7</b>	59,05	0,3472	153,09	0,6528		
<b>18,8</b>	57,76	0,3333	155,74	0,6667		
<b>20,0</b>	61,98	0,3611	162,69	0,6389		
<b>23,0</b>	62,23	0,3562	172,68	0,6438		
<b>26,0</b>	67,03	0,3889	184,98	0,6111		
<b>29,0</b>	66,42	0,3750	191,83	0,6250		
<b>32,0</b>	67,85	0,3889	199,04	0,6111		
<b>35,0</b>	72,70	0,4247	212,98	0,5753		
<b>40,0</b>	71,92	0,4085	216,22	0,5915		

<b>45,0</b>	72,37	0,4110	222,63	0,5890		
<b>50,0</b>	73,71	0,4167	229,17	0,5833		
<b>55,0</b>	77,22	0,4384	238,71	0,5616		
<b>60,0</b>	76,64	0,4306	241,61	0,5694		
<b>65,0</b>	78,72	0,4459	247,67	0,5541		
<b>70,0</b>	78,72	0,4444	250,09	0,5556		
<b>75,0</b>	81,26	0,4583	256,63	0,5417		
<b>80,0</b>	80,13	0,4507	254,53	0,5493		
<b>85,0</b>	79,45	0,4444	256,36	0,5556		
<b>90,0</b>	80,46	0,4507	260,26	0,5493		
<b>95,0</b>	80,22	0,4507	260,11	0,5493		
<b>100,0</b>	79,82	0,4444	261,54	0,5556		
<b>110,0</b>	80,51	0,4583	264,32	0,5417		
<b>120,0</b>	82,80	0,4583	269,88	0,5417		
<b>130,0</b>	82,50	0,4583	269,28	0,5417		
<b>140,0</b>	53,87	0,1831	116,44	0,3662	287,75	0,4507
<b>150,0</b>	53,37	0,1644	108,90	0,3562	282,28	0,4795
<b>160,0</b>	54,16	0,1507	106,41	0,3699	283,59	0,4795
<b>170,0</b>	62,15	0,2466	125,42	0,2877	287,93	0,4658
<b>180,0</b>	61,48	0,2222	120,79	0,3194	292,52	0,4583
<b>190,0</b>	84,25	0,4648	277,21	0,5352		
<b>200,0</b>	52,33	0,1571	110,68	0,3714	288,33	0,4714
<b>220,0</b>	54,76	0,1618	112,61	0,3676	292,61	0,4706
<b>240,0</b>	50,03	0,1250	103,00	0,3889	289,08	0,4861
<b>260,0</b>	82,23	0,4559	275,60	0,5441		
<b>280,0</b>	55,45	0,1806	119,92	0,3750	298,03	0,4444
<b>300,0</b>	56,69	0,1912	115,87	0,3382	291,47	0,4706
<b>350,0</b>	51,80	0,1447	110,76	0,3816	295,64	0,4737
<b>400,0</b>	84,64	0,4737	284,49	0,5263		
<b>450,0</b>	83,83	0,4605	283,17	0,5395		
<b>500,0</b>	85,34	0,4737	283,54	0,5263		
<b>550,0</b>	60,27	0,2297	129,11	0,3243	298,55	0,4459
<b>600,0</b>	84,23	0,4667	278,51	0,5333		
<b>650,0</b>	81,65	0,4533	273,57	0,5467		
<b>700,0</b>	64,37	0,2763	135,82	0,2763	290,36	0,4474
<b>750,0</b>	83,64	0,4667	273,70	0,5333		
<b>800,0</b>	66,05	0,3026	149,86	0,2895	292,72	0,4079
<b>850,0</b>	62,90	0,2533	121,52	0,2800	280,99	0,4667
<b>900,0</b>	79,87	0,4533	263,85	0,5467		
<b>950,0</b>	55,54	0,2000	117,91	0,3467	279,75	0,4533
<b>1000,0</b>	55,64	0,2000	119,35	0,3467	278,94	0,4533
<b>1100,0</b>	78,09	0,4324	252,84	0,5676		
<b>1200,0</b>	50,36	0,1600	106,00	0,3600	263,02	0,4800
<b>1300,0</b>	51,58	0,1447	98,00	0,3421	250,63	0,5132
<b>1400,0</b>	76,29	0,4324	239,63	0,5676		
<b>1500,0</b>	75,85	0,4400	233,90	0,5600		
<b>1600,0</b>	71,21	0,4133	222,82	0,5867		

<b>1700,0</b>	70,55	0,4133	215,37	0,5867
<b>1800,0</b>	65,72	0,3919	198,63	0,6081

<b>TAA-TTC- PDIMe<sub>2</sub></b>	<b>t<sub>1</sub> / ns</b>	<b>a<sub>1</sub></b>	<b>t<sub>2</sub> / ns</b>	<b>a<sub>2</sub></b>	<b>t<sub>3</sub> / ns</b>	<b>a<sub>3</sub></b>
<b>0,0</b>	52,92	0,8382	104,08	0,1618		
<b>0,1</b>	54,82	0,8824	115,75	0,1176		
<b>0,3</b>	54,33	0,8657	109,89	0,1343		
<b>0,5</b>	53,55	0,8507	107,99	0,1493		
<b>0,6</b>	53,74	0,8696	114,93	0,1304		
<b>0,9</b>	51,90	0,8358	107,59	0,1642		
<b>1,2</b>	47,36	0,6970	86,99	0,3030		
<b>1,5</b>	48,21	0,8382	113,00	0,1618		
<b>1,7</b>	43,67	0,7612	98,45	0,2388		
<b>2,0</b>	40,20	0,7353	96,40	0,2647		
<b>2,6</b>	36,09	0,7206	97,08	0,2794		
<b>3,1</b>	29,72	0,6857	92,82	0,3143		
<b>3,5</b>	26,66	0,6901	94,47	0,3099		
<b>3,9</b>	24,83	0,6944	96,75	0,3056		
<b>4,3</b>	26,35	0,6901	96,61	0,3099		
<b>4,8</b>	31,41	0,7000	101,58	0,3000		
<b>5,3</b>	33,21	0,7143	102,68	0,2857		
<b>5,8</b>	45,53	0,7681	116,54	0,2319		
<b>6,3</b>	52,43	0,7910	121,40	0,2090		
<b>6,9</b>	57,67	0,7941	123,19	0,2059		
<b>7,4</b>	61,55	0,7429	117,41	0,2571		
<b>7,9</b>	68,39	0,7794	127,53	0,2206		
<b>8,4</b>	69,26	0,6087	116,19	0,3913		
<b>8,9</b>	68,62	0,5000	115,29	0,5000		
<b>9,4</b>	68,12	0,4706	117,17	0,5294		
<b>10,5</b>	59,50	0,2537	118,09	0,7463		
<b>11,5</b>	59,72	0,2500	123,80	0,7500		
<b>12,5</b>	64,64	0,2836	137,33	0,7164		
<b>13,6</b>	63,98	0,2754	143,52	0,7246		
<b>15,0</b>	65,06	0,2941	151,47	0,7059		
<b>15,6</b>	67,37	0,3088	159,06	0,6912		
<b>16,7</b>	69,83	0,3134	165,51	0,6866		
<b>17,7</b>	70,42	0,3188	169,90	0,6812		
<b>18,8</b>	68,86	0,3043	173,22	0,6957		
<b>20,0</b>	70,77	0,3235	180,73	0,6765		
<b>23,0</b>	72,61	0,3284	193,70	0,6716		
<b>26,0</b>	75,95	0,3529	205,84	0,6471		
<b>29,0</b>	78,51	0,3676	217,36	0,6324		
<b>32,0</b>	81,98	0,3824	228,51	0,6176		
<b>35,0</b>	83,58	0,3944	234,86	0,6056		
<b>40,0</b>	86,36	0,4028	244,26	0,5972		
<b>45,0</b>	87,06	0,4085	253,99	0,5915		



<b>50,0</b>	89,76	0,4225	264,38	0,5775		
<b>55,0</b>	91,59	0,4286	273,63	0,5714		
<b>60,0</b>	91,86	0,4286	277,47	0,5714		
<b>65,0</b>	91,90	0,4286	281,09	0,5714		
<b>70,0</b>	92,28	0,4225	284,46	0,5775		
<b>75,0</b>	94,91	0,4384	290,40	0,5616		
<b>80,0</b>	95,26	0,4429	296,26	0,5571		
<b>85,0</b>	70,20	0,2000	133,92	0,3143	313,81	0,4857
<b>90,0</b>	95,68	0,4429	302,07	0,5571		
<b>95,0</b>	71,00	0,1831	128,25	0,3239	316,32	0,4930
<b>100,0</b>	96,35	0,4493	306,80	0,5507		
<b>110,0</b>	96,47	0,4493	310,59	0,5507		
<b>120,0</b>	97,36	0,4493	312,00	0,5507		
<b>130,0</b>	98,53	0,4493	318,70	0,5507		
<b>140,0</b>	99,22	0,4571	320,91	0,5429		
<b>150,0</b>	98,83	0,4571	322,92	0,5429		
<b>160,0</b>	63,23	0,1429	127,18	0,3714	337,11	0,4857
<b>170,0</b>	77,70	0,2571	160,43	0,3000	348,71	0,4429
<b>180,0</b>	99,50	0,4571	325,28	0,5429		
<b>190,0</b>	67,98	0,1714	134,29	0,3571	346,29	0,4714
<b>200,0</b>	99,85	0,4638	329,12	0,5362		
<b>220,0</b>	102,26	0,4648	331,14	0,5352		
<b>240,0</b>	73,90	0,2394	156,56	0,3239	354,94	0,4366
<b>260,0</b>	98,11	0,4507	326,68	0,5493		
<b>280,0</b>	99,44	0,4571	332,01	0,5429		
<b>300,0</b>	98,39	0,4507	329,31	0,5493		
<b>350,0</b>	98,99	0,4571	329,93	0,5429		
<b>400,0</b>	100,36	0,4571	332,82	0,5429		
<b>450,0</b>	72,73	0,2083	145,98	0,3333	351,27	0,4583
<b>500,0</b>	105,22	0,4583	333,02	0,5417		
<b>550,0</b>	99,71	0,4571	329,67	0,5429		
<b>600,0</b>	97,89	0,4493	325,76	0,5507		
<b>650,0</b>	98,98	0,4429	324,13	0,5571		
<b>700,0</b>	96,95	0,4493	318,07	0,5507		
<b>750,0</b>	97,36	0,4493	319,73	0,5507		
<b>800,0</b>	96,02	0,4412	313,18	0,5588		
<b>850,0</b>	95,62	0,4493	311,71	0,5507		
<b>900,0</b>	93,98	0,4366	306,92	0,5634		
<b>950,0</b>	93,74	0,4348	304,63	0,5652		
<b>1000,0</b>	94,56	0,4429	302,91	0,5571		
<b>1100,0</b>	92,57	0,4366	297,39	0,5634		
<b>1200,0</b>	92,01	0,4286	290,78	0,5714		
<b>1300,0</b>	90,18	0,4286	282,58	0,5714		
<b>1400,0</b>	86,11	0,4143	272,30	0,5857		
<b>1500,0</b>	87,60	0,4143	267,03	0,5857		
<b>1600,0</b>	83,31	0,4000	257,67	0,6000		
<b>1700,0</b>	82,45	0,4000	249,14	0,6000		

<b>1800,0</b>	<b>79,59</b>	<b>0,3944</b>	<b>238,22</b>	<b>0,6056</b>
<b>TAA-TTC-PDI</b>	<b>t<sub>1</sub> / ns</b>	<b>a<sub>1</sub></b>	<b>t<sub>2</sub> / ns</b>	<b>a<sub>2</sub></b>
<b>0,0</b>	128,79	1,0000		
<b>0,2</b>	40,67	0,0455	131,96	0,9545
<b>0,3</b>	64,76	0,1053	131,63	0,8947
<b>0,5</b>	39,40	0,0909	131,29	0,9091
<b>0,7</b>	54,26	0,0909	132,00	0,9091
<b>0,9</b>	50,97	0,0909	131,56	0,9091
<b>1,2</b>	65,83	0,1304	134,78	0,8696
<b>1,5</b>	37,93	0,0909	130,23	0,9091
<b>1,7</b>	44,46	0,0455	128,87	0,9545
<b>2,0</b>	44,00	0,0909	129,76	0,9091
<b>2,6</b>	57,12	0,1304	134,08	0,8696
<b>3,1</b>	52,42	0,0909	130,23	0,9091
<b>3,5</b>	62,40	0,1364	133,81	0,8636
<b>3,9</b>	64,88	0,1739	132,60	0,8261
<b>4,3</b>	60,72	0,1739	131,89	0,8261
<b>4,8</b>	66,72	0,1818	132,48	0,8182
<b>5,3</b>	81,41	0,3913	142,62	0,6087
<b>5,8</b>	64,93	0,2273	131,02	0,7727
<b>6,3</b>	56,54	0,2273	130,55	0,7727
<b>6,9</b>	77,66	0,4783	142,96	0,5217
<b>7,4</b>	77,22	0,5000	146,44	0,5000
<b>7,9</b>	64,70	0,3913	136,81	0,6087
<b>8,4</b>	70,59	0,4545	142,84	0,5455
<b>8,9</b>	62,53	0,4348	139,74	0,5652
<b>9,4</b>	61,61	0,4286	137,62	0,5714
<b>10,5</b>	60,83	0,5000	143,34	0,5000
<b>11,5</b>	59,71	0,5455	146,01	0,4545
<b>12,5</b>	53,08	0,5000	140,13	0,5000
<b>13,6</b>	54,03	0,5263	144,99	0,4737
<b>14,6</b>	56,85	0,5455	147,97	0,4545
<b>15,6</b>	58,36	0,5455	151,50	0,4545
<b>16,7</b>	61,78	0,5000	147,23	0,5000
<b>17,7</b>	66,30	0,4762	148,75	0,5238
<b>18,7</b>	67,63	0,4091	144,69	0,5909
<b>20,0</b>	70,01	0,3636	145,63	0,6364
<b>22,0</b>	58,92	0,1364	140,55	0,8636
<b>24,0</b>	47,34	0,0500	145,31	0,9500
<b>26,0</b>	45,30	0,0455	155,18	0,9545
<b>28,0</b>	30,61	0,0455	161,68	0,9545
<b>30,0</b>	19,34	0,0455	170,78	0,9545
<b>33,0</b>	182,60	1,0000		
<b>36,0</b>	194,12	1,0000		
<b>39,0</b>	20,59	0,0455	204,35	0,9545

<b>42,0</b>	26,54	0,0455	214,68	0,9545
<b>45,0</b>	35,51	0,0455	220,35	0,9545
<b>50,0</b>	44,99	0,0455	231,43	0,9545
<b>55,0</b>	28,14	0,0455	239,04	0,9545
<b>60,0</b>	54,14	0,0476	251,87	0,9524
<b>65,0</b>	73,13	0,0476	259,13	0,9524
<b>70,0</b>	62,29	0,0455	262,72	0,9545
<b>75,0</b>	100,19	0,0909	273,55	0,9091
<b>80,0</b>	95,70	0,0526	276,57	0,9474
<b>85,0</b>	98,69	0,0909	283,17	0,9091
<b>90,0</b>	107,01	0,1000	286,61	0,9000
<b>95,0</b>	106,11	0,0909	288,78	0,9091
<b>100,0</b>	108,90	0,0952	295,38	0,9048
<b>110,0</b>	103,19	0,0909	297,98	0,9091
<b>120,0</b>	108,86	0,0909	300,61	0,9091
<b>130,0</b>	91,90	0,0909	303,15	0,9091
<b>140,0</b>	96,50	0,0909	303,75	0,9091
<b>150,0</b>	118,49	0,0952	312,18	0,9048
<b>160,0</b>	120,18	0,0952	313,19	0,9048
<b>170,0</b>	122,78	0,1364	317,23	0,8636
<b>180,0</b>	88,32	0,0909	312,24	0,9091
<b>190,0</b>	114,38	0,0952	316,63	0,9048
<b>200,0</b>	132,07	0,1364	323,05	0,8636
<b>220,0</b>	114,47	0,1364	322,76	0,8636
<b>240,0</b>	110,96	0,0952	321,07	0,9048
<b>260,0</b>	137,97	0,1429	329,63	0,8571
<b>280,0</b>	110,83	0,0952	321,21	0,9048
<b>300,0</b>	131,01	0,1364	326,40	0,8636
<b>350,0</b>	121,11	0,0909	325,77	0,9091
<b>400,0</b>	132,33	0,1304	330,58	0,8696
<b>450,0</b>	141,24	0,1304	331,16	0,8696
<b>500,0</b>	128,01	0,1304	330,71	0,8696
<b>550,0</b>	124,40	0,1250	331,83	0,8750
<b>600,0</b>	124,38	0,1250	327,58	0,8750
<b>650,0</b>	135,40	0,1304	331,19	0,8696
<b>700,0</b>	123,06	0,1364	326,56	0,8636
<b>750,0</b>	132,04	0,1364	325,32	0,8636
<b>800,0</b>	121,41	0,1304	326,05	0,8696
<b>850,0</b>	106,66	0,0870	320,89	0,9130
<b>900,0</b>	114,45	0,0870	317,70	0,9130
<b>950,0</b>	112,85	0,0870	318,99	0,9130
<b>1000,0</b>	96,79	0,0870	314,09	0,9130
<b>1100,0</b>	106,52	0,1250	317,38	0,8750
<b>1200,0</b>	123,44	0,1304	314,85	0,8696
<b>1300,0</b>	98,15	0,0870	308,11	0,9130
<b>1400,0</b>	114,53	0,1250	311,94	0,8750
<b>1500,0</b>	112,86	0,1250	308,21	0,8750

<b>1600,0</b>	94,64	0,0870	298,68	0,9130
<b>1700,0</b>	99,53	0,1250	298,96	0,8750
<b>1800,0</b>	99,01	0,1250	290,45	0,8750

<b>TAAMe<sub>2</sub>-TTC(OMe)<sub>2</sub>-PDI</b>	<b>t<sub>1</sub> / ns</b>	<b>a<sub>1</sub></b>	<b>t<sub>2</sub> / ns</b>	<b>a<sub>2</sub></b>
<b>0</b>	51,05	0,9886	398,29	0,0114
<b>0,2</b>	50,89	0,9770	315,09	0,0230
<b>0,4</b>	51,48	0,9888	503,54	0,0112
<b>0,6</b>	51,02	0,9787	364,68	0,0213
<b>0,8</b>	50,80	0,9785	387,54	0,0215
<b>1</b>	51,01	0,9778	422,93	0,0222
<b>1,3</b>	50,51	0,9778	315,27	0,0222
<b>1,6</b>	48,62	0,9670	207,79	0,0330
<b>1,9</b>	49,76	0,9783	397,46	0,0217
<b>2,2</b>	48,93	0,9778	402,45	0,0222
<b>2,5</b>	48,09	0,9780	293,61	0,0220
<b>3</b>	45,82	0,9565	212,51	0,0435
<b>3,5</b>	45,14	0,9540	217,28	0,0460
<b>4</b>	39,28	0,8636	111,71	0,1364
<b>4,5</b>	34,80	0,8090	100,20	0,1910
<b>5</b>	32,33	0,7500	85,04	0,2500
<b>5,5</b>	31,21	0,7667	91,81	0,2333
<b>6</b>	27,72	0,7283	85,89	0,2717
<b>6,5</b>	25,19	0,7053	81,62	0,2947
<b>7</b>	24,18	0,7204	85,17	0,2796
<b>7,5</b>	21,25	0,6771	78,80	0,3229
<b>8</b>	20,90	0,6771	79,11	0,3229
<b>8,5</b>	24,65	0,7253	90,45	0,2747
<b>9</b>	25,79	0,7079	86,85	0,2921
<b>9,5</b>	27,77	0,7273	92,17	0,2727
<b>10</b>	29,72	0,7191	90,30	0,2809
<b>11</b>	33,62	0,7412	95,08	0,2588
<b>13</b>	45,88	0,8118	106,94	0,1882
<b>14</b>	51,41	0,8929	132,34	0,1071
<b>15</b>	60,86	0,9302	159,58	0,0698
<b>16</b>	65,86	0,9551	192,89	0,0449
<b>17</b>	62,59	0,8090	117,99	0,1910
<b>18</b>	72,82	0,9419	208,26	0,0581
<b>19</b>	63,90	0,6629	111,74	0,3371
<b>20</b>	70,89	0,7802	133,52	0,2198
<b>22</b>	72,68	0,7093	131,45	0,2907
<b>24</b>	69,07	0,5444	125,23	0,4556
<b>26</b>	71,22	0,5568	135,61	0,4432
<b>28</b>	70,54	0,5172	140,01	0,4828
<b>30</b>	74,19	0,5341	148,28	0,4659
<b>35</b>	72,02	0,4651	158,73	0,5349

<b>40</b>	74,40	0,4615	171,05	0,5385
<b>45</b>	74,50	0,4483	179,26	0,5517
<b>50</b>	76,78	0,4535	190,84	0,5465
<b>55</b>	77,00	0,4444	196,01	0,5556
<b>60</b>	81,24	0,4598	207,34	0,5402
<b>65</b>	82,24	0,4725	214,84	0,5275
<b>70</b>	81,39	0,4607	218,50	0,5393
<b>75</b>	81,71	0,4674	227,27	0,5326
<b>80</b>	84,25	0,4725	231,88	0,5275
<b>85</b>	82,28	0,4667	230,55	0,5333
<b>90</b>	84,50	0,4725	239,17	0,5275
<b>95</b>	84,47	0,4719	244,82	0,5281
<b>100</b>	85,99	0,4889	249,82	0,5111
<b>110</b>	85,59	0,4762	250,42	0,5238
<b>120</b>	87,45	0,4835	255,96	0,5165
<b>130</b>	86,68	0,4831	259,93	0,5169
<b>140</b>	89,15	0,5000	269,41	0,5000
<b>150</b>	88,73	0,4946	269,40	0,5054
<b>160</b>	87,52	0,4828	268,31	0,5172
<b>170</b>	91,19	0,5109	280,71	0,4891
<b>180</b>	90,92	0,4944	278,58	0,5056
<b>190</b>	89,74	0,5055	282,91	0,4945
<b>200</b>	90,49	0,5059	285,29	0,4941
<b>220</b>	93,36	0,5165	294,99	0,4835
<b>240</b>	97,93	0,5465	307,69	0,4535
<b>260</b>	98,21	0,5495	313,51	0,4505
<b>280</b>	96,23	0,5326	303,72	0,4674
<b>300</b>	98,23	0,5254	313,61	0,4746
<b>350</b>	98,35	0,5259	312,53	0,4741
<b>400</b>	98,62	0,5278	313,85	0,4722
<b>450</b>	98,29	0,5304	317,27	0,4696
<b>500</b>	97,58	0,5268	315,18	0,4732
<b>550</b>	95,57	0,5135	307,69	0,4865
<b>600</b>	98,06	0,5304	313,34	0,4696
<b>650</b>	98,17	0,5315	315,04	0,4685
<b>700</b>	96,19	0,5225	308,51	0,4775
<b>750</b>	98,11	0,5340	311,46	0,4660
<b>800</b>	96,97	0,5315	304,37	0,4685
<b>850</b>	94,64	0,5192	297,77	0,4808
<b>900</b>	97,81	0,5421	305,27	0,4579
<b>950</b>	98,13	0,5413	305,54	0,4587
<b>1000</b>	95,24	0,5288	296,26	0,4712
<b>1100</b>	96,73	0,5408	302,65	0,4592
<b>1200</b>	94,28	0,5321	290,63	0,4679
<b>1300</b>	95,27	0,5455	287,38	0,4545
<b>1400</b>	89,21	0,5000	267,79	0,5000
<b>1500</b>	93,02	0,5385	274,38	0,4615

<b>1600</b>	92,20	0,5347	263,87	0,4653
<b>1700</b>	88,84	0,5189	249,74	0,4811
<b>1800</b>	93,20	0,5263	285,65	0,4737

<b>TAAMe<sub>2</sub>-TTCMe<sub>2</sub>-PDI</b>	<b>t<sub>1</sub> / ns</b>	<b>a<sub>1</sub></b>	<b>t<sub>2</sub> / ns</b>	<b>a<sub>2</sub></b>
<b>0</b>	53,63	1,0000		0,0000
<b>0,2</b>	45,58	0,7922	76,86	0,2078
<b>0,4</b>	41,41	0,6389	69,50	0,3611
<b>0,6</b>	40,07	0,6712	75,45	0,3288
<b>0,8</b>	36,53	0,5479	67,36	0,4521
<b>1</b>	37,39	0,5946	67,89	0,4054
<b>1,2</b>	34,20	0,6081	69,92	0,3919
<b>1,5</b>	33,34	0,6486	74,04	0,3514
<b>2</b>	28,02	0,6709	76,42	0,3291
<b>2,3</b>	25,65	0,6974	79,91	0,3026
<b>2,5</b>	22,45	0,6753	78,78	0,3247
<b>2,6</b>	20,57	0,6515	73,30	0,3485
<b>2,8</b>	19,63	0,6667	74,36	0,3333
<b>2,9</b>	20,17	0,6923	77,00	0,3077
<b>3</b>	19,29	0,6667	76,19	0,3333
<b>3,1</b>	18,78	0,6818	76,31	0,3182
<b>3,2</b>	18,50	0,6765	75,42	0,3235
<b>3,3</b>	19,01	0,6716	75,78	0,3284
<b>3,4</b>	19,38	0,7101	80,00	0,2899
<b>3,5</b>	20,74	0,6709	79,09	0,3291
<b>3,6</b>	19,08	0,6667	74,26	0,3333
<b>3,7</b>	20,77	0,6866	79,64	0,3134
<b>3,8</b>	20,05	0,6615	75,26	0,3385
<b>3,9</b>	21,08	0,6667	78,11	0,3333
<b>4</b>	23,50	0,6579	79,74	0,3421
<b>4,2</b>	23,57	0,6508	76,54	0,3492
<b>4,5</b>	27,52	0,6479	80,20	0,3521
<b>5</b>	34,68	0,6622	84,89	0,3378
<b>5,5</b>	39,08	0,6438	84,92	0,3562
<b>6</b>	45,59	0,6761	90,98	0,3239
<b>6,5</b>	46,10	0,5200	84,83	0,4800
<b>7</b>	41,48	0,2877	79,12	0,7123
<b>7,5</b>	44,56	0,3014	84,63	0,6986
<b>8</b>	43,45	0,2703	87,49	0,7297
<b>8,5</b>	42,19	0,2603	92,27	0,7397
<b>9</b>	44,42	0,2533	95,60	0,7467
<b>9,5</b>	43,83	0,2297	98,58	0,7703
<b>10</b>	41,78	0,2027	99,68	0,7973
<b>11</b>	46,19	0,2222	109,53	0,7778

<b>12</b>	48,08	0,2297	114,27	0,7703
<b>13</b>	44,63	0,2381	122,58	0,7619
<b>14</b>	49,49	0,2381	127,80	0,7619
<b>15</b>	46,00	0,2469	132,28	0,7531
<b>16</b>	46,11	0,2439	137,34	0,7561
<b>17</b>	49,08	0,2625	143,75	0,7375
<b>18</b>	50,00	0,2564	147,00	0,7436
<b>19</b>	50,86	0,2821	153,58	0,7179
<b>20</b>	54,07	0,2875	159,41	0,7125
<b>22</b>	58,78	0,3247	173,72	0,6753
<b>24</b>	55,54	0,3026	177,66	0,6974
<b>26</b>	60,20	0,3289	186,89	0,6711
<b>28</b>	65,61	0,3590	197,21	0,6410
<b>30</b>	65,68	0,3649	202,26	0,6351
<b>35</b>	73,28	0,4054	222,80	0,5946
<b>40</b>	72,74	0,3889	228,74	0,6111
<b>45</b>	78,47	0,4189	241,29	0,5811
<b>50</b>	80,01	0,4267	249,63	0,5733
<b>55</b>	80,16	0,4306	254,93	0,5694
<b>60</b>	79,16	0,4225	258,18	0,5775
<b>65</b>	84,55	0,4583	271,80	0,5417
<b>70</b>	83,32	0,4342	269,83	0,5658
<b>75</b>	84,40	0,4429	274,38	0,5571
<b>80</b>	87,40	0,4571	279,25	0,5429
<b>85</b>	83,54	0,4366	277,32	0,5634
<b>90</b>	85,74	0,4559	286,01	0,5441
<b>95</b>	90,49	0,4783	294,37	0,5217
<b>100</b>	88,80	0,4706	292,78	0,5294
<b>110</b>	91,98	0,4853	302,90	0,5147
<b>120</b>	90,44	0,4638	300,21	0,5362
<b>130</b>	92,69	0,4928	310,34	0,5072
<b>140</b>	94,08	0,4853	309,66	0,5147
<b>150</b>	93,19	0,4783	311,78	0,5217
<b>160</b>	94,08	0,4714	313,20	0,5286
<b>170</b>	92,63	0,4706	309,74	0,5294
<b>180</b>	94,53	0,4930	318,86	0,5070
<b>190</b>	96,20	0,4925	318,61	0,5075
<b>200</b>	95,25	0,4925	317,53	0,5075
<b>220</b>	95,48	0,4928	321,02	0,5072
<b>240</b>	92,62	0,4627	314,16	0,5373
<b>260</b>	92,16	0,4776	317,60	0,5224
<b>280</b>	94,91	0,4925	322,57	0,5075
<b>300</b>	94,03	0,4853	322,52	0,5147
<b>350</b>	96,88	0,5000	329,10	0,5000
<b>400</b>	95,48	0,4923	324,02	0,5077

<b>450</b>	96,24	0,5000	325,83	0,5000
<b>500</b>	98,78	0,5152	332,88	0,4848
<b>550</b>	103,08	0,5068	336,87	0,4932
<b>600</b>	101,22	0,5068	335,92	0,4932
<b>650</b>	99,78	0,5000	329,05	0,5000
<b>700</b>	97,85	0,4861	323,83	0,5139
<b>750</b>	94,96	0,4789	315,76	0,5211
<b>800</b>	97,13	0,4857	316,07	0,5143
<b>850</b>	91,79	0,4638	303,90	0,5362
<b>900</b>	94,89	0,4638	306,86	0,5362
<b>950</b>	91,86	0,4638	302,84	0,5362
<b>1000</b>	90,46	0,4571	298,13	0,5429
<b>1100</b>	88,58	0,4493	287,68	0,5507
<b>1200</b>	87,79	0,4478	282,36	0,5522
<b>1300</b>	84,00	0,4348	270,50	0,5652
<b>1400</b>	83,11	0,4265	260,49	0,5735
<b>1500</b>	90,81	0,4925	272,91	0,5075
<b>1600</b>	80,90	0,4242	250,14	0,5758
<b>1700</b>	77,05	0,4127	241,73	0,5873
<b>1800</b>	70,30	0,3651	227,57	0,6349

<b>TAAMe<sub>2</sub>-TTCCl<sub>2</sub>-PDI</b>	<b>t<sub>1</sub> / ns</b>	<b>a<sub>1</sub></b>	<b>t<sub>2</sub> / ns</b>	<b>a<sub>2</sub></b>	<b>t<sub>2</sub> / ns</b>	<b>a<sub>2</sub></b>
<b>0,0</b>	43,56	0,9831	551,82	0,0169		
<b>0,0</b>	44,33	0,9789	337,39	0,0211		
<b>0,1</b>	45,16	0,9894	607,00	0,0106		
<b>0,3</b>	45,17	0,9896	611,37	0,0104		
<b>0,5</b>	44,62	0,9896	585,61	0,0104		
<b>0,7</b>	44,11	0,9892	526,48	0,0108		
<b>1,2</b>	35,08	0,8085	101,15	0,1915		
<b>1,5</b>	30,45	0,8085	88,12	0,1915		
<b>1,7</b>	26,73	0,7684	80,47	0,2316		
<b>2,0</b>	22,12	0,7200	74,85	0,2800		
<b>2,6</b>	16,98	0,6887	69,65	0,3113		
<b>3,1</b>	18,89	0,6970	73,03	0,3030		
<b>3,5</b>	25,96	0,7500	84,49	0,2500		
<b>3,9</b>	33,39	0,8191	98,60	0,1809		
<b>4,3</b>	39,88	0,8804	114,11	0,1196		
<b>4,8</b>	46,15	0,9130	138,84	0,0870		
<b>5,3</b>	48,88	0,7766	113,70	0,2234		
<b>5,8</b>	50,83	0,7766	102,72	0,2234		
<b>6,3</b>	53,54	0,7634	109,46	0,2366		
<b>6,9</b>	53,66	0,6596	100,53	0,3404		
<b>7,4</b>	57,46	0,6989	113,90	0,3011		
<b>7,9</b>	54,49	0,5851	108,39	0,4149		
<b>8,4</b>	54,69	0,5368	109,29	0,4632		



<b>8,9</b>	55,02	0,5213	112,23	0,4787		
<b>9,4</b>	53,05	0,4737	114,63	0,5263		
<b>10,5</b>	57,26	0,5106	125,01	0,4894		
<b>11,5</b>	57,02	0,4731	129,47	0,5269		
<b>12,5</b>	57,04	0,4783	137,29	0,5217		
<b>13,6</b>	58,64	0,4731	142,02	0,5269		
<b>14,6</b>	58,75	0,4565	146,62	0,5435		
<b>15,6</b>	56,32	0,4194	147,60	0,5806		
<b>16,7</b>	57,16	0,4239	152,76	0,5761		
<b>17,7</b>	58,84	0,4516	159,97	0,5484		
<b>18,8</b>	59,90	0,4505	165,38	0,5495		
<b>19,8</b>	62,03	0,4624	170,69	0,5376		
<b>23,0</b>	65,39	0,4778	184,41	0,5222		
<b>26,0</b>	65,16	0,4783	193,44	0,5217		
<b>29,0</b>	65,79	0,4731	199,21	0,5269		
<b>32,0</b>	68,14	0,4835	208,32	0,5165		
<b>35,0</b>	67,35	0,4787	215,17	0,5213		
<b>40,0</b>	69,70	0,4947	224,48	0,5053		
<b>45,0</b>	71,04	0,4889	231,63	0,5111		
<b>50,0</b>	71,60	0,5000	237,20	0,5000		
<b>55,0</b>	72,12	0,4945	241,41	0,5055		
<b>60,0</b>	71,60	0,4889	242,02	0,5111		
<b>65,0</b>	73,17	0,5000	247,26	0,5000		
<b>70,0</b>	72,97	0,5000	253,49	0,5000		
<b>75,0</b>	76,79	0,5222	259,52	0,4778		
<b>80,0</b>	75,76	0,5161	258,69	0,4839		
<b>85,0</b>	75,73	0,5169	262,39	0,4831		
<b>90,0</b>	73,43	0,4944	257,30	0,5056		
<b>95,0</b>	77,20	0,5227	265,38	0,4773		
<b>100,0</b>	73,27	0,4886	255,55	0,5114		
<b>110,0</b>	76,49	0,5111	267,40	0,4889		
<b>120,0</b>	76,62	0,5114	267,33	0,4886		
<b>130,0</b>	75,84	0,5056	265,01	0,4944		
<b>140,0</b>	76,97	0,5114	270,93	0,4886		
<b>150,0</b>	74,66	0,5000	267,01	0,5000		
<b>160,0</b>	77,69	0,5114	271,75	0,4886		
<b>170,0</b>	77,85	0,5222	275,83	0,4778		
<b>180,0</b>	76,40	0,5116	271,76	0,4884		
<b>190,0</b>	56,27	0,2558	118,88	0,3605	300,86	0,3837
<b>200,0</b>	75,98	0,5059	272,12	0,4941		
<b>220,0</b>	75,27	0,5000	270,13	0,5000		
<b>240,0</b>	77,53	0,5109	274,18	0,4891		
<b>260,0</b>	76,19	0,5114	275,25	0,4886		
<b>280,0</b>	76,66	0,5000	270,82	0,5000		
<b>300,0</b>	77,75	0,5287	276,24	0,4713		
<b>350,0</b>	80,10	0,5287	280,23	0,4713		
<b>400,0</b>	75,54	0,4941	268,21	0,5059		

<b>450,0</b>	74,66	0,5000	269,47	0,5000
<b>500,0</b>	75,74	0,5057	270,00	0,4943
<b>550,0</b>	76,59	0,5059	269,32	0,4941
<b>600,0</b>	74,80	0,5000	264,24	0,5000
<b>650,0</b>	75,71	0,5000	264,21	0,5000
<b>700,0</b>	75,63	0,5000	264,82	0,5000
<b>750,0</b>	73,85	0,4881	275,16	0,5119
<b>800,0</b>	76,65	0,5176	264,54	0,4824
<b>850,0</b>	76,00	0,5119	260,45	0,4881
<b>900,0</b>	73,45	0,5000	255,86	0,5000
<b>950,0</b>	74,35	0,5000	254,78	0,5000
<b>1000,0</b>	74,37	0,5059	253,11	0,4941
<b>1100,0</b>	73,53	0,4940	245,00	0,5060
<b>1200,0</b>	72,66	0,4941	242,83	0,5059
<b>1300,0</b>	73,99	0,5116	241,31	0,4884
<b>1400,0</b>	70,83	0,4824	228,71	0,5176
<b>1500,0</b>	71,69	0,5000	230,39	0,5000
<b>1600,0</b>	73,28	0,5172	229,43	0,4828
<b>1700,0</b>	67,92	0,4824	210,44	0,5176
<b>1800,0</b>	58,71	0,4355	180,44	0,5645

<b>TAAMe<sub>2</sub>-TTCAZC-PDI</b>	<b>t<sub>1</sub> / ns</b>	<b>a<sub>1</sub></b>	<b>t<sub>2</sub> / ns</b>	<b>a<sub>2</sub></b>
<b>0</b>	43,72	1,0000		0,0000
<b>0,2</b>	43,46	1,0000		0,0000
<b>0,4</b>	42,41	1,0000		0,0000
<b>0,6</b>	42,14	1,0000		0,0000
<b>1</b>	38,74	0,9909	365,89	0,0091
<b>1,3</b>	28,50	0,7207	59,02	0,2793
<b>1,8</b>	25,30	0,7632	65,91	0,2368
<b>2</b>	21,29	0,6975	62,83	0,3025
<b>2,2</b>	17,49	0,6525	56,26	0,3475
<b>2,4</b>	14,46	0,6129	52,11	0,3871
<b>2,6</b>	16,08	0,6429	55,32	0,3571
<b>2,8</b>	18,54	0,6186	56,47	0,3814
<b>3</b>	19,45	0,6111	58,10	0,3889
<b>3,5</b>	36,92	0,9727	212,27	0,0273
<b>4</b>	42,41	0,9909	345,79	0,0091
<b>4,5</b>	46,90	0,9913	346,87	0,0087
<b>5</b>	50,98	0,9915	294,55	0,0085
<b>5,5</b>	54,17	0,9915	164,93	0,0085
<b>6</b>	59,91	1,0000		0,0000
<b>6,5</b>	61,18	0,9917	171,25	0,0083
<b>7</b>	63,87	0,9831	194,26	0,0169
<b>8</b>	66,89	0,9333	150,16	0,0667
<b>8,5</b>	68,93	0,9328	174,81	0,0672

<b>9</b>	67,90	0,8655	133,53	0,1345
<b>9,5</b>	66,34	0,7563	120,76	0,2437
<b>10</b>	70,19	0,8333	141,04	0,1667
<b>11</b>	69,18	0,7581	141,09	0,2419
<b>12</b>	69,80	0,7258	144,18	0,2742
<b>13</b>	70,06	0,7190	152,32	0,2810
<b>14</b>	64,56	0,6000	139,33	0,4000
<b>15</b>	69,03	0,6446	153,37	0,3554
<b>16</b>	69,78	0,6198	153,49	0,3802
<b>17</b>	67,03	0,5804	154,23	0,4196
<b>18</b>	69,50	0,6050	161,42	0,3950
<b>19</b>	66,11	0,5391	158,59	0,4609
<b>20</b>	69,40	0,5840	169,15	0,4160
<b>22</b>	64,67	0,5299	166,64	0,4701
<b>24</b>	66,77	0,5417	174,90	0,4583
<b>26</b>	63,79	0,5124	174,26	0,4876
<b>28</b>	65,29	0,5040	176,25	0,4960
<b>30</b>	64,95	0,4917	178,54	0,5083
<b>35</b>	63,14	0,4922	187,27	0,5078
<b>40</b>	66,63	0,5000	193,29	0,5000
<b>60</b>	63,61	0,4590	196,09	0,5410
<b>70</b>	62,48	0,4545	198,08	0,5455
<b>80</b>	62,36	0,4677	202,20	0,5323
<b>90</b>	63,57	0,4500	201,85	0,5500
<b>100</b>	61,60	0,4538	202,67	0,5462
<b>130</b>	58,37	0,4202	198,99	0,5798
<b>160</b>	60,78	0,4480	207,87	0,5520
<b>190</b>	63,24	0,4454	207,18	0,5546
<b>230</b>	62,93	0,4483	206,69	0,5517
<b>260</b>	60,57	0,4472	207,98	0,5528
<b>300</b>	62,36	0,4516	209,68	0,5484
<b>400</b>	61,86	0,4426	208,25	0,5574
<b>500</b>	60,62	0,4454	204,45	0,5546
<b>700</b>	64,02	0,4655	206,55	0,5345
<b>900</b>	63,48	0,4711	202,60	0,5289
<b>1100</b>	62,65	0,4701	194,15	0,5299
<b>1300</b>	61,99	0,4701	187,09	0,5299
<b>1500</b>	61,71	0,4874	179,71	0,5126
<b>1800</b>	64,26	0,5323	176,12	0,4677

<b>TAAMe<sub>2</sub>-ATC-PDIME<sub>2</sub></b>	<b>t<sub>1</sub> / ns</b>	<b>a<sub>1</sub></b>	<b>t<sub>2</sub> / ns</b>	<b>a<sub>2</sub></b>
<b>0</b>	74,24	1,0000		
<b>0,2</b>	73,27	1,0000		

0,4	73,70	1,0000		
0,6	74,18	1,0000		
0,8	74,39	1,0000		
1	76,65	1,0000		
1,3	78,28	1,0000		
1,6	80,64	1,0000		
1,9	81,64	1,0000		
2,2	83,09	1,0000		
2,5	85,36	1,0000		
3	88,07	1,0000		
3,5	88,83	1,0000		
4	87,97	0,9762	251,20	0,0238
4,5	92,28	1,0000		
5	94,11	1,0000		
5,5	94,89	1,0000		
6	92,26	0,9500	175,83	0,0500
6,5	93,31	0,9750	210,02	0,0250
7	92,01	0,9286	164,51	0,0714
7,5	90,86	0,9250	188,11	0,0750
8	91,94	0,9048	166,09	0,0952
8,5	90,65	0,8049	136,93	0,1951
9	92,27	0,9000	174,89	0,1000
9,5	92,44	0,8750	161,04	0,1250
10	92,26	0,8500	159,66	0,1500
11	93,50	0,8293	147,02	0,1707
12	104,35	1,0000		
13	84,39	0,5385	125,21	0,4615
14	91,80	0,8409	163,16	0,1591
15	90,57	0,7805	163,43	0,2195
16	92,95	0,8205	164,23	0,1795
17	84,71	0,6098	140,67	0,3902
18	95,82	0,8750	202,93	0,1250
19	91,91	0,8000	170,71	0,2000
20	91,88	0,7949	168,12	0,2051
22	89,05	0,7105	156,38	0,2895
24	85,14	0,6667	160,86	0,3333
26	90,60	0,7250	163,72	0,2750
28	90,89	0,7073	160,80	0,2927
30	90,36	0,6750	158,53	0,3250
35	88,10	0,6842	167,79	0,3158
40	86,39	0,6154	158,86	0,3846
45	81,44	0,5366	152,77	0,4634
50	82,28	0,5641	159,26	0,4359
55	85,20	0,5641	158,51	0,4359
60	85,33	0,6000	164,85	0,4000

<b>65</b>	80,55	0,5526	159,81	0,4474
<b>70</b>	84,30	0,6216	176,35	0,3784
<b>75</b>	77,20	0,4595	153,70	0,5405
<b>80</b>	88,85	0,6757	184,68	0,3243
<b>85</b>	72,76	0,4474	153,38	0,5526
<b>90</b>	77,86	0,5263	161,17	0,4737
<b>95</b>	77,57	0,5135	164,16	0,4865
<b>100</b>	73,96	0,4444	155,00	0,5556
<b>110</b>	83,63	0,5789	169,82	0,4211
<b>120</b>	79,95	0,5526	168,46	0,4474
<b>130</b>	82,96	0,5897	172,13	0,4103
<b>140</b>	80,94	0,5278	163,27	0,4722
<b>150</b>	78,93	0,5405	167,75	0,4595
<b>160</b>	73,79	0,4722	159,12	0,5278
<b>170</b>	76,56	0,5135	164,92	0,4865
<b>180</b>	85,73	0,6486	182,79	0,3514
<b>190</b>	68,67	0,3714	146,58	0,6286
<b>200</b>	65,28	0,3947	149,52	0,6053
<b>220</b>	77,09	0,5143	164,54	0,4857
<b>240</b>	74,11	0,5000	164,11	0,5000
<b>260</b>	78,30	0,5278	168,28	0,4722
<b>280</b>	71,88	0,4595	158,99	0,5405
<b>300</b>	78,78	0,5429	170,41	0,4571
<b>350</b>	80,99	0,5143	167,91	0,4857
<b>400</b>	72,63	0,4444	156,79	0,5556
<b>450</b>	71,55	0,4167	154,74	0,5833
<b>500</b>	80,78	0,5676	172,42	0,4324
<b>550</b>	77,61	0,4865	161,88	0,5135
<b>600</b>	78,23	0,5278	172,64	0,4722
<b>650</b>	73,82	0,5000	166,59	0,5000
<b>700</b>	68,95	0,4054	151,27	0,5946
<b>750</b>	77,34	0,4865	158,85	0,5135
<b>800</b>	67,30	0,4324	156,60	0,5676
<b>850</b>	69,56	0,4118	154,50	0,5882
<b>900</b>	63,02	0,3429	144,18	0,6571
<b>950</b>	77,86	0,5714	174,79	0,4286
<b>1000</b>	71,35	0,4412	159,02	0,5588
<b>1100</b>	67,55	0,3939	152,06	0,6061
<b>1200</b>	69,49	0,3824	147,78	0,6176
<b>1300</b>	82,54	0,5429	167,69	0,4571
<b>1400</b>	74,71	0,4857	162,98	0,5143
<b>1500</b>	72,64	0,4167	150,92	0,5833
<b>1600</b>	68,06	0,3077	142,22	0,6923
<b>1700</b>	72,38	0,4286	150,76	0,5714
<b>1800</b>	73,38	0,4048	147,16	0,5952

<b>TAAMe<sub>2</sub>-ATC(OMe)<sub>2</sub>- PDIME<sub>2</sub><sup>45</sup></b>	<b>t<sub>1</sub> / ns</b>	<b>a<sub>1</sub></b>	<b>t<sub>2</sub> / ns</b>	<b>a<sub>2</sub></b>
0	44,41	0,2273	124,69	0,7727
0,2	83,33	0,5806	151,25	0,4194
0,4	59,93	0,3125	132,57	0,6875
0,6	82,86	0,5333	146,97	0,4667
0,8	34,53	0,1692	120,26	0,8308
1	56,02	0,2500	128,00	0,7500
1,3	62,30	0,3333	132,74	0,6667
1,7	86,11	0,6825	162,12	0,3175
2	68,67	0,3768	134,16	0,6232
2,3	84,95	0,5357	145,72	0,4643
2,6	55,97	0,1864	124,20	0,8136
3	71,88	0,4107	137,78	0,5893
3,5	49,97	0,1930	123,61	0,8070
4	93,78	0,7818	184,18	0,2182
4,5	91,60	0,7656	176,05	0,2344
7	90,80	0,7538	170,99	0,2462
7,5	44,21	0,1786	119,45	0,8214
8	91,35	0,7778	176,00	0,2222
8,5	98,41	0,9074	241,63	0,0926
9	87,75	0,7091	156,59	0,2909
9,5	93,37	0,8636	191,54	0,1364
10	87,44	0,7813	175,88	0,2188
11	86,07	0,7222	155,81	0,2778
12	90,36	0,8438	186,22	0,1563
13	85,26	0,7778	159,91	0,2222
14	68,62	0,4444	126,13	0,5556
15	81,99	0,8095	178,77	0,1905
16	84,37	0,8594	192,66	0,1406
17	68,95	0,6452	140,31	0,3548
18	76,71	0,7581	156,08	0,2419
19	69,33	0,6970	148,68	0,3030
20	72,13	0,7377	156,26	0,2623
22	78,78	0,8571	201,70	0,1429
24	72,84	0,6667	138,61	0,3333
26	77,11	0,7759	170,68	0,2241
28	83,68	0,8197	187,43	0,1803
30	93,17	0,8596	193,01	0,1404
35	51,82	0,2000	130,04	0,8000
40	92,10	0,4364	156,41	0,5636
45	86,60	0,3455	162,21	0,6545

<sup>45</sup> The deconvolution fit was not working for all fields. Only the suitable fits are depicted.

---

<b>50</b>	106,14	0,4545	176,06	0,5455
<b>55</b>	76,18	0,2222	167,25	0,7778
<b>60</b>	74,86	0,1930	171,78	0,8070
<b>70</b>	94,12	0,3273	193,57	0,6727
<b>75</b>	58,36	0,1429	178,53	0,8571
<b>85</b>	58,81	0,1404	184,43	0,8596
<b>90</b>	83,03	0,2321	192,66	0,7679
<b>95</b>	105,13	0,3148	202,55	0,6852
<b>100</b>	49,78	0,1273	184,19	0,8727
<b>110</b>	72,74	0,1818	194,33	0,8182
<b>120</b>	63,63	0,1607	194,53	0,8393
<b>140</b>	78,73	0,2105	203,77	0,7895
<b>170</b>	79,04	0,1636	201,17	0,8364
<b>190</b>	77,20	0,1698	203,34	0,8302
<b>200</b>	57,06	0,1455	200,90	0,8545
<b>220</b>	72,24	0,1636	204,79	0,8364
<b>280</b>	69,34	0,1607	206,45	0,8393
<b>300</b>	75,54	0,1818	207,54	0,8182
<b>400</b>	82,02	0,2069	210,00	0,7931
<b>450</b>	66,60	0,1636	207,55	0,8364
<b>500</b>	71,34	0,1636	208,32	0,8364

---

## 13.1 Conference distributions and distributions to other publications

### Conference distributions

Presentation

KOPO **2022**, Bad Honnef, Germany.

### Other publications

*Electron-Rich 3,4-Ethylenedioxythiophene (EDOT) Linkers in Tetracationic bis-Triarylborane Chromophores: Influence on Water-Stability, Bio-macromolecule Sensing, and Photoinduced Cytotoxicity*

M. Ferger, C. Roger, E. Köster, F. Rauch, S. Lorenzen, I. Krummenacher, A. Friedrich, M. Kosczak, D. Nestic, H. Braunschweig, C. Lambert, I. Piantanida, T. B. Marder

*Chem. Eur. J.* **2022**, 28, e202201130.

*Metal-Based Diversity for Crystalline Metal-Fullerene Frameworks*

Andreas Kraft, Chantal Roger, David Schmidt, Johannes Stange, Klaus Müller-Buschbaum and Florian Beuerle\*

*Chem. Eur. J.* **2017**, 23, 15864–15868.



## 13.2 Danksagung

Mein besonderer Dank gilt Prof. Lambert und den gesamten ehemaligen und aktuellen Doktoranden.

Im besonderen möchte ich mich bedanken bei:

Michael Moos: Danke für die Hilfe bei sämtlichen organisatorischen Hürden und das Umbauen und in Stand halten vieler Technischer Geräte.

Marco Holzapfel: Für die Auswertung der fs-Daten und die Berechnung einiger Molekülparameter.

Alexander Schmiedel: Danke für die Aufnahme der fs-Spektren und das mehrfache Umbauen des ns-Setups sowie die Behebung einiger Fehler die im Laufe der Jahre am ns-Setup aufgetaucht sind.

Danke an meine Auszubildenden Lukas Schmitt und Paula Roth für die Durchführung einiger Synthesen.

Fabian Fella: Für die erfolgreiche Durchführung seiner Bachelorarbeit unter meiner Anleitung. Mein Dank gilt auch all meinen Praktikanten: Jonathan Herpich, Luisa Martin, Konstantinos Rimagmos und Tobias Groß.

Mein besonderer Dank gilt Prof. Dr. U. E. Steiner und Prof. Dr. N. Lukzen für die erfolgreiche Kooperation und die Erläuterung der theoretischen Hintergründe der Spinchemie.

Des Weiteren gilt mein Danke:

Dr. Matthias Grüne, Stephanie Schmitt, Patricia Altenberger und Dr. Juliane Adelman sowie dem gesamten Service-Team der Analytik.

Bernd Brunner, Markus Braun, Bálint Klink, Michael Ramold, Matthias Fromm und dem gesamten Technischen Betrieb.

Dr. Christian Stadler, Dr. Alfons Ledermann, Dr. Michaela Büchner, Anette Krug und Christiana Toussaint für die verwaltungstechnischen Aufgaben.